Vibration Analysis and Control
New Trends and Developments

Edited by Francisco Beltrán Carbajal

VIBRATION ANALYSIS AND CONTROL – NEW TRENDS AND DEVELOPMENTS

Edited by **Francisco Beltrán-Carbajal**

Vibration Analysis and Control - New Trends and Developments
http://dx.doi.org/10.5772/924
Edited by Francisco Beltran-Carbajal

Contributors

Jordi Cusidó I Roura, Miguel Delgado Prieto, Jose Luis Romeral Martínez, Hamid Reza Karimi, José Guilherme Santos Da Silva, Ana Cristina Castro Fontenla Sieira, Luciano Rodrigues Ornelas De Lima, Bruno Dias Rimola, Hisao Hiraba, Philip Bonello, Linsheng Huo, Hongnan Li, Ivan M Diaz, Alexander Schirrer, Martin Kozek, Jürgen Schöftner, Min-Sang Seong, Seung-Bok Choi, Kum-Gil Sung, Kazuhiko Hiramoto, Taichi Matsuoka, Katsuaki Sunakoda, Ragnar Eide, Nuno Maia, Antonio Vale Urgueira, Raquel Albuquerque Almeida, Francisco Beltran-Carbajal, Gerardo Silva-Navarro, Esteban Chavez-Conde, Benjamin Vazquez Gonzalez, Andrea Tonoli, Angelo Bonfitto, Mario Silvagni, Lester Daniel Suarez Cabrera, Enrico Zenerino, Antonio Favela-Contreras, R Sreekala

Notice

Statements and opinions expressed in the chapters are these of the individual contributors and not necessarily those of the editors or publisher. No responsibility is accepted for the accuracy of information contained in the published chapters. The publisher assumes no responsibility for any damage or injury to persons or property arising out of the use of any materials, instructions, methods or ideas contained in the book.

We are IntechOpen,
the world's leading publisher of
Open Access books
Built by scientists, for scientists

4,000+
Open access books available

116,000+
International authors and editors

120M+
Downloads

151
Countries delivered to

Our authors are among the

Top 1%
most cited scientists

12.2%
Contributors from top 500 universities

CLARIVATE ANALYTICS
BOOK CITATION INDEX
INDEXED

WEB OF SCIENCE™

Selection of our books indexed in the Book Citation Index
in Web of Science™ Core Collection (BKCI)

Interested in publishing with us?
Contact book.department@intechopen.com

Numbers displayed above are based on latest data collected.
For more information visit www.intechopen.com

Meet the editor

Francisco Beltrán Carbajal obtained his electromechanical engineer's degree in 1993 from the Instituto Tecnológico de Zacatepec (México) and his PhD. degree in electrical engineering (Mechatronics) in 2004 from the Centro de Investigación y Estudios Avanzados del Instituto Politécnico Nacional (CINVESTAV-IPN) in Mexico City (Mexico). He is currently a titular professor in the Energy Department in the Universidad Autónoma Metropolitana (UAM), Unidad Azcapotzalco in Mexico City, and founder and president of the Technological Innovation Generator for Social and Business Development S.A. de C.V. (Mexico). From 2004 to 2009 he was with the Instituto Tecnológico y de Estudios Superiores de Monterrey, Campus Guadalajara, where he served as professor, Head of the Department of Electronics and Mechatronics, Director of the Mechatronics Program, Associated National Coordinator of the Electronic Academy of the Tecnológico de Monterrey and Leader of the Research Chair in Embedded Systems for Robust Automation of Electronic and Mechatronic Products. Dr. Beltrán has worked in the automotive industry as an electromechanical engineer and as professor in several prestigious universities such as Instituto Politécnico Nacional, Instituto Tecnológico de Zacatepec, Universidad Politécnica de la Zona Metropolitana de Guadalajara. He has published more than 30 technical publications in journals, book chapters and conferences.

Contents

Preface

This book focuses on the very important and diverse field of vibration analysis and control. The sixteen chapters of the book written by selected experts from international scientific community cover a wide range of interesting research topics related to original and innovative design methodologies of passive, semi-active and active vibration control schemes, dynamic vibration absorbers, vehicle suspension systems, structural vibration, identification, vibration control devices, smart materials, fault detection, finite element analysis and several other recent practical applications and theoretical studies of this fascinating field of vibration analysis and control. The book is addressed not only to both academic and industrial researchers and practitioners of this field, but also to undergraduate and postgraduate engineering students and other experts and newcomers in a variety of disciplines seeking to know more about the state of the art, challenging open problems, innovative solution proposals and new trends and developments in this area.

The book is organized into 16 chapters. A brief description of every chapter follows. Chapter 1 presents the basic design principles of adaptive tuned vibration absorbers (ATVA) and a comprehensive review of the various design concepts that have been presented for the ATVA, including the latest innovations contributed by the author. Chapter 2 introduces a design approach for active vibration absorption schemes in linear mass-spring-damper mechanical systems subject to exogenous harmonic vibrations, which can simultaneously be used for vibration attenuation and desired reference trajectory tracking tasks. Chapter 3 deals with the seismic response control of eccentric structures using Circular Tuned Liquid Column Dampers (CTLCD). The optimal control parameters are derived from the motion equation of the CTLCD-structure system and supposing that ground motion is a stochastic process. Chapter 4 presents the practical implementation of an active mass damper to cancel excessive vertical vibrations on an in-service office floor and on an in-service footbridge. In Chapter 5, the authors describe the formulation and experimental evaluation of various vibration control strategies for semi-active vehicle suspension system with magnetorheological (MR) dampers. The design of a back-stepping control scheme for semi-active vehicle suspension systems with MR dampers is the focus of Chapter 6. Chapter 7 proposes a robust control scheme based on the real-time estimation of perturbation signals for active nonlinear or linear vehicle suspension systems subject to unknown exogenous disturbances due to irregular road surfaces. Chapter 8

introduces a methodology for semi-active control system design of civil structures. A semi-active control law based on a one-step-ahead prediction of the seismic response is proposed, which employs a vibration control device developed by the authors. Chapter 9 deals with the seismic response control using smart materials. Mathematical models are developed to predict the maximum energy dissipation capability of the material under study. Chapter 10 presents a general overview on the transmissibility concept for multiple degree-of-freedom systems. It is shown that the various ways in which transmissibility can be defined and applied opens various possibilities for research in different domains, like system identification, structural modification, coupling analysis, damage detection, model updating, vibro-acoustic applications, isolation and vibration attenuation. The focus of Chapter 11 is on design of control schemes for vibration mitigation on wind turbine systems. The main control objective of the proposed schemes is to reduce the torque variations by using speed control with collective blade pitch adjustments. Chapter 12 focuses on the evaluation of an active isolation and vibration damping device on the working cell of a micro-mechanical laser center, using active electromagnetic actuators. Chapter 13 presents an overview of multisensory inference approaches used to characterize motor ball bearings, and their application to a set of motors with distributed fault failure. The results show that a multivariable design contributes positively to damage monitoring of bearings. Chapter 14 investigates the dynamic behavior of an oil production platform submitted to impacts produced by rotating machinery. A computational model is developed for the structural system dynamic analysis. The peak acceleration values and maximum displacements and velocities are employed to evaluate the structural model performance in terms of human comfort, maximum tolerances of the mechanical equipment and vibration serviceability limit states of the structural system. Chapter 15 proposes LQG and weighted H2 MIMO control design methods for the vibration control of lightweight rail car body structures. These designs are studied and compared to achieve vibration reduction and passenger ride comfort improvement in a highly flexible metro rail car body. The metro car body structure is directly actuated via locally mounted Piezo stack actuators. Chapter 16 concludes the book, describing a study on vibrotactile stimuli on the submandibular glands stimulated by vibration with one motor and two motors.

Finally, I would like to express my sincere gratitude to all the authors for their excellent contributions, which I am sure will be valuable to the readers. I would also like to thank the editorial staff at InTech for their great effort and support in the process of edition and publication of the book.

I truly hope that this book can be useful and inspiring for contributing to the development of technology, new academic and industrial research and many inventions and innovations in the field of vibration analysis and control.

Francisco Beltrán Carbajal
Energy Department
Azcapotzalco Unit of the Autonomous Metropolitan University
Mexico

Adaptive Tuned Vibration Absorbers: Design Principles, Concepts and Physical Implementation

Philip Bonello
University of Manchester
United Kingdom

1. Introduction

The tuned vibration absorber (TVA) has been used for vibration control purposes in many sectors of civil/automotive/aerospace engineering for many decades since its inception by (Ormondroyd & Den Hartog, 1928). A tuned vibration absorber (TVA), in its most generic form, is an auxiliary system whose parameters can be tuned to suppress the vibration of a host structure. The auxiliary system is commonly a spring-mass-damper system (or equivalent) and the TVA suppresses the vibration at its point of attachment to the host structure through the application of an interface force. The tuned frequency ω_a of the TVA is defined as its undamped natural frequency with its base (point of attachment) blocked. The TVA can be used in two distinct ways, resulting in different optimal tuning criteria and design requirements (von Flotow et al., 1994):

a. It can be tuned to suppress (*dampen*) the modal contribution from a specific troublesome natural frequency Ω_s of the host structure over a wide band of excitation frequencies.

b. It can be tuned to suppress (*neutralise*) the vibration at a specific troublesome excitation frequency ω, in which case it acts like a notch filter.

When used for application (a), the TVA referred to as a "tuned mass damper" (TMD). ω_a is optimally tuned to a value slightly lower than that of the targeted mode Ω_s and an optimal level of damping needs to be designed into the absorber. When used for application (b), the TVA is referred to as a "tuned vibration neutraliser" (TVN) (Brennan, 1997, Kidner & Brennan, 1999) or "undamped TVA". The optimal tuning condition is in this case is $\omega_a = \omega$ and the TVN suppresses the vibration over a very narrow bandwidth centred at the tuned frequency. Total suppression of the vibration at this frequency is achieved when there is no damping in the TVN.

Deviation from the tuned condition (mistuning) degrades the performance of either variant of the TVA (von Flotow et al., 1994) and it can be shown that a mistuned vibration neutraliser could actually increase the vibration of its host structure (Brennan, 1997). To avoid mistuning, smart or adaptive tunable vibration absorbers (ATVAs) have been developed. Such devices are capable of retuning themselves in real time. Adaptive technology is especially important in the case of the TVN since the low damping requirement in the spring element can raise the host structure vibration to dangerous levels

in the mistuned condition. In this case, mistuning can occur either due to a drift in the forcing frequency or due to a drift in tuned frequency caused by environmental factors (e.g. temperature change). Hence, a TVN needs to be adaptive to be practically useful.

At the heart of an ATVA is a means for adjusting the tuned frequency ω_a in real time. This is frequently done through the variation of the effective mechanical stiffness of the ATVA, although other means are possible. Whatever the retuning method used, the device should be tunable over an adequate range of frequencies, and the adjustment should be rapid and with minimum power requirement. The device must also be cheap and easy to manufacture. To maximise vibration attenuation, the retuning mechanism should add as little as possible to the redundant mass of the device and, in the case of the neutraliser, have a low structural damping (Brennan, 1997). The technical challenge is to design an adaptive device with such attributes.

This chapter continues with a quantitative illustration of the basic design principles of both variants of the TVA. It will then present a comprehensive review of the various design concepts that have been presented for the ATVA, including the latest innovations contributed by the author. This section will cover the use of piezoelectric actuators, shape-memory alloys and servo-actuators within the smart structure of the ATVA. Control algorithms and their implementation through MATLAB® with SIMULINK® will also be discussed.

2. Basic design principles of TVA

With reference to Fig. 1a, the above-defined frequency ω_a coincides exactly with the lowest anti-resonance frequency of the attachment point receptance frequency response function (FRF) of the undamped "free-body" TVA structure, $r_{AA}(\omega) = Y_A/F$, where Y_A and F are complex amplitudes of y_A and the interface force $f(t)$, for harmonic vibration at circular frequency ω. It is for this reason that, for the TVN, the condition $\omega_a = \omega$ defines optimal tuning. For excitation frequencies ω below the first non-zero resonance frequency ω_m of $r_{AA}(\omega)$, the absorber can be represented by the equivalent two-degree-of-freedom model shown in Fig. 1b (Bonello & Groves, 2009). Fig. 1b shows that the absorber mass m_a is split into an effective mass $m_{a,eff} = Rm_a$ and a redundant mass $m_{a,red} = (1-R)m_a$. The latter mass simply adds to the host structure. The effective part of the absorber is the single-degree-of-freedom system constituted by mass $m_{a,eff}$, the spring of stiffness $k_a = \omega_a^2 m_{a,eff}$ and a damping element. In the case of a TMD, where damping is deliberately designed into the device, it is preferable to represent it by viscous damper of frequency-independent coefficient c_a. In the case of a TVN, where the damping is an unwanted inherent feature of the spring element, it is best represented by a structural damping mechanism of loss factor η_a, for which the equivalent viscous damping coefficient is $k_a\eta_a/\omega$. The method for deriving the equivalent two-degree-freedom is detailed in Section 4.1.

2.1 Tuned mass damper

The purpose of the TMD is to dampen a particular resonance peak of the FRF $r_{AP}(\omega)$ connecting the response at A to an external force $f_p(t)$ applied to the host structure at some arbitrary point P. It is useful for applications where the excitation has a broad frequency spectrum containing the targeted mode. The damping in the original host structure (i.e. the

structure prior to the addition of the TMD) is commonly assumed to be negligible relative to that introduced by the TMD. Suppose the TMD is targeted at the sth mode of the original host structure. Let Ω_s be the frequency of this mode and $\psi_A^{(s)}$ denote the value of the corresponding mass-normalised mode-shape at the degree of freedom being targeted (e.g. the vertical displacement at A in Fig. 1). Then, from standard modal theory (Ewins, 1984), the contribution of the targeted mode to the dynamics of the original host structure at the targeted degree of freedom can be represented as the simple mass-spring system of mass $M_A^{(s)} = 1 / \left\{ \psi_A^{(s)} \right\}^2$ and stiffness $K_A^{(s)} = \Omega_s^2 M_A^{(s)}$ (see Fig. 2(a)). The dynamics of the original host structure at the targeted degree of freedom can be accurately modelled in this form for excitation frequencies ω in the vicinity of Ω_s, where the targeted mode is dominant. Addition of the TMD in Fig. 1b to the system in Fig. 2(a) results in the system in Fig. 2(b). Notice that original host structure modal mass $M_A^{(s)}$ needs to be readjusted to $M_A^{(s)} + m_{a,red}$, to account for the addition of the redundant absorber mass to the host structure. The harmonic analysis of the systems in Figs. 2(a,b) (i.e. analysis with $f_P = \mathrm{Re}\left\{ F_P e^{j\omega t} \right\}$) then gives a modal approximation of $r_{AP}(\omega)$, denoted by $r_{AP}^{(s)}(\omega)$, which is accurate for frequencies ω in the vicinity of Ω_s.

(a) Actual arbitrary TVA   (b) Equivalent two-degree-of-freedom model of TVA

Fig. 1. Generic TVA

(a) Host structure   (b) Host structure with TMD
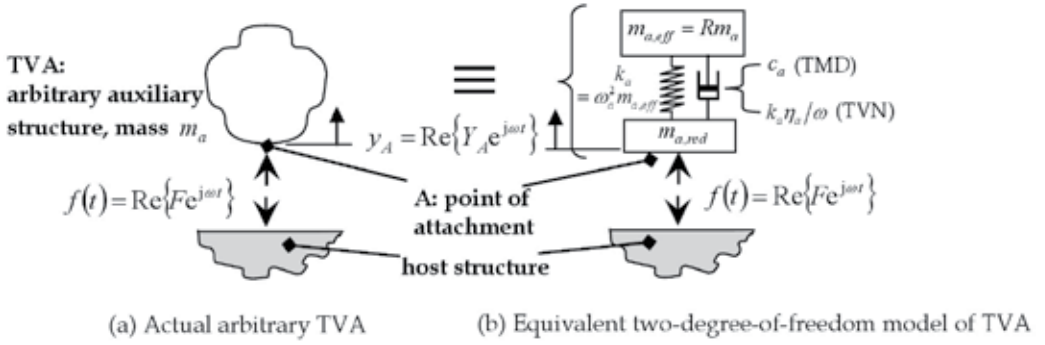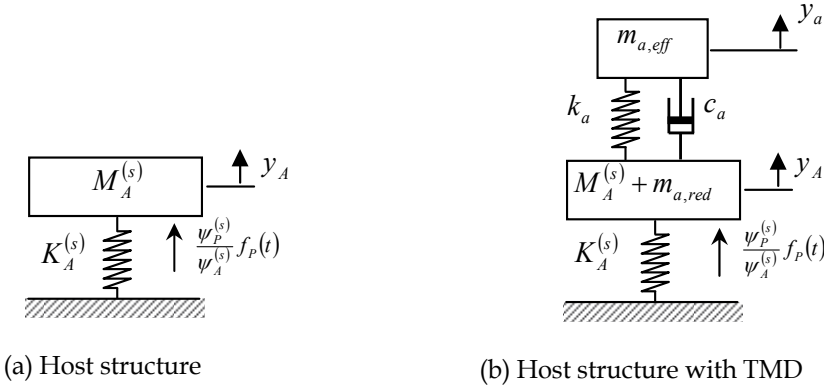
Fig. 2. Dynamic modal model of the host structure without/with TMD for frequencies ω in the vicinity of Ω_s

$r_{AP}^{(s)}(\omega)$ can be dampened by adapting the harmonic analysis in (Den Hartog, 1956) to the system in Fig. 2(b). The optimal tuning condition is found to be:

$$\frac{\omega_{a_{opt}}}{\Omega_s'} = \frac{1}{1+\mu} \tag{1}$$

where

$$\Omega_s' = \Omega_s \sqrt{M_A^{(s)} \Big/ \left\{ M_A^{(s)} + m_{a,red} \right\}} \ , \ \ \mu = m_{a,eff} \Big/ \left\{ M_A^{(s)} + m_{a,red} \right\} \tag{2}$$

The viscous damping coefficient is given by:

$$c_a = 2\zeta_a m_{a,eff} \omega_a \tag{3}$$

The optimal value of the viscous damping ratio ζ_a is given by (Den Hartog, 1956):

$$\zeta_{a_{opt}} = \sqrt{\frac{3\mu}{8(1+\mu)^3}} \tag{4}$$

The optimisation of the modulus of $r_{AP}^{(s)}(\omega)$ is illustrated in Fig. 3. The introduction of the TMD splits the original host structure resonance peak into two peaks separated by an anti-resonance. Points M and N are referred to as the 'fixed points' since, for given μ and ω_a, the function $\left| r_{AP}^{(s)}(\omega) \right|$ of the modified structure passes through them regardless of the value of ζ_a. The optimal tuning condition of eq. (1) ensures that the fixed points are level with each other (this is the case illustrated in Fig. 3). With this condition in place, the optimal damping condition of eq. (4) ensures that the peaks of $\left| r_{AP}^{(s)}(\omega) \right|$ coincide as closely as possible with the fixed points. The height of these optimised peaks is approximately inversely proportional to $\sqrt{\mu}$.

As an illustration of the effect of a TMD on a multimodal (i.e. continuous) system, consider a TMD attached to the tip of a cantilever and tuned to attenuate its second flexural mode (Fig. 4). The cantilever OA is of length 1m and made of steel (Young Modulus 200 GN/m², density 7850 kg/m²) of circular section with diameter 3cm.

Assuming an Euler-Bernoulli beam model, an eigenvalue analysis yields $\Omega_2 / (2\pi) = 132.8$ Hz, $M_A^{(2)} = 1.387$ kg. The mass ratio μ is taken as 2%. For simplicity, the TMD is assumed to have no redundant mass. The TMD parameters were computed according to the above formulae. The receptances $r_{AP}(\omega) = Y_A / F_P$ of the system with and without the TMD were evaluated using the Dynamic Stiffness Method (Bonello & Brennan, 2001) and shown in Fig. 5, where the dampening of the targeted resonance is clearly evident.

Fig. 6 illustrates the effect of mistuning i.e. deviation from the tuned condition of eq. (1). The stiffness k_a of the TMD was varied such that it was mistuned by 10% i.e. ω_a was set to $1.1\omega_{a_{opt}}$, with c_a kept the same as the optimal case of Fig. 5 (considering eqs. (3) and (4), this means that ζ_a of the mistuned case in Fig. 6 is not $\zeta_{a_{opt}}$). It is clear from Fig. 6 that a slight mistuning produces significant deterioration of the TMD performance.

$$\left|r_{AP}^{(s)}(\omega)\right|$$

$$\left(\times \left|\frac{\psi_A^{(s)}}{\psi_P^{(s)}}\right| K_A^{(s)}\right)$$
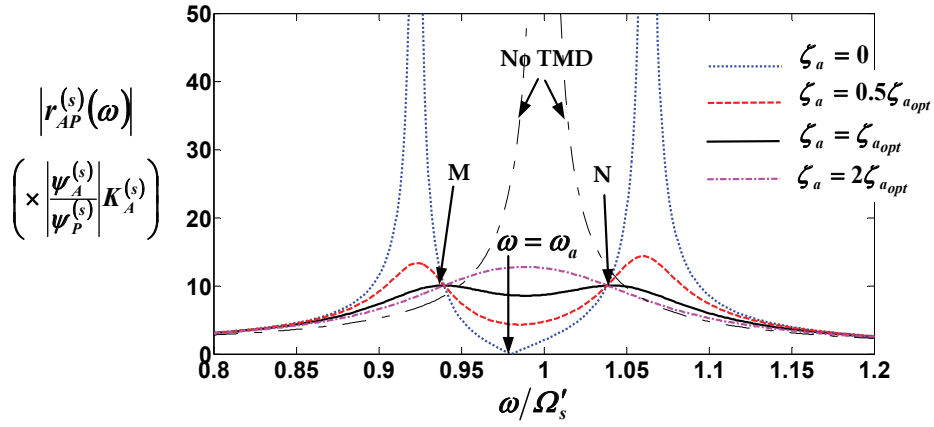
Fig. 3. Effect of damping on the modal approximation of the attachment point FRF (case shown is for the tuned condition, eq. (1), with $\mu = 0.02$
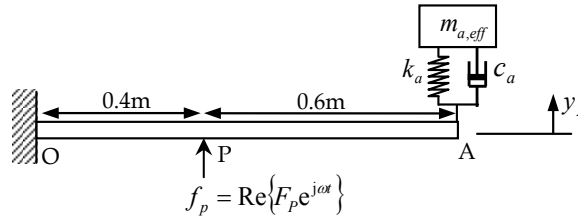
Fig. 4. TMD attached to a cantilever

$$\left|r_{AP}(\omega)\right|$$
$$(\text{m/N})$$
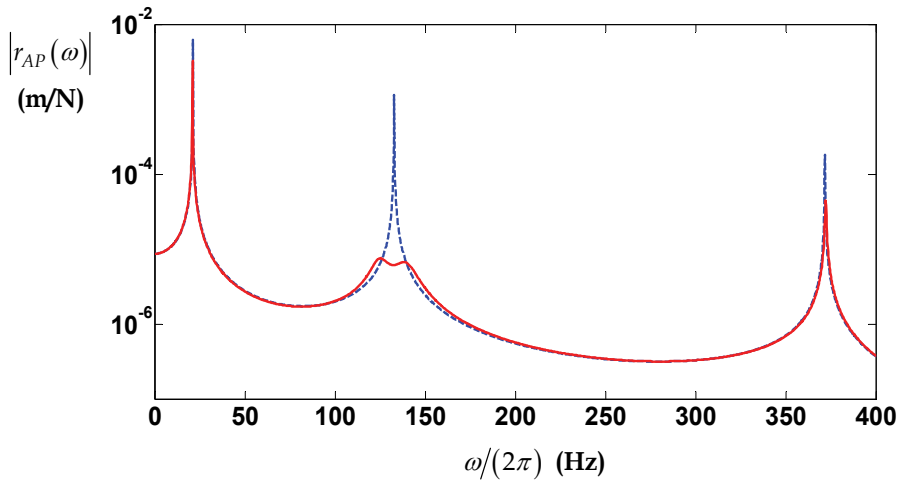
Fig. 5. Effect of TMD targeted against the second flexural mode of cantilever in Figure 4: original system (dashed line); with TMD (solid line)
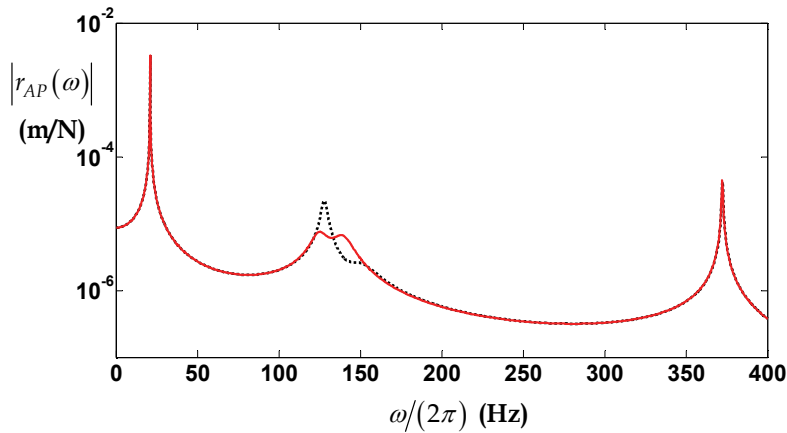
Fig. 6. Effect of a mistuned TMD on cantilever in Figure 4: TMD optimally tuned and damped as per eqs. (1) and (4) (solid line); 10% mistuned TMD (dotted line)

Finally, it is worth mentioning that a similar effect to the TMD can be achieved through an electrical analogue, wherein the auxiliary system is a piezoelectric shunt circuit (Park, 2002). In such an 'electrical' TVA, a piezoelectric patch is bonded to the host structure and connected across an external inductor-resistor circuit. The piezoelectric patch is used to convert the vibration energy of the host structure into electrical energy and introduces a capacitor effect into the circuit, turning it into an L-C-R circuit. The electrical energy is then dissipated most efficiently as heat through the resistor when the electrical resonance produced by the LC components is close to the frequency of the targeted mode and the resistor has an optimum value. One major disadvantage of the electrical TVA is the difficulty in deriving the transfer function of the modified system (on which the optimisation is based); the difficulty increases with the complexity of the host structure. For this reason the electrical TVA has typically been restricted to simple host structures like cantilevers (e.g. Park, 2002). In contrast, the classical theory of the mechanical TMD is readily applicable to any arbitrary host structure since the only host structure data it requires are the frequency and modal mass of the targeted mode.

2.2 Tuned vibration neutraliser
The purpose of the TVN is to plant an anti-resonance in the FRF $r_{AP}(\omega)$ at some particular chosen value of the excitation frequency ω. Hence, the TVN is typically used for applications where the excitation is entirely, or mainly, at a single frequency (i.e. harmonic). For example, suppose that it is required to cancel the tip vibration of the above considered cantilever (Fig. 4) at a frequency of 50 Hz. The optimal condition for a TVN is

$$\omega_a = \omega \tag{5}$$

Hence, in this example, ω_a is optimally set to 100π. Neglecting the redundant TVA mass and assuming an effective mass of the absorber, the absorber stiffness is calculated accordingly. The effect of the TVN is illustrated in Fig. 7, where the absorber mass is assumed to be 2% of the total mass of the beam. It is seen that an anti-resonance is introduced at the desired frequency, in addition to a resonance at a slightly higher

frequency (52 Hz) (the difference between the anti-resonance and resonance frequencies is found to increase with the effective TVN mass).

(Brennan, 1997) defines the attenuation D provided by a TVN for harmonic excitation as the ratio of the vibration amplitude at A without the TVN to the amplitude there with the TVN attached and optimally tuned:

$$D = \frac{|Y_A|_{\text{free}}}{|Y_A|_{\text{TVN, opt}}} \tag{6}$$

In the absence of damping in the absorber $D \rightarrow \infty$ (complete attenuation). The attenuation degrades with increasing absorber damping η_a (since this reduces the depth of the anti-resonance in Fig. 7). Also, for given absorber damping, the TVA's attenuating capability degrades as $m_{a,eff}$ is reduced. In fact, for a host structure that is a rigid machine of mass M mounted on soft isolators, (Brennan , 1997) showed that

$$D \approx \mu/\eta_a \tag{7}$$

where

$$\mu = m_{a,eff}/(M + m_{a,red}) \tag{8}$$

Deviation from the optimally tuned condition $\omega_a = \omega$ (mistuning) can occur due to a change in the excitation frequency (e.g. a change in operating speed of rotating machinery). It is evident from Fig. 7 that even a slight mistuning will drastically degrade the performance of the TVN. In fact, as can be seen in Fig. 7, if the excitation frequency drifts above ω_a then the vibration neutraliser actually increases the vibration of its host structure due to the extra resonance it introduced into the system. This extra resonance is itself made more pronounced by the low damping requirement.
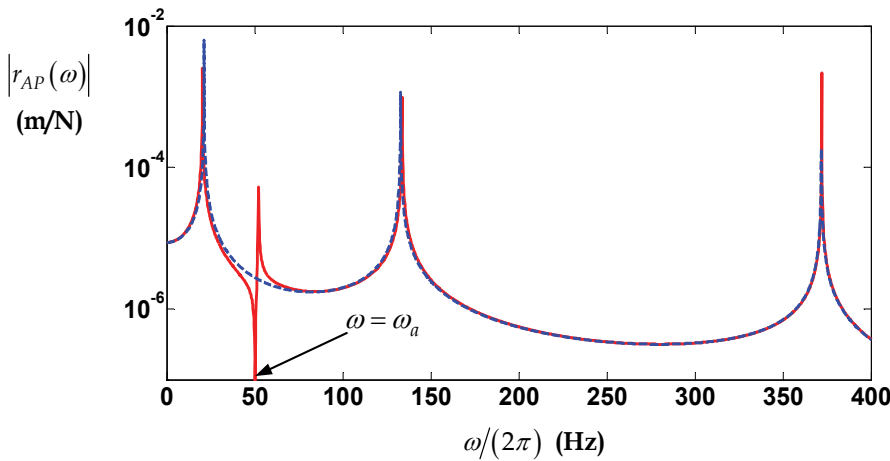
Fig. 7. Effect of TVN tuned to an excitation frequency of 50Hz on the cantilever in Fig. 4: original system (dashed line); with TVN (solid line)

3. Adaptive tuned vibration absorbers – an overview

"Tuning" a TVA involves making the appropriate adjustment of ω_a and this is done through an adjustment in one or more properties of the TVA structure. Mistuning is avoided through the use of adaptive (or "smart") tuneable vibration absorbers (ATVAs) which can automatically perform the necessary adjustment in real time (von Flotow et al., 1994, Brennan et al., 2004a). As demonstrated in the previous section, mistuning is a far more serious issue for the TVN, since the requirement for low absorber damping can raise the host structure vibration to dangerous levels in the mistuned condition. It is for this reason that adaptive technology has been mainly developed in the context of the TVN. *The ATVAs considered in the remainder of the chapter will therefore exclusively be vibration neutralisers*.

In the context of the TVN, adaptive tuning of the device involves maintaining the condition $\omega_a = \omega$ in the presence of variable conditions (typically a time-varying excitation frequency ω, in which case the antiresonance in Fig. 7 is shifted in real time along the frequency axis, in accordance to the current value of the excitation frequency). The challenge for ATVA designers is to produce a device with the following attributes:

i.   low structural damping;
ii.   any actuating mechanism to retune the device should add as little as possible to the redundant mass;
iii.   the device should be tuneable over a wide range of frequencies;
iv.   retuning should be rapid and with minimum power requirement;
v.   the device should be cheap and easy to design and manufacture.

Various design concepts for ATVAs have been proposed (von Flotow et al., 1994, Brennan et al., 2004a). One early variable stiffness element used in a vibration absorber was described in (Longbottom et al., 1990). A mass was sandwiched between a pair of pneumatic rubber bellows (Fig. 8) and the stiffness was adjusted by changing the air pressure inside the bellows. Further work on this device by (Long et al., 1998) resulted in a means of automatically adjusting the stiffness. However, the high amount of damping introduced by the rubber bellows was a major disadvantage.
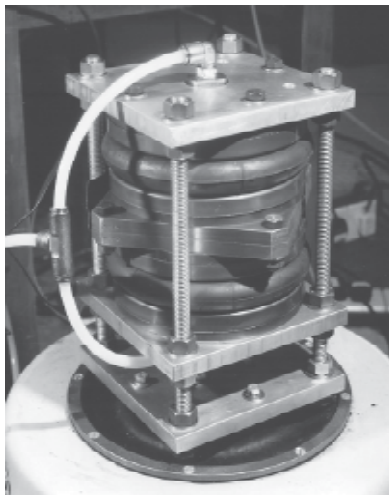
Fig. 8. Pneumatic rubber bellows ATVA (Brennan et al., 2004b)

One recent strategy for adaptation, by (Rustighi et al., 2005), was to utilise the variation with temperature of the Young Modulus of a beam-like ATVA made of a shape memory alloy (SMA) conductor (Fig. 9). The SMA wire formed a double cantilever, projecting from either side of the central attachment point to the host structure. The ATVA stiffness was controlled by adjusting the current through the wire. Despite being strong in attributes (i), (ii) and (v) above, this device could only achieve a maximum variation of around 20% in tuned frequency, taking as long as 2 minutes with a 9A current to do so (Brennan et al., 2004a, Rustighi et al., 2005).
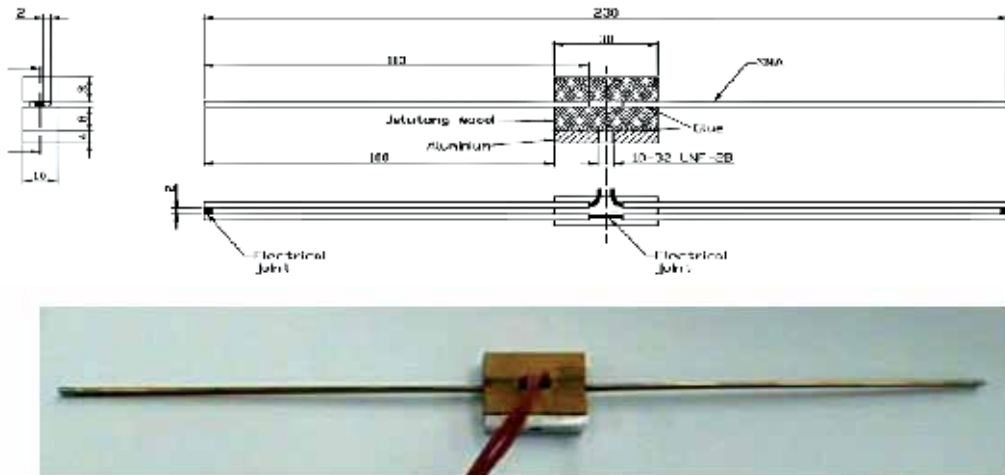
Fig. 9. Shape memory alloy ATVA (Rustighi et al., 2005)

Another recent approach, by (Bonello et al., 2005) was to utilise a mass-spring ATVA in which the stiffness element was composed of parallel curved beams in longitudinal compression (Fig. 10). The longitudinal stiffness was controlled by adjusting the curvature through piezo-ceramic actuators bonded to the beams. This device was capable of very rapid tuning over a frequency range 36-56 Hz (56% variation). However, this design concept was inherently limited to low frequency applications as a result of inertia effects in the curved beams (Bonello et al., 2005).

Other works have focused on the use of a beam-like ATVA controlled through servo-actuation. This concept remains the best approach for applications requiring a wide tuning frequency range (Carneal et al., 2004). Figs. 11-15 show various such ATVA designs. The "moveable-supports" ATVA in Fig. 11 was patented by (Hong & Ryu, 1985). It consisted of a beam with a mass attached to its centre and supports that could be moved relative to each other, thereby altering ω_a .

(Brennan, 2000) performed a theoretical study of the tuning frequency characteristics of the designs in Figs. 12, 13. In Fig. 12, the ATVA beam is composed of two beams and the effective stiffness of the ATVA is adjusted by pushing apart the two constituent beams at the centre, thereby altering the ATVA beam cross-section. Such a device was built and tested in (Kidner et al., 2002), where a maximum adjustment of 35% in tuned frequency was achieved. This concept appears to provide the most rapid tuning of all beam-like designs in Figs. 11-15 since the actuator is required to move the least distance to achieve a given change

in ω_a. However, the actuator has to work against much larger forces and the variability in ω_a is clearly limited by the maximum deformation that the constituent beams can withstand as they are being prised apart. Through elementary analysis, (Brennan, 2000) predicted that a considerably greater tuning range is achievable through the two alternative designs in Fig. 13 ("moveable beam" or "moveable masses"). In the "moveable beam" approach the masses are fixed relative to the beam and the beam lengthens or shortens. This device does not appear to have been built and would require some form of telescoping beam. The "moveable-masses" concept is more feasible: the beam is of fixed length and tuning is achieved by repositioning the attached masses. (Von Flotow et al., 1994) describes devices that appear to match this latter description in operation on the Boeing Chinook helicopter, although the details available are very sketchy.

Fig. 10. ATVA with variable-curvature piezo-actuated beams (Bonello et al., 2005)
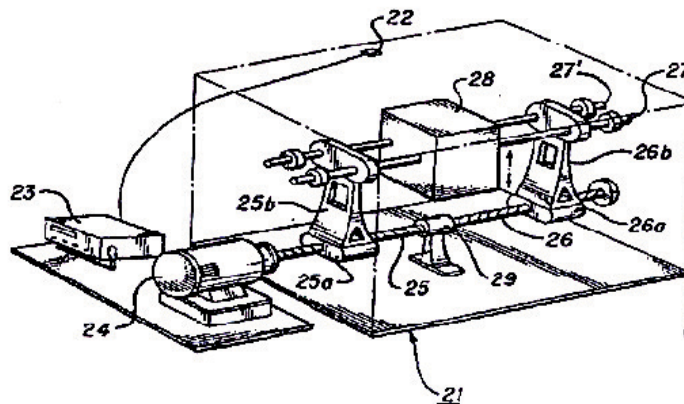
Fig. 11. Servo-actuated beam ATVA: moveable-supports, conventional design (Hong & Ryu, 1985)

In all devices of Figs. 11-13, the actuator is a permanently redundant mass that degrades the attenuating capacity of the ATVA (eq. (7, 8)). This limitation was overcome by (Carneal et al., 2004) who improved the "moveable-supports" concept of (Hong & Ryu, 1985) by incorporating the actuator into the central mass supported by the beam (Fig. 14). This necessitated the use of a "V-Type" undercarriage. The design of this undercarriage (and the one used in Fig. 11) clearly warrants careful consideration. It should be sufficiently rigid so as to avoid introducing unwanted dynamics that would interfere with ATVA operation. Moreover, it needs to be as light as possible to minimise the redundant mass. A far simpler approach would be to utilise a moveable-masses ATVA with actuators incorporated into the masses, as illustrated in Fig. 15, where the device simply attaches directly to the host structure at its centre. Such a novel device was proposed by (Bonello & Groves, 2009). Apart from the constructional simplicity, this concept was shown to provide superior ATVA performance.

Another important contribution of (Bonello & Groves, 2009) was the derivation of the effective mass and tuned frequency characteristics of the moveable-supports and moveable-masses ATVA. This enables the designer to quantify their expected performance for any given application. The derivation of the effective mass of the beam-like ATVAs in Figs. 11-15 requires the derivation of their equivalent two-degree-of-freedom model (Fig. 1b). Such analysis is very important when one considers that, for the devices in Fig. 11-15 (with the possible exception of Fig. 12), the effective mass proportion R will vary as the ATVA is retuned. Although (Carneal et al., 2004) describe their actuator-incorporated mass (Fig. 14) as the "active mass" of the absorber, its degree of activity is actually dependent on the setting of the ATVA. The same can be said of the moveable-masses concept (Fig. 15). With the supports or masses fully retracted in Figs. 14 and 15, the attached masses clearly become entirely redundant and the effective mass proportion R in Fig. 1b is then entirely contributed by the beam itself. This means that, as the ATVA retunes itself, the attenuation it provides will vary due to the consequent variation in μ (eqs. (7, 8)). Hence, the knowledge of an "effective mass characteristic" of a moveable-supports or moveable-masses ATVA is important since it would allow the designer to quantify the expected attenuation provided by an ATVA over a range of frequencies for any given application.

4. ATVA analysis

The aims of this section are two-fold: (i) to illustrate the derivation of the effective mass and tuned frequency characteristics of moveable-supports and moveable-masses ATVAs (Figs. 14 and 15); (ii) to illustrate the physical implementation and testing of the beam-like ATVA with actuator-incorporated moveable masses (Fig. 15). This latter covers the adaptation logic control. The material in this section is based on the work in (Bonello & Groves, 2009), from which further details can be obtained.

4.1 Effective mass and tuned frequency characteristics

Fig. 16 shows the two alternative types of ATVA considered. It shall be assumed that the beam supports of the device in Fig. 16b are simple supports. Let A denote the point/points of attachment of the beam to the host structure and B denote the point/points of attachment of the mass/masses. The aim of the following analysis is the determination of the fractional change in tuned frequency ω_a and the variation of the effective mass proportion R (Fig. 1b) as the setting $\tilde{x} = x/L$ of the actual systems in Fig. 16 is varied. Hence, for this purpose, damping can be omitted from the analysis without loss of accuracy.
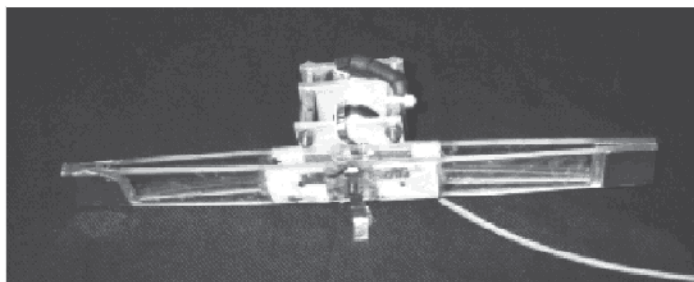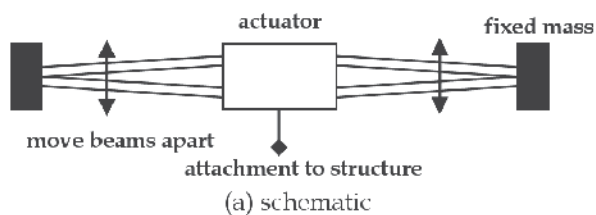
Fig. 12. Servo-actuated beam-like ATVA: adjustable beam-cross-section ATVA (Brennan, 2000, Kidner et al., 2002)
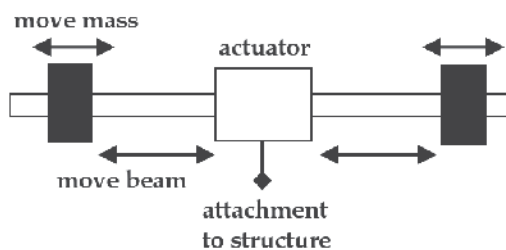
Fig. 13. Servo-actuated beam-like ATVA: moveable-beam or moveable-masses ATVA (Brennan, 2000)
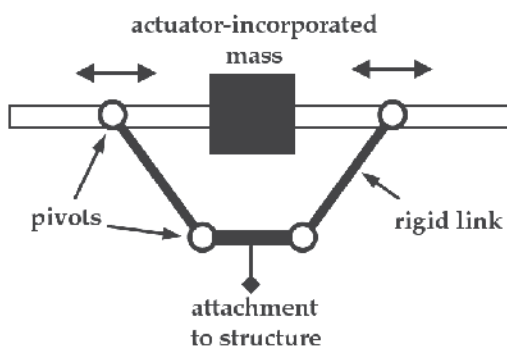
Fig. 14. Servo-actuated beam-like ATVA: moveable supports, "V-Type" design ATVA (Carneal et al., 2004)
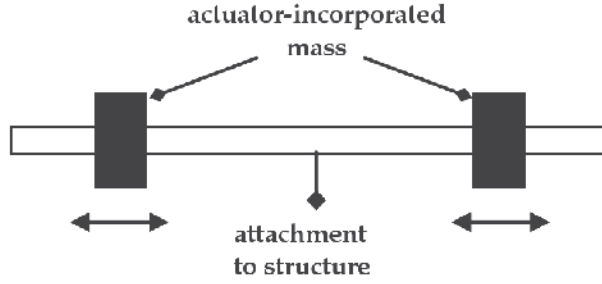
Fig. 15. Servo-actuated beam-like ATVA: actuator-incorporated moveable masses ATVA (Bonello & Groves, 2009)
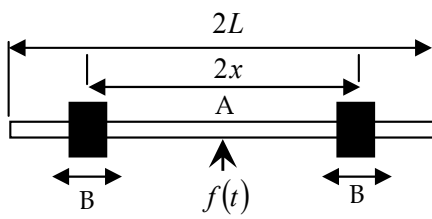
(a) Moveable masses
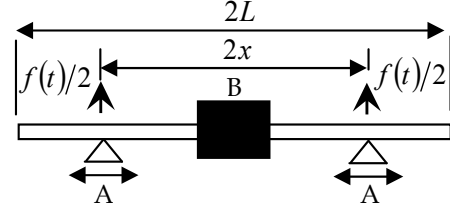
(b) Moveable supports ('V'-type)

Fig. 16. Free-body schematics of two alternative designs for an actuator-incorporated mass ATVA

In either case the system will be regarded as comprising a beam acted upon by: (i) the reaction forces from the lumped mass attachments at B; (ii) the reaction force from the host. If the latter force is $f(t) = \text{Re}\{F e^{j\omega t}\}$, then the response at any point Q on the beam is $y_Q(t) = \text{Re}\{Y_Q e^{j\omega t}\}$. Following the analysis in (Bonello & Groves, 2009), the expression for the receptance of the TVA at its point of attachment to the structure is:

$$r_{AA}(\omega) = \frac{Y_A}{F} = \frac{\left[1 - \tilde{\omega}^2\right]}{m_b \omega_1^2}$$

$$\left\{ \frac{\left[-\dfrac{1}{\tilde{\omega}^2} + \tilde{\beta}_{AA}(\tilde{\omega})\right]\left[1 + \sigma - \sigma\tilde{\omega}^2 \tilde{\beta}_{BB}(\tilde{\omega})\right] + \left[-\dfrac{1}{\tilde{\omega}^2} + \tilde{\beta}_{BA}(\tilde{\omega})\right]\left[-\sigma + \sigma\tilde{\omega}^2 \tilde{\beta}_{AB}(\tilde{\omega})\right]}{\left[1 - \tilde{\omega}^2\right]\left[1 + \sigma - \sigma\tilde{\omega}^2 \displaystyle\sum_{k=3,5,\ldots}^{K} \frac{\left\{\phi_B^{(k)}\right\}^2}{\tilde{\omega}_k^2 - \tilde{\omega}^2}\right] - \sigma\tilde{\omega}^2 \left\{\phi_B^{(1)}\right\}^2} \right\} \tag{9}$$

where:

$$\sigma = \frac{m_{att}}{m_b} \ , \ \tilde{\omega} = \frac{\omega}{\omega_1} \ , \ \tilde{\omega}_k = \frac{\omega_k}{\omega_1} \ , \ \tilde{\beta}_{QS}(\tilde{\omega}) = \sum_{k=1,3,5,\dots}^{K} \frac{\phi_Q^{(k)}\phi_S^{(k)}}{\tilde{\omega}_k^2 - \tilde{\omega}^2} \tag{10a-d}$$

In the above expressions m_{att} is the sum of the attached masses at B (for moveable masses) or simply the mass at B (for moveable supports) and m_b is the mass of the beam alone. $\phi_Q^{(k)}$, $\phi_S^{(k)}$ are the kth flexural non-dimensional mode-shape functions evaluated at arbitrary points Q, S and ω_k is the kth flexural natural frequency. These modal parameters pertain to the *plain* beam (i.e. without lumped mass attachment) under free-free conditions. Notice that only the symmetric modes are considered due to the symmetry of the systems in Fig. 16. The expression in eq. (9) is exact for $K \to \infty$ but, for a given upper limit of the non-dimensional excitation frequency $\tilde{\omega}$, will be virtually exact for a sufficiently large finite value of K (corresponding to a total of $(K+1)/2$ symmetric modes). For the moveable masses absorber, $\phi_A^{(k)}$ is fixed and $\phi_B^{(k)}$ is variable; for the moveable supports absorber $\phi_B^{(k)}$ is fixed and $\phi_A^{(k)}$ is variable. If the Euler-Bernoulli beam model is assumed, then the free-free mode-shape function values tabulated by (Bishop & Johnson, 1960) can be used. In this case, from eq. (9), it is clear that the non-dimensional receptance function

$$\tilde{r}_{AA}(\tilde{\omega},\tilde{x},\sigma) = m_b \omega_1^2 r_{AA}(\omega) \tag{11}$$

is totally independent of the actual material and geometrical properties for either ATVA in Fig. 16.

For given $\tilde{x}$ and σ, the lowest non-dimensional anti-resonance $\tilde{\omega}_a = \omega_a/\omega_1$ (i.e. the tuned frequency of the device) is obtained by finding the lowest value of $\tilde{\omega}$ for which the numerator of eq. (9) is 0:

$$\left[-\frac{1}{\tilde{\omega}^2} + \tilde{\beta}_{AA}(\tilde{\omega})\right]\left[1 + \sigma - \sigma\tilde{\omega}^2\tilde{\beta}_{BB}(\tilde{\omega})\right] + \left[-\frac{1}{\tilde{\omega}^2} + \tilde{\beta}_{BA}(\tilde{\omega})\right]\left[-\sigma + \sigma\tilde{\omega}^2\tilde{\beta}_{AB}(\tilde{\omega})\right] = 0 \tag{12}$$

Similarly, the lowest non-dimensional resonance $\tilde{\omega}_m = \omega_m/\omega_1$ is obtained by finding the lowest value of $\tilde{\omega}$ for which the denominator of eq. (9) is 0:

$$\left[1 - \tilde{\omega}^2\right]\left[1 + \sigma - \sigma\tilde{\omega}^2 \sum_{k=3,5,\dots}^{K} \frac{\left\{\phi_B^{(k)}\right\}^2}{\tilde{\omega}_k^2 - \tilde{\omega}^2}\right] - \sigma\tilde{\omega}^2\left\{\phi_B^{(1)}\right\}^2 = 0 \tag{13}$$

For any given K, the frequencies $\tilde{\omega}_a$, $\tilde{\omega}_m$ can be found by an iteration technique using as initial approximations the corresponding roots $\tilde{\omega}_a|_{K=1}$, $\tilde{\omega}_m|_{K=1}$ obtained for $K = 1$. From eqs. (12, 13) it can be shown that:

$$\tilde{\omega}_a|_{K=1} = \frac{1}{\sqrt{1 + (1+\sigma)\phi_A^2 + \sigma\left(\phi_B^2 - 2\phi_A\phi_B\right)}} \ , \ \tilde{\omega}_m|_{K=1} = \sqrt{\frac{1+\sigma}{1 + \sigma\left(1 + \phi_B^2\right)}} \tag{14a,b}$$

High accuracy is guaranteed here by solving the frequencies $\tilde{\omega}_a$, $\tilde{\omega}_m$ for $K = 39$, which means that 20 symmetric free-free plain beam flexural modes were considered.

Now, for the equivalent two-degree-of-freedom system in Fig. 1b, one can write the attachment point receptance as (Kidner & Brennan, 1997):

$$r_{AA}\left(\omega\right)\Big|_{\text{2-DOF}} = \frac{\omega_a^2 - \omega^2}{m_{a,red}\omega^2\left\{\omega^2 - \left(1 + m_{a,eff}/m_{a,red}\right)\omega_a^2\right\}} \tag{15}$$

where

$$m_{a,eff} = Rm_a \,,\; m_{a,red} = \left(1-R\right)m_a \,,\; m_a = \left(1+\sigma\right)m_b \tag{16a-c}$$

The non-zero resonance of the function in eq. (15) is given by:

$$\omega_m\Big|_{\text{2-DOF}} = \omega_a\sqrt{1 + m_{a,eff}/m_{a,red}} \tag{17}$$

For equivalence, $\omega_m\big|_{\text{2-DOF}} = \omega_m$ in eq. (17). Hence, by substituting this condition and eqs. (16a,b) into eq. (17), an expression can be obtained for the proportion R of the total absorber mass m_a that is effective in vibration attenuation:

$$R\left(\tilde{x},\sigma\right) = 1 - \left(\tilde{\omega}_a/\tilde{\omega}_m\right)^2 \tag{18}$$

…where $\tilde{\omega}_a$, $\tilde{\omega}_m$ are the roots of eqs. (12, 13). Also, from eq. (15) and eqs. (16), the non-dimensional attachment point receptance of the equivalent system can be written as:

$$\tilde{r}_{AA}\left(\tilde{\omega},\tilde{x},\sigma\right)\Big|_{\text{2-DOF}} = m_b\omega_1^2\, r_{AA}\left(\omega\right)\Big|_{\text{2-DOF}} = \frac{\tilde{\omega}_a^2 - \tilde{\omega}^2}{\left(1+\sigma\right)\tilde{\omega}^2\left\{\left(1-R\right)\tilde{\omega}^2 - \tilde{\omega}_a^2\right\}} \tag{19}$$

The equivalent two-degree-of-freedom model is verified in Fig. 17 against the exact theory governing the actual (continuous) ATVA structures of Fig. 16 for $\sigma = 5$ and two given settings $\tilde{x} = 0.25$, 0.5. For each setting of $\tilde{x}$ the corresponding values of $\tilde{\omega}_a$ and R were calculated using eqs. (12, 13, 18) and used to plot the function $\tilde{r}_{AA}\left(\tilde{\omega},\tilde{x},\sigma\right)\big|_{\text{2-DOF}}$ in eq. (19). Comparison with the exact receptance $\tilde{r}_{AA}\left(\tilde{\omega},\tilde{x},\sigma\right)$ (computed from eqs. (9) and (11)) shows that the equivalent two-degree-of-freedom system is a satisfactory representation of the actual systems in Fig. 16 over a frequency range which contains the operational frequency of the ATVA ($\omega = \omega_a$).

Next, using eqs. (12, 13, 18), the variations of ω_a and R with ATVA setting $\tilde{x}$ for various fixed values of σ are investigated for both types of ATVA in Fig. 16. The resulting characteristics are depicted in Fig. 18. With reference to Fig. 18a, it is evident that, as σ is increased, the tuning frequency characteristics of both types of ATVA approach each other. Moreover, for $\sigma \geq 1$, both types of ATVA give roughly the same overall useable variation in ω_a relative to $\omega_a\big|_{\tilde{x}=1}$. The moveable-supports ATVA characteristics in Fig. 18a have a peak (which is more prominent for lower σ values) that gives the impression of a greater variation in ω_a than the moveable-masses ATVA. However, this is a "red herring" since

these peaks coincide with a stark dip to zero in the effective mass proportion R of the moveable-supports ATVA, as can be seen in Fig. 18b. These troughs in R are explained by the fact that, for given σ, the free body resonance ω_m of the moveable-supports ATVA (i.e. the resonance of the free-free beam with central mass attached) is fixed (i.e. independent of $\tilde{x}$), as can be seen from Figs. 17c,d. Hence, the nodes of the associated mode-shape are fixed in position so that when the setting $\tilde{x}$ is such that the attachment points A of the moveable-supports ATVA coincide with these nodes, this ATVA becomes totally useless (i.e. attenuation $D = 0$, eq. (7)).

(a) Moveable masses, $\tilde{x} = 0.25$

(b) Moveable masses, $\tilde{x} = 0.5$

(c) Moveable supports, $\tilde{x} = 0.25$

(d) Moveable supports, $\tilde{x} = 0.25$
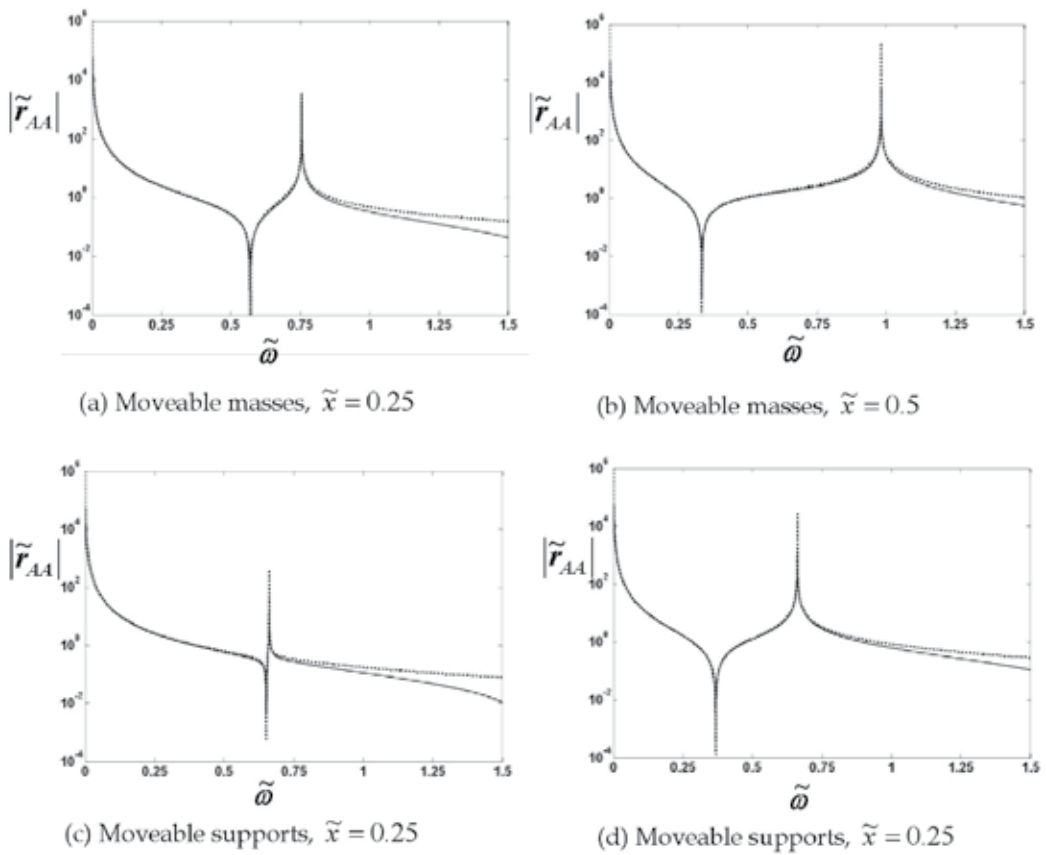
Fig. 17. Verification of equivalent two-degree-of-freedom model - non-dimensional attachment point receptance plotted against non-dimensional excitation frequency for two settings of the ATVAs in Figure 3 with $\sigma = 5$: exact, through eqs. (9) and (11) (———); equivalent 2-degree-of-freedom model, from eq. (19) (••••••••)

The moveable-masses ATVA does not suffer from this problem, and consequently has vastly superior effective mass characteristics, as evident from Fig. 18b. From eqs. (16a, b), one can rewrite the attenuation D in eq. (8) as:

$$D = \frac{1}{\eta_a}\left(\frac{R}{1 - R + M/m_a}\right) \tag{20}$$

It is evident from Fig. 18b and eq. (20) that the degree of attenuation D provided by a given moveable-supports ATVA in any given application undergoes considerable variability over its tuning frequency range, dipping to zero at a critical tuned frequency. On the other hand, the moveable-masses ATVA can be tuned over a comparable tuning frequency range while providing significantly superior vibration attenuation.

(a) Tuned frequency characteristics

(b) Effective mass characteristics
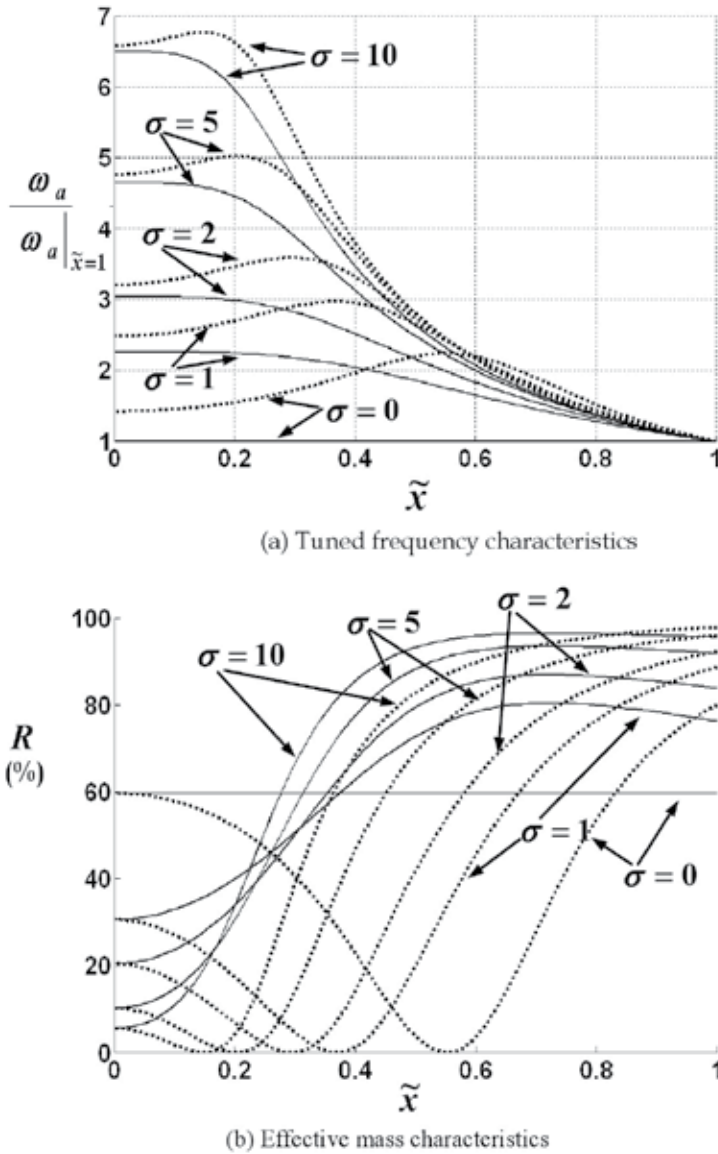
Fig. 18. Tuned frequency and effective mass characteristics for moveable-masses ATVA

4.2 Physical implementation and testing

Fig. 19 shows the moveable-masses ATVA with motor-incorporated masses that was built in (Bonello & Groves, 2009) to lend validation to the theory of the previous section and demonstrate the ATVA operation. The stepper-motors were operated from the same driver circuit board through a distribution box that sent identical signals to the motors, ensuring symmetrically-disposed movement of the masses. Each motor had an internal rotating nut that moved it along a fixed lead-screw. Each motor was guided by a pair of aluminium guide-shafts that, along with the lead-screw, made up the beam section.

The aim of Section 4.2.1 is to validate the theory of Section 4.1 whereas the aim of Section 4.2.2 is to demonstrate real-time ATVA operation.

4.2.1 Tuned frequency and effective mass characteristics

In these tests a random signal v was sent to the electrodynamic shaker amplifier and for each fixed setting $\tilde{x}$ the frequency response function (FRF) H_{Av} relating $\ddot{y}_A$ to v, and the FRF T_{BA} relating $\ddot{y}_B$ to $\ddot{y}_A$ (i.e. the transmissibility) were measured. Fig. 20a shows H_{Av} for different settings. The tuned frequency ω_a of the ATVA is the anti-resonance, which coincides with the resonance in T_{BA}. Fig. 20b shows that, at the anti-resonance, the cosine of the phase of T_{BA} is approximately zero. This is an indication that the absorber damping η_a (Fig. 1b) is low (Kidner et al., 2002). Hence, just like other types of ATVA e.g. (Rustighi et. al., 2005, Bonello et al., 2005, Kidner et al., 2002), the cosine of the phase Φ between the signals $\ddot{y}_A$ and $\ddot{y}_B$ can be used as the error signal of a feedback control system for the ATVA under variable frequency harmonic excitation (Section 4.2.2). It is noted that this result is in accordance with the two-degree-of-freedom modal reduction of the ATVA and, additionally, it could be shown theoretically that the cosine of the phase between $\ddot{y}_A$ and the signal $\ddot{y}_Q$ at any other arbitrary point Q on the ATVA would also be zero in the tuned condition.
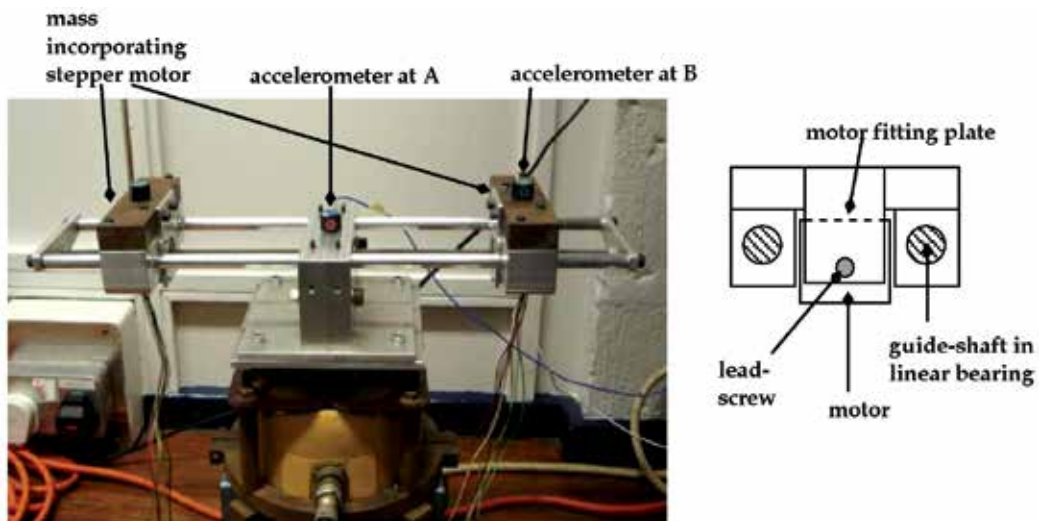
Fig. 19. Moveable-masses ATVA demonstrator mounted on electrodynamic shaker (inset shows motor-incorporated mass and ATVA beam cross-section)

Using the FRFs of Fig. 20a and a lumped parameter model of the ATVA/shaker combination it was possible to estimate the effective mass proportion R of the ATVA for each setting $\tilde{x}$, using the analysis described in (Bonello & Groves, 2009). The estimates varied slightly according to the type of damping assumed for the shaker armature suspension. However, as can be seen in Fig. 21, regardless of the damping assumption, there is good correlation with the effective mass characteristic predicted according to the theory of the previous section. Fig. 22 shows the predicted and measured tuning frequency characteristic, which gives the ratio of the tuned frequency to the tuned frequency at a reference setting. The demonstrator did not manage to achieve the predicted 418 % increase in tuned frequency, although it managed a 255 % increase, which is far higher than other proposed ATVAs e.g. (Rustighi et. al., 2005, Bonello et al., 2005, Kidner et al., 2002) and similar to the percentage increase achieved by the V-Type ATVA in (Carneal et al., 2004). The main reasons for a lower-than-predicted tuned frequency as $\tilde{x}$ was reduced can be listed as follows: (a) the guide-shafts-pair and lead-screw constituting the "beam cross-section" (Fig. 19) would only really vibrate together as one composite fixed-cross-section beam in bending, as assumed in the theory, if their cross-sections were rigidly secured relative to each other at regular intervals over the entire beam length – this was not the case in the real system and indeed was not feasible; (b) shear deformation effects induced by the inertia of the attached masses at B and the reaction force at A became more pronounced as $\tilde{x}$ was reduced; (c) the slight clearance within the stepper-motors. It is noted that the limitation in (a) was exacerbated by the offset of the centroidal axis of the lead-screw from that of the guide-shafts (inset of Fig. 19). Moreover, the limitations described in (a) and (b) are also encountered when implementing the moveable-supports design (Fig. 16b). It is also interesting to observe that, at least for the case studied, the divergence in Fig. 22 did not significantly affect the good correlation in Fig. 21.

4.2.2 Vibration control tests

Fig. 23 shows the experimental set-up for the vibration control tests. The shaker amplifier was fed with a harmonic excitation signal v of time-varying circular frequency ω and fixed amplitude and the ability of the ATVA to attenuate the vibration $\ddot{y}_A$ by maintaining the tuned condition $\omega_a = \omega$ in real time was assessed. The frequency variation occurred over the interval $t_i < t < t_f$ and was linear:

$$\omega = \begin{cases} \omega_i & t \le t_i \\ \omega_i + \left[\left(\omega_f - \omega_i\right)\big/\left(t_f - t_i\right)\right]\left(t - t_i\right) & t_i < t < t_f \\ \omega_f & t \ge t_f \end{cases} \qquad (21)$$

where ω_i, ω_f are the initial and final frequency values. The swept-sine excitation signal was hence as given by:

$$v = V \sin\theta \, , \quad \frac{d\theta}{dt} = \omega \qquad (22a,b)$$

where, by substitution of (21) into (22b) and integration:

$$\theta = \begin{cases} \omega_i t & t \le t_i \\ 0.5\left[\left(\omega_f - \omega_i\right)/\left(t_f - t_i\right)\right]\left(t - t_i\right)^2 + \omega_i t & t_i < t < t_f \\ \omega_f t - 0.5\left[\left(\omega_f - \omega_i\right)/\left(t_f + t_i\right)\right] & t \ge t_f \end{cases} \tag{23}$$
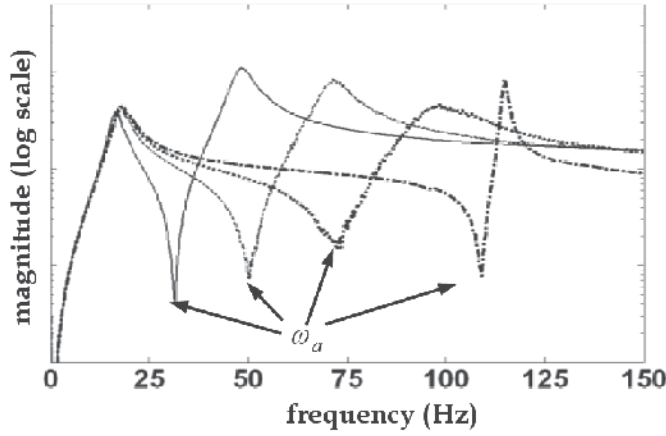
(a) FRF relating to $\ddot{y}_A$ (output) to v (input)
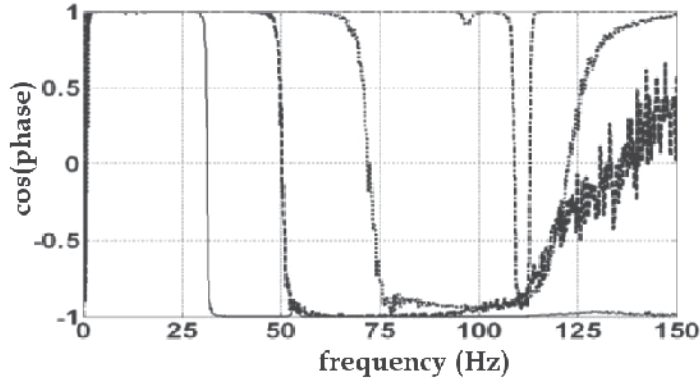
(b) Cosine of phase of FRF relating to $\ddot{y}_B$ (output) to $\ddot{y}_A$ (input)

Fig. 20. Frequency response function measurements for different settings of ATVA of Fig. 19

The inputs to the controller were the signals $\ddot{y}_A$, $\ddot{y}_B$ from the accelerometers. As discussed in Section 4.2.1, the instantaneous error signal fed into the controller was $e(t) = \cos\Phi$ and this was continuously evaluated from $\ddot{y}_A$, $\ddot{y}_B$ by integrating their normalised product over a sliding interval of fixed length T_c, according to the following formula:

$$e(t) = \cos\Phi = \begin{cases} \dfrac{I_{AB}(t)}{\{I_{AA}(t)\}^{0.5}\{I_{BB}(t)\}^{0.5}} & (t \le T_c) \\[4mm] \dfrac{I_{AB}(t) - I_{AB}(t - T_c)}{\{I_{AA}(t) - I_{AA}(t - T_c)\}^{0.5}\{I_{BB}(t) - I_{BB}(t - T_c)\}^{0.5}} & (t > T_c) \end{cases}$$ (24)

where

$$I_{AA}(t) = \int_0^t \ddot{y}_A(\tau)\,\ddot{y}_A(\tau)\,d\tau \;,\; I_{BB}(t) = \int_0^t \ddot{y}_B(\tau)\,\ddot{y}_B(\tau)\,d\tau \;,\; I_{AB}(t) = \int_0^t \ddot{y}_A(\tau)\,\ddot{y}_B(\tau)\,d\tau$$ (25a-c)

…and T_c was taken to be many times the interval Δ between consecutive sampling times of the data acquisition ($T_c = 100\Delta$ typically). Since the difference between the forcing frequency and the tuned frequency, $\omega - \omega_a$ is non-linearly related to $e(t)$, a non-linear control algorithm was necessary to minimise $|e(t)|$. Various such control algorithms for ATVAs have been proposed. For example, (Bonello et al., 2005) used a nonlinear *P-D* controller in which the voltage that controlled the piezo-actuators (Fig. 10) was updated according to a sum of two polynomial functions, one in e and the other in $\dot{e}$, weighted by suitably chosen constants *P* and *D*. (Kidner et al., 2002) formulated a fuzzy logic algorithm based on e to control the servo-motor of the device in Figure 12b. These algorithms were not convenient for the present application since they provided an analogue command signal to the actuator. In the present case, the available motor driver was far more easily operated through logic signals. Each motor had five possible motion states, respectively activated by five possible logic-combination inputs to the driver. Hence, the interval-based control methodology described in Table 1 was implemented, where the error signal computed by eq. (24) was divided into 5 intervals.
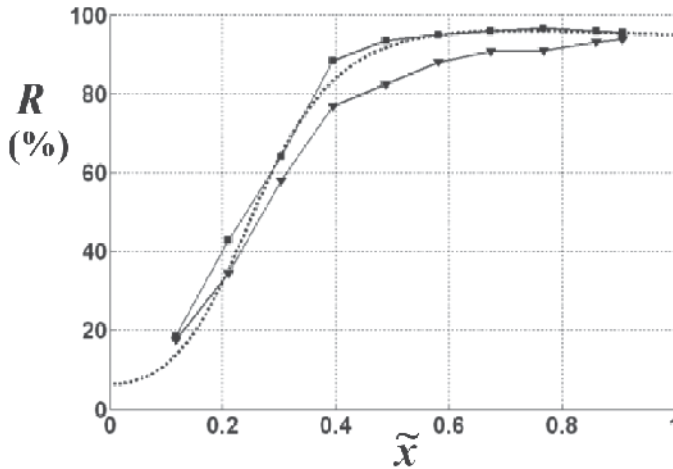
Fig. 21. Effective mass characteristics for prototype moveable masses ATVA: predicted (•••••••); measured, light damping assumption (——■——); measured, proportional damping assumption (——▼——)
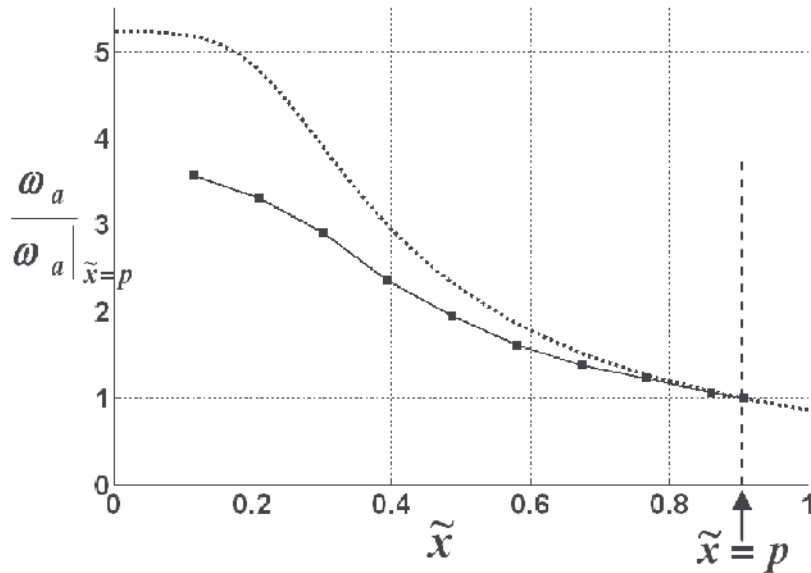
Fig. 22. Tuned frequency characteristic for prototype moveable masses ATVA: predicted (▪▪▪▪▪▪▪); measured (──▪──)
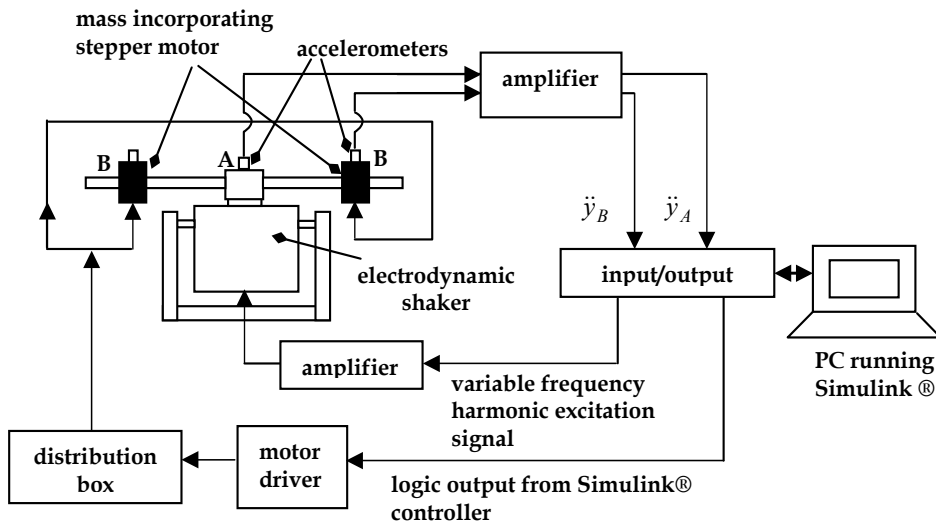
Fig. 23. Experimental set-up for vibration control test

The control system for the experimental set-up of Figure 23 was implemented in MATLAB® with SIMULINK® using the Real Time Workshop® and Real Time Windows Target® toolboxes.

Fig. 24 shows the results obtained for the frequency-sweep in Fig. 24a with the control system turned off and the ATVA tuned to a frequency of 56Hz. It is clear that at the instant

where the excitation frequency sweeps through 56 Hz, the amplitude of the acceleration $\ddot{y}_A$ is at a minimum value and $\cos\Phi$ is approximately equal to zero (i.e. the ATVA is momentarily tuned to the excitation).

(a) excitation frequency

(b) acceleration at attachment point A of ATVA, normalised with respect to $\left.\widehat{\ddot{y}}_A\right|_{peak}$

(c) cosine of phase shift Φ between $\ddot{y}_B$ and $\ddot{y}_A$
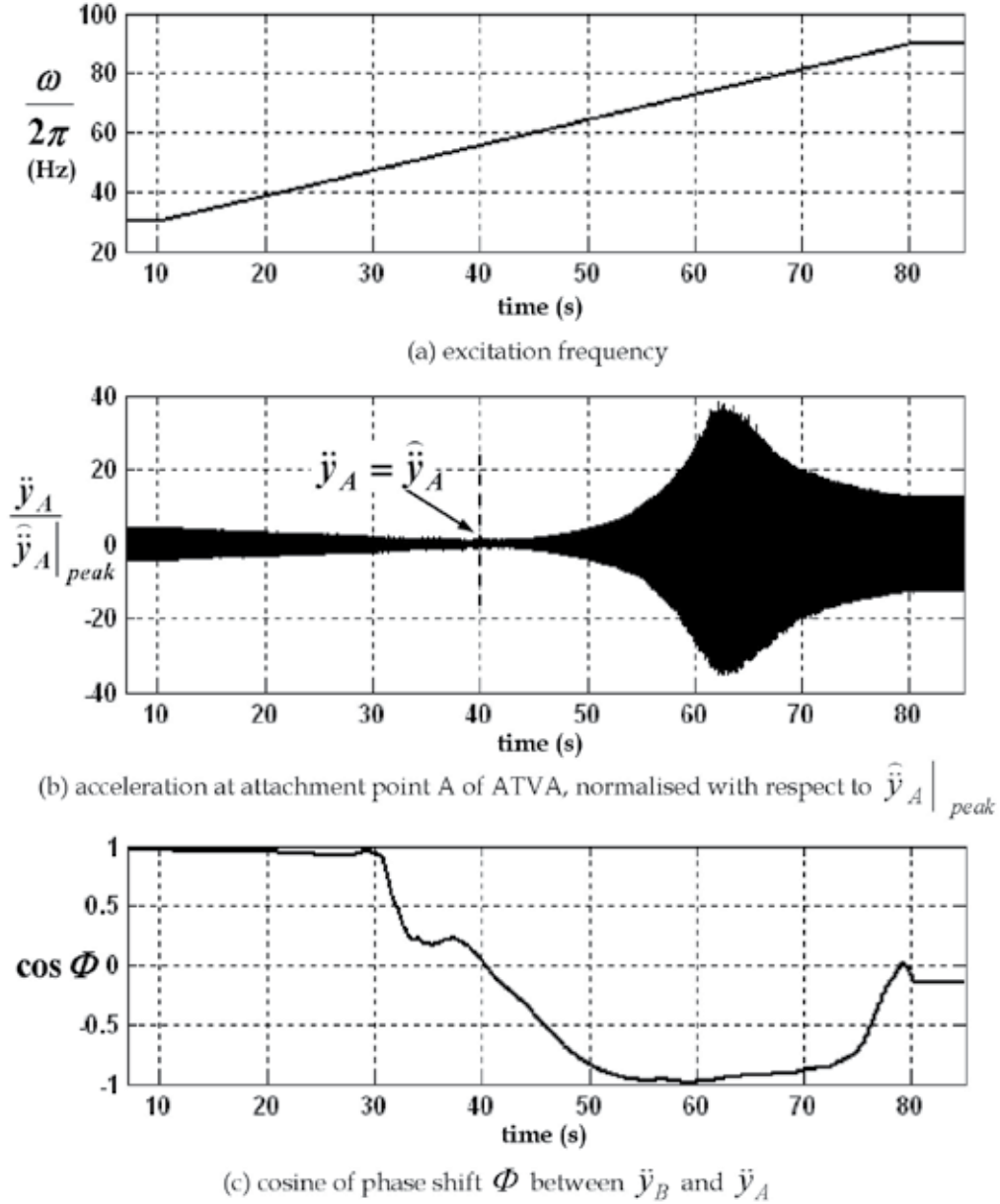
Fig. 24. Swept-sine test with controller turned off and ATVA tuned to a fixed frequency of 56 Hz ($\left.\widehat{\ddot{y}}_A\right|_{peak}$ is the amplitude of $\widehat{\ddot{y}}_A$, the tuned acceleration at A at an excitation frequency of 56 Hz)

$\cos \Phi$	Motion State
$c_1 \leq \cos \Phi \leq 1$	Fast CW
$c_2 \leq \cos \Phi < c_1$	Slow CW
$-c_2 < \cos \Phi < c_2$	Stopped
$-c_2 \geq \cos \Phi > -c_1$	Slow CCW
$-c_1 \geq \cos \Phi \geq -1$	Fast CCW

Table 1. Interval-based control methodology for stepper-motor driver (CW: clockwise; CCW: counter-clockwise)
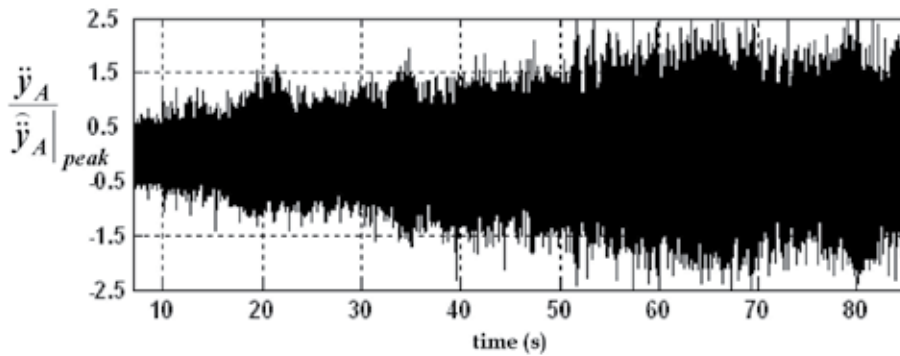
(a) acceleration at attachment point A of ATVA, normalised with respect to $\left. \hat{\ddot{y}}_A \right|_{peak}$ (defined in Figure 24)
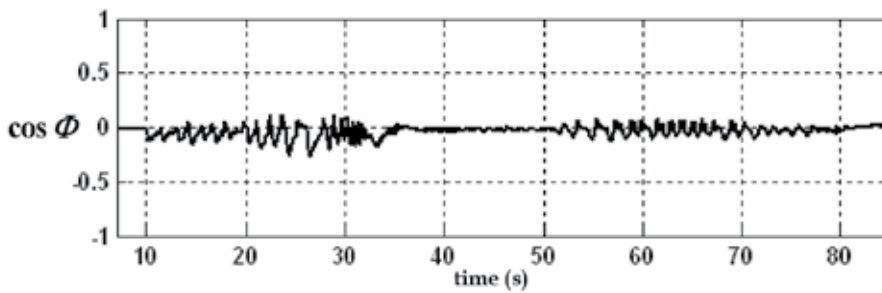
(b) cosine of phase shift Φ between $\ddot{y}_B$ and $\ddot{y}_A$

Fig. 25. Response to swept sine excitation (Figure 24a) with controller turned on and ATVA initially tuned to the excitation frequency (controller parameters in Table 1 are $c_1 = 0.04$, $c_2 = 0.02$).

Fig. 25 shows the response to the same frequency-sweep of Fig. 24a with the controller turned on. Prior to the start of the frequency-sweep at $t = 10$, the ATVA was allowed to tune itself, from whatever initial setting it had, to the prevailing excitation frequency of 30 Hz. As the sweep progressed, the controller retuned the ATVA accordingly to reasonable accuracy, as illustrated in Fig. 25b. This resulted in minimised vibration over the entire sweep, as evident by comparing the scales of the vertical axes of Fig. 25a and 24b. However, it is evident from

Fig. 25a that the amplitude of the tuned vibration increases steadily over the frequency sweep between start and finish. Further studies revealed that this observed degradation in attenuation produced by the ATVA was due to the reduction in its effective mass proportion R as it retuned itself to a higher frequency, decreasing the effective mass ratio μ of the ATVA-shaker combination. This illustrated the importance of knowing the effective mass characteristic of a moveable-masses or moveable-supports ATVA. It is noted that the tests in this subsection (4.2.2) were made with an earlier version of the prototype wherein the ATVA beam came in two halves i.e. one separate lead-screw and a separate guide-shaft-pair for each symmetric half of the ATVA, each secured into the central block (see Fig. 19). The tests in section 4.2.1 were made with an improved version wherein the ATVA beam was one continuous piece, as in the theory (Fig. 16a) i.e. one long lead-screw and guide-shaft pair running straight through the central block, where they were tightly secured, ensuring a horizontal slope (see Fig. 19). Based on the validated results of Fig. 21, the observed degradation in attenuation in Fig. 25a is expected to be much less for the improved version.

5. Conclusion

This chapter started with a quantitative illustration of the basic design principles of both variants of the TVA: the TMD and the TVN. The importance of adaptive technology, particularly with regard to the TVN, was justified. The remainder of the chapter then focussed on adaptive (smart) technology as applied to the TVN. A comprehensive review of the various design concepts that have been proposed for the ATVA was presented. The latest ATVA concept introduced by the author, involving a beam-like ATVA with actuator-incorporated moveable masses, was then studied theoretically and experimentally. The variation in tuned frequency was shown to be significantly higher than most other proposed ATVAs and at least as high as that reported in the literature for the alternative moveable-supports beam ATVA design. Moreover, the analysis revealed that the moveable-masses beam concept offers significantly superior vibration attenuation relative to the moveable-supports beam concept, apart from constructional simplicity. Vibration control tests with logic-based feedback control demonstrated the efficacy of the device under variable frequency excitation. Current efforts by the author are being directed at introducing smart technology to TMDs.

6. References

Bishop, R.E.D. & Johnson, D.C. (1960). *The Mechanics of Vibration*, Cambridge University Press, Cambridge, UK

Bonello, P. & Brennan, M. J. (2001). Modelling the dynamic behaviour of a supercritical rotor on a flexible foundation using the mechanical impedance technique. *J. Sound and Vibration*, Vol.239, No.3, pp. 445-466

Bonello, P.; Brennan, M. J. & Elliott, S. J. (2005). Vibration control using an adaptive tuned vibration absorber with a variable curvature stiffness element. *Smart Mater. Struct.*, Vol.14, No.5, pp. 1055-1065

Bonello, P. & Groves, K.H. (2009). Vibration control using a beam-like adaptive tuned vibration absorber with actuator-incorporated mass-element. *Proceedings of the Institution of Mechanical Engineers - Part C: Journal of Mechanical Engineering Science.*,Vol.223.,No.7, pp 1555-1567

Brennan, M.J. (1997). Vibration control using a tunable vibration neutraliser. *Proc. IMechE Part C, Journal of Mechanical Engineering Science*, Vol.211, pp. 91-108

Brennan, M.J. (2000). Actuators for active control – tunable resonant devices. *Applied Mechanics and Engineering*, Vol.5, No.1, pp. 63-74

Brennan, M.J.; Bonello, P.; Rustighi, E., Mace, B.R. & Elliott, S.J. (2004a). Designs of a variable stiffness element for a tunable vibration absorber, *Proceedings of ICA2004 (The 18th International Congress on Acoustics)*, Vol.IV, pp. 2915-2918, Kyoto, Japan, 4-9 April , 2004

Brennan, M.J.; Bonello, P.; Rustighi, E., Mace, B.R. & Elliott, S.J. (2004b). Designs of a variable stiffness element for a tunable vibration absorber, *Presentation given at ICA2004 (The 18th International Congress on Acoustics)*, Vol.IV, pp. 2915-2918, Kyoto, Japan, 4-9 April , 2004

Carneal, J.P.; Charette, F. & Fuller, C.R. (2004). Minimization of sound radiation from plates using adaptive tuned vibration absorbers. *J. Sound and Vibration*, Vol.270, pp. 781-792

Den Hartog, J.P. (1956). *Mechanical Vibrations*, McGraw Hill (4th Edition), New York, USA

Ewins, D.J. (1984). *Modal Testing: Theory and Practice*, Letchworth: Research Student Press, UK

Hong, D.P. & Ryu, Y.S. (1985). Automatically controlled vibration absorber. *US Patent No. 4935651*

Kidner, M.R.F. & Brennan, M.J. (1999). Improving the performance of a vibration neutraliser by actively removing damping. *J. Sound and Vibration*, Vo.221, No.4, pp. 587-606

Kidner, M. R. F. & Brennan, M. J. (2002). Variable stiffness of a beam-like neutraliser under fuzzy logic control. *Trans. of the ASME, J. Vibration and Acoustics*, Vol.124, pp. 90-99

Ormondroyd, J. & den Hartog, J.P. (1928). Theory of the dynamic absorber. *Trans. of the ASME*, Vol. 50, pp. 9-22

Long, T.; Brennan, M.J. & Elliott, S.J. (1998). Design of smart machinery installations to reduce transmitted vibrations by adaptive modification of internal forces. *Proceedings of the Institution of Mechanical Engineering - Part I: Journal of Systems and Control Engineering*, Vol.212, No.13, pp. 215-228

Longbottom, C.J.; Day M.J. & Rider, E. (1990). A self tuning vibration absorber. *UK Patent No. GB218957B*

Park, C.H. (2003). Dynamics modelling of beams with shunted piezoelectric elements. *J. Sound and Vibration*, Vol.268, pp. 115-129

Rustighi, E.; Brennan, M.J. & Mace, B.R. (2005). A shape memory alloy adaptive tuned vibration absorber: design and implementation. *Smart Mater. Struct.*, Vol.14, No.1, pp. 19–28

von Flotow, A.H.; Beard, A.H. & Bailey, D. (1994). Adaptive tuned vibration absorbers: tuning laws, tracking agility, sizing and physical implementation, *Proc. Noise-Con 94*, pp. 81-101, Florida, USA, 1994

Design of Active Vibration Absorbers Using On-Line Estimation of Parameters and Signals

Francisco Beltran-Carbajal[1], Gerardo Silva-Navarro[2],
Benjamin Vazquez-Gonzalez[1] and Esteban Chavez-Conde[3]
[1] *Universidad Autonoma Metropolitana, Plantel Azcapotzalco, Departamento de Energia, Mexico, D.F.*
[2] *Centro de Investigacion y de Estudios Avanzados del I.P.N., Departamento de Ingenieria Electrica, Seccion de Mecatronica, Mexico, D.F.*
[3]*Universidad del Papaloapan, Campus Loma Bonita, Departamento de Mecatronica, Oaxaca*
Mexico

1. Introduction

Many engineering systems undergo undesirable vibrations. Vibration control in mechanical systems is an important problem by means of which vibrations are suppressed or at least attenuated. In this direction, the dynamic vibration absorbers have been widely applied in many practical situations because of their low cost/maintenance, efficiency, accuracy and easy installation (Braun et al., 2001; Preumont, 1993). Some of their applications can be found in buildings, bridges, civil structures, aircrafts, machine tools and many other engineering systems (Caetano et al., 2010; Korenev & Reznikov, 1993; Sun et al., 1995; Taniguchi et al., 2008; Weber & Feltrin, 2010; Yang, 2010).

There are three fundamental control design methodologies for vibration absorbers described as passive, semi-active and active vibration control. Passive vibration control relies on the addition of stiffness and damping to the primary system in order to reduce its dynamic response, and serves for specific excitation frequencies and stable operating conditions, but is not recommended for variable excitation frequencies and/or parametric uncertainty. Semiactive vibration control deals with adaptive spring or damper characteristics, which are tuned according to the operating conditions. Active vibration control achieves better dynamic performance by adding degrees of freedom to the system and/or controlling actuator forces depending on feedback and feedforward real-time information of the system, obtained from sensors. For more details about passive, semiactive and active vibration control we refer to the books (Braun et al., 2001; Den Hartog, 1934; Fuller et al, 1997; Preumont, 1993).

On the other hand, many dynamical systems exhibit a structural property called differential flatness. This property is equivalent to the existence of a set of independent outputs, called flat outputs and equal in number to the control inputs, which completely parameterizes every state variable and control input (Fliess et al., 1993; Sira-Ramirez & Agrawal, 2004). By means of differential flatness techniques the analysis and design of a controller is greatly

simplified. In particular, the combination of differential flatness with the control approach called Generalized Proportional Integral (GPI) control, based on output measurements and integral reconstructions of the state variables (Fliess et al., 2002), qualifies as an adequate control scheme to achieve the robust asymptotic output tracking and, simultaneously, the cancellation/attenuation of harmonic vibrations. GPI controllers for design of active vibration absorbers have been previously addressed in (Beltran et al., 2003). Combinations of GPI control, sliding modes and on-line algebraic identification of harmonic vibrations for design of adaptive-like active vibration control schemes have been also proposed in (Beltran et al., 2010). A GPI control strategy implemented as a classical compensation network for robust perturbation rejection in mechanical systems has been presented in (Sira-Ramirez et al., 2008). In this chapter a design approach for active vibration absorption schemes in linear mass-spring-damper mechanical systems subject to exogenous harmonic vibrations is presented, which are based on differential flatness and GPI control, but taking the advantage of the interesting energy dissipation properties of passive vibration absorbers. Our design approach considers a mass-spring active vibration absorber as a dynamic controller, which can simultaneously be used for vibration attenuation and desired reference trajectory tracking tasks. The proposed approach allows extending the vibrating energy dissipation property of a passive vibration absorber for harmonic vibrations of any excitation frequency, by applying suitable control forces to the vibration absorber. Two different active vibration control schemes are synthesized, one employing only displacement measurements of the primary system and other using measurements of the displacement of the primary system as well as information of the excitation frequency. The algebraic parametric identification methodology reported by (Fliess & Sira-Ramirez, 2003), which employs differential algebra, module theory and operational calculus, is applied for the on-line estimation of the parameters associated to the external harmonic vibrations, using only displacement measurements of the primary system. Some experimental results on the application of on-line algebraic identification of parameters and excitation forces in vibrating mechanical systems were presented in (Beltran et al., 2004), which show their success in practical implementations.

The real-time algebraic identification of the excitation frequency is combined with a certainty equivalence controller to cancel undesirable harmonic vibrations affecting the primary mechanical system as well as to track asymptotically and robustly a specified output reference trajectory. The adaptive-like control scheme results quite fast and robust against parameter uncertainty and frequency variations.

The main virtue of the proposed identification and adaptive-like control scheme for vibrating systems is that only measurements of the transient input/output behavior are used during the identification process, in contrast to the well-known persisting excitation condition and complex algorithms required by most of the traditional identification methods (Isermann & Munchhof, 2011; Ljung, 1987; Soderstrom, 1989). It is important to emphasize that the proposed results are now possible thanks to the existence of high speed DSP boards with high computational performance operating at high sampling rates.

Finally, some simulation results are provided to show the robust and efficient performance of the proposed active vibration control schemes as well as of the proposed identifiers for on-line estimation of the unknown frequency and amplitude of resonant harmonic vibrations.

2. Vibrating mechanical system

2.1 Mathematical model

Consider the vibrating mechanical system shown in Fig. 1, which consists of an active undamped dynamic vibration absorber (secondary system) coupled to the perturbed mechanical system (primary system). The generalized coordinates are the displacements of both masses, x_1 and x_2, respectively. In addition, u represents the force control input and $f(t)$ some harmonic perturbation, possibly unknown. Here m_1, k_1 and c_1 denote mass, linear stiffness and linear viscous damping on the primary system, respectively. Similarly, m_2, k_2 and c_2 denote mass, stiffness and viscous damping of the dynamic vibration absorber. Note also that, when $u \equiv 0$ the active vibration absorber becomes only a passive vibration absorber.
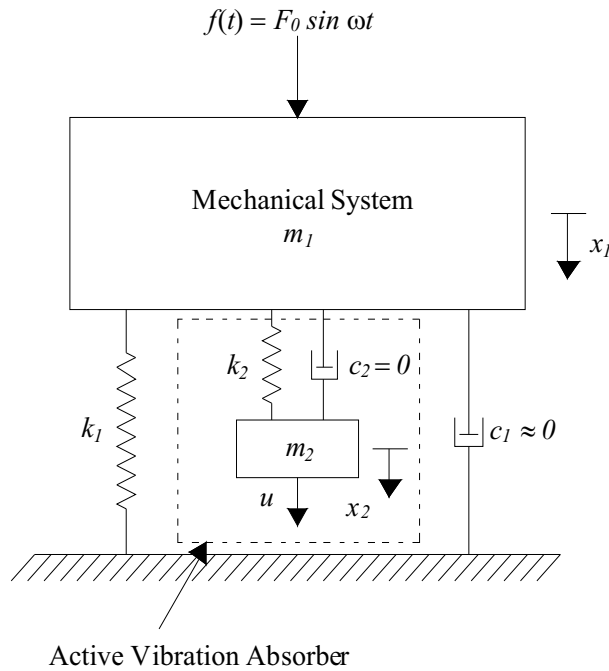
Fig. 1. Schematic diagram of the vibrating mechanical system with active vibration absorber.

The mathematical model of this two degrees-of-freedom system is described by the following two coupled ordinary differential equations

$$m_1\ddot{x}_1 + c_1\dot{x}_1 + k_1x_1 + k_2(x_1 - x_2) = f(t)$$
$$m_2\ddot{x}_2 + k_2(x_2 - x_1) = u(t)$$

(1)

where $f(t) = F_0 \sin \omega t$, with F_0 and ω denoting the amplitude and frequency of the excitation force, respecively. In order to simplify the analysis we have assumed that $c_1 \approx 0$.

Defining the state variables as $z_1 = x_1, z_2 = \dot{x}_1, z_3 = x_2$ and $z_4 = \dot{x}_2$, one obtains the following state-space description

$$\dot{z}_1 = z_2$$
$$\dot{z}_2 = -\frac{k_1+k_2}{m_1}z_1 - \frac{c_1}{m_1}z_2 + \frac{k_2}{m_1}z_3 + \frac{1}{m_1}f(t)$$
$$\dot{z}_3 = z_4 \tag{2}$$
$$\dot{z}_4 = \frac{k_2}{m_2}z_1 - \frac{k_2}{m_2}z_3 + \frac{1}{m_2}u(t)$$
$$y = z_1$$

It is easy to verify that the system (2) is completely controllable and observable as well as marginally stable in case of $c_1 = 0$, $f \equiv 0$ and $u \equiv 0$ (asymptotically stable when $c_1 > 0$). Note that, an immediate consequence is that, the output $y = z_1$ has relative degree 4 with respect to u and relative degree 2 with respect to f and, therefore, the so-called disturbance decoupling problem of the perturbation $f(t)$ from the output $y = z_1$, using state feedback, is not solvable (Isidori, 1995).

To cancel the exogenous harmonic vibrations on the primary system, the dynamic vibration absorber should apply an equivalent force to the primary system, with the same amplitude but in opposite phase (sign). This means that the vibration energy injected to the primary system, by the exogenous vibration $f(t)$, is transferred to the vibration absorber through the coupling elements (i.e., spring k_2). Of course, this vibration control method is possible under the assumption of perfect knowledge of the exogenous vibrations and stable operating conditions (Preumont, 1993).

In this work we will apply the algebraic identification method to estimate the parameters associated to the harmonic force $f(t)$ and then, propose the design of an active vibration controller based on state feedback and feedforward information of $f(t)$.

2.2 Passive vibration absorber

It is well known that a passive vibration absorber can only cancel the vibration $f(t)$ affecting the primary system if and only if the excitation frequency ω coincides with the uncoupled natural frequency of the absorber (Den Hartog, 1934), that is,

$$\omega_2 = \sqrt{\frac{k_2}{m_2}} = \omega \tag{3}$$

See Fig. 2, where X_1 denotes the steady-state maximum amplitude of $x_1(t)$ and δ_{st} the static deflection of the primary system under the constant force F_0. Note, however, that the interconnection of the passive vibration absorber to the primary system slightly changes the natural frequencies in both uncoupled subsystems and, hence, when $\omega \neq \omega_2$ and close to those resonant frequencies the amplitudes might be large or theoretically infinite. This situation clearly leads to large displacements and could damage of any physical system.

In what follows we shall use an active vibration absorber based on Generalized PI control (GPI) to provide some robustness with respect to variations on the excitation frequency ω, uncertain system parameters and initial conditions.
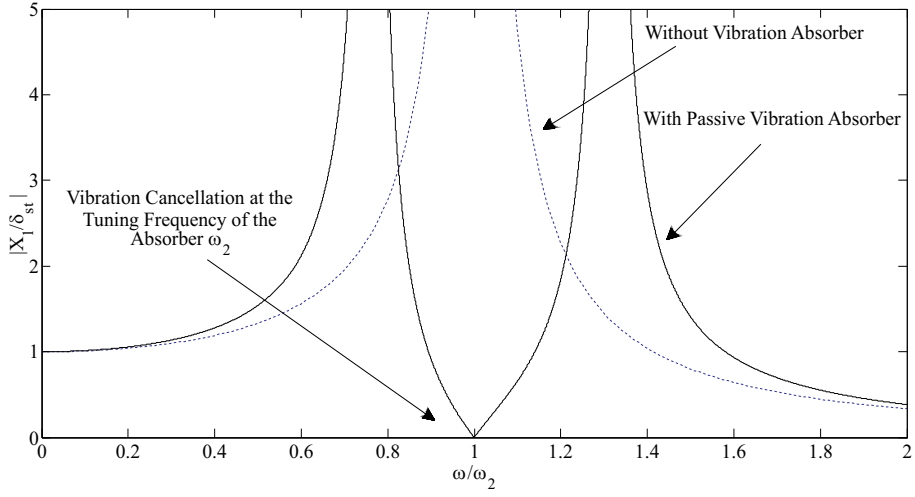
Fig. 2. Frequency response of the vibrating mechanical system with passive vibration absorber.

2.3 Differential flatness

Because the system (2) is completely controllable from u then, it is differentially flat, with flat output given by $y = z_1$. Then, all the state variables and the control input can be differentially parameterized in terms of the flat output y and a finite number of its time derivatives (Fliess et al., 1993; Sira-Ramirez & Agrawal, 2004).

In fact, from y and its time derivatives up to fourth order one can obtain that

$$
\begin{aligned}
y &= z_1 \\
\dot{y} &= z_2 \\
\ddot{y} &= -\frac{k_1+k_2}{m_1}z_1 + \frac{k_2}{m_1}z_3 \\
y^{(3)} &= -\frac{k_1+k_2}{m_1}z_2 + \frac{k_2}{m_1}z_4 \\
y^{(4)} &= \left[\frac{(k_1+k_2)^2}{m_1^2} + \frac{k_2^2}{m_1 m_2}\right]z_1 - \left[\frac{k_2(k_2+k_1)}{m_1^2} + \frac{k_2^2}{m_1 m_2}\right]z_3 + \frac{k_2}{m_1 m_2}u
\end{aligned}
\tag{4}
$$

where $c_1 = 0$ and $f \equiv 0$. Therefore, the differential parameterization results as follows

$$
\begin{aligned}
z_1 &= y \\
z_2 &= \dot{y} \\
z_3 &= \frac{k_1+k_2}{k_2}y + \frac{m_1}{k_2}\ddot{y} \\
z_4 &= \frac{k_1+k_2}{k_2}\dot{y} + \frac{m_1}{k_2}y^{(3)} \\
u &= k_1 y + \left(m_1 + m_2 + \frac{k_1}{k_2}m_2\right)\ddot{y} + \frac{m_1 m_2}{k_2}y^{(4)}
\end{aligned}
\tag{5}
$$

Then, the flat output y satisfies the following input-output differential equation

$$
y^{(4)} = a_0 y + a_2 \ddot{y} + bu
\tag{6}
$$

where

$$a_0 = -\frac{k_1 k_2}{m_1 m_2}$$

$$a_2 = -\left(\frac{k_1 + k_2}{m_1} + \frac{k_2}{m_2}\right)$$

$$b = \frac{k_2}{m_1 m_2}$$

From (6) one obtains the following differential flatness-based controller to asymptotically track some desired reference trajectory $y^*(t)$:

$$u = b^{-1}\left(v - a_0 y - a_2 \ddot{y}\right) \tag{7}$$

with

$$v = (y^*)^{(4)}(t) - \beta_6\left[y^{(3)} - (y^*)^{(3)}(t)\right] - \beta_5\left[\ddot{y} - \ddot{y}^*(t)\right] - \beta_4\left[\dot{y} - \dot{y}^*(t)\right] - \beta_3\left[y - y^*(t)\right]$$

The use of this controller yields the following closed-loop dynamics for the trajectory tracking error $e = y - y^*(t)$:

$$e^{(4)} + \beta_6 e^{(3)} + \beta_5 \ddot{e} + \beta_4 \dot{e} + \beta_3 e = 0 \tag{8}$$

Therefore, selecting the design parameters β_i, $i = 3, ..., 6$, such that the associated characteristic polynomial for (8) be *Hurwitz*, i.e., all its roots lying in the open left half complex plane, one can guarantee that the error dynamics be globally asymptotically stable.

Nevertheless, this controller is not robust with respect to exogenous signals or parameter uncertainties in the model. In case of $f(t) \neq 0$, the parameterization should explicitly include the effect of f and its time derivatives up to second order. In addition, the implementation of this controller requires measurements of the time derivatives of the flat output up to third order and vibration signal and its time derivatives up to second order.

Remark. In spite of the linear models under study, it results important to emphasize the great potential of the differential flatness approach for nonlinear flat systems, which can be analyzed using similar arguments (Fliess & Sira-Ramirez, 2003). In fact, the proposed results can be generalized to some classes of nonlinear mechanical systems.

Next, we will synthesize two controllers based on the Generalized PI (GPI) control approach combined with differential flatness and passive absorption, in order to get robust controllers against external vibrations.

3. Generalized PI control

3.1 Control scheme using displacement measurement on the primary system

Since the system (2) is observable for the flat output y then, all the time derivatives of the flat output can be reconstructed by means of integrators, that is, they can be expressed in terms of the flat output y, the input u and iterated integrals of the input and the output variables (Fliess et al., 2002).

For simplicity, we will denote the integral $\int_0^t \varphi(\tau)\,d\tau$ by $\int \varphi$ and $\int_0^t \int_0^{\sigma_1} \cdots \int_0^{\sigma_{n-1}} \varphi(\sigma_n)\,d\sigma_n \cdots d\sigma_1$ by $\int^{(n)} \varphi$ with n a positive integer. The integral input-output

parameterization of the time derivatives of the flat output is given, modulo initial conditions, by

$$\widehat{\dot{y}} = a_0 \int^{(3)} y + a_2 \int y + b \int^{(3)} u$$

$$\widehat{\ddot{y}} = a_0 \int^{(2)} y + a_2 y + b \int^{(2)} u \tag{9}$$

$$\widehat{y^{(3)}} = a_0 \int y + a_2 \widehat{\ddot{y}} + b \int u$$

These expressions were obtained by successive integrations of the last equation in (6). For non-zero initial conditions, the relations linking the actual values of the time derivatives of the flat output to the structural estimates in (9) are given as follows

$$\dot{y} = \widehat{\dot{y}} + e_{12} t^2 + e_{11} t + e_{11}$$

$$\ddot{y} = \widehat{\ddot{y}} + g_{11} t + g_{10} \tag{10}$$

$$y^{(3)} = \widehat{y^{(3)}} + h_{12} t^2 + h_{11} t + h_{10}$$

where $e_{1i}, g_j, h_i, i = 0, \ldots, 2, j = 0, \ldots, 1$, are real constants depending on the unknown initial conditions.

For the design of the GPI controller, the time derivatives of the flat output are replaced for their structural estimates (9) into (7). This, however, implies that the closed-loop system would be actually excited by constant values, ramps and quadratic functions. To eliminate these destabilizing effects of such structural estimation errors, one can use the following controller with iterated integral error compensation:

$$u = b^{-1} \left(v - a_0 y - a_2 \widehat{\ddot{y}} \right)$$

$$v = (y^*)^{(4)} (t) - \beta_6 \left[\widehat{y^{(3)}} - (y^*)^{(3)} (t) \right] - \beta_5 \left[\widehat{\ddot{y}} - \ddot{y}^* (t) \right] - \beta_4 \left[\widehat{\dot{y}} - \dot{y}^* (t) \right]$$

$$-\beta_3 \left[y - y^* (t) \right] - \beta_2 \xi_1 - \beta_1 \xi_2 - \beta_0 \xi_3$$

$$\dot{\xi}_1 = y - y^* (t), \quad \xi_1 (0) = 0 \tag{11}$$

$$\dot{\xi}_2 = \xi_1, \qquad\qquad \xi_2 (0) = 0$$

$$\dot{\xi}_3 = \xi_2, \qquad\qquad \xi_3 (0) = 0$$

The use of this controller yields the following closed-loop system dynamics for the tracking error, $e = y - y^* (t)$, described by

$$e^{(7)} + \beta_6 e^{(6)} + \beta_5 e^{(5)} + \beta_4 e^{(4)} + \beta_3 e^{(3)} + \beta_2 \ddot{e} + \beta_1 \dot{e} + \beta_0 e = 0 \tag{12}$$

The coefficients β_i, $i = 0, \ldots, 6$, have to be selected in such way that the characteristic polynomial of (12) be *Hurwitz*. Thus, one can conclude that $\lim_{t \to \infty} e(t) = 0$, i.e., the asymptotic output tracking of the reference trajectory $\lim_{t \to \infty} y(t) = y^* (t)$.

3.1.1 Robustness analysis with respect to external vibrations

Now, consider that the passive vibration absorber is tuned at the uncoupled natural frequency of the primary system, that is, $\omega_2 = \omega_1$. The transfer function of the closed-loop system from

the perturbation $f(t)$ to the output $y = z_1$ is then given by

$$
\begin{aligned}
G(s) &= \frac{x_1(s)}{f(s)} \\
&= \frac{\mu \left(m_2 s^2 + k_2\right) \left(m_2 s^3 + \beta_6 m_2 s^2 + \beta_5 m_2 s - \beta_6 k_2 \mu - 2\beta_6 k_2 + \beta_4 m_2 - 2k_2 s - k_2 s \mu\right)}{m_2^3 \left(s^7 + \beta_6 s^6 + \beta_5 s^5 + \beta_4 s^4 + \beta_3 s^3 + \beta_2 s^2 + \beta_1 s + \beta_0\right)}
\end{aligned}
\tag{13}
$$

where $\mu = m_2/m_1$ is the mass ratio.

Then, for the harmonic perturbation $f(t) = F_0 \sin \omega t$, the steady-state magnitude of the primary system is computed as

$$
|X_1| = \frac{\mu}{m_2^3} F_0 \sqrt{\frac{A(\omega)}{B(\omega)}}
\tag{14}
$$

where

$$
\begin{aligned}
A(\omega) &= \left(k_2 - m_2 \omega^2\right)^2 \left[\left(-\beta_6 m_2 \omega^2 - \beta_6 k_2 \mu - 2\beta_6 k_2 + \beta_4 m_2\right)^2 \right. \\
&\quad \left. + \left(-m_2 \omega^3 + \beta_5 m_2 \omega - 2k_2 \omega - k_2 \omega \mu\right)^2 \right] \\
B(\omega) &= \left(-\beta_6 \omega^6 + \beta_4 \omega^4 - \beta_2 \omega^2 + \beta_0\right)^2 + \left(-\omega^7 + \beta_5 \omega^5 - \beta_3 \omega^3 + \beta_1 \omega\right)^2
\end{aligned}
$$

Note that $X_1 \equiv 0$ exactly when $\omega = \omega_2 = \sqrt{\frac{k_2}{m_2}}$, independently of the selected gains of the control law in (11), corresponding to the dynamic performance of the passive vibration control scheme. This clearly corresponds to a finite zero in the above transfer function $G(s)$, situation where the passive vibration absorber is well tuned.

Thus, the control objective for (11) is to add some robustness when $\omega \neq \omega_2$ and improve the performance of the closed-loop system using small control efforts and taking advantage of the passive vibration absorber (when $\omega = \omega_2$ the system can operate with $u \equiv 0$).

In Fig. 3 we can observe that, the active vibration absorber can attenuate vibrations for any excitation frequency, including vibrations with multiple harmonic signals. In fact, it is still possible to minimize the attenuation level by adding a proper viscous damping to the absorber (Korenev & Reznikov, 1993; Rao, 1995).

3.2 Control scheme using displacement measurement on the primary system and excitation frequency

Consider the perturbed system (2). The state variables and the control input u can be expressed in terms of the flat output y, the perturbation f and their time derivatives:

$$
\begin{aligned}
z_1 &= y \\
z_2 &= \dot{y} \\
z_3 &= \frac{k_1 + k_2}{k_2} y + \frac{m_1}{k_2} \ddot{y} - \frac{1}{k_2} f(t) \\
z_4 &= \frac{k_1 + k_2}{k_2} \dot{y} + \frac{m_1}{k_2} y^{(3)} - \frac{1}{k_2} \dot{f}(t) \\
u &= \frac{m_1 m_2}{k_2} y^{(4)} + k_1 y + \left(m_1 + m_2 + \frac{k_1}{k_2} m_2\right) \ddot{y} - f(t) - \frac{m_2}{k_2} \ddot{f}(t)
\end{aligned}
\tag{15}
$$
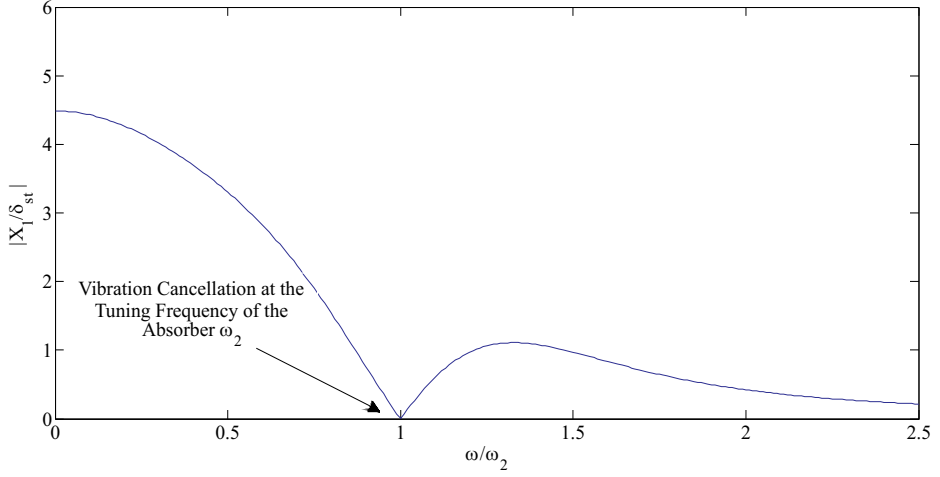
Fig. 3. Frequency response of the vibrating mechanical system using an active vibration absorber with controller (11).

Furthermore, when $f(t) = F_0 \sin \omega t$ the flat output y satisfies the following input-output differential equation:

$$y^{(4)} = -\frac{k_1 k_2}{m_1 m_2} y - \left(\frac{k_1 + k_2}{m_1} + \frac{k_2}{m_2} \right) \ddot{y} + \left(\frac{k_2}{m_1 m_2} - \frac{\omega^2}{m_1} \right) F_0 \sin \omega t + \frac{k_2}{m_1 m_2} u \qquad (16)$$

Taking two additional time derivatives of (16) results in

$$y^{(6)} = -\frac{k_1 k_2}{m_1 m_2} \ddot{y} - \left(\frac{k_1 + k_2}{m_1} + \frac{k_2}{m_2} \right) y^{(4)} + \frac{k_2}{m_1 m_2} \ddot{u} - \left(\frac{k_2}{m_1 m_2} - \frac{\omega^2}{m_1} \right) \omega^2 F_0 \sin \omega t \qquad (17)$$

Multiplication of (16) by ω^2 and adding it to (17) leads to

$$y^{(6)} + d_1 y^{(4)} + d_2 \ddot{y} + d_3 y = d_4 \left(\ddot{u} + \omega^2 u \right) \qquad (18)$$

where

$$d_1 = \frac{k_1 + k_2}{m_1} + \frac{k_2}{m_2} + \omega^2$$
$$d_2 = \left(\frac{k_1 + k_2}{m_1} + \frac{k_2}{m_2} \right) \omega^2 + \frac{k_1 k_2}{m_1 m_2}$$
$$d_3 = \frac{k_1 k_2}{m_1 m_2} \omega^2$$
$$d_4 = \frac{k_2}{m_1 m_2}$$

A differential flatness-based dynamic controller, using feedback measurements of the flat output y and its time derivatives up to fifth order as well as feedforward measurements of the excitation frequency ω, is proposed by the following dynamic compensator:

$$\ddot{u} + \omega^2 u = d_4^{-1} v + d_4^{-1} \left(d_1 y^{(4)} + d_2 \ddot{y} + \frac{k_1 k_2}{m_1 m_2} \omega^2 y \right)$$
$$v = y^{*(6)} - \alpha_{10} \left[y^{(5)} - y^{*(5)} \right] - \alpha_9 \left[y^{(4)} - y^{*(4)} \right] - \alpha_8 \left[y^{(3)} - y^{*(3)} \right] \qquad (19)$$
$$- \alpha_7 \left[\ddot{y} - \ddot{y}^* \right] - \alpha_6 \left[\dot{y} - \dot{y}^* \right] - \alpha_5 \left[y - y^* \right]$$

with zero initial conditions (i.e., $u(0) = \dot{u}(0) = 0$). It is important to remark that, the above differential equation resembles an exosystem (linear oscillator) tuned at the known excitation frequency ω (feedforward action) and injected by feedback terms involving the flat output y and its desired reference trajectory y^*.

On the other hand, one can note that the time derivatives of the flat output admit an integral input-output parameterization, obtained after some algebraic manipulations, given by

$$
\begin{aligned}
\widehat{y} &= -d_1 \int y - d_2 \int^{(3)} y - d_3 \int^{(5)} y + d_4 \int^{(3)} u \\
\widehat{\dot{y}} &= -d_1 y - d_2 \int^{(2)} y - d_3 \int^{(4)} y + d_4 \int^{(2)} u + d_4 \omega^2 \int^{(4)} u \\
\widehat{y}^{(3)} &= -d_1 \widehat{\dot{y}} - d_2 \int y - d_3 \int^{(3)} y + d_4 \int u + d_4 \omega^2 \int^{(3)} u \\
\widehat{y}^{(4)} &= -d_1 \widehat{\ddot{y}} - d_2 y - d_3 \int^{(2)} y + d_4 u + d_4 \omega^2 \int^{(2)} u \\
\widehat{y}^{(5)} &= -d_1 \widehat{y}^{(3)} - d_2 \widehat{\dot{y}} - d_3 \int y + d_4 \dot{u} + d_4 \omega^2 \int u
\end{aligned}
\tag{20}
$$

The differences in the structural estimates of the time derivatives of the flat output with respect to the actual time derivatives are given by

$$
\begin{aligned}
\dot{y} &= \widehat{\dot{y}} + p_4 t^4 + p_3 t^3 + p_2 t^2 + p_1 t + p_0 \\
\ddot{y} &= \widehat{\ddot{y}} + p_4 t^3 + p_3 t^2 + p_2 t + p_1 \\
y^{(3)} &= \widehat{y}^{(3)} + q_4 t^4 + q_3 t^3 + q_2 t^2 + q_1 t + q_0 \\
y^{(4)} &= \widehat{y}^{(4)} + r_3 t^3 + r_2 t^2 + r_1 t + r_0 \\
y^{(5)} &= \widehat{y}^{(5)} + s_4 t^4 + s_3 t^3 + s_2 t^2 + s_1 t + s_0
\end{aligned}
$$

where p_i, q_i, r_j, s_i, $i = 0,...,4$, $j = 0,...,3$, are real constants depending on the unknown initial conditions.

Finally, the differential flatness based GPI controller is obtained by replacing the actual time derivatives of the flat output in (19) by their structural estimates in (20) but using additional iterated integral error compensations as follows

$$
\begin{aligned}
\ddot{u} + \omega^2 u &= d_4^{-1} v + d_4^{-1} \left(d_1 \widehat{y}^{(4)} + d_2 \widehat{\ddot{y}} + d_3 y \right) \\
v &= y^{*(6)} - \alpha_{10} \left[\widehat{y^{(5)}} - y^{*(5)} \right] - \alpha_9 \left[\widehat{y^{(4)}} - y^{*(4)} \right] - \alpha_8 \left[\widehat{y^{(3)}} - y^{*(3)} \right] \\
&\quad - \alpha_7 \left[\widehat{\ddot{y}} - \ddot{y}^* \right] - \alpha_6 \left[\widehat{\dot{y}} - \dot{y}^* \right] - \alpha_5 \left[y - y^* \right] \\
&\quad - \alpha_4 \xi_1 - \alpha_3 \xi_2 - \alpha_2 \xi_3 - \alpha_1 \xi_4 - \alpha_0 \xi_5 \\
\dot{\xi}_1 &= y - y^*, \quad \xi_1(0) = 0 \\
\dot{\xi}_2 &= \xi_1, \qquad \xi_2(0) = 0 \\
\dot{\xi}_3 &= \xi_2, \qquad \xi_3(0) = 0 \\
\dot{\xi}_4 &= \xi_3, \qquad \xi_4(0) = 0 \\
\dot{\xi}_5 &= \xi_4, \qquad \xi_5(0) = 0
\end{aligned}
\tag{21}
$$

This feedback and feedforward active vibration controller depends on the measurements of the flat output y and the excitation frequency ω, therefore, this dynamic controller can compensate simultaneously two harmonic components, corresponding to the tuned (passive) vibration absorber (ω_2) and the actual excitation frequency (ω).

The closed-loop system dynamics, expressed in terms of the tracking error $e = y - y^*(t)$, is described by

$$
\begin{aligned}
&e^{(11)} + \alpha_{10}e^{(10)} + \alpha_9 e^{(9)} + \alpha_8 e^{(8)} + \alpha_7 e^{(7)} + \alpha_6 e^{(6)} + \alpha_5 e^{(5)} + \alpha_4 e^{(4)} \\
&+ \alpha_3 e^{(3)} + \alpha_2 \ddot{e} + \alpha_1 \dot{e} + \alpha_0 e = 0
\end{aligned}
\tag{22}
$$

Therefore, the design parameters α_i, $i = 0, ..., 10$, have to be selected such that the associated characteristic polynomial for (22) be *Hurwitz*, thus guaranteeing the desired asymptotic output tracking when one can measure the excitation frequency ω.

3.2.1 Robustness with respect to external vibrations

Fig. 4 shows the frequency response of the closed-loop system, using an active vibration absorber based on differential flatness and measurements of y and ω. Note that this active
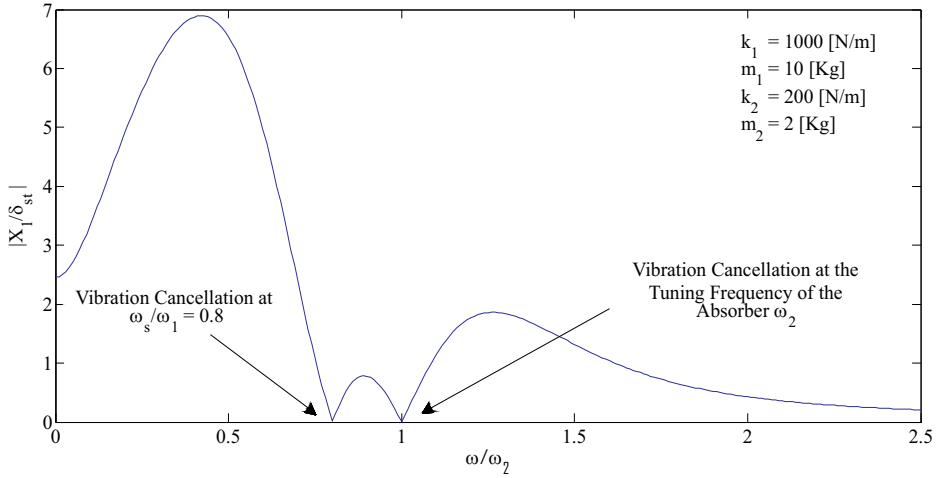
Fig. 4. Frequency response of the vibrating mechanical system using the active vibration absorber with controller (21).

vibration absorber employs the measurement of the excitation frequency ω and, therefore, such harmonic vibrations can always be cancelled (i.e., $X_1 = 0$). Moreover, this absorber is also useful to eliminate vibrations of the form $f(t) = F_0 \left[\sin(\omega_s t) + \sin(\omega_2 t) \right]$, where ω_s is the measured frequency (affecting the feedforward control action) and ω_2 is the design frequency of the passive absorber.

3.3 Simulation results

Some numerical simulations were performed on a vibrating mechanical platform from *Educational Control Products (ECP), model 210/210a Rectilinear Control System*, characterized by the set of system parameters given in Table 1.

The controllers (11) and (21) were specified in such a way that one could prove how the active vibration absorber cancels the two harmonic vibrations affecting the primary system and the asymptotic output tracking of the desired reference trajectory.

$m_1 = 10\text{kg}$	$m_2 = 2\text{kg}$
$k_1 = 1000\frac{\text{N}}{\text{m}}$	$k_2 = 200\frac{\text{N}}{\text{m}}$
$c_1 \approx 0\frac{\text{N}}{\text{m/s}}$	$c_2 \approx 0\frac{\text{N}}{\text{m/s}}$

Table 1. System parameters for the primary and secondary systems.

The planned trajectory for the flat output $y = z_1$ is given by

$$y^*(t) = \begin{cases} 0 & \text{for } 0 \leq t < T_1 \\ \psi(t, T_1, T_2)\,\bar{y} & \text{for } T_1 \leq t \leq T_2 \\ \bar{y} & \text{for } t > T_2 \end{cases}$$

where $\bar{y} = 0.01\text{m}$, $T_1 = 5\text{s}$, $T_2 = 10\text{s}$ and $\psi(t, T_1, T_2)$ is a Bézier polynomial, with $\psi(T_1, T_1, T_2) = 0$ and $\psi(T_2, T_1, T_2) = 1$, described by

$$\psi(t) = \left(\frac{t - T_1}{T_2 - T_1}\right)^5 \left[r_1 - r_2\left(\frac{t - T_1}{T_2 - T_1}\right) + r_3\left(\frac{t - T_1}{T_2 - T_1}\right)^2 - \dots - r_6\left(\frac{t - T_1}{T_2 - T_1}\right)^5 \right]$$

with $r_1 = 252$, $r_2 = 1050$, $r_3 = 1800$, $r_4 = 1575$, $r_5 = 700$, $r_6 = 126$.

Fig. 5 shows the dynamic behavior of the closed-loop system with the controller (11). One can observe the vibration cancellation on the primary system and the output tracking of the pre-specified reference trajectory. The controller gains were chosen so that the characteristic polynomial of the closed-loop tracking error dynamics (12) is a *Hurwitz* polynomial given by

$$p_{d1}(s) = (s + p_1)\left(s^2 + 2\zeta_1\omega_{n1}s + \omega_{n1}^2\right)^3$$

with $\zeta_1 = 0.5$, $\omega_{n1} = 12\text{rad/s}$, $p_1 = 6$.
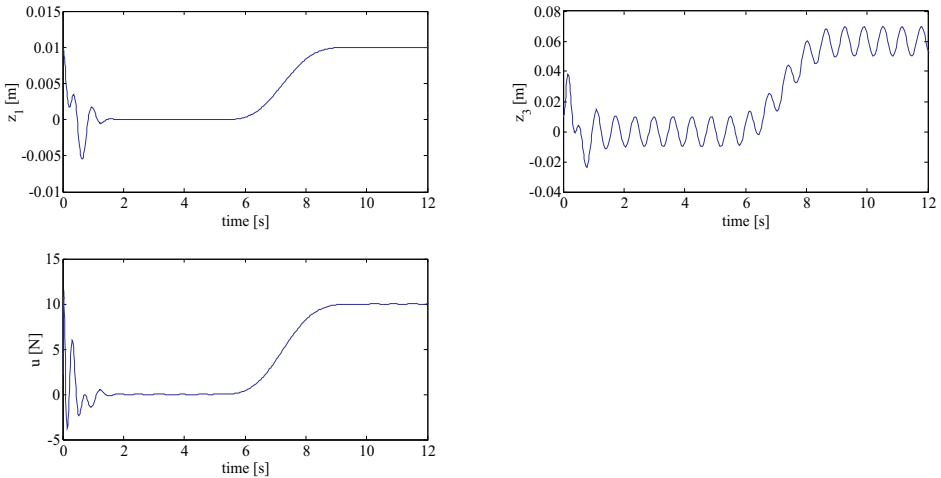
Fig. 5. Active vibration absorber using measurements of y and ω for harmonic vibration $f = 2\sin(10t)\,\text{N}$.

Fig. 6 shows the robust performance of closed-loop system employing the controller (21). One can see that the active vibration absorber eliminates vibrations containing two different harmonics. The design parameters were selected to have a sixth order closed-loop characteristic polynomial

$$p_{d2}(s) = (s + p_2)\left(s^2 + 2\zeta_2\omega_{n2}s + \omega_{n2}^2\right)^5$$

with

$$\zeta_2 = 0.5, \quad \omega_{n2} = 10\,\text{rad/s}, \quad p_2 = 5.$$
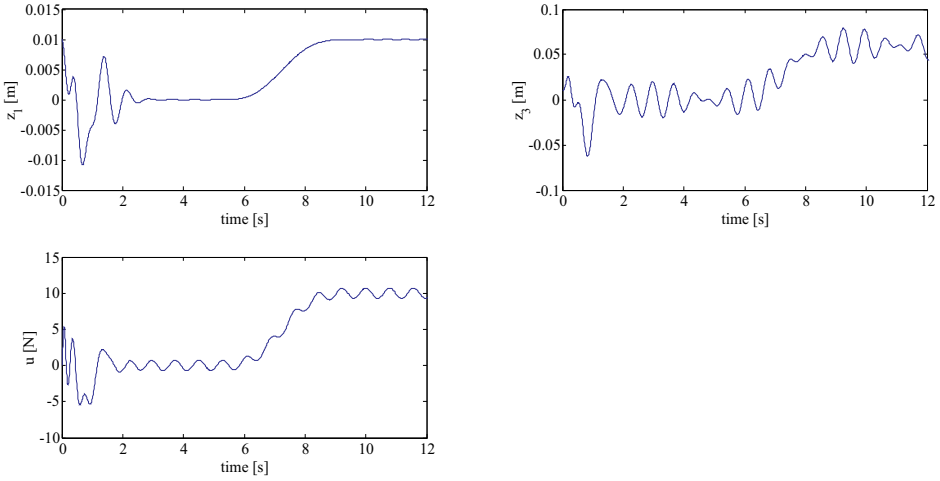
Fig. 6. Active vibration absorber using measurements of y and ω, for external vibration $f = 2\left[\sin\left(8.0109t\right) + \sin\left(10t\right)\right]$ N.

4. Algebraic identification of harmonic vibrations

The algebraic identification methodology (Fliess & Sira-Ramirez, 2003) can be applied to estimate the parameters associated to exogenous harmonic vibrations affecting a mechanical vibrating system (Beltran et al., 2004).

To do that, consider the input-output differential equation (16), where only displacement measurements of the primary system $y = z_1$ and the control input u are available for the identification process of the parameters associated with the harmonic signal $f(t) = F_0 \sin \omega t$, that is,

$$y^{(4)} = -\frac{k_1 k_2}{m_1 m_2}y - \left(\frac{k_1 + k_2}{m_1} + \frac{k_2}{m_2}\right)\ddot{y} + \left(\frac{k_2}{m_1 m_2} - \frac{\omega^2}{m_1}\right)F_0 \sin \omega t + \frac{k_2}{m_1 m_2}u \qquad (23)$$

Next we will proceed to synthesize two algebraic identifiers for the excitation frequency ω and amplitude F_0.

4.1 Identification of the excitation frequency ω

The differential equation (23) is expressed in notation of operational calculus as

$$
m_1 s^4 Y(s) + \left(k_1 + k_2 + \frac{m_1 k_2}{m_2} \right) s^2 Y(s) + \frac{k_1 k_2}{m_2} Y(s)
$$

$$
= \frac{k_2}{m_2} U(s) + \left(\frac{k_2}{m_2} - \omega^2 \right) F_0 \frac{\omega}{s^2 + \omega^2} + a_3 s^3 + a_2 s^2 + a_1 s + a_0 \tag{24}
$$

where a_i, $i = 0,...,3$, denote unknown real constants depending on the system initial conditions. Now, equation (24) is multiplied by $\left(s^2 + \omega^2 \right)$, leading to

$$
\left(s^2 + \omega^2 \right) \left[\left(s^4 Y + \frac{k_2}{m_2} s^2 Y \right) m_1 + \left(s^2 Y + \frac{k_2}{m_2} Y \right) k_1 + k_2 s^2 Y \right]
$$

$$
= \frac{k_2}{m_2} \left(s^2 + \omega^2 \right) u + \left(\frac{k_2}{m_2} - \omega^2 \right) F_0 \omega + \left(s^2 + \omega^2 \right) \left(a_3 s^3 + a_2 s^2 + a_1 s + a_0 \right) \tag{25}
$$

This equation is then differentiated six times with respect to s, in order to eliminate the constants a_i and the unknown amplitude F_0. The resulting equation is then multiplied by s^{-6} to avoid differentiations with respect to time in time domain, and next transformed into the time domain, to get

$$
\left[a_{11}(t) + \omega^2 a_{12}(t) \right] m_1 + \left[a_{12}(t) + \omega^2 b_{12}(t) \right] k_1 = c_1(t) + \omega^2 d_1(t) \tag{26}
$$

where $\Delta t = t - t_0$ and

$$
a_{11}(t) = m_2 g_{11}(t) + k_2 g_{12}(t)
$$

$$
a_{12}(t) = m_2 g_{12}(t) + k_2 g_{13}(t)
$$

$$
b_{12}(t) = m_2 g_{13}(t) + k_2 \int_{t_0}^{(6)} (\Delta t)^6 z_1
$$

$$
c_1(t) = k_2 g_{14}(t) - k_2 m_2 g_{12}(t)
$$

$$
d_1(t) = k_2 \int_{t_0}^{(6)} (\Delta t)^6 u - k_2 m_2 g_{13}(t)
$$

with

$$
g_{11}(t) = 720 \int_{t_0}^{(6)} y - 4320 \int_{t_0}^{(5)} (\Delta t)\, y + 5400 \int_{t_0}^{(4)} (\Delta t)^2 y - 2400 \int_{t_0}^{(3)} (\Delta t)^3 y
$$

$$
+ 450 \int_{t_0}^{(2)} (\Delta t)^4 y - 36 \int_{t_0} (\Delta t)^5 y + (\Delta t)^6 y
$$

$$
g_{12}(t) = 360 \int_{t_0}^{(6)} (\Delta t)^2 y - 480 \int_{t_0}^{(5)} (\Delta t)^3 y + 180 \int_{t_0}^{(4)} (\Delta t)^4 y
$$

$$
- 24 \int_{t_0}^{(3)} (\Delta t)^5 y + \int_{t_0}^{(2)} (\Delta t)^6 y
$$

$$g_{13}(t) = 30 \int_{t_0}^{(6)} (\Delta t)^4 \, y - 12 \int_{t_0}^{(5)} (\Delta t)^5 \, y + \int_{t_0}^{(4)} (\Delta t)^6 \, y$$

$$g_{14}(t) = 30 \int_{t_0}^{(6)} (\Delta t)^4 \, u - 12 \int_{t_0}^{(5)} (\Delta t)^5 \, u + \int_{t_0}^{(4)} (\Delta t)^6 \, u$$

Finally, solving for the excitation frequency ω in (26) leads to the following on-line algebraic identifier:

$$\omega_e^2 = \frac{N_1(t)}{D_1(t)} = \frac{c_1(t) - a_{11}(t)\, m_1 - a_{12}(t)\, k_1}{a_{12}(t)\, m_1 + b_{12}(t)\, k_1 - d_1(t)} \tag{27}$$

This estimation is valid if and only if the condition $D_1(t) \neq 0$ holds in a sufficiently small time interval $(t_0, t_0 + \delta_0]$ with $\delta_0 > 0$. This nonsingularity condition is somewhat similar to the well-known persistent excitation property needed by most of the asymptotic identification methods (Isermann & Munchhof, 2011; Ljung, 1987; Soderstrom, 1989). In particular, this obstacle can be overcome by using numerical resetting algorithms or further integrations on $N_1(t)$ and $D_1(t)$ (Sira-Ramirez et al., 2008).

4.2 Identification of the amplitude F_0

To synthesize an algebraic identifier for the amplitude F_0 of the harmonic vibrations acting on the mechanical system, the input-output differential equation (23) is expressed in notation of operational calculus as follows

$$m_1 s^4 Y(s) + \left(k_1 + k_2 + \frac{m_1 k_2}{m_2} \right) s^2 Y(s) + \frac{k_1 k_2}{m_2} Y(s)$$

$$= \frac{k_2}{m_2} U(s) + \left(\frac{k_2}{m_2} - \omega^2 \right) F(s) + a_3 s^3 + a_2 s^2 + a_1 s + a_0 \tag{28}$$

Taking derivatives, four times, with respect to s makes possible to remove the dependence on the unknown constants a_i. The resulting equation is then multiplied by s^{-4}, and next transformed into the time domain, to get

$$m_1 P_1(t) + \left(k_1 + k_2 + \frac{m_1 k_2}{m_2} \right) P_2(t) + \frac{k_1 k_2}{m_2} \int_{t_0}^{(4)} (\Delta t)^4 \, z_1$$

$$= \frac{k_2}{m_2} \int_{t_0}^{(4)} (\Delta t)^4 \, u + F_0 \left(\frac{k_2}{m_2} - \omega^2 \right) \int_{t_0}^{(4)} (\Delta t)^4 \sin \omega t \tag{29}$$

where

$$P_1(t) = 24 \int_{t_0}^{(4)} z_1 - 96 \int_{t_0}^{(3)} (\Delta t) \, z_1 + 72 \int_{t_0}^{(2)} (\Delta t)^2 \, z_1 - 16 \int_{t_0} (\Delta t)^3 \, z_1 + (\Delta t)^4 \, z_1$$

$$P_2(t) = 12 \int_{t_0}^{(4)} (\Delta t)^2 \, z_1 - 8 \int_{t_0}^{(3)} (\Delta t)^3 \, z_1 + \int_{t_0}^{(2)} (\Delta t)^4 \, z_1$$

It is important to note that equation (29) still depends on the excitation frequency ω, which can be estimated from (27). Therefore, it is required to synchronize both algebraic identifiers for ω and F_0. This procedure is sequentially executed, first by running the identifier for ω and, after some small time interval with the estimation $\omega_e(t_0 + \delta_0)$ is then started the algebraic identifier

for F_0, which is obtained by solving

$$N_2(t) - D_2(t)F_0 = 0 \tag{30}$$

where

$$N_2(t) = m_1 P_1(t) + \left(k_1 + k_2 + \frac{m_1 k_2}{m_2} \right) P_2(t) + \frac{k_1 k_2}{m_2} \int_{t_0+\delta_0}^{(4)} (\Delta t)^4 z_1 - \frac{k_2}{m_2} \int_{t_0+\delta_0}^{(4)} (\Delta t)^4 u$$

$$D_2(t) = \left(\frac{k_2}{m_2} - \omega_e^2 \right) \int_{t_0+\delta_0}^{(4)} (\Delta t)^4 \sin[\omega_e(t_0+\delta_0)t]$$

In this case if the condition $D_2(t) \neq 0$ is satisfied for all $t \in (t_0 + \delta_0, t_0 + \delta_1]$ with $\delta_1 > \delta_0 > 0$, then the solution of (30) yields an algebraic identifier for the excitation amplitude

$$F_{0e} = \frac{N_2(t)}{D_2(t)}, \ \ \forall t \in (t_0 + \delta_0, t_0 + \delta_1] \tag{31}$$

4.3 Adaptive-like active vibration absorber for unknown harmonic forces

The active vibration control scheme (21), based on the differential flatness property and the GPI controller, can be combined with the on-line algebraic identification of harmonic vibrations (27) and (31), where the estimated harmonic force is computed as

$$f_e(t) = F_{0e} \sin(\omega_e t) \tag{32}$$

resulting some certainty equivalence feedback/feedforward control law. Note that, according to the algebraic identification approach, providing fast identification for the parameters associated to the harmonic vibration (F_0, ω) and, as a consequence, a fast estimation of this perturbation signal, the proposed controller is similar to an adaptive control scheme. From a theoretical point of view, the algebraic identification is instantaneous (Fliess & Sira-Ramirez, 2003). In practice, however, there are modelling errors and many other factors that complicate the real-time algebraic computation. Fortunately, the identification algorithms and closed-loop system are robust against such difficulties.

4.4 Simulation results

Fig. 7 shows the identification process of the excitation frequency of the resonant harmonic perturbation $f(t) = 2\sin(8.0109t)$ N and the robust performance of the adaptive-like control scheme (21) for reference trajectory tracking tasks, which starts using the nominal frequency value $\omega = 10\text{rad/s}$, which corresponds to the known design frequency for the passive vibration absorber, and at $t > 0.1$s this controller uses the estimated value of the resonant excitation frequency. Here it is clear how the frequency identification is quickly performed (before $t = 0.1$s and it is almost exact with respect to the actual value.

One can also observe that, the resonant vibrations affecting the primary mechanical system are asymptotically cancelled from the primary system response in a short time interval. It is also evident the presence of some singularities in the algebraic identifier, i.e., when its denominator $D_1(t)$ is zero. The first singularity, however, occurs about $t = 0.727$s, which is too much time (more than 7 times) after the identification has been finished.

Fig. 8 illustrates the fast and effective performance of the on-line algebraic identifier for the amplitude of the harmonic force $f(t) = 2\sin(8.0109t)$ N. First of all, it is started the identifier for ω, which takes about $t < 0.1$s to get a good estimation. After the time interval $(0, 0.1]$s, where $t_0 = 0$s and $\delta_0 = 0.1$s with an estimated value $\omega_e(t_0 + \delta_0) = 8.0108$rad/s, it is activated the identifier for the amplitude F_0.
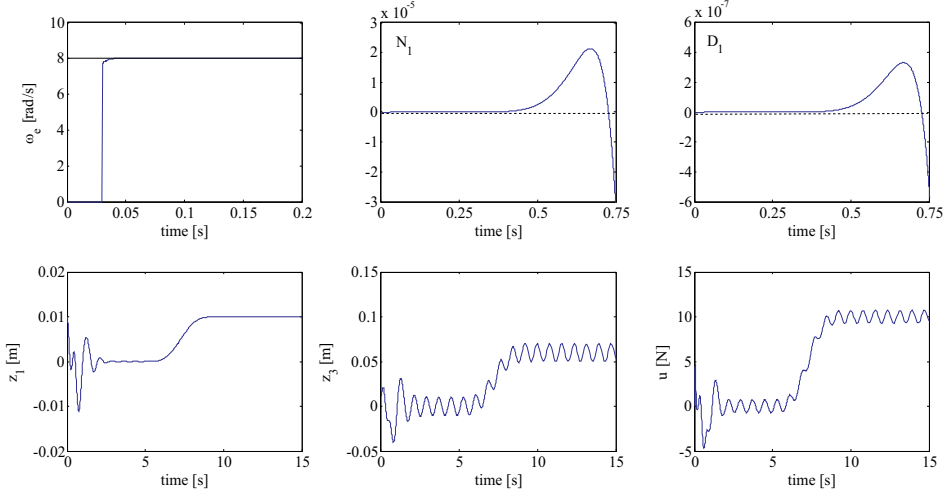
Fig. 7. Controlled system responses and identification of frequency for $f(t) = 2\sin(8.0109t)$ [N].
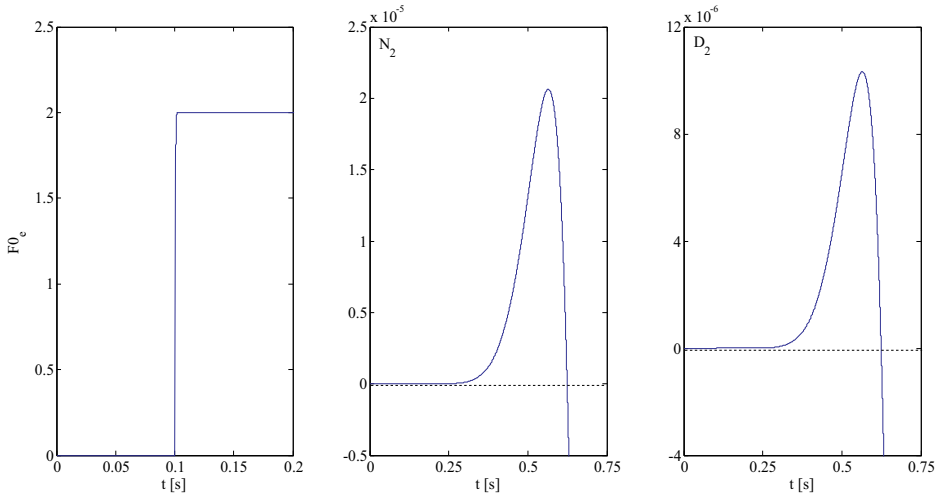
Fig. 8. Identification of amplitude for $f(t) = 2\sin(8.0109t)$ [N].

One can also observe that the first singularity occurs when the numerator $N_2(t)$ and denominator $D_2(t)$ are zero. However the first singularity is presented about $t = 0.702$s, and therefore the identification process is not affected.

Now, Figs. 9 and 10 present the robust performance of the on-line algebraic identifiers for the excitation frequency ω and amplitude F_0. In this case, the primary system was forced by external vibrations containing two harmonics, $f(t) = 2\left[\sin\left(8.0109t\right) + 10\sin\left(10t\right)\right]$ N. Here, the frequency $\omega_2 = 10\,$rad/s corresponds to the known tuning frequency of the passive vibration absorber, which does not need to be identified. Once again, one can see the fast and effective estimation of the resonant excitation frequency $\omega = 8.0109\,$rad/s and amplitude $F_0 = 2$N as well as the robust performance of the proposed active vibration control scheme (21) based on differential flatness and GPI control, which only requires displacement measurements of the primary system and information of the estimated excitation frequency.
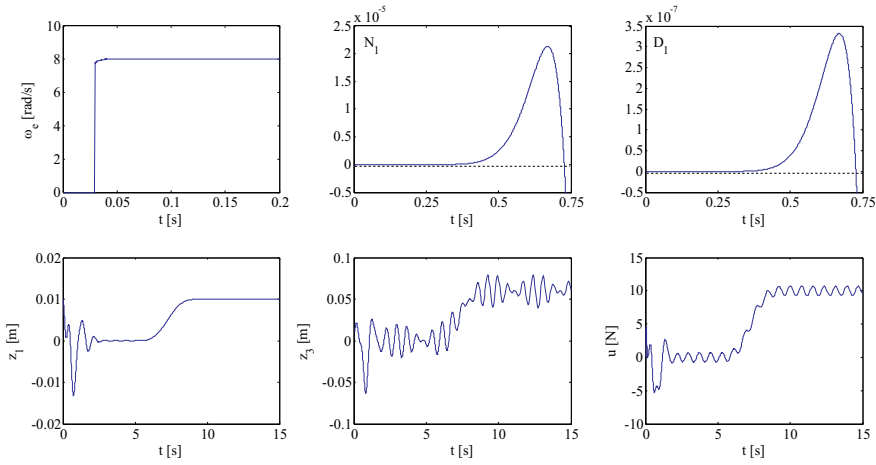
Fig. 9. Controlled system responses and identification of the unknown resonant frequency for $.f(t) = 2\left[\sin\left(8.0109t\right) + 10\sin\left(10t\right)\right]$ [N].
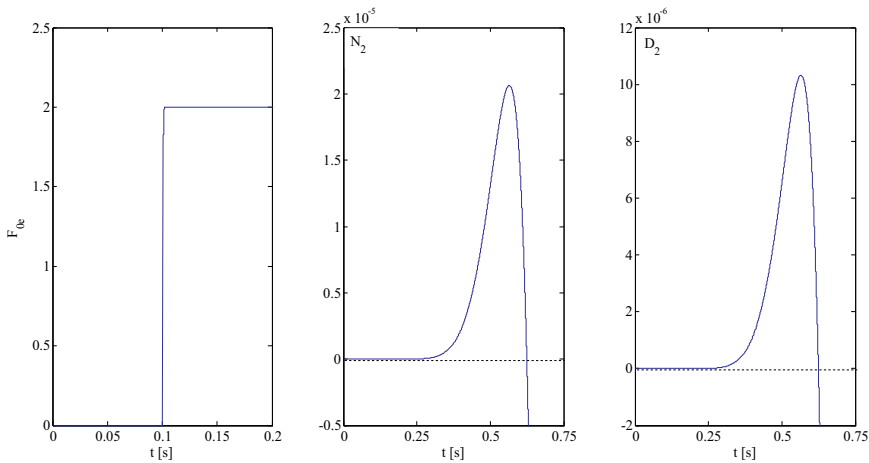
Fig. 10. Identification of amplitude for $f(t) = 2\left[\sin\left(8.0109t\right) + 10\sin\left(10t\right)\right]$ [N].

5. Conclusions

In this chapter we have described the design approach of a robust active vibration absorption scheme for vibrating mechanical systems based on passive vibration absorbers, differential flatness, GPI control and on-line algebraic identification of harmonic forces.

The proposed adaptive-like active controller is useful to completely cancel any harmonic force, with unknown amplitude and excitation frequency, and to improve the robustness of passive/active vibrations absorbers employing only displacement measurements of the primary system and small control efforts. In addition, the controller is also able to asymptotically track some desired reference trajectory for the primary system.

In general, one can conclude that the adaptive-like vibration control scheme results quite fast and robust in presence of parameter uncertainty and variations on the amplitude and excitation frequency of harmonic perturbations.

The methodology can be applied to rotor-bearing systems and some classes of nonlinear mechanical systems.

6. References

Beltran-Carbajal, F., Silva-Navarro, G. & Sira-Ramirez, H. (2003). Active Vibration Absorbers Using Generalized PI and Sliding-Mode Control Techniques, *Proceedings of the American Control Conference 2003*, pp. 791-796, Denver, CO, USA.

Beltran-Carbajal, F., Silva-Navarro, G. & Sira-Ramirez, H. (2004). Application of On-line Algebraic Identification in Active Vibration Control, *Proceedings of the International Conference on Noise & Vibration Engineering 2004*, pp. 157-172, Leuven, Belgium, 2004.

Beltran-Carbajal, F., Silva-Navarro, G., Sira-Ramirez, H., Blanco-Ortega, A. (2010). Active Vibration Control Using On-line Algebraic Identification and Sliding Modes, *Computación y Sistemas*, Vol. 13, No. 3, pp. 313-330.

Braun, S.G., Ewins, D.J. & Rao, S.S. (2001). *Encyclopedia of Vibration*, Vols. 1-3, Academic Press, San Diego, CA.

Caetano, E., Cunha, A., Moutinho, C. & Magalhães, F. (2010). Studies for controlling human-induced vibration of the Pedro e Inês footbridge, Portugal. Part 2: Implementation of tuned mass dampers, *Engineering Structures*, Vol. 32, pp. 1082-1091.

Den Hartog, J.P. (1934). *Mechanical Vibrations*, McGraw-Hill, NY.

Fliess, M., Lévine, J., Martin, P. & Rouchon, P. (1993). Flatness and defect of nonlinear systems: Introductory theory and examples, *International Journal of Control*, Vol. 61(6), pp. 1327-1361.

Fliess, M., Marquez, R., Delaleau, E. & Sira-Ramirez, H. (2002). Correcteurs Proportionnels-Integraux Généralisés, *ESAIM Control, Optimisation and Calculus of Variations*, Vol. 7, No. 2, pp. 23-41.

Fliess, M. & Sira-Ramirez, H. (2003). An algebraic framework for linear identification, *ESAIM: Control, Optimization and Calculus of Variations*, Vol. 9, pp. 151-168.

Fuller, C.R., Elliot, S.J. & Nelson, P.A. (1997). *Active Control of Vibration*, Academic Press, San Diego, CA.

Isermann, R. & Munchhpf, M. (2011). *Identification of Dynamic Systems*, Springer-Verlag, Berlin.

Isidori, A. (1995). *Nonlinear Control Systems*, Springer-Verlag, NY.

Ljung, L. (1987). *Systems Identification: Theory for the User*, Prentice-Hall, Englewood Cliffs, NJ.

Korenev, B.G. & Reznikov, L.M. (1993). *Dynamic Vibration Absorbers: Theory and Technical Applications*, Wiley, London.

Preumont, A. (2002). *Vibration Control of Active Structures: An Introduction*, Kluwer, Dordrecht, 2002.

Rao, S.S. (1995). *Mechanical Vibrations*, Addison-Wesley, NY.

Sira-Ramirez, H. & Agrawal, S.K. (2004). *Differentially Flat Systems*, Marcel Dekker, NY.

Sira-Ramirez, H., Beltran-Carbajal, F. & Blanco-Ortega, A. (2008). A Generalized Proportional Integral Output Feedback Controller for the Robust Perturbation Rejection in a Mechanical System, *e-STA*, Vol. 5, No. 4, pp. 24-32.

Soderstrom, T. & Stoica, P. (1989). *System Identification*, Prentice-Hall, NY.

Sun, J.Q., Jolly, M.R., & Norris, M.A. (1995). Passive, adaptive and active tuned vibration absorbers Ű a survey. *In: Transaction of the ASME, 50th anniversary of the design engineering division*, Vol. 117, pp. 234Ű42.

Taniguchi, T., Der Kiureghian, A. & Melkumyan, M. (2008). Effect of tuned mass damper on displacement demand of base-isolated structures, *Engineering Structures*, Vol. 30, pp. 3478-3488.

Weber, B. & Feltrin, G. (2010). Assessment of long-term behavior of tuned mass dampers by system identification. *Engineering Structures*, Vol. 32, pp. 3670-3682.

Wright, R.I. & Jidner, M.R.F. (2004). Vibration Absorbers: A Review of Applications in Interior Noise Control of Propeller Aircraft, *Journal of Vibration and Control*, Vol. 10, pp. 1221-1237.

Yang, Y., Muñoa, J., & Altintas, Y. (2010). Optimization of multiple tuned mass dampers to suppress machine tool chatter, *International Journal of Machine Tools & Manufacture*, Vol. 50, pp. 834-842.

Seismic Response Reduction of Eccentric Structures Using Liquid Dampers

Linsheng Huo and Hongnan Li
Dalian University of Technology
China

1. Introduction

The installation of vibration absorbers on tall buildings or other flexible structures can be a successful method for reducing the effects of dynamic excitations, such as wind or earthquake, which may exceed either serviceability or safety criteria. Tuned liquid column damper (TLCD) is an effective passive control device by the motion of liquid in a column container. The potential advantages of liquid vibration absorbers include: low manufacturing and installation costs; the ability of the absorbers to be incorporated during the design stage of a structure, or to be retrofitted to serve a remedial role; relatively low maintenance requirements; and the availability of the liquid to be used for emergency purposes, or for the everyday function of the structure if fresh water is used (Hitchcock et al., 1997a, 1997b).

A TLCD is a U-shaped tube of uniform rectangular or circle cross-section, containing liquid. Vibration energy is transferred from the structure to the TLCD liquid through the motion of the rigid container exciting the TLCD liquid. And the vibration of a structure is suppressed by a TLCD through the gravitational restoring force acting on the displaced TLCD liquid and the energy is dissipated by the viscous interaction between the liquid and the rigid container, as well as liquid head loss due to orifices installed inside the TLCD container.

Analytical and experimental researches on this type of vibration reduction approach has been conducted, in which viscous interaction between a liquid and solid boundary has been investigated and used to control vibration (Sakai et al., 1989; Qu et al., 1993). Their experiments, defining the relationship between the coefficient of liquid head loss (as well as its dependence on the orifice opening ratio) and the liquid damping, confirms the validity of their proposed equation of motion in describing liquid column relative motion under moderate excitation. A variation of TLCD, called a liquid column vibration absorber (LCVA) has also been investigated, which has different cross sectional areas in its vertical and horizontal sections depending on performance requirements (Gao and Kwok, 1997; Yan et al., 1998; Chang and Hsu, 1998; Chang 1999). Yan et al. presented the adjustable frequency tuned liquid column damper by adding springs to the TLCD system, which modified the frequency of TLCD and expended its application ranges (Yan and Li, 1999).

Multiple tuned mass damper (MTMD) which consists of a number of tuned mass damper whose natural frequencies are distributed over a certain range around the fundamental frequency of the structure has been proposed and investigated (Kareem and Kline, 1995). The results showed that an optimized MTMD can be more efficient than a single optimized TMD and the sensitivity of a MTMD to the tuning ratio is diminished. A multiple tuned

liquid damper (MTLD) system is investigated by Fujino and Sun(Fujino and Sun, 1993). They found that in situations involving small amplitude liquid motion the MTLD has similar characteristics to that of a MTMD including more effectiveness and less sensitivity to the frequency ratio. However, in a large liquid motion case, the MTLD is not much more effective than a single optimized TLD and a MTLD has almost the same effectiveness as a single TLD when breaking waves occur. Gao et al analyzed the characteristics of multiple liquid column dampers (both U-shaped and V-shaped types) (Gao et al., 1999). It was found that the frequency of range and the coefficient of liquid head loss have significant effects on the performance of a MTLCD; increasing the number of TLCD can enhance the efficiency of MTLCD, but no further significant enhancement is observed when the number of TLCD is over five. It was also confirmed that the sensitivity of an optimized MTLCD to its central frequency ratio is not much less than that of an optimized single TLCD to its frequency ratio, and an optimized MTLCD is even more sensitive to the coefficient of head loss.

2. Circular Tuned Liquid Dampers

Circular Tuned Liquid Column Dampers (CTLCD) is a type of damper that can control the torsional response of structures (Jiang and Tang, 2001). The results of free vibration and forced vibration experiments showed that it is effective to control structural torsional response (Hochrainer et al., 2000), but how to determine the parameters of CTLCD to effectively reduce torsionally coupled vibration is still necessary to be further investigated. In this section, the optimal parameters of CLTCD for vibration control of structures are presented based on the stochastic vibration theory.

2.1 Equation of motion for control system

The configuration of CTLCD is shown in Fig.1. Through Lagrange principle, the equation of motion for CTLCD excited by seismic can be derived as

$$\rho A \left(2H + 2\pi R \right) \ddot{h} + \frac{1}{2} \rho A \xi \left| \dot{h} \right| \dot{h} + 2\rho A g h = -2\rho A\pi R^2 \left(\ddot{u}_\theta + \ddot{u}_{g\theta} \right) \tag{1}$$

where h is the relative displacement of liquid in CTLCD; ρ means the density of liquid; H denotes the height of liquid in the vertical column of container when the liquid is quiescent; A expresses the cross-sectional area of CTLCD; g is the gravity acceleration; R represents the radius of horizontal circular column; ξ is the head loss coefficient; $\ddot{u}_\theta$ denotes the torsional acceleration of structure; $\ddot{u}_{g\theta}$ is the torsional acceleration of ground motion.

Because the damping in the above equation is nonlinear, equivalently linearize it and the equation can be re-written as

$$m_T \ddot{h} + c_{Teq} \dot{h} + k_T h = -\alpha m_T R \left(\ddot{u}_\theta + \ddot{u}_{g\theta} \right) \tag{2}$$

where $m_T = \rho A L_{ee}$ is the mass of liquid in CTLCD; $L_{ee} = 2H + 2\pi R$ denotes the total length of liquid in the column; $c_{Teq} = 2m_T \omega_T \zeta_T$ is the equivalent damping of CTLCD; $\omega_T = \sqrt{2g / L_{ee}}$ is the natural circular frequency of CTLCD; $\zeta_T = \dfrac{\xi}{2\sqrt{\pi g L_{ee}}} \sigma_{\dot{h}}$ is equivalent linear damping ratio

(Wang, 1997); σ_h means the standard deviation of the liquid velocity; $k_T = 2\rho Ag$ is the "stiffness" of liquid in vibration; $\alpha = 2\pi R / L_{ee}$ is the configuration coefficient of CTLCD.
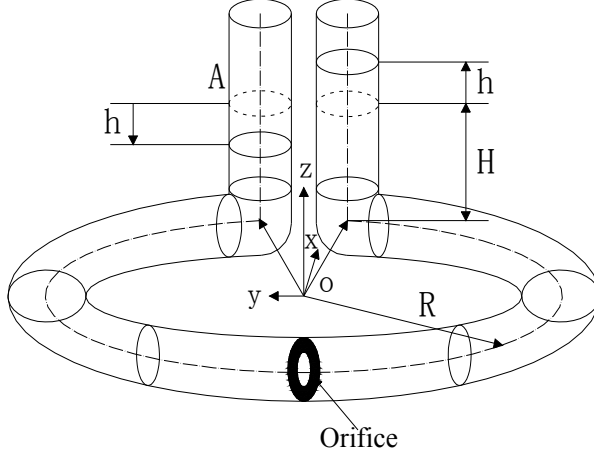
Fig. 1. Configuration of Circular TLCD

For a single-story offshore platform, the equation of torsional motion installed CTLCD can be written as

$$J_\theta \ddot{u}_\theta + c_\theta \dot{u}_\theta + k_\theta u_\theta = -J_\theta \ddot{u}_{\theta g} + F_\theta \tag{3}$$

where J_θ is the inertia moment of platform to vertical axis together with additional inertial moment of sea fluid; c_θ denotes the summation of damping of platform and additional damping caused by sea fluid; k_θ expresses the stiffness of platform; $\dot{u}_\theta$ and u_θ are velocity and displacement of platform, respectively; F_θ is the control force of CTLCD to offshore platform, given by

$$F_\theta = -m_T R \left(R\ddot{u}_\theta + R\ddot{u}_{g\theta} + \alpha \ddot{h} \right) \tag{4}$$

Combining equation (1) to (4) yields:

$$\begin{bmatrix} 1+\lambda & \alpha\lambda / R \\ \alpha\lambda / R & \lambda / R^2 \end{bmatrix} \begin{Bmatrix} \ddot{u}_\theta \\ \ddot{h} \end{Bmatrix} + \begin{bmatrix} 2\zeta_s \omega_\theta & 0 \\ 0 & 2\lambda\zeta_T \omega_T / R^2 \end{bmatrix} \begin{Bmatrix} \dot{u}_\theta \\ \dot{h} \end{Bmatrix} + \begin{bmatrix} \omega_\theta^2 & 0 \\ 0 & \lambda\omega_T^2 / R^2 \end{bmatrix} \begin{Bmatrix} u_\theta \\ h \end{Bmatrix} = -\begin{Bmatrix} 1+\lambda \\ \alpha\lambda / R \end{Bmatrix} \ddot{u}_{g\theta} \tag{5}$$

where $\lambda = \dfrac{m_T R^2}{J_\theta}$ denotes inertia moment ratio. Let $\ddot{u}_{g\theta}(t) = e^{i\omega t}$, then

$$\begin{Bmatrix} u_\theta \\ h \end{Bmatrix} = \begin{Bmatrix} H_\theta(\omega) \\ H_h(\omega) \end{Bmatrix} e^{i\omega t} \tag{6}$$

where $H_\theta(\omega)$ and $H_h(\omega)$ are transfer functions in the frequency domain. Substituting equation (6) into equation (5) leads to

$$\begin{bmatrix} -(1+\lambda)\omega^2 + 2\zeta_s\omega_\theta i\omega + \omega_\theta^2 & -\alpha\lambda\omega^2 / R \\ -\alpha\lambda\omega^2 / R & -\lambda\omega^2 / R^2 + 2\lambda\zeta_T\omega_T i\omega / R^2 + \lambda\omega_T^2 / R^2 \end{bmatrix} \cdot \begin{Bmatrix} H_\theta \\ H_h \end{Bmatrix} = -\begin{Bmatrix} 1+\lambda \\ \alpha\lambda / R \end{Bmatrix} \quad (7)$$

From the above equation, the transfer function of structural torsional response can be expressed by

$$H_\theta(\omega) = \frac{\left[\lambda(1+\lambda) - \alpha^2\lambda^2\right]\omega^2 - 2(1+\lambda)\lambda\zeta_T\omega_T i\omega - \lambda(1+\lambda)\omega_T^2}{\left[-(1+\lambda)\omega^2 + 2\zeta_\theta\omega_\theta i\omega + \omega_\theta^2\right]\left[-\lambda\omega^2 + 2\lambda\zeta_T\omega_T i\omega + \lambda\omega_T^2\right] - \alpha^2\lambda^2\omega^4} \quad (8)$$

Then, the torsional response variance of structure installed CTLCD can be obtained as

$$\sigma_{u_\theta}^2 = \int_{-\infty}^{\infty} |H_\theta|^2 S_{\ddot{u}_{g\theta}}(\omega) d\omega \quad (9)$$

If the ground motion is assumed to be a Gauss white noise random process with an intensity of S_0 and define the frequency ratio $\gamma = \omega_T / \omega_\theta$, the value of $\sigma_{u_\theta}^2$ can be calculated by

$$\sigma_{u_\theta}^2 = \frac{\pi S_0}{2\omega_\theta^3} \cdot$$

$$\cdot \frac{2(1+\lambda)^4\zeta_T\gamma^4 + 2A_1\zeta_\theta(1+\lambda)^2\gamma^3 + 2\zeta_T(1+\lambda)^2(2B_1+\alpha^2\lambda)\gamma^2 + 2C_1\zeta_\theta\gamma + 2\zeta_T(1+\lambda-\alpha^2\lambda)^2}{2(1+\lambda)^2\zeta_\theta\zeta_T\gamma^4 + 2A_1\zeta_\theta^2\gamma^3 + 4B_1\zeta_\theta\zeta_T\gamma^2 + 2D_1\zeta_T^2\gamma + 2\zeta_\theta\zeta_T} \quad (10)$$

where $A_1 = \alpha^2\lambda + 4\zeta_T^2(1+\lambda)$, $B_1 = (2\zeta_T^2 - 1)(1+\lambda) + 2\zeta_\theta^2 + \alpha^2\lambda$, $C_1 = 4\zeta_T^2(1+\lambda)^2 + \alpha^4\lambda^2$, $D_1 = 4\zeta_\theta^2 + \alpha^2\lambda$

2.2 Optimal parameters of circular tuned liquid column dampers

The optimal parameters of CTLCD should make the displacement variance of offshore platform $\sigma_{u_\theta}^2$ minimum, so the optimal parameters of CTLCD can be obtained according to the following condition

$$\frac{\partial \sigma_{u_\theta}^2}{\partial \zeta_T} = 0 \quad \frac{\partial \sigma_{u_\theta}^2}{\partial \gamma} = 0 \quad (11)$$

Neglecting the damping ratio of offshore platform ζ_θ and solving above equation, the optimal damping ratio ζ_T^{opt} and frequency ratio γ^{opt} for CTLCD can be formulized as

$$\zeta_T^{opt} = \frac{1}{2}\sqrt{\frac{\lambda\alpha^2(1+\lambda-\frac{5}{4}\lambda\alpha^2)}{(1+\lambda)(1+\lambda-\frac{3}{2}\lambda\alpha^2)}} \quad \gamma^{opt} = \frac{\sqrt{1+\lambda-\frac{3}{2}\lambda\alpha^2}}{1+\lambda} \quad (12)$$

Fig. 2 shows the optimal damping ratio ζ_T^{opt} and optimal frequency ratio γ^{opt} of CTLCD as a function of inertia moment ratio λ ranging between 0 to 5% for α =0.2, 0.4, 0.6 and 0.8. It can be seen that as the value of λ increases the optimal damping ratio ζ_T^{opt} increases and the optimal frequency ratio γ^{opt} decreases. For a given value of λ, the optimal damping ratio ζ_T^{opt} increases and the optimal frequency ratio decreases with the rise of α. It can also be seen that the value of γ^{opt} is always near 1 for different values of α and λ in Fig.2. If let $\gamma = 1$ and solve $\dfrac{\partial \sigma_\theta^2}{\partial \zeta_T} = 0$, the optimal damping ratio of CTLCD ζ_T^{opt} is obtained as

$$\zeta_T^{opt} = \frac{1}{2}\sqrt{\frac{\lambda^2(a^2+1+\lambda)+a^2\lambda(1+\lambda)^2}{(1+\lambda)^3}} \tag{13}$$
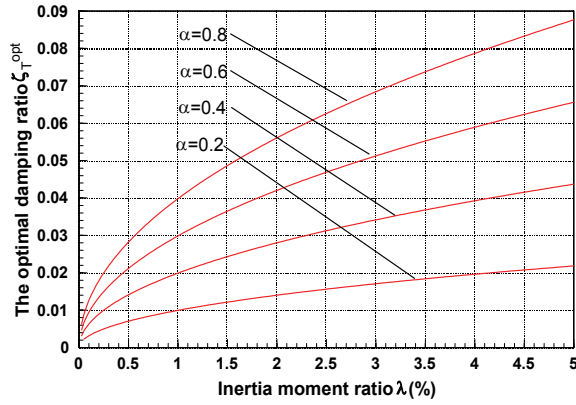
(a) The optimal damping ratio with inertia moment
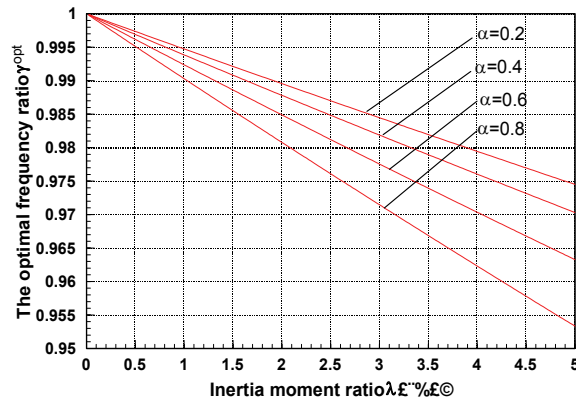
(b) The optimal frequency ratio with inertia moment

Fig. 2. The optimal parameters of CTLCD with inertia moment ratio λ

The optimal parameters of CTLCD cannot be expressed with formulas when considering the damping of offshore platform for the complexity of equation (10), so we can only get numerical results for different values of structural damping, as shown in Table 1. Table 1 shows that for different damping of platform system, the optimal damping ratio of CTLCD increases and the optimal frequency ratio decreases with the rise of λ, which is the same as Fig. 2. Table 1 also suggests the damping of platform has little effect on the optimal parameters of CTLCD, especially on the optimal damping ratio ζ_T^{opt}.

	$\zeta_\theta = 0$		$\zeta_\theta = 1\%$		$\zeta_\theta = 2\%$		$\zeta_\theta = 5\%$	
	γ^{opt}	ζ_T^{opt}	γ^{opt}	ζ_T^{opt}	γ^{opt}	ζ_T^{opt}	γ^{opt}	ζ_T^{opt}
$\lambda = 0.5\%$	0.9951	0.0282	0.9935	0.0283	0.9915	0.0283	0.9832	0.0283
$\lambda = 1\%$	0.9903	0.0398	0.9881	0.0398	0.9856	0.0398	0.9755	0.0398
$\lambda = 1.5\%$	0.9855	0.0487	0.9829	0.0487	0.9799	0.0487	0.9687	0.0487
$\lambda = 2\%$	0.9808	0.0561	0.9778	0.0561	0.9745	0.0561	0.9622	0.0561
$\lambda = 5\%$	0.9533	0.0876	0.9490	0.0877	0.9442	0.0877	0.9278	0.0877

Table 1. The optimal parameters of CLTCD ($\alpha = 0.8$)

2.3 Analysis of structural torsional response control using CTLCD

The objective of dampers installed in the offshore platform is to increase the damping of the structural system and reduce the response of structure. To analyze the effects of different system parameters on the torsional response of structure, the damping of a platform structure with CTLCD is expressed by equivalent damping ratio ζ_e (Wang, 1997):

$$\zeta_e = \frac{\pi S_0}{2\omega_\theta^3 \sigma_\theta^2} \tag{14}$$

The relationships between ζ_e and different parameters of control system are shown in Fig. 3 to Fig. 7.
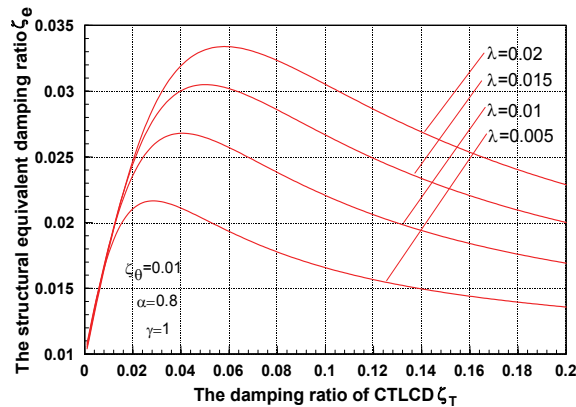

Fig. 3. The structural equivalent damping ratio with the damping ratio of CTLCD
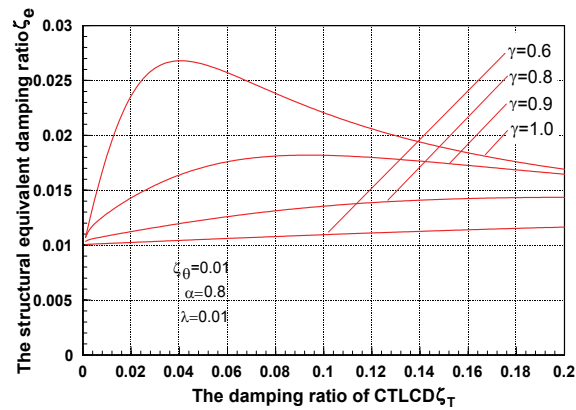
Fig. 4. The structural equivalent damping ratio with the damping ratio of CTLCD
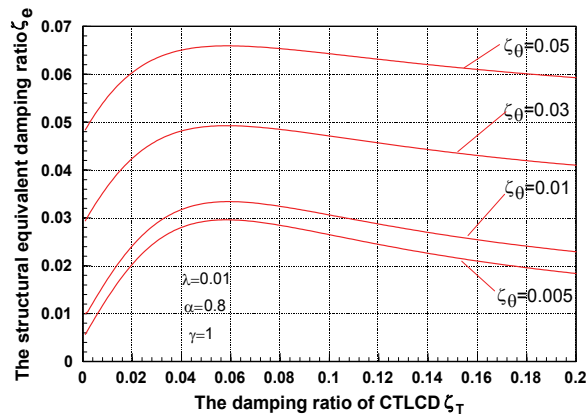

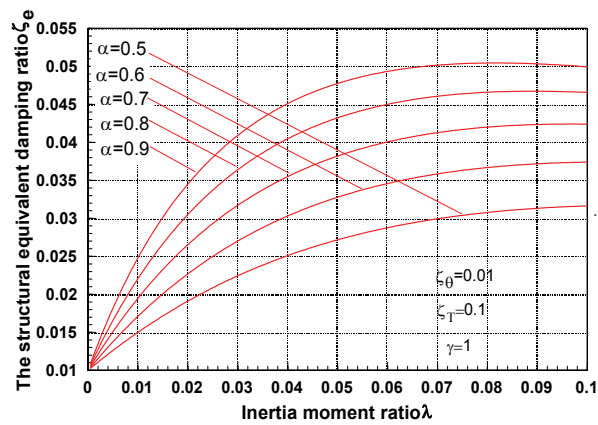Fig. 5. The structural equivalent damping ratio with the damping ratio of CTLCD

Fig. 6. The structural equivalent damping ratio with the inertia moment ratio

Fig. 3 shows the equivalent damping ratio of a platform structure ζ_e as a function of the damping ratio of CTLCD for λ =0.005, 0.01, 0.015, 0.02. It is seen from the figure that the equivalent damping ratio ζ_e increases rapidly with the increase of ζ_T initially, whereas it decreases if the damping ratio of CTLCD ζ_T is greater than a certain value.

Fig. 4 shows the equivalent damping ratio of a platform structure ζ_e as a function of the damping ratio of CTLCD for γ =0.6, 0.8, 0.9, 1.0. It is seen from the figure that the value of ζ_e increases with the rise of frequency ratio γ .

Fig. 5 shows the equivalent damping ratio of structure ζ_e as a function of the damping ratio of CTLCD for ζ_θ =0.005, 0.01, 0.03 and 0.05. It is seen from the figure that as the rise of the damping ratio of structure ζ_θ , the equivalent damping ratio ζ_e increases.

Fig. 6 shows the equivalent damping ratio of structure ζ_e as a function of λ for α =0.5, 0.6, 0.7, 0.8 and 0.9. It can be seen from the figure that the damping ratio of structure ζ_e increases with λ initially. Whereas, the curve of ζ_e with λ will be gentle when the value of λ is greater than a certain value. It can also be concluded from the figure that the damping ratio of structure ζ_e increases with the rise of configuration coefficient α .
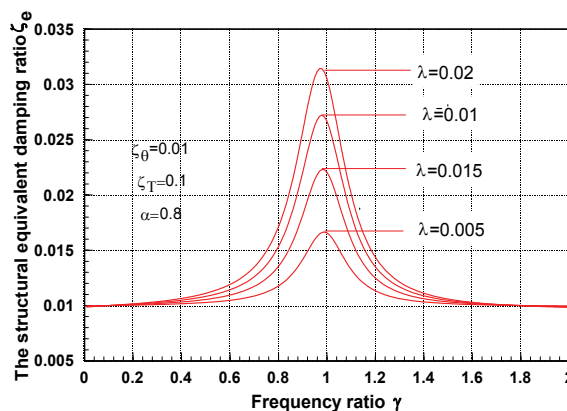
Fig. 7. The structural equivalent damping ratio with the frequency ratio

Fig. 7 shows the equivalent damping ratio of structure ζ_e as a function of frequency ratio between CTLCD and structure. It is seen from the figure that the value of ζ_e will be maximum at the condition of $\gamma = 1$. So, the value of γ can be set to approximate 1 in the engineering application to get the best control performance.

2.4 Structural torsionally coupled response control using CTLCD

The torsional response of structure is usually coupled with translational response in engineering, so it is necessary to consider torsionally coupled response for vibration control of eccentric platform structure. In this paper, a single-story structure only eccentric in x direction is taken as an example, which means that the displacement in y direction is coupled with the torsional response of platform. The equation of torsionally coupled motion for the eccentric platform installed CTLCD can be written as

$$\begin{bmatrix} m_s & 0 \\ 0 & m_s r^2 \end{bmatrix} \begin{Bmatrix} \ddot{u}_y \\ \ddot{u}_\theta \end{Bmatrix} + \begin{bmatrix} C_{11} & C_{12} \\ C_{21} & C_{22} \end{bmatrix} \begin{Bmatrix} \dot{u}_y \\ \dot{u}_\theta \end{Bmatrix} + \begin{bmatrix} K_y & K_y e_s \\ K_y e_s & K_\theta \end{bmatrix} \begin{Bmatrix} u_y \\ u_\theta \end{Bmatrix} = -\begin{bmatrix} m_s & 0 \\ 0 & m_s r^2 \end{bmatrix} \begin{Bmatrix} \ddot{u}_{gy} \\ \ddot{u}_{g\theta} \end{Bmatrix} + \begin{Bmatrix} F_y \\ F_\theta \end{Bmatrix} \quad (15)$$

The above equation can be simplified as

$$\mathbf{M_s}\ddot{\mathbf{u}} + \mathbf{C_s}\dot{\mathbf{u}} + \mathbf{K_s}\mathbf{u} = -\mathbf{M_s}\ddot{\mathbf{u}}_\mathbf{g} + \mathbf{F} \quad (16)$$

where m_s means the mass of platform together with additional mass of sea fluid; e_s is eccentric distance; u_y, $\ddot{u}_{gy}$ and K_y are the displacement, ground acceleration and stiffness of offshore platform in y direction, respectively; The control force $\mathbf{F}$ is calculated by

$$\begin{Bmatrix} F_y = -m_T(\ddot{u}_y + \ddot{u}_{gy}) \\ F_\theta = -m_T R(R\ddot{u}_\theta + R\ddot{u}_{g\theta} + \alpha\ddot{h}) \end{Bmatrix} \quad (17)$$

It is assumed that the damping matrix in Equation (16) is directly proportional to the stiffness matrix, that is

$$\mathbf{C_s} = a\mathbf{K_s} \quad (18)$$

where the proportionality constant a has units of second. The proportionality constant a was chosen such that the uncoupled lateral mode of vibration has damping equal to 2% of critical damping. This was to account for the nominal elastic energy dissipation that occurs in any real structure (Bugeja *et al.*, 1997). The critical damping coefficient c_c for a single degree-of-freedom (SDOF) system is given by

$$c_c = 2m_s\omega_y \quad (19)$$

where $\omega_y = \sqrt{K_y / m_s}$ is natural frequency of the uncoupled lateral mode. From the equation (18) and (19), the constant a is determined by

$$a = \frac{0.02 \times 2m_s\sqrt{\dfrac{K_y}{m_s}}}{K_y} \quad (20)$$

Combining the Equation (2) and (15), the equation of motion for torsionally coupled system can be written as

$$\begin{bmatrix} 1+\mu & 0 & 0 \\ 0 & 1+\dfrac{\mu R^2}{r^2} & \dfrac{\alpha\mu R}{r^2} \\ 0 & \alpha\mu R & \mu \end{bmatrix} \begin{Bmatrix} \ddot{u}_y \\ \ddot{u}_\theta \\ \ddot{h} \end{Bmatrix} + \begin{bmatrix} a\omega_y^2 & a\omega_y^2 e_s & 0 \\ \dfrac{a\omega_y^2 e_s}{r^2} & a\omega_\theta^2 & 0 \\ 0 & 0 & 2\mu\zeta_T\omega_T \end{bmatrix} \begin{Bmatrix} \dot{u}_y \\ \dot{u}_\theta \\ \dot{h} \end{Bmatrix} +$$

$$\begin{bmatrix} \omega_y^2 & \omega_y^2 e_s & 0 \\ \dfrac{\omega_y^2 e_s}{r^2} & \omega_\theta^2 & 0 \\ 0 & 0 & \mu\omega_T^2 \end{bmatrix} \begin{Bmatrix} u_y \\ u_\theta \\ h \end{Bmatrix} = -\begin{bmatrix} 1+\mu & 0 \\ 0 & 1+\dfrac{\mu R^2}{r^2} \\ 0 & \alpha\mu R \end{bmatrix} \begin{Bmatrix} \ddot{u}_{gy} \\ \ddot{u}_{g\theta} \end{Bmatrix} \quad (21)$$

where $\mu = m_T / m_s$ is a ratio between the mass of CTLCD and the mass of structure; $\omega_\theta = \sqrt{k_\theta / (m_T r^2)}$ denotes the natural frequency of the uncoupled torsional mode. The following assumptions are made in this paper: $\ddot{u}_{gy}$ and $\ddot{u}_{g\theta}$ are two unrelated Gauss white noise random processes with intensities of S_1 and S_2, respectively; H_{yy}, $H_{y\theta}$, $H_{\theta y}$ and $H_{\theta\theta}$ are transfer functions from $\ddot{u}_{gy}$ to u_y, $\ddot{u}_{g\theta}$ to u_y, $\ddot{u}_{gy}$ to u_θ and $\ddot{u}_{g\theta}$ to u_θ, respectively. Then, the displacement variance of structure can be obtained by

$$\sigma^2_{u_{yy}} = S_1 \int_{-\infty}^{\infty} \left| H_{yy} \right|^2 d\omega \qquad \sigma^2_{u_{y\theta}} = S_2 \int_{-\infty}^{\infty} \left| H_{y\theta} \right|^2 d\omega$$

$$\sigma^2_{u_{\theta y}} = S_1 \int_{-\infty}^{\infty} \left| H_{\theta y} \right|^2 d\omega \qquad \sigma^2_{u_{\theta\theta}} = S_2 \int_{-\infty}^{\infty} \left| H_{\theta\theta} \right|^2 d\omega \tag{22}$$

where $\sigma_{u_{yy}}$ and $\sigma_{u_{y\theta}}$ are displacement variances in y direction caused by the ground motion in y direction and θ direction, respectively; $\sigma_{u_{\theta y}}$ and $\sigma_{u_{\theta\theta}}$ are displacement variances in θ direction caused by the ground motion in y direction and θ direction, respectively. So, the equivalent damping ratios of structure are given as

$$\zeta_{eyy} = \frac{\pi S_1}{2\omega_y^3 \sigma^2_{u_{yy}}} \ ; \ \zeta_{ey\theta} = \frac{\pi S_2 r^2}{2\omega_y^3 \sigma^2_{u_{y\theta}}} \ ; \ \zeta_{e\theta y} = \frac{\pi S_1}{2\omega_y^3 r^2 \sigma^2_{u_{\theta y}}} \ ; \ \zeta_{e\theta\theta} = \frac{\pi S_2}{2\omega_y^3 \sigma^2_{u_{\theta\theta}}} \tag{23}$$

where ζ_{eyy} and $\zeta_{ey\theta}$ are equivalent damping ratios in y direction caused by the ground motions in y direction and θ direction, respectively; $\zeta_{e\theta y}$ and $\zeta_{e\theta\theta}$ are equivalent damping ratios in θ direction caused by the ground motions in y direction and θ direction, respectively. Then, the total equivalent damping ratio ζ_{ey} in y direction and $\zeta_{e\theta}$ in θ direction can be defined as

$$\zeta_{ey} = \zeta_{eyy} + \zeta_{ey\theta}$$

$$\zeta_{e\theta} = \zeta_{e\theta y} + \zeta_{e\theta\theta} \tag{24}$$

Define $\Omega = \omega_\theta / \omega_x$ as the frequency ratio between the uncoupled torsional mode and uncoupled translational mode and ω_1 as the first frequency of torsionally coupled structure. The relationships of equivalent damping ratio ζ_{ey} and $\zeta_{e\theta}$ with parameters of control system are shown in Fig. 8 to Fig. 11.

Fig. 8 shows the equivalent damping ratio ζ_{ey} and $\zeta_{e\theta}$ as functions of frequency ratio ω_T / ω_1 for mass ratio μ =0.005, 0.01, 0.015 and 0.02. It is seen from the figure that the values of ζ_{ey} and $\zeta_{e\theta}$ are maximum when the value of frequency ratio ω_T / ω_1 is approximate 1. The Fig. 8 also suggests that damping ratio ζ_{ey} and $\zeta_{e\theta}$ increase with the rise of mass ratio μ.

Fig. 9 shows equivalent damping ratio ζ_{ey} and $\zeta_{e\theta}$ as functions of mass ratio μ for configuration coefficient α =0.5, 0.6, 0.7 and 0.8. It is seen from the figure that the values of ζ_{ey} and $\zeta_{e\theta}$ increase initially and approach constants finally with the rise of mass ratio μ.

It can also be concluded that the values of ζ_{ey} and $\zeta_{e\theta}$ both increase with the rise of configuration coefficient α.
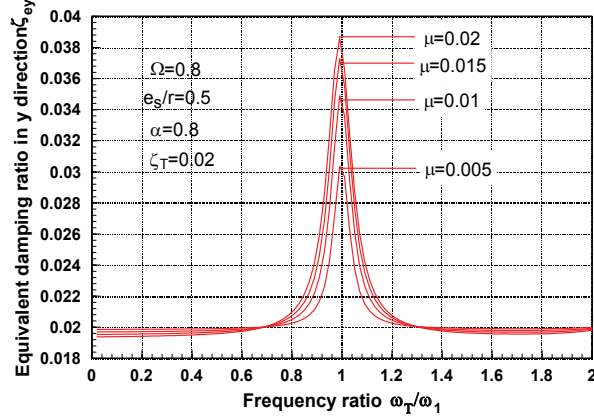
(a) Equivalent damping ratio in y direction

(b) Equivalnet damping ratio in θ direction

Fig. 8. Equivalent damping ratio of structure with frequency ratio ω_T / ω_1
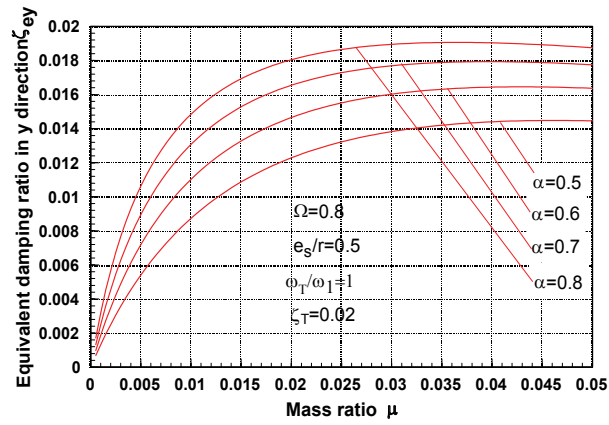
(a) Equivalent damping ratio in y direction
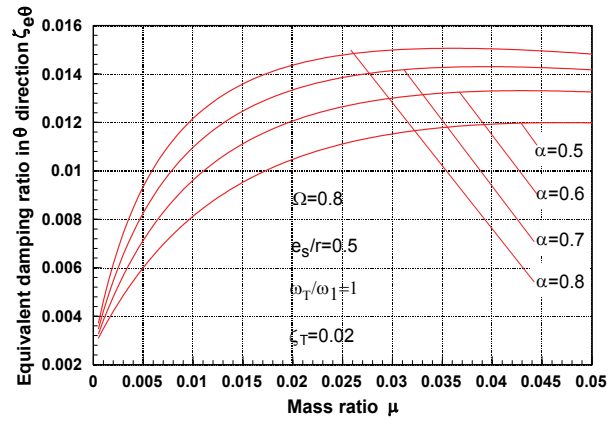
(b)Equivalnet damping ratio in θ direction

Fig. 9. Equivalent damping ratio of structure with mass ratio μ
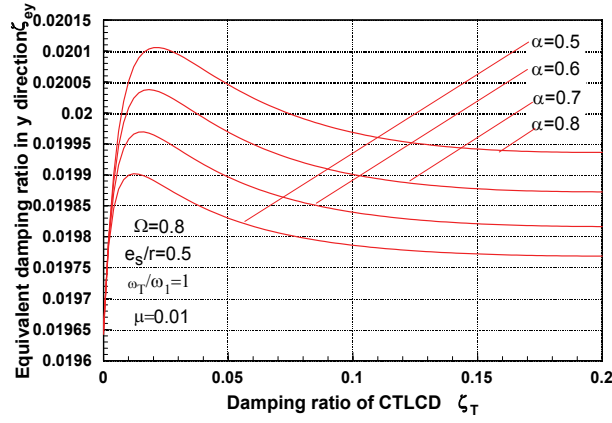
(a) Equivalent damping ratio in y direction
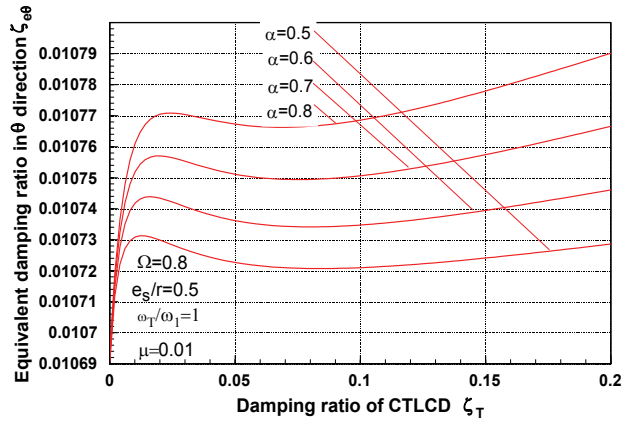
(b) Equivalnet damping ratio in θ direction

Fig. 10. Equivalent damping ratio of structure with damping ratio ζ_T

Fig. 10 shows equivalent damping ratio ζ_{ey} and $\zeta_{e\theta}$ as functions of damping ratio ζ_T for α =0.5, 0.6, 0.7 and 0.8. It is seen from the figure that the values of ζ_{ey} and $\zeta_{e\theta}$ rapidly increase initially with the rise of ζ_T; whereas, after a certain value of ζ_T, ζ_{ey} will decrease to a constant and $\zeta_{e\theta}$ decrease first, then increase gradually.
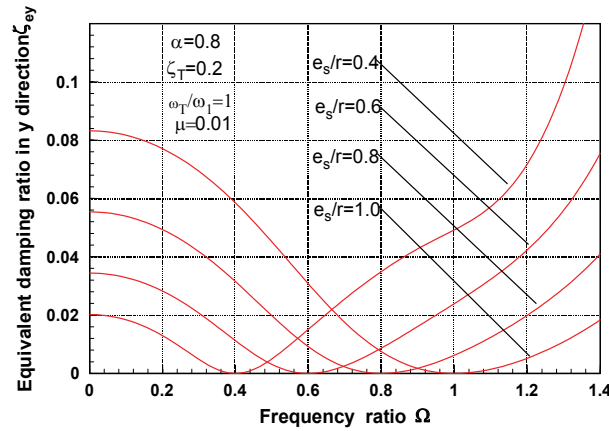
(a) Equivalent damping ratio in y direction
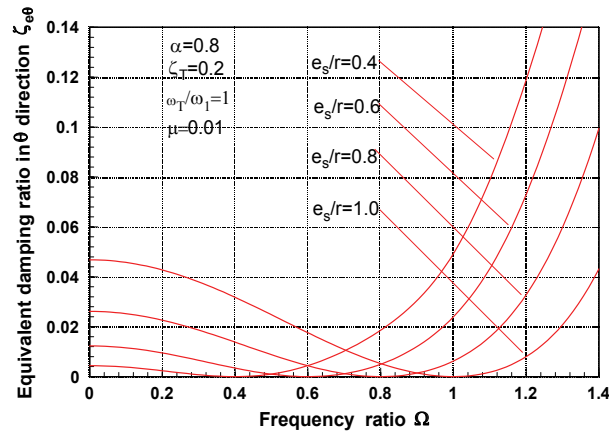
(b) Equivalnet damping ratio in θ direction

Fig. 11. Equivalent damping ratio of structure with frequency ratio Ω
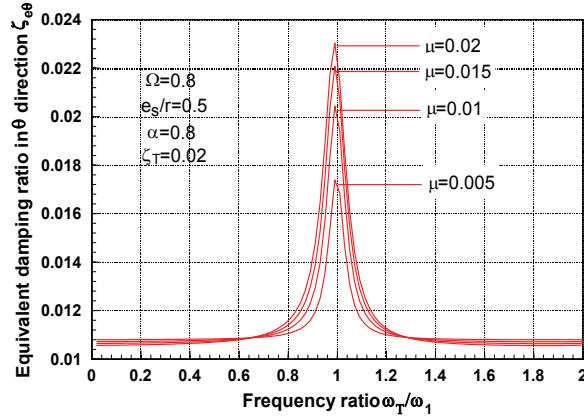
Fig 11 shows equivalent damping ratio ζ_{ey} and $\zeta_{e\theta}$ as functions of frequency ratio Ω for e_s / r =0.4, 0.6 0.8 and 1.0. It is seen from the figure that the values of ζ_{ey} and $\zeta_{e\theta}$ are approximate zero for the structure with Ω near to e_s / r; for the structure $\Omega < e_s / r$, the values of ζ_{ey} and $\zeta_{e\theta}$ decrease with the rise of frequency ratio Ω and increase with the rise of e_s / r; for the structure with $\Omega > e_s / r$, the values of ζ_{ey} and $\zeta_{e\theta}$ increase with the rise of frequency ratio Ω and decrease with the rise of e_s / r.

3. Torsionally coupled vibration control of eccentric buildings

The earthquake is essentially multi-dimensional and so is the structural response excited by earthquake, which will result in the torsionally coupled vibration that cannot be neglected. So, the torsional response for structure is very important (Li and Wang, 1992). Previously, Li et al. presented the method of reducing torsionally coupled response by installing TLCDs in structural orthogonal directions (Huo and Li, 2001). Circular Tuned Liquid Column

Dampers (CTLCD) is a type of control device sensitive to torsional response. The results of free vibration and forced vibration experiments showed that it is effective to control structural torsional response (Liang, 1996; Hochrainer, 2000). However, how to determine the parameters of CTLCD to effectively reduce torsionally coupled vibration is still necessary to be further investigated.

3.1 Equation of motion for control system

The configuration of TLCD is shown in Fig. 12(a). According to the Lagrange theory, the equation of motion for TLCD excited by seismic can be derived as

$$\rho A (2H + B)\ddot{h} + \frac{1}{2}\rho A \xi |\dot{h}|\dot{h} + 2\rho A g h = -\rho A B (\ddot{u} + \ddot{u}_g) \tag{25}$$

where h is the relative displacement of liquid in TLCD; ρ means the density of liquid; H expresses the height of liquid in the container when the liquid is quiescent; A denotes the cross-sectional area of TLCD; g is the acceleration of gravity; B represents the length of horizontal liquid column; ξ is the head loss coefficient; $\ddot{u}$ and $\ddot{u}_g$ mean the acceleration of structure and ground motion, respectively

(a)   (b)
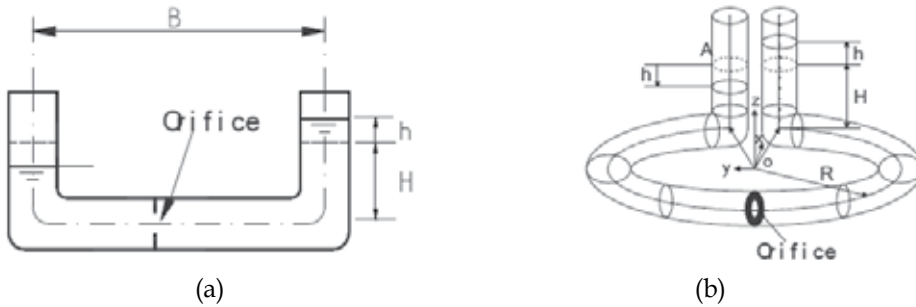
Fig. 12. Configuration of Liquid Column Dampers

The shape of CTCD is shown in Fig. 12(b). In the same way, the equation of motion for CTLCD is derived as

$$\rho A (2H + 2\pi R)\ddot{h} + \frac{1}{2}\rho A \xi |\dot{h}|\dot{h} + 2\rho A g h = -2\rho A \pi R^2 (\ddot{u}_\theta + \ddot{u}_{g\theta}) \tag{26}$$

Two TLCDs are set in the longitudinal direction and transverse direction of n-story building, respectively, and a CTLCD is installed in the center of mass, as shown in Fig.13. The equation of motion of system excited by multi-dimensional seismic inputs can be written as

$$[M_s]\{\ddot{u}\} + [C_s]\{\dot{u}\} + [K_s]\{u\} = -[M_s][E_s]\{\ddot{u}_g\} + \{F_T\} \tag{27}$$

Where, $[M_s]$, $[C_s]$ and $[K_s]$ are the mass, damping and stiffness matrices of the system with dimension of $3n\times 3n$, respectively. $\{u\}$ means hte displacement vector of the strucutre, $\{u\} = \{u_{x1} \quad \cdots \quad u_{xn} \quad u_{y1} \quad \cdots \quad u_{yn} \quad u_{\theta 1} \quad \cdots \quad u_{\theta n}\}^T$; [Es] is the influence matrix of the ground

excitation; $\left\{ \ddot{u}_g \right\} = \left\{ \ddot{u}_{xg} \quad \ddot{u}_{yg} \quad \ddot{u}_{\theta g} \right\}$ is   the   three-dimensional   siesmic   inputs;

$F_T = \left\{ 0 \quad \cdots \quad F_x \quad 0 \quad \cdots \quad F_y \quad 0 \quad \cdots \quad F_\theta \right\}$ is the three-dimensional control vector, where

$$
\begin{aligned}
F_x &= -m_{Ttot}(\ddot{u}_{xn} + \ddot{u}_{xg}) - \alpha_x m_{Tx}\ddot{h}_x + (m_{Tx}l_{1y} + m_{Ty}l_{2y})(\ddot{u}_{\theta n} + \ddot{u}_{\theta g}) \\
F_y &= -m_{Ttot}(\ddot{u}_{yn} + \ddot{u}_{yg}) - \alpha_y m_{Ty}\ddot{h}_y - (m_{Tx}l_{1x} + m_{Ty}l_{2x})(\ddot{u}_{\theta n} + \ddot{u}_{\theta g}) \\
F_\theta &= (m_{Tx}l_{1y} + m_{Ty}l_{2y})(\ddot{u}_{xn} + \ddot{u}_{xg}) - (m_{Tx}l_{1x} + m_{Ty}l_{2x})(\ddot{u}_{yn} + \ddot{u}_{yg}) \\
&\quad + \alpha_x m_{Tx}l_{1y}\ddot{h}_x - \alpha_y m_{Ty}l_{2x}\ddot{h}_y - (m_{Tx}r_1^2 + m_{Ty}r_2^2 + m_T R^2)(\ddot{u}_{\theta n} + \ddot{u}_{\theta g}) - \alpha_\theta m_T R\ddot{h}_\theta
\end{aligned}
\tag{28}
$$

where (l_{1x}, l_{1y}) means the location of the TLCD in x direction; (l_{2x}, l_{2y}) means the location of the TLCD in y direction; $r_1^2 = l_{1x}^2 + l_{1y}^2$; $r_2^2 = l_{2x}^2 + l_{2y}^2$.

Combining Equation (1) to (3), the equation of motion for the control system can be written as

$$\mathbf{M\ddot{x} + C\dot{x} + Kx = -ME\ddot{u}_g} \tag{29}$$

where **M**, **C** and **K** are the mass, damping and stiffness matrices of the combined and damper system. Although the damping of the structure is assumed to be classical, the combined structure and damper system represented by the above equation will be non-classically damped. To analyze a non-classical damped system, it is convenient to work with the system of first order state equations

$$\mathbf{\dot{Z} = AZ + B\ddot{u}_g} \tag{30}$$

where

$$\mathbf{Z = \left\{ \begin{matrix} x \\ \dot{x} \end{matrix} \right\}} \; , \; \mathbf{A = \begin{bmatrix} 0 & I \\ -M^{-1}K & -M^{-1}C \end{bmatrix}} \; , \; \mathbf{B = \begin{bmatrix} 0 \\ -E \end{bmatrix}} \tag{31}$$
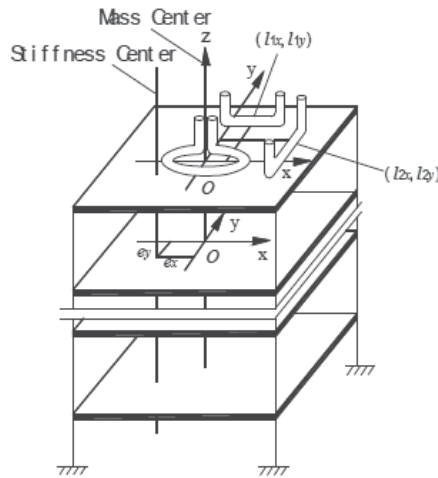
Fig. 13. An eccentric structure with liquid Dampers

3.2 Dynamical characteristics of the structure

The structure analyzed in this paper is an 8-story moment-resisting steel frame with a plan irregularity and a height of 36m created in this study and shown in Figure 14 and Figure 15(Kim, 2002). The structure has 208 members, 99 nodes, and 594 DOFs prior to applying boundary conditions, rigid diaphragm constrains, and the dynamic condensation. Applying boundary conditions and rigid diaphragm constraints results in 288 DOFs. They are further reduced 24 DOFs by the Guyan reduction of vertical DOFs and the rotational DOFs about two horizontal axes.

The static loading on the building consists of uniformly distributed floor dead and live load of 4.78 Kpa and 3.35 Kpa, respectively. A total lateral force (base force) of 963 KN is obtained and distributed over the structure using the equivalent linear static load approach. Each floor shear force is distributed to the nodes in that floor in proportion to nodal masses.
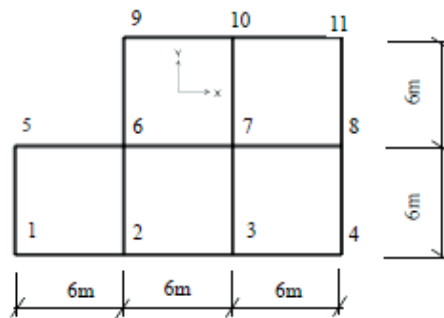
Fig. 14. Plan of the structure
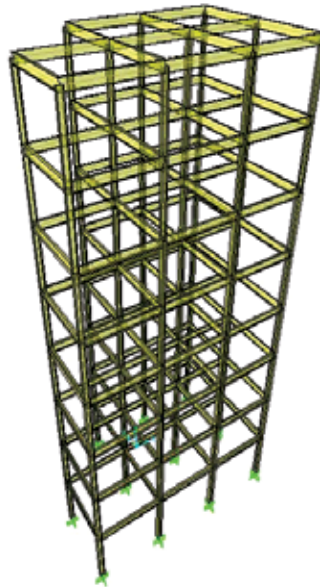
Fig. 15. FEM figure of the structure

        (a) Mode 1   (b) Mode 2   (c)Mode 3
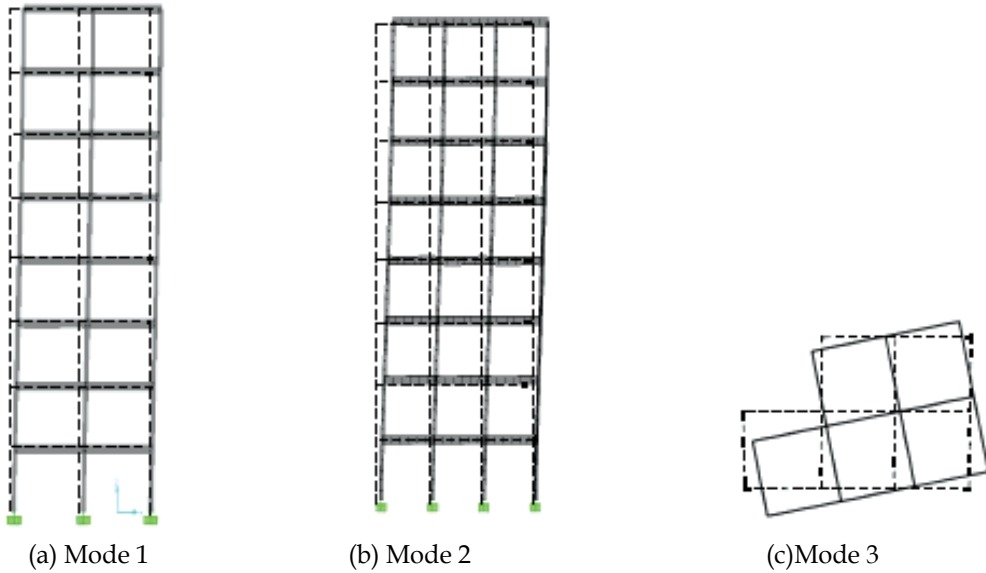
Fig. 16. The first three modes of the structure

Because of plan irregularity substantially more translational and torsional coupling effect is expected in this example. Figure 16 shows the first three modes of vibrations: (a) mode 1 with a frequency of 0.57 Hz, (b) mode 2 with a frequency of 0.72 Hz, (c) mode 3 with a frequency of 0.75 Hz.

3.3 Optimization of the damper parameters

To reduce the torsionally coupled vibration of the 8-story eccentric buildings, two TLCDs are respectively installed on the top story of the structure along x and y direction and one CTLCD on the mass center of the top story. Hence, there are many parameters of the control system to be optimized. The focus of the paper is how to optimize the parameters of liquid dampers to effectively control the dynamical responses of structures. Genetic Algorithm (GA) provides a general framework for the optimization of complicated systems, which is independent of specific areas and robust for the types of problems. In this section, parameters of liquid dampers are optimized by use of GA.

The following form of performance function is used, primarily because it is easy to evaluate the responses of structures

$$f_2 = 1 - \frac{\sqrt{\sum_{i=1}^{n}(d_x^2 + d_y^2 + d_\theta^2)_{i,\text{controlled}}}}{\sqrt{\sum_{i=1}^{n}(d_x^2 + d_y^2 + d_\theta^2)_{i,\text{uncontrolled}}}} \quad i = 1,2,3,\cdots,n \tag{32}$$

where, d_x, d_y and d_θ are the drifts of a story in x, y and torsion direction.

Both, the stochastic model and the design response spectra have been used to define the base input motion. For the stochastic model, the ground motions in x and y directions are descried by two identical but uncorrelated zero-mean stationary processes with power spectral density function $\Phi_l(\omega)$ of the Kanai-Tajimi form:

$$\Phi_l(\omega) = \frac{1 + 4\beta^2 \left(\dfrac{\omega}{\omega_g}\right)^2}{\left[1 - \left(\dfrac{\omega}{\omega_g}\right)^2\right]^2 + 4\beta^2 \left(\dfrac{\omega}{\omega_g}\right)^2} S_0 \tag{33}$$

The parameters of this function are: $\omega_g = 5\pi$, $\beta = 0.5$, $S_0 = 0.01$.

As mentioned before, two TLCDs and one CTLCD are installed at the top of the building. The objective of the study is to design the optimum parameters of these dampers that would maximize the performance function stated earlier. The possible ranges for the design parameters are fixed as follows:

1. Mass ratio, μ: The mass ratio is defined as the ratio of the damper mass to the total building mass. It is assumed that each damper ratio can vary in the range of 0.1 percent to 1 percent of the building mass. Thus the maximum mass of the damper system consisting of three dampers could be as high as 3 percent of the building mass.
2. Frequency tuning ratio, f: The frequency ratio for each damper is defined as the ratio its own natural frequency to the fundamental frequency of the building structure. Here it is assumed that this ratio could vary between 0-1.5.
3. Damping ratio, d: This is a ratio of the damping coefficient to its critical value. It is assumed that this ratio can vary in the range of 0-10 percent.
4. Damper positions from the mass center, lx in x axis and ly: in y axis: It is assumed that lx can vary between –8 and 5 meters and ly can vary between –4 and 3 meters

The optimization process starts with a population of these individuals. For the problem at hand, 30 individuals were selected to form the population. The probability of crossover and mutation are 0.95 and 0.05, respectively. The process of iteration is determined to be 300 steps. The final optimum parameters for the two optimum design criteria are given in Table 2.

	Performance Criteria i (f1=0.47769)		
	TLCD in x direction	TLCD in y direction	CTLCD
μ	0.008519	0.0095655	0.0014362
f_r	1.2334	0.96607	1.1137
d_r	0.053803	0.061988	0.052886
l_x	-7.38	0.45567	—
l_y	-6.479	-2.2431	—

Table 2. The optimal parameters of liquid dampers

3.4 Seismic analysis in time domain

The parameters of liquid dampers on the 8-story building structure have been optimized in the previous section and the results are listed in the Table 2. The control results of liquid dampers on the building are analyzed in time domains in this section. The El Centro, Tianjin and Qian'an earthquake records are selected to input to the structure as excitations, which represent different site conditions.

The structural response without liquid dampers subjected to earthquake in x, y and θ directions are expressed with x_0, y_0 and θ_0, respectively. Also, the response with liquid

dampers subjected to earthquake in x, y and θ directions are expressed with x, y and θ, respectively. The response reduction ratio of the structure is defined as

$$J = \frac{x_0 - x}{x_0} \times 100\% \qquad (34)$$

The maximum displacements of the structure and response reduction ratios are computed for three earthquake records and the results listed from Table 3 to Table 5. It can be seen

Story Number	x_0 (cm)	x (cm)	J (%)	y_0 (cm)	y (cm)	J (%)	θ_0 (10^{-4}Rad)	θ (10^{-4}Rad)	J (%)
1	0.57	0.53	6.14	1.18	0.99	15.94	1.71	1.56	8.77
2	1.11	1.03	7.24	2.28	1.94	15.12	3.30	3.04	7.88
3	1.77	1.58	10.71	3.43	2.96	13.73	5.02	4.61	8.17
4	2.38	2.04	14.20	4.30	3.76	12.59	6.42	5.87	8.57
5	2.98	2.54	15.01	4.95	4.39	11.34	7.62	6.90	9.45
6	3.48	3.03	12.77	5.64	4.69	16.76	8.50	7.46	12.24
7	4.03	3.67	8.86	6.58	4.89	25.64	10.05	8.63	14.13
8	4.37	4.06	7.00	7.10	5.47	22.98	10.96	9.63	12.14

Table 3. Maximum displacements of the structure (El Centro)

Story Number	x_0 (cm)	x (cm)	J (%)	y_0 (cm)	y (cm)	J (%)	θ_0 (10^{-4}Rad)	θ (10^{-4}Rad)	J (%)
1	2.49	1.85	25.64	2.10	1.83	12.57	4.67	4.22	9.64
2	4.91	3.66	25.49	4.05	3.52	13.03	9.14	8.25	9.74
3	7.71	5.78	25.06	6.30	5.48	13.12	14.21	12.73	10.42
4	10.26	7.69	24.98	8.36	7.23	13.59	18.83	16.75	11.05
5	12.77	9.58	24.97	10.36	8.90	14.08	23.21	20.60	11.25
6	14.79	11.09	24.97	11.98	10.27	14.25	26.55	23.56	11.26
7	16.88	12.66	24.96	14.10	12.13	13.91	30.45	27.05	11.17
8	17.98	13.51	24.89	15.22	13.41	11.90	32.44	29.02	10.54

Table 4. Maximum displacements of the structure (Tianjin)

Story Number	x_0 (cm)	x (cm)	J (%)	y_0 (cm)	y (cm)	J (%)	θ_0 (10^{-4}Rad)	θ (10^{-4}Rad)	J (%)
1	0.11	0.10	6.91	0.10	0.091	6.93	0.132	0.12	4.10
2	0.19	0.17	6.57	0.19	0.16	16.00	0.25	0.24	1.25
3	0.23	0.21	6.66	0.28	0.22	24.60	0.39	0.38	2.82
4	0.24	0.21	11.48	0.38	0.28	25.86	0.51	0.50	1.45
5	0.29	0.22	23.54	0.48	0.36	24.89	0.63	0.61	1.40
6	0.34	0.26	24.76	0.56	0.43	23.54	0.72	0.70	2.20
7	0.39	0.34	14.17	0.70	0.54	21.70	0.83	0.79	4.45
8	0.43	0.39	8.15	0.77	0.62	19.47	0.93	0.87	5.60

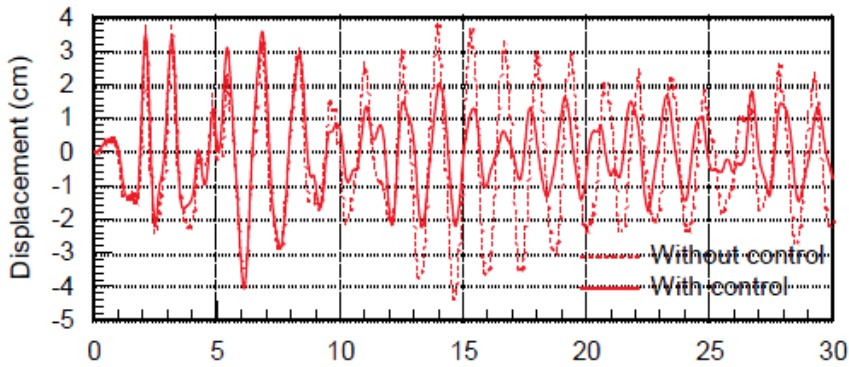Table 5. Maximum displacements of the structure (Qian'an)

Fig. 17. Time history of the displacement on the *x* direction of top floor (El Centro)
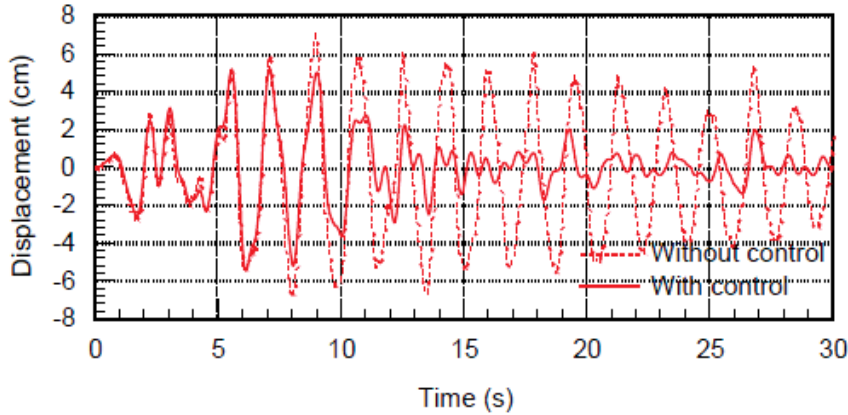
Fig. 18. Time history of the displacement on the *y* direction of top floor (El Centro)
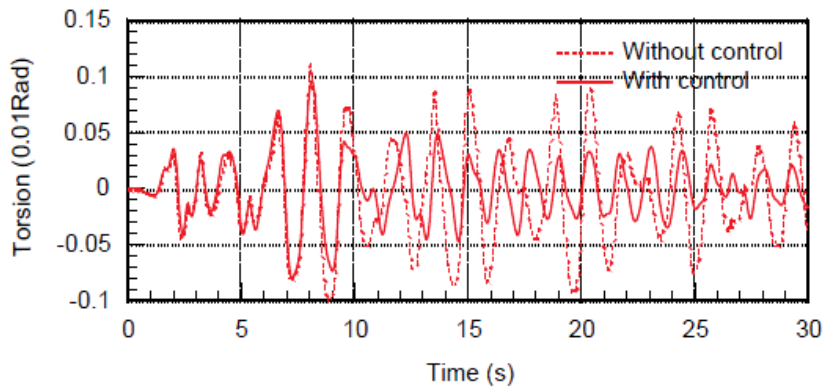
Fig. 19. Time history of the torsional displacement of top floor (El Centro)

from the tables that the responses of the structure in each degree of freedom are reduced with the installation of liquid dampers. However, the reduction ratios are different for the different earthquake records.

The displacement time history curves of the top story are shown from Fig. 6 to Fig. 8 and acceleration time history curves in Fig. 17 to Fig. 19 for El Centro earthquake. It can be seen from these figures that the structural response are reduced in the whole time history.

4. Conclusion

From the theoretical analysis and seismic disasters, it can be concluded that the seismic response is not only in translational direction, but also in torsional direction. The torsional components can aggravate the destroy of structures especially for the eccentric structures. Hence, the control problem of eccentric structures under earthquakes is very important. This paper focus on the seismic response control of eccentric structures using tuned liquid dampers. The control performance of Circular Tuned Liquid Column Dampers (CTLCD) to torsional response of offshore platform structure excited by ground motions is investigated. Based on the equation of motion for the CTLCD-structure system, the optimal control parameters of CTLCD are given through some derivations supposing the ground motion is stochastic process. The influence of systematic parameters on the equivalent damping ratio of the structures is analyzed with purely torsional vibration and translational-torsional coupled vibration, respectively. The results show that Circular Tuned Liquid Column Dampers (CTLCD) is an effective torsional response control device. An 8-story eccentric steel building, with two TLCDs on the orthogonal direction and one CTLCD on the mass center of the top story, is analyzed. The optimal parameters of liquid dampers are optimized by Genetic Algorithm. The structural response with and without liquid dampers under bi-directional earthquakes are calculated. The results show that the torsionally coupled response of structures can be effectively suppressed by liquid dampers with optimal parameters.

5. Acknowledgment

6. References

Bugeja, N.; Thambiratnam, D.P. & Brameld G.H. (1999). The Influence of Stiffness and Strength Eccentricities on the Inelastic Earthquake Response of Asymmetric Structures, *Engineering Structures*, Vol. 21,No.9, pp.856–863

Chang, C. C. & Hsu, C. T.(1998). Control Performance of Liquid Column Vibration Absorbers. *Engineering Structures*. Vol.20, No.7, pp.580-586

Chang, C. C.(1999). Mass Dampers and Their Optimal Design for Building Vibration Control. *Engineering Structures*, Vol.21, No.5, pp.454-463

Fujina, Y. & Sun, L. M.(1993). Vibration Control by Multiple Tuned Liquid Dampers(MTLDs). *J. of Structural Engineering*, ASCE, Vol.119, No.12, pp.3482-3502

Gao H. & Kwok K. C. S.(1997). Optimization of Tuned Liquid Column Dampers. *Engineering Structures*, Vol.19, No.6, pp. 476-486

Gao, H.; Kwok, K. S. C. & Samali B.(1999). Characteristics Of Multiple Tuned Liquid Column Dampers In Suppressing Structural Vibration. *Engineering Structures*, Vol.21, No.4, pp.316-331

Hitchcock, P. A.; Kwok, K. C. S. & Watkins R. D. (1997). Characteristics Of Liquid Column Vibration Absorbers (LCVA)-I. *Engineering Structures*, Vol.19, No.2, pp.126-134

Hitchcock, P. A.; Kwok, K. C. S. & Watkins R. D. (1997). Characteristics Of Liquid Column Vibration Absorbers (LCVA)-II. *Engineering Structures*, Vol.19, No.2, pp.135-144

Hochrainer, M. J.; Adam, C. & Ziegler, F. (2000). Application of Tuned Liquid Column Dampers for Passive Structural Control, *Proc. of 7th International Congress on Sound and Vibration (ICSV 7)*, Garmisch-Partenkirchen, Germany, pp.3107-3114

Huo, L.S. & Li H.N. (2001). Parameter Study of TLCD Control System Excited by Multi-Dimensional Ground Motions. *Earthquake Engineering and Engineering Vibration*, Vol.21, No.4, pp.147-153

Jiang, Y. C. & Tang, J. X. (2001). Torsional Response of the Offshore Platform with TMD, *China Ocean Engineering*, Vol.15, No.2, pp.309-314

Kareem, A. & Kline, S.(1995). Performance Of Multiple Mass Dampers Under Random Loading. *J. of Structural Engineering*, ASCE, Vol.121, No.2, pp.348-361

Kim, H. (2002). Wavelet-based adaptive control of structures under seismic and wind loads. Notre Dame: The Ohio State University

Li, H.N. & Wang, S.Y. (1992). Torsionally Coupled Stochastic Response Analysis of Irregular Buildings Excited by Multiple Dimensional Ground Motions. *Journal of Building Structures*, Vol.13, No.6, pp.12-20

Liang, S.G. (1996).Experiment Study of Torsionally Structural Vibration Control Using Circular Tuned Liquid Column Dampers, *Special Structures*, Vol.13, No.3, pp. 33-35

Qu, W. L.; Li, Z. Y. & Li, G. Q. (1993). Experimental Study on U Type Water Tank for Tall Buildings and High-Rise Structures, *China Journal of Building Structures*, Vol.14, No.5, pp.37-43

Sakai, F.; Takaeda, S. & Tamake, T. (1989). Tuned Liquid Column Damper — New Type Device For Suppression Of Building Vibrations. *Proc. Int. Conf. On High-rise Buildings*, Nanjing, China, pp.926-931

Wang, Z. M. (1997). *Vibration Control of Towering Structures*, Shanghai: Press of Tongji University.

Yan, S. & Li H. N.(1999). Performance of Vibration Control for U Type Water Tank with Variable Cross Section. *Earthquake Engineering and Engineering Vibration*, Vol.19, No.1, pp.197-201

Yan, S.; Li, H. N. & Lin, G. (1998). Studies on Control Parameters of Adjustable Tuned Liquid Column Damper, *Earthquake Engineering and Engineering Vibration*, Vol18, No.4, pp. 96-101

Active Control of Human-Induced Vibrations Using a Proof-Mass Actuator

Iván M. Díaz
Universidad de Castilla-La Mancha
Spain

1. Introduction

Advances in structural technologies, including construction materials and design technologies, have enabled the design of light and slender structures, which have increased susceptibility to human-induced vibration. This is compounded by the trend toward open-plan structures with fewer non-structural elements, which have less inherent damping. Examples of notable vibrations under human-induced excitations have been reported in floors, footbridges and grandstands, amongst other structures (Bachmann, 1992; Bachmann, 2002; Hanagan et al., 2003a). Such vibrations can cause a serviceability problem in terms of disturbing the users, but they rarely affect the fatigue behaviour or safety of structures.

Solutions to overcome human-induced vibration serviceability problems might be: (i) designing in order to avoid natural frequencies into the habitual pacing rate of walking, running or dancing, (ii) stiffening the structure in the appropriate direction resulting in significant design modifications, (iii) increasing the weight of the structure to reduce the human influence being also necessary a proportional increase of stiffness and (iv) increasing the damping of the structure by adding vibration absorber devices. The addition of these devices is usually the easiest way of improving the vibration performance. Traditionally, passive vibration absorbers, such as tuned mass dampers (TMDs) (Setareh & Hanson, 1992; Caetano et al., 2010), tuned liquid dampers (Reiterer & Ziegler, 2006) or visco-elastic dampers, etc., have been employed. However, the performance of passive devices is often of limited effectiveness if they have to deal with small vibration amplitude (such as those produced by human loading) or if vibration reduction over several vibration modes is required since they have to be tuned to a single mode. Semi-active devices, such semi-active TMDs, have been found to be more robust in case of detuning due to structural changes, but they exhibit only slightly improved performance over passive TMDs and they still have the fundamental problem that they are tuned to a single problematic mode (Setareh, 2002; Occhiuzzi et al., 2008). In these cases, an active vibration control (AVC) system might be more effective and then, an alternative to traditional passive devices (Hanagan et al., 2003b). A state-of-the-art review of technologies (passive, semi-active and active) for mitigation of human-induced vibration can be found in (Nyawako & Reynolds, 2007). Furthermore, techniques to cancel floor vibrations (especially passive and semi-active techniques) are reviewed in (Ebrahimpour & Sack, 2005) and the usual adopted solutions to cancel footbridge vibrations can be found in (FIB, 2005).

An AVC system based on direct velocity feedback control (DVFC) with saturation has been studied analytically and implemented experimentally for the control of human-induced vibrations via an active mass damper (AMD) (also known as inertial actuator or proof-mass actuator) on a floor structure (Hanagan & Murray, 1997) and on a footbridge (Moutinho et al., 2010). This actuator generates inertial forces in the structure without need for a fixed reference. The velocity output, which is obtained by an integrator circuit applied to the measured acceleration response, is multiplied by a constant gain and feeds back to a collocated force actuator. The term collocated means that the actuator and sensor are located physically at the same point on the structure. The merits of this method are its robustness to spillover effects due to high-order unmodelled dynamics and that it is unconditionally stable in the absence of actuator and sensor (integrator circuit) dynamics (Balas, 1979). Nonetheless, when such dynamics are considered, the stability for high gains is no longer guaranteed and the system can exhibit limit cycle behaviour, which is not desirable since it could result in dramatic effects on the system performance and its components (Díaz & Reynolds, 2010a). Then, DVFC with saturation is not such a desirable solution. Generally, the actuator and sensor dynamics influence the system dynamics and have to be considered in the design process of the AVC system. If the interaction between sensor/actuator and structure dynamics is not taken into account, the AVC system might exhibit poor stability margins, be sensitive to parameter uncertainties and be ineffective. A control strategy based on a phase-lag compensator applied to the structure acceleration (Díaz & Reynolds, 2010b), which is usually the actual magnitude measured, can alleviated such problems. This compensator accounts for the interaction between the structure and the actuator and sensor dynamics in such a way that the closed-loop system shows desirable properties. Such properties are high damping for the fundamental vibration mode of the structure and high stability margins. Both properties lead to a closed-loop system robust with respect to stability and performance (Preumont, 1997). This control law is completed by: (i) a high-pass filter, applied to the output of the phase-lag compensator, designed to avoid actuator stroke saturation due to low-frequency components and (ii) a saturation nonlinearity applied to the control signal to avoid actuator force overloading at any frequency. This methodology will be referred as to compensated acceleration feedback control (CAFC) from this point onwards.

This chapter presents the practical implementation of an AMD to cancel excessive vertical vibrations on an in-service office floor and on an in-service footbridge. The AMD consists of a commercial electrodynamic inertial actuator controlled via CAFC. The remainder of this chapter is organised as follows. The general control strategy together with the structure and actuator dynamic model are described in Section 2. The control design procedure is described in Section 3. Section 4 deals with the experimental implementation of the AVC system on an in-service open-plan office floor whereas Section 5 deals with the implementation on an in-service footbridge. Both sections contain the system dynamic models, the design of CAFC and results to assess the design. Finally, some conclusions are given in Section 6.

2. Control strategy and system dynamics

The main components of the general control strategy adopted in this work are shown in Fig. 1. The output of the system is the structural acceleration since this is usually the most convenient quantity to measure. Because it is rarely possible to measure the system state

and due to simplicity reasons, direct output measurement feedback control might be preferable rather than state-space feedback in practical problems (Chung & Jin, 1998). In this Fig., G_A is the transfer function of the actuator, G is of the structure, C_D is of the direct compensator and C_F is of the feedback compensator. The direct one is merely a phase-lead compensator (high-pass property) designed to avoid actuator stroke saturation for low-frequency components. It is notable that its influence on the global stability will be small since only a local phase-lead is introduced. The feedback one is a phase-lag compensator designed to increase the closed-loop system stability and to make the system more amenable to the introduction of significant damping by a closed-loop control. The control law is completed by a nonlinear element f that is assumed to be a saturation nonlinearity to account for actuator force overloading.

$r(t):$	Reference command	$\ddot{y}(t):$	Acceleration response
$V(t):$	Control voltage	$\ddot{y}_c(t):$	Compensated acceleration
$F(t):$	Actuator force	$V_0(t):$	Initial control voltage
$p(t):$	Plant disturbance	$f(\ddot{y}_c):$	Nonlinear element
$C_D(s):$	Transfer function of the direct compensator		
$G_A(s):$	Transfer function of the AMD		
$G(s):$	Transfer function of the structure		
$C_F(s):$	Transfer function of the feedback compensator		
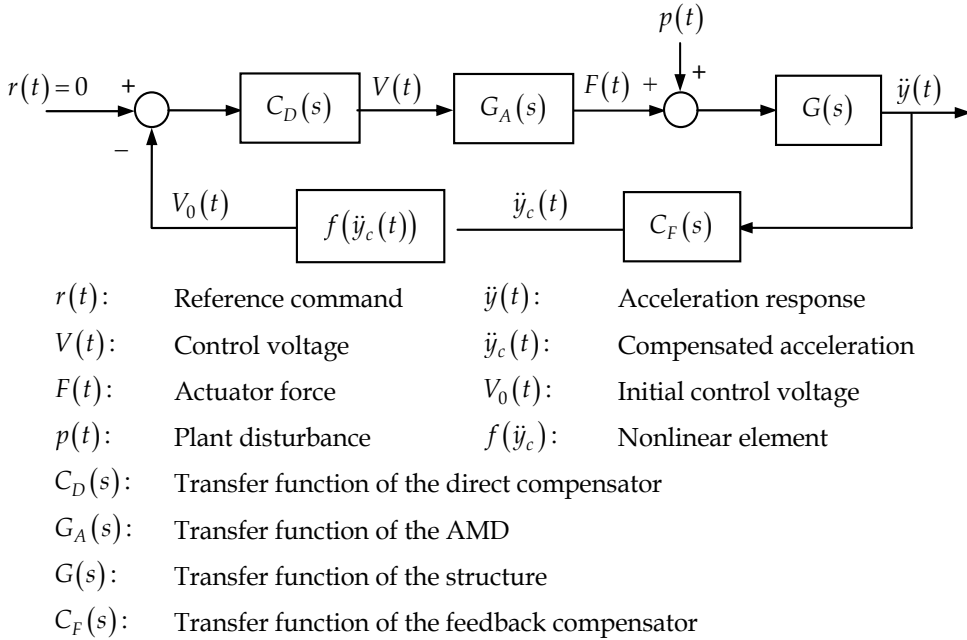
Fig. 1. General control scheme

2.1 Structure dynamics

If the collocated case between the acceleration (output) and the force (input) is considered and using the modal analysis approach, the transfer function of the structure dynamics can be represented as an infinitive sum of second-order systems as follows (Preumont, 1997)

$$G(s) = \sum_{i=1}^{\infty} \frac{\chi_i s^2}{s^2 + 2\zeta_i \omega_i s + \omega_i^2}, \qquad (1)$$

where $s = j\omega$, ω is the frequency, χ_i, ζ_i and ω_i are the inverse of the modal mass, damping ratio and natural frequency associated to the i-th mode, respectively. For practical application, N vibration modes are considered in the frequency bandwidth of interest. The transfer function G (1) is thus approximated by a truncated one as follows

$$G(s) \simeq \sum_{i=1}^{N} \frac{\chi_i s^2}{s^2 + 2\zeta_i \omega_i s + \omega_i^2} \,. \tag{2}$$

2.2 Proof-mass actuator dynamics

The actuator consists of a reaction (moving) mass attached to a current-carrying coil moving in a magnetic field created by an array of permanent magnets. The linear behaviour of a proof-mass actuator can be closely described as a linear third-order model (Reynolds et al., 2009). That is, a low-pass element is added to a linear second-order system in order to account for the low-pass property exhibited by these actuators. The cut-off frequency of this element is not always out of the frequency bandwidth of interest since it is approximately 10 Hz (APS). Such a low-pass behaviour might affect importantly the global stability of the AVC system. Thus, the actuator is proposed to be modelled by

$$G_A(s) = \left(\frac{K_A s^2}{s^2 + 2\zeta_A \omega_A s + \omega_A^2} \right) \left(\frac{1}{s + \varepsilon} \right) = \frac{K_A s^2}{s^3 + (2\zeta_A \omega_A + \varepsilon)s^2 + (2\zeta_A \omega_A \varepsilon + \omega_A^2)s + \varepsilon \omega_A^2} \tag{3}$$

where $K_A > 0$, and ζ_A and ω_A are, respectively, the damping ratio and natural frequency which take into consideration the suspension system and internal damping. The pole at $-\varepsilon$ provides the low-pass property.

3. Controller design

The purpose of this section is to show a procedure to design the compensators C_D and C_F (see Fig. 1). The design of C_D is undertaken in the frequency domain and the design of C_F is carried out through the root locus technique. The root locus maps the complex linear system roots of the closed-loop transfer function for control gains from zero (open-loop) to infinity (Bolton, 1998). In the design of C_F, it is assumed that the natural frequency of the actuator ω_A (see Eq. (3)) is below the first natural frequency of the structure ω_1 (see Eq. (2)) (Hanagan, 2005).

3.1 Direct compensator

The transfer function between the inertial mass displacement and input voltage to the actuator can be considered as follows

$$G_d(s) = \frac{1}{m_A} \frac{G_A(s)}{s^2}, \tag{4}$$

with m_A being the mass value of the inertial mass. Fig. 2a shows an example of magnitude of G_d. The inertial mass displacement at low frequencies should be limited due to stroke saturation. A transfer function with the following magnitude is defined

$$\left| \hat{G}_d(j\omega) \right| = \begin{cases} d & 0 \le \omega \le \hat{\omega} \\ \left| G_d(j\omega) \right| & \hat{\omega} < \omega < \infty \end{cases}, \tag{5}$$

in which d is the maximum allowable stroke for harmonic input per unit voltage and $\hat{\omega}$ is the higher frequency that fulfils $\left|G_d(j\omega)\right| = d$. A high-pass compensator of the form

$$C_D(s,\lambda,\eta) = \frac{s+\lambda}{s+\eta} \text{ with } \eta > \lambda \geq 0, \tag{6}$$

is applied to the initial control voltage V_0 and its output is the filtered input V to the actuator (see Fig. 1). Fig. 2b shows an example of C_D. The following error function is defined

$$e(\omega,\lambda,\eta) = \left(\left|\hat{G}_d(j\omega)\right| - \left|C_D(j\omega,\lambda,\eta)G_d(j\omega)\right|\right)^2, \tag{7}$$

with $\omega \in (\omega_L,\omega_U)$, $\omega_L < \hat{\omega}$, $\omega_U > \hat{\omega}$, and ω_L and ω_U being, respectively, the lower and upper value of the frequency range that is considered in the design. The lower frequency ω_L must be selected in such a way that the actuator resonance is sufficiently included and the upper frequency ω_U must be chosen so that the structure dynamics that are prone to be excited are included. Parameters λ and η of the compensator are obtained by minimising the error function (7)

$$\min_{(\lambda,\eta) \in \mathbb{R}^+} e(\omega,\lambda,\eta), \forall \omega \in (\omega_L,\omega_U), \tag{8}$$

with $\lambda \in [0,\lambda_{max})$, $\eta \in [0,\eta_{max})$, λ_{max}, $\eta_{max} \leq \varepsilon$ and λ_{max} and η_{max} being, respectively, the maximum considered value of λ and η for the optimisation problem (8). Note that λ and η are delimited by the low-pass property of the actuator ε in order to minimise the influence of C_D on the global stability properties. By and large, the objective is to fit $C_D(j\omega)G_d(j\omega)$ to d for $\omega_L < \omega < \hat{\omega}$ and not to affect the dynamics for $\hat{\omega} < \omega < \omega_U$ (see Fig. 2a). The result is a high-pass compensator that introduces dynamics mainly in the frequency range $\omega_L < \omega < \hat{\omega}$ in such a way that the global stability is not compromised.
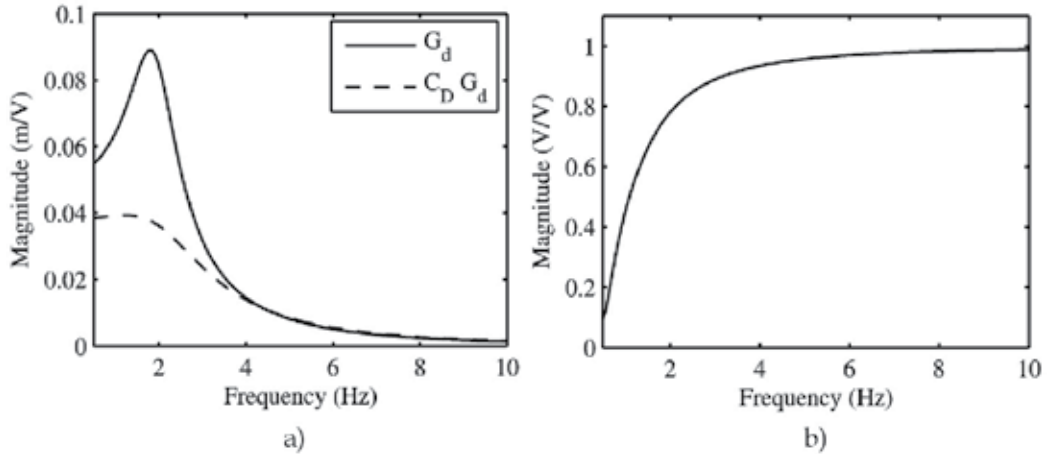
Fig. 2. Effect of the high-pass compensator on the actuator dynamics. a) Magnitude of G_d and $C_D G_d$. b) Magnitude of C_D

3.2 Feedback compensator

To illustrate the selection of the form of the compensator C_F, the root locus map (s-plane) for four different cases is shown in Fig. 3. A realistic structure is assumed with two significant vibration modes. The modal mass and damping ratio for both modes are assumed to be 20 tonnes and 0.03, respectively. The four cases are: a) direct acceleration feedback control (DAFC) considering two vibration modes at 4 and 10 Hz, respectively; b) DVFC for the same structure as in a); c) DAFC considering two vibration modes at 7 and 10 Hz, respectively; and d) DVFC for the same structure as in c). The actuator dynamics (Eq. (3)) is represented by a pair of high-damped poles, two zeros at the origin and a real pole and the structure is represented by two zeros at the origin and interlacing low-damped poles and zeros. It is clearly shown that the resulting root locus has non-collocated system features due to the influence of the actuator dynamics on the structure dynamics. That is, when the actuator dynamics are considered, the interlacing pole-zero pattern exhibited by collocated systems is

DAFC	
First frequency	4 Hz
Second frequency	10 Hz
Maximum damping	0.047

DVFC	
First frequency	4 Hz
Second frequency	10 Hz
Maximum damping	0.205

DAFC	
First frequency	7Hz
Second frequency	10 Hz
Maximum damping	0.242

DVFC	
First frequency	7Hz
Second frequency	10 Hz
Maximum damping	0.070

Fig. 3. Examples of root loci. (×) poles; (o) zeros

no longer accomplished. On one hand, it is observed that for a structure with a fundamental frequency of 4 Hz, direct output feedback (DAFC since the 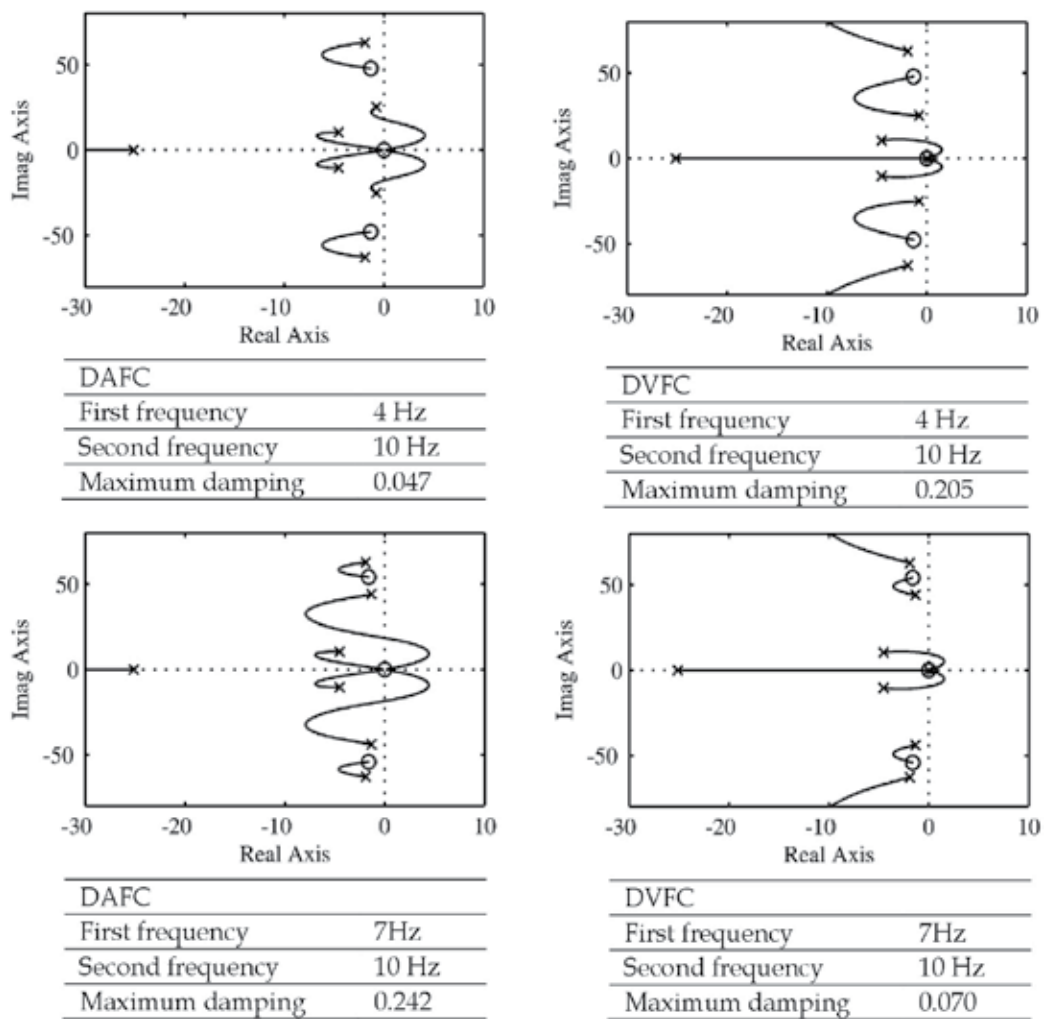actual measurement is the acceleration) will provide very small relative stability (the distance of the poles to the imaginary axis in the s-plane) and low damping (Bolton, 1998). However, the inclusion of an integrator circuit (a pole at the origin for an ideal integrator), which results in DVFC, improves substantially such properties. On the other hand, for a structure with a higher fundamental frequency (7 Hz), DAFC provides much better features than DVFC.

Fig. 3 shows the fact that DVFC might not be a good solution and supports the use of CAFC. It is applied the following phase-lag compensator to the measured acceleration

$$C_F(s) = \frac{s+\gamma}{s} \text{ with } \gamma \geq 0 .$$

(9)

If $\gamma = 0$, the control scheme will be DAFC since $C_F(s) = 1$. If $\gamma \gg \varepsilon$, which means that the zero of the compensator does not affect the dominant system dynamics, the control scheme will then be considered DVFC. Parameter γ has to be chosen according to the closed-loop poles corresponding to the fundamental frequency of the structure in order to: 1) improve substantially their relative stability, 2) decrease their angles with respect to the negative real axis to allow increasing damping, and 3) increase the distance to the origin to allow increasing natural frequency. Note that increasing values both of the frequency and the damping result in decreasing the settling time of the corresponding dynamics (Bolton, 1998). The possible values of γ that provide the aforementioned features can be bound through the departure angle at zero gain of the locus corresponding to the fundamental structure vibration mode. This angle must point to negative values of the real axis. To obtain this angle, the argument equation of the closed-loop characteristic equation is used. That is, any point s_1 of a specific trajectory verifies the following equation

$$\sum_{i=1}^{n_z} \angle (s_1 + z_i) - \sum_{j=1}^{n_p} \angle (s_1 + p_j) = \pm(2k+1)\pi \text{ with } k \in \mathbb{N} ,$$

(10)

in which n_z is the number of zeros, n_p is the number of poles and $\angle (s_1 + z_i)$ and $\angle (s_1 + p_j)$ are the angles of vectors drawn from the zeros and poles, respectively, to point s_1. The departure angle can be determined by letting s_1 be a point very close to one of the poles of the fundamental structure vibration mode. As an example, the dominant dynamics are considered without the direct compensator. Fig. 4 shows the map of zeros and poles under the aforementioned conditions. Eq. (10) can be written as follows

$$(\beta_1 + \beta_2 + \beta_3 + \beta_4) - (\alpha_1 + \alpha_2 + \alpha_3 + \alpha_4 + \alpha_5) = \pm(2k+1)\pi \text{ with } k \in \mathbb{N} .$$

(11)

If it is considered that the damping of the fundamental vibration mode is $\zeta_1 \simeq 0$, the following assumptions can be done: $\beta_1 = \beta_2 = \beta_3 \simeq \pi/2$ and $\alpha_5 \simeq \pi/2$. Therefore, Eq. (11) can be rewritten as

$$\beta_4 - (\alpha_1 + \alpha_2 + \alpha_3 + \alpha_4) = \pm 2k\pi \text{ with } k \in \mathbb{N} .$$

(12)

Considering transfer functions (2) and (3), the angles α_1, α_2 and α_3 are of the following form

$$\alpha_1 = \mathrm{atan}\left(\frac{\omega_1}{\varsigma_A\omega_A} - \frac{\sqrt{1-\varsigma_A^2}}{\varsigma_A}\right), \; \alpha_2 = \mathrm{atan}\left(\frac{\omega_1}{\varsigma_A\omega_A} + \frac{\sqrt{1-\varsigma_A^2}}{\varsigma_A}\right), \text{ and } \alpha_3 = \mathrm{atan}\left(\frac{\omega_1}{\varepsilon}\right) \quad (13)$$

Considering transfer functions (2) and (9), the angle β_4 is obtained as

$$\beta_4 = \mathrm{atan}\left(\frac{\omega_1}{\gamma}\right) \quad (14)$$

Then, by imposing a minimum $\alpha_{4,\min}$ and a maximum $\alpha_{4,\max}$ value of the departure angle α_4 of the fundamental structure vibration mode, a couple of values of β_4 can be obtained

$$\beta_{4,\min} = -2\pi + \left(\alpha_1 + \alpha_2 + \alpha_3 + \alpha_{4,\min}\right), \; \beta_{4,\max} = -2\pi + \left(\alpha_1 + \alpha_2 + \alpha_3 + \alpha_{4,\max}\right) \quad (15)$$

in which it is assumed $k = 1$. Therefore, the variation interval of β_4 is derived as follows

$$\beta_4 \in \left(\max\left(0; \beta_{4,\min}\right), \; \min\left(\pi/2; \beta_{4,\max}\right)\right) \quad (16)$$

and using Eq. (14), the corresponding variation interval of $\gamma \in \left(\gamma_{\min}, \gamma_{\max}\right)$ is determined. The final value of γ must be chosen so that the attractor properties of the zero are focussed on the fundamental vibration mode.
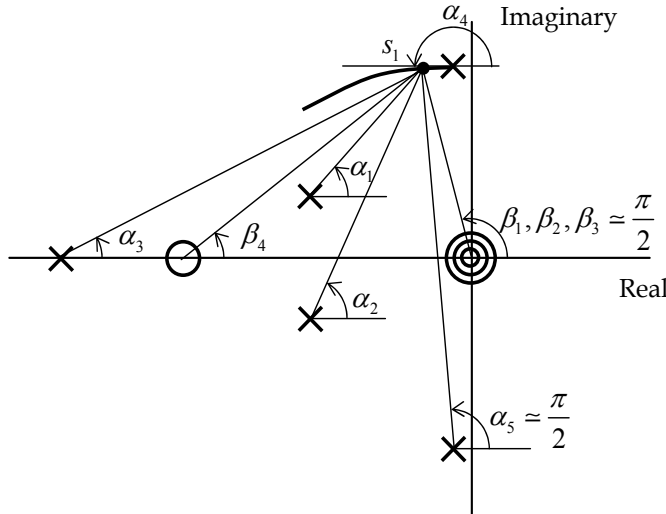
Fig. 4. Departure angle of the locus corresponding to the fundamental structure vibration mode (not to scale). (×) pole; (o) zeros

3.3 Stability
Stability is the primary concern in any active control system applied to civil engineering structures, mainly due to safety and serviceability reasons. The control scheme of Fig. 1, assuming that the nonlinear element f is a saturation nonlinearity, is analysed in this section. The nonlinear element can be written as

$$f\left(\ddot{y}_c(t)\right) = \begin{cases} K_c\ddot{y}_c(t) & \left|\ddot{y}_c(t)\right| \le V_s/K_c \\ V_s sign\left(\ddot{y}_c(t)\right) & \left|\ddot{y}_c(t)\right| > V_s/K_c \end{cases} \tag{17}$$

where K_c is the control gain and V_s is the maximum allowable control voltage to the actuator (saturation level). The saturation nonlinearity is introduced to avoid actuator force saturation and to keep the system safe under any excitation and independently of selection of control parameters. The stability can be studied using the Describing Function (DF) tool in its basic form (Slotine & Li, 1991). Firstly, the total transfer function of the linear part (Eqs. (2), (3), (6) and (9)) is obtained (see Fig .1)

$$G_T(j\omega) = C_D(j\omega)G_A(j\omega)G(j\omega)C_F(j\omega). \tag{18}$$

Then, from the root locus of G_T, the limit gain $K_{c,\text{limit}}$ for which the closed-loop system becomes unstable is derived. This is the minimum value of the control gain K_c (see Eq. (17)) for which at least one of the loci intersects the imaginary axis.

Secondly, the DF, denoted by $N(A,\omega)$, for the nonlinear element is obtained. The DF is the ratio between the fundamental component of the Fourier series of the nonlinear element output and a sinusoidal input given by $x(t) = A\sin(\omega t)$. If the nonlinearity is hard, odd and single-valued (the case of saturation nonlinearity), the DF depends only on the input amplitude $N(A,\omega) = N(A)$, i.e., it is a real function. The DF for a saturation nonlinearity is (Slotine & Li, 1991)

$$N(A) = \begin{cases} K_c & A \le a \\ \dfrac{2K_c}{\pi}\left[\arcsin\left(\dfrac{a}{A}\right) - \dfrac{a}{A}\sqrt{1 - \dfrac{a^2}{A^2}}\right] & A > a \end{cases} \tag{19}$$

with $a = V_s/K_c$ (see Eq. (17)). The normalised DF $N(A)/K_c$ (19) is plotted in Fig. 5a as a function of A/a. If the input amplitude is in the linear range $(A \le a)$, $N(A)$ is constant and equal to the control gain $N(A) = K_c$. $N(A)$ then decreases as the input amplitude increases when $A > a$. That is, saturation does not occur for small signals and it reduces the ratio of the output to input as the input increases.

Thirdly, the extended Nyquist criterion using the DF is applied

$$G_T(j\omega) = -1/N(A). \tag{20}$$

Each solution of Eq. (20) predicts a limit cycle behaviour (self-sustained periodic undesirable vibration). The total transfer function $G_T(j\omega)$ will intersect the real axis at $-1/K_{c,\text{limit}}$. With regards to the plot of $-1/N(A)$, it will start at $-1/K_c$ and go to $-\infty$ as A increases. Depending on the value of K_c, both plots $G_T(j\omega)$ and $-1/N(A)$ can intersect. Fig. 5b illustrates this fact. The conclusion is that: if $K_c < K_{c,\text{limit}}$, the system is asymptotically stable and goes to zero vibration (no intersection); otherwise, a limit cycle is predicted (intersection). Such a limit cycle is deduced to be stable by using the limit cycle stability criterion (Slotine & Li, 1991; Díaz & Reynolds, 2010a). The properties of the limit cycle, frequency and amplitude, can be obtained by Eq. (20) particularised to the intersection point.
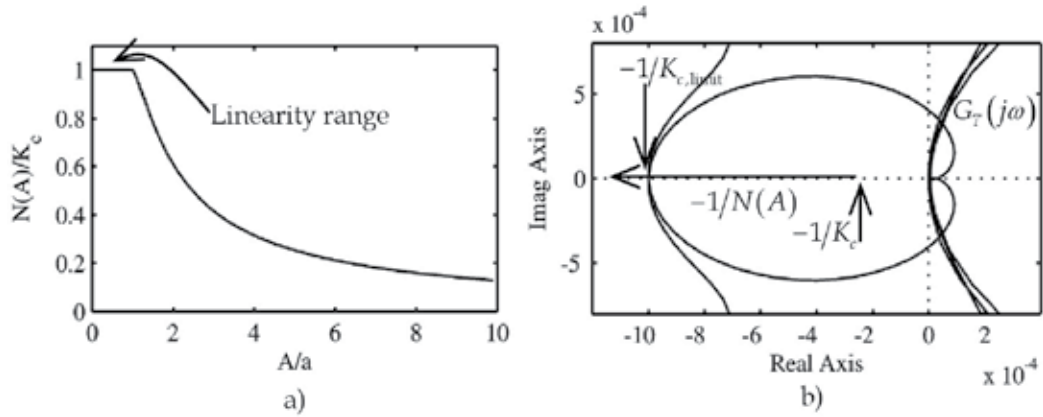
Fig. 5. a) DF for the saturation nonlinearity. b) Nyquist diagram of $G_T(j\omega)$ and $-1/N(A)$

3.4 Design process

The design process of the control scheme represented in Fig. 1 can be summarised in the following steps:

Step 1: Identify the actuator G_A and structure dynamics G.

Step 2: Design the direct compensator (phase-lead) C_D accounting for the actuator stroke saturation. This design is carried out following the procedure described in Subsection 3.1.

Step 3: Design the feedback (phase-lag) compensator C_F to increase the damping and robustness with respect to stability and performance of the closed-loop system by following Subsection 3.2.

Step 4: Design the nonlinear element f according to stability and performance. If f is a saturation nonlinearity, take a saturation value to avoid actuator force overloading and select a suitable gain K_c using the root locus method.

4. Implementation on a floor structure

This Section presents the design and practical implementation of an AVC system based on the procedure presented in Section 3 on an in-service open-plan office floor sited in the North of England.

4.1 Structure description and modal properties

The test structure is a composite steel-concrete floor in a steel frame office building. A plan of the floor is shown in Fig. 6a, in which the measurement points used for the experimental modal analysis (EMA) are indicated. Columns are located along the two sides of the building (without point numbers) and along the centreline (18-27-end), at every other test point (TP) location (i.e, 18, 20, 22, etc.). Fig 6b shows a photograph from TP 44 towards TP 28 and Fig. 6c shows a photograph from TP 12 towards TP 01. The EMA of this structure is explained in detail in (Reynolds et al., 2009). The floor is considered by its occupants to be quite lively, but not sufficiently lively to attract complaints. Special attention is paid to TP 04 (see Fig. 6a) and its surroundings because it is perceived to be a particularly lively location

on the floor. Because the vibration perception is particularly acute at this point, this is the candidate for the installation of the AVC system.
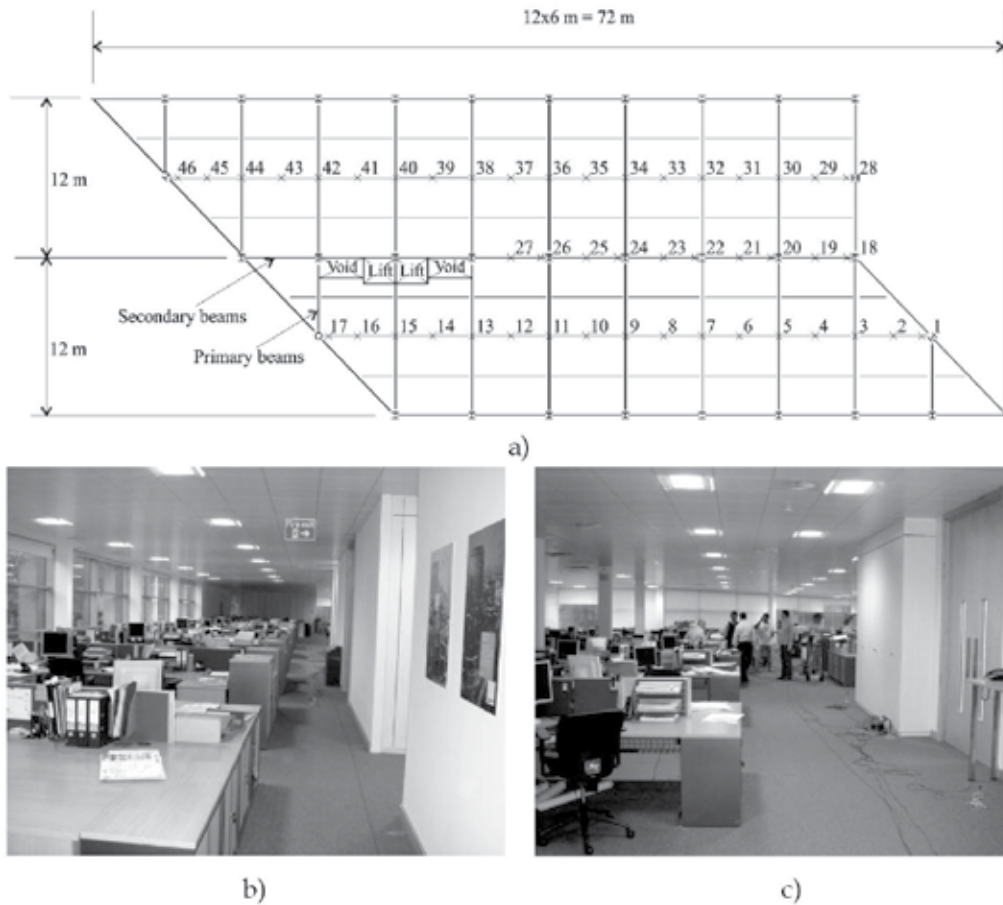
Fig. 6. Floor structure. a) Plan of the floor (not to scale); (×) measurement point used in the EMA. b) View from TP 44 towards TP 28. c) View from TP 12 to TP 01

A multi-input multi-output modal testing is carried out with four excitation points placed at TPs 04, 07, 31 and 36 and responses measured at all TPs. The artificial excitation is supplied by APS Dynamics Model 400 electrodynamic shakers (Fig. 7b) and responses are measured by QA750 force-balance accelerometers (Fig. 7c). Fig 7a shows a photograph of the multishaker modal testing carried out. Fig. 8 shows the magnitudes of the point accelerance FRFs acquired. Interestingly, the highest peak occurs at TP 04 at approximately 6.4 Hz, which is the point on the structure where the response has been subjectively assessed to be highest. Parameter estimation is carried out using the multiple reference orthogonal polynomial algorithm already implemented in ME'scope suite of software. Fig. 9 shows the estimated vibration modes which are dominant at TP 04.

Fig. 7. a) Multishaker modal testing of the floor structure. b) APS Dynamics Model 400 electrodynamic shaker. c) QA750 force-balance accelerometer

Fig. 8. Magnitudes of the point accelerance FRFs at TP 04, 07, 31 and 36

Fig. 9. Estimated vibration modes prone to be excited by human walking at TP 04. a) Vibration mode at 6.37 Hz. b) Vibration mode at 9.19 Hz
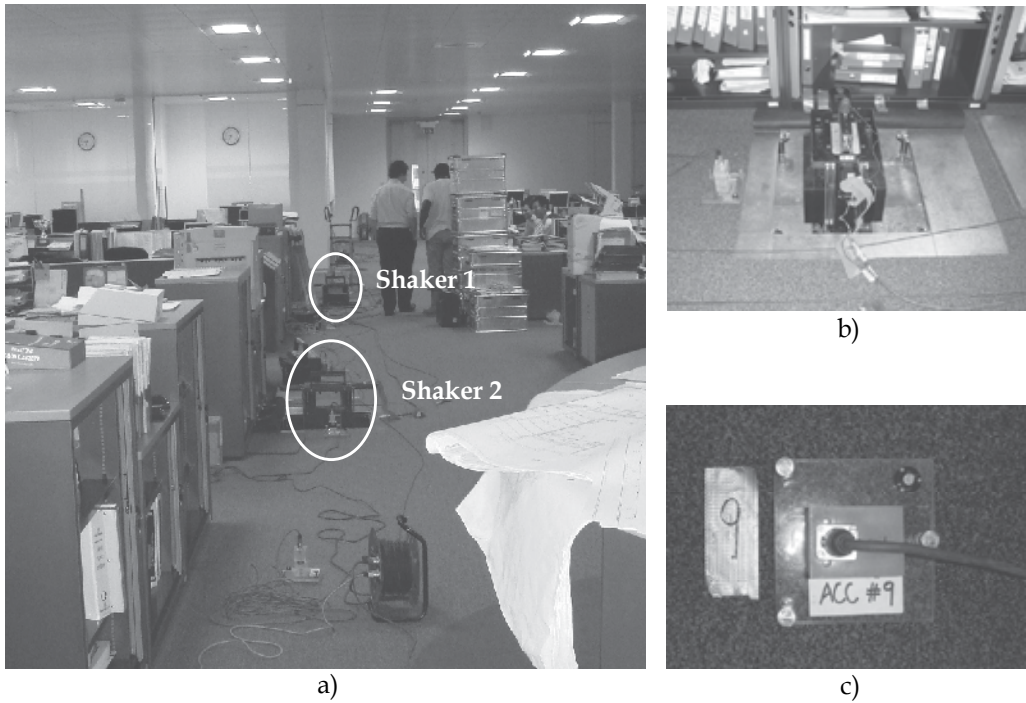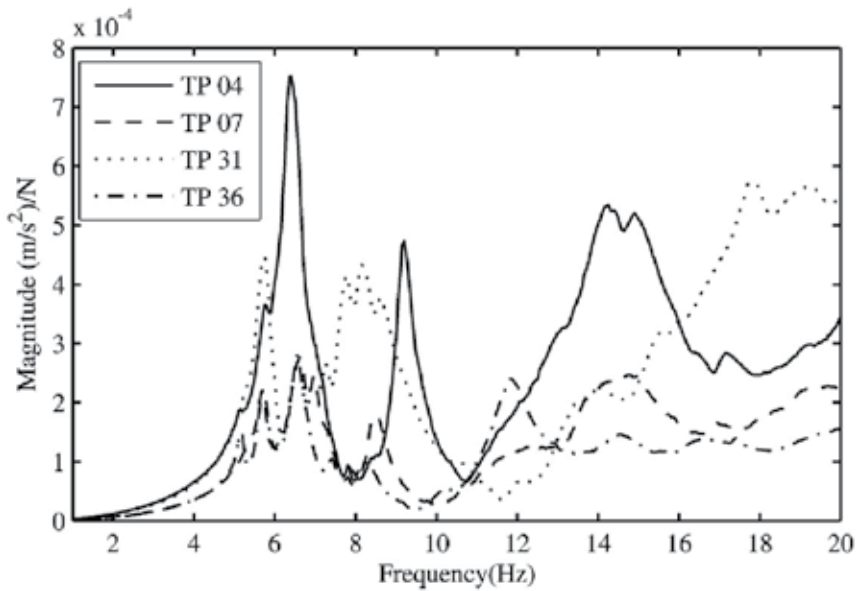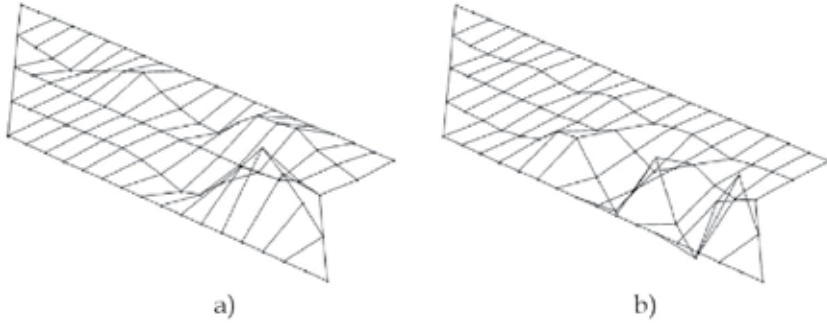
4.2 System dynamics

The AVC system is placed at TP 04. The floor dynamics at the AVC location (Eq. (2)) and the actuator dynamics (Eq. (3)) are identified. Using the modal parameters obtained from the EMA, the transfer function of the floor is modelled considering three vibration modes $N = 3$ in the frequency range of 0–20 Hz

$$G(s) = \frac{4.49 \cdot 10^{-5} s^2}{s^2 + 2.36s + 1627} + \frac{1.74 \cdot 10^{-5} s^2}{s^2 + 2.09s + 3341} + \frac{1 \cdot 10^{-4} s^2}{s^2 + 17.59s + 7738} \tag{21}$$

The inertial actuator is an APS Dynamics Model 400 electrodynamic shaker (operated in inertial mode and driven using voltage mode) with an inertial mass of $m_A = 30.4$ kg (APS Manual). The actuator model is obtained to be

$$G_A(s) = \frac{12600 s^2}{s^3 + 62.16 s^2 + 728.6s + 6573}. \tag{22}$$

The natural frequency of the actuator is estimated as 1.80 Hz and the pole that provides the low pass property is estimated to be $\varepsilon = 50.26$ rad/s (Eq. (3)).

4.3 Controller design

Compensators C_D and C_F are obtained following Section 3. Firstly, C_D is obtained. From (22), the transfer function G_d (Eq. (4)) is derived. By assuming a value of $d = 0.05$ m, which is appropriate considering the actual stroke limit of the actuator is 0.075 m, its magnitude $|\hat{G}(j\omega)|$ (Eq. (5)) is obtained with $\hat{\omega} = 14.74$ rad/s. The compensator parameters are thus derived from the optimisation problem (8) in which it is assumed $\omega_L = 1.25$ rad/s, $\omega_U = 62.83$ rad/s and $\lambda_{max} = \eta_{max} = \varepsilon = 50.26$. The control parameters are then found to be $\lambda = 6.87$ and $\eta = 14.34$.

Secondly, the feedback compensator C_F (Eq. (9)) is obtained. Taking into account the dominant dynamics: G_A, C_D and the fundamental floor vibration mode of (21) (the first one of the three considered mode), and restricting the departure angle of the locus corresponding to the structure vibration mode as $\alpha_4 \in (180, 225)$ deg (see Fig. 4), then the angle corresponding to the zero of the compensator β_4 can be bounded. It is obtained

84 Vibration Analysis and Control – New Trends and Developments

$\beta_4 \in (10.24, 55.24)$ deg and consequently $\gamma \in (27.9, 223.2)$ using Eq. (14). A value of $\gamma = 55$ is chosen since it must be higher than the inferior limit but it should not be so high that the attractor effect of the zero is focussed on the fundamental vibration mode. The root locus technique is used here. The root locus of G_T (Eq. (18)) for CAFC is plotted in Fig. 10. It can be observed that the linear system might be critically damped for the fundamental floor vibration mode.
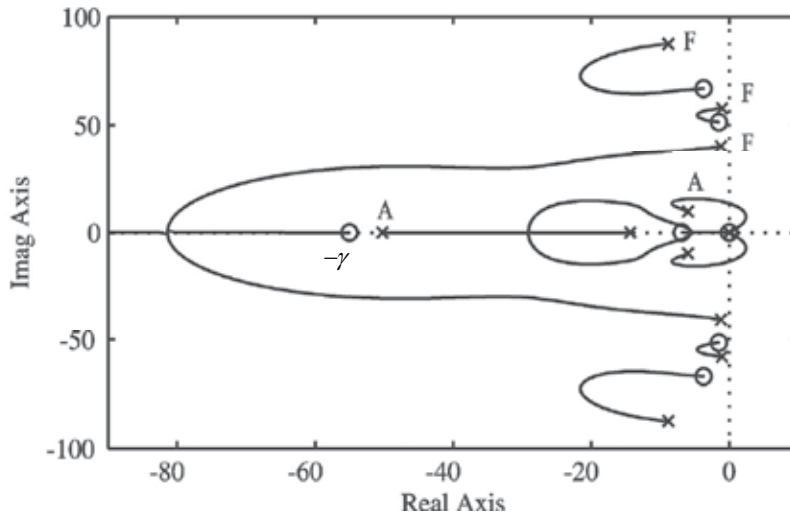
Fig. 10. Root locus of the total transfer function G_T for CAFC. (×) pole; (o) zero; (F) floor; (A) actuator

Finally, the nonlinear element is chosen as a saturation nonlinearity (17) with $V_s = 1$ V, which is a convenient value to avoid actuator force overloading at any frequency of the excitation. Therefore, the stability is guaranteed just by taking a safe control gain $K_c < K_{c,\text{limit}}$. The limit gain is predicted to be $K_{c,\text{limit}} = 44.4$ V/(m/s^2). Values of damping of the actuator poles smaller than 0.30 are not recommended (Hanagan, 2005). This damping is reached for $K_c = 18.6$ V/(m/s^2).

A digital computer is used for the on-line calculation of the control signal V. The system output is sampled with a period $\Delta t = 0.001$ s and the control signal is calculated once every sampling period. Then, the discrete-time control signal is converted into a zero-order-hold continuous-time signal. Likewise, the continuous transfer functions of the compensators are converted to discrete transfer function using the zero-order-hold approximation. Note that the sampled period used is sufficiently small to not consider the delay introduced by the digital implementation of the control scheme.

4.4 Results

The AVC system is assessed firstly by carrying out several simulations using different values of the control gain K_c. MATLAB/Simulink is used for this purpose. The control scheme shown in Fig. 1 is simulated using the transfer function models of the compensators given by Eqs. (6) and (9) with the parameters obtained in Section 4.3 and Eqs. (21) and (22)

obtained from FRF identifications. The control scheme is perturbed by a real walking excitation obtained from an instrumented treadmill (Brownjohn et al., 2004) ($p(t)$ in Fig. 1). Table 1 shows the results obtained. Two different pacing frequencies (1.58 and 2.12 Hz) are used in such a way that the first floor vibration mode might be excited by the third or the fourth harmonic. The results are compared in terms of the maximum transient vibration value (MTVV) calculated from the 1 s running RMS acceleration and from the vibration dose value (VDV) obtained from the total period of the excitation (BS 6472, 2008). The BS 6841 W_b weighted acceleration is used for both measures (BS 6841, 1987). The results predicted that the AVC are quite insensitive to the gain value. The reduction in vibration is approximately 60 % for slow walking (1.58 Hz) and 53 % for fast walking (2.12 Hz) in terms of MTVV. The results in terms of the VDV provide similar reductions as for the MTVV.

Control gain (V/(m/s²))	Uncontrolled	5	10	15	20
Walking at 1.58 Hz					
MTVV[1] (m/s²)	0.030	0.0122	0.0115	0.0115	0.0116
Reduction MTVV (%)	—	59	62	62	61
VDV[2] (m/s¹·⁷⁵)	0.063	0.029	0.027	0.027	0.027
Reduction VDV (%)	—	55	58	58	57
Walking at 2.12 Hz					
MTVV (m/s²)	0.033	0.0154	0.0150	0.0156	0.0160
Reduction MTVV (%)	—	53	55	53	52
VDV (m/s¹·⁷⁵)	0.073	0.034	0.032	0.033	0.033
Reduction VDV (%)	—	54	56	55	55

Table 1. Simulation performance assessment for the floor structure using several control gains and walking excitation. [1] Maximum Transient Vibration value defined as the maximum value of 1s running RMS acceleration. [2] Cumulative Vibration Dose Value

Actual walking tests are carried out on the test structure using the same walking excitation frequencies as in the simulations. The walking path consists of walking from TP 01 to TP 09 and then back from TP 09 to TP 01 (see Fig. 6). A gain of $K_c = 15$ V/$\left(m/s^2\right)$ is found to give good performance so that is used in the experiments. Fig. 11 shows BS 6841 W_b weighted response time histories (including the 1s RMS and the cumulative VDV), uncontrolled and controlled, for a pacing frequency of 1.58 Hz, which is controlled using a metronome set to 95 beats per minute (bpm). The MTVV is reduced from 0.031 m/s² to 0.010 m/s², a reduction of 68 %, and the VDV is reduced from 0.050 m/s¹·⁷⁵ to 0.019 m/s¹·⁷⁵, a reduction of 62 %. The same test is carried out for a pacing frequency of 2.12 Hz (127 bpm). The achieved reduction in terms of the MTVV is now 52 %, from 0.033 m/s² to 0.016 m/s², and in terms of the VDV is 51 %, from 0.057 m/s¹·⁷⁵ to 0.028 m/s¹·⁷⁵. The experimental reductions agreed very well with the numerical predictions (see Table 1).

Continuous whole-day monitoring has been carried out to assess the vibration reduction achieved by the AVC system. The acceleration is measured from 6:00 am to 6:00 pm during four working days, two without and two with the AVC system. The R-factor is used to quantify the vibration reduction. This factor is defined as the ratio between the 1 s running RMS of the BS 6841 W_b weighted acceleration response and 0.005 m/s² (Wyatt, 1989). Fig. 12 shows the percentage of time during which the R-factor is over 1, 2, 3, 4 and 5. The values
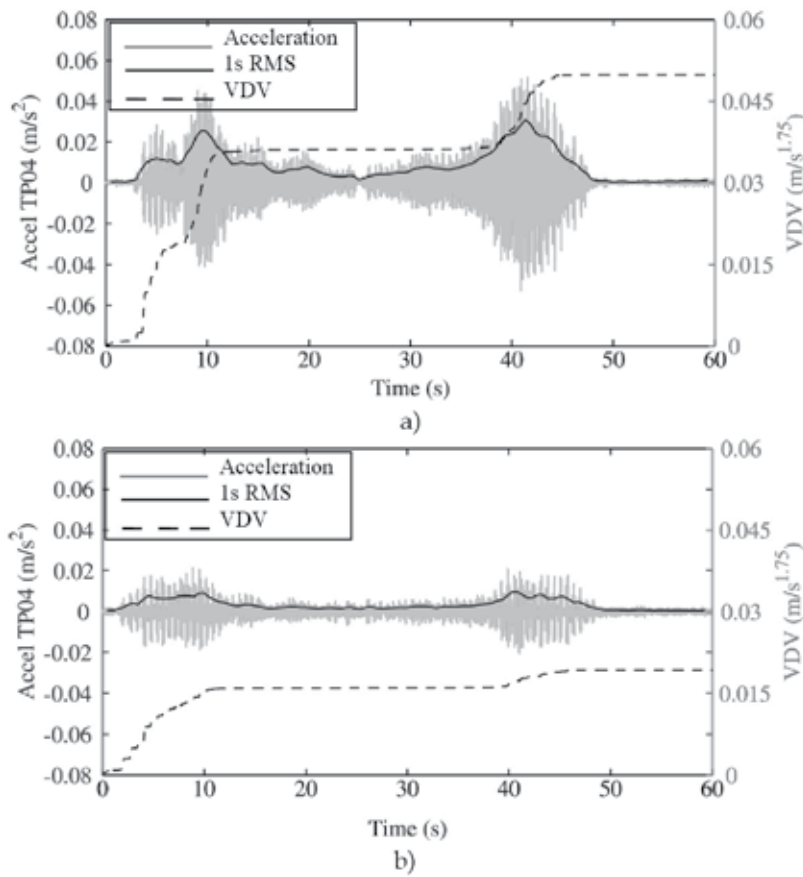
Fig. 11. Experimental results on the floor structure. Walking at 1.58 Hz (95 bpm). a) Uncontrolled $\text{MTVV} = 0.031 \text{ m/s}^2$ and $\text{VDV} = 0.050 \text{ m/s}^{1.75}$. b) Controlled $\text{MTVV} = 0.010 \text{ m/s}^2$ and $\text{VDV} = 0.019 \text{ m/s}^{1.75}$
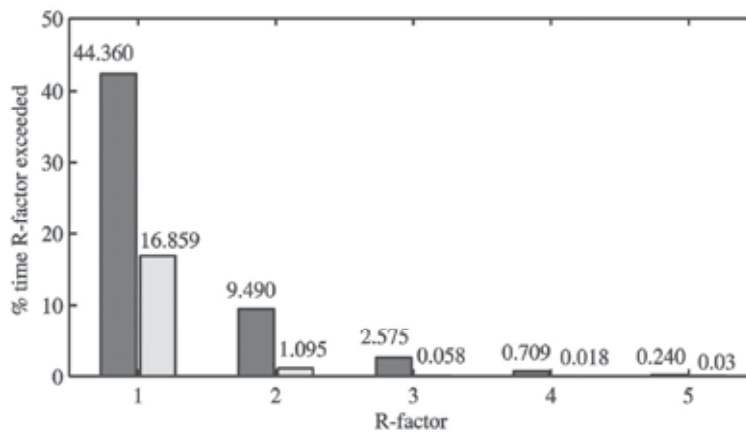

Fig. 12. Whole-day monitoring: percentage of time of exceedance of R-factors

shown in the Fig. are the mean values between the two corresponding days. It is observed that the time for which the R-factor is over 1 is reduced by 60 % and the time for which it is over 4 is significantly reduced by over 97 %. Note that the second reduction is very important since an R-factor of 4 is a commonly used vibration limit for a high quality office floor (Pavic & Willford, 2005). Hence, these results clearly illustrate the effectiveness of the AVC system designed. In addition, the cumulative VDV is also calculated for the same exposure to vibration and using the W_b weighted acceleration. The VDV obtained when the AVC system is disconnected is 0.162 m/s$^{1.75}$ whereas such a value is 0.101 m/s$^{1.75}$ when the system is engaged. The reduction achieved is almost 40 %. Note that the VDV is much more strongly influenced by vibration magnitude than duration (BS 6472, 2008). This fact results in less vibration reduction in terms of the VDV than using the MTVV.

5. Implementation on a footbridge

This Section presents the design and practical implementation of an AVC system based on the procedure presented in Section 3 on an in-service footbridge sited in Valladolid (Spain).

5.1 Structure description and modal properties

The test structure, sited in Valladolid (Spain), is a footbridge that creates a pedestrian link over The Pisuerga River between the Science Museum and the city centre (see Fig. 13). This bridge, built in 2004, is a 234 m truss structure composed of four spans: three made of tubular steel beams and one made of white concrete, all of them with a timber walkway. The main span (Span 3 in Fig. 1), post-tensioning by two external cable systems (transversal and longitudinal), is 111 m, the second span (Span 2 from this point onwards) is 51 m and the other two spans are shorter and stiffer (Gómez, 2004). The external cable systems of Span 3 has both aesthetical reasons (the original design by the architect José Rafael Moneo was based on the form of a fish basket) and structural reasons (making Span 3 stiffer).

Because of its slenderness, this footbridge, especially Span 2, represents a typical lightweight structure sensitive to dynamic excitations produced by pedestrians. Annoying levels of vibration are sometime perceived in Span 2. Special attention is paid to the point of maximum amplitude of the first bending mode (close to mid-span) since the vibration perception is acute at this point, particularly when runners cross the bridge. Therefore, it is decided to study the dynamic properties of this span and implement the AVC system at that point.
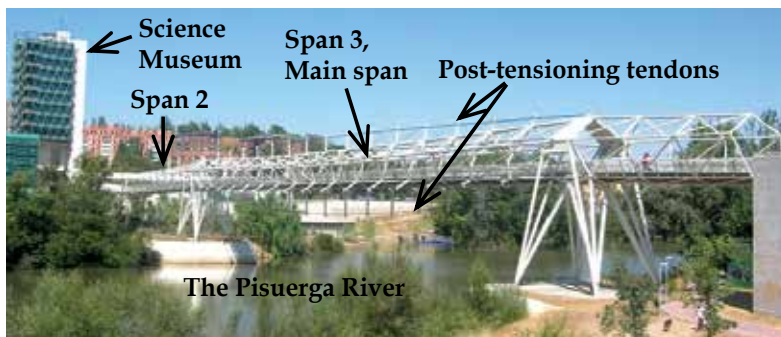

Fig. 13. General view of the Valladolid Science Museum Footbridge

The operational modal analysis of Span 2 is carried out in order to obtain the natural frequencies, damping ratios and modal shapes of the lower vibration modes. The analysis is carried out with five roving and two reference accelerometers. Preliminary spectral analyses and time history recordings indicates that the vertical vibration is considerably higher than the horizontal one, thus, only vertical response measurements are performed. A measurement grid of 3 longitudinal lines with 9 equidistant test points is considered, resulting in 27 test points. Five setups with an acquisition time of 720 seconds and a sampling frequency of 100 Hz are recorded. Thus, it is expected to successfully identify vibration modes up to 30 Hz. The modal parameter estimation is carried out using the ARTeMIS suite of software. In particular, frequency domain methods (Frequency domain decomposition-FDD, enhanced frequency domain decomposition-EFDD and curve-fit frequency domain decomposition-CFDD) are used. Table 2 shows the modal parameters estimated through the modal analysis for the first four vibration modes. Fig. 14 shows the corresponding estimated modal shapes.

		Mode 1	Mode 2	Mode 3	Mode 4
FDD	Frequency (Hz)	3.516	6.250	7.373	9.351
	Damping ratio (%)	—	—	—	—
EFDD	Frequency (Hz)	3.506	6.278	7.386	9.365
	Damping ratio (%)	0.7221	0.4167	0.6571	0.5528
CFDD	Frequency (Hz)	3.508	6.274	7.389	9.367
	Damping ratio (%)	0.7984	0.2599	0.4319	0.3869

Table 2. Natural frequencies and damping ratios identified by the operational modal analysis of the footbridge

1st bending mode: 3.5 Hz

1st torsional mode: 6.3 Hz

2nd bending mode: 7.4 Hz
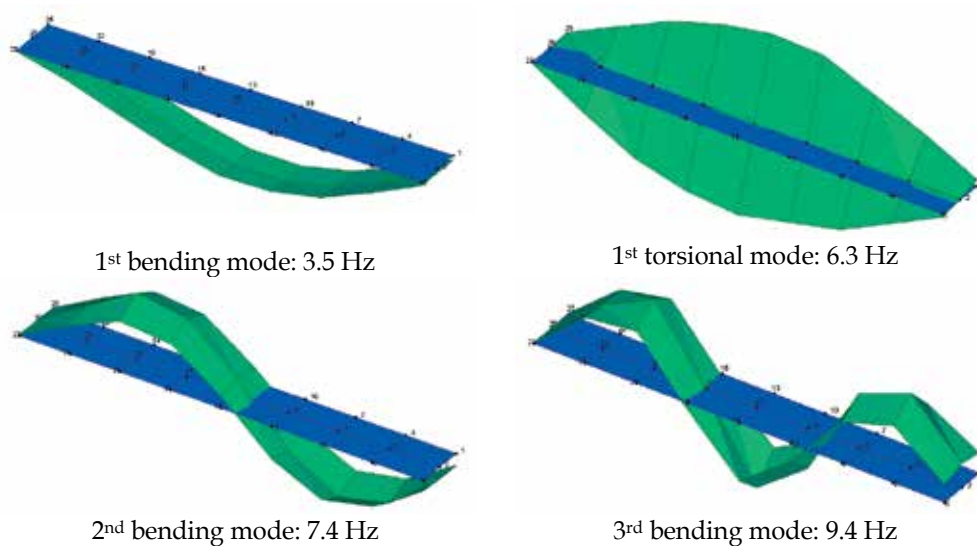

3rd bending mode: 9.4 Hz

Fig. 14. Estimated modal shapes for the footbridge structure

5.2 System dynamics

The FRF between the structure acceleration and the input force is obtained at the middle of the transversal steel beam sited closest to the point of maximum value of the first vibration mode (close to mid-span). A chirp signal with frequency content between 1 and 15 Hz is used to excite the first vibration modes. The force is generated by an APS Dynamics Model 400 electrodynamic (as was used for the floor) and the structure acceleration is measured by a piezoelectric accelerometer (as those used for the modal analysis). The force induced by the shaker is estimated by measuring the acceleration of the inertial mass and multiplying this by the magnitude of the inertial mass (30.4 kg). Thus, the structure dynamics for the collocated case between the acceleration (output) and the force (input) can be identified from model (2) as follows

$$G(s) = \frac{5.40 \cdot 10^{-5} s^2}{s^2 + 0.3079s + 483.6} + \frac{5.85 \cdot 10^{-5} s^2}{s^2 + 0.5887s + 3451} \tag{23}$$

The vibration modes at 6.3 and 7.4 Hz (see Fig. 14) are not clearly observed and they are not included into this model. The same shaker that is used to obtain the FRF for the structure is used as inertial actuator. The transfer function between the output force and the input voltage is the one given by Eq. (22).

5.3 Controller design

The design process shown in Section 3 is now followed. The direct compensator of the form of (6) is assumed. Again, a maximum stroke for harmonic excitation of d = 0.05 m is considered in the design. The compensator parameters are obtained from the optimisation problem (8) using the parameter used in Subsection 4.3. The controller parameters are found to be $\lambda = 5.6$ and $\eta = 24.6$. These parameters are selected in such a way that the likelihood of stroke saturation is reduced significantly. The stroke saturation leads to collisions of the inertial mass with its stroke limits, imparting highly undesirable shocks to the structure and possibly causing damage to the actuator.

Once the direct compensator is designed, the feedback one (9) is designed considering the dynamics of the actuator, structure and the direct compensator dynamics. As in Subsection 4.3, the departure angle of the locus corresponding to the structure vibration mode is restricted to $\alpha_4 \in (180, 225)$ deg (see Fig. 4). It is obtained $\gamma \geq 35.5$. A value of $\gamma = 50$ is finally chosen. The root locus technique is now used. The root locus of the total transfer function of the linear part (18) is plotted in Fig. 15 (only the dominant dynamics are shown). It is observed that a couple of branches in the root locus corresponding to the actuator dynamics go to the right-half plane provoking unstable behaviour in the actuator. The gain for which the control system is unstable is the limit gain $K_{c,\text{limit}} = 82 \text{ V}/(\text{m/s}^2)$. Finally, a gain of $K_{c,\text{limit}} = 40 \text{ V}/(\text{m/s}^2)$ is chosen. The saturation level is set to $V_s = 1 \text{ V}$.

5.4 Results

Once both compensators and the control parameters are selected, simulations are carried out in order to assess the AVC performance. MATLAB/Simulink is again used for this purpose. Table 3 shows controlled acceleration response for walking and running excitation. Moreover, the AMD displacement estimation is included.
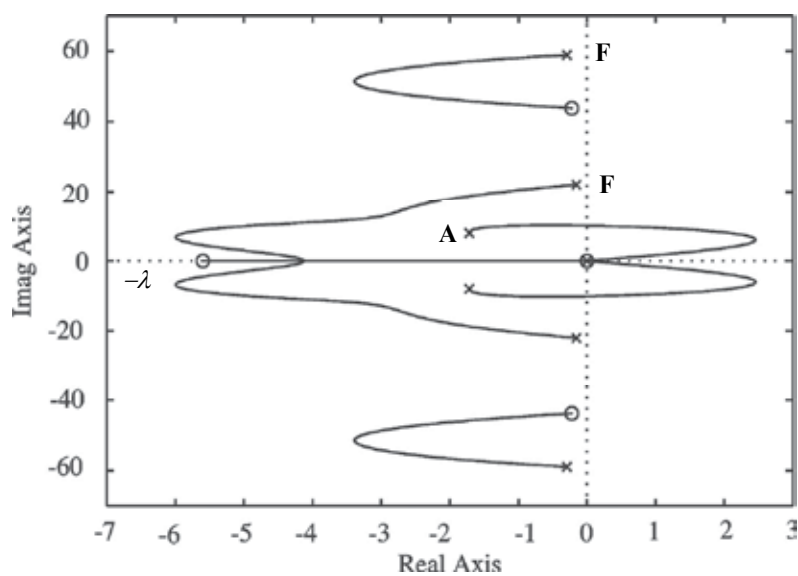
Fig. 15. Root locus of the total transfer function G_T for CAFC on the footbridge. (×) pole; (o) zero; (F) footbridge; (A) actuator

	Uncontrolled (m/s²)	Controlled (m/s²)	Reduction (%)	Mass displacement (m)
Walking at 1.75 Hz	0.39	0.04	89	± 0.034
Running at 3.50 Hz	6.16	3.75	40	± 0.022

Table 3. Simulation performance assessment for the footbridge using the peak acceleration for walking and running excitation

Walking and running tests are carried out to assess the efficacy of the AVC system. The walking tests consist of walking at 1.75 Hz such that the first vibration mode of the structure (3.5 Hz) could be excited by the second harmonic of walking. A frequency of 3.5 Hz is used for the running tests so that the structure is excited by the first harmonic of running. The walking/running tests consisted of walking/running from one end of Span 2 to the other and back again. The pacing frequency is controlled using a metronome set to 105 beats per minute (bpm) for 1.75 Hz and to 210 bpm for 3.5 Hz. Each test is repeated three times.

	Uncontrolled	Controlled	Reduction (%)
Walking at 1.75 Hz			
Peak acceleration (m/s²)	0.41	0.16	70
MTVV[1] (m/s²)	0.21	0.06	67
Running at 3.50 Hz			
Peak acceleration (m/s²)	3.34	1.19	64
MTVV (m/s²)	2.20	0.69	68

Table 4. Experimental performance assessment for walking and running excitation. [1] Maximum Transient Vibration value defined as the maximum value of 1s running RMS acceleration

The results are compared by means of the maximum peak acceleration and the MTVV computed from the 1 s running RMS acceleration. Table 4 shows the result obtained for the uncontrolled and controlled case. It is observed that the AMD designed (with a moving mass of 30 kg) performs well for both excitations, achieving reductions of approximately 70 %. Fig. 16 shows the response time histories (including the 1 s RMS) uncontrolled and controlled for a walking test. Fig. 17 shows the same plots for a running test.
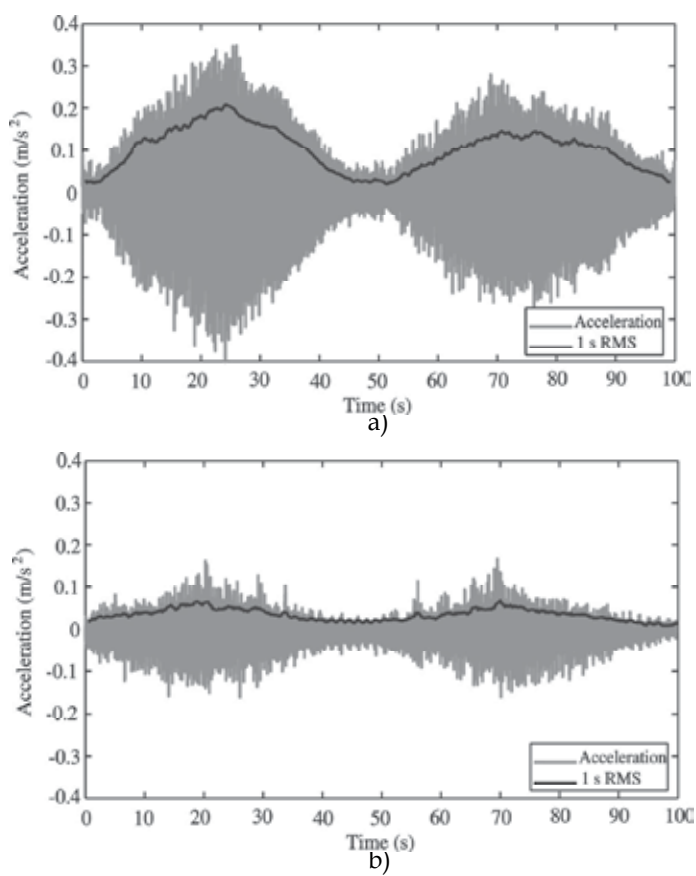
Fig. 16. Walking test on the footbridge. a) Uncontrolled $MTVV = 0.207 \ m/s^2$. b) Controlled $MTVV = 0.067 \ m/s^2$
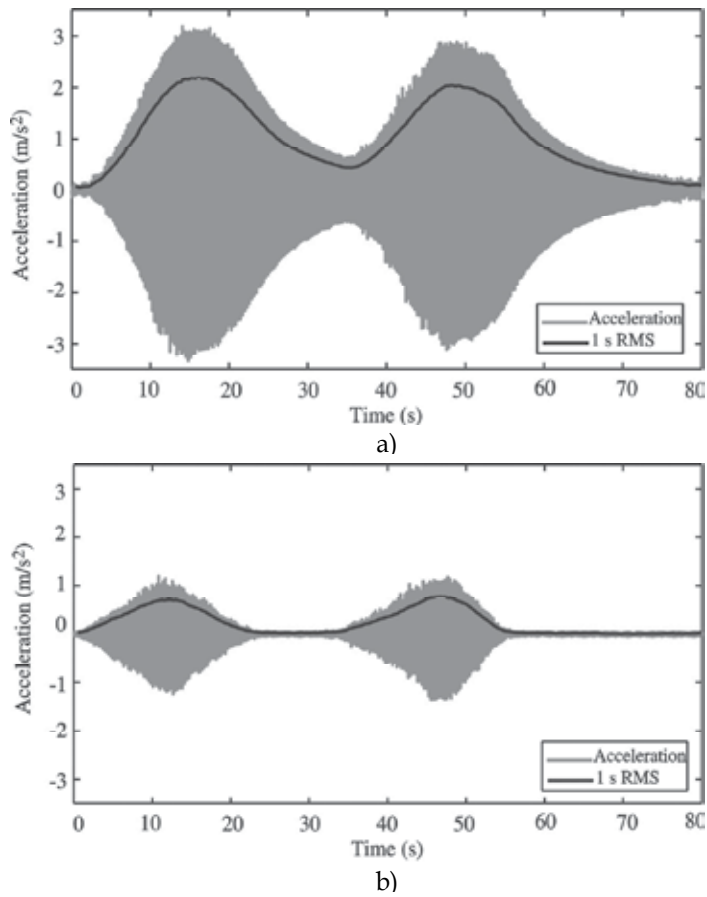
Fig. 17. Running test on the footbridge. a) Uncontrolled $MTVV = 2.198 \ m/s^2$. b) Controlled $MTVV = 0.773 \ m/s^2$

6. Conclusion

The active cancellation of human-induced vibrations has been considered in this chapter. Even velocity feedback has been used previously for controlling human-induced vibrations, it has been shown that this is not a desirable solution when the actuator dynamics influence the structure dynamics. Instead of using velocity feedback, here, it is used a control scheme base on the feedback of the acceleration (which is the actual measured output) and the use of a first-order compensator (phase-lag network) conveniently designed in order to achieve significant relative stability and damping. Note that the compensator could be equivalent to an integrator circuit leading to velocity feedback, depending on the interaction between actuator and structure dynamics. Moreover, the control scheme is completed by a phase-lead network to avoid stroke saturation due to low-frequency components of excitations and a nonlinear element to account for actuator overloading. An AVC system based on this control scheme and using a commercial inertial actuator has been tested on two in-service structures, an office floor and a footbridge.

The floor structure has a vibration mode at 6.4 Hz which is the most likely to be excited. This mode has a damping ratio of 3% and a modal mass of approximately 20 tonnes. Reductions of approximately 60 % have been observed in MTVV and cumulative VDV for controlled walking tests. For in-service whole-day monitoring, the amount of time that an R-factor of 4 is exceeded, which is a commonly used vibration limit for high quality office floor, is reduced by over 97 %. The footbridge has a vibration mode at 3.5 Hz which is the most likely to be excited. This mode has a damping ratio of 0.7 % and a modal mass of approximately 18 tonnes. Reductions close to 70 % in term of the MTVV has been achieved for walking and running tests.

It has been shown that AVC could be a realistic and reasonable solution for flexible lightweight civil engineering structures such as light-weight floor structure or lively footbridges. In these cases, in which low control forces are required (as compared with other civil engineering applications such as high-rise buildings or long-span bridges), electrical actuators can be employed. These actuators present advantages with respect to hydraulic ones such as lower cost, maintenance and level of noise. However, AVC systems for human-induced vibrations needs much further research and development to jump into building and construction technologies considered by designers. With respect to passive systems, such as TMDs, cost is still the mayor disadvantage. However, it is expected that this technology will become less expensive and more reasonable in the near future. Research projects involving the development of new affordable and compact actuators for human-induced vibration control are currently on the go (Research Grant EP/H009825/1, 2010).

7. Acknowledgment

8. References

APS. *Instruction Manual Electro-Seis Model 400 Shaker*, APS Dynamics, USA, available from http://www.apsdynamics.com

Bachmann, H. (1992). Case studies of structures with man-induced vibrations. *Journal of Structural Engineering*, Vol.118, No.3, pp. 631-647, ISNN 0733-0445

Bachmann, H. (2002). Lively footbridges—a Real Challenge, *Proceedings of the International Conference on the Design and Dynamic Behaviour of Footbridges*, OTUA, Paris, France, November 20-22

Balas, M.J. (1979). Direct velocity feedback control of large space structures, *Journal of Guidance and Control*, Vol.2, No.3, pp. 252–53

Bolton, W. (1998). *Control engineering*, Logman, ISBN 978-0-582-32773-3, United Kingdom

Brownjohn, J.M.W., Pavic, A. & Omenzetter, P. (2004). A spectral density approach for modelling continuous vertical forces on pedestrian structures due to walking, *Canadian Journal of Civil Engineering*, Vol.31, No.1, pp. 65–77, ISSN 0315-1468

BS 6841. (1987). *Measurement and evaluation of human exposure to whole-body mechanical vibration and repeated shock*, British Standards Institution, ISBN 0-580-16049-1, United Kingdom

BS 6472. (2008). *Guide to evaluation of human exposure to vibration in buildings. Part 1: Vibration sources other than blasting*, British Standards Institution, ISBN 978-0-580-53027-2, United Kingdom

Caetano, E., Cunha, A., Moutinho, C. & Magalhães, F. (2010) Studies for controlling human-induced vibration of the Pedro e Inês footbridge, Portugal. Part 2: Implementation of tuned mass dampers, *Engineering Structures*, Vol.32, pp. 1082–1091, ISSN 0141-0296

Chung, L.Y. & Jin, T.G. (1998). Acceleration feedback control of seismic structures, *Engineering Structures*, Vol.20, No.1, pp. 62–74, ISSN 0141-0296

Díaz, I.M. & Reynolds, P. (2010a). On-off nonlinear active control of floor vibrations, *Mechanical Systems and Signal Processing*, 24: 1711–1726, ISSN 0888-3270

Díaz, I.M. & Reynolds, P. (2010b). Acceleration feedback control of human-induced floor vibrations, *Engineering Structures*, Vol.32, No.1, pp. 163–173, ISSN 0141-0296

Ebrahimpour, A. & Sack, R.L. (2005). A review of vibration serviceability criteria for floor structures, *Computers and Structures*, Vol.83, pp. 2488–94, ISSN 0045-7949

FIB-Bulletin 32. (2005). *Guidelines for the design of footbridges*, International Federation for Structural Concrete, Lausanne, Switzerland

Gómez, M. (2004). A new and unusual cable-stayed footbridge at Valladolid (Spain). *Steelbridge 2004: Symposium International sur les Ponts Metálliques*, Milau, France, June, pp. 23-25

Hanagan, L.M. & Murray, T.M. (1997) Active control for reducing floor vibrations, *Journal of Structural Engineering*, Vol.123, No.11, pp. 1497–1505, ISSN 0733-9445

Hanagan, L.M., Raebel, C.H. & Trethway, M.W. (2003a). Dynamic measurements of in-place steel floors to assess vibration performance, *Journal of Performance of Constructed Facilities*, Vol.17, pp. 126–135, ISSN - 0887-3828

Hanagan, L.M., Murray, T.M. & Premaratne, K. (2003b). Controlling floor vibration with active and passive devices, *The Shock and Vibration Digest*, Vol.35, No.5, pp. 347–65, ISSN 0583-1024

Hanagan, L.M. (2005). *Active floor vibration system*, United States Patent 6874748

Moutinho, C., Cunha, A. & Caetano, E. (2010). Analysis and control of vibrations in a stress-ribbon footbridge, *Structural Control and Health Monitoring*, doi: 10.1002/stc.390

Nyawako, D. & Reynolds, P. (2007) Technologies for mitigation of human-induced vibration in civil engineering structures, *The Shock and Vibration Digest*, Vol.36, No.(6), pp. 465–93, ISSN 0583-1024

Occhiuzzi, A., Spizzuoco, M. & Ricciardelli, F. (2008). Loading models and response control of footbridges excited by running pedestrians, *Structural Control and Health Monitoring*, Vol.15, pp. 349–368, ISSN 1545-2263

Pavic, A. & Willford, M. (2005). *Appendix G in Post-tensioned concrete floors design handbook– Technical Report 43*, Concrete Society, Slough, United Kingdom

Preumont, A. (1997). *Vibration Control of Active Structures: An introduction*, Kluwer Academic, Dordrecht, ISBN 1-4020-0496-9, The Netherlands

Reiterer, M. & Ziegler, F. (2006). Control of pedestrian-induced vibrations of long-span bridges, *Structural Control and Health Monitoring*, Vol.13, pp. 1003–1027, ISSN 1545-2263

Research Grant EP/H009825/1. (2010). *Active control of human-induced vibration*, PI: Dr Paul Reynolds, Engineering and Physical Sciences Research Council, 2010–2012, United Kingdom

Reynolds, P., Díaz, I.M. & Nyawako, D.S. (2009). Vibration testing and active control of an office floor, *Proceedings of the 27th International Modal Analysis Conference*, Orlando, Florida, USA

Setareh, M. & Hanson, R.D. (1992). Tuned mass damper to control floor vibration from humans, *Journal of Structural Engineering*, Vol.118, No.3, pp. 741–62, ISSN 0733-9445

Setareh, M. (2002). Floor vibration control using semi-active tuned mass dampers, *Canadian Journal of Civil Engineering*, Vol.29, No.1, pp. 76–84, ISSN 0315-1468

Slotine, J.J. & Li, W. (1991). *Applied non linear control*, Prentice-Hall, Chapter 5, ISBN 013-040890-5, USA

Wyatt, T.A. (1989). *Design guide on the vibration of floors*, The Steel Construction Institute, ISBN 1-870004-34-5, United Kingdom

Control Strategies for Vehicle Suspension System Featuring Magnetorheological (MR) Damper

Min-Sang Seong[1], Seung-Bok Choi[1] and Kum-Gil Sung[2]
[1]Inha University
[2]Yeungnam College of Science and Technology
Korea

1. Introduction

Vehicle suspension is used to attenuate unwanted vibrations from various road conditions. So far, three types of suspension system have been proposed and successfully implemented; passive, active and semiactive. Though the passive suspension system featuring oil damper provides design simplicity and cost-effectiveness, performance limitations are inevitable due to the lack of damping force controllability. On the other hand, the active suspension system can provides high control performance in wide frequency range. However, this type may require high power sources, many sensors and complex actuators such as servovalves. Consequently, one way to resolve these requirements of the active suspension system is to adopt the semiactive suspension system. The semiactive suspension system offers a desirable performance generally enhanced in the active mode without requiring large power sources and expensive hardware.

One of very attractive and effective semiactive vehicle suspension systems is to utilize magnetorheological (MR) fluid. MR fluids are currently being studied and implemented as actuating fluids for valve systems, shock absorbers, engine mounts, haptic systems, structure damper, and other control systems. The rheological properties of MR fluids are reversibly and instantaneously changed by applying a magnetic field to the fluid domain. Recently, a very attractive and effective semi-active suspension system featuring MR fluids has been researched widely. Carlson et al., 1996 proposed a commercially available MR damper which is applicable to on-and-off-highway vehicle suspension system. They experimentally demonstrated that sufficient levels of damping force and also superior control capability of the damping force by applying control magnetic field. Spencer Jr. et al., 1997 proposed dynamic model for the prediction of damping force of a MR damper. They compared the measured damping forces with the predicted ones in time domain. Kamath et al., 1998 proposed a semi-active MR lag mode damper. They proposed dynamic model and verified its validity by comparing the predicted damping force with the measured one. Yu et al., 2006 evaluated the effective performance of the MR suspension system by road testing. Guo & Hu, 2005 proposed nonlinear stiffness model of a MR damper. They proposed nonlinear stiffness model and verified it using simulation and experiment. Du et al., 2005

proposed H-infinity control algorithm for vehicle MR damper and verified its effectiveness using simulation. Shen et al., 2007 proposed load-levelling suspension with a magnetorheological damper. Pranoto et al., 2005 proposed 2DOF-type rotary MR damper and verified its efficiencies. Ok et al., 2007 proposed cable-stayed bridges using MR dampers and verified its effectiveness using semi-active fuzzy control algorithm. Choi et al., 2001 manufactured an MR damper for a passenger vehicle and presented a hysteresis model for predicting the field-dependent damping force. Hong et al., 2008 derived a nondimensional Bingham model for MR damper and verified its effectiveness through experimental investigation. Yu et al., 2009 developed human simulated intelligent control algorithm and successfully applied it to vibration control of vehicle suspension featuring MR dampers. Seong et al., 2009 proposed hysteretic compensator of MR damper. They developed nonlinear Preisach hysteresis model and hysteretic compensator and demonstrated its damping force control performance.

As is evident from the previous research work, MR damper is very effective solution for vibration control of vehicle suspension system. So in this chapter, we formulate various vibration control strategies for vibration control of MR suspension system and evaluate their control performances. In order to achieve this goal, material characteristics of MR fluid are explained. Then the MR damper for vehicle suspension system is designed, modelled and manufactured. The characteristics of manufactured MR damper are experimentally evaluated. For vibration control, the quarter vehicle suspension system featuring MR damper is modelled and constructed. Then, various vibration control strategies such as skyhook control, PID control, LQG control, H_∞ control, Sliding mode control, moving sliding mode control and fuzzy moving sliding mode control are formulated. Finally, control performances of the proposed control algorithms are experimentally evaluated and compared.

2. Suspension modelling

2.1 MR fluid

Since Jacob Rabinow discovered MR fluid in the late 1940s, of which yield stress and viscosity varies in the presence of magnetic field, various applications using MR fluid have been developed such as shock absorbers, clutches, engine mounts, haptic devices and structure dampers, etc (Kim et al., 2002). Physical property changes of MR fluid are resulted from the chain-like structures between paramagnetic MR particles in the low permeability solvent. At the normal condition, MR fluid shows the isotropic Newtonian behavior because the MR particles move freely as shown in Fig. 1 (a). However, when the magnetic field applied to the MR fluid, MR fluid shows the anisotropic Bingham behavior and resist to flow or external shear force because the MR particles make a chain structure as shown in Fig. 1 (b). From this property, force or torque of application devices can be easily controlled by the intensity of the magnetic field.

2.2 MR damper

The schematic configuration of the cylindrical type MR damper proposed in this work is shown in Fig. 2. The MR damper is composed of the piston, cylinder and gas chamber. The floating piston between the cylinder and the gas chamber is also used in order to compensate for the volume induced by the motion of the piston. Also the gas chamber

(a) no magnetic field applied
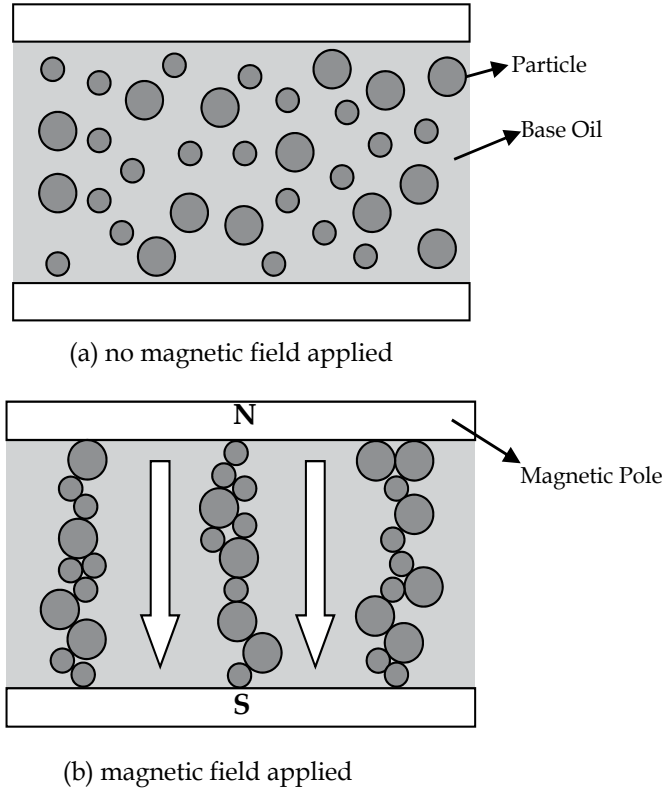

(b) magnetic field applied

Fig. 1. Phenomenological behavior of MR fluid

which is filled with nitrogen gas acts as an accumulator for absorbing sudden pressure variation of lower chamber of the MR damper induced by the rapid motion of the piston. The MR damper is divided into the upper and lower chambers by piston, and it is fully filled with the MR fluid. By the motion of the piston, the MR fluid flows through the annular duct between inner and outer piston from one chamber to the other. The magnetic poles in the piston head is placed to control the yield stress of the MR fluid by supplying current to the coil. In order effectively to generate the magnetic field in the magnetic pole, the outer cylinder and both ends of inner piston are made of ferromagnetic substance, while the center of the inner piston is a paramagnetic substance. In the absence of a magnetic field, the MR damper produces a damping force caused only by fluid viscous resistance. However, if a certain level of magnetic field is supplied to the MR damper, the MR damper produces an additional damping force owing to the yield stress of the MR fluid. This damping force of the MR damper can be continuously tuned by controlling the intensity of the magnetic field.

In order to simplify the analysis of the MR damper, it is assumed that the MR fluid is incompressible and that pressure in one chamber is uniformly distributed. The pressure drops due to the geometric shape of the annular duct and the fluid inertia are assumed to be negligible. For laminar flow in the annular duct, the fluid resistance is given by (Liu et al., 2006; White, 1994)

$$R_e = 8\eta \frac{L}{\pi\left[R_o^4 - R_i^4 - \frac{\left(R_o^2 - R_i^2\right)^2}{ln(R_o/R_i)}\right]} \qquad (1)$$
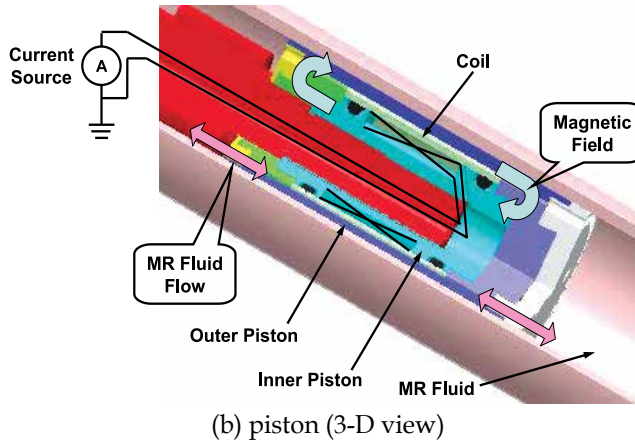
(a) MR damper

(b) piston (3-D view)
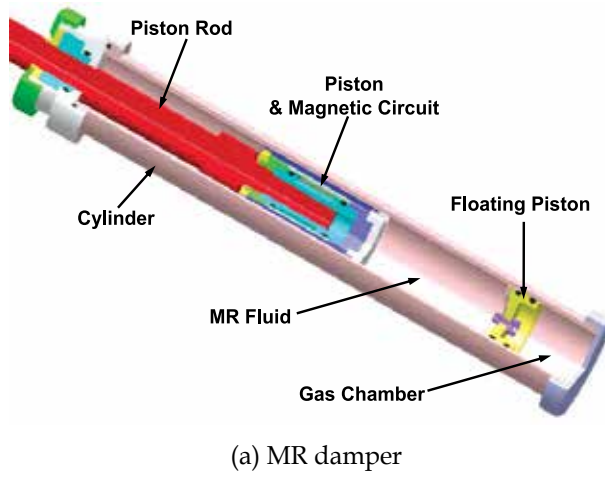
Fig. 2. Schematic configuration of the proposed MR damper

where η is the viscosity of the MR fluid and L is the length of the annular duct. R_o and R_i are the inner radius of the outer piston and outer radius of the inner piston respectively. By assuming that the gas does not exchange much heat with its surroundings, and hence considering its relation as adiabatic variation, the compliance of the gas chamber is obtained by

$$C_g = \frac{V_0}{P_0 \kappa} \tag{2}$$

where V_0 and P_0 are the initial volume and pressure of the gas chamber respectively, and κ is the specific heat ratio. On the other hand, the pressure drop due to the increment of the yield stress of the MR fluid is given by

$$P_{MR} = 2 \frac{c L_p}{h} \tau_y(B) \tag{3}$$

where c is a coefficient that depends on flow velocity profile and has a value range from 2.0 to 3.0, L_p is the length of the magnetic pole, h is the gap of the annular duct, and $\tau_y(B)$ is the

yield stress caused by the magnetic flux density B. Therefore, the damping force of the proposed MR damper can be written as

$$F_D = k_e x_p + c_e \dot{x}_p + F_{MR} \tag{4}$$

where

Parameter	Value
Duct Length (L)	82mm
Piston Area (A_p)	1661.90mm²
Piston Rod Area (A_r)	380.13mm²
Duct Width (b)	123.53mm
Maximum Stroke	164mm

Table 1. Design parameters of the MR damper

$$k_e = \frac{A_r^2}{C_g}, \quad c_e = \left(A_p - A_r\right)^2 R_e$$

$$F_{MR} = \left(A_p - A_r\right) P_{MR} sgn\left(\dot{x}_p\right) \tag{5}$$

where x_p and $\dot{x}_p$ are the piston displacement and velocity respectively, A_p and A_r represent the piston and piston rod areas respectively, and $sgn(\cdot)$ is a signum function.
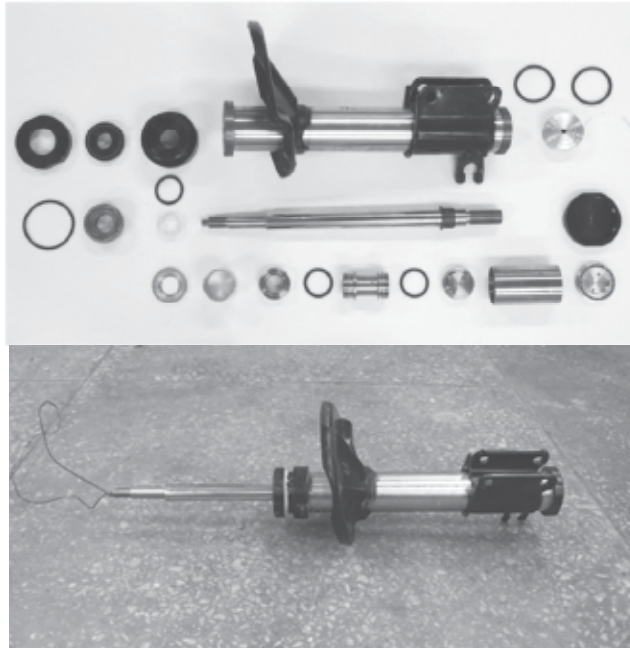

Fig. 3. Photograph of the manufactured MR damper

The photograph of the manufactured MR damper with optimally obtained design parameters are shown in Fig. 3. The principal design parameters of the manufactured MR damper, which can be applied to a mid-sized commercial passenger vehicle, are presented

in Table 1. Fig. 4 presents the measured and analysed damping force F_D characteristics of the MR damper with respect to the piston velocity at various magnetic fields. This is obtained by calculating the maximum damping force at each velocity. The piston velocity is changed by increasing the excitation frequency from 0.5 to 4.0Hz, while the excitation amplitude is kept constant ±20mm. This type of plot is frequently used in the damper manufacturing industry to evaluate the level of damping performance. It is clearly observed that the damping force is increased as the magnetic field increases, as expected. The damping force response of the MR damper is measured as shown in Fig. 5. It can be found that the time constant is about 23ms, which is obtained by inspecting the required time when the damping force reaches 63.2percent of its final steady state value.
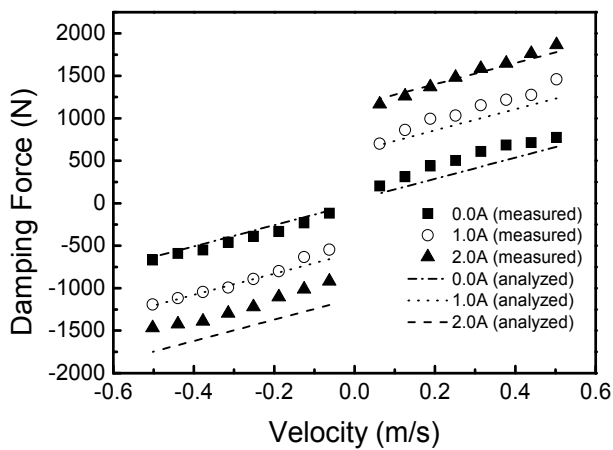

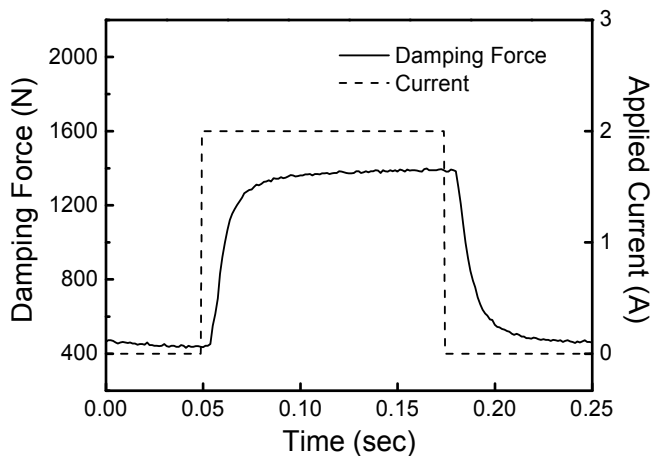Fig. 4. Field-dependent damping force of the MR damper

Fig. 5. Damping force responses of the MR damper

2.3 Quarter vehicle MR suspension

In order to investigate the effectiveness of vibration control algorithm, a quarter vehicle MR suspension system is constructed as shown in Fig. 6. It shows that the proposed quarter vehicle suspension model with the MR damper has two degrees of freedom. The spring for the suspension is assumed to be linear and the tire is also modelled as linear spring component. From the mechanical model, dynamic equation of system considering time constant can be expressed as follows:
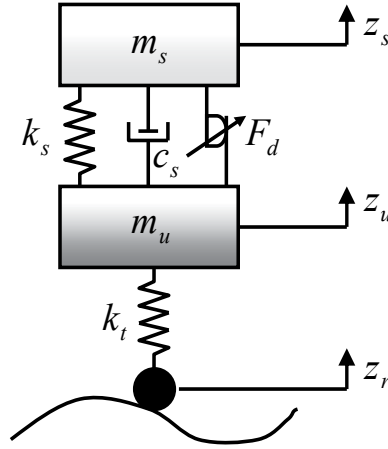
Fig. 6. Mechanical model of a quarter vehicle MR suspension system

$$m_s \ddot{z}_s = -k_s z_s - c_s \dot{z}_s + k_s z_u + c_s \dot{z}_u - F_{MR}$$

$$m_u \ddot{z}_u = k_s z_s + c_s \dot{z}_s - (k_t + k_s) z_u - c_s \dot{z}_u + F_{MR} + k_t z_r \qquad (6)$$

$$\dot{F}_{MR} = -\frac{1}{\tau_{MRD}} F_{MR} + \frac{1}{\tau_{MRD}} u$$

Parameter	Value
Sprung Mass (m_s)	373.5kg
Unsprung Mass (m_u)	40kg
Stiffness Coefficient (k_s)	27358N/m
Tire Stiffness Coefficient (k_t)	211625N/m
Damping Coefficient (c_s)	570Ns/m

Table 2. System parameters of the quarter vehicle suspension system

where τ_{MRD} is time constant of the MR damper, k_s is the total stiffness coefficient of the suspension, including the effective stiffness k_e of the MR damper in equation (4), c_s is the damping coefficient of the suspension and is assumed to be equal to c_e, k_t is the vertical stiffness of the tire, and z_s, z_u and z_r are the vertical displacements of sprung mass, unsprung mass and road excitation respectively. The state space equation of proposed quarter vehicle suspension can be expressed using dynamic equation (Lee et al., 2011):

$$\dot{x} = Ax + Bu + Lz_r, \ y = Cx \qquad (7)$$

where

$$x = [z_s \quad \dot{z}_s \quad z_u \quad \dot{z}_u \quad F_{MR}]^T$$

$$A = \begin{bmatrix} 0 & 1 & 0 & 0 & 0 \\ -k_s/m_s & -c_s/m_s & k_s/m_s & c_s/m_s & -1/m_s \\ 0 & 0 & 0 & 1 & 0 \\ k_s/m_u & c_s/m_u & -(k_t + k_s)/m_u & -c_s/m_u & 1/m_u \\ 0 & 0 & 0 & 0 & -1/\tau_{MRD} \end{bmatrix}, \tag{8}$$

$$B = \begin{bmatrix} 0 & 0 & 0 & 0 & 1/\tau_{MRD} \end{bmatrix}^T, L = \begin{bmatrix} 0 & 0 & 0 & k_t/m_u & 0 \end{bmatrix}^T,$$

$$C = \begin{bmatrix} 1 & 0 & 0 & 0 & 0 \end{bmatrix}$$

The system parameters of the quarter vehicle MR suspension system are chosen on the basis of the conventional suspension system for a mid-sized passenger vehicle, and listed in Table 2.

3. Control strategies

In order to evaluate vibration control performance of the quarter vehicle MR suspension system, various control strategies are formulated and experimentally implemented.

3.1 Skyhook controller

Skyhook controller is simple but very effective control algorithm. It is well known that the logic of the skyhook controller is easy to implement in the real field. The principle of skyhook control is to design the active or semiactive suspension control so that the sprung mass is linked to the sky in order to reduce the vertical oscillations of the sprung mass. Fig. 7 shows the conceptual scheme of skyhook controller for vehicle suspension system. The desired damping force is set by
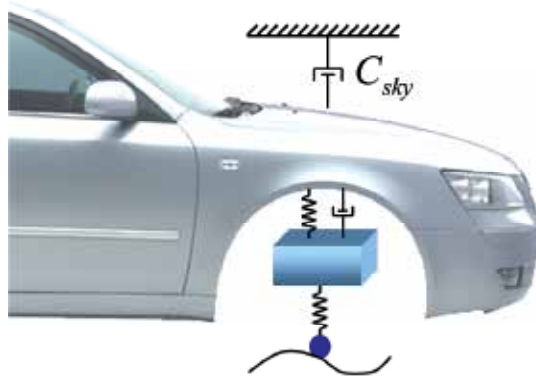
$$u = C_{sky} \dot{z}_s \tag{9}$$

Fig. 7. Scheme of the skyhook controller for vehicle suspension system

where C_{sky} is the control gain, which physically indicates the damping coefficient. In this work, the value is chosen as 2470 using trial-and-error method.

3.2 LQG controller

Optimal control of a linear system with respect to the quadratic objective function under incomplete measurements corrupted by white Gaussian noise is generally referred to as the linear quadratic Gaussian (LQG) problem. The optimal control is a linear function of the state estimates obtained from the Kalman-Bucy filter. The LQR (linear quadratic regulation) is a state feedback problem, whereas LQG is an output feedback problem, which is more realistic (Bahram & Michael, 1993). Fig. 8 shows the block diagram of an LQG controller. In this study, the control input is formulated as follows:

$$u = -K_{LQG}\hat{x} \tag{10}$$

where $\hat{x}$ is the estimated state. Control gain K_{LQG} is set as
$[-1248.3 \quad 1150.3 \quad -4121.8 \quad 15.5 \quad 0.4]$ in this work.

3.3 H∞ controller

In reality, the sprung mass of the vehicle is varied by the loading conditions such as the number of riding persons and payload. And it makes the pitch and roll mass moment of inertia to be changed. Therefore, in order to successfully control the vibration, a robust control algorithm is required by considering the parameter variations of the system. From the structured suspension model, a desirable damping force required to effectively suppress the vibration is determined by adopting H∞ controller. Fig. 9 shows the nominal plant, perturbed plant, shaped plant and loop gain graph. As shown in Fig., loop gain and perturbed plant are well matched and it means loop perturbation is successfully constructed.

For reducing the steady state error and suppressing the effectiveness of disturbance, weighting function can be designed as follows (Choi et al., 1999; 2002):

$$W = 180\frac{s+88}{s} \tag{11}$$

For the design of controller, design index γ is set as 2.99. Fig. 10 shows the sensitivity and complementary sensitivity of the closed loop system. Therefore, control gain can be calculated as follows:

$$u = K_{H\infty}x, \ K_{H\infty} = \frac{N(s)}{D(s)} \tag{12}$$

where $N(s) = -1.45e2s^6 - 2.29e4s^5 - 1.82e6s^4 - 1.12e8s^3 - 2.10e9s^2 + 5.20e10s - 6.91e6, D(s) = s^7 + 92.03s^6 + 8.34e3s^5 + 3.83e5s^4 + 3.47e6s^3 + 3.48e7s^2 + 7.51e2s$.

3.4 Sliding mode controller (SMC)

Fig. 11 shows the conceptual scheme of sliding mode control algorithm. After the initial reaching phase, the system states slides along the sliding surface. The first step to formulate the SMC is to design a stable sliding surface. The stable sliding surface for the control system is defined as follows:

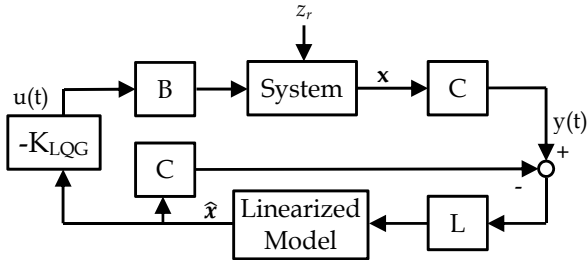$$s = c_1x_1 + c_2x_2 + c_3x_3 + c_4x_4 + x_5 \tag{13}$$

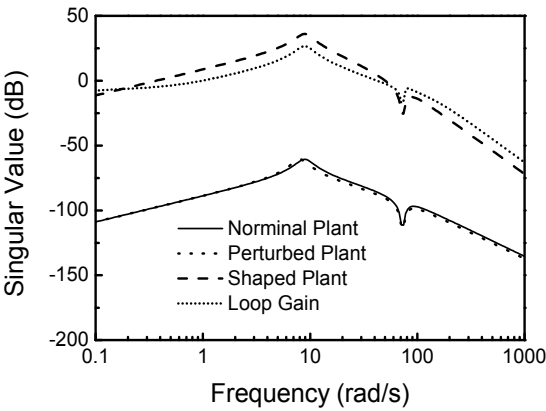Fig. 8. Block diagram of LQG controller

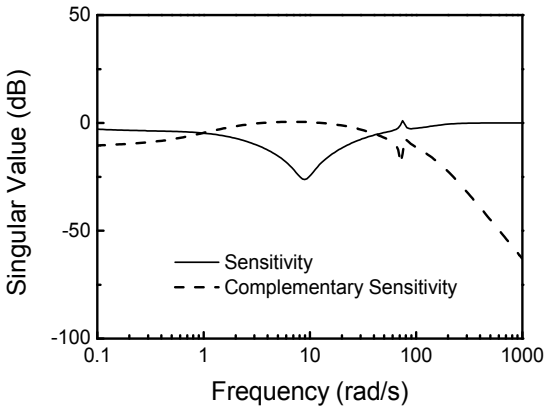Fig. 9. Singular value plots of the quarter vehicle MR suspension system

Fig. 10. Frequency domain indicators of the quarter vehicle MR suspension system
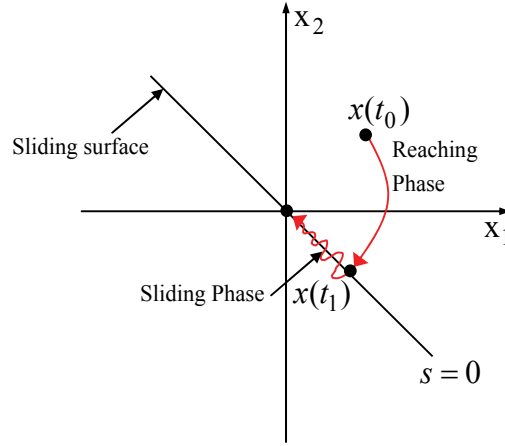
Fig. 11. Scheme of the sliding mode control

where $c_i(i = 1, 2, 3, 4)$ are sliding surface coefficients to be determined so that the sliding surface is stable. Then the sliding mode controller can be formulated which satisfies sliding mode condition $s\dot{s} < 0$ as follows (Choi et al., 2000):

$$u = -\frac{\tau_{MRD}}{c_5}\left(c_1 x_2 + \frac{c_2}{m_s}(-k_s x_1 - c_s x_2 + k_s x_3 + c_s x_4 - x_5) + c_3 x_4 + \frac{c_4}{m_u}(k_s x_1 + c_s x_2 - (k_t + k_s)x_3 - c_s x_4 + x_5) + \frac{1}{\tau_{MRD}}x_5\right) - k sgn(s), \ (k > 0) \tag{14}$$

where k stands for the discontinuous gain which is a positive number. The discrete gain can be changed to continuous gain for reducing the chattering problem.

$$\text{sat(s)} = \begin{cases} s/\varepsilon & for \ |s/\varepsilon| \le 1 \\ sgn(s) & for \ |s/\varepsilon| > 1 \end{cases} \tag{15}$$

3.5 Moving sliding mode controller (MSMC)
It is required to reduce reaching phase to improve the performance and robustness of the SMC. Reaching time can be successfully reduced in case that sliding surface is rotated or shifted by considering reaching phase. Fig. 12 illustrates two moving patterns of the sliding surface: rotating and shifting. The sliding surface for moving sliding mode controller can be determined as follows:

$$s = c_1(x_1, x_2)x_1 + c_2 x_2 + c_3 x_3 + c_4 x_4 + x_5 + \alpha(x_1, x_2)$$

$$c_1(x_1, x_2) = \frac{(\Delta_{fr} - x_2)}{x_1}, \alpha(x_1, x_2) = c_{1o} x_1 + x_2 - \Delta_{fs} \tag{16}$$

where Δ_{fr} and Δ_{fs} are gain for surface rotating and surface shifting respectively. c_{1o} is initial value of c_1. The moving sliding mode controller can be formulated as follows:

$$u = -\frac{\tau_{MRD}}{c_5}\left(c_1(x_1, x_2)x_2 + \frac{c_2}{m_s}(-k_s x_1 - c_s x_2 + k_s x_3 + c_s x_4 - x_5) + c_3 x_4 + \frac{c_4}{m_u}(k_s x_1 + c_s x_2 - (k_t + k_s)x_3 - c_s x_4 + x_5) + \frac{1}{\tau_{MRD}}x_5 + \alpha(x_1, x_2)\right) - k sgn(s), \ (k > 0) \tag{17}$$

3.6 Fuzzy moving sliding mode controller (FMSMC)

The fuzzy moving sliding mode controller, which can change the coefficients and intercepts of sliding surface by fuzzy tuning which takes into account for location of reaching phase, is developed. Fig. 13 presents the block diagram of the proposed FMSMC. The basic configuration of fuzzy control consists of three components: a fuzzification interface, a decision-making logic and a deffuzification interface. In this study, the coefficient of sprung mass displacement x_1 is considered with priority while other coefficients of sliding surface are fixed. Rotating algorithm, which can change the sliding surface c_1 as a function of x_1, is applied to reduce the reaching phase. However, it is hard to expect that the robustness is enhanced in case that initial condition of reaching phase is located in quadrant 1 or quadrant 3. Hence, shifting algorithm, which can change the intercept α as a function of x_1, is adopted and determined according to the relative place of sliding surface, and this will sufficiently reduce the reaching phase. Therefore, the sliding surface can be written as follows (Cho et al., 2007):

$$s = c_1(x_1)x_1 + c_2x_2 + c_3x_3 + c_4x_4 + \alpha(x_1) \tag{18}$$
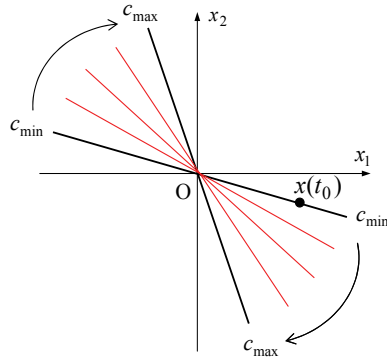
(a) rotating sliding surface
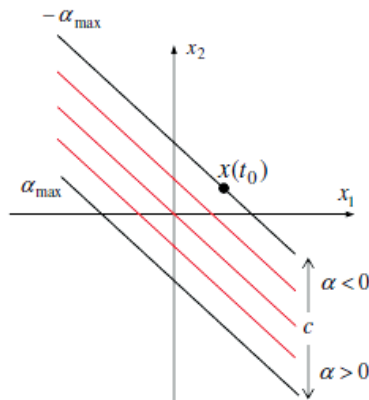
(b) shifting sliding surface

Fig. 12. Scheme of the moving sliding mode control
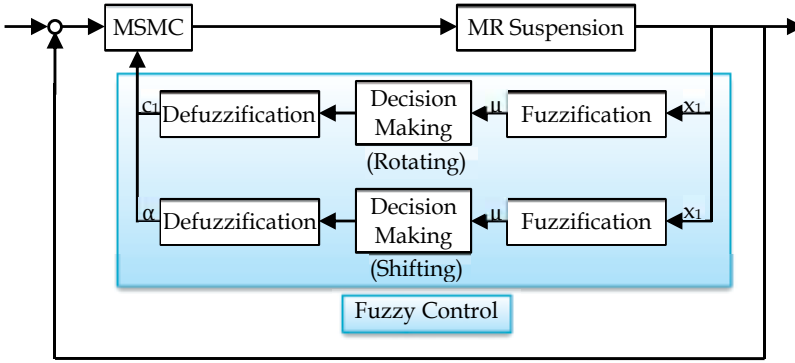
Fig. 13. Block-diagram of the proposed FMSMC

where c_1 and α are determined by tuning of fuzzy logic which takes into account for displacement and direction of sprung mass displacement of x_1. In this case, the sliding surface should maintain stability, although c_1 and α are changed according to time. In order to reduce reaching time in the rotating algorithm, c_1 should be high in case of the opposite case. In the letter case, the sprung displacement x_1 can be converted toward 0 more quickly. In the shifting control algorithm, absolute value of α should be high in case that absolute value of x_1 is large and vice versa. Furthermore, sliding surface is moved upward for positive x_1 and sliding surface is moved downward for the opposite case. Consequently, we can formulate the following control input of the proposed FMSMC, which is combined rotating and shifting algorithm:

$$u = -\frac{\tau_{MRD}}{c_5}\left\{\left(c_1(x_1) + \frac{\Delta c_1 \chi_{1r}\sinh(\chi_{1r})}{\cosh^2(\chi_{1r})} - \frac{(\alpha_{max}/\sigma_s)}{\cosh^2(\chi_{1s})}\right)x_2 + \frac{c_2}{m_s}(-k_s x_1 - c_s x_2 + k_s x_3 + c_s x_4 - x_5) + \right.$$
$$\left. c_3 x_4 + \frac{c_4}{m_u}(k_s x_1 + c_s x_2 - (k_t + k_s)x_3 - c_s x_4 + x_5) - \frac{1}{\tau_{MRD}}x_5\right\} - ksgn(s), \ (k > 0) \qquad (19)$$

The control input determined from the FMSMC is to be applied to the MR damper depending upon the motion of suspension travel. The detailed control algorithm was described by Cho et al., 2007.

3.7 Semi-active condition

The control input u directly represents the damping force of F_{MR}. On the other hand, the damping of the suspension system needs to be controlled depending upon the motion of suspension travel. Therefore, the following semi-active actuating condition is imposed:

$$u = \begin{cases} u & for \ u(\dot{z}_s - \dot{z}_u) > 0 \\ 0 & for \ u(\dot{z}_s - \dot{z}_u) \le 0 \end{cases} \qquad (20)$$

This semi-active condition can assure the increment of damping characteristic of the suspension system and hence increase the stability of the system.

4. Control performances

Vibration control performances of the quarter vehicle MR suspension system are evaluated under two types of excitation (road) conditions. The first excitation, normally used to reveal the transient response characteristic, is a bump described by

$$z_r = A_m[1 - \cos(\omega t)] \tag{21}$$

where $\omega = 2\pi f$, $f = 1/T$ and $T = D/V$. $A_m(= 0.07\text{m})$ is the bump height, $D(= 0.8m)$ is the width of the bump and V is the vehicle velocity. In the bump excitation, the vehicle travels the bump with a constant vehicle velocity of 3.08km/h(=0.856m/s). The second excitation is a random road conditions.

Fig. 14 shows the experimental apparatus of the quarter vehicle MR suspension system to evaluate and compare the effectiveness of vibration isolation of the proposed control algorithms. The MR suspension (assembly of the MR damper and spring), sprung mass and tire are installed on the hydraulic excitation system. The sprung mass displacement and excitation displacement are measured by LVDT (linear variable differential transformer) and the suspension travel is measured by a wire sensor. The hydraulic system applies the road profile to the MR suspension system. The current amplifier applies the control current determined from the control algorithm to the MR damper.
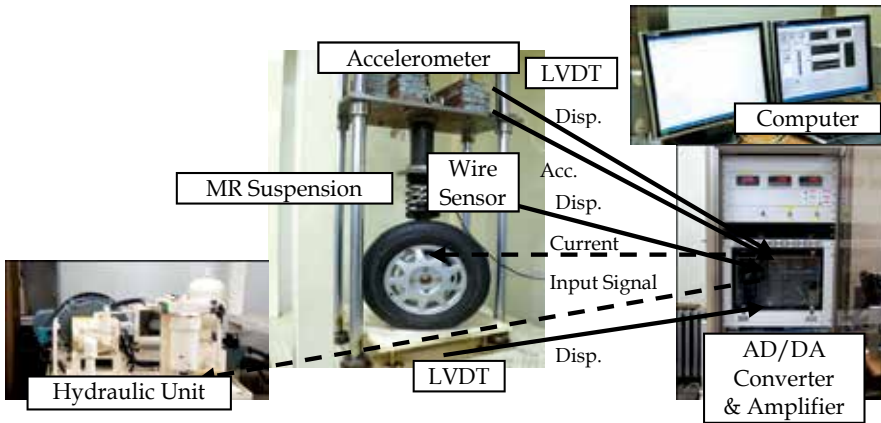
Fig. 14. Experimental apparatus of the quarter vehicle MR suspension system

Fig. 15 presents vertical displacement, vertical acceleration of sprung mass and suspension travel versus time responses of the MR suspension system for the bump excitation. As shown in the Fig., it can obviously be found that unwanted vibrations induced from the bump excitation are well suppressed by adopting the control algorithms in the MR suspension system. Fig. 16 shows the performance comparison of vertical acceleration RMS of the quarter vehicle MR suspension system for the bump excitation. The RMS value is calculated from:

$$RMS = \sqrt{\frac{x_1^2 + x_2^2 + \cdots + x_n^2}{n}} \tag{22}$$

As shown in Fig., skyhook control algorithm shows quite good vibration control performance. Also, Fig. 17 shows the PSD (power spectrum density) of sprung mass acceleration in frequency domain for the random excitation and Fig. 18 shows the performance comparison of vertical acceleration RMS of the quarter vehicle MR suspension system for the random excitation. As expected, the PSD of the vertical acceleration has been
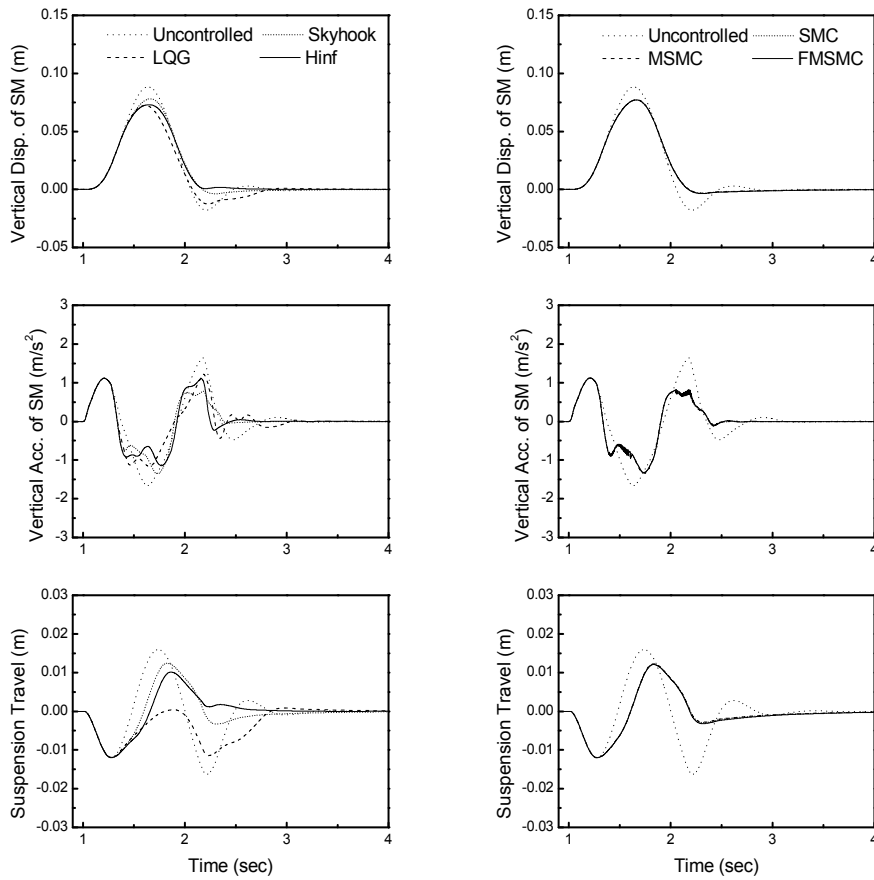
Fig. 15. Bump responses of the quarter vehicle MR suspension system
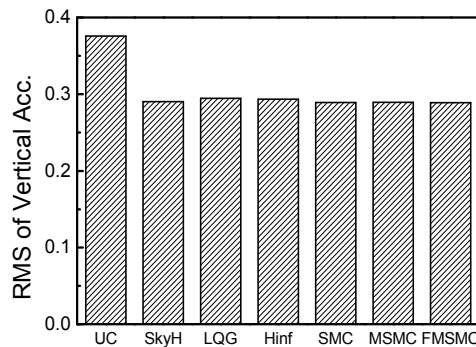
Fig. 16. Performance comparison of vertical acceleration RMS of the quarter vehicle MR suspension system (bump)
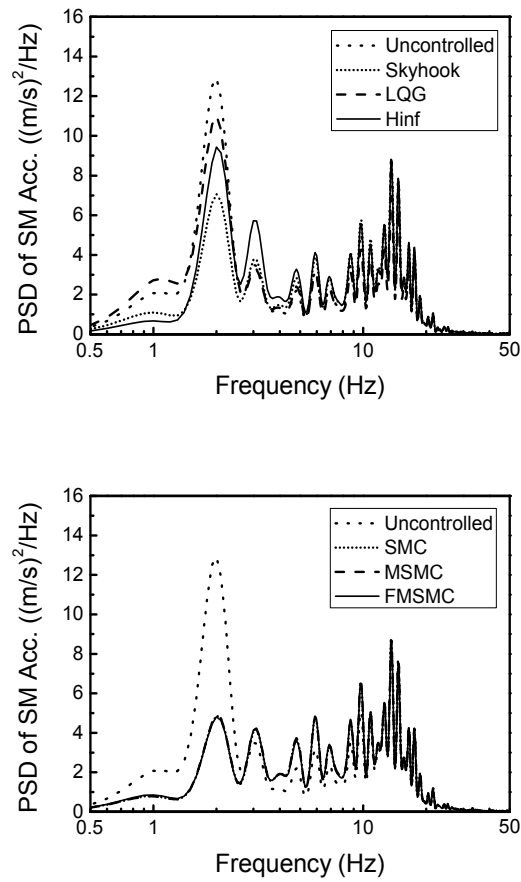
Fig. 17. Random responses of the quarter vehicle MR suspension system (72km/h)
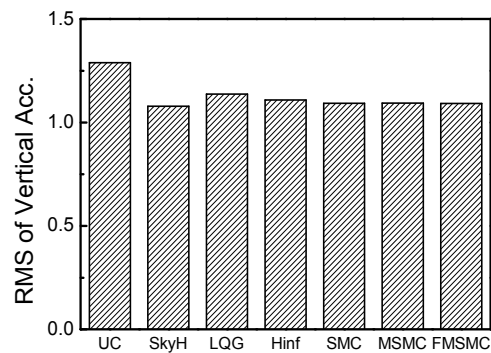
Fig. 18. Performance comparison of vertical acceleration RMS of the quarter vehicle MR suspension system (random, 72km/h)

considerably reduced in the neighbourhood of body resonance (1~2Hz) by applying control input. The control results presented in Figs. 15~18 indicate that ride comfort of a vehicle system can be substantially improved by employing the MR suspension system associated with the proposed control algorithms.

5. Conclusion

In this chapter, control algorithms for vibration control of the quarter vehicle MR suspension system were proposed and its effectiveness was experimentally verified and compared. In order to achieve this goal, a cylindrical MR damper was designed and manufactured. After evaluating the field-dependent damping characteristics of the MR damper, a quarter vehicle suspension system was then constructed and its governing equations of motion were derived. In order to obtain a favourable control performance of the MR suspension system, skyhook controller, LQG controller, H∞ controller, sliding mode controller, moving sliding mode controller and fuzzy moving sliding mode controller were designed and experimentally realized to the quarter vehicle MR suspension system. It has been experimentally shown that the proposed control algorithms can reduce the unwanted vibration under bump excitation. In addition, it has been demonstrated that using the proposed control methodologies vibration levels such as sprung mass acceleration under random excitation can be significantly reduced at body resonance region. The results presented here are self-explanatory justifying that the control strategies implemented in this work can produce very similar vibration control performance. This directly indicates that ride comfort of the vehicle system can be substantially improved by adopting the MR suspension system associated with the proposed control strategies.

6. References

Bahram, S. and Michael, H. (1993). *Control System Design Using MATLAB*, Prentice Hall, ISBN 0-13-174061-X, New Jersey

Carlson, J. D., Cantanzarite, D. M. and St.Clair, K. A. (1996). Commercial Magnetorheological Fluid Devices. *Electro-Rheological Fluids, Magneto-Rheological Suspensions and Associated Technology*, Vol.1996, pp. 20-28, ISBN 981-02-2676-4

Cho, J. W., Pang, Y. S., Choi, S. B. and Kim, K. S. (2007). Fuzzy Moving Sliding Mode Control of Vehicle Suspension Featuring ER Shock Absorber. *International Conference on Electro-Rheological Fluids and Magneto-Rheological Suspensions*, ISBN 978-981-2771-19-3, Lake Tahoe, USA

Choi, S. B., Han, S. S., Kim, H. K. and Cheong, C. C. (1999). H∞ Control of a Flexible Gantry Robot Arm Using Smart Actuators. *Mechatronics: Mechanics, Electronics, Control*, Vol.9, No.3, pp. 271-286, ISSN 0957-4158

Choi, S. B., Choi, Y. T. and Park, D. W. (2000). A Sliding Mode Control of a Full-Car Electrorheological Suspension System Via Hardware in-the-Loop Simulation. *Journal of Dynamic Systems, Measurement, and Control*, Vol.122, No.1, pp. 114-121, ISSN 0022-0434

Choi, S. B., Lee, S. K. and Park, Y. P. (2001). A Hysteresis Model for the Field-Dependent Damping Force of a Magnetorheological Damper. *Journal of Sound and Vibration*, Vol.245, No.2, pp. 375-383, ISSN 0022-460x

Choi, S. B., Lee, H. S. and Park, Y. P. (2002). H∞ Control Performance of a Full-Vehicle Suspension Featuring Magnetorheological Dampers. *Vehicle System Dynamics*, Vol.38, No.5, pp. 341-360, ISSN 0042-3114

Du, H., Yim, S. K. and Lam, J. (2005). Semi-Active H∞ Control of Vehicle Suspension with Magneto-Rheological Dampers. *Journal of Sound and Vibration*, Vol.283, No.3/5, pp. 981-996, ISSN 0022-460x

Guo, D. and Hu, H. (2005). Nonlinear Stiffness of a Magneto-Rheological Damper. *Nonlinear Dynamics*, Vol.40, No.3, pp. 241-249, ISSN 0924-090x

Hong, S. R., Wereley, N. M., Choi, Y. T. and Choi, S. B. (2008). Analytical and Experimental Validation of a Nondimensional Bingham Model for Mixed-Mode Magnetorheological Dampers. *Journal of Sound and Vibration*, Vol.312, No.3, pp. 399-417, ISSN 0022-460x

Kamath, G. M., Wereley, N. M. and Jolly, M. R. (1998). Characterization of Semiactive Magnetorheological Helicopter Lag Mode Dampers. *Smart Structures and Integrated Systems*, Vol.1998, pp. 356-377, ISSN 0277-786x

Kim, J. H., Kang, B. W., Park, K. M., Choi, S. B. and Kim, K. S. (2002). MR Inserts For Shock Wave Reduction in Warship Structures. *Journal of Intelligent Material Systems and Structures*, Vol.13, No.10, pp. 661-666, ISSN 1045-389x

Lee, H. G., Sung, K. G., Choi, S. B., Park, M. K. and Park, M. K. (2011). Performance Evaluation of a Quarter-Vehicle MR Suspension System with Different Tire Pressure. *International Journal of Precision Engineering and Manufacturing*, Vol.12, No.2, pp. 203-210, ISSN 1229-8557

Liu, B., Li, W. H., Kosasih, P. B. and Zhang, X. Z. (2006). Development of an MR-Brake-Based Haptic Device. *Smart Materials and Structures*, Vol.15, No.6, pp. 1960-1966, ISSN 0964-1726

Ok, S. Y., Kim, D. S., Park, K. S. and Koh, H. M. (2007). Semi-Active Fuzzy Control of Cable-Stayed Bridges Using Magneto-Rheological Dampers. *Engineering Structures*, Vol.29, No.5, pp. 776-788, ISSN 0141-0296

Pranoto, T. and Nagaya, K. (2005). Development on 2DOF-Type and Rotary-Type Shock Absorber Damper Using MRF and Their Efficiencies. *Journal of Materials Processing Technology*, Vol.161, No.1/2, pp. 146-150, ISSN 0924-0136

Seong, M. S., Choi, S. B. and Han, Y. M. (2009). Damping Force Control of a Vehicle MR Damper Using a Preisach Hysteretic Compensator. *Smart Materials and Structures*, Vol.18, No.7, pp. 1-13, ISSN 0964-1726

Shen, Y., Golnaraghi, M. F. and Heppler, G. R. (2007). Load-Leveling Suspension System with a Magnetorheological Damper. *Vehicle System Dynamics*, Vol.45, No.4, pp. 297-312, ISSN 0042-3114

Spencer Jr., B. F., Dyke, S. J., Sain, M. K. and Carlson, J. D. (1997). Phenomenological Model for Magnetorheological Dampers. *Journal of Engineering Mechanics*, Vol.123, No. 3, pp. 230-238, ISSN 0733-9399

White, F. M. (2003). *Fluid Mechanics* (Fifth Edition), Mcgraw-Hill, ISBN 0-07-240217-2, New York

Yu, M., Liao, C. R., Chen, W. M. and Huang, S. L. (2006). Study on MR Semi-Active Suspension System and its Road Testing. *Journal of Intelligent Material Systems and Structures*, Vol.17, No.8/9, pp. 801-806, ISSN 1045-389x

Yu, M., Dong, X. M., Choi, S. B. and Liao, C. R. (2009). Human Simulated Intelligent Control of Vehicle Suspension System with MR Dampers. *Journal of Sound and Vibration*, Vol.319, No.3/5, pp. 753-767, ISSN 0022-460x

A Semiactive Vibration Control Design for Suspension Systems with Mr Dampers

Hamid Reza Karimi

Department of Engineering, Faculty of Engineering and Science
University of Agder
Norway

1. Introduction

In an automotive system, the vehicle suspension usually contributes to the vehicle's handling and braking for good active safety and driving pleasure and keeps the vehicle occupants comfortable and reasonably well isolated from road noise, bumps and vibrations. The design of vehicle suspension systems is an active research field in automotive industry (Du and Zhang, 2007; Guglielmino, *et al.*, 2008). Most conventional suspensions use passive springs to absorb impacts and shock absorbers to control spring motions. The shock absorbers damp out the motions of a vehicle up and down on its springs, and also damp out much of the wheel bounce when the unsprung weight of a wheel, hub, axle and sometimes brakes and differential bounces up and down on the springiness of a tire.

Semiactive suspension techniques (Karkoub and Dhabi, 2006; Shen, *et al.*, 2006; Zapateiro, *et al.*, 2009) promise a solution to the problem of vibration absorption with some comparatively better features than active and passive devices. Compared with passive dampers, active and semiactive devices can be tuned due to their flexible structure. One of the drawbacks of active dampers is that they may become unstable if the controller fails. On the contrary, semiactive devices are inherently stable, because they cannot inject energy to the controlled system, and will act as pure passive dampers in case of control failure. Among semiactive control devices, magnetorheological (MR) dampers are particularly interesting because of the high damping force they can produce with low energy requirements (being possible to operate with batteries), simple mechanical design and low production costs. The damping force of MR dampers is produced when the MR fluid inside the device changes its rheological properties in the presence of a magnetic field. In other words, by varying the magnitude of an external magnetic field, the MR fluid can reversibly go from a liquid state to a semisolid one or vice versa (Carlson, 1999). Despite the above advantages, MR dampers have a complex nonlinear behavior that makes modeling and control a challenging task. In general, MR dampers exhibit a hysteretic force - velocity loop response whose shape depends on the magnitude of the magnetic field and other variables. Diverse MR damper models have been developed for describing the nonlinear dynamics and formulating the semiactive control laws (Dyke, *et al.*, 1998; Zapateiro and Luo, 2007; Rodriguez, *et al.*, 2009). Most of the MR damper's models found in literature are the so-called phenomenological models which are based on the mechanical behavior of the device (Spencer, *et al.*, 1997; Ikhouane and Rodellar, 2007).

The objective of the work is to mitigate the vibration in semiactive suspension systems equipped with a MR damper. Most conventional suspensions use passive devices to absorb impacts and vibrations, which is generally difficult to adapt to the uncertain circumstances. Semiactive suspension techniques promise a solution to the above problem with some comparatively better features than active and passive suspension devices. To this aim, a backstepping control is proposed to mitigate the vibration in this application. In the design of backstepping control, the Bouc-Wen model of the MR damper is used to estimate the damping force of the semiactive device taking the control voltage and velocity inputs as variables and the semiactive control law takes into account the hysteretic nonlinearity of the MR damper. The performance of the proposed semiactive suspension strategy is evaluated through an experimental platform for the semiactive vehicle suspension available in our laboratory.

The chapter is organized as follows. In the section 2, physical study of MR dampers is proposed. The mathematical model for the semiactive suspension experimental platform is introduced in the section 3. In the section 4, details on the formulation of the backstepping control are given. The results of control performance verification are presented and discussed in the section 5. Finally, conclusions are drawn at the end of the paper.

2. MR damper

Nowadays dampers based on MagnetoRheological (MR) fluids are receiving significant attention especially for control of structural vibration and automotive suspension systems. . In most cases it is necessary to develop an appropriate control strategy which is practically implementable when a suitable model of MR damper is available. It is not a trivial task to model the dynamic of MR damper because of their inherent nonlinear and hysteretic dynamics. In this work, an alternative representation of the MR damper in term of neural network is developed. Training and validating of the network models are achieved by using data generated from the numerical simulation of the nonlinear differential equations proposed for MR damper. The MR damper is a controllable fluid damper which belongs in the semi-active category. A brief overview of the physical buildup of an MR damper is seen in this section.

2.1 Physical study

The MR damper has a physical structure much like a typical passive damper: an outer casing, piston, piston rod and damping fluid confined within the outer casing. The main difference lies in the use of MR fluid and an electromagnet.

2.1.1 MR fluid

A magneto rheological fluid is usually a type of mineral or silicone oil that carries magnetic particles. These magnetic particles may be iron particles that can measure 3-10 microns in diameter, shown in Fig. 1. In addition to these particles it might also contain additives to keep the iron particles suspended. When this fluid is subject to a magnetic field the iron particles behave like dipoles and start aligning along the constant flux, shown in Fig. 2.When the fluid is contained between the dipoles, its movement is restricted by the chain of the particles thus increasing its viscosity. Thus it changes its state from liquid to a viscoelastic solid.
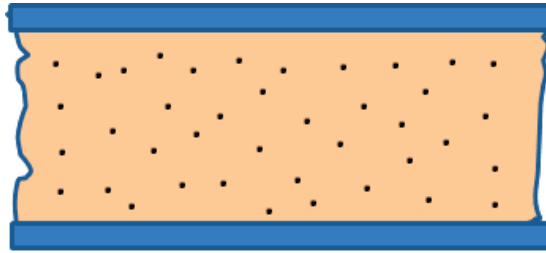
Fig. 1. Magnetic particles in the MR fluid.
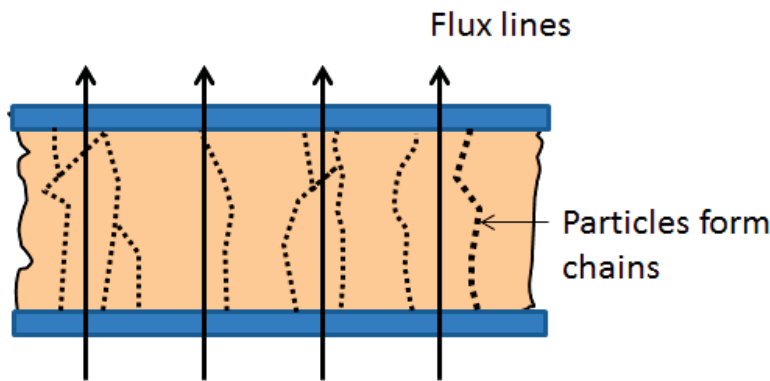
Fig. 2. Particles aligning along the flux lines.

Mechanical properties of the fluid in its 'on' state are anisotropic i.e. it is directly dependent on the direction. Hence while designing a MR device it is important to ensure that the lines of flux are perpendicular to the direction of the motion to be restricted. This way the yield stress of the fluid can be controlled very accurately by varying the magnetic field intensity. Controlling the yield stress of a MR fluid is important because once the peek of the yield stress is reached the fluid cannot be further magnetized and it can result in shearing. It is also known that the MR Fluids can operate at temperatures ranging from -40 to 150° C with only slight changes in the yield stress. Hence it is possible to control the fluids ability to transmit force with an electromagnet and make use of it in control-based applications.

2.1.2 Electromagnet
The electromagnet in the MR damper can be made with coils wound around the piston. An example is the MR damper design by Gavin et. al (2001), seen in Fig. 3. The wire connecting this electromagnet is then lead out through the piston shaft.

2.2 Modes of operation
MR Fluids can be used in three different modes (Spencer et al, 1997):
*Flow mode***:** Fluid is flowing as a result of pressure gradient between two stationary plates. It can be used in dampers and shock absorbers, by using the movement to be controlled to force the fluid through channels, across which a magnetic field is applied, see Fig. 4.

Shear mode: In this mode the fluid is between two plates moving relative to one another. It is used in clutches and brakes i.e. in places where rotational motion must be controlled, see Fig. 5.
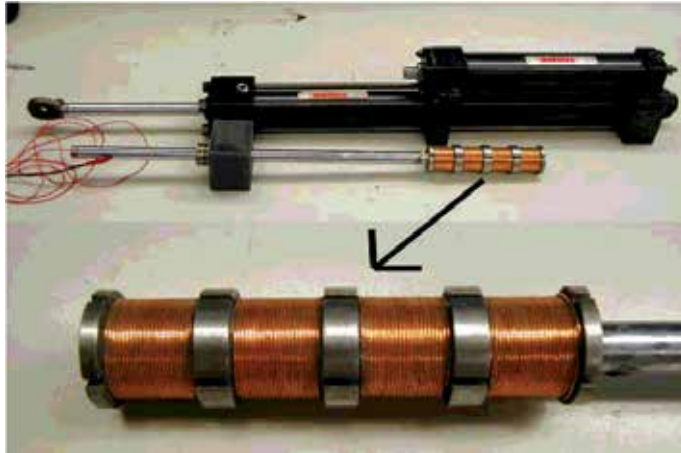
Fig. 3. Electromagnetic piston.
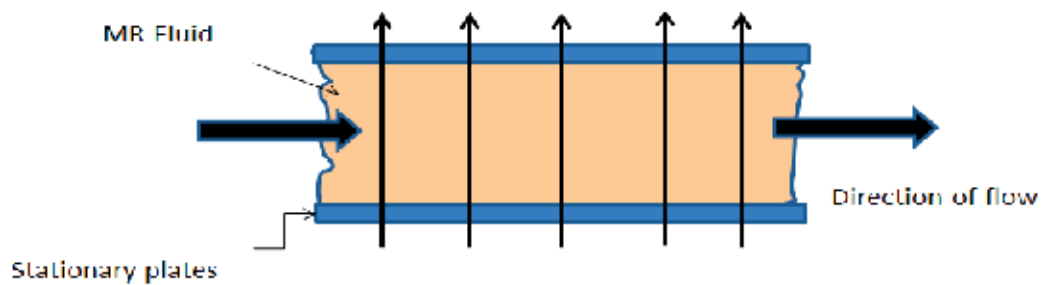
Fig. 4. Flow mode.
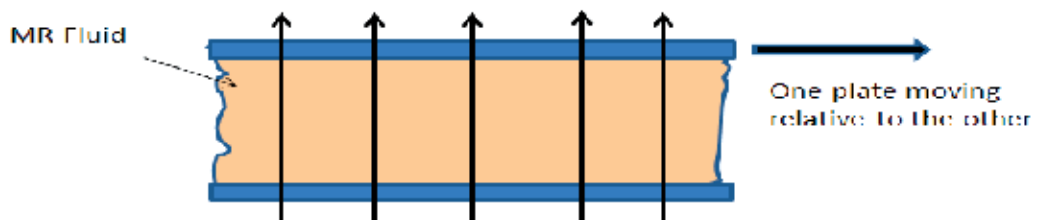
Fig. 5. Shear mode.

Squeeze-flow mode: In this mode the fluid is between two plates moving in the direction perpendicular to their planes. It is most useful for controlling small movements with large forces, see Fig. 6.
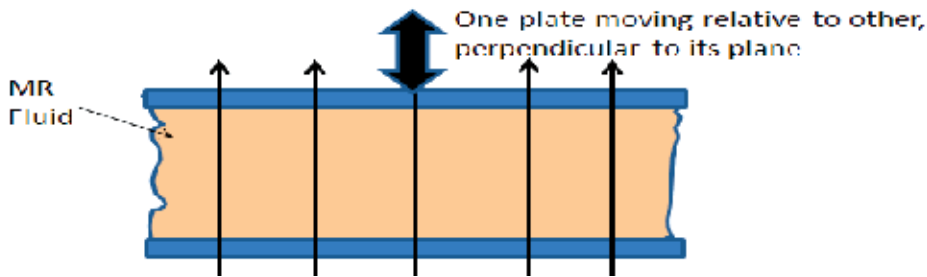
Fig. 6. Squeeze flow mode.

2.3 MR damper categories
2.3.1 Linear MR dampers
There are three main types of linear MR dampers, the mono, twin and double-ended MR dampers (Ashfak et. al, 2011). All of these have the same physical structure of an outer casing, piston rod, piston, electromagnet and the MR fluid itself.

2.3.2 Mono and twin
The mono damper is named because of its single MR fluid reservoir. As the piston displaces due to an applied force, the MR liquid compresses the gas in the gas reservoir. Just like the other two MR damper types, the mono MR damper has its electromagnets located in the piston. Fig. 7 shows a schematic diagram of the mono MR damper.

The twin MR damper has two housings, see Fig. 8. Other than this, it is identical to the mono MR damper.
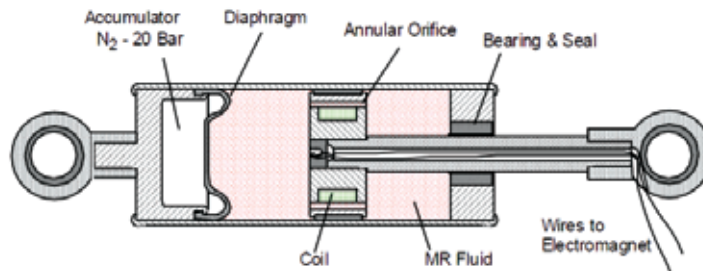
Fig. 7. The mono MR damper.
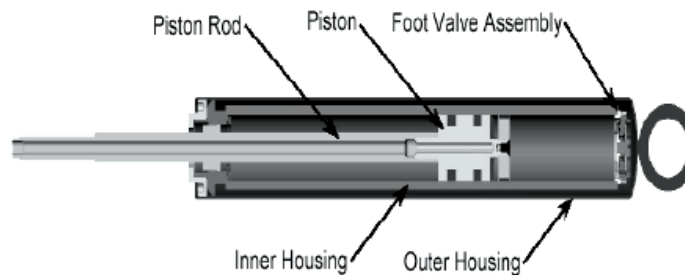
Fig. 8. The twin MR damper.

2.3.3 Double-ended

The double-ended MR damper is named so because of the double protruding pistons from both ends of the piston, see Fig. 9. No gas accumulators are used in this setup because the MR fluid is able to squeeze from one chamber to the other. In an experimental design by Lord Corp, a thermal expansive accumulator is used. This is to store the expanded liquid due to heat generation, see Fig. 10.
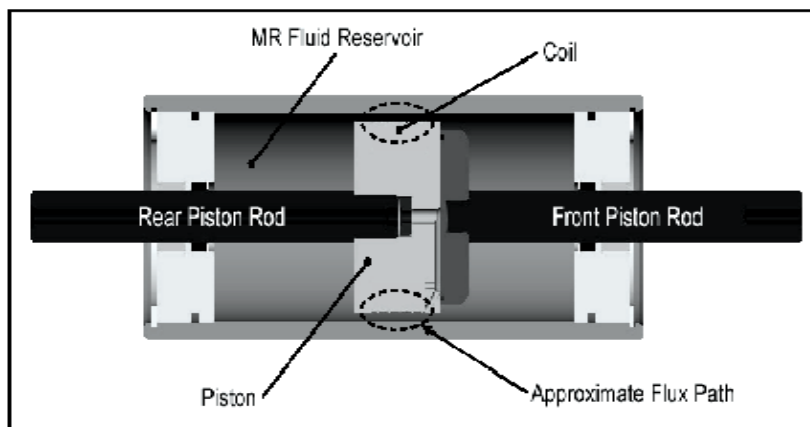
Fig. 9. Double-ended MR damper.
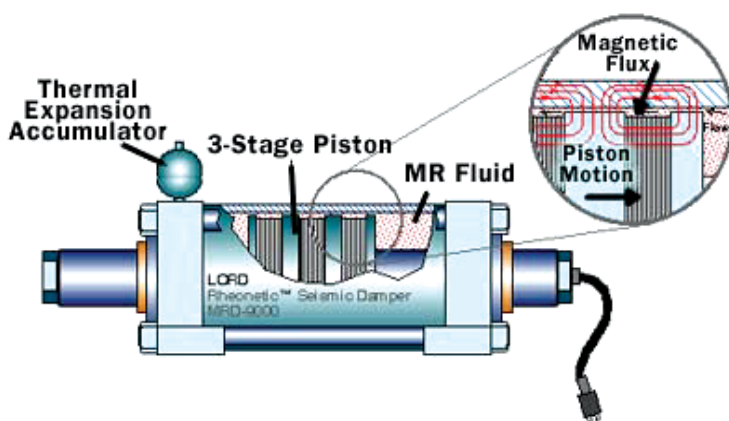
Fig. 10. Double-ended MR damper with thermal expansion accumulator.

2.3.4 Rotary dampers

Rotary dampers, as the name suggests, are used when rotary motion needs damping. There exist several types of rotary dampers, but the one that will be described is the disk brake. This is also the type that is used on the SAS platform.

The disk brake is one of the most commonly used rotary dampers. It has a disk shape and contains MR fluid and a coil as shown in Fig. 11. Different setups have been proposed for the MR disk brake. A comparison of these has been done by Wang et al (2004) and Carlson et al (1998).
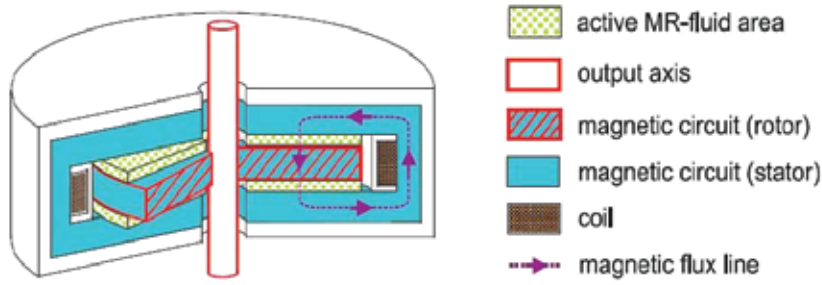
Fig. 11. MR brake disk.

3. Problem formulation

The experimental platform used in this work is fabricated by the Polish company Inteco Limited, see Fig. 12. It consists of a rocking lever that emulates the car body, a spring, and an MR damper that makes the semiactive vibration control. A DC motor coupled to an eccentric wheel is used to simulate the vibrations induced to the vehicle. Thus, the higher is the motor angular velocity, the higher is the frequency of the car (rocking lever) vibrations. The detailed definitions of the angles and distances can be found in the appendix.

Fig. 12. Picture of the SAS system (Inteco Ltd., Poland).

The equations of motion of the upper rocking lever are given by:

$$
\begin{aligned}
\dot{\alpha}_2 &= \omega_2 \\
\dot{\omega}_2 &= J_2^{-1}\left(M_{21} + M_{22} + M_{s2}\right) + J_2^{-1} r_{2f} F_{eq} f_{mr} \sin\left(\pi - \alpha_{2f} - \alpha_2 - \gamma_f\right)
\end{aligned}
\tag{1}
$$

where α_2 and ω_2 are the angular position and angular speed of the upper lever, respectively. M_{21}, M_{22} and M_{s2} are the viscous friction damping torque, the gravitational forces torque and the spring torque acting on the lower rocking lever, respectively and their equations are:

$$
\begin{aligned}
M_{21} &= -k_2\omega_2 \\
M_{22} &= -G_2 R_2 \cos(\alpha_2) \\
M_{s2} &= r_{2s} F_s \sin(\pi - \alpha_2 + \alpha_{2s} - \gamma_s)
\end{aligned}
\tag{2}
$$

F_s is the force generated by the spring and γ_s is the slope angle of the spring operational line, which are given by:

$$
F_s = K_s\left(l_{0s} - \sqrt{\left(r_{2s}\sin(\alpha_2 - \alpha_{2s}) + r_{1s}\sin(\alpha_1 - \alpha_{1s})\right)^2 + \left(b - r_{1s}\cos(\alpha_1 - \alpha_{1s}) - r_{2s}\cos(\alpha_2 - \alpha_{2s})\right)}\right) \tag{3}
$$

$$
\gamma_s = abs\left(\tan^{-1}\left(\frac{-r_{1s}\sin(\alpha_1 - \alpha_{1s}) - r_{2s}\sin(\alpha_2 - \alpha_{2s})}{b - r_{1s}\cos(\alpha_1 - \alpha_{1s}) - r_{2s}\cos(\alpha_2 - \alpha_{2s})}\right)\right) \tag{4}
$$

$F_{eq}\cdot f_{mr}$ is the force generated by the MR damper:

$$
F_{eq}\cdot f_{mr} = f_{mr}\left(\omega_2 r_{2f}\cos\left(-\frac{\pi}{2} + \alpha_2 + \alpha_{2f} + \gamma_f\right) + \omega_1 r_{1f}\cos\left(-\frac{\pi}{2} + \alpha_1 + \alpha_{1f} + \gamma_f\right)\right) \tag{5}
$$

$$
\gamma_f = abs\left(\tan^{-1}\left(\frac{-r_{1f}\sin(\alpha_1 + \alpha_{1f}) - r_{2f}\sin(\alpha_2 + \alpha_{2f})}{b - r_{1f}\cos(\alpha_1 + \alpha_{1f}) - r_{2f}\cos(\alpha_2 + \alpha_{2f})}\right)\right) \tag{6}
$$

The model is completed with the equations of motion of the lower rocking lever:

$$
\begin{aligned}
\dot{\alpha}_1 &= \omega_1 \\
\dot{\omega}_1 &= J_1^{-1}\left(M_{11} + M_{12} + M_{13} + M_{14} + M_{s1} + M_{f1}\right)
\end{aligned}
\tag{7}
$$

with

$$
\begin{aligned}
M_{11} &= -k_1\omega_1 \\
M_{12} &= -G_2 R_2 \cos(\alpha_2) \\
M_{13} &= -R_1\cos(\alpha_1 + \beta)\left(K_g\left(l_0 + r + R_1\sin(\alpha_1 + \beta) - D_x + e(t)\right)\right) \\
M_{14} &= f_g\left(\frac{de(t)}{dt} - R_1\cos(\alpha_1 + \beta)\right) \\
M_{s1} &= r_{1s} F_s \sin(\pi - (\alpha_1 - \alpha_{1s}) - \gamma_s) \\
M_{f1} &= r_{1f} F_f \sin(\pi - (\alpha_1 + \alpha_{1f}) - \gamma_f)
\end{aligned}
\tag{8}
$$

where M_{11} is the viscous friction damping torque; M_{12} is the gravitational forces torque; M_{13} is the actuating kinematic torque transferred through the tire; M_{14} is the damping torque generated by the gum of tire; M_{s1} is the torque generated by the spring; M_{f1} is the torque generated by the damper, and $e(t)$ is the disturbance input.

The objective of the semiactive suspension is to reduce the vibrations of the car body (the upper rocking lever). This can be achieved by reducing the angular velocity of the lever ω_2.

Thus, the system to be controlled is that of (1) by assuming that the lower rocking lever dynamics constitute the disturbances.

4. Backstepping control design

For making the backstepping control design, define z_1 and z_2 as the new coordinates according to:

$$(z_1, z_2) = \left(\alpha_2 - \alpha_{2equ}, \omega_2\right) \tag{9}$$

where the equilibrium point of the system is $\left(\alpha_{2equ}, \omega_{2equ}\right) = (0.55\ rad,\ 0)$, $f_{mr} = 0$. The above change of coordinates is made so that the equilibrium point is set to (0, 0). In the new coordinates, (1) becomes:

$$\begin{aligned}
\dot{z}_1 &= z_2 \\
\dot{z}_2 &= J_2^{-1}\left(M_{21} + M_{22} + M_{s2}\right) + J_2^{-1} r_{2f} F_{eq} \sin\left(\pi - \alpha_{2f} - z_1 - \alpha_{2equ} - \gamma_f\right) f_{mr} = f + g \cdot f_{mr}
\end{aligned} \tag{10}$$

The backstepping technique can now be applied to the system (10). First, define the following standard backstepping variables and their derivatives:

$$\begin{aligned}
e_1 &= z_1 & \dot{e}_1 &= z_2 \\
e_2 &= z_2 - \delta_1 & \dot{e}_2 &= \dot{z}_2 + h_1 z_2 \\
\delta_1 &= -h_1 e_1,\ \ h_1 > 0 & \dot{\delta}_1 &= -h_1 z_2
\end{aligned} \tag{11}$$

For the control design, the following Bouc-Wen model of the MR damper (Ikhouane and Dyke, 2007) is used:

$$f_{mr} = \alpha(v)w + c(v)\dot{x} \tag{12a}$$

$$\dot{w} = -\gamma|\dot{x}|w|w|^n - \beta\dot{x}|w|^n + \delta\dot{x} \tag{12b}$$

$$c(v) = c_0 + c_1 v \tag{12c}$$

$$\alpha(v) = \alpha_0 + \alpha_1 v \tag{12d}$$

where v is the control voltage and w is a variable that accounts for the hysteretic dynamics. $\alpha, c, \beta, \gamma, n, \delta$ are parameters that control the shape of the hysteresis loop. From control design point of view, it is desirable to count on the inverse model, i.e., a model that predicts the control voltage for producing the damping force required to reduce the vibrations. This is because the force cannot be commanded directly; instead, voltage or current signals are used as the control input to approximately generate the desired damping force.

Now, define the following Lyapunov function candidate:

$$V = \frac{1}{2}V_1^2 + \frac{1}{2}V_2^2 = \frac{1}{2}e_1^2 + \frac{1}{2}e_2^2 \tag{13}$$

Deriving (13) and substituting (10)-(11) in the result yields:

$$
\begin{aligned}
\dot{V} &= e_1\dot{e}_1 + e_2\dot{e}_2 = e_1e_2 - h_1e_1^2 + e_2f + e_2g\cdot f_{mr} + h_1z_2e_2 \\
&= -h_1e_1^2 - h_2e_2^2 + e_2\left[(\alpha_2 - \alpha_{2equ})(1+h_1h_2) + (h_1+h_2)\omega_2 + f + g\cdot f_{mr}\right]
\end{aligned}
\tag{14}
$$

In order to make $\dot{V}(t)$ negative, the following control law is proposed to generate the force f_{mr} :

$$
f_{mr} = -\frac{\left(\alpha_2 - \alpha_{2equ}\right)\left(1+h_1h_2\right) + \left(h_1+h_2\right)\omega_2 + f}{g}
\tag{15}
$$

Substitution of (15) into (14) yields:

$$
\dot{V} = -h_1e_1^2 - h_2e_2^2 < 0, \qquad \forall h_1,\, h_2 > 0
\tag{16}
$$

Thus, according to the Lyapunov stability theory, the system is asymptotically stable. Therefore, $e_1 \to 0$ and $e_2 \to 0$, and consequently $\alpha_2 \to \alpha_{2equ}$ and $\omega_2 \to 0$ by using the control law (15).

Note that the control force f_{mr} in (15) cannot be commanded directly, thus voltage or current commanding signals are used as the control input to approximately generate the desired damping force. Concretely, by making use of the Dahl model (12), the following voltage commanding signal is obtained from (15):

$$
v(t) = \begin{cases}
-\dfrac{\left(\alpha_2 - \alpha_{2equ}\right)\left(1+h_1h_2\right) + \left(h_1+h_2\right)\omega_2 + f - g\left(c_0\dot{x} + \alpha_0 w\right)}{(\alpha_1 w + c_1\dot{x})g} & \forall g \neq 0 \\
0 \qquad \text{otherwise}
\end{cases}
\tag{17}
$$

which is the control signal that can be sent to the MR damper.

5. Simulation results

In this section, MR damper parameters $\alpha_0 = 1,8079$, $\alpha_1 = 8,0802$, $c_0 = 0,0055$, $c_1 = 0,0055$, $\gamma = 84,0253$, $\beta = 100$, $n = 1$ and $\delta = 80,7337$ (Ikhouane and Dyke, 2007) are taken for the simulation. The displacement curves and velocity curves showing hysteresis of the three last simulations, with different values of voltage, are given in Fig. 13 and Fig. 14, respectively. The blue curve is for no current, and gives the effect of the passive damper. We notice that the higher current the higher torque and less hysteresis width. All of the curves starts wide, and gets smaller and closer to zero by time. This is because of the damping. The system is stable.

Now, the backstepping control law (17) was applied to the experimental platform with the parameters $h_1 = 1$ and $h_2 = 10$ for the simulation.

The effectiveness of the backstepping controller for the vibration reduction can be seen in Fig. 15. It shows the system response (angular position and velocity) for three different excitation inputs: step, pulse train and random excitation. The figures show the comparison of the system response in two cases: "no control", when the current to MR damper is 0 A at all times (or equivalently, the voltage is set to 0 V) and "Backstepping", when the controller

is activated. The reduction in the RMS angular velocity achieved in each case is 43.5%, 37.3% and 40.7%, respectively.
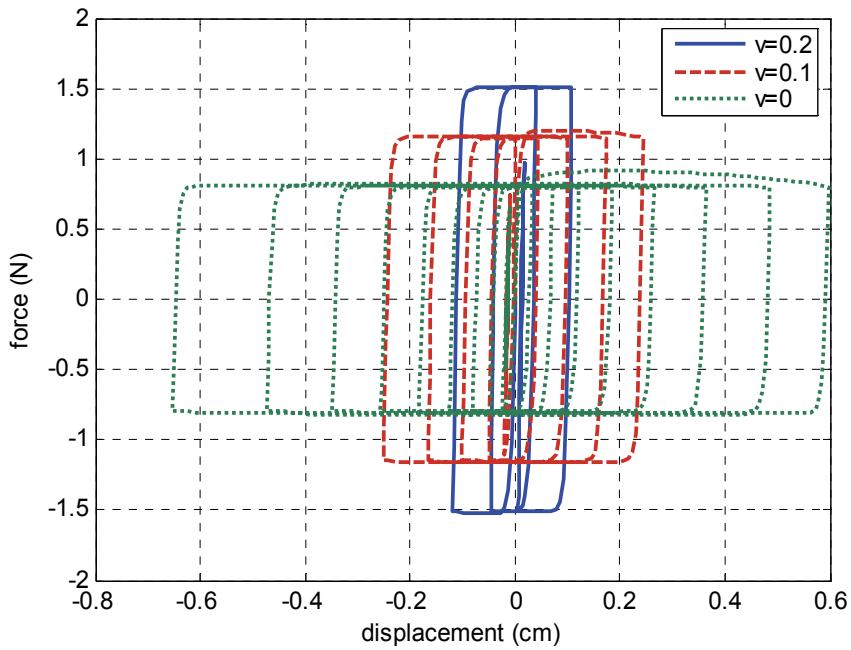
Fig. 13. Displacement vs torque.
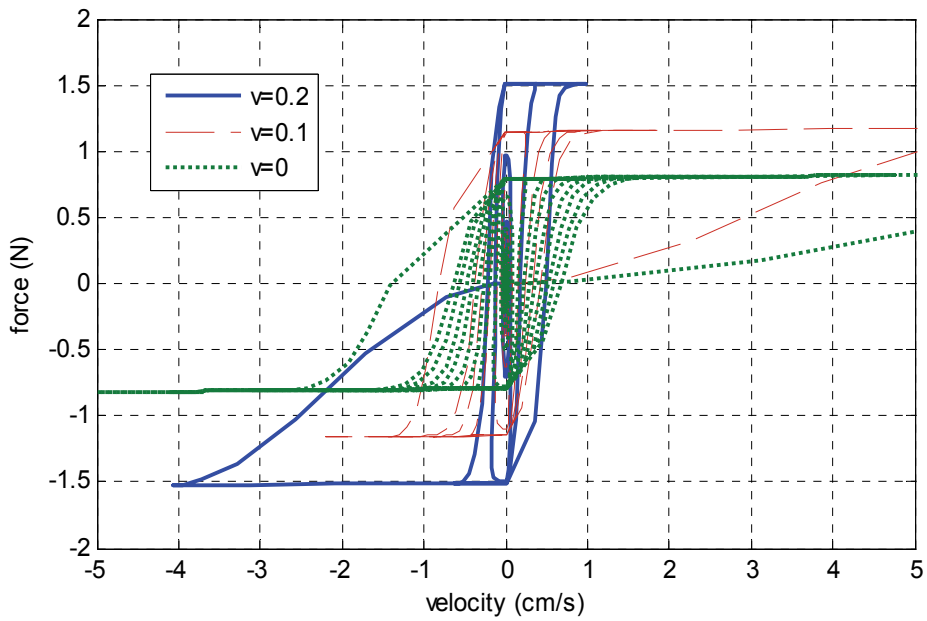
Fig. 14. Velocity vs torque.
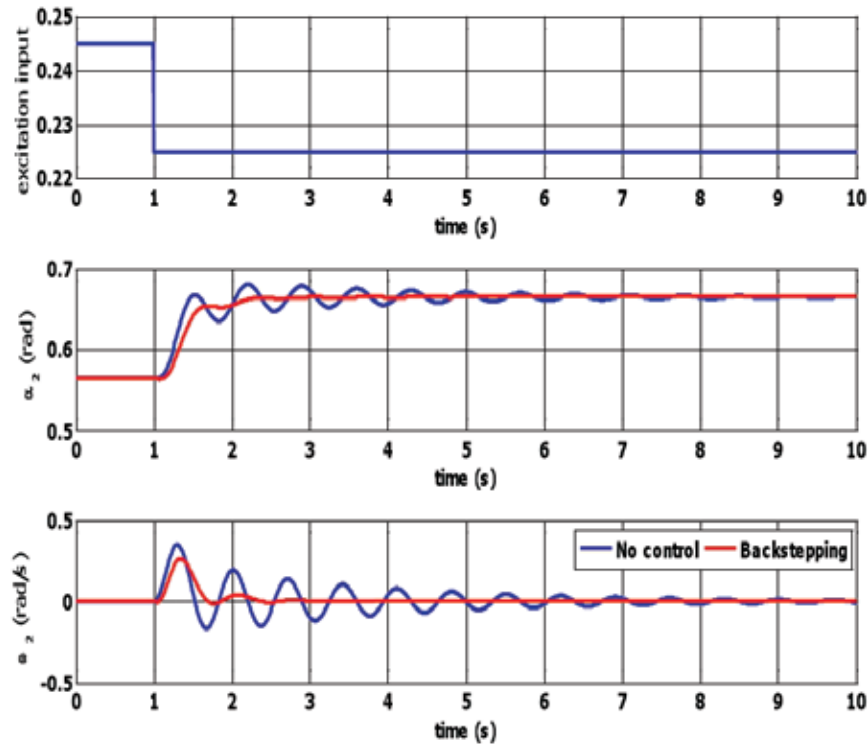
(a)
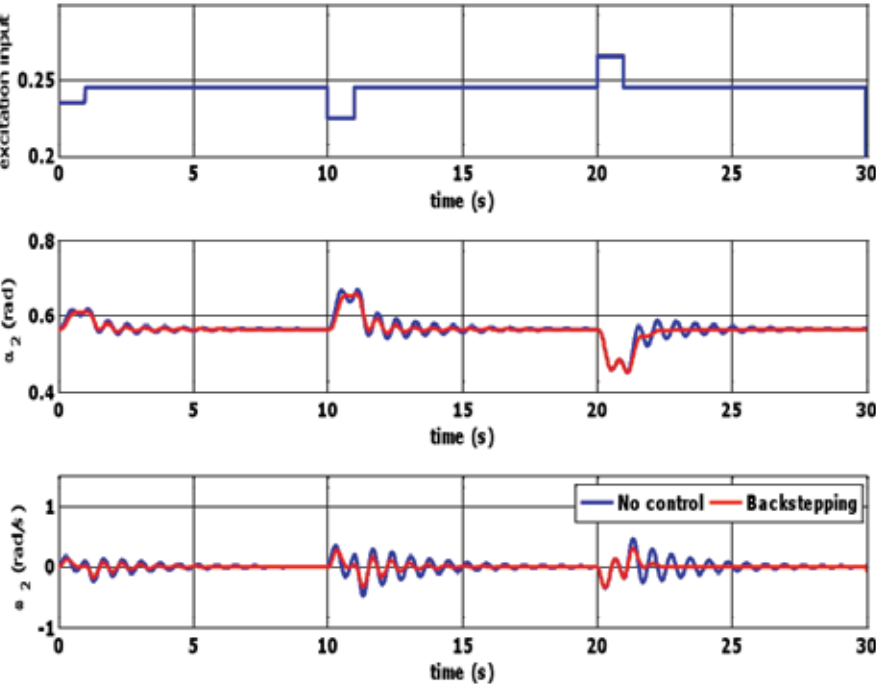
(b)
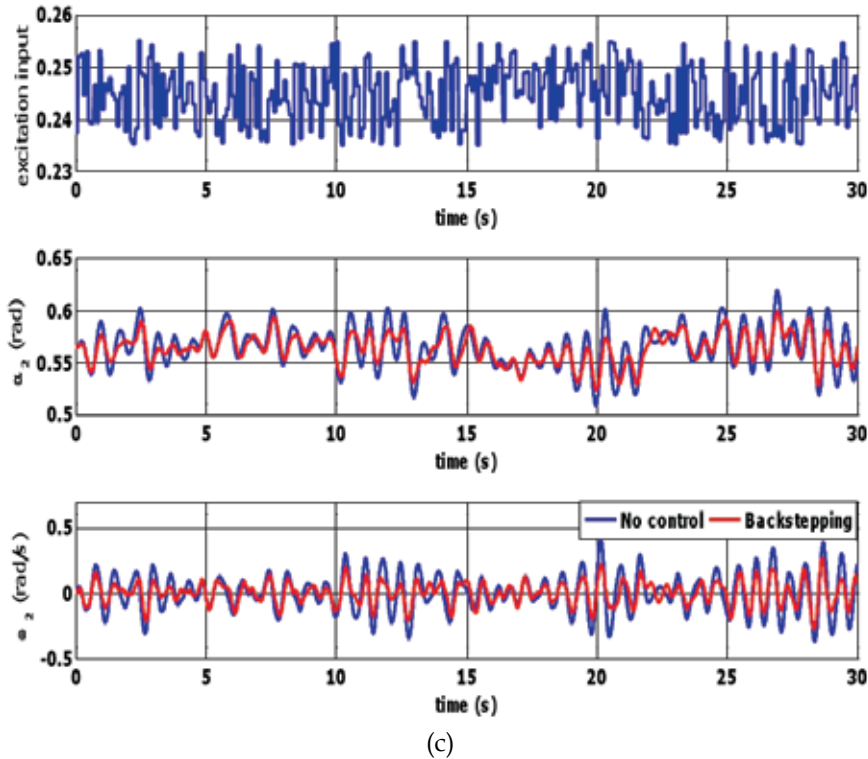
Fig. 15. Suspension systems response with the backstepping control: (a) Step input; (b) Pulse train input; (c) Random input.

6. Conclusions

In this paper we have studied the application of semiactive suspension for the vibration reduction in a class of automotive systems by using MR dampers. Backstepping and heuristic controllers have been proposed: the first one is able to account for the MR damper's nonlinearities and the second one needs only the information of the measured vibration. The control performance has been evaluated through the simulations on an experimental vehicle semiactive suspension platform. It has been shown that the proposed semiactive control strategies are capable of reducing the suspension deflection with a significantly enhanced control performance than the passive suspension system.

7. Appendix. Geometrical diagram (Inteco SAS manual)
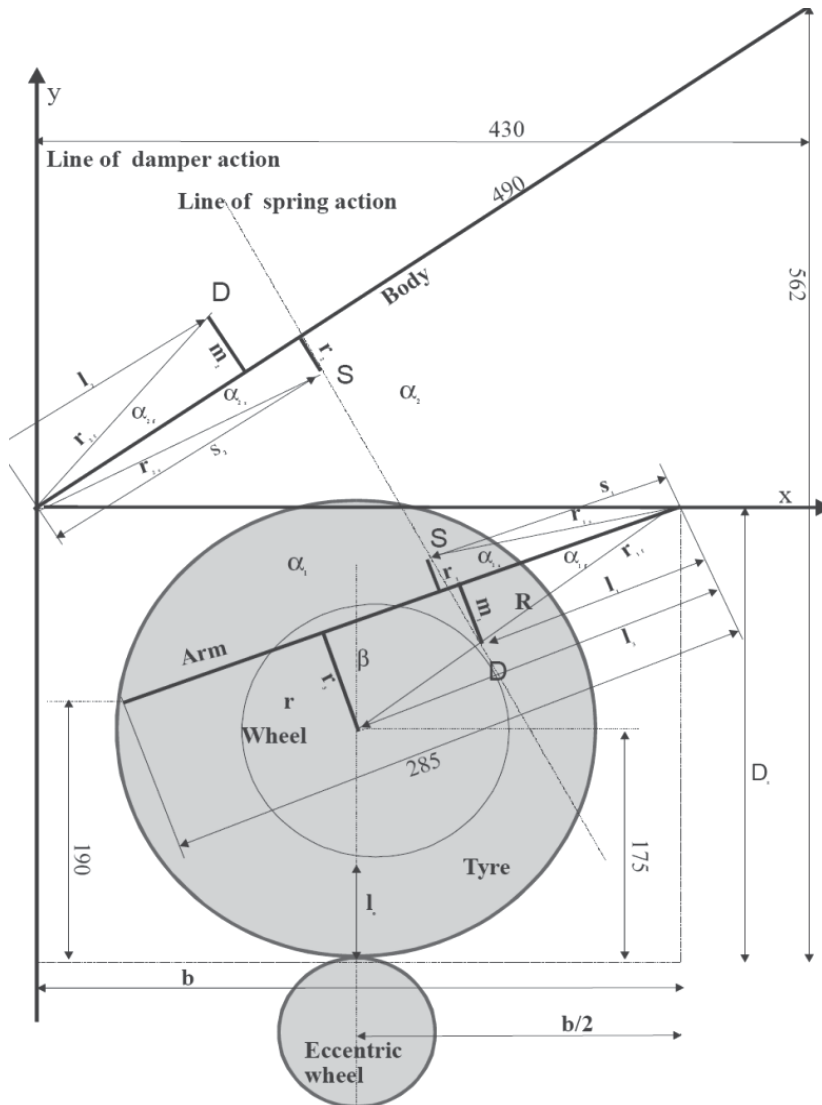
Geometrical diagram (Inteco SAS Manual)

where

- $r_1 = r_2 = 0.025$ m: distance between the spring joint and the lower and upper rocking lever line.
- $r_3 = 0.050$ m: distance between the wheel axis and the lower rocking lever line.
- $l_1 = 0.125$ m: distance between the damper joint and the lower rocking lever line.
- $l_2 = 0.130$ m: distance between the damper joint and the upper rocking lever line.
- $l_3 = 0.200$ m: distance between the wheel axis and the lower rocking lever line.
- $s_1 = 0.135$ m: distance between the spring joint and the lower rocking lever line.
- $s_2 = 0.160$ m: distance between the spring joint and the upper rocking lever line.

- α_{1f} = 0.2730 rad: damper fixation angle.
- α_{2f} = 0.2630 rad: damper fixation angle.
- α_{1s} = 0.1831 rad: spring fixation angle.
- α_{2s} = 0.1550 rad: spring fixation angle.
- β = 0.2450 rad: wheel axis fixation angle.
- r_{1f} = 0.1298 m: lower rotational radius of the damper suspension.
- r_{2f} = 0.1346 m: upper rotational radius of the damper suspension.
- r_{1s} = 0.1373 m: lower rotational radius of the spring suspension.
- r_{2s} = 0.1619 m: upper rotational radius of the spring suspension.
- R = 0.2062 m: rotational radius of the wheel axis.
- D_x = 0.249 m: distance between the rocking lever rota-tional axis and the wheel bottom (minimal eccentricity).
- r = 0.06 m: radius of rim.
- l_0 = 0.07 m: tire thickness.
- b = 0.330 m: distance between the rocking lever rotational axis and car body.

8. References

A. Ashfak, A. Saheed, K. K. Abdul Rasheed, and J. Abdul Jaleel (2011). Design, Fabrication and Evaluation of MR Damper. *International Journal of Aerospace and Mechanical Engineering*. 1, vol. 5, pp. 27-33.

J.D. Carlson (1999), Magnetorheological fluid actuators, in *Adaptronics and Smart Structures. Basics, Materials, Design and Applications*, edited by H. Janocha, London: Springer.

J.D. Carlson, D.F. LeRoy, J.C. Holzheimer, D.R. Prindle, and R.H. Marjoram. Controllable brake. *US patent* 5,842,547, 1998.

H. Du and N. Zhang (2007), H$_\infty$ control of active vehicle suspensions with actuator time delay, *J. Sound and Vibration*, vol. 301, pp. 236-252.

S.J. Dyke, B.F. Spencer Jr., M.K. Sain and J.D. Carlson (1998), An experimental study of MR dampers for seismic protection, *Smart Materials and Structures*, vol. 7, pp. 693-703.

H. Gavin, J. Hoagg and M. Dobossy (2001). *Optimal Design of MR Dampers. Proc. U.S.-Japan Workshop on Smart Structures for Improved Seismic Performance in Urban Regions*, Seattle, WA, 2001. pp. 225-236.

E. Guglielmino, T. Sireteanu, C.W. Stammers and G. Ghita (2008), *Semi-active Suspension Control: Improved Vehicle Ride and Road Friendliness*, London: Springer.

F. Ikhouane and J. Rodellar (2007), *Systems with hysteresis: Analysis, Identification and Control Using the Bouc-Wen Model*, West Sussex: John Wiley & Sons.

F. Ikhouane and S.J. Dyke (2007), Modeling and identification of a shear mode magnetorheological damper, *Smart Materials and Structures*, vol. 16, pp. 1-12.

INTECO Limited (2007), *Semiactive Suspension System (SAS): User's Manual*.

A. Karkoub and A. Dhabi (2006), Active/semiactive suspension control using magnetorheological actuators, *Int. J. Systems Science*, vol. 37, pp. 35-44.

A. Rodriguez, F. Ikhouane, J. Rodellar and N. Luo (2009), Modeling and identification of a small-scale magneto-rheological damper, *J. Intelligent Material Systems and Structures*, vol. 20, pp. 825-835.

Y. Shen, M.F. Golnaraghi and G.R. Heppler (2006), Semiactive vibration control schemes for suspension system using magnetorheological damper, *J. Vibration and Control*, vol. 12, pp. 3-24.

B.F. Spencer, S.J. Dyke, M.K. Sain and J.D. Carlson (1997), Phenomenological model of a magnetorheological damper, *ASCE J. Engineering Mechanics*, vol. 123, pp. 230-238.

H. Wang, X.L. Gong, Y.S. Zhu, and P.Q. Zhang (2004). A route to design rotary magnetorheological dampers. In Proceedings of the Ninth International Conference on Electrorheological Fluids and Magnetorheological Suspensions, pages 680–686, Beijing, China.

M. Zapateiro and N. Luo (2007), Parametric and non-parametric characterization of a shear mode MR damper, *J. Vibroengineering*, vol. 9, pp. 14-18.

M. Zapateiro, N. Luo, H.R. Karimi and J. Vehi (2009), Vibration control of a class of semiactive suspension system using neural network and backstepping techniques, *Mechanical Systems and Signal Processing*, vol. 23, pp. 1946-1953.

Control of Nonlinear Active Vehicle Suspension Systems Using Disturbance Observers

Francisco Beltran-Carbajal[1], Esteban Chavez-Conde[2],
Gerardo Silva Navarro[3], Benjamin Vazquez Gonzalez[1]
and Antonio Favela Contreras[4]

[1]*Universidad Autonoma Metropolitana, Plantel Azcapotzalco,*
Departamento de Energia, Mexico, D.F.
[2]*Universidad del Papaloapan, Campus Loma Bonita, Departamento de Ingenieria en*
Mecatronica, Instituto de Agroingenieria, Loma Bonita, Oaxaca
[3]*Centro de Investigacion y de Estudios Avanzados del I.P.N., Departamento de Ingenieria*
Electrica, Seccion de Mecatronica, Mexico, D.F.
[4]*ITESM Campus Monterrey, Monterrey, N.L.*
Mexico

1. Introduction

The main control objectives of active vehicle suspension systems are to improve the ride comfort and handling performance of the vehicle by adding degrees of freedom to the passive system and/or controlling actuator forces depending on feedback and feedforward information of the system obtained from sensors.

Passenger comfort is provided by isolating the passengers from the undesirable vibrations induced by irregular road disturbances and its performance is evaluated by the level of acceleration by which vehicle passengers are exposed. Handling performance is achieved by maintaining a good contact between the tire and the road to provide guidance along the track.

The topic of active vehicle suspension control system, for linear and nonlinear models, in general, has been quite challenging over the years and we refer the reader to some of the fundamental works in the vibration control area (Ahmadian, 2001). Some active control schemes are based on neural networks, genetic algorithms, fuzzy logic, sliding modes, H-infinity, adaptive control, disturbance observers, LQR, backstepping control techniques, etc. See, e.g., (Cao et al., 2008); (Isermann & Munchhof, 2011); (Martins et al., 2006); (Tahboub, 2005); (Chen & Huang, 2005) and references therein. In addition, some interesting semiactive vibration control schemes, based on Electro-Rheological (ER) and Magneto-Rheological (MR) dampers, have been proposed and implemented on commercial vehicles. See, e.g., (Choi et al., 2003); (Yao et al., 2002).

In this chapter is proposed a robust control scheme, based on the real-time estimation of perturbation signals, for active nonlinear or linear vehicle suspension systems subject to unknown exogenous disturbances due to irregular road surfaces. Our approach differs

from others in that, the control design problem is formulated as a bounded disturbance signal processing problem, which is quite interesting because one can take advantage of the industrial embedded system technologies to implement the resulting active vibration control strategies. In fact, there exist successful implementations of automotive active control systems based on embedded systems, and this novel tendency is growing very fast in the automotive industry. See, e.g., (Shoukry et al., 2010); (Basterretxea et al., 2010); (Ventura et al., 2008); (Gysen et al., 2008) and references therein.

In our control design approach is assumed that the nonlinear effects, parameter variations, exogenous disturbances and possibly input unmodeled dynamics are lumped into an unknown bounded time-varying disturbance input signal affecting a so-called differentially flat linear simplified dynamic mathematical model of the suspension system. The lumped disturbance signal and some time derivatives of the flat output are estimated by using a flat output-based linear high-gain dynamic observer. The proposed observer-control design methodology considers that, the perturbation signal can be locally approximated by a family of Taylor polynomials. Two active vibration controllers are proposed for hydraulic or electromagnetic suspension systems, which only require position measurements.

Some numerical simulation results are provided to show the efficiency, effectiveness and robust performance of the feedforward and feedback linearization control scheme proposed for a nonlinear quarter-vehicle active suspension system.

This chapter is organized as follows: Section 2 presents the nonlinear mathematical model of an active nonlinear quarter-vehicle suspension system. Section 3 presents the proposed vehicle suspension control scheme based on differential flatness. Section 4 presents the main results of this chapter as an alternative solution to the vibration attenuation problem in nonlinear and linear active vehicle suspension systems actuated electromagnetically or hydraulically. Computer simulation results of the proposed design methodology are included in Section 5. Finally, Section 6 contains the conclusions and suggestions for further research.

2. A quarter-vehicle active suspension system model

Consider the well-known nonlinear quarter-vehicle suspension system shown in Fig. 1. In this model, the sprung mass m_s denotes the time-varying mass of the vehicle-body and the unsprung mass m_u represents the assembly of the axle and wheel. The tire is modeled as a linear spring with equivalent stiffness coefficient k_t linked to the road and negligible damping coefficient. The vehicle suspension, located between m_s and m_u, is modeled by a damper and spring, whose nonlinear damping and stiffness force functions are given by

$$\mathcal{F}_k(z) = kz + k_n z^3$$

$$\mathcal{F}_c(\dot{z}) = c\dot{z} + c_n \dot{z}^2 \mathrm{sgn}(\dot{z})$$

The generalized coordinates are the displacements of both masses, z_s and z_u, respectively. In addition, $u = F_A$ denotes the (force) control input, which is applied between the two masses by means of an actuator, and $z_r(t)$ represents a bounded exogenous perturbation signal due
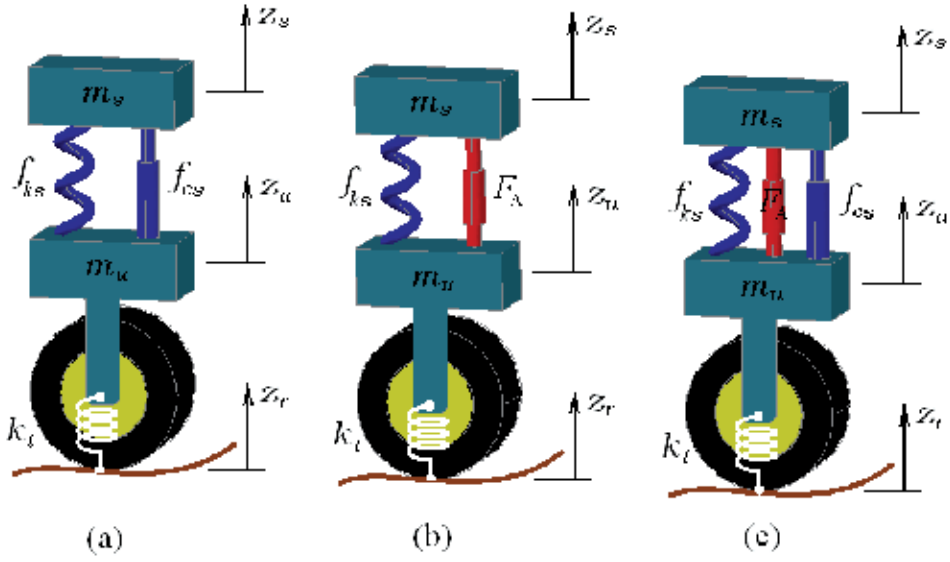
Fig. 1. Schematic diagram of a quarter-vehicle suspension system: (a) passive suspension system, (b) electromagnetic active suspension system and (c) hydraulic active suspension system.

to irregular road surfaces satisfying:

$$\|z_r(t)\|_\infty = \gamma_1$$
$$\|\dot{z}_r(t)\|_\infty = \gamma_2$$
$$\|\ddot{z}_r(t)\|_\infty = \gamma_3$$

where

$$\gamma_1 = \sup_{t\in[0,\infty)} |z_r(t)|$$
$$\gamma_2 = \sup_{t\in[0,\infty)} |\dot{z}_r(t)|$$
$$\gamma_3 = \sup_{t\in[0,\infty)} |\ddot{z}_r(t)|$$

For an electromagnetic active suspension system, the damper is replaced by an electromagnetic actuator (Martins et al., 2006). In this configuration, it is assumed that $\mathcal{F}_c(\dot{z}) \approx 0$.
The mathematical model of the two degree-of-freedom suspension system is then described by the following two coupled nonlinear differential equations:

$$m_s\ddot{z}_s + \mathcal{F}_{sc} + \mathcal{F}_{sk} = u$$
$$m_u\ddot{z}_u + k_t(z_u - z_r) - \mathcal{F}_{sc} - \mathcal{F}_{sk} = -u \tag{1}$$

with

$$\mathcal{F}_{sk}\left(z_s, z_u\right) = k_s(z_s - z_u) + k_{ns}\left(z_s - z_u\right)^3$$
$$\mathcal{F}_{sc}\left(\dot{z}_s, \dot{z}_u\right) = c_s(\dot{z}_s - \dot{z}_u) + c_{ns}(\dot{z}_s - \dot{z}_u)^2 \text{sgn}(\dot{z}_s - \dot{z}_u)$$

where $sgn(\cdot)$ denotes the standard signum function.

Defining the state variables as $x_1 = z_s$, $x_2 = \dot{z}_s$, $x_3 = z_u$ and $x_4 = \dot{z}_u$, one obtains the following state-space description:

$$\begin{aligned}
\dot{x}_1 &= x_2 \\
\dot{x}_2 &= -\frac{1}{m_s}\left(\mathcal{F}_{sc} + \mathcal{F}_{sk}\right) + \frac{1}{m_s}u \\
\dot{x}_3 &= x_4 \\
\dot{x}_4 &= -\frac{k_t}{m_u}x_3 + \frac{1}{m_u}\left(\mathcal{F}_{sc} + \mathcal{F}_{sk}\right) - \frac{1}{m_u}u + \frac{k_t}{m_u}z_r
\end{aligned} \qquad (2)$$

with

$$\mathcal{F}_{sk}\left(x_1, x_3\right) = k_s(x_1 - x_3) + k_{ns}\left(x_1 - x_3\right)^3$$
$$\mathcal{F}_{sc}\left(x_2, x_4\right) = c_s(x_2 - x_4) + c_{ns}(x_2 - x_4)^2 \text{sgn}(x_2 - x_4)$$

It is easy to verify that the nonlinear vehicle suspension system (2) is completely controllable and observable and, therefore, is differentially flat and constructible. For more details on this topics we refer to (Fliess et al., 1993) and the book by (Sira-Ramirez & Agrawal, 2004). Both properties can be used extensively during the synthesis of different controllers based on differential flatness, trajectory planning, disturbance and state reconstruction, parameter identification, Generalized PI (GPI) and sliding mode control, etc. See, e.g., (Beltran-Carbajal et al., 2010a); (Beltran-Carbajal et al., 2010b); (Chavez-Conde et al., 2009a); (Chavez-Conde et al., 2009b).

In what follows, a feedforward and feedback linearization active vibration controller, as well as a disturbance observer, will be designed taking advantage of the differential flatness property exhibited by the vehicle suspension system.

3. Differential flatness-based control

The system (2) is differentially flat, with a flat output given by

$$L = m_s x_1 + m_u x_3$$

which is constructed as a linear combination of the displacements of the sprung mass x_1 and the unsprung mass x_3.

Then, all the state variables and the control input can be parameterized in terms of the flat output L and a finite number of its time derivatives (Sira-Ramirez & Agrawal, 2004). As a matter of fact, from L and its time derivatives up to fourth order one can obtain:

$$\begin{aligned}
L &= m_s x_1 + m_u x_3 \\
\dot{L} &= m_s x_2 + m_u x_4 \\
\ddot{L} &= k_t\left(z_r - x_3\right) \\
L^{(3)} &= k_t\left(\dot{z}_r - x_4\right) \\
L^{(4)} &= \frac{1}{m_u}u + \frac{k_t}{m_u}x_3 - \frac{1}{m_u}\left(\mathcal{F}_{sc} + \mathcal{F}_{sk}\right) - \frac{k_t}{m_u}z_r + k_t\ddot{z}_r
\end{aligned} \qquad (3)$$

Therefore, the differential parameterization of the state variables and the control input in the vehicle dynamics (2) results as follows

$$
\begin{aligned}
x_1 &= \frac{m_u}{k_t m_s} \ddot{L} + \frac{1}{m_s} L - \frac{m_u}{m_s} z_r \\
x_2 &= \frac{m_u}{k_t m_s} L^{(3)} + \frac{1}{m_s} \dot{L} - \frac{m_u}{m_s} \dot{z}_r \\
x_3 &= -\frac{1}{k_t} \ddot{L} + z_r \\
x_4 &= -\frac{1}{k_t} L^{(3)} + \dot{z}_r \\
u &= \frac{1}{b} \left(L^{(4)} + a_3 L^{(3)} + a_2 \ddot{L} + a_1 \dot{L} + a_0 L - \xi(t) \right)
\end{aligned}
\tag{4}
$$

with

$$
\begin{aligned}
a_0 &= \frac{k_s k_t}{m_s m_u} \\
a_1 &= \frac{c_s k_t}{m_s m_u} \\
a_2 &= \frac{k_s}{m_s} + \frac{k_s + k_t}{m_u} \\
a_3 &= \frac{c_s}{m_s} + \frac{c_s}{m_u} \\
b &= \frac{k_t}{m_u}
\end{aligned}
$$

and

$$
\begin{aligned}
\xi(t) = &-\frac{k_{ns} k_t}{m_u} (x_1 - x_3)^3 - \frac{c_{ns} k_t}{m_u} (x_2 - x_4)^2 \mathrm{sgn}(x_2 - x_4) \\
&+ k_t \ddot{z}_r + \left(\frac{k_t}{m_s} + \frac{k_t}{m_u} \right) c_s \dot{z}_r + \left(\frac{k_t}{m_s} + \frac{k_t}{m_u} \right) k_s z_r
\end{aligned}
$$

Now, note that from the last equation in the differential parameterization (4), one can see that the flat output satisfies the following perturbed input-output differential equation:

$$
L^{(4)} + a_3 L^{(3)} + a_2 \ddot{L} + a_1 \dot{L} + a_0 L = bu + \xi(t)
\tag{5}
$$

Then, the flat output dynamics can be described by the following 4th order perturbed linear system:

$$
\begin{aligned}
\dot{\eta}_1 &= \eta_2 \\
\dot{\eta}_2 &= \eta_3 \\
\dot{\eta}_3 &= \eta_4 \\
\dot{\eta}_4 &= -a_0 \eta_1 - a_1 \eta_2 - a_2 \eta_3 - a_3 \eta_4 + bu + \xi(t) \\
y &= \eta_1 = L
\end{aligned}
\tag{6}
$$

To formulate the vibration control problem, let us assume, by the moment, a perfect knowledge of the perturbation term ξ, as well as the time derivatives of the flat output up to third order. Then, from (6) one obtains the following differential flatness-based controller:

$$
u = \frac{1}{b} v + \underline{\frac{1}{b} \left(a_3 \eta_4 + a_2 \eta_3 + a_1 \eta_2 + a_0 \eta_1 - \xi(t) \right)}
\tag{7}
$$

with

$$
v = -\alpha_3 \eta_4 - \alpha_2 \eta_3 - \alpha_1 \eta_2 - \alpha_0 \eta_1
$$

The use of this controller yields the following closed-loop dynamics:

$$
L^{(4)} + \alpha_3 L^{(3)} + \alpha_2 \ddot{L} + \alpha_1 \dot{L} + \alpha_0 L = 0
\tag{8}
$$

The closed-loop characteristic polynomial is then given by

$$p(s) = s^4 + \alpha_3 s^3 + \alpha_2 s^2 + \alpha_1 s + \alpha_0 \tag{9}$$

Therefore, by selecting the design parameters α_i, $i = 0, \cdots, 3$, such that the associated characteristic polynomial for (8) be *Hurwitz*, one can guarantee that the flat output dynamics be globally asymptotically stable, i.e.,

$$\lim_{t \to \infty} L(t) = 0$$

Now, the following Hurwitz polynomial is proposed to get the corresponding controller gains:

$$p_c(s) = \left(s^2 + 2\zeta_c \omega_c s + \omega_c^2 \right)^2 \tag{10}$$

where $\omega_c > 0$ *and* $\zeta_c > 0$ are the natural frequency and damping ratio of the desired closed-loop dynamics, respectively.

Equating term by term the coefficients of both polynomials (9) and (10), one obtains that

$$\alpha_0 = \omega_c^4$$
$$\alpha_1 = 4\omega_c^3 \zeta_c$$
$$\alpha_2 = 4\omega_c^2 \zeta_c^2 + 2\omega_c^2$$
$$\alpha_3 = 4\omega_c \zeta_c$$

On the other hand, it is easy to show that the closed-loop system (2)-(7) is L_∞-stable or bounded-input-bounded-state, that is,

$$\|x_1\|_\infty = \frac{m_u}{m_s} \gamma_1$$
$$\|x_2\|_\infty = \frac{m_u}{m_s} \gamma_2$$
$$\|x_3\|_\infty = \gamma_1$$
$$\|x_4\|_\infty = \gamma_2$$
$$\|u\|_\infty = \left(k_{ns} \gamma_1^3 \rho^2 + c_{ns} \rho \gamma_2^2 + c_s \gamma_2 + k_s \gamma_1 \right) \rho + m_u \gamma_3$$

where $\rho = \frac{m_u}{m_s} + 1$.

It is evident, however, that the controller (8) requires the perfect knowledge of the exogenous perturbation signal z_r and its time derivatives up to second order, revealing several disadvantages with respect to other control schemes. Nevertheless, one can take advantage of the design methodology of robust observers with respect to unmodeled perturbation inputs, of the polynomial type affecting the observed plant, proposed by (Sira-Ramirez et al., 2008b). The proposed disturbance observer is called Generalized Proportional Integral (GPI) observer, because its design approach is the dual counterpart of the so-called GPI controllers (Fliess et al., 2002) and whose robust performance, with respect to unknown perturbation inputs, nonlinear and linear unmodeled dynamics and parametric uncertainties, have been evaluated extensively through experiments for trajectory tracking tasks on a vibrating mechanical system by (Sira-Ramirez et al., 2008a) and on a dc motor by (Sira-Ramirez et al., 2009).

4. Disturbance observer design

In the observer design process it is assumed that the perturbation input signal $\xi(t)$ can be locally approximated by a family of Taylor polynomials of $(r-1)$th degree:

$$\xi(t) = \sum_{i=0}^{r-1} p_i t^i \tag{11}$$

where all the coefficients p_i are completely unknown.

The perturbation signal could then be locally described by the following state-space based linear mathematical model:

$$\begin{aligned}
\dot{\xi}_1 &= \xi_2 \\
\dot{\xi}_2 &= \xi_3 \\
&\;\;\vdots \\
\dot{\xi}_{r-1} &= \xi_r \\
\dot{\xi}_r &= 0
\end{aligned} \tag{12}$$

where $\xi_1 = \xi,\; \xi_2 = \dot{\xi},\; \xi_3 = \ddot{\xi},\; \cdots,\; \xi_r = \xi^{(r-1)}$.

An extended approximate state model for the perturbed flat output dynamics is then given by

$$\begin{aligned}
\dot{\eta}_1 &= \eta_2 \\
\dot{\eta}_2 &= \eta_3 \\
\dot{\eta}_3 &= \eta_4 \\
\dot{\eta}_4 &= -a_0\eta_1 - a_1\eta_2 - a_2\eta_3 - a_3\eta_4 + \xi_1 + bu \\
\dot{\xi}_1 &= \xi_2 \\
\dot{\xi}_2 &= \xi_3 \\
&\;\;\vdots \\
\dot{\xi}_{r-1} &= \xi_r \\
\dot{\xi}_r &= 0 \\
y &= \eta_1 = L
\end{aligned} \tag{13}$$

A Luenberger observer for the system (13) is given by

$$\begin{aligned}
\dot{\widehat{\eta}}_1 &= \widehat{\eta}_2 + \beta_{r+3}(y - \widehat{y}) \\
\dot{\widehat{\eta}}_2 &= \widehat{\eta}_3 + \beta_{r+2}(y - \widehat{y}) \\
\dot{\widehat{\eta}}_3 &= \widehat{\eta}_4 + \beta_{r+1}(y - \widehat{y}) \\
\dot{\widehat{\eta}}_4 &= -a_0\widehat{\eta}_1 - a_1\widehat{\eta}_2 - a_2\widehat{\eta}_3 - a_3\widehat{\eta}_4 + \widehat{\xi}_1 + bu + \beta_r(y - \widehat{y}) \\
\dot{\widehat{\xi}}_1 &= \widehat{\xi}_2 + \beta_{r-1}(y - \widehat{y}) \\
\dot{\widehat{\xi}}_2 &= \widehat{\xi}_3 + \beta_{r-2}(y - \widehat{y}) \\
&\;\;\vdots \\
\dot{\widehat{\xi}}_{r-1} &= \widehat{\xi}_r + \beta_1(y - \widehat{y}) \\
\dot{\widehat{\xi}}_r &= \beta_0(y - \widehat{y}) \\
\widehat{y} &= \widehat{\eta}_1
\end{aligned} \tag{14}$$

The dynamical system describing the state estimation error is readily obtained by subtracting the observer dynamics (14) from the extended linear system dynamics (6). One then obtains, with $e_1 = y - \widehat{y}$ and $e_{zi} = \xi_i - \widehat{\xi}_i$, $i = 1, 2, \cdots, r$, that

$$
\begin{aligned}
\dot{e}_1 &= -\beta_{r+3}e_1 + e_2 \\
\dot{e}_2 &= -\beta_{r+2}e_1 + e_3 \\
\dot{e}_3 &= -\beta_{r+1}e_1 + e_4 \\
\dot{e}_4 &= -\left(\beta_r + a_0\right)e_1 - a_1 e_2 - a_2 e_3 - a_3 e_4 + e_{z_1} \\
\dot{e}_{z_1} &= -\beta_{r-1}e_1 + e_{z_2} \\
\dot{e}_{z_2} &= -\beta_{r-2}e_1 + e_{z_3} \\
&\vdots \\
\dot{e}_{z_{r-1}} &= -\beta_1 e_1 + e_{z_r} \\
\dot{e}_{z_r} &= -\beta_0 e_1
\end{aligned}
\tag{15}
$$

From this expression, it is not difficult to see that the dynamics of output observation error $e_1 = y - \hat{y}$ satisfies the following differential equation:

$$
\begin{aligned}
&e_1^{(r+4)} + \left(\beta_{r+3} + a_3\right) e_1^{(r+3)} + \left(\beta_{r+2} + a_2 + \beta_{r+3}a_3\right) e_1^{(r+2)} \\
&+ \left(\beta_{r+1} + a_1 + \beta_{r+2}a_3 + \beta_{r+3}a_2\right) e_1^{(r+1)} \\
&+ \left(\beta_r + a_0 + \beta_{r+1}a_3 + \beta_{r+2}a_2 + \beta_{r+3}a_1\right) e_1^{(r)} \\
&+ \beta_{r-1}e_1^{(r-1)} + \cdots + \beta_2 \ddot{e}_1 + \beta_1 \dot{e}_1 + \beta_0 e_1 = 0
\end{aligned}
\tag{16}
$$

which is completely independent of any coefficients p_i, $i = 0, \cdots, r - 1$, of the Taylor polynomial expansion of $\xi(t)$. This means that, the high-gain observer continuously self-updates. Therefore, as time goes on, the bounded perturbation input signal $\xi(t)$ is approximated in the form of a $(r-1)$th degree time polynomial.

Clearly, the coefficients of the associated characteristic polynomial for (16) can be adjusted, by means of a suitable specification of the design gains $\{\beta_{r+3}, \ldots, \beta_1, \beta_0\}$, sufficiently far from the imaginary axis in the left half of the complex plane, so that the output estimation error e_1 exponentially asymptotically converges to zero.

A fifth-order local mathematical model for the real-time estimation of the perturbation input signal is proposed in this chapter. Then, the characteristic polynomial for the dynamics of output observation error is simply given by

$$
\begin{aligned}
p_{o1}(s) = s^9 &+ (\beta_8 + a_3)s^8 + (\beta_7 + a_2 + \beta_8 a_3)s^7 + (\beta_6 + a_1 + \beta_7 a_3 + \beta_8 a_2)s^6 \\
&+ (\beta_5 + a_0 + \beta_6 a_3 + \beta_7 a_2 + \beta_8 a_1)s^5 + \beta_4 s^4 + \beta_3 s^3 + \beta_2 s^2 + \beta_1 s + \beta_0
\end{aligned}
\tag{17}
$$

Equating the coefficients of the characteristic polynomial (17) with the corresponding ones of the following ninth-order Hurwitz polynomial:

$$
p_{do1}(s) = (s + p_1)\left(s^2 + 2\zeta_1 \omega_1 s + \omega_1^2\right)^4
\tag{18}
$$

one gets the observer gains as follows

$$\beta_0 = p_1 \omega_1^8$$

$$\beta_1 = \omega_1^8 + 8 p_1 \zeta_1 \omega_1^7$$

$$\beta_2 = 8\omega_1^7 \zeta_1 + 24 p_1 \omega_1^6 \zeta_1^2 + 4 p_1 \omega_1^6$$

$$\beta_3 = 24\omega_1^6 \zeta_1^2 + 4\omega_1^6 + 32 p_1 \omega_1^5 \zeta_1^3 + 24 p_1 \omega_1^5 \zeta_1$$

$$\beta_4 = 32\omega_1^5 \zeta_1^3 + 24\omega_1^5 \zeta_1 + 16 p_1 \omega_1^4 \zeta_1^4 + 48 p_1 \omega_1^4 \zeta_1^2 + 6 p_1 \omega_1^4$$

$$\beta_5 = 16\omega_1^4 \zeta_1^4 + 48\omega_1^4 \zeta_1^2 + 6\omega_1^4 + 32 p_1 \omega_1^3 \zeta_1^3 + 24 p_1 \omega_1^3 \zeta_1 - a_0 - \beta_6 a_3 - \beta_7 a_2 - \beta_8 a_1$$

$$\beta_6 = 32\omega_1^3 \zeta_1^3 + 24\omega_1^3 \zeta_1 + 24 p_1 \omega_1^2 \zeta_1^2 + 4 p_1 \omega_1^2 - a_1 - \beta_7 a_3 - \beta_8 a_2$$

$$\beta_7 = 24\omega_1^2 \zeta_1^2 + 4\omega_1^2 + 8 p_1 \omega_1 \zeta_1 - a_2 - \beta_8 a_3$$

$$\beta_8 = p_1 + 8\omega_1 \zeta_1 - a_3$$

with $p_1, \omega_1, \zeta_1 > 0$.

Now, consider that the system (6) is being perturbed by the unknown input signal $\varpi(t)$ as follows

$$\begin{aligned}
\dot{\eta}_1 &= \eta_2 \\
\dot{\eta}_2 &= \eta_3 \\
\dot{\eta}_3 &= \eta_4 \\
\dot{\eta}_4 &= bu + \varpi(t) \\
y &= \eta_1 = L
\end{aligned} \tag{19}$$

with

$$\varpi(t) = -a_0 \eta_1 - a_1 \eta_2 - a_2 \eta_3 - a_3 \eta_4 + \xi(t)$$

Then, by the perfect knowledge of $\varpi(t)$, one gets the following differential flatness-based controller with feedforward of the perturbation signal $\varpi(t)$:

$$u = \frac{1}{b}(v - \varpi(t)) \tag{20}$$

with

$$v = -\alpha_3 \eta_4 - \alpha_2 \eta_3 - \alpha_1 \eta_2 - \alpha_0 \eta_1$$

Similarly as before, the perturbation input signal ϖ could be locally reconstructed by the following family of Taylor polynomial of $(r-1)$th degree:

$$\varpi(t) = \sum_{i=0}^{r-1} \gamma_i t^i \tag{21}$$

where all the coefficients γ_i are completely unknown.

Then, one can use the following extended mathematical model described in state-space form to design a robust observer for real-time estimation of the disturbance $\varpi(t)$ and time

derivatives of the flat output required for implementation of the controller (20):

$$\begin{aligned}
\dot{\eta}_1 &= \eta_2 \\
\dot{\eta}_2 &= \eta_3 \\
\dot{\eta}_3 &= \eta_4 \\
\dot{\eta}_4 &= \varpi_1 + bu \\
\dot{\varpi}_1 &= \varpi_2 \\
\dot{\varpi}_2 &= \varpi_3 \\
&\vdots \\
\dot{\varpi}_{r-1} &= \varpi_r \\
\dot{\varpi}_r &= 0 \\
y &= \eta_1 = L
\end{aligned} \tag{22}$$

where $\varpi_1 = \varpi, \varpi_2 = \dot{\varpi}, \varpi_3 = \ddot{\varpi}, \cdots, \varpi_r = \varpi^{(r-1)}$.

A Luenberger observer for the system (22) is then given by

$$\begin{aligned}
\dot{\widehat{\eta}}_1 &= \widehat{\eta}_2 + \lambda_{r+3}\left(y - \widehat{y}\right) \\
\dot{\widehat{\eta}}_2 &= \widehat{\eta}_3 + \lambda_{r+2}\left(y - \widehat{y}\right) \\
\dot{\widehat{\eta}}_3 &= \widehat{\eta}_4 + \lambda_{r+1}\left(y - \widehat{y}\right) \\
\dot{\widehat{\eta}}_4 &= \widehat{\varpi}_1 + bu + \lambda_r\left(y - \widehat{y}\right) \\
\dot{\widehat{\varpi}}_1 &= \widehat{\varpi}_2 + \lambda_{r-1}\left(y - \widehat{y}\right) \\
\dot{\widehat{\varpi}}_2 &= \widehat{\varpi}_3 + \lambda_{r-2}\left(y - \widehat{y}\right) \\
&\vdots \\
\dot{\widehat{\varpi}}_{r-1} &= \widehat{\varpi}_r + \lambda_1\left(y - \widehat{y}\right) \\
\dot{\widehat{\varpi}}_r &= \lambda_0\left(y - \widehat{y}\right) \\
\widehat{y} &= \widehat{\eta}_1
\end{aligned} \tag{23}$$

The estimation error dynamics $e_1 = y - \widehat{y}$ satisfies the following dynamics:

$$\begin{aligned}
&e_1^{(r+4)} + \lambda_{r+3}e_1^{(r+3)} + \lambda_{r+2}e_1^{(r+2)} + \lambda_{r+1}e_1^{(r+1)} + \lambda_r e_1^{(r)} \\
&+ \lambda_{r-1}e_1^{(r-1)} + \cdots + \lambda_2\ddot{e} + \lambda_1\dot{e}_1 + \lambda_0 e_1 = 0
\end{aligned} \tag{24}$$

Therefore, the design parameters λ_i, $i = 0, \cdots, r+3$, can be chosen so that the output estimation error e_1 exponentially asymptotically converges to zero.

On the other hand, it is assumed that the perturbation input signal $\varpi(t)$ can be locally approximated by a family of Taylor polynomials of fourth degree. Therefore, the characteristic polynomial for the dynamics of output observation error (24) is given by

$$p_{o2} = s^9 + \lambda_8 s^8 + \lambda_7 s^7 + \lambda_6 s^6 + \lambda_5 s^5 + \lambda_4 s^4 + \lambda_3 s^3 + \lambda_2 s^2 + \lambda_1 s + \lambda_0 \tag{25}$$

It is then proposed the following Hurwitz polynomial to compute the proper gains for the observer:

$$p_{o2}\left(s\right) = \left(s + p_2\right)\left(s^2 + 2\zeta_2\omega_2 s + \omega_2^2\right)^4 \tag{26}$$

One then obtains that

$$\lambda_0 = p_2 \omega_2^8$$
$$\lambda_1 = \omega_2^8 + 8p_2\zeta_2\omega_2^7$$
$$\lambda_2 = 8\omega_2^7\zeta_2 + 24p_2\omega_2^6\zeta_2^2 + 4p_2\omega_2^6$$
$$\lambda_3 = 24\omega_2^6\zeta_2^2 + 4\omega_2^6 + 32p_2\omega_2^5\zeta_2^3 + 24p_2\omega_2^5\zeta_2$$
$$\lambda_4 = 32\omega_2^5\zeta_2^3 + 24\omega_2^5\zeta_2 + 16p_2\omega_2^4\zeta_2^4 + 48p_2\omega_2^4\zeta_2^2 + 6p_2\omega_2^4$$
$$\lambda_5 = 16\omega_2^4\zeta_2^4 + 48\omega_2^4\zeta_2^2 + 6\omega_2^4 + 32p_2\omega_2^3\zeta_2^3 + 24p_2\omega_2^3\zeta_2$$
$$\lambda_6 = 32\omega_2^3\zeta_2^3 + 24\omega_2^3\zeta_2 + 24p_2\omega_2^2\zeta_2^2 + 4p_2\omega_2^2$$
$$\lambda_7 = 24\omega_2^2\zeta_2^2 + 4\omega_2^2 + 8p_2\omega_2\zeta_2$$
$$\lambda_8 = p_2 + 8\omega_2\zeta_2$$

with $p_2, \omega_2, \zeta_2 > 0$.

From the practical viewpoint, main advantage of this high-gain observer is that it could be employed for hydraulic or electromagnetic active vehicle suspension systems, requiring only information of the stiffness constant of tire k_t and the unsprung mass m_u. In addition, it can be shown that the proposed observer design methodology is quite robust with respect to parameter uncertainty and unmodeled dynamics, by considering the parameter variations into the perturbation input signal $\varpi(t)$. In fact, in (Sira-Ramirez et al., 2008a) has been presented through some experimental results that the polynomial disturbance signal-based GPI control scheme, implemented as a classical compensation network, is robust enough with respect to parameter uncertainty and unmodeled dynamics in the context of an off-line and pre-specified reference trajectory tracking tasks.

It is important to emphasize that, the proposed results are now possible thanks to the existence of commercial embedded system for automatic control tasks based on high speed FPGA/DSP boards with high computational performance operating at high sampling rates. The proposed observer could be implemented via embedded software applications without many problems.

5. Simulation results

Some numerical simulations were performed on a nonlinear quarter-vehicle suspension system characterized by the following set of realistic parameters (Tahboub, 2005) to verify the effectiveness of the proposed disturbance observer-control design methodology (see Table 1):

Parameters	Values
Sprung mass (m_s)	216.75 $[kg]$
Unsprung mass (m_u)	28.85 $[kg]$
Spring stifness (k_s)	21700 $[\frac{N}{m}]$
Damping constant (c_s)	1200 $[\frac{N \cdot s}{m}]$
Tire stifness (k_t)	184000 $[\frac{N}{m}]$
nonlinear spring stiffness (k_{ns})	2170 $[\frac{N}{m}]$
nonlinear damping constant (c_{ns})	120 $[\frac{N \cdot s}{m}]$

Table 1. Parameters of the vehicle suspension system.

Fig. 2 shows some schematic diagram for the implementation of the proposed active vibration controllers based on on-line disturbance estimation using a flatness-based controller and GPI observers.
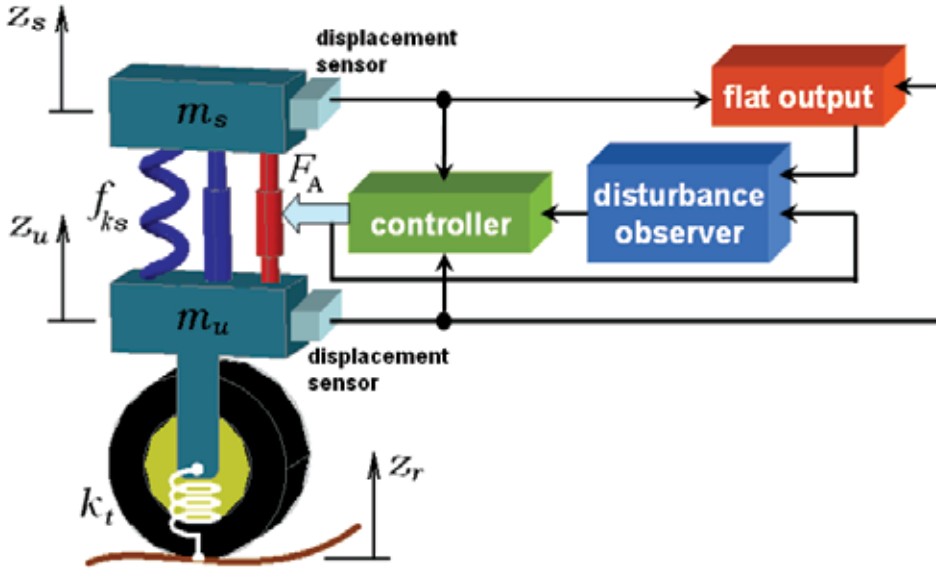
Fig. 2. Schematic diagram of the instrumentation for active vehicle suspension control implementation.

The following trajectory was utilized to simulate the unknown exogenous disturbance excitations due to irregular road surfaces (Chen & Huang, 2005):

$$z_r(t) = \begin{cases} f_1(t) + f(t) & \text{for } t \in [3.5, 5) \\ f_2(t) + f(t) & \text{for } t \in [5, 6.5) \\ f_3(t) + f(t) & \text{for } t \in [8.5, 10) \\ f_3(t) + f(t) & \text{for } t \in [10, 11.5 \\ f(t) & \text{else} \end{cases}$$

with

$$f_1(t) = -0.0592(t - 3.5)^3 + 0.1332(t - 3.5)^2$$
$$f_2(t) = 0.0592(t - 6.5)^3 + 0.1332(t - 6.5)^2$$
$$f_3(t) = 0.0592(t - 8.5)^3 - 0.1332(t - 8.5)^2$$
$$f_3(t) = -0.0592(t - 11.5)^3 - 0.1332(t - 11.5)^2$$
$$f(t) = 0.002\sin(2\pi t) + 0.002\sin(7.5\pi t)$$

Figs. 3-9 describe the robust performance of the controller (7) using the observer (14). It can be seen the high vibration attenuation level of the active vehicle suspension system compared with the passive counterpart.

Moreover, one can observe a robust and fast on-line estimation of the disturbance $\xi(t)$ as well as the corresponding time derivatives of the flat output up to third order. Similar results on the implementation of the controller (20) with disturbance observer (23) for estimation of the perturbation $\varpi(t)$ and time derivatives of the flat output are shown in Figs. 10-23.

In the computer simulations it is assumed that the perturbation input signals $\xi(t)$ and $\varpi(t)$ can be locally approximated by a family of Taylor polynomials of fourth degree.

The characteristic polynomials for the ninth order observation error dynamics were all set to be of the following form:

$$p_o(s) = (s + p_o)\left(s^2 + 2\zeta_o\omega_o s + \omega_o^2\right)^4$$

with $p_o = \omega_o = 300\text{rad/s}$ and $\zeta_o = 20$.

The characteristic polynomials associated with the closed-loop dynamics were all set to be of the form: $p_c(s) = \left(s^2 + 2\zeta_c\omega_c s + \omega_c^2\right)^2$, with $\omega_c = 10\text{rad/s}$ and $\zeta_c = 0.7071$.
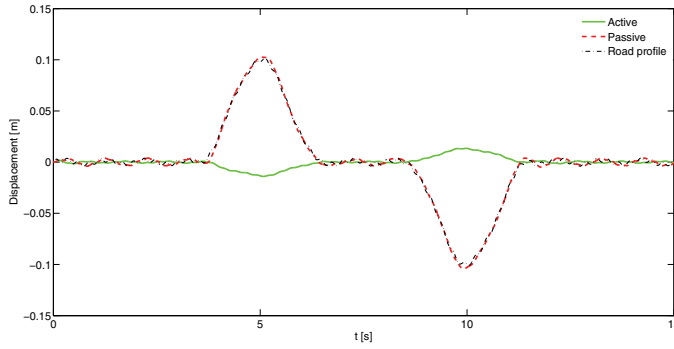
Fig. 3. Sprung mass displacement response using controller (7) and observer (14).
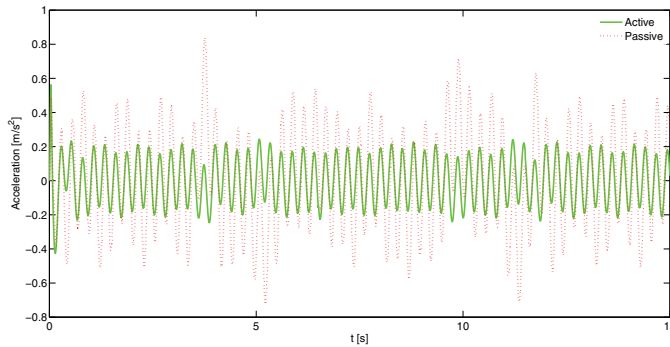
Fig. 4. Sprung mass acceleration response using controller (7) and observer (14).

In general, the proposed active vehicle suspension using a flatness-based controller and GPI observers for the estimation of unknown perturbations yields good attenuation properties and an overall robust performance.
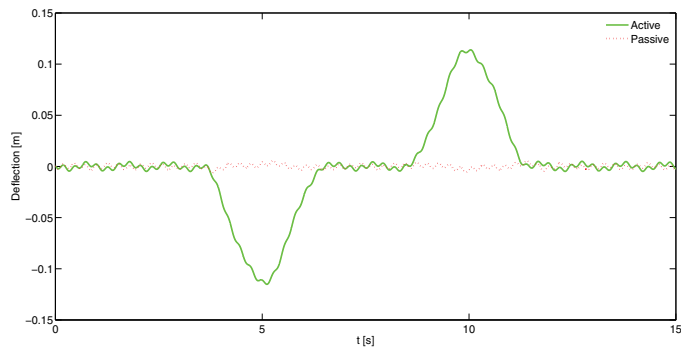
Fig. 5. Suspension deflection response ($x_1 - x_3$) using controller (7) and observer (14).
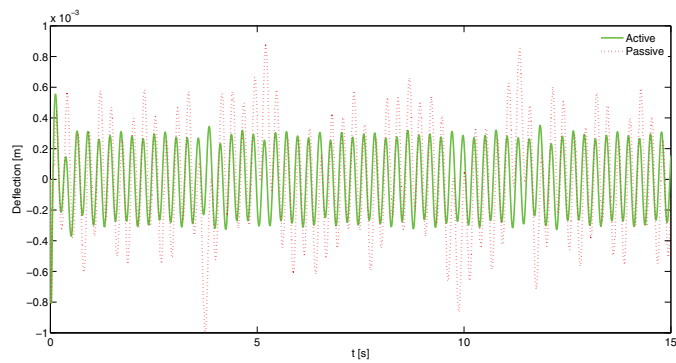
Fig. 6. Tire deflection response ($x_3 - z_r$) using controller (7) and observer (14).
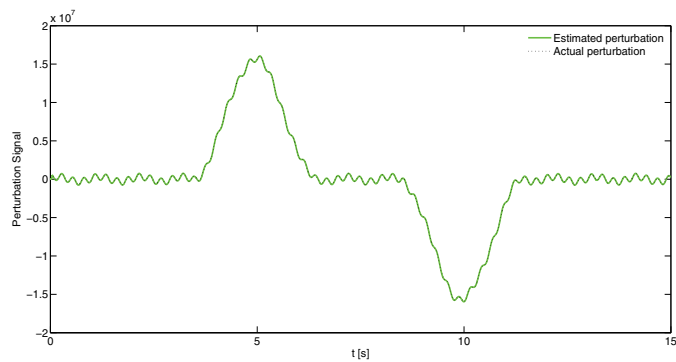
Fig. 7. Perturbation estimation $\xi(t)$ using observer (14).
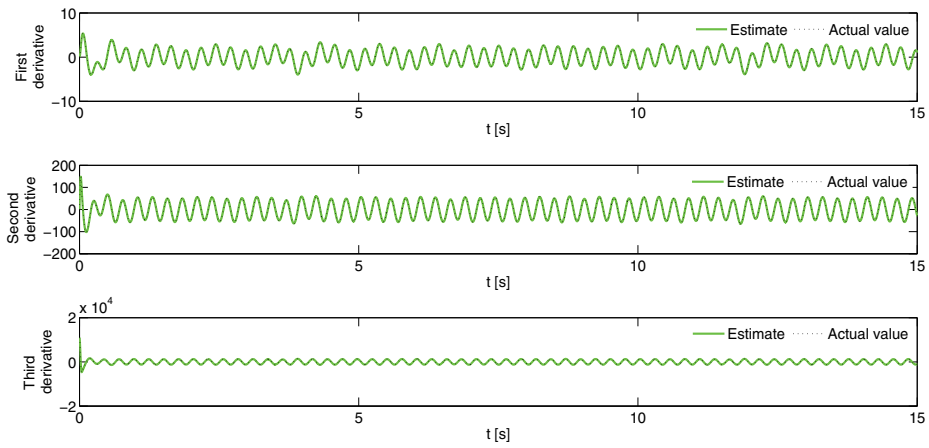
Fig. 8. Estimation of time derivatives of the flat output using the observer (14).
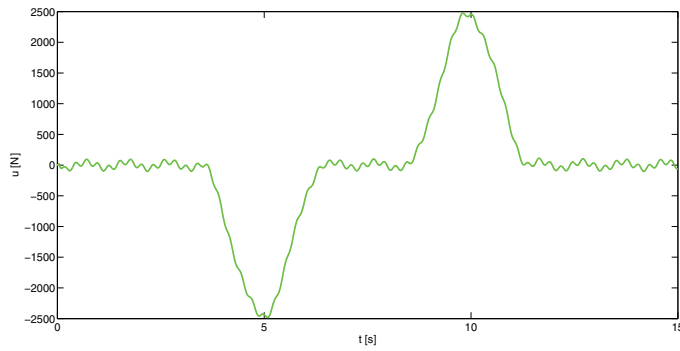
Fig. 9. Control force using the observer (14).
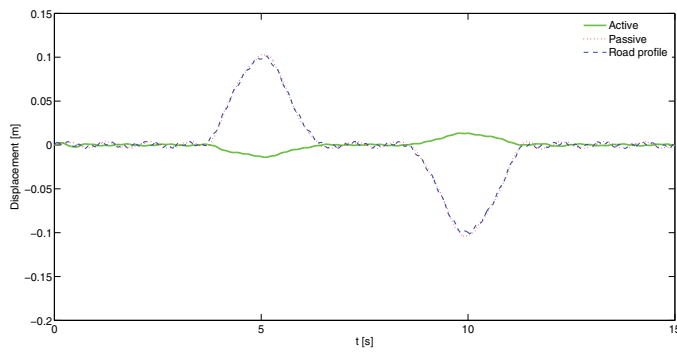
Fig. 10. Sprung mass displacement response using controller (20) and observer (23).).
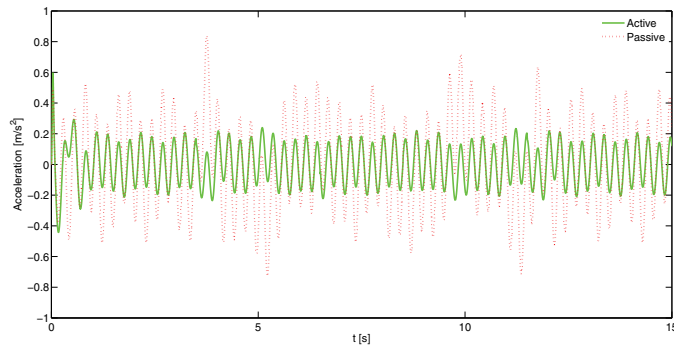
Fig. 11. Sprung mass acceleration response using controller (20) and observer (23).
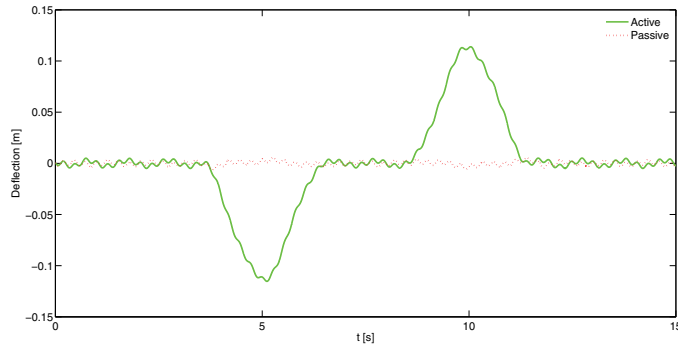
Fig. 12. Suspension deflection response $(x_1 - x_3)$ using controller (20) and observer (23).
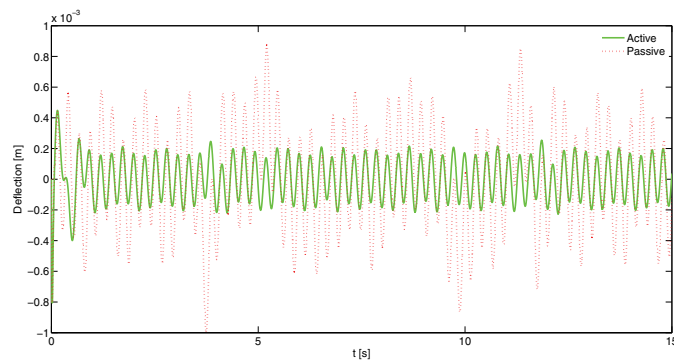
Fig. 13. Tire deflection response $(x_3 - z_r)$ using controller (20) and observer (23).
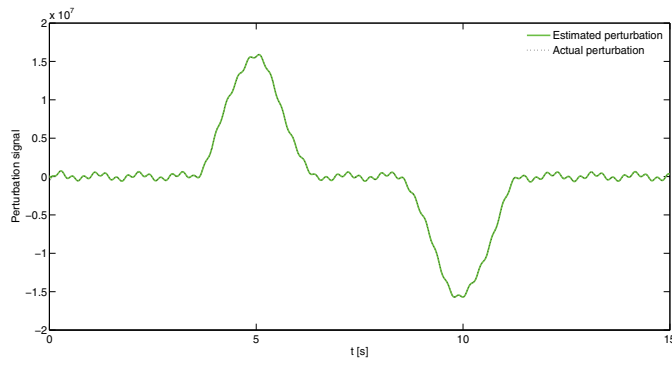
Fig. 14. Perturbation estimation $\varpi\left(t\right)$ using observer (23).
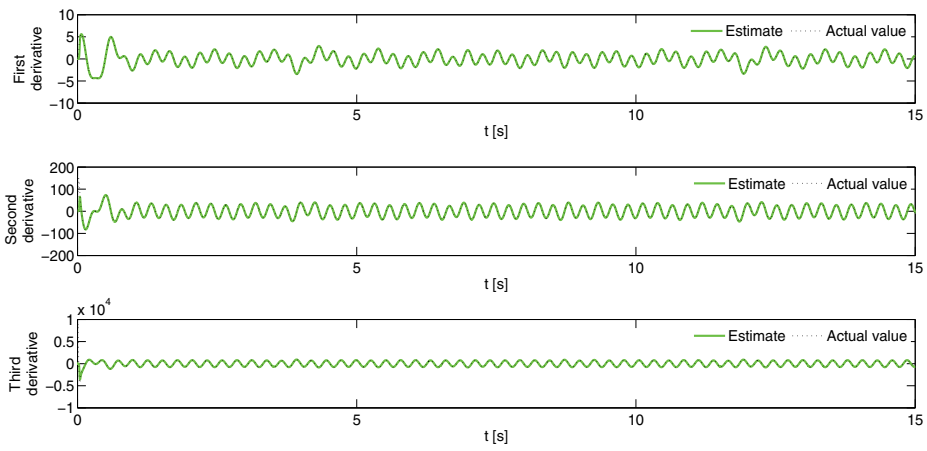
Fig. 15. Estimation of time derivatives of the flat output using the observer (23).
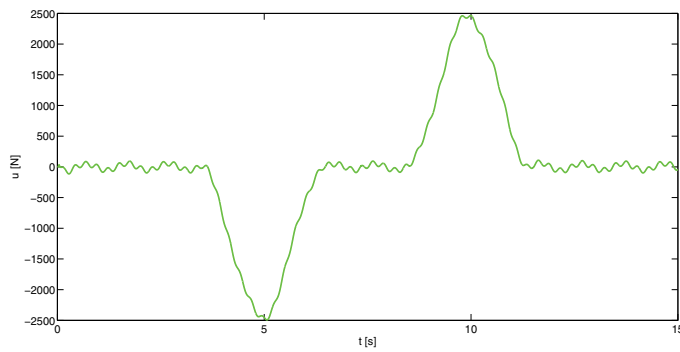
Fig. 16. Control force using the observer (23).

6. Conclusions

In this chapter a robust active vibration control scheme, based on real-time estimation and rejection of perturbation signals, of nonlinear vehicle suspension systems is described. The proposed approach exploits the structural property of differential flatness exhibited by the suspension system fot the synthesis of a flatness based controller and a robust observer. Therefore, a perturbed input-output differential equation describing the dynamics of the flat output is obtained for design purposes of the control scheme. The exogenous disturbances due to irregular road surfaces, nonlinear effects, parameter variations and unmodeled dynamics are lumped into an unknown bounded time-varying perturbation input signal affecting the differentially flat linear simplified dynamic mathematical model of the suspension system. A family of Taylor polynomials of (r-1)th degree is used to locally approximate this perturbation signal. Hence the perturbation signal is described by a rth-order mathematical model. Then, the perturbed suspension system model is expressed as a (r+4)th-order extended mathematical model.

The design of high-gain Luenberger observers, based on this kind of extended models, is proposed to estimate the perturbation signal and some time derivatives of the flat output required for implementation of differential flatness-based disturbance feedforward and feedback controllers for attenuation of vibrations in electromagnetic and hydraulic active vehicle suspension systems.

Two high-gain disturbance observer-based controllers have been proposed to attenuate the vibrations induced by unknown exogenous disturbance excitations due to irregular road surfaces, which could be employed for nonlinear quarter-vehicle active suspension models by using hydraulic or electromagnetic actuators. Computer simulations were included to show the effectiveness of the proposed controllers, as well as of the disturbance observers based on Taylor polynomials of fourth degree.

The results show a high vibration attenuation level of the active vehicle suspension system compared with the passive counterpart and, in addition, a robust and fast real-time estimation of the disturbance and time derivatives of the flat output.

7. References

Ahmadian, M. Active control of vehicle suspensions. In: *Encyclopedia of Vibration*, Edited by Braun, S.G., Ewins, D.J. & Rao, S.S. (2001), Vols. 1-3, Academic Press, San Diego, CA.

Basterretxea, K., Del Campo, I. & Echanobe, J. (2010). A semi-active suspension embedded controller in a FPGA, *2010 IEEE International Symposium on Industrial Embedded Systems*, pp. 69-78, Trento, July 7-9.

Beltran-Carbajal, F., Silva-Navarro, G., Blanco-Ortega, A. & Chavez-Conde, E. (2010a). Active Vibration Control for a Nonlinear Mechanical System using On-line Algebraic Identification, In: *Vibration Control*, M. Lallart, (Ed.), 201-214, Sciyo, Rijeka, Croatia.

Beltran-Carbajal, F., Silva-Navarro, G., Sira-Ramirez, H. & Blanco-Ortega, A. (2010b). Application of on-line algebraic identification in active vibration control, *Computación y Sistemas*, Vol. 13, No. 3, pp. 313-330.

Cao, J., Liu, H., Li, P. & Brown, D. (2008). State of the Art in Vehicle Active Suspension Adaptive Control Systems Based on Intelligent Methodologies, *IEEE Transaction on Intelligent Transportation Systems*, Vol. 9, No. 3, pp. 392-405.

Choi, S.B., Lee, H.K. & Chang, E.G. (2001). Field test results of a semi-active ER suspension system associated with skyhook controller, *Mechatronics*, Vol. 11, pp. 345-353.

Chavez-Conde, E., Beltran-Carbajal, F., Garcia-Rodriguez, C. & Blanco-Ortega, A. (2009a). Sliding Mode Based Differential Flatness Control and State Estimation of Vehicle Active Suspensions System, *IEEE International Conference on Electrical Engineering, Computing Science and Automatic Control*, pp. 544-549, Toluca, Mexico, November 10-13.

Chavez-Conde, E., Beltran-Carbajal, F., Blanco-Ortega, A. & Mendez-Azua, H. (2009b). Sliding Mode and Generalized PI Control of Vehicle Active Suspensions, *18th IEEE International Conference on Control Applications*, pp. 1726-1731, Saint Petersburg, Russia, July 8-10.

Chen, P. & Huang, A. (2005). Adaptive sliding control of non-autonomous active suspension systems with time-varying loadings, *Journal of Sound and Vibration*, Vol. 282, pp. 1119-1135.

Fliess, M., Marquez, R., Delaleau, E. & Sira-Ramirez, H. (2002). Correcteurs Proportionnels-Integraux Généralisés, *ESAIM Control, Optimisation and Calculus of Variations*, Vol. 7, pp. 23-41.

Fliess, M., Marquez, R. & Delaleau, E. (2001). State feedbacks without asymptotic observers and generalized PID regulators, Nonlinear Control in the Year 2000, *Lecture Notes in Control and Information Sciences*, Vol. 258, pp. 367-384, Springer, London.

Fliess, M., Lévine, J., Martin, Ph. & Rouchon, P. (1993). Flatness and defect of nonlinear systems: introductory theory and examples, *International Journal of Control*, Vol. 61, No. 6, pp. 1327-1361.

Gysen, B.L.J., Paulides, J.J.H., Janssen, J.L.G. & Lomonova, E. A. (2008). Active Electromagnetic Suspension System for Improved Vehicle Dynamics, *IEEE Vehicle Power and Propulsion Conference (VPPC)*, Harbin, China, September 3-5.

Isermann, R. & Munchhpf, M. (2011). *Identification of Dynamic Systems*, Springer-Verlag, Berlin.

Martins, I., Esteves, J., Marques, D.G. & Da Silva, F. P. (2006). Permanent-Magnets Linear Actuators Applicability in Automobile Active Suspensions, *IEEE Trans. on Vehicular Technology*, Vol. 55, No. 1, pp. 86-94.

Sira-Ramirez, H., Beltran-Carbajal, F. & Blanco-Ortega, A. (2008a). A Generalized Proportional Integral Output Feedback Controller for the Robust Perturbation Rejection in a Mechanical System, *e-STA Sciences et Technologies de l'Automatique*, Vol. 5, No. 4, pp. 24-32.

Sira-Ramirez, H., Feliu-Batlle, V., Beltran-Carbajal, F. & Blanco-Ortega, A. (2008b). Sigma-Delta modulation sliding mode observers for linear systems subject to locally unstable inputs, *16th Mediterranean Conference on Control and Automation*, pp. 344-349, Ajaccio, France, June 25-27.

Sira-Ramirez, H., Barrios-Cruz, E. & Marquez-Contreras, R.J. (2009). Fast adaptive trajectory tracking control for a completely uncertain DC motor via output feedback, *Computación y Sistemas*, Vol. 12, No. 4, pp. 397-408.

Sira-Ramirez, H., Silva-Navarro, G. & Beltran-Carbajal, F. (2007). On the GPI balancing control of an uncertain Jeffcot rotor model, *2007 4th International Conference on Electrical and Electronics Engineering (ICEEE)*, pp. 306-309, Mexico City, Mexico, September 5-7.

Sira-Ramirez, H. & Agrawal, S.K. (2004). *Differentially Flat Systems*, Marcel Dekker, New York.

Shoukry, Y., El-Kharashi, M. W. & Hammad, S. (2010). MPC-On-Chip: An Embedded GPC Coprocessor for Automotive Active Suspension Systems, *IEEE Embedded Systems Letters*, Vol. 2, No. 2, pp. 31-34.

Tahboub, K. A. (2005). Active Nonlinear Vehicle-Suspension Variable-Gain Control, *13th Mediterranean Conference on Control and Automation*, pp. 569-574, Limassol, Cyprus, June 27-29.

van der Schaft, A. (2000). L_2-Gain *and Passivity Techniques in Nonlinear Control*, Springer, London.

Ventura, P.J.C., Ferreira, C.D.H., Neves, C. F. C. S., Morais, R.M.P., Valente, A.L.G. & Reis, M.J.C.S. (2008). An embedded system to assess the automotive shock absorber condition under vehicle operation, *IEEE Sensor 2008 Conference*, pp. 1210-1213, Lecce, October 26-29.

Yao, G.Z., Yap, F.F., Chen, G., Li, W.H. & Yeo, S.H. (2002). MR damper and its application for semi-active control of vehicle suspension system, *Mechatronics*, Vol. 12, pp. 963-973.

Semi-Active Control of Civil Structures Based on the Prediction of the Structural Response: Integrated Design Approach

Kazuhiko Hiramoto[1], Taichi Matsuoka[2] and Katsuaki Sunakoda[3]
[1]*Department of Mechanical and Production Engineering, Niigata University*
[2]*Department of Mechanical Engineering Informatics, Meiji University*
[3]*Sanwa Tekki Corporation**
Japan

1. Introduction

Various methodologies for vibration control of civil structures have been proposed so far. The traditional scheme is passive vibration control, i.e., dissipation of the vibration energy to the outside of the structural systems with dampers or mass dampers etc.. Passive control is quite simple and popular still, however it has some limitations, e.g., insufficient performance and/or difficulty in tuning such devices for a case of multi-mode vibration control etc..

Active vibration control is a candidate for a breakthrough to overcome the above drawbacks of passive control and has been studied extensively these decades ((Spencer et al., 1998) and the references therein). Although many studies show that the active control methodology achieves the quite high control performance on vibration suppression, it requires a large energy source to produce the control force and this fact has been an obstacle in applying active methods to general vibration control problems.

Semi-active control, which is not necessarily new (Karnop et al., 1974) either, can be recognized as an intermediate between passive and active schemes in the sense of not only the performance on vibration suppression but also the complexity of the control system. In most semi-active control vibration suppression is achieved by changing the damping coefficient of the semi-active damper. In civil structures semi-active control technique is getting more realistic recently (Casciati et al., 2006) along with the development of a large scale damper whose damping property is able to be changed (Sodeyama et al., 1997). In semi-active control, the damping coefficient of the semi-active damper is changed mainly based on the following two strategies:

- An active controller is synthesized with a standard control theory (e.g., sky-hook, LQ or $\mathcal{H}_\infty$ control, etc.) firstly as a target for the semi-active control. Then the semi-active damper is operated so as to emulate the targeted active control force as much as possible(Dyke et al., 1996; Karnop et al., 1974; Kurata et al., 1999).

- The damping coefficient of the semi-active damper is determined so as to maximally *accelerate* energy dissipation of the structural systems(Gavin, 2001).

---

*A professor emeritus at Akita University, Japan

The latter method is based on the Lyapunov theory. The Lyapunov function has been defined as the total energy, i.e., the sum of the kinetic and potential energies of the structural system in most cases. The control law for maximizing the rate of energy dissipation is generally given as a bang-bang type change of the damping coefficient.

In this chapter we propose a new semi-active control method that is based on a one-step-ahead prediction of the structural response for the seismic disturbance. In the present semi-active control the vibration control device (VCD), which has been developed by the authors to reduce the structural vibration, is employed. The VCD is a mechanism consists of a ball screw, a flywheel and an electric motor connected to the ball screw. The VCD is installed between neighboring two floors of buildings as general dampers. Unlike general dampers, the VCD generates two types of resistance forces, i.e., a damping force proportional to the relative velocity and an inertial force proportional to the relative acceleration between two floors. The damping force is generated by the electric motor and the inertial force is produced by the mechanism of the ball screw and the flywheel. The damping coefficient of the VCD can be adjusted in a real-time manner by changing the electric resistance connected to the motor and we use this capability of the VCD for the semi-active control.

We assume the command signal for changing the damping coefficient of each VCD takes two values, i.e., the command to take the maximum or minimum damping coefficient in the present chapter. Under the assumption we obtain the optimal command signal among all possible combinations of command signals ($2^{n_{VCD}}$, n_{VCD}: The number of VCDs) in a real-time manner. The optimal command signal is selected from all candidates of the command signals so that the weighted Euclidean norm of the predicted one-step-ahead structural response, calculated by a numerical integration method, e.g., Runge-Kutta method, is minimized.

To accomplish the further performance improvement of the semi-active control system an integrated design approach of structural and semi-active control systems using the above predictive control law is proposed. The stiffness distribution between neighboring two floors of the structure and some parameters of the VCDs are taken as adjustable structural design parameters. The weighting matrix that is used in the predictive semi-active control law is defined as the control design parameters. Those design parameters are simultaneously optimized so that the seismic responses of the semi-active control system subject to various recorded and artificial earthquake waves become good. The control performance is evaluated by an objective function that is calculated by the simulated structural response of the semi-active control system. The Genetic Algorithm (GA) is adopted for the optimization.

As a design example the a simulation study for a fifteen-story building with three VCDs is presented. The control performance of the semi-active control system is significantly improved by the proposed integrated design methodology.

The rest of the chapter is organized as follows: In §2 the principle of the VCD and the mathematical model of the civil structure with the VCD are introduced. The semi-active control law based on the prediction of the structural response is given in §3. The integrated design problem of the structural and the semi-active control is formulated in §4. The simulation results for a fifteen-story building are shown in §5 and the conclusion of the chapter is presented in §6.

Notations are as follows: t: time, $\mathbf{R}^{m \times n}$: the set of $m \times n$ real matrices, $\mathbf{R}^m$: the set of m-dimensional real vectors, $\mathbf{S}^n$: the set of n-dimensional real symmetric matrices, $\mathbf{0}_{m \times n}$: an $m \times n$ zero matrix, $\mathbf{I}$: an identity matrix with an appropriate dimension, $\mathbf{1}_{m \times n}$: an $m \times n$ matrix whose all elements equal to 1, ^{T}: the transposition of a vector or a matrix.

2. Mathematical model

2.1 Vibration Control Device (VCD)

The schematic diagram of the VCD is shown in Fig. 1. The VCD is installed between neighboring two floors of a structure, e.g., the i-th and $(i-1)$-th floors. In Fig. 1, $q_i(t)$, m_j^{VCD} and $d_j^{\text{VCD}}(t)$ are the displacement of the i-th floor, an equivalent mass and a time-varying damping coefficient of the VCD_j (j-th VCD, $j = 1\ldots,n_{\text{VCD}}$) respectively. The resistance force produced by the relative motion of the two floors is denoted by $f_j^{\text{VCD}}(t)$. The VCD is a dynamic system which has two input signals, i.e., the relative acceleration and velocity between two floors. The output signal of the VCD is the resistance force $f_j^{\text{VCD}}(t)$. The mathematical model of the VCD is described as the following:

$$f_j^{\text{VCD}}(t) = m_j^{\text{VCD}}(\ddot{q}_i(t) - \ddot{q}_{i-1}(t)) + d_j^{\text{VCD}}(t)(\dot{q}_i(t) - \dot{q}_{i-1}(t)) \tag{1}$$

The VCD whose resistance force property is given as Eq. (1) has been developed by the authors in recent years (Ohtake et al., 2006). The assembly and the design parameters of the VCD in (Ohtake et al., 2006) are shown in Fig. 2 and Table 1 respectively. The VCD is a mechanism consists of a ball screw, a flywheel, an electric motor and an electric circuit to control the damping property of the VCD. The ball screw and the flywheel produce a large inertia force (the term $m_j^{\text{VCD}}(\ddot{q}_i(t) - \ddot{q}_{i-1}(t))$ in Eq. (1)) which is proportional to the relative acceleration between two floors. The damping force denoted by $d_j^{\text{VCD}}(t)(\dot{q}_i(t) - \dot{q}_{i-1}(t))$ in Eq. (1) is generated by the electric motor (generator) and the electric circuit for the energy dissipation. The coefficients m_j^{VCD} and $d_j^{\text{VCD}}(t)$ in Eq. (1) are given as (Ohtake et al., 2006):

$$m_j^{\text{VCD}} = K_s(I_1 + r^2 I_2), \quad d_j^{\text{VCD}}(t) = K_s \frac{r^2 K_t K_e}{R_a + R}, \tag{2}$$

where K_s, r, I_1 and I_2 are the constant related to the ball screw, the gear ratio, the moment of inertia of the flywheel and that of the electric motor respectively. In the damping coefficient $d_j^{\text{VCD}}(t)$, K_t, K_e, R_a and R are the torque constant, the back-emf (back electromotive force) constant, the electric resistance of the motor and the resistance connected to the motor terminal respectively. From Eq. (2) the damping coefficient of the VCD can be controlled by changing the resistance R. We have developed an electronic circuit to change the electronic resistance according to a command voltage that is produced by an implemented semi-active control law. More detailed dynamical properties of the VCD are presented in (Ohtake et al., 2006) and we are currently developing the VCD that can produce a larger resistance force.

2.2 Model of civil structures with VCD

Consider a civil structure with the n_{VCD} VCDs, whose inertial and variable damping coefficients are denoted by m_j^{VCD} and $d_j^{\text{VCD}}(t)$ ($j = 1, \ldots, n_{\text{VCD}}$) respectively. The equation of motion of the structure is given as

$$\mathbf{M}\ddot{\mathbf{q}}(t) + \mathbf{D}(t)\dot{\mathbf{q}}(t) + \mathbf{K}\mathbf{q}(t) = \mathbf{b}_2\ddot{\mathbf{w}}(t) + \mathbf{b}_1(t)\dot{\mathbf{w}}(t) + \mathbf{b}_0\mathbf{w}(t), \tag{3}$$

$$\mathbf{M} = \mathbf{M}^0 + \mathbf{M}^{\text{VCD}}, \ \mathbf{D}(t) = \mathbf{D}^0 + \mathbf{D}^{\text{VCD}}(t), \ \mathbf{b}_1(t) = \mathbf{b}_1^0 + \mathbf{b}_1^{\text{VCD}}(t), \ \mathbf{b}_2 = \mathbf{b}_2^0 + \mathbf{b}_2^{\text{VCD}}, \tag{4}$$

where $\mathbf{q}(t) \in \mathbf{R}^n$ and $\mathbf{w}(t) \in \mathbf{R}^{n_w}$ are the displacement and the disturbance vectors of the structure respectively. Matrices $\mathbf{M}, \mathbf{D}, \mathbf{K} \in \mathbf{S}^n$ and $\mathbf{b}_j \in \mathbf{R}^{n \times n_w}$ ($j = 0, 1, 2$) are the
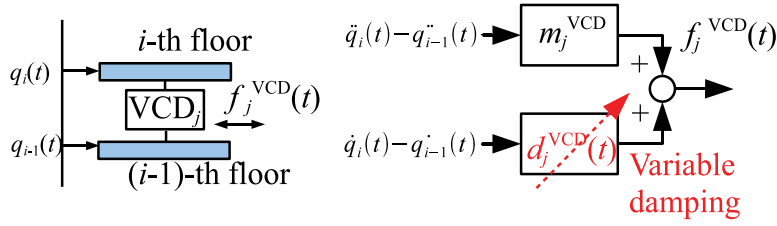
Fig. 1. Schematic diagram of the VCD

Design parameters	Value [Unit]
Length	0.699 [m]
Weight	16.8 [kg]
Maximum load	30 [kN]
Stroke	$\pm 6.0 \times 10^{-2}$ [m]

Table 1. Design parameters of the VCD(Ohtake et al., 2006)

mass, damping, stiffness and influence coefficient matrices of the structure with the VCDs respectively. In Eq. (4) the matrices $\mathbf{M}^0$, $\mathbf{D}^0$, $\mathbf{b}_1^0$ and $\mathbf{b}_2^0$ are the mass, damping and influence coefficient matrices of the original structure without VCDs and the matrices $\mathbf{M}^{\text{VCD}}$, $\mathbf{D}^{\text{VCD}}(t)$, $\mathbf{b}_1^{\text{VCD}}(t)$ and $\mathbf{b}_2^{\text{VCD}}$ are those of the installed VCDs respectively. Note that the matrices $\mathbf{D}$ and $\mathbf{b}_1$ accordingly become time varying because they contain the variable damping coefficient of the VCD.

With the equation of motion in Eq. (3) the state-space form of the structure with n_{VCD} VCDs is given by

$$\begin{cases} \dot{\mathbf{x}}(t) = \mathbf{A}\mathbf{x}(t) + \mathbf{B}\mathbf{u}_x(t) \\ \mathbf{z}(t) = \mathbf{C}_z\mathbf{x}(t) + \mathbf{D}_z\mathbf{u}_z(t) \end{cases} , \tag{5}$$

where

$$\mathbf{x}(t) := \begin{bmatrix} \mathbf{q}(t) \\ \dot{\mathbf{q}}(t) \end{bmatrix}, \ \mathbf{u}_x(t) := \begin{bmatrix} \mathbf{w}(t) \\ \dot{\mathbf{w}}(t) \\ \ddot{\mathbf{w}}(t) \end{bmatrix}, \ \mathbf{u}_z(t) := \begin{bmatrix} \mathbf{w}(t) \\ \dot{\mathbf{w}}(t) \end{bmatrix},$$

$$\mathbf{A} := \begin{bmatrix} \mathbf{0}_{n \times n} & \mathbf{I}_n \\ -\mathbf{M}^{-1}\mathbf{K} & -\mathbf{M}^{-1}\mathbf{D}(t) \end{bmatrix}, \ \mathbf{B} := \begin{bmatrix} \mathbf{0}_{n \times 3n_w} \\ \mathbf{M}^{-1}\begin{bmatrix} \mathbf{b}_0 & \mathbf{b}_1(t) & \mathbf{b}_2 \end{bmatrix} \end{bmatrix}.$$

The vector $\mathbf{z}(t) \in \mathbf{R}^{n_z}$ is the output vector to evaluate the performance of the structural system with VCDs. The output vector $\mathbf{z}(t)$ will be used to construct the semi-active control law that will be proposed in the next section. Note that all coefficient matrices in Eq. (5) can become time varying because possibly they contain the variable damping coefficient of the VCDs, i.e., matrices $\mathbf{A}$, $\mathbf{B}$, $\mathbf{C}_z$, $\mathbf{D}_z$ are functions on the variable damping coefficient ($d_j^{\text{VCD}}(t)$, $j = 1, \ldots, n_{\text{VCD}}$) of the VCDs. In this chapter we assume each variable damping coefficient of the VCD can be controlled in a following range:

$$\underline{d_j^{\text{VCD}}} \leq d_j^{\text{VCD}}(t) \leq \overline{d_j^{\text{VCD}}}, \ j = 1, \ldots, n_{\text{VCD}} \tag{6}$$

where $\overline{d_j^{\text{VCD}}} \geq 0$ and $\underline{d_j^{\text{VCD}}} \geq 0$ are the maximum and minimum damping coefficients of the j-th VCD respectively.
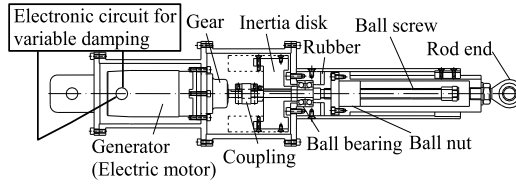
Fig. 2. Assembly of the VCD(Ohtake et al., 2006)

3. Semi-active control methodology

We propose a semi-active control using the variable damping capability of the VCD. The control law is based on a prediction of the seismic response of the structure. The prediction of the structural response can be obtained through a numerical integration of the state-space model defined in Eq. (5) with the current sensor data of the state variable and the earthquake disturbance. The prediction of the structural response is obtained for all candidates of command signals each VCD. Then the optimal (combination of) command signal is selected among all candidates of the command signals in a real time manner. Essentially the command signal for the VCD can take a continuous value in the range given as Eq. (6). In this chapter, however, to make the prediction-based semi-active control realistic, the command signal for each VCD denoted by $d_j^c(t)$, $j = 1, \ldots, n_{\mathrm{VCD}}$ is quantized to the following one bit signal:

$$d_j^c(t) = \begin{cases} \overline{d_j^{\mathrm{VCD}}} \\ \underline{d_j^{\mathrm{VCD}}} \end{cases}, \ j = 1, \ldots, n_{\mathrm{VCD}} \tag{7}$$

With the above quantization the possible number of command combinations for n_{VCD} VCDs becomes $2^{n_{\mathrm{VCD}}}$. In the present chapter the optimal combination is selected among all possible combinations so that the following performance index J_p is minimized:

$$J_p := \sqrt{\mathbf{z}^T(t_0 + \Delta t)\mathbf{Q}_w\mathbf{z}(t_0 + \Delta t)} \tag{8}$$

where t_0 and $\Delta t > 0$ are the current time instant and the length of the prediction respectively. The matrix $\mathbf{Q}_w = \mathbf{Q}_w^T \geq 0$ is an weighting matrix, defined by a control system designer, for evaluating the predicted control performance.
From Eq. (5) the prediction of the output vector $\mathbf{z}(t_0)$ is given as

$$\mathbf{z}(t_0 + \Delta t) = \mathbf{C}_z\mathbf{x}(t_0 + \Delta t) + \mathbf{D}_z\mathbf{u}_z(t_0 + \Delta t), \tag{9}$$

where the prediction of the state vector $\mathbf{x}(t_0 + \Delta t)$ and the output vector $\mathbf{z}(t_0 + \Delta t)$ are approximated by

$$\mathbf{x}(t_0 + \Delta t) \simeq \mathbf{x}(t_0) + \Delta t\dot{\mathbf{x}}(t_0), \ \mathbf{u}_z(t_0 + \Delta t) \simeq \mathbf{u}_z(t_0) + \Delta t\dot{\mathbf{u}}_z(t_0). \tag{10}$$

To have the (approximated) predicted output vector $\mathbf{z}(t_0 + \Delta t)$ we need to obtain $\dot{\mathbf{x}}(t_0)$ and $\dot{\mathbf{u}}_z(t_0)$. The time derivative of the state vector can be obtained with the current state vector $\mathbf{x}(t_0)$ and the disturbance $\mathbf{u}_x(t_0)$ at $t = t_0$ by using the state-space form Eq. (5), that is,

$$\dot{\mathbf{x}}(t_0) = \mathbf{A}\mathbf{x}(t_0) + \mathbf{B}\mathbf{u}_x(t_0). \tag{11}$$

We can apply various numerical integration methods, e.g., Euler method or Runge-Kutta method etc., to obtain (the approximated) $\dot{\mathbf{x}}_0(t_0)$. Furthermore the time derivative of the disturbance $\mathbf{u}_z(t_0)$ can be obtained from the following simple relationship:

$$\dot{\mathbf{u}}_z(t_0) = \frac{\mathrm{d}}{\mathrm{d}t} \begin{bmatrix} \mathbf{w}(t_0) \\ \dot{\mathbf{w}}(t_0) \end{bmatrix} = \begin{bmatrix} \dot{\mathbf{w}}(t_0) \\ \ddot{\mathbf{w}}(t_0) \end{bmatrix} \tag{12}$$

In the present chapter all $2^{n_{\text{VCD}}}$ values of J_p's, the weighted Euclidean norm of the predicted output vector $\mathbf{z}(t_0 + \Delta t)$, are computed for all possible combinations of the command signals for the VCDs at every time instant. Then the optimal combination that minimizes J_p in Eq. (8) is selected among all $2^{n_{\text{VCD}}}$ candidates of command signals.

Similar to currently available devices that realize a variable damping property, such as MR damper etc., the VCD in the present chapter also has a dynamic delay for a given command signal. In other words the i-th damping coefficient of the VCD, denoted by $d_i^{\text{VCD}}(t)$, cannot perfectly track the command signal $d_i^c(t)$ defined as Eq. (7). We assume the characteristic of the delay is modeled as the following first order dynamics:

$$\frac{\mathrm{d}(d_j^{\text{VCD}}(t))}{\mathrm{d}t} = -\frac{1}{T_d}d_j^{\text{VCD}}(t) + \frac{1}{T_d}d_j^c(t), \; j = 1, \ldots, n_{\text{VCD}} \tag{13}$$

where $T_d > 0$ is the time constant representing the delay of the VCD.

Several features of the proposed prediction-based semi-active control are summarized as follows:

- In the semi-active control the predicted performance index J_p in Eq. (8) is obtained for all possible combinations of the command signals and the optimal command that achieves the minimum J_p is selected. As shown in §1 conventional semi-active control laws consider the norm of the closed-loop system (in the phase of the targeted active control design) or the energy dissipation rate of the structural systems. Such performance indices are used in general control system design (not only in semi-active control design) as a measure for evaluating the closed-loop performance. However in the semi-active control of civil structures we can not know if a satisfactory result is obtained or not with the adopted semi-active control in the sense of the vibration control of civil structures when we employ one of the conventional semi-active control methods because a mismatch exists between the above performance index and key performance measures used in vibration control of civil structures, e.g., the relative displacement between neighboring two floors and the absolute acceleration of each floor. In other words there is a gap between the performance index for the control system design and the quantities for the performance evaluation in a semi-active control of civil structural systems. On the other hand the performance index J_p is the Euclidean norm of the predicted output vector $\mathbf{z}(t)$ in Eq. (5). The elements of the vector $\mathbf{z}(t)$ can be defined as the relative displacement and velocity between neighboring two floors and the absolute displacement and velocity of each floor, etc. (Note: Clearly, there is a strong relationship between the absolute acceleration and the displacement or velocity of each floor.). Therefore the gap mentioned above is small in the proposed control method. By comparing the proposed prediction-based approach with the conventional semi-active control laws in §1 the prediction-based method is a more direct method because the performance measure on vibration suppression of the civil structural systems can be directly dealt with to obtain the optimal command for the VCDs in a real-time manner.

- The proposed semi-active control is quite flexible because it is a fully algorithm-based control law. As the most noteworthy example of the flexibility we show that a robust performance property within the present semi-active control framework can be recovered easily with a simple method that is shown as follows. In general model-based semi-active control methods including the proposed prediction-based approach the performance of the control system depends on the accuracy of the model of the control object. Because the perfect mathematical model of the control object is generally unavailable we need to make the control law to be robust in some sense. In the present semi-active control the predicted performance index J_p in Eq. (8) is obtained for all $2^{n_{\mathrm{VCD}}}$ candidates of the command signals and the optimal command that achieves the minimum J_p is selected. Let $J_p^{\max}$ denote the predicted performance index obtained by setting the command signals for all VCDs to their maximum values, i.e., $d_i^c(t) = \overline{d_i^{\mathrm{VCD}}}$, $i = 1,\ldots,n_{\mathrm{VCD}}$. As a simple method to recover the robustness we redefine the performance index $J_p^{\max}$ as $\alpha J_p^{\max}$, $0 \leq \alpha < 1$ and then the optimal command signal is selected in the same way. After the redefinition the command signal corresponding to (the redefined) $J_p^{\max}$ tends to be selected more often because the command $d_i^c(t) = \overline{d_i^{\mathrm{VCD}}}$, $\forall\, i = 1,\ldots,n_{\mathrm{VCD}}$ is overvalued among all candidates of the optimal command signals. By making $0 \leq \alpha < 1$ smaller, the performance of the semi-active control approaches asymptotically to that the case where all damping coefficients are kept their maximum. Actually in $\alpha = 0$ the semi-active control is coincident with the *passive control* where all damping coefficients are fixed their maximum because the command signal $d_i^c(t) = \overline{d_i^{\mathrm{VCD}}}$, $\forall\, i = 1,\ldots,n_{\mathrm{VCD}}$ is always selected during the semi-active control as a result. The above methodology is reasonable because the maximum damping case guarantees a certain level of vibration suppression *independent* of the mathematical model of the structural system although the resulted performance of the semi-active control becomes conservative. Note that in general control design there is a trade-off between the performance and the robustness like this situation. As the authors' knowledge, among so many studies about semi-active control of civil structures classified in §1 there are no theoretical considerations about the robustness of the semi-active control system although all model-based semi-active control laws highly rely on the mathematical model of the structural systems. The authors would like to emphasize the fact that we *should not expect* the semi-active control methodologies aiming to realize the desired active control as much as possible, e.g., clipped optimal control(Dyke et al., 1996), have a performance robustness comparable with the targeted active control even if the targeted active control law is robustly designed in some sense. It is because the semi-active devices can not produce the same control force as the targeted active control perfectly. With the above discussion we can say that the present approach is simple but useful because the performance robustness of the present semi-active control can be easily recovered by making the factor α smaller and the degree of the robustness also can be adjusted by tuning the parameter α.

- As other examples of the flexibility of the control law we present following two features:
  - A constraint on the hardware can be included quite easily, e.g., a constraint on the command signal such that all commands for VCDs must take the same value at some instant.
  - In the present study we use the Euclidean norm (2-norm) of the predicted output. Other norms such as 1-norm and ∞-norm also can be used.

- Additionally, with the bang-bang control nature of the method the implementation of the control law is relatively easier than general feedback control methods that require the continuous controller output.

4. Integrated design approach

Under the predictive semi-active control law in §3, an integrated design problem of structural and control systems is formulated. The integrated design problem is the control system design problem that the controller and the structural parameters, e.g., the stiffness and the damping characteristics of structural systems, are dealt with as adjustable design parameters.

The integrated design problem was firstly considered in the control system design of large space structures (LSS) in 1980's and has been studied around this three decades in the control system and the structural design communities(Grogoriadis et al., 1996; Hiramoto et al., 2000; Hiramoto & Grigoriadis, 2006; Onoda & Haftka, 1987). In the integrated design paradigm we can expect better control performance than that of the standard structural or control design because we can adjust the design parameters simultaneously, i.e., we can use the full design freedom of the formulated design problem. However, we currently have the result that the general integrated design problem becomes a BMI (Bilinear Matrix Inequality) optimization problem that cannot be obtained the globally optimal solution with the practically acceptable amount of computation even in the simplest case. Several methods have been proposed so far to obtain a locally optimal solution(Grogoriadis et al., 1996; Hiramoto et al., 2000; Hiramoto & Grigoriadis, 2006; Onoda & Haftka, 1987).

In this chapter the integrated design problem of the civil structural system with the predictive semi-active control presented in the previous section is formulated. As the structural design parameters we take the structural stiffness between neighboring two floors denoted by k_i, $i = 1, \ldots, n$, the equivalent mass and the maximum value of the variable damping coefficient of each VCD that are denoted by m_j^{VCD} and $\overline{d_j^{VCD}}$, $j = 1, \ldots, n_{VCD}$ respectively. Each structural design parameter is able to be adjusted in the ranges as follows:

$$(k_i)_l \leq k_i \leq (k_i)_u \,, \, i = 1, \ldots, n \tag{14}$$

$$\left(m_j^{VCD} \right)_l \leq m_j^{VCD} \leq \left(m_j^{VCD} \right)_u \,, \, j = 1, \ldots n_{VCD} \tag{15}$$

$$\left(\overline{d_j^{VCD}} \right)_l \leq \overline{d_j^{VCD}} \leq \left(\overline{d_j^{VCD}} \right)_u \,, \, j = 1, \ldots n_{VCD} \tag{16}$$

Note that subscripts $_u$ and $_l$ mean that the maximum and minimum values of the structural design parameters respectively.

The control design parameters are defined as $[\mathbf{Q}_w]_{kk}$, $k = 1, \ldots, n_z$ that are the diagonal elements of the weighting matrix $\mathbf{Q}_w$ in Eq. (8). The range of $[\mathbf{Q}_w]_{kk}$, $k = 1, \ldots, n_z$ is given by

$$0 \leq ([\mathbf{Q}_w]_{kk})_l \leq [\mathbf{Q}_w]_{kk} \leq ([\mathbf{Q}_w]_{kk})_u \,, k = 1, \ldots, n_z. \tag{17}$$

The objective function in the present integrated design problem is defined as the following:

$$J = \lambda J^s + (1 - \lambda) J^h, \, 0 < \lambda < 1, \tag{18}$$

$$J^s = \sum_{i=1}^{n_e} J_i^s, \, J_i^s = \sum_{j=1}^{4} g_i^j \left(J_i^s \right)_j, \, g_i^j \geq 0, \, i = 1, \ldots, n_e, \, j = 1, \ldots, 4, \tag{19}$$

$$(J_i^s)_1 = \sum_{k=1}^{n} \left(\frac{\text{RMS}\left({}^s r_k^i(t)\right)}{\text{RMS}\left({}^0 r_k^i(t)\right)} \right), \tag{20}$$

$$(J_i^s)_2 = \sum_{k=1}^{n} \left(\frac{\text{RMS}\left({}^s a_k^i(t)\right)}{\text{RMS}\left({}^0 a_k^i(t)\right)} \right), \tag{21}$$

$$(J_i^s)_3 = \sum_{k=1}^{n} \left(\frac{\max_{0 \le t \le t_f}\left|{}^s r_k^i(t)\right|}{\max_{0 \le t \le t_f}\left|{}^0 r_k^i(t)\right|} \right), \tag{22}$$

$$(J_i^s)_4 = \sum_{k=1}^{n} \left(\frac{\max_{0 \le t \le t_f}\left|{}^s a_k^i(t)\right|}{\max_{0 \le t \le t_f}\left|{}^0 a_k^i(t)\right|} \right), \tag{23}$$

$$J^h = \sum_{i=1}^{n_e} J_i^h, \quad J_i^h = \sum_{j=1}^{4} h_i^j \left(J_i^h\right)_j, \quad h_i^j \ge 0, \tag{24}$$

$$(J_i^h)_1 = \sum_{k=1}^{n} \left(\frac{\text{RMS}\left({}^h r_k^i(t)\right)}{\text{RMS}\left({}^0 r_k^i(t)\right)} \right), \tag{25}$$

$$(J_i^h)_2 = \sum_{k=1}^{n} \left(\frac{\text{RMS}\left({}^h a_k^i(t)\right)}{\text{RMS}\left({}^0 a_k^i(t)\right)} \right), \tag{26}$$

$$(J_i^h)_3 = \sum_{k=1}^{n} \left(\frac{\max_{0 \le t \le t_f}\left|{}^h r_k^i(t)\right|}{\max_{0 \le t \le t_f}\left|{}^0 r_k^i(t)\right|} \right), \tag{27}$$

$$(J_i^h)_4 = \sum_{k=1}^{n} \left(\frac{\max_{0 \le t \le t_f}\left|{}^h a_k^i(t)\right|}{\max_{0 \le t \le t_f}\left|{}^0 a_k^i(t)\right|} \right), \tag{28}$$

where n_e and T_f^i, $i = 1, \ldots, n_e$ are the number and the duration time of the i-th earthquake waves that are used to obtain the simulated structural response in the present integrated design respectively. The relative displacement between neighboring k-th and $(k-1)$-th floors and the absolute acceleration of k-th floor are denoted by r_k^i and a_k^i, $i = 1, \ldots, n_e$, $k = 1, \ldots, n$ respectively. Superscripts ^{s}, ^{h} and ^{0} show the case of semi-active control, the case where the damping coefficient of all VCDs are kept their maximum throughout the earthquake event (Passive on) and the case without VCDs. The scalar $0 < \lambda < 1$ and g_i^j, $i = 1, \ldots, n_e$ are weighting factors that are determined by the designer.

The components J_i^s, $i = 1, \ldots, n_e$ are the sum of ratios between the RMS or the peak values of structural responses (r_k^i and a_k^i, $i = 1, \ldots, n_e$, $k = 1, \ldots, n$) that are obtained respectively in the semi-active control case and the passive on case for the i-th earthquake wave. Hence, if we get a solution to the integrated design problem that the component J_i^s, $i = 1, \ldots, n_e$ is small, the amount of the performance improvement is large when the predictive semi-active control law is applied.

On the other hand the components J_i^h, $i = 1, \ldots, n_e$ are the sum of ratios between the RMS or the peak values of r_k^i and a_k^i, $i = 1, \ldots, n_e$, $k = 1, \ldots, n$ in the passive on case and the case without VCDs. When the component J_i^h, $i = 1, \ldots, n_e$ is small, the performance enhancement by installing VCDs (and keeping the damping coefficients maximum) is large.

The performance index J in Eq. (18) is the weighted sum of J^s representing the performance improvement with the semi-active control and J^h related to the effect of the VCD itself. By minimizing the performance index J we can obtain the structural and control design parameters that achieve the good control performance on vibration suppression.

The formulated integrated design problem that minimizes the objective function J in Eq. (18) is a highly nonlinear and non-convex optimization problem on structural and the control design parameters because of the form of the objective function itself and the nonlinear nature of the semi-active control law. Furthermore the number of the design parameters is relatively high in the formulated optimization problem compared to the standard structural or the control system design problem because we need to optimize not only the structural or control design parameters only but parameters both in the structural and control system simultaneously. Therefore it is difficult to apply gradient-based optimization methods that achieve a local convergence of the objective function J because the amount of computation to get the gradient of J on the structural and control design parameters become enormous. In the present chapter the Genetic Algorithm (GA) is applied to obtain an optimal solution. In GA the global optimality of the obtained solution is not guaranteed. However no gradient information is required to get the solution and many successful applications of GA have been reported so far for various types of optimization problems.

5. Design example

Let us consider a fifteen-story building with three VCDs shown in Fig. 3. The one-dimensional earthquake disturbance whose displacement is defined as $w(t)$ is assumed in the present example. The mass of each floor m_i and the nominal inter-story stiffness k_i^{nom}, $i = 1, \ldots, 15$ are shown in Table 2. In the present design example the structural damping matrix $\mathbf{D}_0$ is defined as

$$\mathbf{D}_0 = \beta \mathbf{K}, \ \beta > 0, \tag{29}$$

where the scaler $\beta > 0$ is determined so that the damping ratio of the 1st mode of vibration becomes 2%. The nominal parameter values of the VCDs are determined as

$$\left(m_j^{VCD} \right)^{nom} = 9.0 \times 10^6 \ [\text{kg}], \tag{30}$$

$$\left(\overline{d_j^{VCD}} \right)^{nom} = 3.6 \times 10^7 \ [\text{Ns/m}], \ \left(\underline{d_j^{VCD}} \right)^{nom} = 0, \ j = 1, 2, 3. \tag{31}$$

The maximum and minimum values of the structural design parameters in Eqs. (14)-(16) are defined as follows:

$$(k_i)_l = 0.5 k_i^{nom}, \ (k_i)_u = 2 k_i^{nom}, \ i = 1, \ldots, 15 \tag{32}$$

$$\left(m_j^{VCD} \right)_l = 0.5 \left(m_j^{VCD} \right)^{nom}, \ \left(m_j^{VCD} \right)_u = 2 \left(m_j^{VCD} \right)^{nom}, \tag{33}$$

$$\left(\overline{d_j^{VCD}} \right)_l = 0.5 \left(\overline{d_j^{VCD}} \right)^{nom}, \ \left(\overline{d_j^{VCD}} \right)_u = 2 \left(\overline{d_j^{VCD}} \right)^{nom}, \ j = 1, 2, 3 \tag{34}$$
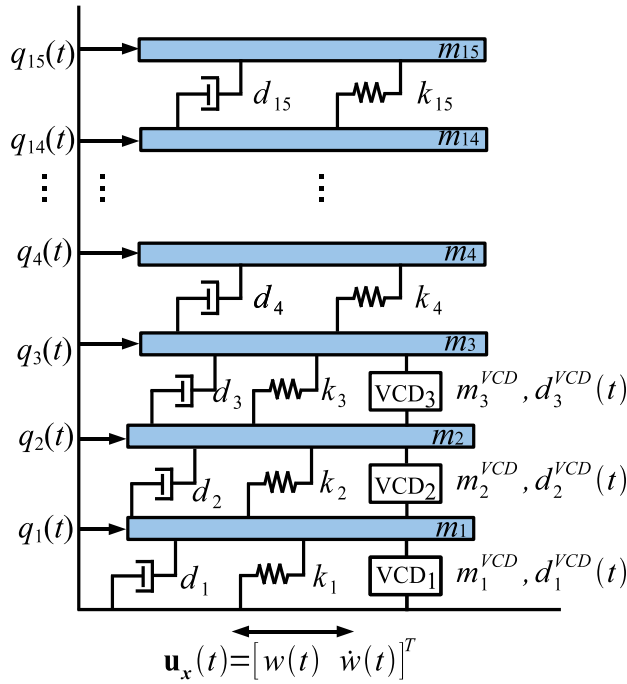
Fig. 3. Fifteen story building with 3-VCDs

Story	$m_i \times 10^3$ [kg]	$k_i^{nom} \times 10^6$ [N/m]
15	882	291
14	470	294
13	470	305
12	470	313
11	470	352
10	480	412
9	485	427
8	485	435
7	485	448
6	485	483
5	500	544
4	505	561
3	505	580
2	505	644
1	900	1098

Table 2. Nominal structural parameters of the fifteen story building ($i = 1, \ldots, 15$)

The control output vector $\mathbf{z}(t)$ in Eq. (5) is defined as

$$\mathbf{z}(t) = \begin{bmatrix} \mathbf{r}(t) \\ \dot{\mathbf{r}}(t) \\ \mathbf{q}(t) \\ \dot{\mathbf{q}}(t) \end{bmatrix} = \mathbf{C}_z \mathbf{x}(t) + \mathbf{D}_z \mathbf{u}_z(t), \tag{35}$$

Design parameter [Unit]	Nominal	Optimal
m_1^{VCD} [kg]	9.00×10^6	5.04×10^6
m_2^{VCD} [kg]	9.00×10^6	4.78×10^6
m_3^{VCD} [kg]	9.00×10^6	4.78×10^6
d_1^{VCD} [Ns/m]	3.60×10^7	6.79×10^7
d_2^{VCD} [Ns/m]	3.60×10^7	6.78×10^7
d_3^{VCD} [Ns/m]	3.60×10^7	7.04×10^7

Table 3. Nominal and optimal design parameters of VCDs

where $\mathbf{q}(t)$ and $\mathbf{r}(t)$ are the vector of the absolute displacement of each floor and the relative displacement between neighboring two floors given as

$$\mathbf{q}(t) = \begin{bmatrix} q_1(t) \\ q_2(t) \\ \vdots \\ q_{15}(t) \end{bmatrix}, \ \mathbf{r}(t) = \begin{bmatrix} r_1(t) \\ r_2(t) \\ \vdots \\ r_{15}(t) \end{bmatrix} = \begin{bmatrix} q_1(t) - w(t) \\ q_2(t) - q_1(t) \\ \vdots \\ q_{15}(t) - q_{14}(t) \end{bmatrix}. \tag{36}$$

Then coefficient matrices $\mathbf{C}_z$ and $\mathbf{D}_z$ in Eq. (5) are given by

$$\mathbf{C}_z = \begin{bmatrix} \mathbf{R} & \mathbf{0}_{15 \times 15} \\ \mathbf{0}_{15 \times 15} & \mathbf{R} \\ & \mathbf{I}_{30} \end{bmatrix}, \ \mathbf{D}_z = \begin{bmatrix} \mathbf{s} & \mathbf{0}_{15 \times 1} \\ \mathbf{0}_{15 \times 1} & \mathbf{s} \\ & \mathbf{0}_{30 \times 30} \end{bmatrix} \tag{37}$$

where

$$\mathbf{R} = \begin{bmatrix} 1 & 0 & 0 & 0 & \dots & 0 \\ 0 & 1 & -1 & 0 & \dots & 0 \\ 0 & 0 & 1 & -1 & \dots & 0 \\ \vdots & \ddots & \ddots & \ddots & \ddots & \vdots \\ 0 & \dots & \dots & \dots & 1 & -1 \end{bmatrix}, \ \mathbf{s} = \begin{bmatrix} -1 \\ \mathbf{0}_{14 \times 1} \end{bmatrix}. \tag{38}$$

The time constant T_d in Eq. (13) to model the delay of the VCD for the command signal $d_c^j(t)$, $j = 1, 2, 3$ is defined as $T_d = 0.02$ [s].
From the definition of $\mathbf{z}(t)$ in Eq. (35) the weighting matrix $\mathbf{Q}_w$ in Eq. (8) has 60 diagonal elements. Because the number of elements is too many to conduct the GA-based optimization the matrix $\mathbf{Q}_w$ is parameterized as

$$\mathbf{Q}_w = \mathrm{diag}\big(w_r^l \mathbf{1}_{1 \times 5}, \ w_r^m \mathbf{1}_{1 \times 5}, \ w_r^h \mathbf{1}_{1 \times 5}, \ w_{dr}^l \mathbf{1}_{1 \times 5}, \ w_{dr}^m \mathbf{1}_{1 \times 5}, \ w_{dr}^h \mathbf{1}_{1 \times 5},$$
$$w_q^l \mathbf{1}_{1 \times 5}, \ w_q^m \mathbf{1}_{1 \times 5}, \ w_q^h \mathbf{1}_{1 \times 5}, \ w_{dq}^l \mathbf{1}_{1 \times 5}, \ w_{dq}^m \mathbf{1}_{1 \times 5}, \ w_{dq}^h \mathbf{1}_{1 \times 5} \big), \tag{39}$$

where $w_r^l, w_r^m, w_r^h, w_{dr}^l, w_{dr}^m, w_{dr}^h, w_q^l, w_q^m, w_q^h, w_{dq}^l, w_{dq}^m, w_{dq}^h > 0$ are the weighting factors for the relative displacement and velocity for lower (1st-5th), middle (6th-10th) and higher (11th-15th) floors, and those for the absolute displacement and velocity for the floors divided like the above way respectively. With the parameterization the number of the control design parameters becomes 12. The maximum and minimum values of those weighting factors are determined to be 1 and 0 respectively.
To obtain the simulated structural responses that are used in the proposed GA-based optimal design we take four recorded or artificial earthquake waves ($n_e = 4$ in Eqs. (19) and (24)), i.e.,

El Centro NS (1940) ($i = 1$), BCJL1 (artificial) ($i = 2$), Hachinohe NS (1968) ($i = 3$) and JMA kobe NS (1995) ($i = 4$) waves. All earthquake waves are scaled such that the peak ground acceleration (PGA) becomes 4.0 [m/s^2].

The optimal structural and control design parameters are obtained by minimizing the objective function J in Eq. (18) with GA. The optimized design parameters are shown in Figs. 4, 5 and Table 3. To compare the performance on vibration suppression between the optimal semi-active control system obtained by the present integrated design approach and some other cases, structural responses are obtained for the scaled BCJL2 (artificial, PGA: 4.0 [m/s^2]) earthquake wave[1] shown in Fig. 6 for seven cases given as follows:

- **NC (Nominal structure):** The case of the nominal structural design parameters without VCD

- **NC (Optimized structure):** The case of the optimized structural design parameters without VCD

- **Pon (Nominal structure):** The passive on case with the nominal structural design parameters

- **Pon (Optimized structure):** The passive on case with the optimized structural design parameters

- **SA (Nominal structure):** The semi-active control case with the nominal structural and control design parameters

- **SA (Optimized structure):** The semi-active control case with the optimized structural and control design parameters

- **Energy-based SA (Optimized structure):** The case of the semi-active control for the maximum energy dissipation(Gavin, 2001) with the optimized structural design parameters

The time histories of the structural responses $r_{15}(t)$ (the relative displacement between the 15th and 14th floors) and $a_{15}(t)$ (the absolute acceleration of the 15th floor) for the optimized structure are presented in Fig. 7. By comparing between the case NC, Pon and SA the structural responses are suppressed by introducing the VCDs. It is also clear that the further performance improvement is achieved with the proposed predictive semi-active control by comparing the responses of the case Pon and SA. The time histories of the variable damping coefficients of the three VCDs are also shown in Fig. 8. The damping coefficients of the VCDs are frequently changed between their maximum and minimum values by the predictive semi-active control. The intermediate values between the maximum and minimum values of the variable damping coefficients come from the delay of the VCDs modeled as Eq. (13).

To make a more quantitative evaluation of the control performance the RMS and the peak values of the relative displacement between neighboring two floors and the absolute acceleration of each floor for all the above seven cases are shown in Figs. 9-12. The results of the integrated design for the fifteen story building are summarized as follows:

1. By introducing VCDs the structural response for the earthquake disturbance is highly suppressed both in the nominal and the optimized structures. This result shows that the effectiveness of the VCD as the vibration control device for civil structures.

---

[1] Note that this earthquake wave is not employed in the GA-based optimization.
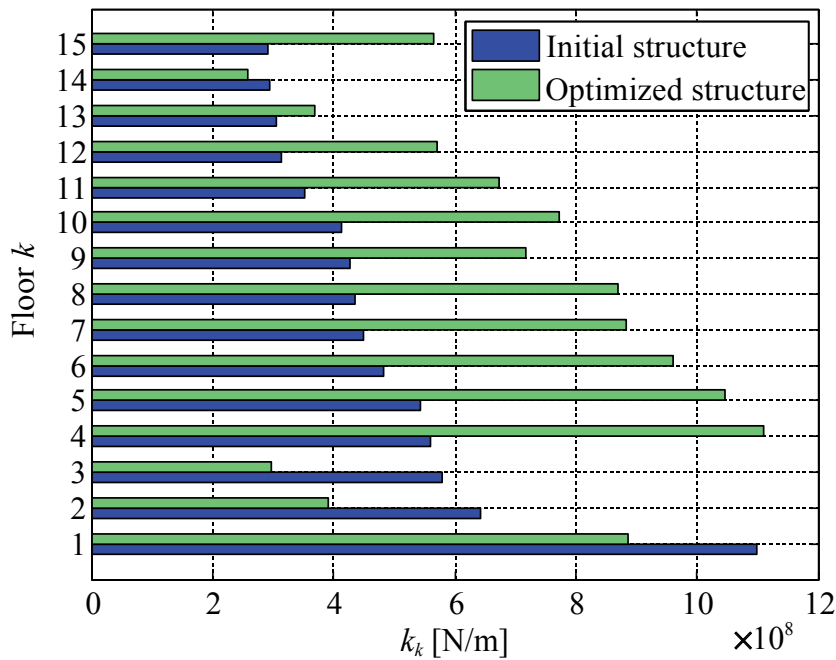
Fig. 4. Nominal and optimal stiffness parameters k_k, $k = 1, \ldots, 15$

2. In the case Pon and the case SA the relative displacement r_k, $k = 1, \ldots, 15$ and the absolute acceleration a_k, $k = 1, \ldots, 15$ of the optimized structure are significantly improved compared to those of nominal structure especially in middle and higher floors.

3. In lower floors (1-3F) the values of the optimized stiffness k_k becomes much lower than those of the nominal values while the stiffness in upper floors are increased. The result implies that so called "soft-story" type structure (Iwata et al., 1999), that aims at concentrating the structural deformation in lower floors by adopting small stiffness k_k and moreover suppressing the vibration and the deformation in higher floors by adopting large stiffness k_k, is obtained as the result of the integrated design. Hence the relative displacement in lower floors becomes larger in the case NC for the optimized structure than that of the nominal structure. However, we can see that the large amount of the relative displacement in the lower floors of the optimized structure are well suppressed by the VCDs with the proposed predictive semi-active control.

4. From Figs. 9-12 the optimized semi-active control system (SA (Opt. str.)) shows the better performance on vibration suppression compared to that of the semi-active control proposed by (Gavin, 2001) (Energy-based SA (Opt. str.))[2]. Especially the fairly better control performance on the absolute acceleration of each floor is achieved with the predictive semi-active control compared to that achieved with the he semi-active control law proposed in (Gavin, 2001). This result indicates that the importance of the proposed integrated design approach, i.e., the design of the structural system (the control object) with taking the employed control law into consideration.

---

[2] In the semi-active control law in (Gavin, 2001) the command signal for the VCD also becomes the bang-bang type that is same as the present predictive semi-active control.
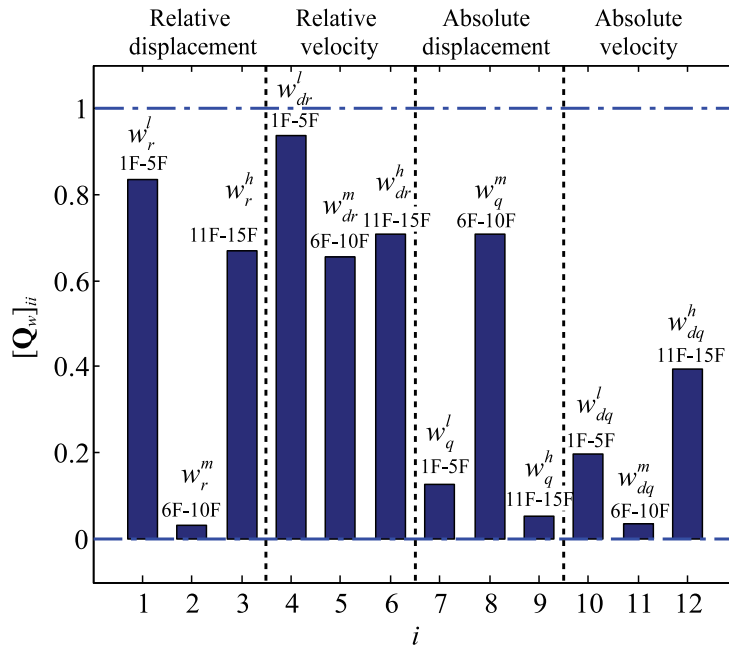
Fig. 5. Optimal control design parameters
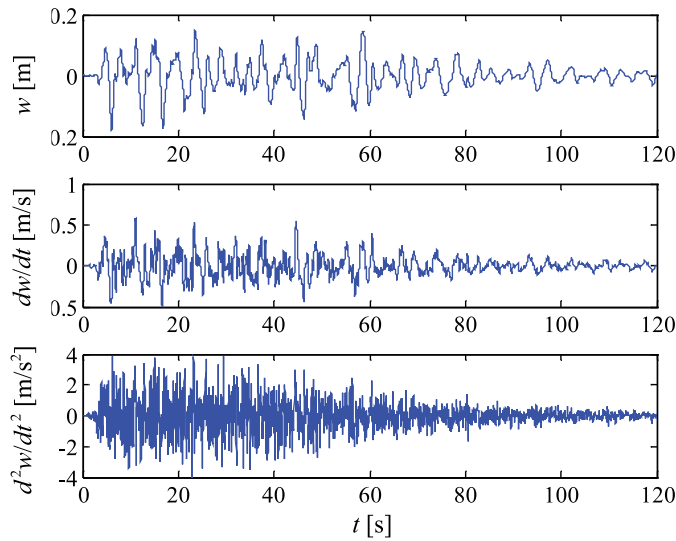
Fig. 6. BCJL2 wave (PGA=4.0 $[\text{m/s}^2]$)
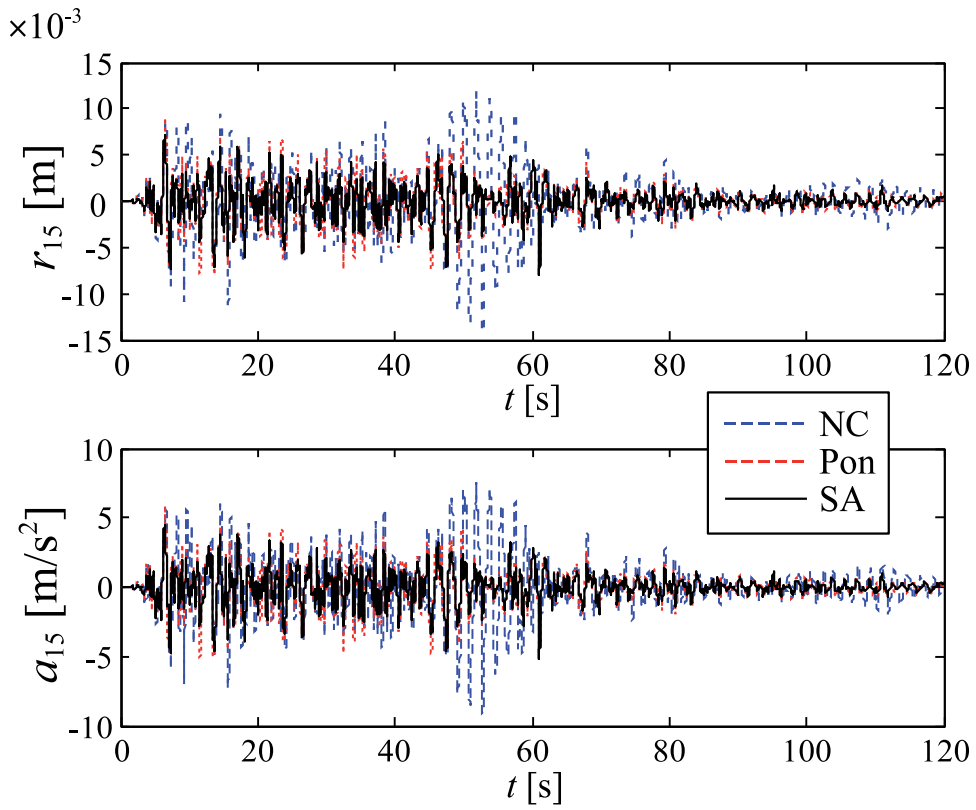
Fig. 7. Time histories of r_{15} and a_{15} for BCJL2 wave (Optimized structure, PGA=4.0 [m/s^2])
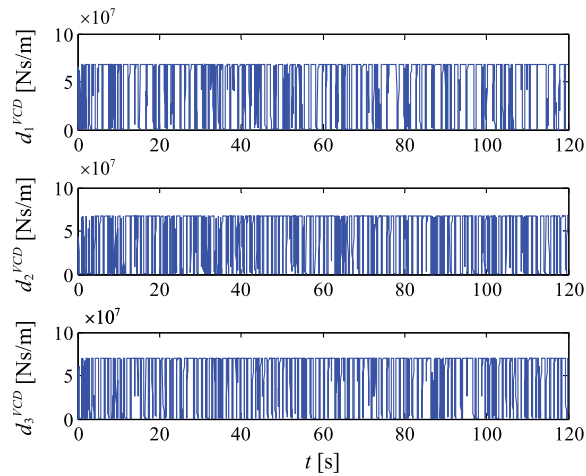
Fig. 8. Time histories of the variable damping coefficients of VCDs for BCJL2 wave (Optimized structure PGA=4.0 [m/s^2])
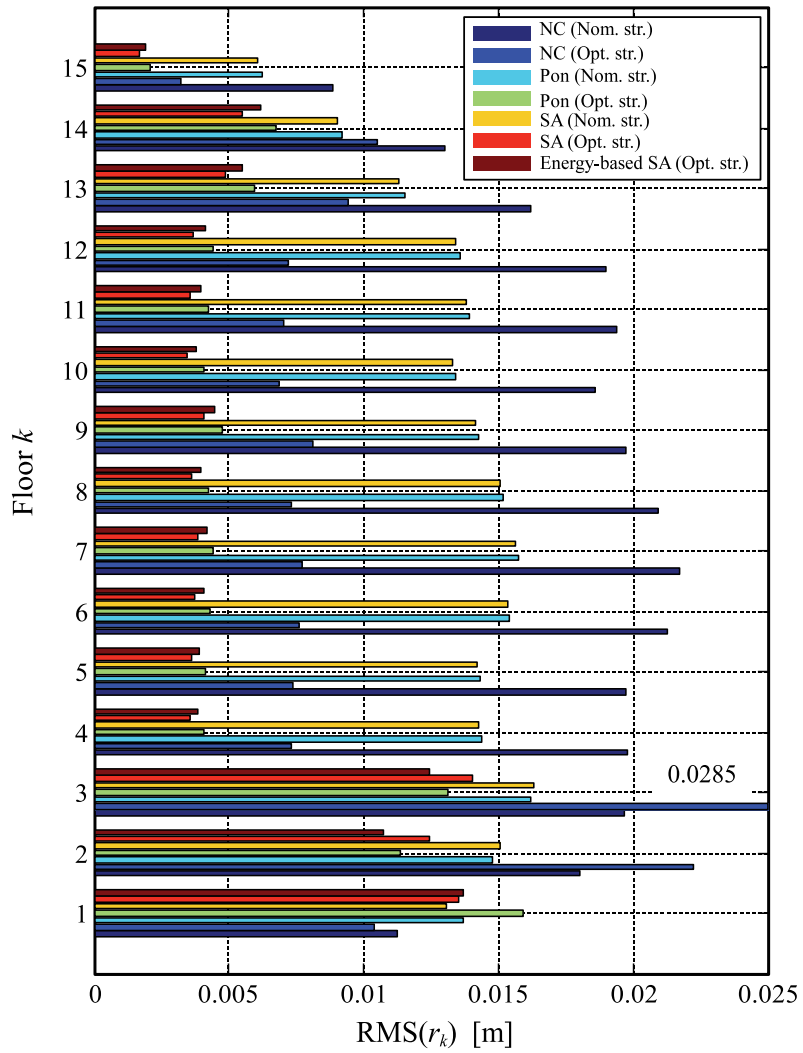
Fig. 9. RMS values of the relative displacement RMS(r_k), $k = 1, \ldots, 15$ (BCJL2 wave)
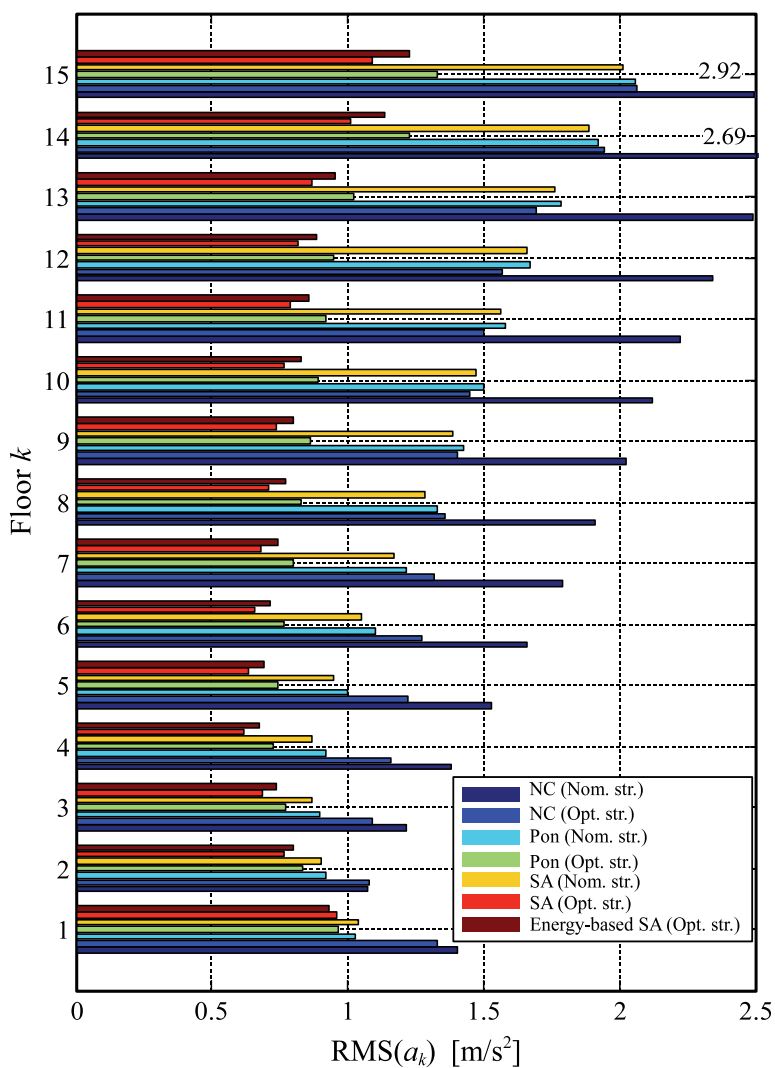
Fig. 10. RMS values of the absolute acceleration RMS(a_k), $k = 1, \ldots, 15$ (BCJL2 wave)
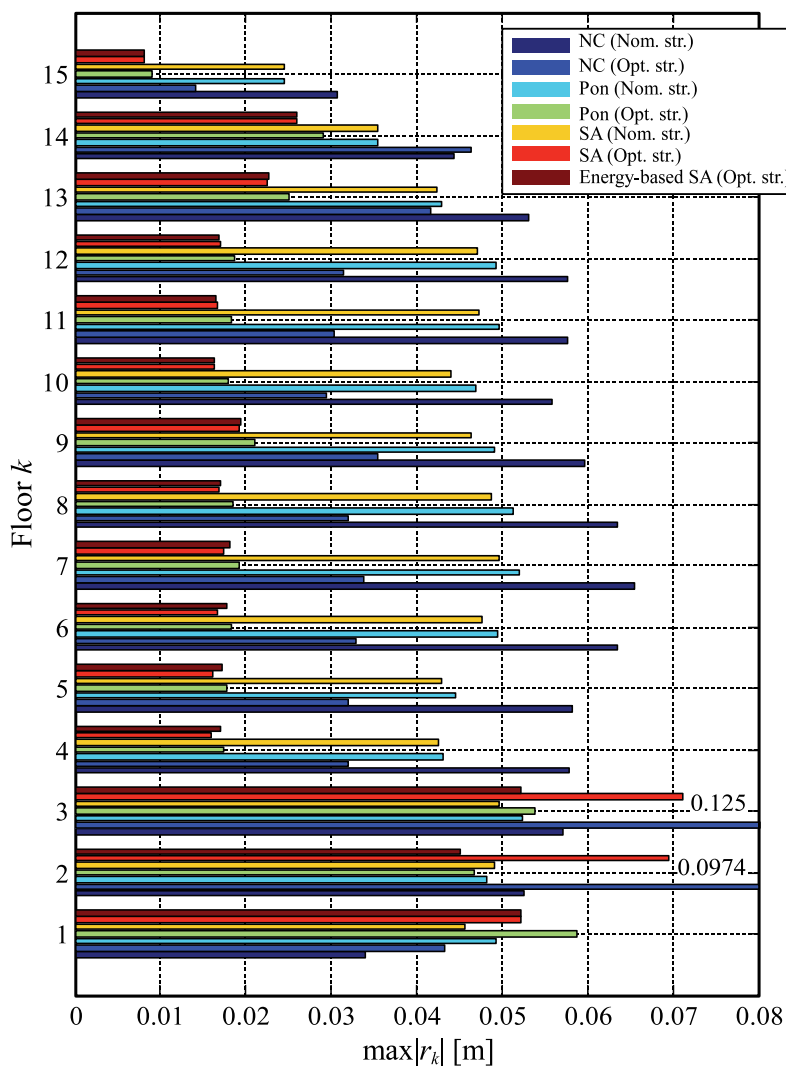
Fig. 11. Peak values of the relative displacement max $|r_k|$, $k = 1, \ldots, 15$ (BCJL2 wave)
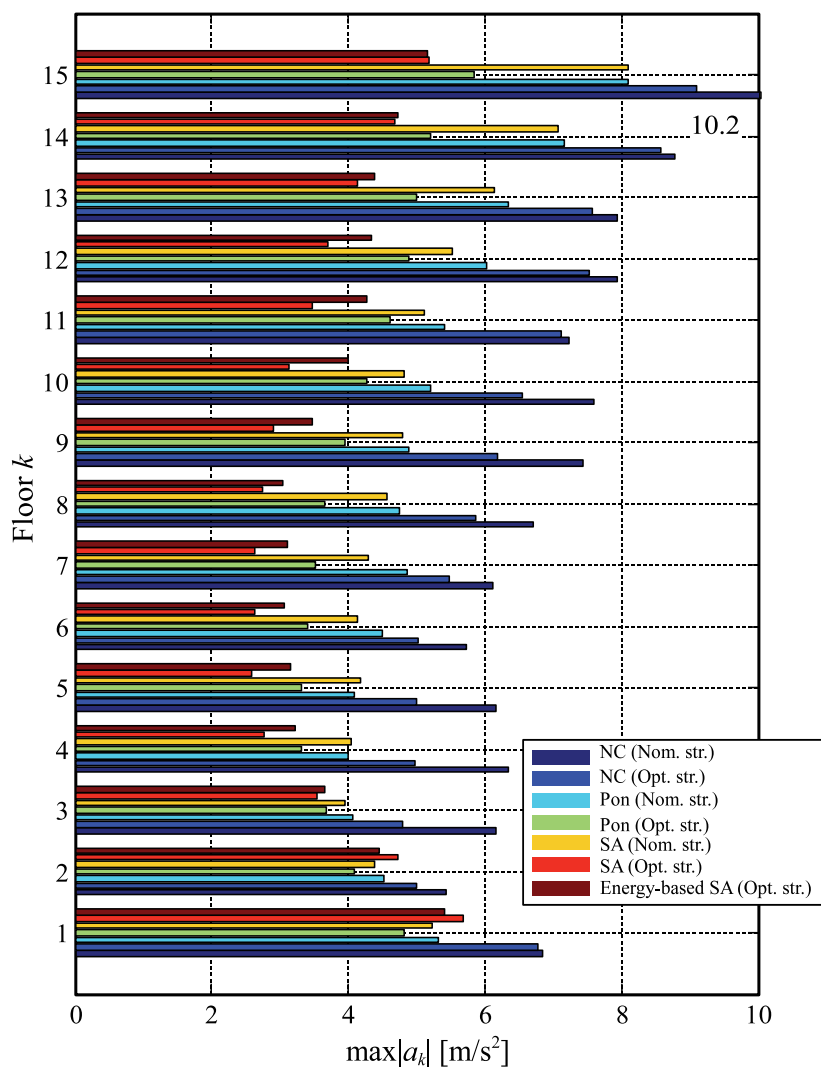
Fig. 12. Peak values of the absolute acceleration $\max |a_k|$, $k = 1, \ldots, 15$ (BCJL2 wave)

6. Conclusion

In this chapter the integrated design of civil structural systems and the semi-active control law is considered. The vibration control device (VCD) that is under development by the authors is adopted for the semi-active control. The VCD is the mechanism consists of the ball-screw and the flywheel that is for the inertial resistance force and the electric motor and the electric circuit for the damping resistance force with the variable damping coefficient. The semi-active control based on the one-step ahead prediction of the structural response is proposed. With the predictive semi-active control the stiffness property of the building, the parameters of VCDs and the weighting matrix used in the semi-active control are simultaneously optimized so that the control performance on vibration suppression for various recorded and artificial earthquake disturbances is optimized. The Genetic Algorithm is adopted for the optimization. The simulation study is conducted for the fifteen story building. The performance on vibration suppression of the semi-active control system obtained by the integrated design method is verified with the earthquake wave that is not employed in the GA-based optimization. The result of the simulation study shows the effectiveness of the proposed design methodology and the importance of the integrated design approach for control system design including semi-active control.

The future research subjects are summarized as follows:

- Integrated design of the semi-active control system including the optimization of the location of the VCDs

- Semi-active control for a simplified model of the real structural system

- Experimental study using a full-scale building with VCDs

7. References

Casciati, F., Magonette, G., & Marazzi, F. (2006). *Technology of Semiactive Devices and Application in Vibration Mitigation,* Wiley, New York.

Dyke, S.J., Spencer, Jr., B.F., Sain M.K. & Carlson J.D. (1996). Modeling and control of magnetorheological dampers for seismic response reduction, *Smart Materials and Structures*, Vol. 5: 565-575.

Gavin H.P. (2001). Control of seismically excited vibration using electrorheological materials and Lyapunov methods, *IEEE Transactions on Control Systems Technology,* Vol. 9: 27-36.

Grigoriadis, K.M., Zhu, G. & Skelton, R.E. (1996). Optimal Redesign of Linear Systems, *Transactions of the ASME, Journal of Dynamics, Systems, Measurement and Control,* Vol. 118: 598-605.

Hiramoto, K., Doki, H. & Obinata, G. (2000). Optimal Sensor/Actuator Placement for Active Vibration Control Using Explicit Solutions of Algebraic Riccati Equation, *Journal of Sound and Vibration,* Vol. 299: 1057-1075.

Hiramoto, K. & Grigoriadis, K.M. (2006). Integrated Design of Structural and Control Systems with a Homotopy Like Iterative Method, *International Journal of Control,* Vol. 79: 1062-1073.

Karnopp, D., Crosby, M.J., & Harwood, R.A. (1974). Vibration control using semi-active force generator, *Transactions of the ASME, Journal of Engineering for Industry,* Vol. 96: 619-626.

Kurata, N., Kobori, T., Takahashi M., Niwa N. & Midorikawa H. (1999). Actual seismic response controlled building with semi-active damper system, *Earthquake Engineering & Structural Dynamics,* Vol. 28: 1427-1447.

Ohtake T., Sunakoda K. & Matsuoka, T. (2006). Study on vibration control device using power generator, *Proceedings of ASME PVP 2006,* Vancouver, #PVP2006-ICPVT-11-93534.

Iwata, N., Hama, T. & Soda, S. (1999). Seismic control of the soft-first-story building by sifting method in sliding mode control, *Journal of Structural and Construction Engineering,* (No. 816): 83-90.

Onoda, J. & Hattka R.T. (1987). An Approach to Structure/Control Simultaneous Optimization for Large Flexible Spacecraft, *AIAA Journal,* Vol. 25: 1133-1138.

Sodeyama, H., Suzuki, K. & Sunakoda, K. (2004). Development of large capacity semi-active seismic damper using magneto-rheological fluid, *Transactions of the ASME, Journal of Pressure Vessel Technology,* Vol. 126: 105-109.

Spencer, B.F., Dyke, S.J. & Deoskar, H.S. (1998). Benchmark problems in structural control: Part I - Active mass driver system, *Earthquake Engineering & Structural Dynamics,* Vol. 27: 1127-1139.

Seismic Response Control Using Smart Materials

Sreekala R, Muthumani K, Nagesh R Iyer
CSIR/Structural Engineering Research Centre
India

1. Introduction

Earthquakes are highly destructive natural phenomena resulting in the massive deterioration of civil infrastructure, which becomes highly significant wih increasing urban population. Performance of structural systems needs to be improved recalling the huge loss of life and destruction to constructed facilities caused by various earthquakes. Protection of lifelines and infrastructural facilities are of utmost importance during a seismic event. There have been considerable research efforts in seismic vibration control for the past several decades. Developments of new techniques and new materials, which are not traditionally used in civil engineering structures, offer significant promise in reducing the seismic risk. Smart materials may be described as materials that can sense an external stimulus (e.g:- stress, pressure, temperature change, magnetic field, etc.) and initiate a response. They may belong to one of the four classes namely metals or alloys, polymers, ceramics or composites. Metals and alloys of different metals are considered as classical materials with lot of research activities around the globe . Shape Memory Alloys (SMA) belongs to the class of smart materials which are well known for its peculiar characteristics, which can be stress or temperature, induced. The research area which deals with structural applications of this variety of smart materials are promising (Sreekala& Muthumani, 2009) for structural health monitoring and vibration control.

Nickel Titanium (NiTi) Alloys are well known for its super elastic and shape memory properties and they belong to the class of Shape Memory Alloys (SMA). Presently SMA's are mainly applied in medical sciences, electrical, aerospace and mechanical engineering and also can open new applications in civil engineering specifically in seismic protection of buildings. Super elastic nitinol is found to be very effective for passive vibration control, as it can sustain large amounts of inelastic deformation and recover that deformation at the end of the process with good energy dissipation compared to regular metallic materials.

Various tests are conducted on NiTi wires in CSIR-SERC to evaluate the possibility of using SMA as an energy dissipating material with re-centering capabilities. Ability to sustain and recover large amounts of inelastic deformation during reversed cyclic loading with extra ordinary fatigue resistance make super elastic NiTi suitable candidate for seismic risk reduction. Quasi static and dynamic tests conducted with various parameters like pre strain, amplitudes and frequency for a number of cycles establishes the behavior which is suitable for seismic applications. It is interesting to find that from the quasi-static behavior of the material an optimum value of pre strain, which is material dependent, can be selected and

adopted in vibration control applications. Mathematical models were developed to predict the maximum energy dissipation capability of the material under study. The tests verify the potential of pre-strained NiTi wires as kernel components in seismic protection devices. It also highlights the effects of repeated cycling on pre strained wires, as special devices for passive protection during earthquake are meant for repeated cycling. Various types of vibration control devices can be made with the material used.

The technologies using smart materials are useful for both new and existing constructions. The chapter highlights various structural applications of this class of smart materials available in addition to the suitability of this material for vibration control applications. Protection of structures from damage during earthquakes can be addressed using passive protection devices designed to have maximum energy dissipation capacity with re centering capabilities. Innovative means of structural control scheme can be developed through passive systems, consisting of materials and devices useful in the context of seismic design and retrofit of structures

Ductility and energy dissipation are important parameters to be evaluated and quantified for seismic resistant design of structural components. Equivalent viscous damping is a significant quantity usually employed in earthquake engineering to characterize the dissipation capability of the material under investigation. This parameter expresses the effectiveness of the material in vibration damping. The relevance of the study is made clear with the associated terms in earthquake engineering

2. Properties, which enable SMA for civil engineering application

1. Repeated absorption of large amounts of strain energy under loading without permanent deformation
2. Possibility to obtain a wide range of cyclic behaviour from supplemental and fully re centering to highly dissipating by simply varying the characteristics of SMA components.
3. Strain range of 2 to 10%
4. Extraordinary fatigue resistance under large strain cycles.
5. Their greater durability and reliability in the long run.

2.1 Shape memory alloys in structural control

The existence of SMA property in certain alloys has been known from 1932(when it was first observed in Gold-Cadmium alloy exhibits a rubber like behavior). SMA's have unique properties, which are not present in many materials traditionally used in engineering applications; especially shape memory effect and super elasticity. While shape memory alloys have been commercially available since the 1960s, their application has been limited (Pelton et al., 2000). Early literatures on SMA materials shows successful uses of these for the design of biomedical and clinical devices, particularly for fixing body fractures internally with various 'NiTi' SMA interlocking intramedullary nails(Da et al,2001). Among other designs, research related to the use of SMA materials as micro-pumps, micro-grippers, flexible SMA active catheters, micro nano-tribological devices and SMA thin films for electromechanical system have been increasingly revealed in recent years (Stockel & Melzer, 1995). Those achievements exhibited an excellent reliability and confidence in using these materials for other primarily structural elements. The SMA materials possess many unique mechanical and geometrical properties such as shape memory effects which provide a large recovery strain and force simultaneously, pseudo-elastic behavior upon heating and super-

elastic properties in ambient conditions for specified SMA materials. Birman (1997) and Humbeeck (2001) gave comprehensive reviews on the properties of SMA materials. Based on the studies under MANSIDE project, 1999(Italian Department for National technical services) Ni–Ti SMA's appear to be the best candidates for use in seismic applications. But selection of the SMA wires for energy dissipation with or without pre strain had to be addressed separately (Sreekala et al., 2010). So the need arose for finding the effect of pre strain as well as repeated cycling in the energy dissipation of SMA wires.

2.2 Mechanism behind super elasticity

Super elasticity is related to the isothermal response of SMA specimens to applied mechanical loads. The phase transformations are solid to solid diffusionless processes between a crystallographically more ordered phase, the austenite (A) and a crystallographically less ordered phase the martensite (M). Fig. 1 shows a schematic stress–strain cyclic curve of a super elastic SMA. It is characterized by five branches. Branches 1 and 4 correspond to the elastic deformation of the two stable phases of SMA, respectively, austenite and martensite. Branches 2 and 3 correspond, respectively, to the forward (from austenite to detwinned martensite) and inverse (from detwinned martensite to austenite) phase transformation. Branch 5 corresponds to the onset of plastic deformation of detwinned martensite. In the figure σ_{Fs} and σ_{Ff} represent the critical stresses at which the forward transformation, respectively, starts and finishes, while σ_{Is} and σ_{If} are those at which the inverse transformation, respectively, starts and finishes. Since loading and unloading paths are different from each other, a certain amount of energy is dissipated over the cycle.

3. Research significance

Most of the applications of SMA have focused on developing various types of actuators. However, most of the commercially successful applications - such as couplings, electrical connectors, cardiovascular stents and eyeglass frames - use the full shape- memory effect or the full super elastic cycle only a few times. This indicates that SMA components can be used successfully for several non-actuator applications as well. One such area is the use of SMA components for damage control in structures. The SMA component can undergo finite deformations either due to super-elasticity or due to rearrangement of martensite variants at relatively small stresses. This can be used to prevent permanent plastic deformation due to unexpected loads in the rest of the structure. The ability of the SMA component to recover its original dimensions may be an additional advantage, during the seismic events.

Shape Memory Alloys (SMA) show the potential to eliminate some limitations involved in present technologies, allowing a broader application. The limitations of existing technologies for passive protection devices can be summarized as follows

1. Problems related to ageing and durability (e.g., rubber components)
2. Difficulty in maintenance(those based on fluid viscosity)
3. Installation complexity or replacement and geometry restoration after strong events (those based on steel yielding or lead extrusion)
4. Variable performances depending on temperature(polymer based devices)

The usable strain range in the order of 10% in shape memory alloys provide them very high energy dissipation per unit mass of material. Comparing the well known rubber isolators and steel hysteretic dampers which belong to the class of quasi-elastic devices and elasto-plastic devices respectively, re-centering devices gain the best mechanical characteristics of

both. The shortcomings of the traditional restrainers can potentially be addressed with the use of SMAs (Fig.2). The comparative behaviour of steel, rubber and SMA is given in Fig.2.
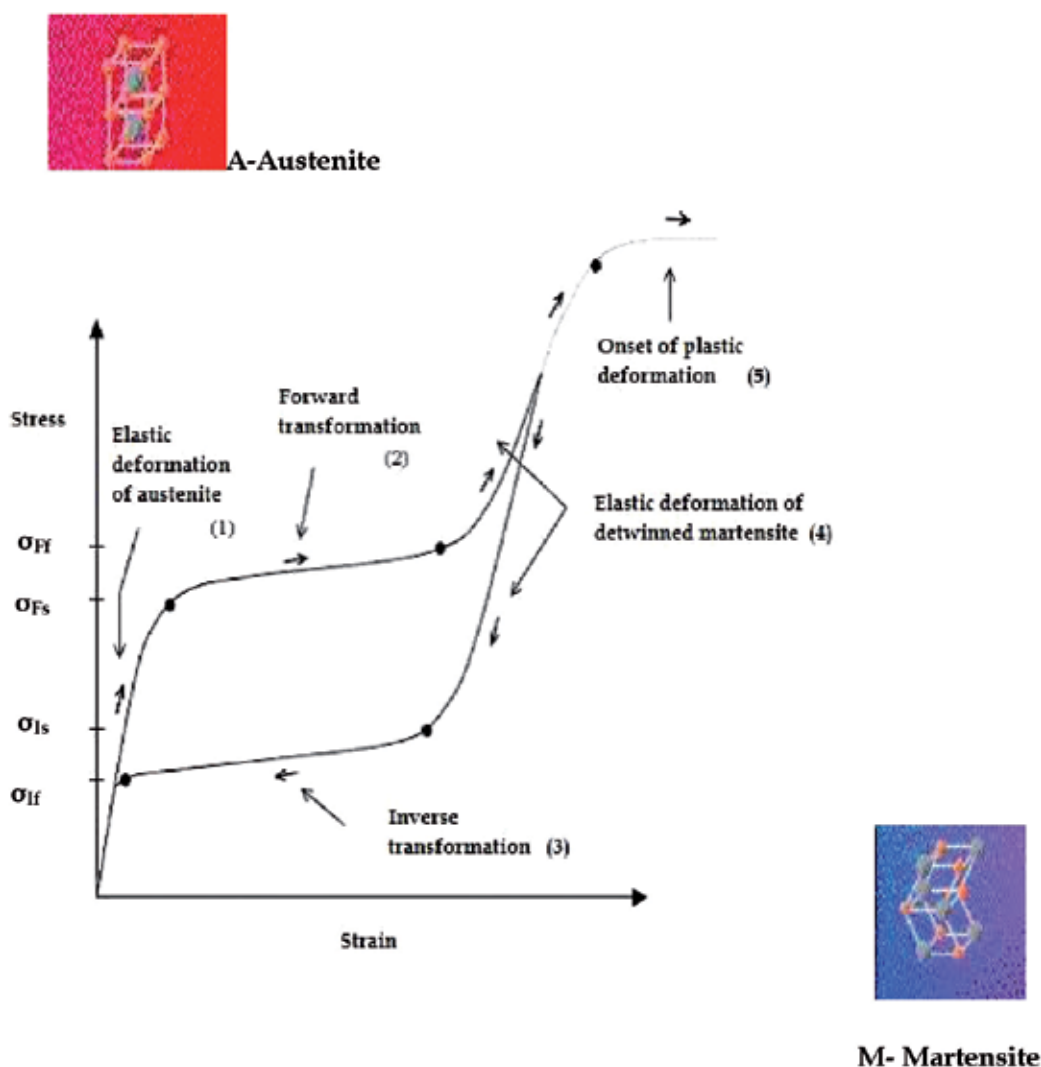
Fig. 1. Stress-strain curve showing super elasticity of SMA-Schematic sketch describing the phase change with the deformation process and the associated crystal structure

On the one hand, they recover the initial position of the structure, with a good control of the displacements; on the other hand they put a threshold to the force transmitted to the super-structure. The full possibility of designing the mechanical behavior combining the self-centering and the energy dissipation capability, permit to calibrate the desired features and fit the specific needs. The availability of such features opens considerable room for improvement of the structural system design. But the mechanical behavior of SMAs is strongly dependent upon the alloy composition and the thermo-mechanical treatment. Special care should be taken while alloy selection is made.
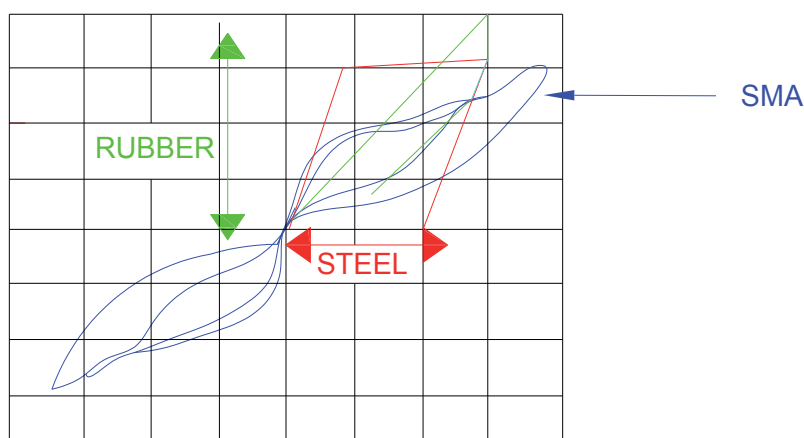
Fig. 2. Comparative behaviour of Steel, Rubber and SMA

4. Experimental investigation and inferences

The experimental tests were carried out on austenite wire samples of 0.4mm diameter and 1.2mm. The wires were available in spool form. The typical photograph of the material – wires in spool form-is shown in fig.3. The compositions of wires were NiTi alloy with 55 % Ni and balance titanium spooled NiTi. The wire selection is made in such a way that Ni-Ti alloy wire with equi-atomic composition possesses better dissipation property and higher resistance to corrosion and fatigue. The material is straight annealed super elastic NiTi wires and has its latent heat and specific gravity 14500 J/kg and 6479.85 kg/m^3 (0.234 lbs/in^3) respectively. The test was carried out under ambient temperature conditions around 27^0 C. Quasi-Static and dynamic tests were conducted to evaluate the super-elastic properties and energy dissipation capabilities under ambient temperature. Dynamic tests were carried out by applying sinusoidal cyclic deformation to wire samples. A displacement controlled test set up was used to perform the tests. The typical test sequence is characterized in terms of number of cycles, strain amplitude and frequency as they could provide very important information regarding earthquake applications.

The test programme on SMA wires of two diameters namely 0.4 and 1.2 mm can be summarized as follows:

1. Quasi-static tests
2. Dynamic tests -frequency of operation 0.5 Hz (sinusoidal cyclic deformation)
    a. Tests to evaluate the number of cycles to failure for a constant amplitude
    b. Variable amplitude tests to evaluate the energy dissipation capability for increased amplitudes.
3. Tests on pre-strained wires –frequency of operation 0.5 Hz .
4. Tests on wires for varying frequencies.

The quasi-static (slow rate) tests were performed till the failure of the specimen. The test was run in a position controlled test set up at constant rate of loading 0.025mm/sec. Fig.4 shows the stress strain curve for quasi-static loading. It is compared with the behavior of the 1mm diameter steel wire which is used for binding purposes in construction A sinusoidal cyclic test on SMA wires was performed for maximum amplitude of 5 mm.
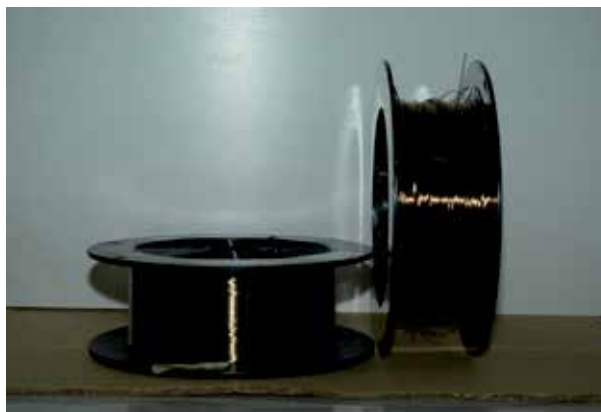
Fig. 3. The photograph of the super elastic SMA wire samples (Available in spool form)
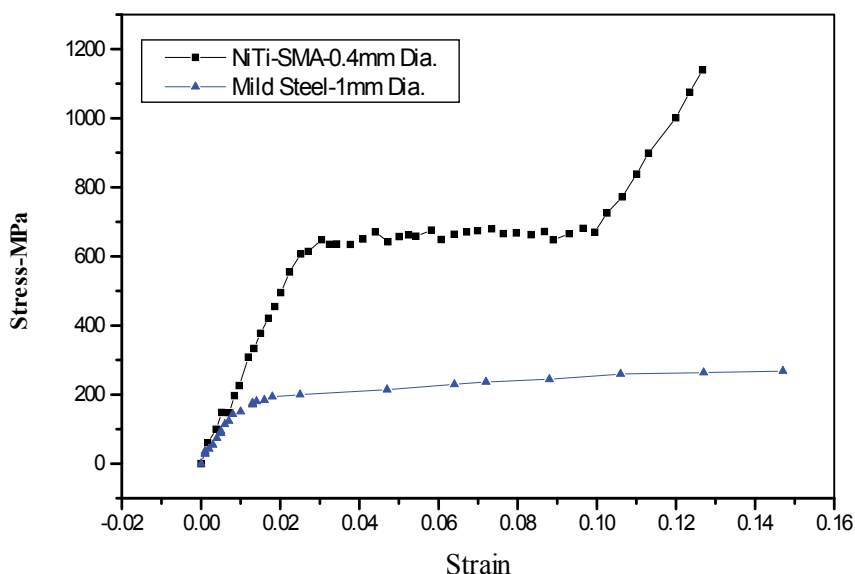
Fig. 4. Behaviour of Ni-Ti wires – quasi static tests- Comparison with 1 mm mild- steel binding wire used for reinforcement stirrup tying in structural construction.

The mechanical behavior such as the transformation stress levels, fatigue behaviour and the frequency dependence were found to be similar in both diameter wires. The tests were also carried out with increasing number of cycles to obtain the fatigue characteristics.

Typical load deformation characteristics of 1.2mm diameter wire with 11 mm amplitude are shown in Fig.6. As the displacement amplitude increased as observed in the force deformation behaviour, presence of the martensitic phase -after completion of the phase transformation- provides additional stiffness. Strain hardening is observed towards higher amplitudes which correspond to 8-9% strain in both the wires seen in Fig.4 & Fig.6. The increase in stress levels is quite evident in Fig.6. Here cycling up to 9% strain variation fetches a stress of 830 Mpa.
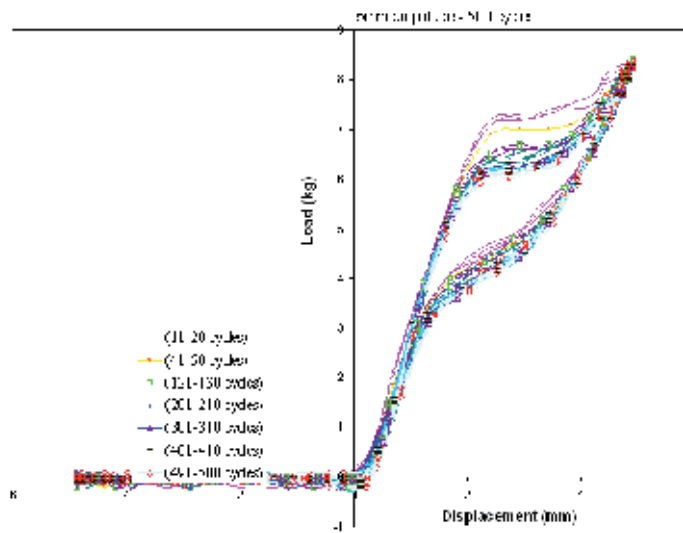
Fig. 5. Load deformation curves for 0.4mm diameter wire with 5mm amplitude (strain variation 3%, maximum stress 650 Mpa)- frequency of loading 0.5 Hz-0.4mm diameter wires
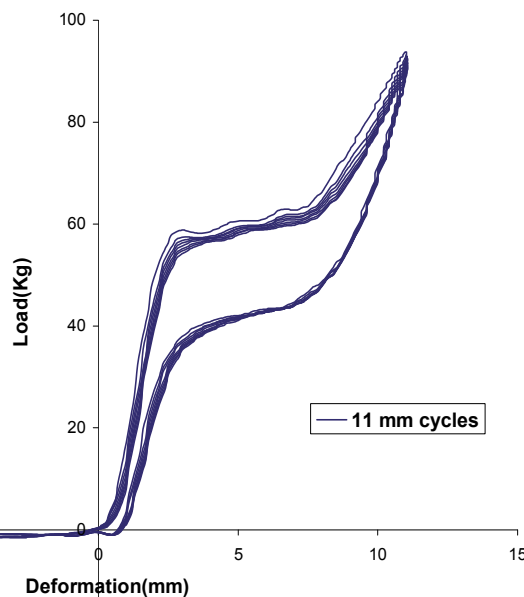
Fig. 6. Load-deformation curves for 1.2 mm diameter wire with 11mm amplitude cycles (strain range 9%, max. stress 830MPa)- frequency of loading 0.5 Hz Cycles (strain range 9%, max. stress 830MPa)

The various parameters and the testing scheme are selected in a way to understand the behavior of the material during earthquakes. Initially a sinusoidal cyclic test on SMA wires was performed for constant amplitude of 5 mm [Fig.7(a)- 7(d)]. Usually earthquake

vibrations are dynamic- reversed cyclic in nature which consists many number of cycles. The tests were also carried out with increasing number of cycles to obtain the fatigue characteristics. Further tests were carried out with increasing amplitude from 5 mm to 11 mm [i.e increasing the total strains from 4% to 9%, Fig.7 (e)]. Strain measurements were based on the actuator displacement as the wires were having very smooth oxide finish surface
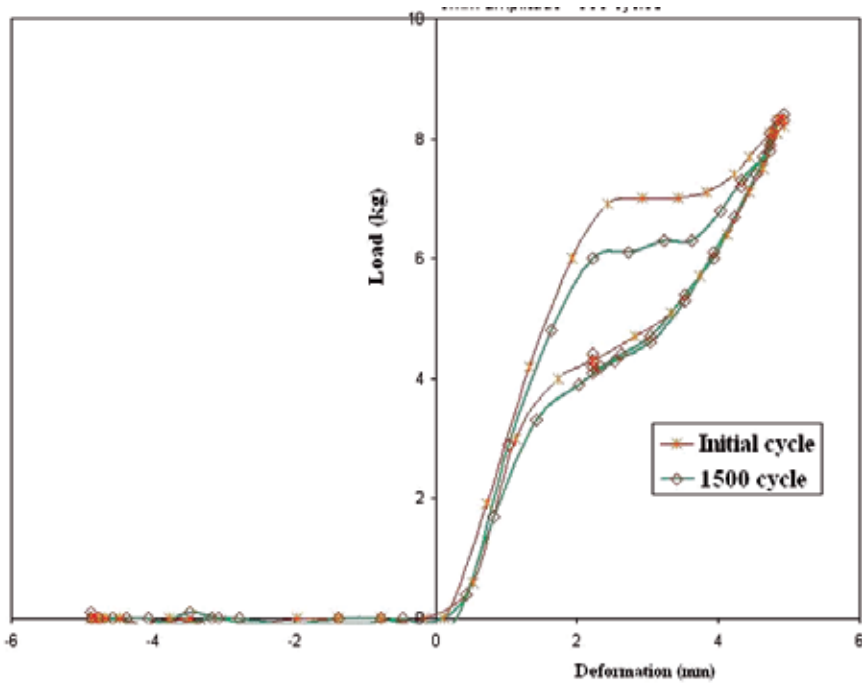
(a)
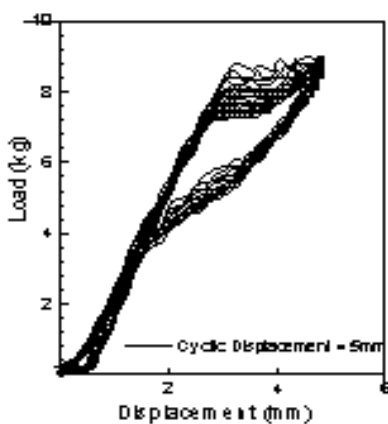
(b) Initial 28 cycles
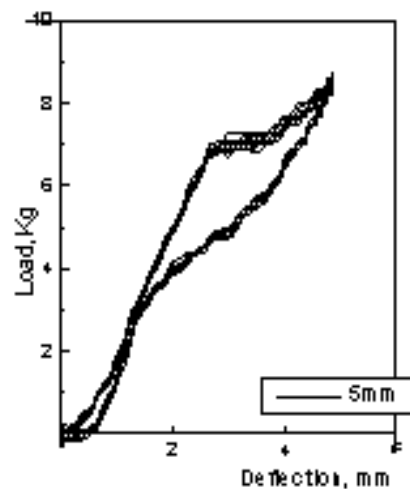
(c) Subsequent cycles

(d) (e)
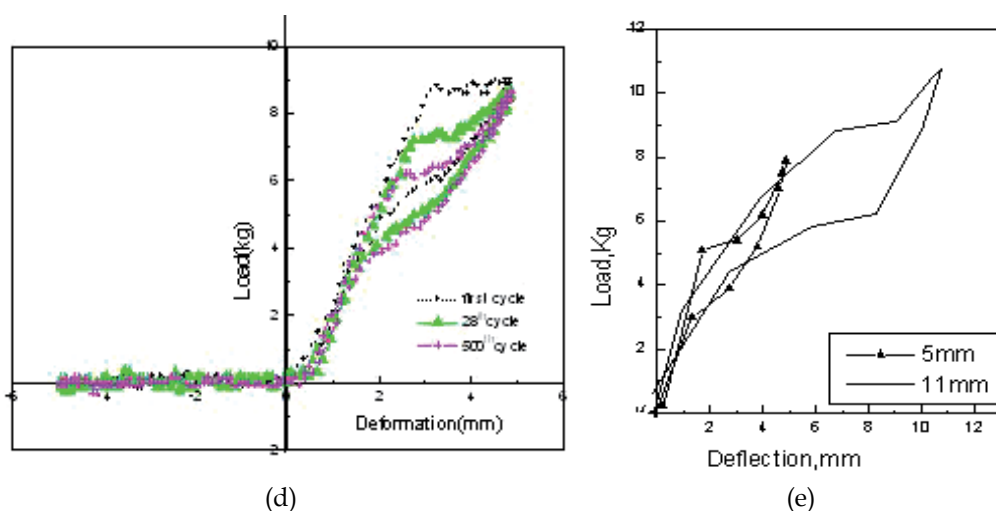
Fig. 7. (a) to (d) Cyclic tests on non pre-strained wires cycling for +/- 3 percentage strain variation (5mm amplitude). (e) Effect of increasing the amplitude beyond 1500 cycles.

Due to the repeated cyclic deformation of the same amplitude it is observed that the hysteresis loops translate downwards and narrows (Fig.7a-7d). Consequently the stress levels for the transformation decreases. Energy dissipation capacity under constant amplitude loading remained same up to 500 cycles, 20% reduction was observed in the next 500 cycles and around 30% reduction towards the failure from the initial value. Effect of increasing the amplitude beyond 1500 cycles can be observed in figure.7e.

4.1. Effect of pre-strain
The effect of pre-strain was found out by imposing pre-strain amplitude in the wire. The wire is held at that point of pre-strain and reversed-cycling performed for various amplitudes (Fig.8b). Like wise for various pre strain values the dynamic tests were performed by giving sinusoidal deformation to the wire samples (Fig.8a). These tests help to simulate the characteristics of earthquake loading and understand the behaviour of the material. The frequency dependence on loading is also investigated during the experiment (Fig.9). The frequency of loading was varied from 0.5 Hz to 3 Hz, at intervals of 0.5 Hz, since most of the earthquake applications come within this range. Table.1 gives the test programme for the nitinol wire and the parameters evaluated in the study are tabulated. Temperature variation during cycling was observed using a thermocouple for quite a few cycles.

5. Discussion of test results

Quasi-static tests of the wire clearly shows the super elastic property of the SMA wire. Fig.4. presents the stress strain curves obtained under quasi-static loading using a hydraulically driven test system (instron make). The shape of the stress strain curve exhibits some of the fundamental characteristics of SMA. Test result shows the super elastic property of the SMA wires in the strain range 2% to 10 %. The initial elastic to plateau transition, that is the

transition from linearly elastic to super-elastic occurs at a stress of approximately 597 MPa. The yield stress of 597 Mpa and ultimate stress of 1100 Mpa is comparable with the idealized behavior of SMA (Dolce, 1994).
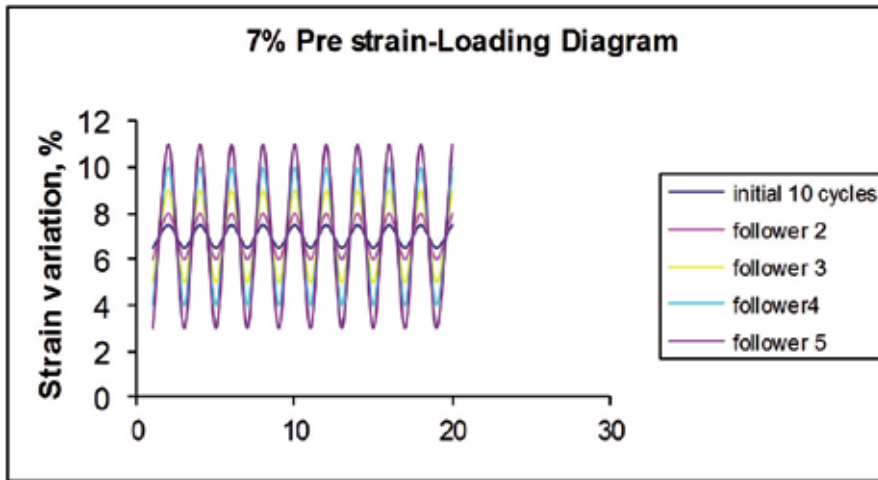
(a)
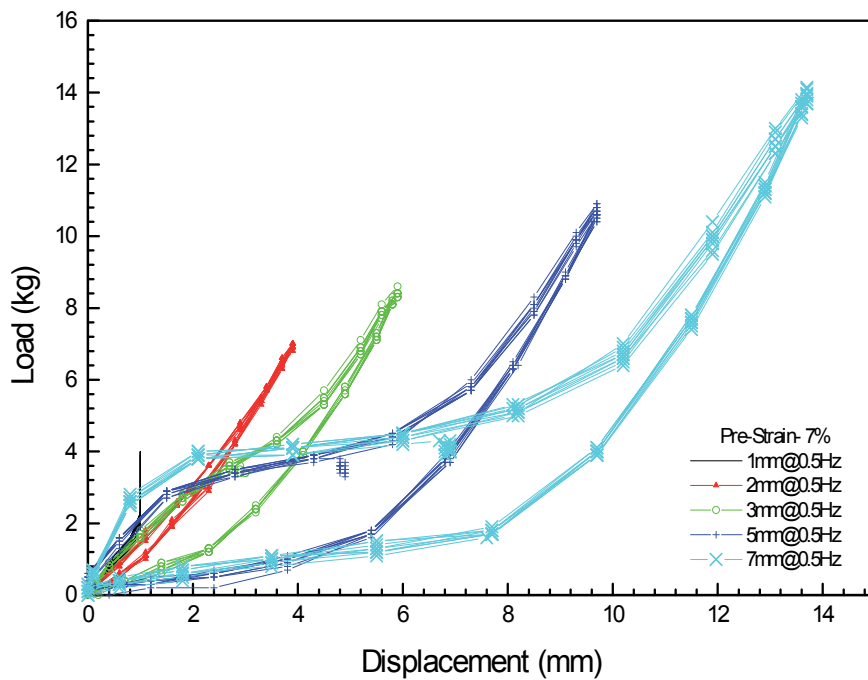
(b)

Fig. 8. Typical sketch showing the loading and the hysteretic curves obtained at 7% pre-strain –variable amplitudes.

If the material is unloaded after being loaded into the super elastic region, the unloading portion of the stress strain curve does not follow the loading portion, but follows a lower path back to the origin which indicates the transformation of stress induced martensite back to the austenite (Fig.5,6). This makes the hysteretic energy dissipation which is an important parameter to be assessed for earthquake applications and hence in passive control devices. The super elasticity based applications take advantage of the following features 1) the possibility of recovering large deformations 2) the existence of a transformation stress plateau, which guarantees constant stress over non-negligible strain intervals. The frequency dependence on loading is also investigated during the experiment (Fig.9). The frequency of loading was varied from 0.5 Hz to 3 Hz, at intervals of 0.5 Hz, since most of the earthquake applications come within this range. It is interesting to note that the number of cycles for the same amplitude is not sensitive to the frequencies in the range 0.5-3 Hz as observed in both the diameter wires.
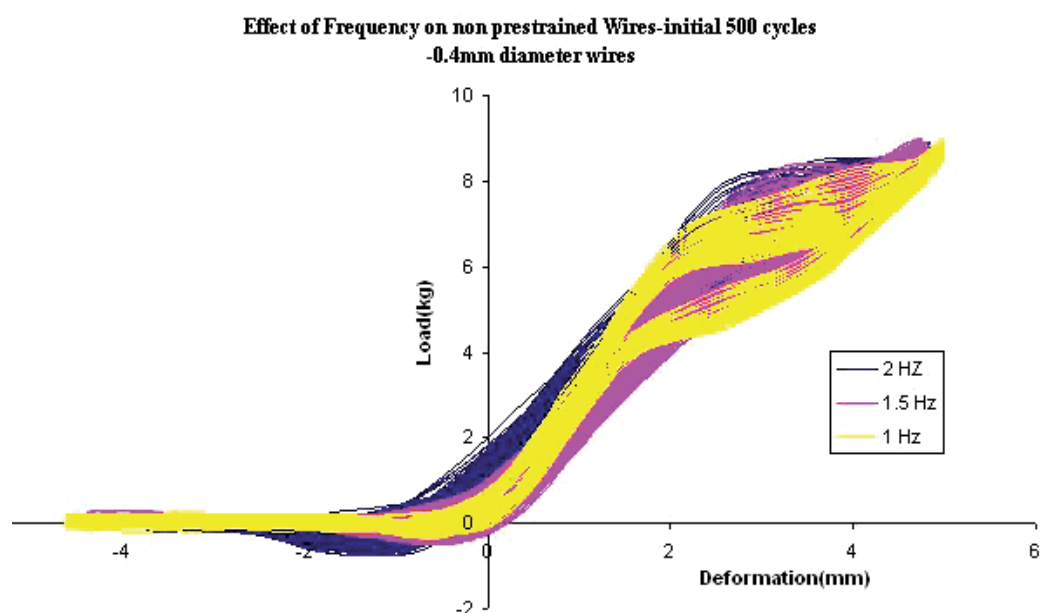
Fig. 9. Typical Cyclic behavior (tension compression tests) of non pre-strained wires for varying frequencies.

It is reported in the literature that the effect of frequency is negligible in the energy dissipation in the range of interest 0.5 - 3 Hz for seismic applications (Cardone et al,1999) . But it is observed from the test that the dissipated energy during the sinusoidal loading at 0.5 Hz is 25 % more than the energy dissipated at 1Hz to 3Hz, which is almost a constant value. Effect of increasing the amplitude beyond 1500 cycles can be observed in figure.7e. The high fatigue resistance combined with negligible residual deformation, observed in SMA material help to reduce the post earthquake repair costs, if dampers are made out using these.

It is found from the experiment that the hysteresis loops narrow and translate upwards when there is an increase in strain amplitude, while the branches of the curve relevant to the

phase transformations harden, thus yielding an increase in the stress levels (Sreekala et al,2008). This trend is observed in the case of cycling around 7% pre-strain, as the strain reaches to 10% the end of the transformation range (Fig.8). This phenomenon is related to the elastic deformation of the de-twinned martensite found at the end of the phase transformation. This is true for pre strained wires as well as without pre strained. It is a favorable aspect in seismic applications as the system stiffens rather than softening, if the expected design seismic action is exceeded, thus ensuring a good control of displacements.

Constant amplitude tests for many cycles for varying frequencies indicated that there is slight variation in the shape of the loops. Different heat exchange modalities with ambient temperature, at different strain rates are the causes of these effects from quasi-static to dynamic range (0.5-3 Hz). As strain rate increases, the heat-exchange condition increasingly digresses from the isothermal one. The latent heat of transformation causes the specimen to self-heat and then increase its average temperature during test. At the same time, during each loading cycle, the specimen temperature oscillates around an average value, according to the sinusoidal variation of strain. The temperature variation is found to be 9^0c.While the instantaneous temperature of the wire oscillates around the ambient temperature (27^0c) with excursions of the order of 9^0c, the average temperature remains practically unchanged during all the loading history equal to the ambient temperature.

As a result of the self heating (cooling) there occurs instantaneous increase (decrease) of the stress required for transformation. It is observed from the test that the dissipated energy during the sinusoidal loading at 0.5 Hz is 25 % more than the energy dissipated at 1Hz to 3Hz, which is almost a constant value. The hardening of the transformation branches, the narrowing of the cycle, apparent change in the shape of the loop resulting in a reduced energy loss all of which are associated with slight temperature variation due to different heat exchange modalities are caused by the stabilization of the material due to repeated cyclic loading(Fig.10). Possible increase of average temperature during cycling at higher strain rates produces an upward translation [Miyazaki et al,1986b].

Stabilization of the material behavior due to repeated cyclic loading also can be observed from the shape change of the loops in the tests on non-pre strained wires (Fig.10). The effect of pre-strain is found at 2.5% pre strain applied in the form of deformation to the sample, on two cyclic strains namely 4 % and 6 % (Fig.11.).

The figure reveals the fact that the hysteresis loops translate upwards as it near the transformation stress level. The comparison between the energy dissipation capability at various pre strain under different amplitudes, namely 3mm and 7mm is shown in Fig.12.

It is interesting to find that the quasi-static curve serves as the envelope curve in this process and as and when the stress reaches the transformation stress level, as marked in fig.12, further stiffening happens in the material. This is an added advantage for seismic applications that the material gets stiffen, rather softening to have good control of displacements. Fig. 12 also shows the hysteresis curve for the wire pre strained at 6% and cycled between 2 % and 10% along with other strain variations.

Tests on wires pre strained to different levels, indicated a particular value of pre-strain, from which cycling in the pseudo-elastic range fetches maximum energy dissipation (Fig.8.). The equivalent viscous damping expresses the effectiveness of the material in vibration damping. It is calculated based on the average energy dissipated per cycle and the damping values observed are also found to be significant. Looking into 6% pre strain one can see the higher equivalent damping values. Cyclic variation of 4% strain on either direction at 6% pre strain gives higher equivalent damping due to higher energy dissipation (Table.1). An
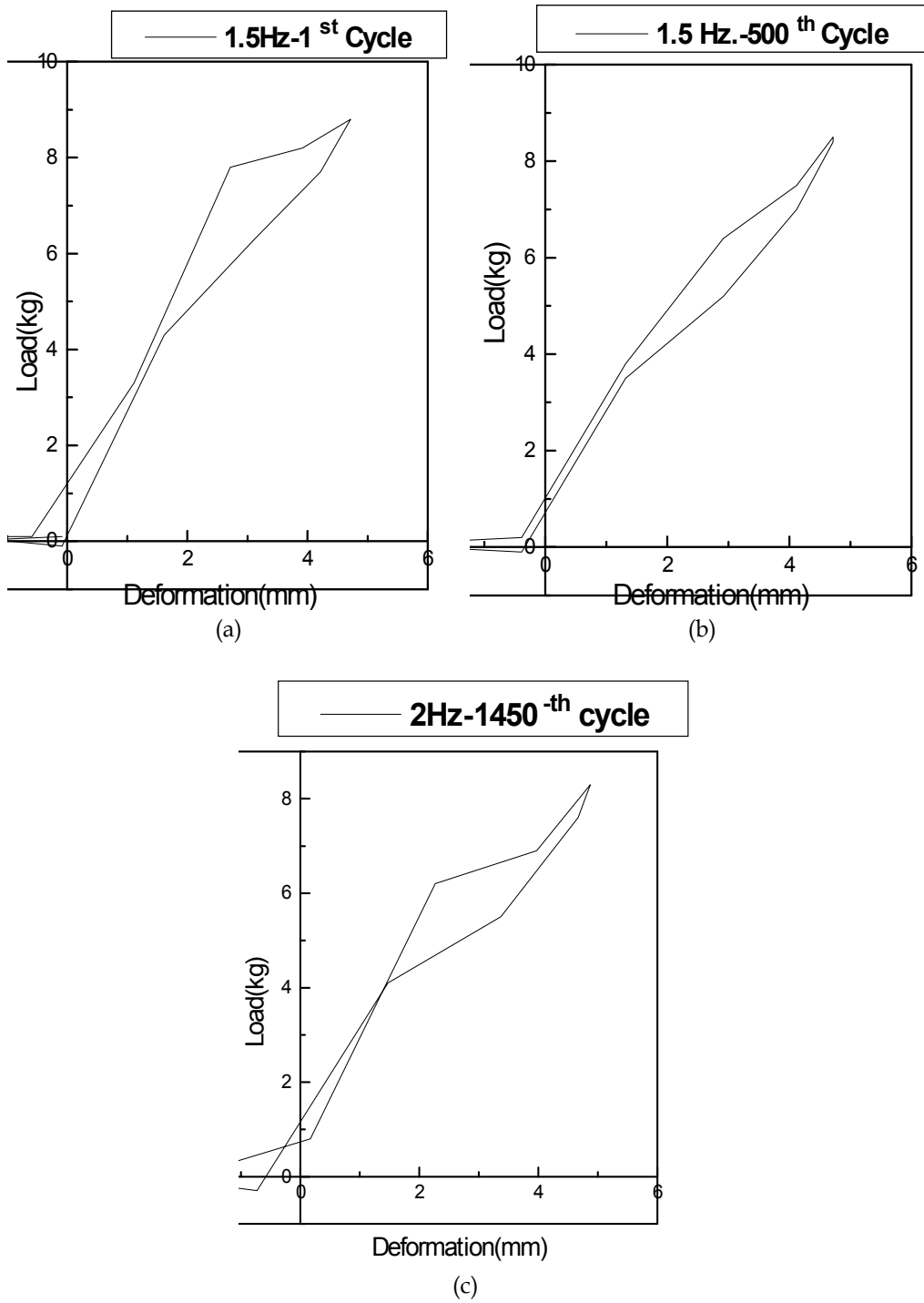
Fig. 10. (a) to (c) Changes in the shape of the curve during varying frequencies.
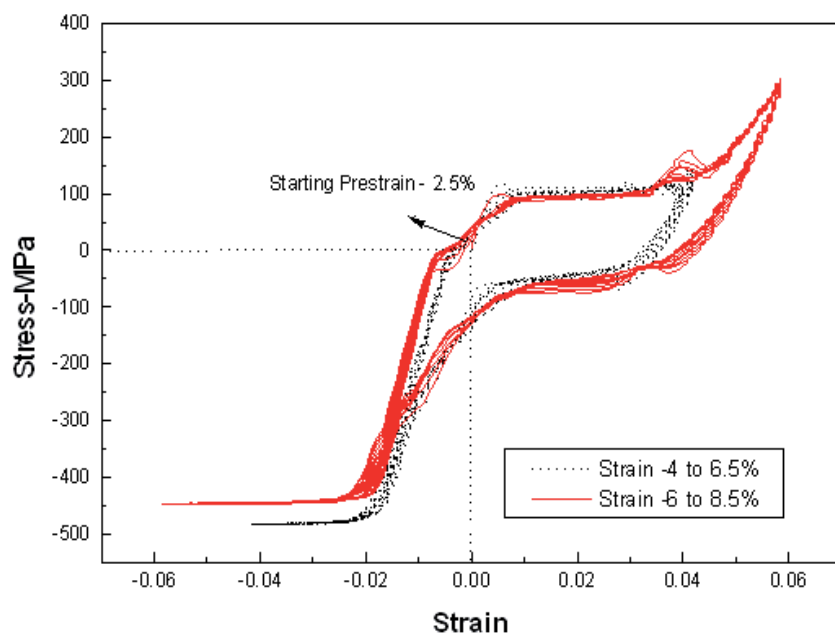
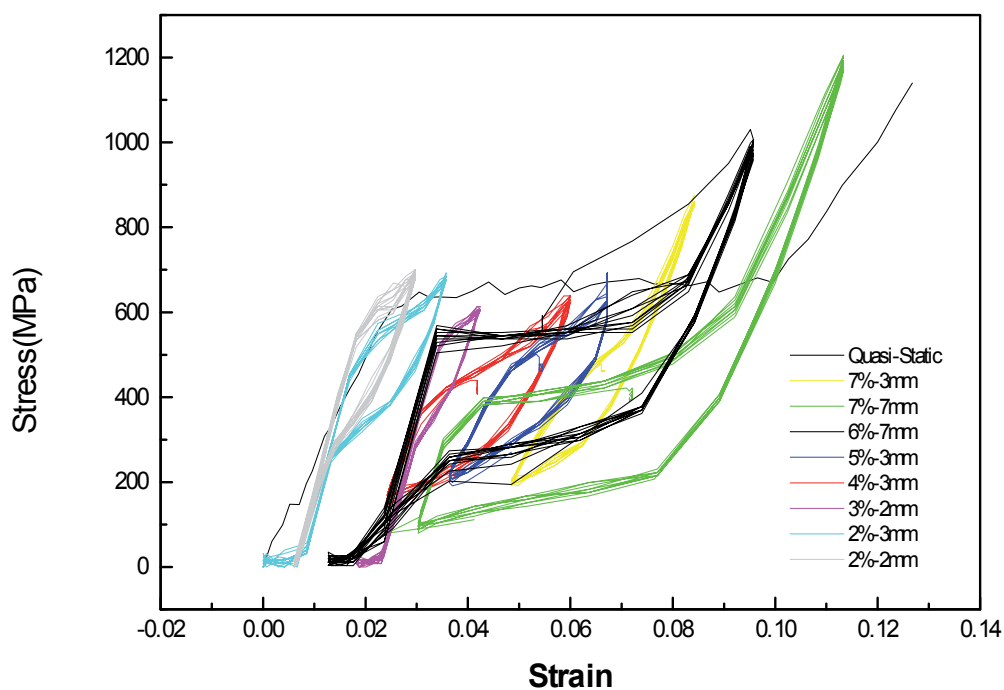Fig. 11. Effect of pre-strain on the energy dissipation (1.2 mm diameter wires)- frequency of loading 0.5 Hz

Fig. 12. Cyclic behavior of pre strained wires for varying pre strains. [The legend denotes pre strain %-reverse displacement cycles from that prestrain (mm)]

average equivalent damping ratio of 16% was realized during the test [Sreekala et al, 2008]. It is found to be nearer to half the super-elastic range obtained from quasi-static tests. Results indicate that if the super elastic wires have to play an energy-dissipating role, cycling around the threshold pre-strain value within this range is desirable [Sreekala et al,2010]. In this case the energy dissipation is dependent on the strain value in the super-elastic range from where cycling the entire range fetches maximum, as seen in figure 4.

For wires without pre strain, the equivalent damping ratio observed is in the order of 3%. This is because during cycling, the reverse direction (compressive region) does not contribute for the energy dissipation in non pre-strained wires. Tests on virgin wires shows lesser damping and energy dissipation capacity and these results can be compared with those under MANSIDE project. The design of the SMA based devices can be made by choosing the mechanical properties such as transformation stress levels/ plateau strength as design variables. Fig.14 shows the hysteretic behaviour of the different types of devices that can be developed using the properties of the SMA material. A variety of hysteretic behaviour can be obtained from the material tested and its application can be made suitable for seismic devices like re-centering, supplemental re-centering or in the case of non re-centering devices. These results reveal the suitability of using pre strained SMA wires in vibration control applications, especially for Non Re-Centering Devices-NRCD as seen in Fig.14. Normally pre straining of wires in vibration control devices requires highly skilled labour and maintenance becomes a difficult procedure. As far as the numbers of cycles are concerned, pre strained wires also goes beyond 900 cycles under constant amplitude loading. e.g.:-in 6% pre strained wire, under the maximum pseudo-elastic range goes up to 940 cycles before failure. No reduction in the energy dissipation is observed up to 30 cycles, but towards the failure 30 % reduction is observed as in non-pre strained wire. Usually for seismic applications, the numbers of cycles to be considered are less than 500 cycles as per various codal spectrums for seismic design in different countries. Table 1 summarizes the number of cycles, energy dissipation capacity per cycle, the strain variation and the equivalent damping. These results reveal the suitability of using SMA wires in seismic vibration control applications.

The usable strain range of the order of 10% in the alloys provide them very high energy dissipation per unit mass of material. Re-centering devices gain the best mechanical characteristics of both quasi-elastic devices (e.g., rubber isolators) and elasto-plastic devices (e.g., steel hysteretic dampers). On the one hand, they recover the initial position of the structure, with a good control of the displacements; on the other hand they put a threshold to the force transmitted to the super-structure. The full possibility of designing the mechanical behavior combining the self-centering and the energy dissipation capability, permit to calibrate the desired features and fit the specific needs. The availability of such features opens considerable room for improvement of the structural system design. Fig 7 indicates the various device options for passive vibration control using this material. But the mechanical behavior of SMAs is strongly dependent upon the alloy composition and the thermo-mechanical treatment. Special care should be taken while alloy selection is made.

6. Equivalent viscous damping

Some significant quantities usually employed in earthquake engineering to characterize the dissipation capability of the material under investigation are equivalent viscous damping, secant stiffness and energy loss per cycle. The equivalent viscous damping expresses the

effectiveness of the material in vibration damping. It is calculated based on the average energy dissipated per cycle. It is calculated as

$$\xi_{eq.} = W_D / (2\Pi \, K_S \delta^2) \tag{1}$$

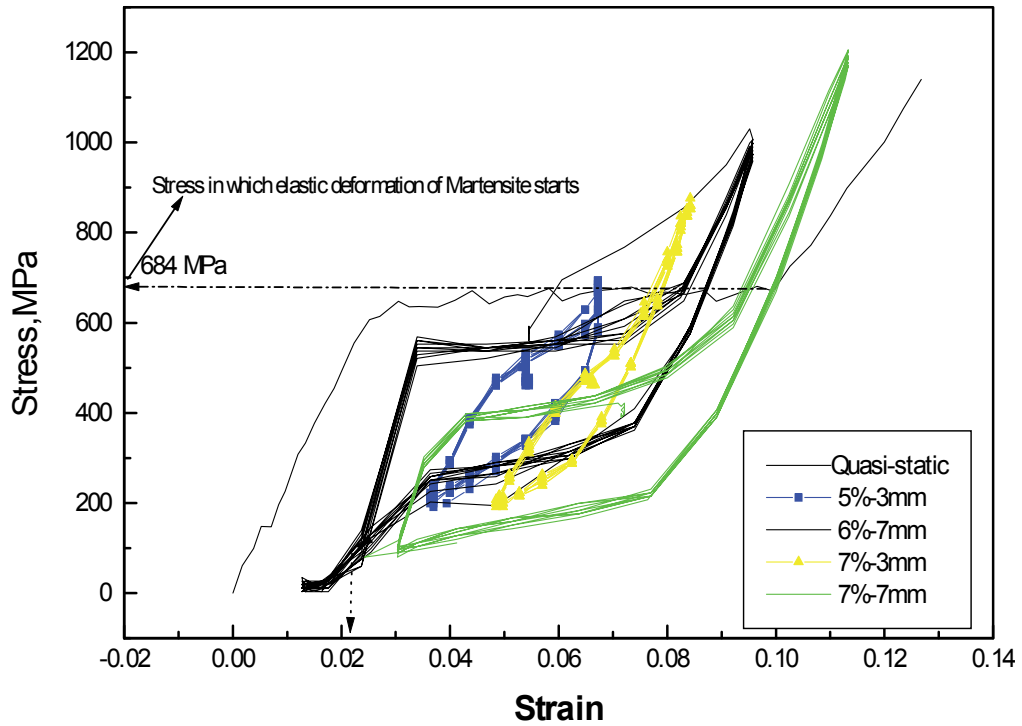Fig. 13. Cyclic behavior of pre strained wires –maximum energy dissipation when pre-strained almost at the middle of the pseudo-elastic range. [The legend denotes pre strain %-displacement cycles (mm)]
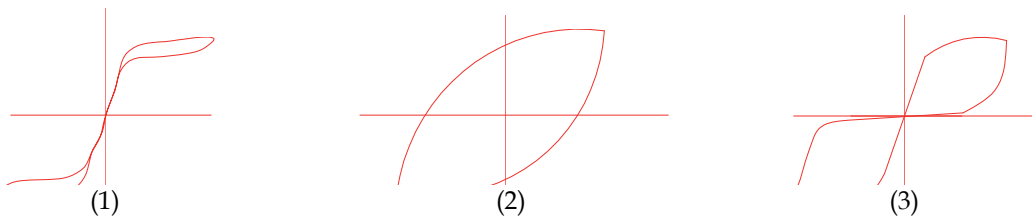

Fig. 14. Load –deformation behavior (Hysterisis curves) for various types of   Devices based on SMA, SRCD-Supplementary Re-Centering Device, NRCD-Non Re-centering Devices, and RCD-Re-centering Devices

where W_D is the energy loss per cycle and δ is the maximum cyclic displacement under consideration. The secant stiffness (K_s) is computed as

K_s = (F_{max} - F_{min}) / (δ_{max} - δ_{min}) where F_{max} and F_{min} are the forces attained for the maximum cyclic displacements δ_{max} and δ_{min}. The associated energy dissipation and the equivalent viscous damping calculated are included in Table.1.

The effect of pre-strain is found at 2.5% pre strain applied in the form of deformation to the sample, on two cyclic strains namely 4 % and 6 % (Fig.11.). An increase in the energy dissipation can be observed as the cyclic strain amplitude increases. The energy dissipated during cycling in pre-strained wires is considerably high compared to non-pre strained wires as observed from the experiment. It is interested to observe that (Fig.13) leaving the flat plateau; the response follows the elastic curve below 2% strain as obtained from the quasi-static test. Hence the quasi- static behaviour gives the envelope curve for the cyclic actions and a variety of hysteretic behaviour suitable for seismic devices can be obtained with pre straining effect [Sreekala et al, 2010].

7. Modeling the maximum energy dissipation for the material under study

It is observed from the experiment that the wires pre strained to the middle of the strain range gives the maximum energy dissipation(fig. 8). The behaviour can be predicted using the following mathematical expressions.

$$\sigma = E\left[\varepsilon - |\varepsilon| \{ 1 / \left(\frac{\sigma - \beta}{Y} \right)^n \} + \sigma_* \right] \tag{2}$$

$$\varepsilon = \left[\frac{\sigma}{E} + |\varepsilon| \{ 1 / \left(\frac{\sigma - \beta}{Y} \right)^n \} - \frac{\sigma_*}{E} \right] \tag{3}$$

σ_* denotes the stress in the pre strained wire at the beginning of the cycling. Here β can be expressed as

$$\beta = E\alpha \left\{ \varepsilon^{in} + f_T \left| \varepsilon^c \right| erf(\alpha\varepsilon) \left[u\left(-\varepsilon\dot{\varepsilon} \right) \right] \right\} \tag{4}$$

β denotes the one dimensional back stress, Y is the "yield" stress ,that is the beginning of the stress- induced transition from austenite to martensite, n is the overstress power. In equation (4) the unit step function activates the added term only during unloading processes. In the descending curve it contributes to the back stress in a way that allows for SMA stress-strain description. The term with (.) shows the ordinary time derivative.

$\alpha = \dfrac{E_y}{\left(E - E_y \right)}$ is a constant controlling the slope of σ – ε, where E is the elastic modulus of

austenite and E_y is the slope after yielding.

Inelastic strain, ε^{in} ,is given by

$$\varepsilon^{in} = \varepsilon - \frac{\sigma}{E} \tag{5}$$

The error function, erf(x) ,and the unit step function, u(x) are defined as follows.

$$erf(x) = \frac{2}{\sqrt{\Pi}} \int e^{-t^2} dt \qquad (6)$$

$$u(x) = 1 \ , x \geq 0 \qquad (7)$$

$$u(x) = 0 \ , x < 0 \qquad (8)$$

The basic expression obtained here for pre-strained wires is a modified form of the model suggested by wilde et al, [12] which is used for predicting the tensile behaviour of SMA materials. This mathematical expression describes the mechanical response of materials showing hysteresis.

$$\dot{\sigma} = E\left[\dot{\varepsilon} - \left|\dot{\varepsilon}\right| \left(\frac{\sigma - \beta}{Y}\right)^n \right] \qquad (9)$$

where σ is the one dimensional stress and ε is the one-dimensional strain, β is the one dimensional back stress , E elastic modulus , Y the yield stress and n the constant controlling the sharpness of the transition from elastic to plastic states.

The modified Cozzarelli model suggested by Wilde et al represents the hardening of the material after the transition from austenite to martensite is completed. Here in this case for pre strained wires for maximum energy dissipation, the hardening branch has not been considered which requires additional terms containing further unit step functions. The model is rate and temperature independent. The requirement of zero residual strain at the end of the loading process motivated the selection of the particular form of back stress through the unit step function. The coefficients f_t, and c are material constants controlling the recovery of the elastic strain during unloading. Since the stress and strain were found to be independent of the rate, the time differential can be eliminated. Hence equation (2) and (3) can be used for predicting the behaviour after many cycles by appropriately changing the values of 'n' and the starting stress value which follows the trend as in fig. 15. The material constants for the wires tested were obtained as

f_t = 0.115, C =0.001, n = 0.25,   α = 0.055. Using Equations (2) and (3) the curves are fitted. Fig. 15 gives the fitted curve for the maximum energy dissipation for the material tested.

8. Various seismic response mitigation strategies

Earthquake engineering has witnessed significant development during the course of the last two decades. Seismic isolation and energy dissipation are proved to be the most efficient tools in the hands of design engineer in seismic areas to limit both relative displacements as well as transmitted forces between adjacent structural elements to desired values. Parallel development of new design strategies (the seismic software) and the perfection of suitable mechanical devices to implement the strategies (the seismic hardware) made it possible to achieve efficient seismic response control. An optimal combination of isolator and the energy dissipater ensures complete protection of the structure during earthquake. Energy dissipation and re-centering capability are the two important functions to cater this need.

Most of the devices now in practice have poor re-centering capabilities. Instead of using a single device a combination of devices can provide significant advantages
The chart shown below Fig.18 illustrates the various seismic response mitigation strategies.
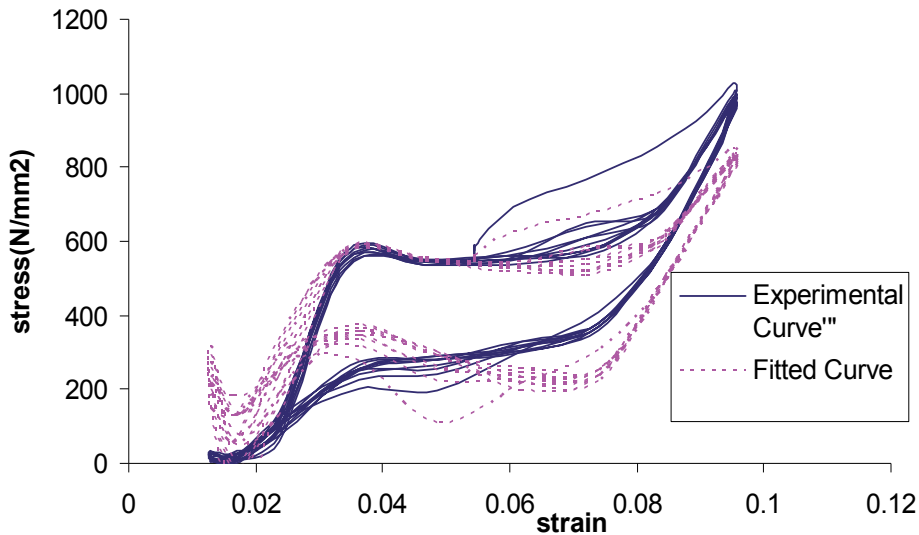
Fig. 15. Cyclic behaviour of prestrained wires –maximum energy dissipation obtained and the fitted curve.
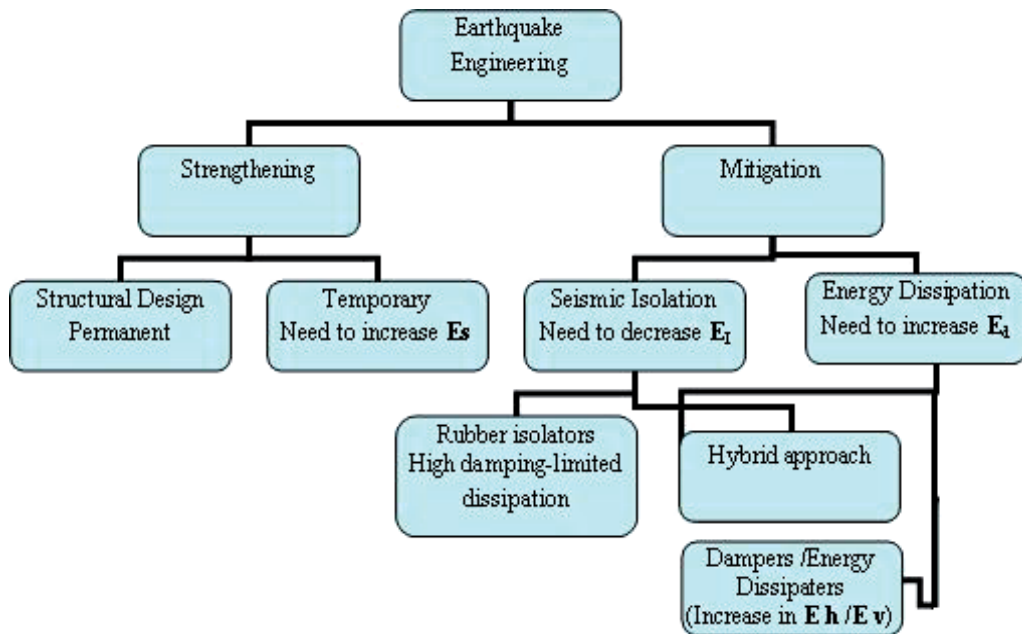
Fig. 16. Various seismic response mitigation strategies

Sl.no:	Nature of Test	Pre- strain in the wire	Cycling Strain range (%)	Average energy dissipated per cycle X10^{-2} J	No: of cycles	Equivalent viscous damping
1		7%	6.5-7.5	00.30	10	0.02
			6.0-8.0	00.60	10 [a]	0.02
			5.0-9.0	06.70	10 [a]	0.06
			4.0-10.0	18.60	10 [a]	0.07
			3.0-11.0	33.00	10 [a]	0.09
			1.3-12.0	-	-	-
2	Dynamic Tests	6%	2-10	33.80	10	0.16
				27.00	50 [a]	0.11
				21.00	500 [a]	0.09
3		5%	4.5-5.5	00.50	10	0.04
			4.0-6.0	04.60	10 [a]	0.13
			3.0-7.0	07.70	10 [a]	0.12
4	Freq. of operation 0.5 Hz. (Sinusoidal cyclic)	4%	3.5-4.5	00.33	10	0.02
			3.0-5.0	05.40	10 [a]	0.16
			2.0-6.0	10.35	10 [a]	0.16
5		3%	2.5-3.5	01.01	10	0.05
			2.0-4.0	01.91	10 [a]	0.04
6		2%	1.5-2.5	01.50	10	0.10
			1.0-3.0	04.40	10 [a]	0.10
			0.0-4.0	05.10	10 [a]	0.07
7		Nil	-3 - +3	07.30	25.	0.03
			-3 - +3	06.40	328 [a]	0.03
			-4 - +4	05.10	560 [a]	0.04
8		Nil	-3 - +3	05.60	1500	0.03
			-7 - +7	10.90	140 [a]	0.045

Table 1. Evaluated parameters of the Nitinol wire.
[a] - denotes the number of cycles which are followed by the cumulative previous cycles.

From this diagram it is clear that for seismic mitigation, a combination of Seismic isolation and Energy Dissipation is beneficial. Seismic Isolation can be implemented as explained below:
-    Through the reduction of the seismic response subsequent to the shift of the fundamental period of the structure in an area of the spectrum poor in energy content
-    Through the limitation of the forces transmitted to the base of the structure. A high level of energy dissipation also characterizes this approach. So it represents a combination of the two strategies of seismic mitigation. Isolation systems must be capable of ensuring the following functions:
    1.   transmit vertical loads,
    2.   provide lateral flexibility,
    3.   provide restoring force,
    4.   provide significant energy dissipation.

In each device, the constituent elements assume one or more of the four fundamental functions listed above. Some of the cases hybrid systems prove to be very much beneficial. For example, the strategy need to be adopted in suspension bridges is that of isolation and energy dissipation as the vertical cables did not provide energy dissipation characteristics. Hence dampers need to be provided and the hybrid system provide adequate protection during seismic response. The Table 2 below provide various energy dissipators/dampers along with their principle of operation

Classification	Principles of operation
Hysteritic devices	Yielding of metals Friction
Visco elastic devices	Deformation of visco elastic solids Deformation of visco elastic fluids Fluid orificing
Re centering Devices	Fluid pressurization and orificing Friction spring action **Phase transformation of metals (Shape memory alloys belong to this category)**
Dynamic vibration absorbers	Tuned mass dampers Tuned liquid dampers

Table 2.Various energy dissipation devices/damper

Fig. 17. Example of Composite Rubber/SMA spring damper

The unique constitutive behaviors of Shape Memory Alloys have attracted the attention of researchers in the civil engineering community. The collective results of these studies suggest that they can be used effectively for vibration control of structures through vibration isolation and energy absorption mechanisms. Possible applications of SMA based devices on Various structures for vibration control is shown in Fig.18,

For the analysis of structures, an equivalent Single Degree Of Freedom (SDOF) system can be utilized. The following mechanical model can represent the behavior of the energy dissipating system (Fig.19a). If re centering device is utilized the hysterisis should be adequately represented using mathematical models.

(i)

(ii)

(iii)
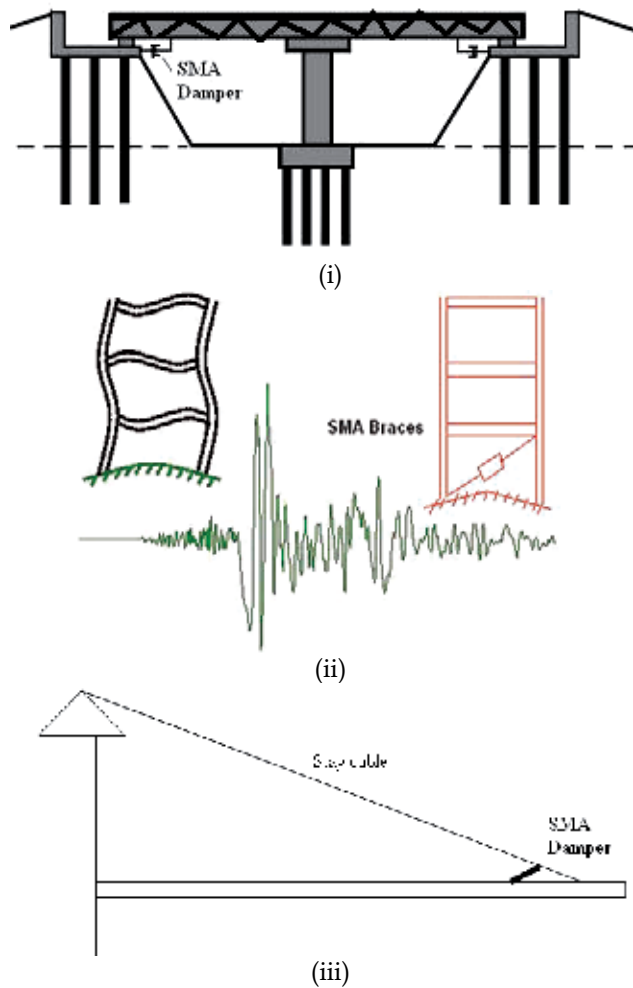
Fig. 18. Possible Applications of the Devices (i) Restrainers in Bridges (ii) Diagonal braces in buildings (iii) Cable stays (iv) combination of isolators and dampers in bridges

a)   b)
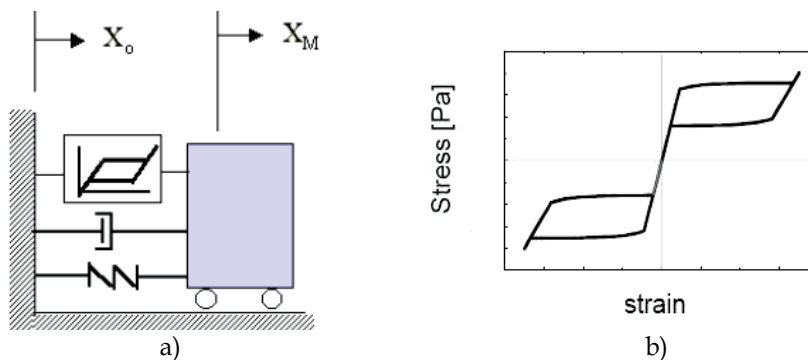
Fig. 19. a) Equivalent mechanical model of the SDOF scaled structure
b) The hysterisis /energy dissipation behavior of the re-centering device

9. Conclusion

There have been considerable research efforts in seismic response control for the past several decades. Due to the distinctive macroscopic behaviour like super elasticity, Shape Memory Alloys are the basis for innovative applications such as devices for protecting buildings from structural vibrations. Super elastic properties of Nitinol wires have been established from the experiments conducted and the salient features to be highlighted from the study are

- The material's application can be made suitable for seismic devices like recentering, supplementally recentering or in the case of non-recentering devices, as a variety of hysteretic behaviors were obtained from the tests.
- Cyclic behavior of the non pre strained wires especially energy dissipation capability, equivalent viscous damping and secant stiffness are not very sensitive to the number of cycles in the frequency range of interest (0.5- 3Hz.) as observed from constant amplitude loading.
- Pre-strained super elastic wires shows higher energy dissipation capability and equivalent damping when cycled around the midpoint of the strain range obtained from quasi-static curve. It is found from the experiment that the pre strain value of 6 %, with amplitude cycles which covers 2-10% gives higher energy dissipation.
- For possible application of vibration control devices in structural systems, a judicious selection of the wire under tension mode can be selected between pre strained and non-pre strained wires. However application of pre strained wires in the system provides excellent energy dissipation characteristics but it requires skilled and sophisticated mechanism to maintain/provide the required pre strain.
- The mathematical model predicts the maximum energy dissipation capability of the material namely pre strained nitinol wires under study.
- The test results shows immense promise on SMA based devices which can be used for vibration control of variety of structures(New designs and restoration of structures). SMA structural elements/devices can be located at key locations of the structure to reduce the seismic vibrations.

10. Acknowledgment

11. References

Birman, V (1997) Review of Mechanics of Shape Memory Alloy Structures *Applied Mechanics Review* 50 629-645

Birman, V (1997) Effect of SMA dampers on nonlinear vibrations of elastic structures *Proceedings of SPIE* 3038 ,268-76

Clark, P W; Aiken, I D; Kelly, J M; Higashino, M and Krumme, R C(1996) Experimental and analytical studies of shape memory alloy damper for structural control *Proc. Passive damping (San Diego,CA 1996)*

Cardone D, Dolce M, Bixio A and Nigro D 1999 Experimental tests on SMA elements *MANSIDE Project (Rome, 1999) (Italian Department for National Technical Services)* II85-104 Da GZ, Wang TM, Liu Y, Wamg CM(2001) Surgical treatment of tibial and femoral fractures with TiNi Shape memory alloy interlocking intra medullary nails *The international conference on Shape Memory and Superelastic Technologies and Shape Memory materials, Kunming, China*

Dolce M (1994) Passive Control of Structures Proceedings of the 10th European Conference on Earthquake Engineering, Vienna, 1994.

Duerig, T; Tolomeo, D and Wholey, M. (2000), An overview of superelastic stent design *Minimally Invasive Therapy & Allied Technologies. , 2000:9(3/4) 235–246.*

Eaton, J P. (1999) Feasibility study of using passive SMA absorbers to minimize secondary system structural response , *Master Thesis ,Worcester polytechnic Institute, M A*

Humbeeck, JV (2001) Shape Memory Alloys: a material and a technology *Advanced Engieering Materials* 3 837-850

Miyazaki, S; Imai, T; Igo, Y. And Otsuka, K(1986b), Effect of cyclic deformation on the pseudoelasticity characteristics of Ti–Ni alloys. *Metall. Trans. A.* 17115–120.

Pelton, A; DiCello,J; and Miyazaki,S. , (2000), Optimisation of processing and properties of medical grade nitinol wire. *Minimally Invasive Therapy & Allied Technologies. ,* 2000:9(1) 107–118.

Sreekala, R; Avinash, S; Gopalakrishnan, N; and Muthumani, K(2004) Energy Dissipation and Pseudo Elasticity in NiTi Alloy Wires *SERC Research Report* MLP 9641/19, October 2004

Sreekala, R; Avinash, S; Gopalakrishnan, N; Sathishkumar, K and Muthumani, K(2005) Experimental Study on a Passive Energy Dissipation Device using Shape Memory Alloy Wires, *SERC Research Report* MLP 9641/21, April 2005

Sreekala,. R;. Muthumani, K; Lakshmanan, N; Gopalakrishnan, N & Sathishkumar, K (2008),. Orthodontic arch wires for seismic risk reduction, *Current Science*, ISSN:0011-3891, Vol. 95, No:11, pp 1593-1599.

Sreekala,. R,;. Muthumani,. K(2009),. Structural Application of Smart materials,. In:. *Smart Materials,.* Edited by Mel Shwartz, . CRC press, Taylor & Francis Group,. pp. 4-1 to 4-7,. Taylor &Francis Publications,. ISBN-13:978-1-4200-4372-3,. Boca raton, FL,USA

Sreekala,. R;. Muthumani, K; Lakshmanan, N; Gopalakrishnan, N; Sathishkumar, K; Reddy, G,R & Parulekar Y M. (2010),. A Study on the suitability of NiTi wires for Passive Seismic Response Control *Journal of Advanced Materials*, ISSN 1070-9789, Vol. 42, No:2,pp. 65-76.

Stöckel,D. and Melzer, *A. ,, Materials in Clinical Applications. ,* ed. P. Vincentini Techna Srl. ,1995, 791–98.

Wilde, K; Gardoni, P. , and Fujino Y. ,(2000) Base isolation system with shape memory alloy device for elevated highway bridges *Engineering Structures* 22 222-229.

Whys and Wherefores of Transmissibility

N. M. M. Maia[1], A. P. V. Urgueira[2] and R. A. B. Almeida[2]
[1]IDMEC-Instituto Superior Técnico, Technical University of Lisbon
[2]Faculdade de Ciências e Tecnologia, Universidade Nova de Lisboa
Portugal

1. Introduction

The present chapter draws a general overview on the concept of transmissibility and on its potentialities, virtues, limitations and possible applications. The notion of transmissibility has, for a long time, been limited to the single degree-of-freedom (SDOF) system; it is only in the last ten years that the concept has evolved in a consistent manner to a generalized definition applicable to a multiple degree-of-freedom (MDOF) system. Such a generalization can be and has been not only developed in terms of a relation between two sets of harmonic responses for a given loading, but also between applied harmonic forces and corresponding reactions. Extensions to comply with random motions and random forces have also been achieved. From the establishment of the various formulations it was possible to deduce and understand several important properties, which allow for diverse applications that have been envisaged, such as evaluation of unmeasured frequency response functions (FRFs), estimation of reaction forces and detection of damage in a structure. All these aspects are reviewed and described in a logical sequence along this chapter.

The notion of transmissibility is presented in every classic textbook on vibrations, associated to the single degree-of-freedom system, when its basis is moving harmonically; it is defined as the ratio between the modulus of the response amplitude and the modulus of the imposed amplitude of motion. Its study enhances some interesting aspects, namely the fact that beyond a certain imposed frequency there is an attenuation in the response amplitude, compared to the input one, i.e., one enters into an isolated region of the spectrum. This enables the design of modifications on the dynamic properties so that the system becomes "more isolated" than before, as its transmissibility has decreased.

Usually, the transmissibility of forces, defined as the ratio between the modulus of the transmitted force magnitude to the ground and the modulus of the imposed force magnitude, is also deduced and the conclusion is that the mathematical formula of the transmissibility of forces is exactly the same as for the transmissibility of displacements. As it will be explained, this is not the case for multiple degree of freedom systems.

The question that arises is how to extend the idea of transmissibility to a system with N degrees-of-freedom, i.e., how to relate a set of unknown responses to another set of known responses, for a given set of applied forces, or how to evaluate a set of reaction forces from a set of applied ones. Some initial attempts were given by Vakakis et al. (Paipetis & Vakakis, 1985; Vakakis, 1985; Vakakis & Paipetis, 1985; 1986), although that generalization was still

limited to a very particular type of N degree-of-freedom system, one where a set constituted by a mass, stiffness and damper is repeated several times in the vertical direction. The works of (Liu & Ewins, 1998), (Liu, 2000) and (Varoto & McConnell, 1998) also extend the initial concept to N degrees-of-freedom systems, but again in a limited way, the former using a definition that makes the calculations dependent on the path taken between the considered co-ordinates involved, the latter by making the set of co-ordinates where the displacements are known coincident to the set of applied forces.

An application where the transmissibility seems of great interest is when in field service one cannot measure the response at some co-ordinates of the structure. If the transmissibility could be evaluated in the laboratory or theoretically (numerically) beforehand, then by measuring in service some responses one would be able to estimate the responses at the inaccessible co-ordinates.

To the best knowledge of the authors, the first time that a general answer to the problem has been given was in 1998, by (Ribeiro, 1998). Surprisingly enough, as the solution is very simple indeed. In what follows, a chronological description of the evolution of the studies on this subject is presented.

2. Transmissibility of motion

In this section and next sub-sections the main definitions, properties and applications will be presented.

2.1 Fundamental formulation

The fundamental deduction (Ribeiro, 1998), based on harmonically applied forces (easy to generalize to periodic ones), begins with the relationships between responses and forces in terms of receptance: if one has a vector $\boldsymbol{F}_A$ of magnitudes of the applied forces at co-ordinates A, a vector $\boldsymbol{X}_U$ of unknown response amplitudes at co-ordinates U and a vector $\boldsymbol{X}_K$ of known response amplitudes at co-ordinates K, as shown in Fig. 1.
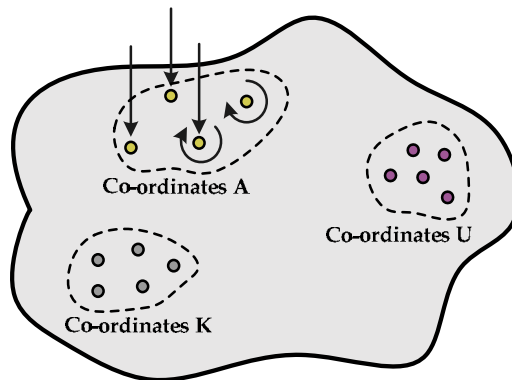
Fig. 1. System with co-ordinates A, U, K

One may establish the following relationships:

$$\boldsymbol{X}_U = \boldsymbol{H}_{UA}\,\boldsymbol{F}_A \qquad (1)$$

$$X_K = H_{KA}\, F_A \tag{2}$$

where H_{UA} and H_{KA} are the receptance frequency response matrices relating co-ordinates U and A, and K and A, respectively. Eliminating F_A between (1) and (2), it follows that

$$X_U = H_{UA}\, H_{KA}^+\, X_K \tag{3}$$

or

$$X_U = T_{UK}^{(A)}\, X_K \tag{4}$$

where H_{KA}^+ is the pseudo-inverse of H_{KA}. Thus, the transmissibility matrix is defined as:

$$T_{UK}^{(A)} = H_{UA}\, H_{KA}^+ \tag{5}$$

Note that the set of co-ordinates where the forces are (or may be) applied (A) need not coincide with the set of known responses (K). The only restriction is that – for the pseudo-inverse to exist – the number of K co-ordinates must be greater or equal than the number of A co-ordinates.

An important property of the transmissibility matrix is that it does not depend on the magnitude of the forces, one simply has to know or to choose the co-ordinates where the forces are going to be applied (or not, as one can even choose more co-ordinates A if one is not sure whether or not there will be some forces there and, later on, one states that those forces are zero) and measure the necessary frequency-response-functions.

2.2 Alternative formulation

An alternative approach, developed by (Ribeiro et al., 2005) evaluates the transmissibility matrix from the dynamic stiffness matrices, where the spatial properties (mass, stiffness, etc.) are explicitly included.

The dynamic behaviour of an *MDOF* system can be described in the frequency domain by the following equation (assuming harmonic loading):

$$Z\, X = F \tag{6}$$

where Z represents the dynamic stiffness matrix, X is the vector of the amplitudes of the dynamic responses and F represents the vector of the amplitudes of the dynamic loads applied to the system.

From the set of dynamic responses, as defined before, it is possible to distinguish between two subsets of co-ordinates K and U; from the set of dynamic loads it is also possible to distinguish between two subsets, A and B, where A is the subset where dynamic loads may be applied and B is the set formed of the remaining co-ordinates, where dynamic loads are never applied. One can write X and F as:

$$X = \begin{Bmatrix} X_K \\ X_U \end{Bmatrix}, \quad F = \begin{Bmatrix} F_A \\ F_B \end{Bmatrix} \tag{7}$$

With these subsets, Eq. (6) can be partitioned accordingly:

$$\begin{bmatrix} \boldsymbol{Z}_{AK} & \boldsymbol{Z}_{AU} \\ \boldsymbol{Z}_{BK} & \boldsymbol{Z}_{BU} \end{bmatrix} \begin{Bmatrix} \boldsymbol{X}_K \\ \boldsymbol{X}_U \end{Bmatrix} = \begin{Bmatrix} \boldsymbol{F}_A \\ \boldsymbol{F}_B \end{Bmatrix} \tag{8}$$

Taking into account that co-ordinates B represent the ones where the dynamic loads are never applied, and considering that the number of these co-ordinates is greater or equal to the number of co-ordinates U, from Eq. (8) it is possible to obtain the unknown response vector:

$$\boldsymbol{F}_B = \boldsymbol{0}, \quad \#B \geq \#U$$
$$\Downarrow \tag{9}$$
$$\boldsymbol{X}_U = -\boldsymbol{Z}_{BU}^+ \, \boldsymbol{Z}_{BK} \, \boldsymbol{X}_K$$

where $\boldsymbol{Z}_{BU}^+$ is the pseudo-inverse of $\boldsymbol{Z}_{BU}$. Therefore, this means that the transmissibility matrix can also be defined as

$$\boldsymbol{T}_{UK}^{(A)} = -\boldsymbol{Z}_{BU}^+ \, \boldsymbol{Z}_{BK} \tag{10}$$

Eq. (10) is an alternative definition of transmissibility, based on the dynamic stiffness matrices of the structure. Therefore,

$$\boldsymbol{T}_{UK}^{(A)} = \boldsymbol{H}_{UA} \, \boldsymbol{H}_{KA}^+ = -\boldsymbol{Z}_{BU}^+ \, \boldsymbol{Z}_{BK} \tag{11}$$

Taking into account that the dynamic stiffness matrix for an undamped system is described in terms of the stiffness and mass matrices, $\boldsymbol{Z} = \boldsymbol{K} - \omega^2 \boldsymbol{M}$, one can now relate the transmissibility functions to the spatial properties of the system. To make this possible, one must bear in mind that it is mandatory that both conditions regarding the number of co-ordinates be valid, i. e.,

$$\#B \geq \#U \quad \text{and} \quad \#K \geq \#A \tag{12}$$

2.3 Numerical example

An MDOF mass-spring system, presented in Fig. 2, will be used to illustrate the principal differences observed between the transmissibilities and FRFs curves. This is a six mass-spring system (designated as original system), possessing the characteristics described in Table 1.

The subsets of known and unknown responses are assumed as:

$$\boldsymbol{X}_K^T = \{X_2 \quad X_4 \quad X_6\}^T \quad \text{and} \quad \boldsymbol{X}_U^T = \{X_1 \quad X_3 \quad X_5\}^T \tag{13}$$

The number of loads can be grouped in the sub-set $\boldsymbol{F}_A$ (even if some of them are, in certain cases, null) and in subset $\boldsymbol{F}_B$.

$$\boldsymbol{F}_A^T = \{F_4 \quad F_5 \quad F_6\}^T \quad \text{and} \quad \boldsymbol{F}_B^T = \{F_1 \quad F_2 \quad F_3\}^T \tag{14}$$

According to Eq. (11), and considering the above-defined subsets, the transmissibility matrix is given by:

		Original System
kg	m_1	7
	m_2	7
	m_3	4
	m_4	3
	m_5	6
	m_6	8
N/m	k_1	10^5
	k_2	10^5
	k_3	4.0×10^5
	k_4	5.0×10^5
	k_5	7.0×10^5
	k_6	2.0×10^5
	k_7	8.0×10^5
	k_8	3.0×10^5
	k_9	6.0×10^5
	k_{10}	3.0×10^5
	k_{11}	5.0×10^5

Table 1. Characteristics of the original system
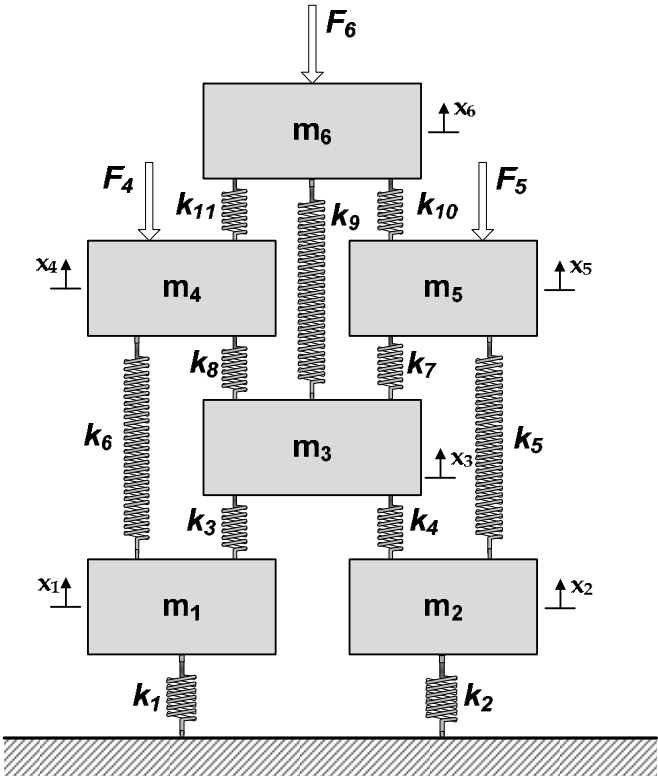

Fig. 2. Mass-spring MDOF system

$$
\begin{bmatrix} T_{12}^{(A)} & T_{14}^{(A)} & T_{16}^{(A)} \\ T_{32}^{(A)} & T_{34}^{(A)} & T_{36}^{(A)} \\ T_{52}^{(A)} & T_{54}^{(A)} & T_{56}^{(A)} \end{bmatrix} = \begin{bmatrix} H_{14} & H_{15} & H_{16} \\ H_{34} & H_{35} & H_{36} \\ H_{54} & H_{55} & H_{56} \end{bmatrix} \begin{bmatrix} H_{24} & H_{25} & H_{26} \\ H_{44} & H_{45} & H_{46} \\ H_{64} & H_{65} & H_{66} \end{bmatrix}^{+}
$$

$$
= - \begin{bmatrix} Z_{11} & Z_{13} & Z_{15} \\ Z_{21} & Z_{23} & Z_{25} \\ Z_{31} & Z_{33} & Z_{35} \end{bmatrix}^{+} \begin{bmatrix} Z_{12} & Z_{14} & Z_{16} \\ Z_{22} & Z_{24} & Z_{26} \\ Z_{32} & Z_{34} & Z_{36} \end{bmatrix}
\tag{15}
$$

The characteristics of the system of Fig. 2 are presented in Table 1.

It may be noted from Fig. 3 that the maxima of the transmissibility curves occur all at the same frequencies. It can also be observed that the maxima and minima of the transmissibility curves do not coincide with the maxima and minima of the FRF curves. No simple relationships (if any) can be established between the picks and anti-picks of the transmissibilities and FRFs. Transmissibilities have a local nature and therefore they do not reflect the existence of the global properties of the system (natural frequencies and damping ratios).
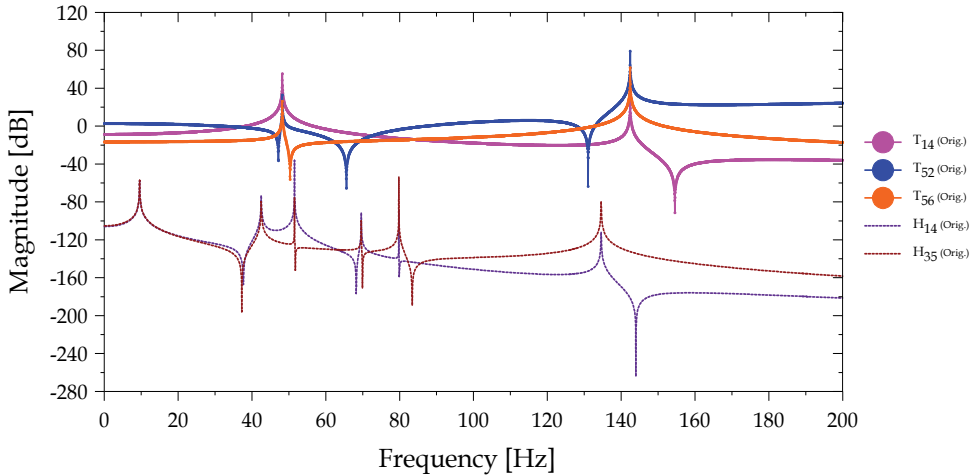
Fig. 3. Some transmissibilities and FRFs curves of the original system

2.4 Transmissibility properties

The formulation presented in section 2.1 allows us to extract some important properties for the transmissibility matrix $\boldsymbol{T}_{UK}^{(A)}$. From Eq. (3) and (5) it is possible to conclude that the *transmissibility matrix is independent from the force vector* $\boldsymbol{F}_A$ (Note that $\boldsymbol{F}_A$ is eliminated between eqs. (1) and (2)). This means that any change verified in one of the force values, acting along with co-ordinates of set A, will not affect $\boldsymbol{T}_{UK}^{(A)}$. This change can be due, for instance, to the alteration of mass values associated to co-ordinates A or stiffness values of springs interconnecting those co-ordinates.

Additionally, to highlight that characteristic of matrix $\boldsymbol{T}_{UK}^{(A)}$, it can be verified from Eq. (10) that there is no part of matrix $\mathbf{Z}$ involving co-ordinates of set A (neither $\boldsymbol{Z}_{AK}$ nor $\boldsymbol{Z}_{AU}$). This statement reinforces the previous conclusion extracted from Eq. (5) and will lead to the formulation of two properties, as follows:

Property 1. *The transmissibility matrix does not change if some modification is made on the mass values of the system where the loads can be applied – subset A.*

Property 2. *The transmissibility matrix does not change if some modification is made on the stiffness values of springs interconnecting co-ordinates of subset A – (where the loads can be applied).*

In fact, any changes in the mass values associated to co-ordinates A and/or any changes in the stiffness values of springs interconnecting co-ordinates A, will affect the inertia forces and elastic forces, respectively, acting along those co-ordinates and thus belonging to F_A.

The same MDOF system presented in Fig. 2 will be used to illustrate the transmissibility properties. In Table 2 four different modifications are made in the original system.

Situations I and II correspond to modifications on the original masses; situations III and IV correspond to modifications on stiffness. Situations I and III only involve co-ordinates A, whereas situations II and IV involve co-ordinates pertaining to both sets A and B.

Choosing, for instance, the transmissibility function $T_{52}^{(A)}$, one obtains the results presented in Figs. 4 and 5, where one can see that $T_{52}^{(A)}$ and $T_{14}^{(A)}$ remain the same only when changes are made at co-ordinates A, where the forces are applied.

2.5 Evaluation of the transmissibility from measurement responses

In 1999, (Ribeiro et al., 1999) and (Maia et al., 1999) showed how the transmissibility matrix could be evaluated directly from the measurement of the responses, rather than measuring the frequency response functions. In Eq. (4), the problem is to evaluate the $U \times K$ values of $T_{UK}^{(A)}$ knowing X_U and X_K. This can be achieved by applying various sets of forces, at a time, on co-ordinates A. Let $F_A^{(1)}$ be the first set of applied forces (amplitudes). Then,

$$X_U^{(1)} = T_{UK}^{(A)} X_K^{(1)} \tag{16}$$

		Original System	Situation I	Situation II	Situation III	Situation IV
kg	m_1	7	--	14	14	--
	m_2	7	--	--	--	--
	m_3	4	--	--	--	--
	m_4	3	13	--	--	--
	m_5	6	12	--	--	--
	m_6	8	--	13	13	--
			--	--	--	--
N/m	k_1	10^5	--	--	--	--
	k_2	10^5	--	--	--	--
	k_3	4.0×10^5	--	--	--	--
	k_4	5.0×10^5	--	--	--	10.0×10^5
	k_5	7.0×10^5	--	--	--	--
	k_6	2.0×10^5	--	--	--	--
	k_7	8.0×10^5	--	--	--	--
	k_8	3.0×10^5	--	--	--	--
	k_9	6.0×10^5	--	--	--	--
	k_{10}	3.0×10^5	--	--	9.0×10^5	--
	k_{11}	5.0×10^5	--	--	9.0×10^6	--

-- unchanged value

Table 2. Characteristics of the modifications made in the original system
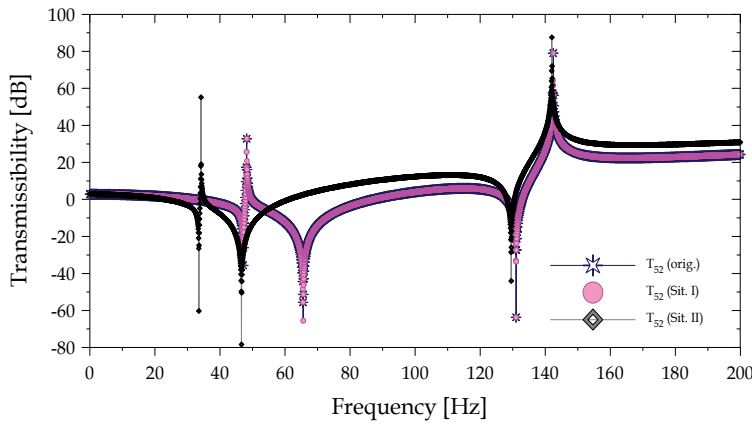
Fig. 4. Transmissibility $T_{52}^{(A)}$, for the original system and the modified systems I e II
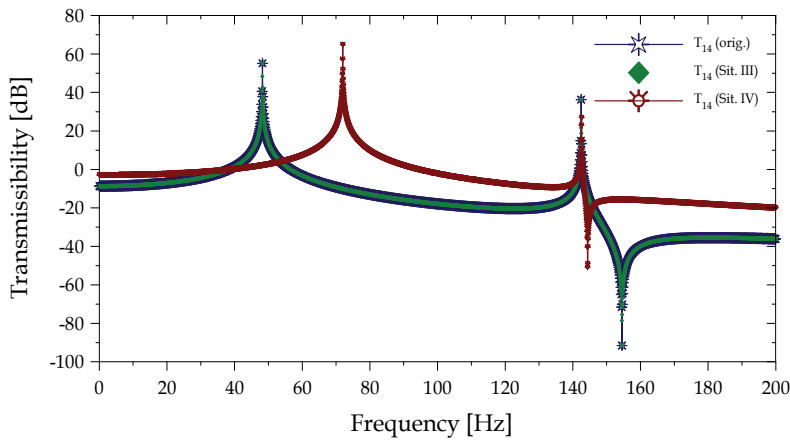
Fig. 5. Transmissibility $T_{14}^{(A)}$, for the original system and the modified systems III e IV

However, when forces change, the transmissibility matrix does not, although the responses themselves do. Therefore, if another test is performed, with a set of forces *linearly independent* of the first one – though applied at the same co-ordinates – $F_A^{(2)}$, a new set of U equations can be obtained, which are linearly independent of the first ones. If K tests are undertaken on the structure, with linearly independent forces always applied at the A set of co-ordinates, one can obtain a system of $U \times K$ equations to solve for the same number of $T_{UK}^{(A)}$ unknowns:

$$\begin{bmatrix} X_U^{(1)} & X_U^{(2)} & \cdots & X_U^{(K)} \end{bmatrix} = T_{UK}^{(A)} \begin{bmatrix} X_K^{(1)} & X_K^{(2)} & \cdots & X_K^{(K)} \end{bmatrix} \tag{17}$$

From which

$$T_{UK}^{(A)} = \begin{bmatrix} X_U^{(1)} & X_U^{(2)} & \cdots & X_U^{(K)} \end{bmatrix} \begin{bmatrix} X_K^{(1)} & X_K^{(2)} & \cdots & X_K^{(K)} \end{bmatrix}^{-1} \tag{18}$$

Note: an easy way to obtain the K sets of linearly independent forces is to apply a single force at each of the A locations at a time.

2.6 The distributed forces case

In (Ribeiro, Maia, & Silva, 2000b) the authors discussed the transmissibility between the two sets of co-ordinates U and K when a distributed force is applied to the structure. Such a force should be discretized to form the A set of applied forces. The issue was then to study what happened if one only took a subset of those co-ordinates A, which implies the reduction or condensation of the applied forces to such a subset and to ask the question: "how to study the transmissibility of responses from a set of condensed forces?". Let the set A be composed by the set C to where one wishes to condense the forces and the set D of the remaining co-ordinates, so that:

$$F_A = \begin{Bmatrix} F_C \\ F_D \end{Bmatrix} \tag{19}$$

If one wishes to condense F_A to F_C, one needs to assume some relationship between F_D and F_C, i.e, one cannot contemplate the case where all the applied forces are completely independent from each other. However, this is not a big restriction, as it seems reasonable to expect that the applied forces exhibit a more or less fixed spatial pattern along the structure. Therefore, let us assume a linear relationship between the sets of forces F_D and F_C, through the matrix P_{DC}:

$$F_D = P_{DC}\, F_C \tag{20}$$

If matrices H_{UA} and H_{KA} from eqs. (1) and (2) are partitioned into

$$H_{UA} = \begin{bmatrix} H_{UC} & \vdots & H_{UD} \end{bmatrix} \tag{21}$$

$$H_{KA} = \begin{bmatrix} H_{KC} & \vdots & H_{KD} \end{bmatrix} \tag{22}$$

and one has Eq. (19) into account, then eqs. (1) and (2) become

$$X_U = H_{UC}\, F_C + H_{UD}\, F_D \tag{23}$$

$$X_K = H_{KC}\, F_C + H_{KD}\, F_D \tag{24}$$

Substituting Eq. (20) in eqs. (23) and (24) and eliminating F_C, it follows that

$$X_U = \left(H_{UC} + H_{UD}\, P_{DC} \right)\left(H_{KC} + H_{KD}\, P_{DC} \right)^{+} X_K \tag{25}$$

Therefore, one has now, instead of Eq. (4), another one relating X_U and X_K, through a new transmissibility matrix referred to the new subset of co-ordinates C:

$$X_U = T_{UK}^{(C)}\, X_K \tag{26}$$

where

$$T_{UK}^{(C)} = \left(H_{UC} + H_{UD} \, P_{DC} \right) \left(H_{KC} + H_{KD} \, P_{DC} \right)^{+} \tag{27}$$

Note: for the pseudo-inverse to exist, the number of K co-ordinates must be higher than the number of C co-ordinates. This is obviously verified, as $\#K \geq \#A$ and $\#A > \#C$. It should also be stressed that although referred to a reduced set of co-ordinates C where the forces are applied, the transmissibility matrix still relates the responses U and K and so it keeps the same size.

In (Ribeiro, Maia, & Silva, 2000a), (Ribeiro, Maia, & Silva, 2000b) and (Maia et al., 2001) the authors summarize some of the previous works and suggest some other possible applications for the transmissibility concept, namely in the area of damage detection. In this area, there has been some activity trying to use the transmissibility as defined, as well as some other variations of it, with limited results in [(Sampaio et al., 1999; 2000; 2001)], but with some promising evolution in [(Maia et al., 2007)].

An example is presented in order to illustrate the above discussion: a cantilevered beam is subjected to the loading shown in Fig. 6.
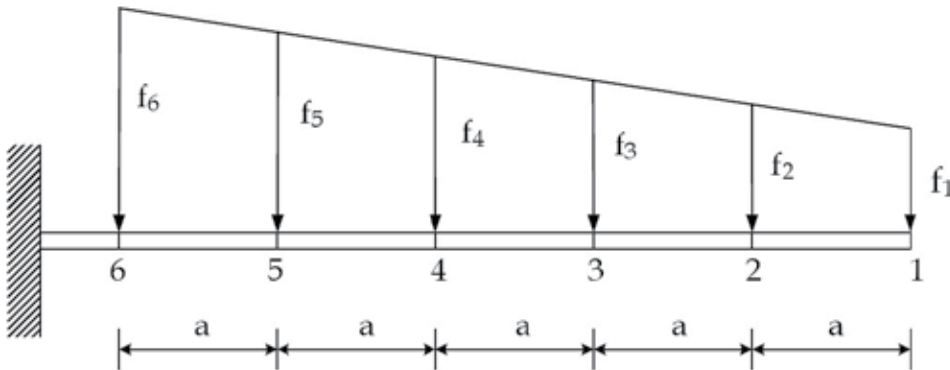
Fig. 6. Example of a loaded beam

It is assumed that forces are applied at co-ordinates 1 to 6 but the forces at co-ordinates 2 to 5 can be related to those applied at 1 and 6 through the expression:

$$F_D = P_{DC} \, F_C \quad \Rightarrow \quad \begin{Bmatrix} f_2 \\ f_3 \\ f_4 \\ f_5 \end{Bmatrix} = \frac{1}{5} \begin{bmatrix} 4 & 1 \\ 3 & 2 \\ 2 & 3 \\ 1 & 4 \end{bmatrix} \begin{Bmatrix} f_1 \\ f_6 \end{Bmatrix} \tag{28}$$

One can further assume that the responses at co-ordinates 1 and 2 can be measured and those at co-ordinates 4 and 5 can be computed through the transmissibility, i.e.,

$X_U = T_{UK}^{(C)} \, X_K$, with $X_U = \begin{Bmatrix} X_4 \\ X_5 \end{Bmatrix}$, $X_K = \begin{Bmatrix} X_1 \\ X_2 \end{Bmatrix}$ and

$$\boldsymbol{T}_{UK}^{(C)} = \left(\boldsymbol{H}_{UC} + \boldsymbol{H}_{UD}\,\boldsymbol{P}_{DC}\right)\left(\boldsymbol{H}_{KC} + \boldsymbol{H}_{KD}\,\boldsymbol{P}_{DC}\right)^{+} \;\Rightarrow$$

$$\boldsymbol{T}_{UK}^{(C)} = \left(\begin{bmatrix} H_{41} & H_{46} \\ H_{51} & H_{56} \end{bmatrix} + \frac{1}{5}\begin{bmatrix} H_{42} & H_{43} & H_{44} & H_{45} \\ H_{52} & H_{53} & H_{54} & H_{55} \end{bmatrix}\begin{bmatrix} 4 & 1 \\ 3 & 2 \\ 2 & 3 \\ 1 & 4 \end{bmatrix}\right)\left(\begin{bmatrix} H_{11} & H_{16} \\ H_{21} & H_{26} \end{bmatrix}\right.$$

$$\left. + \frac{1}{5}\begin{bmatrix} H_{12} & H_{13} & H_{14} & H_{15} \\ H_{22} & H_{23} & H_{24} & H_{25} \end{bmatrix}\begin{bmatrix} 4 & 1 \\ 3 & 2 \\ 2 & 3 \\ 1 & 4 \end{bmatrix}\right)^{+} \tag{29}$$

2.7 The random forces case

Often one has to deal with random forces, for instance when a structure is submitted to environmental loads. The cases that have been addressed so far were limited to harmonic or periodic forces. The generalization to random forces has been derived in [(Ribeiro et al., 2002; Fontul et al., 2004)], now in terms of power spectral densities, rather than in terms of response amplitudes. Let $\boldsymbol{S}_{KK}$ denote the auto-spectral density of the responses $\boldsymbol{X}_K$ and $\boldsymbol{S}_{KU}$ the cross-spectral density between responses $\boldsymbol{X}_K$ and $\boldsymbol{X}_U$. Then, it can be shown (see [(Fontul, 2005)] for specific details) that both are related through the same transmissibility matrix as before (using Eq. (5), for instance):

$$\boldsymbol{S}_{KU}^{T} = \boldsymbol{T}_{UK}^{(A)}\,\boldsymbol{S}_{KK}^{T} \tag{30}$$

2.8 Some possible applications
2.8.1 Transmissibility of motion in structural coupling

This topic has been addressed in (Devriendt, 2004; Ribeiro et al., 2004; Devriendt & Fontul, 2005). Let us consider a main structure, to which an additional structure is coupled though some coupling co-ordinates, i.e., the additional structure applies a set of forces (and moments) to the main structure. As the transmissibility between two sets of responses on the main structure does not depend on the magnitude of those forces, the transmissibility matrix of the main structure is equal to the transmissibility matrix of the total structure (main + additional). In other words, under certain conditions, the transmissibility matrix of the main structure remains unchanged, even if an additional structure is coupled to the main one. To make this property valid it is necessary to consider a sufficient number of coupled co-ordinates. Although it might be argued that a reduced number of coupling co-ordinates would hamper the results since it would not include information about some modes, it has been shown in (Devriendt, 2004; Ribeiro et al., 2004; Devriendt & Fontul, 2005) that, as long as there is enough information regarding the modes included in the frequency range of interest the minimum number of coupling co-ordinates can be reduced without deterioration of the results.

2.8.2 Evaluation of unmeasured frequency response functions

Recent papers [(Maia et al., 2008; Urgueira et al., 2008)] have explored some invariance properties of the transmissibility, namely when modifications are made in terms of masses

and/or stiffnesses at the co-ordinates where the forces are applied, to be able to estimate the new FRFs in locations that become no longer accessible. For instance, if one calculates the transmissibility matrix at some stage between two sets of responses for a given set of applied forces and later on there are some modifications at the force co-ordinates due to some added masses, the FRFs will change but the transmissibility remains the same. This allows the estimation of the new FRFs. So, initially one has $X_U{}^{(1)} = H_{UA}{}^{(1)} H_{KA}{}^{+}{}^{(1)} X_K{}^{(1)}$ and later on one has $X_U{}^{(2)} = H_{UA}{}^{(2)} H_{KA}{}^{+}{}^{(2)} X_K{}^{(2)}$. As the transmissibility remains unchanged, one has

$$T_{UK}^{(A)} = H_{UA}{}^{(1)} H_{KA}^{+}{}^{(1)} = H_{UA}{}^{(2)} H_{KA}^{+}{}^{(2)} \tag{31}$$

and one can calculate, for instance, $H_{UA}{}^{(2)}$, given by:

$$H_{UA}{}^{(2)} = T_{UK}^{(A)} H_{KA}{}^{(2)} \tag{32}$$

2.9 Direct transmissibility
From the definition given before one has,

$$X_U = H_{UA} H_{KA}^{+} X_K = T_{UK}^{(A)} X_K \tag{33}$$

which, as explained, is a generalisation from the one degree of freedom system. However, in some cases it might be useful to divide two responses directly. In strict sense that is a transmissibility only if a single force is applied. Otherwise, one has to name it differently, like pseudo-transmissibility (e.g. (Sampaio et al., 1999)), scalar transmissibility (Devriendt et al., 2010) or direct transmissibility, which is the one we shall adopt.

Direct transmissibilities will depend on the force magnitudes (as well as location, of course). For example, dividing Eq. (33) by one of the amplitudes X_K, say X_s, one has:

$$X_U/X_s = T_{UK}^{(A)} X_K/X_s \quad \text{or} \quad \tau_{Us} = T_{UK}^{(A)} \tau_{Ks} \tag{34}$$

It is easier to understand the implications of both definitions through an example: let X_U, X_K, and F_A be given respectively by

$$X_U = \begin{Bmatrix} X_1 \\ X_2 \end{Bmatrix} \quad X_K = \begin{Bmatrix} X_3 \\ X_4 \end{Bmatrix} \quad F_A = \begin{Bmatrix} F_5 \\ F_6 \end{Bmatrix} \tag{35}$$

The relation between X_U and X_K would be:

$$\begin{Bmatrix} X_1 \\ X_2 \end{Bmatrix} = \begin{bmatrix} T_{13} & T_{14} \\ T_{23} & T_{34} \end{bmatrix} \begin{Bmatrix} X_3 \\ X_4 \end{Bmatrix} \quad \Rightarrow \quad \begin{matrix} X_1 = T_{13}X_3 + T_{14}X_4 \\ X_2 = T_{23}X_3 + T_{24}X_4 \end{matrix} \tag{36}$$

Dividing Eq. (36) by, say, X_3, it follows that

$$\begin{matrix} X_1/X_3 = T_{13} + T_{14} X_4/X_3 \\ X_2/X_3 = T_{23} + T_{24} X_4/X_3 \end{matrix} \quad \text{or} \quad \begin{matrix} \tau_{13} = T_{13} + T_{14}\tau_{43} \\ \tau_{23} = T_{23} + T_{24}\tau_{43} \end{matrix} \tag{37}$$

One can also write:

$$\begin{cases} X_1 = H_{15}F_5 + H_{16}F_6 \\ X_3 = H_{35}F_5 + H_{36}F_6 \end{cases} \quad \Rightarrow \quad \tau_{13} = \frac{X_1}{X_3} = \frac{H_{15}F_5 + H_{16}F_6}{H_{35}F_5 + H_{36}F_6} \tag{38}$$

From Eq. (38) it is clear that the direct transmissibility τ_{13} depends on the magnitudes of F_5 and F_6, unless the relation F_5/F_6 remains constant. Only in the case where there is just a single force one has a coincidence between both types of transmissibility.

Both kinds of definitions can be useful. For instance, concerning now the direct transmissibilities, one can see that from Eq. (37) one can calculate τ_{13} and τ_{23} from τ_{43}, and one can eliminate τ_{43} between both equations and establish a relationship between τ_{13} and τ_{23}, therefore allowing the evaluation of one of them from the other. Moreover and similarly to what was mentioned in section 2.5, the direct transmissibilities allow the calculation of the other ones.

To illustrate the main differences between the curves of general and the direct transmissibilities, the MDOF system presented in Fig. 2 has been used. In Fig. 7 some direct transmissibility curves are presented.
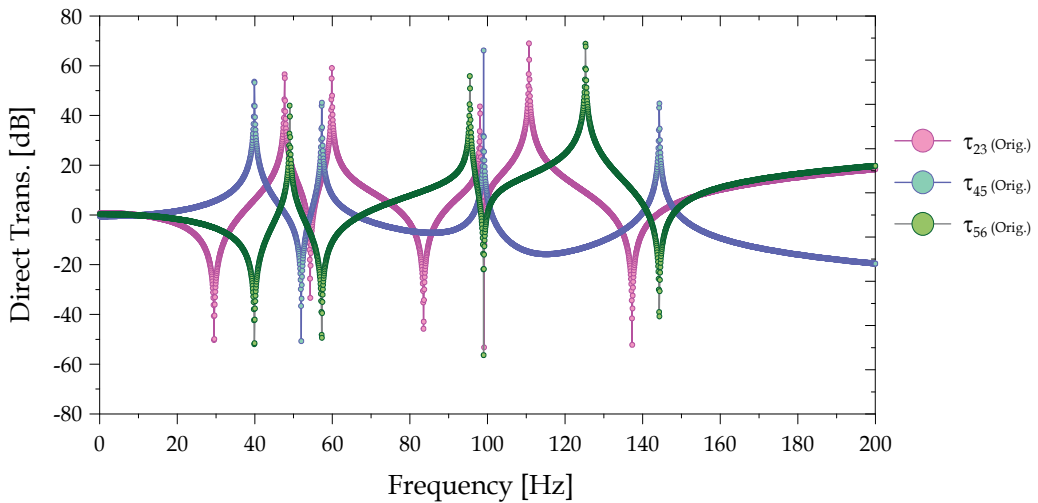
Fig. 7. Some direct transmissibility curves from the system of Fig. 2

By comparing the results of the transmissibilities of Fig. 3 with the curves obtained with the direct transmissibilities, Fig. 7, one can see that both look like FRFs, though it may be noted that in the case of the transmissibilities all the maxima occur at the same frequencies; the same is not true with the direct transmissibilities, where each curve presents distinct maxima.

2.10 Other applications

Other works have presented the possibility of using the transmissibility concept for model updating (Steenackers et al., 2007) and to identify the dynamic properties of a structure (Devriendt & Guillaume, 2007; Devriendt, De Sitter, et al., 2009; Devriendt et al., 2010).

Other recent studies have applied the transmissibility to the problem of transfer path analysis in vibro-acoustics (Tcherniak & Schuhmacher, 2009) and for damage detection (Canales et al., 2009; Devriendt, Vanbrabant, et al., 2009; Urgueira et al., 2011).

3. Transmissibility of forces

3.1 In terms of frequency response functions

Another important topic may be the prediction of the dynamic forces transmitted to the ground when a machine is working. For a single degree of freedom, the solution is well known and the transmissibility is defined as the ratio between the transmitted load (the ground reaction) and the applied one, for harmonic excitation. For an MDOF system, one has to relate the known applied loads (F_K) to the unknown reactions (F_U), Fig. 8.

The displacements at the co-ordinates of one set (the set of the reactions) are constrained, so they must also be known (possibly zero).

The inverse problem may also be of interest, i.e., to estimate the loads applied to a structure (wind, traffic, earthquakes, etc.) from the measured reaction loads. Once the load transmissibility matrix is established between the appropriate sets, the measurement of the reactions is expected to allow for the estimation of the external loads.
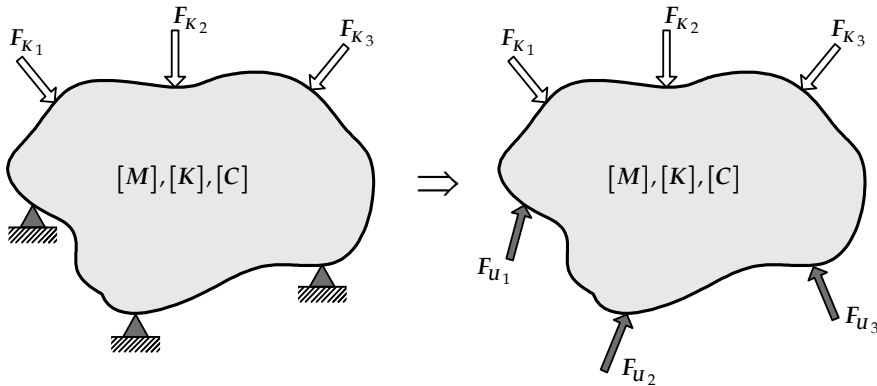
Fig. 8. Structure with applied loads and reactions in dynamic equilibrium

This topic has been addressed in (Maia et al., 2006); the force transmissibility may also be defined either in terms of FRFs or in terms of dynamic stiffnesses. Let X_K and X_U be the responses corresponding to F_K and F_U, respectively, and X_C the responses at the remaining co-ordinates; then,

$$\begin{Bmatrix} X_K \\ X_U \\ X_C \end{Bmatrix} = \begin{bmatrix} H_{KK} & H_{KU} \\ H_{UK} & H_{UU} \\ H_{CK} & H_{CU} \end{bmatrix} \begin{Bmatrix} F_K \\ F_U \end{Bmatrix} \tag{39}$$

Assuming the responses at the reactions co-ordinates as zero, i.e., $X_U = 0$, it follows that:

$$F_U = -H_{UU}^{-1} H_{UK} F_K \tag{40}$$

Therefore, the force transmissibility is defined as:

$$T_{UK} = -H_{UU}^{-1} H_{UK} \tag{41}$$

If the displacements at the co-ordinates of the reactions are not zero, or in the more general case when the two sets of loads are not the applied loads and the reactions, but any disjoint sets that encompass all the loads applied to the structure, it is easy to show (Maia et al., 2006) that:

$$F_U = T_{UK} F_K + H_{UU}^{-1} X_U \tag{42}$$

3.2 In terms of dynamic stiffness
Instead of Eq. (39) one has now:

$$\begin{Bmatrix} F_K \\ F_U \end{Bmatrix} = \begin{bmatrix} Z_{KK} & Z_{KU} & Z_{KC} \\ Z_{UK} & Z_{UU} & Z_{UC} \end{bmatrix} \begin{Bmatrix} X_K \\ X_U \\ X_C \end{Bmatrix} \tag{43}$$

Assuming fictitious loads F_C at the remaining co-ordinates and rearranging, one obtains:

$$\begin{Bmatrix} F_K \\ F_C \\ F_U \end{Bmatrix} = \begin{bmatrix} Z_{KK} & Z_{KC} & Z_{KU} \\ Z_{CK} & Z_{CC} & Z_{CU} \\ Z_{UK} & Z_{UC} & Z_{UU} \end{bmatrix} \begin{Bmatrix} X_K \\ X_C \\ X_U \end{Bmatrix} \tag{44}$$

Defining $X_E = \{X_K \quad X_C\}^T$ and $F_E = \{F_K \quad F_C\}^T$ and assuming, as before, that at the reaction co-ordinates there is no motion ($X_U = 0$), one can write:

$$F_E = Z_{EE} X_E$$
$$F_U = Z_{UE} X_E \tag{45}$$

Eliminating X_E between eqs.(45), it follows that

$$F_U = Z_{UE} Z_{EE}^{-1} F_E \tag{46}$$

and the force transmissibility becomes now:

$$T_{UE} = Z_{UE} Z_{EE}^{-1} \tag{47}$$

Note that because $F_C = 0$, $F_E = \{F_K \quad 0\}^T$, and thus only the columns of T_{UE} corresponding to F_K are relevant to the transmissibility between the two sets of loads, the sub-matrix T_{UK}. One should also note that, in contrast with the SDOF system, the transmissibility of forces is different from the transmissibility of displacements.

Simply to illustrate the application of the concept, a numerical example is presented. The model is shown in Fig. 9, similar to the one of Fig. 3, where the displacements at co-ordinates 1 and 2 are now zero, i.e., $X_1 = X_2 = 0$. External forces are applied at co-ordinates 5 and 6 and the reactions happen at co-ordinates 1 and 2.
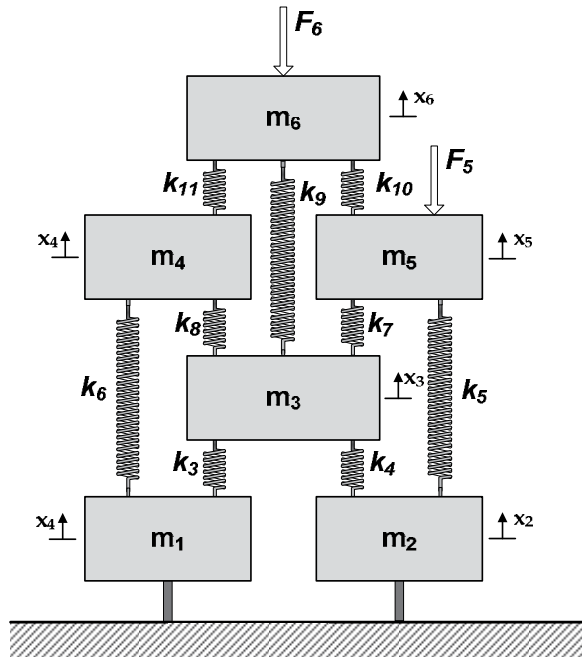
Fig. 9. Structure model in study

The force transmissibility between the two sets of loads – forces at 5 and 6 being known (set K) and forces at 1 and 2 being unknown (set U) – was computed using both described methods.

$$\boldsymbol{F}_K = \begin{Bmatrix} F_5 \\ F_6 \end{Bmatrix}, \quad \boldsymbol{F}_U = \begin{Bmatrix} F_1 \\ F_2 \end{Bmatrix}, \quad \boldsymbol{F}_E = \begin{Bmatrix} F_5 \\ F_6 \\ 0 \\ 0 \end{Bmatrix}, \quad \boldsymbol{X}_K = \begin{Bmatrix} X_5 \\ X_6 \end{Bmatrix}, \quad \boldsymbol{X}_U = \begin{Bmatrix} X_1 \\ X_2 \end{Bmatrix}, \quad \boldsymbol{X}_E = \begin{Bmatrix} X_5 \\ X_6 \\ X_3 \\ X_4 \end{Bmatrix} \tag{48}$$

Equation (41) becomes:

$$\boldsymbol{T}_{UK} = -\begin{bmatrix} H_{11} & H_{12} \\ H_{21} & H_{22} \end{bmatrix}^{-1} \begin{bmatrix} H_{15} & H_{16} \\ H_{25} & H_{26} \end{bmatrix} = \begin{bmatrix} T_{H_{11}} & T_{H_{12}} \\ T_{H_{21}} & T_{H_{22}} \end{bmatrix} \tag{49}$$

where the subscript H means that the transmissibility has been computed using FRFs. Equation (47) becomes:

$$\boldsymbol{T}_{UE} = \begin{bmatrix} Z_{15} & Z_{16} & Z_{13} & Z_{14} \\ Z_{25} & Z_{26} & Z_{23} & Z_{24} \end{bmatrix} \begin{bmatrix} Z_{55} & Z_{56} & Z_{53} & Z_{54} \\ Z_{65} & Z_{66} & Z_{63} & Z_{64} \\ Z_{35} & Z_{36} & Z_{33} & Z_{34} \\ Z_{45} & Z_{46} & Z_{43} & Z_{44} \end{bmatrix}^{-1} = \begin{bmatrix} T_{Z_{11}} & T_{Z_{12}} & T_{Z_{13}} & T_{Z_{14}} \\ T_{Z_{21}} & T_{Z_{22}} & T_{Z_{23}} & T_{Z_{24}} \end{bmatrix} \tag{50}$$

from which

$$\boldsymbol{T}_{UK} = \begin{bmatrix} T_{Z_{11}} & T_{Z_{12}} \\ T_{Z_{21}} & T_{Z_{22}} \end{bmatrix} \tag{51}$$

where the subscript Z means that the transmissibility has been computed using dynamic stiffness matrices. The results obtained by using equations (49) and (51) superimpose perfectly, as expected. Two of the four transmissibilities are presented in Fig. 10 to illustrate this fact.
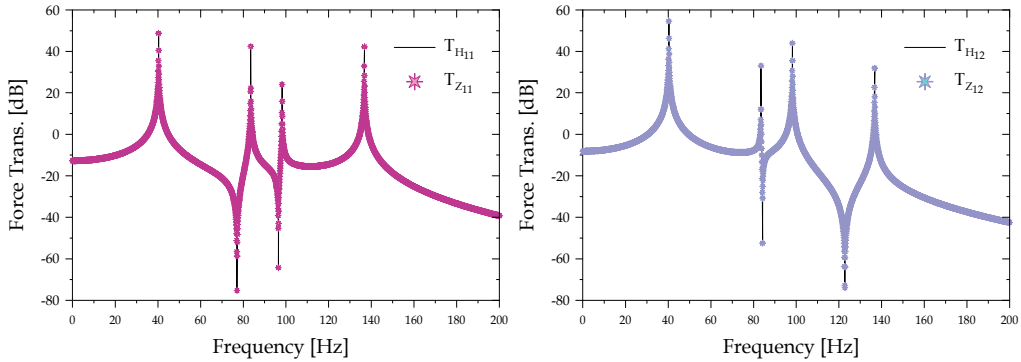
Fig. 10. Comparison between corresponding force transmissibility terms computed from FRFs ($T_{H_{11}}$ and $T_{H_{22}}$) and dynamic stiffness matrices ($T_{Z_{11}}$ and $T_{Z_{22}}$).

It may be noted from Fig. 10 that the maxima of the force transmissibility curves also occur all at the same frequencies.

4. Conclusions

The transmissibility concept for multiple degree-of-freedom systems has been developed and applied for the last ten years and the interest in this matter is continuously growing. In this paper a general overview has been given, concerning the main achievements so far and it has been shown that the various ways in which transmissibility can be defined and applied opens various possibilities for research in different domains, like system identification, structural modification, coupling analysis, damage detection, model updating, vibro-acoustic applications, isolation and vibration attenuation.

5. Acknowledgment

6. References

Canales, G., Mevel, L., Basseville, M. (2009). Transmissibility Based Damage Detection, *Proceedings of the 27th International Operational Modal Analysis Conference (IMAC XXVII)*, Orlando, Florida, U.S.A.

Devriendt, C.M.G., Fontul, M. (2005). Transmissibility in Structural Coupling: Identification of the Sufficient Set of Coupling Forces, *Proceedings of the 1st International Operational Modal Analysis Conference (IOMAC 1)*, Copenhagen, Denmark.

Devriendt, C., Vanbrabant, K., De Sitter, G., Presznzk, F., De Troyer, T., Deckers, K., Steenackers, G., Vanlanduit, S., Guillaume, P. (2009). Structural Health Monitoring in Changing Operational Conditions Using Transmissibility measurements, *Proceedings of International Conference on Engineering Dynamic (ICEDyn 2009)*, Ericeira, Portugal.

Devriendt, C. (2004). Transmissibility on Coupled Structures (Final Project Report). Instituto Superior Técnico, Portugal.

Devriendt, C., De Sitter, G., Guillaume, P. (2010). An Operational Modal Analysis Approach Based on Parametrically Identified Multivariable Transmissibilities, *Mechanical Systems and Signal Processing,* Vol. 24, No. 5, pp. 1250-1259, ISSN: 0888-3270.

Devriendt, C., De Sitter, G., Vanlanduit, S., Guillaume, P. (2009). Operational Modal Analysis in the Presence of Harmonic Excitations by the Use of Transmissibility Measurements, *Mechanical Systems and Signal Processing,* Vol. 23, No. 3, pp. 621-635, ISSN:0888-3270.

Devriendt, C., Guillaume, P. (2007). The use of Transmissibility Measurements in Output-Only Modal Analysis, *Mechanical Systems and Signal Processing*, Vol. 21, No. 7, pp. 2689-2696, ISSN: 0888-3270.

Fontul, M. (2005). Transmissibility in Multi-Degree-of-Freedom Systems (Ph. D Thesis).

Fontul, M., Ribeiro, A.M.R., Silva, J.M.M., Maia, N.M.M. (2004). Transmissibility Matrix in Harmonic and Random Processes, *Shock and Vibration*, Vol. 11, No. 5-6, pp. 563–572, ISSN: 1070-9622.

Liu, W. (2000). Structural Dynamic and Testing of Coupled Structures (Ph. D Thesis).

Liu, W., Ewins, D. J. (1998). Transmissibility Properties of MDOF Systems, *Proceedings of the 16th International Operational Modal Analysis Conference (IMAC XVI)*, Santa Barbara, California, pp. 847-854.

Maia, N.M.M., Almeida, R.A.B., Urgueira, A.P.V. (2008). Understanding Transmissibility Properties, *Proceedings of the 26th International Modal Analysis Conference (IMAC XXVI)*, ISBN: 0-912053-98-4, Orlando, Florida, U.S.A.

Maia, N.M.M., Fontul, M., Ribeiro, A.M.R. (2006). Transmissibility of Forces in Multiple-Degree-of Freedom Systems, *Proceedings of International Conference on Noise and Vibration Engineering (ISMA 2006)*, Leuven, Belgium.

Maia, N.M.M., Ribeiro, A.M.R., Fontul, M., Montalvão, D., Sampaio, R.P.C. (2007). Using the Detection and Relative Damage Quantification Indicator (DRQ) with Transmissibility, *Key Engineering Materials*, Vol. 347, pp. 455-460, ISSN: 1662-9795.

Maia, N.M.M., Silva, J.M.M., Ribeiro, A.M.R. (1999). The Transmissibility Concept in Multi-Degree-of-Freedom *Proceedings of Systems, Inverse Methods in Structural Dynamics, European Mechanics Colloquium, EUROMEC 401*, Liverpool, UK.

Maia, N.M.M., Silva, J.M.M., Ribeiro, A.M.R. (2001). The Transmissibility Concept in Multi-Degrees-of-Freedom Systems, *Mechanical Systems and Signal Processing,* Vol. 15, No. 1, pp. 129-137, ISSN: 0888-3270.

Paipetis, S.A., Vakakis, A.F. (1985). A Method of Analysis for Unidirectional Vibration Isolators with Many Degrees of Freedom, *Journal of Sound and Vibration*, Vol. 98, No. 1, pp. 13-23, ISSN: 0022-460X.

Ribeiro, A.M.R., Fontul, M., Silva, J.M.M., Maia, N.M.M. (2002). Transmissibility Matrix in Harmonic and Random Processes, *Proceedings of the International Conference on Structural Dynamics Modelling (SDM)*, Funchal, Madeira, Portugal.

Ribeiro, A.M.R., Silva, J.M.M., Maia, N.M.M., Fontul, M. (2004). Transmissibility in Structural Coupling, *Proceedings of International Conference on Noise and Vibration Engineering (ISMA 2004)*, Leuven, Belgium.

Ribeiro, A.M.R., Maia, N.M.M., Silva, J.M.M. (2000a). On the Generalisation of the Transmissibility Concept, *Mechanical Systems and Signal Processing*, Vol. 14, No. 1, pp. 29-35, ISSN: 0888-3270.

Ribeiro, A.M.R. (1998). On the Generalization of the Transmissibility Concept, *Proceedings of the NATO/ASI Conference on Modal Analysis and Testing*, Sesimbra, Portugal.

Ribeiro, A.M.R., Fontul, M., Maia, N.M.M., Silva, J.M.M. (2005). Further Developments on the Transmissibility Concept for Multiple Degree of Freedom Systems, *Scientific Bulletin of the «Politehnica» University of Timisoara, Transactions on Mechanics*, Vol. 50, No. 64, pp. 1224–6077, Timisoara, Romania.

Ribeiro, A.M.R., Maia, N.M.M., Silva, J.M.M. (1999). Experimental Evaluation of the Transmissibility Matrix, *Proceedings of the 17th International Modal Analysis Conference (IMAC XVII)*, Kissimmee FL, USA, pp. 1126-1129, ISBN: 0-912053-64-X.

Ribeiro, A.M.R., Maia, N.M.M., Silva, J.M.M. (2000b). Response Prediction From a Reduced Set of Known Responses Using the Transmissibility, *Proceedings of. the 18th International Modal Analysis Conference (IMAC XVIII)*, pp. 425-427, ISBN: 0-912053-67-4, San Antonio TX, USA.

Sampaio, R.P.C., Maia, N.M.M., Ribeiro, A.M.R., Silva, J.M.M. (1999). Damage Detection Using the Transmissibility Concept, *Proceedings of the Sixth International Congress on Sound and Vibration (ICSV 6)*, Copenhagen, Denmark.

Sampaio, R.P.C., Maia, N.M.M., Ribeiro, A.M.R., Silva, J.M.M. (2001). Transmissibility Techniques for Damage Detection, *Proceedings of 19th International Modal Analysis Conference (IMAC XIX)*, Kissimmee, Florida, USA, pp. 1524-1527.

Sampaio, R.P.C., Maia, N.M.M., Silva, J.M.M., Ribeiro, A.M.R. (2000). On the Use of Transmissibility for Damage Detection and Location, *Proceedings of the European COST F3 Conference on System Identification & Structural Health Monitoring*, Polytechnic University of Madrid, Spain, pp. 363-376.

Steenackers, G., Devriendt, C., Guillaume, P. (2007). On the Use of Transmissibility Measurements for Finite Element Model Updating, *Journal of Sound and Vibration*, Vol. 303, No. 3-5, pp. 707-722, ISSN: 0022-460X.

Tcherniak, D., Schuhmacher, A.P. (2009). Application of Transmissibility Matrix Method to NVH Source Contribution Analysis, *Proceedings of the 27th International Modal Analysis Conference (IMAC XXVII)*, Orlando, Florida, U.S.A.

Urgueira, A.P.V., Almeida, R.A.B., Maia, N.M.M. (2008). Experimental Estimation of FRFs Using the Transmissibility Concept, *Proceedings of International Conference on Modal Analysis Noise and Vibration Engineering (ISMA 2008)*, ISBN: 978-90-73802-86-5, Leuven, Belgium.

Urgueira, A.P.V., Almeida, R.A.B., Maia, N.M.M. (2011). On the use of the transmissibility concept for the evaluation of frequency response functions, *Mechanical Systems and Signal Processing*, Vol. 25, No. 3, ISSN: 0888-3270, 940-951.

Vakakis, A.F. (1985). Dynamic Analysis of a Unidirectional Periodic Isolator, Consisting of Identical Masses and Intermediate Distributed Resilient Blocks. *Journal of Sound and Vibration*, Vol. 103, No. 1, pp. 25-33, ISSN: 0022-460X.

Vakakis, A.F., Paipetis, S.A. (1985). Transient Response of Unidirectional Vibration Isolators with Many Degrees of Freedom, *Journal of Sound and Vibration*, Vol. 99, No. 4, pp. 557-562, ISSN: 0022-460X.

Vakakis, A.F., Paipetis, S.A. (1986). The Effect of a Viscously Damped Dynamic Absorber on a Linear Multi-Degree-of-Freedom System, *Journal of Sound and Vibration*, Vol. 105, No. 1, pp. 49-60, ISSN: 0022-460X.

Varoto, P.S., McConnell, K.G. (1998). Single Point vs Multi Point Acceleration Transmissibility Concepts in Vibration Testing, *Proceedings of the 12th International Modal Analysis Conference (IMAC XVI)*, pp. 83-90, ISBN 0-912053-59-3, Santa Barbara, California, USA.

Control Design Methodologies for Vibration Mitigation on Wind Turbine Systems

Ragnar Eide and Hamid Reza Karimi

Department of Engineering, Faculty of Engineering and Science University of Agder
Postboks Grimstad
Norway

1. Introduction

The world's energy consumption from the beginning of the industrial revolution in the 18 th. century and until today has increased at a tremendous degree. Since a large part of the energy has come from sources like oil and coal have the negative impacts on the environment increased proportionally. Therefore, more sustainable and climate friendly energy production methods are emphasized among researchers and environmentalists throughout the world. This is the reason why renewable energies, and wind power particularly, have now become an essential part of the energy programs for most of governments all over the world. One example is seen by the outcome of the European Conference for Renewable Energy in Berlin in 2007 where EU countries defined ambitious goals when it comes to the increase in use of renewable energy resources. One of the goals was that by 2020, the EU would seek to get 20% of energy consumption from renewable energies.

Wind power, in conjunction with other renewable power production methods, has been suggested to play a more and more important role in the future power supply (Waltz, 2008) and (Lee & Kim, 2010). One of the reasons for these expectations is the enormous available potential when it comes to wind resources. One of the most comprehensive study on this topic (Archer & Jacobson, 2005) found the potential of wind power on land and near-shore to be 72TW, which alone could have provided over five times the world's current energy use in all forms averaged over a year.

The World Wind Energy Association (WWEA) estimates the wind power investment worldwide to expand from approximately 160 GW installed capacity at the end of 2010 to 1900 GW installed capacity by 2020. One example is from the USA, where the current contribution of electricity from wind power is merely 1,8% in (2009). However, the U.S Department of Energy is now laying a framework to get as much as 20% contribution by the year 2030.

Due to the economical advantages of installing larger wind turbines (WTs), the typical size of utility-scale turbines has grown dramatically over the last three decades. In addition to the increasing turbine-sizes, cost reduction demands imply use of lighter and hence more flexible structures. If the energy-price from WTs in the coming years are to be competitive with other power production methods, an optimal balance must be made between maximum power capture on one side, and load-reduction capability on the other side. To be able to obtain this is a well defined control-design needed to improve energy capture and reduce

dynamic loads. This combined with the fact that maintenance and constant supervision of WTs at offshore locations is expensive and very difficult, which has further increased the need of a reliable control system for fatigue and load reduction. New advanced control approaches must be designed such as to achieve to the 20- to 25-year operational life required by todayŠs machines (Wright, 2004).

In this paper an above rated wind speed (Region III) regulation of a Horizontal Axis Wind Turbine (HAWT) is presented. The first method is Disturbance Accommodating Control (DAC) which is compared to the LQG controller. The main focus in this work is to use these control techniques to reduce the torque variations by using speed control with collective blade pitch adjustments. Simulation results show effects of the control methodologies for vibration mitigation on wind turbine systems.

The paper is organized as follows. Section 2 will be devoted to the modeling phase. The aim is to come up with a simplified state space model of the WT appropriate to be used in the control design in the subsequent sections. The control system design is covered in Section 3. After a historical overview and a state-of-the-art presentation of WT control are the elements involved in the practical control designed merged with a theoretical description of each topic. The model will then be implemented into a simulation model in the in the MATLAB/Simulink environment in Section 4. Finally, the conclusions and further improvement suggestions are drawn in Section 5.

2. Modeling of the wind turbine

2.1 Introduction

There are different methods available for modeling purposes. Large multi-body dynamics codes, as reported in (Elliot & Wright, 2004), divide the structure into numerous rigid body masses and connect these parts with springs and dampers. This approach leads to dynamic models with hundreds or thousands of DOFs. Hence, the order of these models must be greatly reduced to make them practical for control design (Wright & Fingersh, 2008). Another approach is an assumed modes method. This method discretize the WT structure such that the most important turbine dynamics can be modeled with just a few degrees of freedom. Designing controllers based on these models is much simpler, and captures the most important turbine dynamics, leading to a stable closed-loop system (Wright & Fingersh, 2008). The method is for instance used in FAST, a popular simulation program for design and simulation of control system (Jonkman & Buhl, 2005).

This section presents a simplified control-oriented model. In this approach, a state space representation of the dynamic system is derived from of a quite simple mechanical description of the WT. This state space model is totally non-linear due to the aerodynamics involved, and will thus be linearized around a specific operation point. As reported in (Wright & Fingersh, 2008) with corresponding references, good results are obtained by using linearized time invariant models for the control design.

When modeling a WT one may need to combine different models, each representing interacting subsystems, as Figure 1 below depicts. Here we can see how the WT is simplified to consist of the aerodynamic-, mechanical- (drive train), and electric subsystem, and that the blade pitch angle reference and the power reference in this case are controllable inputs.

The WT is a complicated mechanical system with many interconnecting DOF. However, some of the couplings are rather weak and can be neglected (Ekelund, 1997). For instance, the
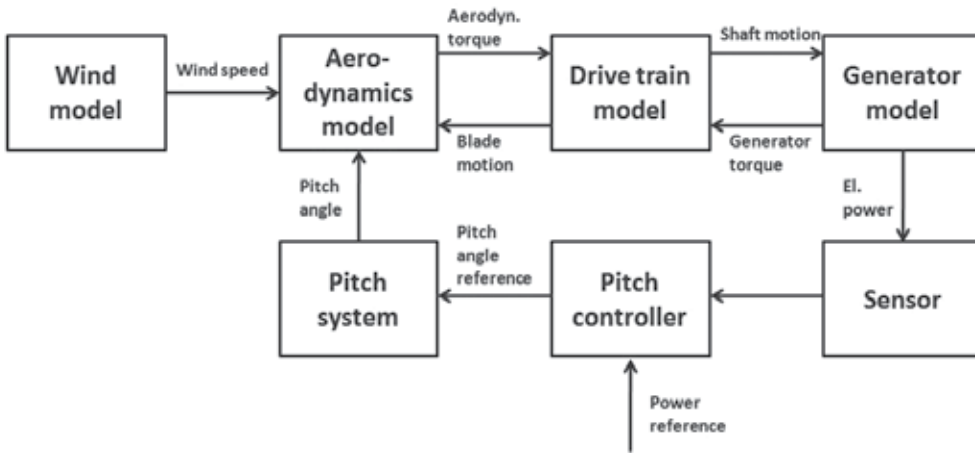
Fig. 1. WT subsystems with corresponding models

connection between the dynamics of the transmission and the tower is neglected in modeling of the mechanical system. The dynamics of the generator and the electrical system are also neglected by regarding the reaction torque from the generator as a fixed value. Also when considering the wind, the approach is to model the wind as simply a scalar input affecting the rotor state.

2.2 State space representation

The nonlinearities of a WT system, for instance due to the aerodynamics, may bring along challenges when it comes to the control design. Since the control input gains of a pitch control usually is the partial derivative of the rotor aerodynamic torque with respect to blade pitch angle variations, these input gains will depend on the operating condition, described by a specific wind and rotor speed. A controller designed for a turbine at one operating point may give poor results at other operating conditions. In fact, a controller which has shown to stabilize the plant for a limited range of operation points, may cause unstable closed-loop behavior in other conditions.

A method which bypasses the challenges of directly involving the nonlinear equations is by using a linear time invariant system (LTI) on state space form. Such a system relates the control input vector u and output of the plant y using first-order vector ordinary differential equation on the form

$$\begin{aligned}
\dot{x} &= Ax + Bu + \Gamma u_D \\
y &= Cx + Du
\end{aligned}$$

(1)

where x is the system states and matrices A, B, Γ, C and D are the state-, input-, disturbance-, output- and feedthrough- matrix, respectively, and u_D is the disturbance input vector.

The representation of the system as given in Eqns. (1) has many advantages. Firstly, it allows the control designer to study more general models (i.e., not just linear or stationary ODEs). Having the ODEs in state variable form gives a compact, standard form for the control design. State space systems also contain a description of the internal states of the system along with the input-output relationship. This helps the control designer to keep track of all the modes

(which is important to do since a system can be internally unstable, although it is input-output stable). As shall be shown in the following is a description of the dynamics on state-space a good starting point for the further controller and observer designs.

The WT drive-train modeled with its high and low speed shaft separated by a gearbox is shown in Figure 2. As it's seen, the drive train is modeled as a simple spring-damper configuration with the constants K_r and C_r denoting the spring stiffness and damping in the rotor shaft, and similarly; K_g and C_g as representing the spring stiffness and damping in the generator shaft. Figure 2 also shows the inertia, torque, rot. speed and displacement of the rotor and generator shafts. The parameters named as T1, ω_1, q1, N1,I1 are the torque, speed, displacement, number of teeth, and inertia of gear 1, and similarly for gear 2.
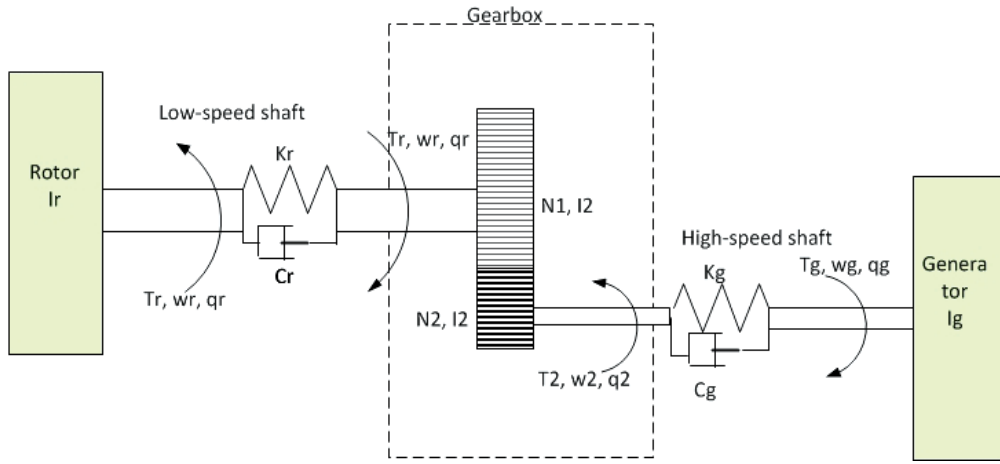
Fig. 2. Model of the drive train with the high and low speed shafts. (For definition of the parameters, see text)

The model in Figure 2 results in the following equation of motion for the rotor torque

$$T_r = I_r \ddot{q}_r + K_r(q_r - q_1) + C_r(\dot{q}_r - \dot{q}_1) + T_1 + I_1 \ddot{q}_1 \tag{2}$$

where the factor $K_r(q_r - q_1) + C_r(\dot{q}_r - \dot{q}_1)$ is the reaction torque in the low speed shaft. Equivalently, the equation for generator motion is as follows

$$T_g = I_g \ddot{q}_g + K_g(q_g - q_2) + C_g(\dot{q}_g - \dot{q}_2) + T_2 + I_2 \ddot{q}_2 \tag{3}$$

where the factor $K_g(q_g - q_2) + C_g(\dot{q}_g - \dot{q}_2)$ is the reaction torque at the high speed shaft.

The relationship between T_1 and T_2 is derived based on the equation describing a constrained motion between two gears in the following way

$$\frac{T_2}{T_1} = \frac{\omega_1}{\omega_2} \rightarrow T_1 = \frac{\omega_1}{\omega_2} T_2 \tag{4}$$

From Eqn. (3) we find

$$T_2 = T_g - I_g \ddot{q}_g - K_r(q_g - q_2) - C_r(\dot{q}_g - \dot{q}_2) - I_2 \ddot{q}_2 \tag{5}$$

then, the following equation for the rotor rotation holds

$$T_r = I_r\ddot{q}_r + K_r(q_r - q_1) + C_r(\dot{q}_r - \dot{q}_1) + \frac{\omega_1}{\omega_2}(T_g - I_g\ddot{q}_g - K_r(q_g - q_2) - C_r(\dot{q}_g - \dot{q}_2) - I_2\ddot{q}_2) + I_1\ddot{q}_1 \tag{6}$$

Since the goal of the modeling is to use it for control design, this equation will be simplified in the following. First, it can be assumed that the the high speed shaft is stiff. This will imply that $T_g = T_2$, $\omega_g = \omega_2$ and so on. Secondly, the gearbox can be assumed lossless, hence the terms involving I_1 and I_2 can be omitted. This reduces Eqn. 6 to the following equation

$$T_r = I_r\ddot{q}_r + K_r(q_r - q_1) + C_r(\dot{q}_r - \dot{q}_1) + \frac{\omega_1}{\omega_2}(T_g - I_g\ddot{q}_g) \tag{7}$$

The model is now of three degrees of freedom (DOF); rotor speed, generator speed, and a DOF describing the torsional spring stiffness of the drive train. These DOFs correspond with the three states shown in Figure 3
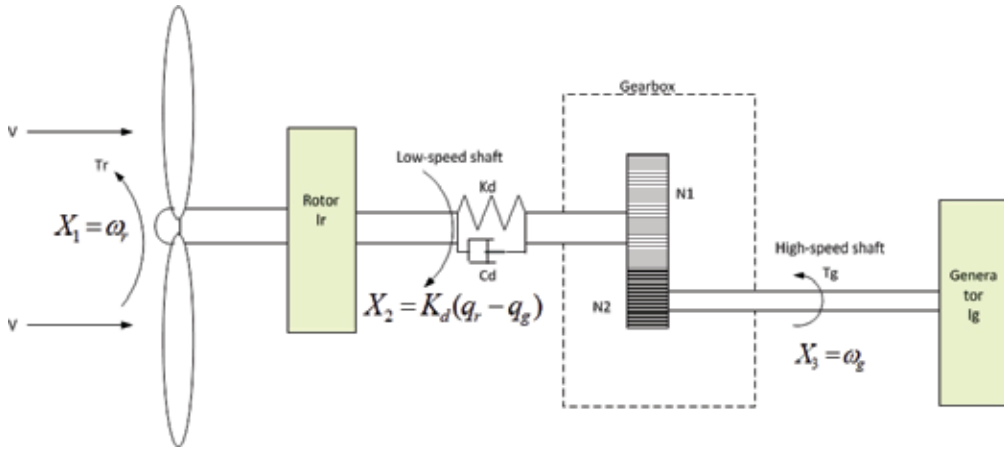
Fig. 3. Illustration of the 3-state model used in the control design having K_d and C_d as drive train torsional stiffness and damping constants, respectively

The states in Figure 3 will in the following be regarded as *perturbations* from an steady-state equilibrium point (operating point), around which the linearization is done. Hence the states are assigned with the δ notation and describes the following DOFs

$X_1 = \delta\omega_r$ is the perturbed rotor speed

$X_2 = K_d(\delta q_r - \delta q_g)$ is the perturbed drive train torsional spring stiffness

$X_3 = \delta\omega_g$ is the perturbed generator speed

where $\delta\dot{q}_r = \delta\omega_r$ and $\delta\dot{q}_g = \delta\omega_g$.
Now, from the Newtons second law, the following relation holds

$$I_r\ddot{q}_r = T_r - T_{sh} \tag{8}$$

where the left hand side expresses the difference between the aerodynamic torque on the rotor caused by the wind force, and the reaction torque in the shaft. This reaction torque can be expressed according to Eqn. (7) as

$$T_{sh} = K_d(q_r - q_g) + C_d(\dot{q}_r - \dot{q}_g) = K_d(q_r - q_g) + C_d(X_1 - X_3) + \frac{\omega_1}{\omega_2}(T_g - I_g\ddot{q}_g) \qquad (9)$$

This equation can, when expressed in terms of deviations from the steady state operation point, be written as:

$$\delta T_{sh} = K_d(\delta q_r - \delta q_g) + C_d(\delta\dot{q}_r - \delta\dot{q}_g) + \frac{\omega_1}{\omega_2}(T_g - I_g\delta\ddot{q}_g) \qquad (10)$$

Hence the BEM theory provides a way to calculate the power coefficient C_P based on the combination of a momentum balance and a empirical study of how the lift and drag coefficients depend on the the collective pitch angle, β, and tip speed ratio, λ . In this way an expression of the aerodynamic torque can be found to be

$$T_r(V, \omega_r, \beta) = \frac{1}{2}\frac{\pi\rho R^2 C_P(\beta, \lambda)}{\lambda}V^2 \qquad (11)$$

where ρ is the air density, R is the rotor radius, and V is the wind speed.
Let us now assume an operating point at $(V_0, \omega_{r,0}, \beta_0)$ such that Eqn. (11) can be written as

$$T_r = T_r(V_0, \omega_{r,0}, \beta_0) + \delta T_r \qquad (12)$$

where δT_r is deviations in the torque from the equilibrium point $(\delta T_r = T_r - T_{r,0})$ and consists of partial derivatives of the torque with respect to the different variables, i.e Taylor series expansion (Henriksen, 2007) and (Wright, 2004), in the following way

$$\delta T_r = \frac{\partial T_r}{\partial V}\delta V + \frac{\partial T_r}{\partial \omega_r}\delta\omega_r + \frac{\partial T_r}{\partial \beta}\delta\beta \qquad (13)$$

where $\delta V = V - V_0$, $\delta\omega = \omega_r - \omega_{r,0}$, and $\delta\beta = \beta - \beta_0$. By assigning α, γ, and ζ to denote the partial derivatives of the torque at the chosen operating point $(V_0, \omega_{rot,0}, \beta_0)$, Eqn. (12) becomes

$$T_r = T_r(V_0, \omega_{r,0}, \beta_0) + \alpha(\delta V) + \gamma(\delta\omega_r) + \zeta(\delta\beta) \qquad (14)$$

If the above expression is put into Eqn.(8), it follows that

$$I_r\ddot{q}_r = T_r(V_0, \omega_{r,0}, \beta_0) + \delta T_r - T_{sh,0} - \delta T_{sh} \qquad (15)$$

At the operation point is $T_r(V_0, \omega_{r,0}, \beta_0) = T_{sh,0}$ since this is a steady state situation. This reduces Eqn. (15) to

$$I_r\ddot{q}_r = \alpha(\delta V) + \gamma(X_1) + \zeta(\delta\beta) - X_2 - C_d(X_1 - X_3) \qquad (16)$$

when substituting with the corresponding state equations. The following expressions for the derivatives of the state variables can now be set up

$$\dot{X}_1 = \frac{(\gamma - C_d)X_1 - X_2 + C_d X_3 + \gamma(\delta\beta) + \alpha(\delta\omega_r)}{I_r} \tag{17}$$

$$\dot{X}_2 = K_d(\delta\dot{q}_r - \delta\dot{q}_g) = K_d X_1 - K_d X_3 \tag{18}$$

$$\dot{X}_3 = \frac{C_d X_1 + X_2 - C_d X_3}{I_g} \tag{19}$$

Note that in the derivative of the generator speed state X_3 is it used that $I_g \ddot{q}_g = I_g X_3 = \delta T_{sh} - \delta T_g = \delta T_{sh}$ when assuming a constant generator torque.

The dynamic system can now be represented in a state space system on the form as described by Eqns (1) yielding

$$\begin{bmatrix} \dot{X}_1 \\ \dot{X}_2 \\ \dot{X}_3 \end{bmatrix} = \begin{bmatrix} \frac{\gamma - C_d}{I_r} & -\frac{1}{I_r} & \frac{C_d}{I_r} \\ K_d & 0 & -K_d \\ \frac{C_d}{I_g} & \frac{1}{I_g} & -\frac{C_d}{I_g} \end{bmatrix} \begin{bmatrix} X_1 \\ X_2 \\ X_3 \end{bmatrix} + \begin{bmatrix} \frac{\zeta}{I_r} \\ 0 \\ 0 \end{bmatrix} \delta\beta + \begin{bmatrix} \frac{\alpha}{I_r} \\ 0 \\ 0 \end{bmatrix} \delta V$$

$$\tag{20}$$

$$y = \begin{bmatrix} 0 & 0 & 1 \end{bmatrix} \begin{bmatrix} X_1 \\ X_2 \\ X_3 \end{bmatrix}$$

where the disturbance input vector u_D from the general form in Eqns. (1) now is given as δV, which is the perturbed wind disturbance (i.e deviations from the operating point, $\delta V = V - V_0$), and the control input vector u from Eqns. (1) now given as $\delta\beta$ (i.e perturbed (collective) pitch angle, $\delta\beta = \beta - \beta_0$).

The parameters will be assigned when coming to Section 4. It is worth no notice that the the measured output signal here is the generator speed. This can be seen from the form of the output vector C. It will be shown later that this will lead to a non-minimum phase plant, i.e a plant with an asymptotically unstable zero in the right complex plane (Lee, 2004). Such plant is in general not suitable for the LTR approach such that a revision of this is required.

3. Wind turbine control

3.1 Introduction

In order to have a power production which ensures that speed, torque and power are within acceptable limits for the different wind speed regions, is it necessary to control the WT. This control system should be complex enough to meet the intended control objectives, but at the same time simple enough to easy interpret the results. A frequently used approach, which will also be applied in this work, is to start with a simple model and a simple controller that can be developed further by adding more degrees of freedom into the model.

Optimally speaking, if the control system shall be able to meet the requirement of reduced energy cost, it must find a good balance between (a) a long working life without failures and (b) an efficient (optimal power output) and stable energy conversion. The first point can be regarded as the main focus in this work. This requirement can be further crystallized to the following properties which the control system should possess

- good closed loop performance in terms of stability, disturbance attenuation, and reference tracking, at an acceptable level of control effort.

- low dynamic order (because of hardware constraints)

- good robustness

To meet the objective of long working life should the control system be designed to be efficiently mitigate loads in order to reduce the fatigue stresses (especially in shaft and blade rotor) due to varying wind disturbances. Before going into the specific control design, an historical overview of WT control with a special view toward the objective of load reduction, will be presented in the following.

3.2 History of WT control

The history of WT control and research within this field have emerged from the simplest form of passive stall control to advanced controllers, like so-called smart rotor control. The latter is well described in for instance (Wilson, Berg, Barone, Berg, Resor & Lobitz, 2009a) and (Lackner & van Kuik, 2010). As these references portrays does this control scheme involve active aerodynamic flow control by implementation of numerous sensors and actuators, bringing along a high level of complexity. Although these advanced control methods have been investigated for ten to fifteen years, most commercial systems are still implemented using multiple single-input-single-output (SISO) loops with classical PID controllers (Bossanyi, 2000). Actually, as reported in (Bossanyi, 2004), PID showed to give competitive results compared to some of the new advanced techniques.

The traditional way of controlling a WT with multiple control objectives, such as speed control for maximum power tracking and load mitigation by pitch control, is to design independent control loops in a way illustrated in Figure 4(a).
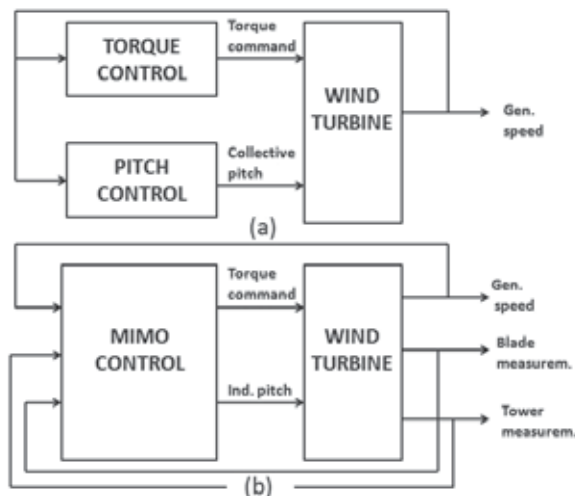

Fig. 4. Illustration of difference between SISO and MIMO controllers

The PID controllers (i.e. the SISO controllers shown in Figure 4 (a)) are traditionally used for the individual torque and pitch control and have shown to have a good effect when carefully tuned and adjusted to its specific application. One disadvantage is, however, that the PID

control loops must be designed not to interfere with each other. If this happen to be the case will the result often be a destabilized turbine. This problem can be solved in an efficient manner within the modern and so-called advanced control techniques (Wright & Fingersh, 2008) using MIMO controllers (cf. Figure 4 (b)). In these more advanced control designs, multiple control objectives is seen to be met with fewer control loops leading to stable closed loop behavior (Wright & Stol, 2008).

With increasing turbine sizes, much research is done to find new and better ways of load control compared to the classical methods (see (Wright & Stol, 2008) and (Bossanyi, 2003) with references). Large turbine sizes will give rise to loads that vary along the blade and change quickly due to wind gusts and other varying wind conditions. Rapidly changing loads can cause fatigue damage and reduce the life of the WT, which in turn may decide the lifetime of the other turbine components. Because of the inertia of the system, as well as the limitations of the actuators, active pitch control alone can only control ŞaverageŤ loads on the blade. On the other hand, passive load control strategies cannot respond to local load variations. Active aerodynamic load control (AALC) is therefore suggested to have a good potential as an addition the existing control strategies when it comes to load reduction (Wilson, Berg, Barone, Berg, Resor & Lobitz, 2009b). One approach where AALC has been combined with an individual blade pitch control scheme has shown to reduce the root flap bending moment significantly (Wilson, Berg, Resor, Barone & Berg, 2009).

A well known MIMO controller, the Linear Quadratic Gaussian (LQG) regulator, is suggested in (Selvam, 2007) to be used in load control. This paper presents that this regulation policy can have a good load reduction capability for a large frequency range. Reports as (Bossanyi, 2003) and (Bossanyi, 2004) suggest load mitigation when using individual pitch actuators. A thorough study has been performed by Bossanyi in (Bossanyi, 2003) where the classical PI control is compared with a multi-variable LQG control approach. Although this work has shown to yield good results when applying LQG, the design process is not straightforward and the resulting algorithm is relatively difficult.

One of the disadvantages of LQG design, however, is that it cannot directly take into account robustness margins (like the gain- and the phase margin). Due to this poor robustness properties of LQG control it was been necessary to search after other methods which could handle model uncertainties in a better way. One method which can be traced back to the early 1980s is the H_∞ approach. In this approach does the control designer from the very beginning specify a model of system uncertainties, which can be for instance additive perturbations or output disturbance (D.-W.Gu et al., 2005). Connor, Iyer, Leithead and Grimble were among the first to suggest an application of H_∞ control on a WT model (see Connor et al., 1992). Their main concern in this work were how to reduce the matter of fatigue loading. Although they encountered some overshoot problems did they prove that the method was applicable to a WT control problem. Suggestions of how H_∞ control can be used for load reduction has later been reported in (Bianchi et al., 2004). The method has also been shown to be applicable in advanced power control to enhance a better power capture for a wider range of wind speeds (Liu et al., 2008).

One particular problem the WT control designers must be able to handle is that WT control generally involves a multi-objective optimization problem, each objective having different goals. For instance, the control objective can be alleviate loads due to large scale gusts over the whole disk area, while others can be more slowly varying and low frequency loads over only one blade. To handle this problem does (Bottasso et al., 2010) propose an approach based

on a multi-layer architecture. In this method are three control layers designed, each aiming at a specific control target and cooperates with the other layers to obtain various control goals. In this way, the choice of the controller used on each layer can be optimized and tailored to the specific control goal of that layer, thereby improving performance and simplify tuning (Bottasso et al., 2010).

What the control designer in all of the above mentioned controlling methods are actually trying to do is to compensate for the stochastic fluctuations in the wind. To do this in a perfect way is of course more or less impossible. One method called Disturbance Accommodating Control (DAC) take into account the fluctuations in the wind by an estimation of the disturbance for an assumed above-rated wind speed situation (Balas et al., 1998). DAC has shown to have a good effect on load mitigation and is therefore used to obtain special attention when it comes to fatigue load reduction. The theory was thoroughly compared with PI control by Alan Wright in his PhD thesis from 2004 (Wright, 2004). He concluded in his paper that the analytic results obtained using DAC appeared to be "extremely promising". For instance, it was shown how DAC has much better performance compared to the PI control in reducing drive-train shaft torsional moments and blade root flapwise-bending moments (Wright, 2004). A brief description of the theory behind the DAC will be given shortly, while an implementation and testing of DAC for the WT system will be done in Section 4.

In addition to the above mentioned control schemes are methods as Model Predictive Control (MPC) (Henriksen, 2007), Generalized Predictive Controller (GPC), and Fuzzy Logic Control (Karimi-Davijani et al., 2009) proposed for WT control. A comparison of different control techniques will not be done in this work (please refer to (Bottasso et al., 2007) for more on this).

3.3 The Linear Quadratic Regulator (LQR)

The LQR controller was among the first of the so-called advanced control techniques used in control of wind turbines. Liebst presented in 1985 a pitch control system for the KaMeWa wind turbine using LQR design (Wright, 2004). The objective of this controller was to alleviate blade loads due to wind shear, gravity, and tower deflection using individual blade pitch control. Results of this work included a reduction of blade and tower cyclic responses as well as the reduction of a large 2-per-revolution variation in power (Liebst, 1985).

The practical application of this technique is limited by the challenges of obtaining accurate measurements of the states needed in the controller. One way to solve this is to add extra sensors and measurement arrangements. However, since this extra sensors and measurements will add considerable cost and complexity to a WT, is this most often not regarded as a good solution. In addition, errors in the measurement of these states can result in poor controller behavior (Wright, 2004). To avoid these problems, a state estimator is added in any practical LQR implementation (Laks et al., 2009). This approach was described by Mattson in his Ph.D thesis as early as in 1984, where power-regulation for a fixed-speed WT using blade pitch is presented (Mattson, 1984). The proposed solution to the WT control problem was here based on linear models containing drive-train torsion and tower fore-aft bending DOF. The same report also describes the use of state estimation to estimate wind speed.

The principles of a LQR controller is given in Figure 5. Here the state space system is represented with its matrices A, B, and C, together with the LQR controller (shown with the $-K$).

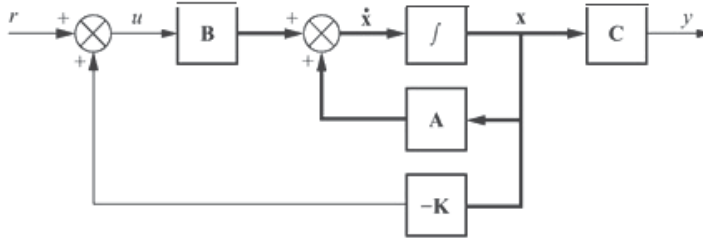The LQR problem rests upon the following three assumptions (Athans, 1981):

Fig. 5. State space control using a LQR controller where K is the LQR gain matrix

1. All the states are available for feedback, i.e it can be measured by sensors etc.

2. The system are *stabilizable* which means that all of its unstable modes are controllable

3. The system are *detectable* having all its unstable modes observable

LQR design is a part of what in the control area is called *optimal control*. This regulator provides an *optimal control law* for a linear system with quadratic performance index yielding a cost function on the form (Burns, 2001)

$$J = \int_0^\infty x^T(t)Qx(t) + u^T(t)Ru(t)\,dt \tag{21}$$

where $Q = Q^T$ and $R = R^T$ are weighting parameters that penalize the states and the control effort, respectively. These matrices are therefore controller tuning parameters.

It is crucial that Q must be chosen in accordance to the emphasize we want to give the response of certain states, or in other words; how we will penalize the states. Likewise, the chosen value(s) of R will penalize the control effort u. As an example, if Q is increased while keeping R at the same value, the settling time will be reduced as the states approach zero at a faster rate. This means that more importance is being placed on keeping the states small at the expense of increased control effort. On the other side, if R is very large relative to Q, the control energy is penalized very heavily. Hence, in an optimal control problem the control system seeks to maximize the return from the system with *minimum cost*.

In a LQR design, because of the quadratic performance index of the cost function, the system has a mathematical solution that yields an *optimal control law* given as

$$u(t) = -Kx(t) \tag{22}$$

where u is the control input and K is the state feedback gain matrix given as $K = R^{-1}B^TS$. It can be shown (see (Burns, 2001))that S can be found by solving the following algebraic Riccati Equation (ARE)

$$SA + A^TS + Q - SBR^{-1}B^TS = 0 \tag{23}$$

The process of minimizing the cost function by solving this equation can easily be done using the built-in MATLAB function `lqr`.

As can be seen from the above description does the LQR algorithm take care of the tedious work of optimizing the controller, which for the case of the PID controller can be a time consuming task. However, the control designer still needs to specify the weighting factors

and compare the results with the specified design goals. This means that controller synthesis will often tend to be an iterative process where the designed "optimal" controllers are tested through simulations and will be adjusted according to the specified design goals.

The optimal control solution from the LQR approach yields some impressive properties. Firstly the controller guarantees at least $60°$ phase margin in each input channel (Saberi et al., 1993), which means that as much as $60°$ phase changes can be tolerated in each input channel without violating the stability. In addition, the LQR has infinite gain margin which implies that the LQR is still able to guarantee the stability, even though the gain increases indefinitely. Hence, LQR guarantees a very robust controller, capable of handling various kinds of uncertainties in the modeling. However, when an state estimator is implemented with measurement feedback, these properties just described is often lacking. But, as will be shown later; the robustness properties can be recovered!

3.4 State estimation

As mentioned for the case of the LQR controller, all sensors for measuring the different states are in this case assumed to be available. This is not a valid assumption in practice. A void of sensors means that all states (full-order state observers), or some of the states (reduced order observer), are not immediately available for use in the control task. In such cases, a state observer must be implemented to supply accurate estimations of the states at all wind-rotor positions. The observer state equations are given by

$$\dot{\hat{x}} = A\hat{x} + Bu + L(y - C\hat{x}) \tag{24}$$

$$\hat{y} = C\hat{x} \tag{25}$$

where $\hat{x}$ is the estimate of the actual state x. Furthermore, equations (24) and (25) can be re-written to become

$$\dot{\hat{x}} = (A - LC)\hat{x} + Bu + Ly \tag{26}$$

These are the governing equations for a *full order observer*, having two inputs u and y and one output, $\hat{x}$. Since we already know A, B, and u, observers of this kind is simple in design and provides accurate estimation of all the states around the linearized point. The proportional observer gain matrix, L, can be found for instance by pole placement procedure, or as will be shown in the following; by applying the Kalman filter design.

3.5 Kalman estimator

In the previous design of the state observer, the measurements $y = Cx$ were assumed to be noise free. This is not usually the case in practical life. Other unknown inputs yielding the state equations to be on the general stochastic state space form, which is already defined in Eqn. (1) as

$$\dot{x} = Ax + Bu + \Gamma u_D$$

$$y = Cx + Du + n$$

here the D matrix relating the input u to the output y most commonly is set to zero, the disturbance input vector u_D is stationary, zero mean Gaussian white process noise (i.e wind disturbance), and n is zero mean Gaussian white sensor noise.

The Kalman filter can be applied to yield the estimated state vector $\hat{x}$ and output vector $\hat{y}$ (cf. Eqns (24) and (25), by using the known inputs u and the measurements y. The Kalman filter is optimal in the sense that it minimizes the estimated error covariance when some presumed conditions are met (see Bottasso & Croce 2009). The mean-square estimation error is given by

$$J = E[(x(t) - \hat{x}(t))^T (x(t) - \hat{x}(t))] \tag{27}$$

 where

$$E[(x(t) - \hat{x}(t))^T y(t) = 0 \tag{28}$$

The optimal Kalman gain is given by

$$L(t) = S_e(t) C^T R^{-1} \tag{29}$$

where $S_e(t)$ is the same as J given in (3.5). Furthermore, when $t \to \infty$, the algebraic Riccati equation can be written as

$$0 = S_e A^T + A S_e + Q_n - S_e C^T R_n^{-1} C S_e \tag{30}$$

where Q_n and R_n are the process and measurement noise covariances, respectively. Tuning of the Kalman filter are required if these are not known. Finally, the sub-optimal Kalman gain for a steady state Kalman filter can be expressed as $L = S_e C^T R^{-1}$.

3.6 Disturbance accommodating control

This section will explain the principles of DAC and for more details, please refer to e.g. (Johnson, 1976). The DAC method will be utilized together with a LQR regulator and is a straightforward way to model and simulate a system with an assumed-wind disturbance.

Recalling from the state space system described by Eqns. (1), which included the vector Γ. This vector describes the magnitude of the disturbance, while the input signal u_D is the disturbance quantity (which in our case is the wind speed perturbation). The Γ vector will in the DAC procedure be used as a free design parameter.

The basic thought in DAC theory is that disturbances are described by an assumed-waveform model on state space form. Such a wind model can be described according to the following equations (Wright, 2004)

$$\dot{z}_D = F z_D \tag{31}$$
$$u_D = \Theta z_D \tag{32}$$

where z_D denotes the disturbance state, F the state matrix, u_D is disturbance output vector (input to the plant), and Θ relates disturbance model input to disturbance states. Note that it is necessary to know something about the initial condition of the disturbance state, z_D^0, in order to know the amplitude of the disturbance.

Since the state variables x and the disturbance variable z_D cannot be measured directly, observers will be utilized to estimate these. The mathematical description of the observer

will in this case according to Eqns (24) and (25) be given as

$$\dot{\hat{x}} = A\hat{x} + Bu + \Gamma\hat{u}_D + K_x(y - \hat{y}) \tag{33}$$

$$\hat{y} = C\hat{x} \tag{34}$$

where the estimator gains K_x can be chosen according to for instance the pole placement method using the `place` command in MATLAB.

Furthermore, the disturbance observer is described as

$$\dot{\hat{z}}_D = Fz_D + K_D(y - \hat{y}) \tag{35}$$

$$\hat{u}_D = \Theta\hat{z}_D \tag{36}$$

where the disturbance state estimator gain K_D is a scalar.

The estimated variables can then be fed into the controller to minimize the effect of the disturbances. The result of this is that the state feedback now also include the feedback of disturbance observer yielding a "new" feedback control law on the form

$$u(t) = G\hat{x}(t) + G_D\hat{z}_D(t) \tag{37}$$

where the LQR gain G is computed in MATLAB, and the full state feedback gain (i.e disturbance gain) G_D must be chosen as to minimize the norm $|BG_D + \Gamma\Theta|$. Calculated numerical values will be given in Section 4.

3.7 The LQG controller

Another well-known method of handling noise inputs is the Linear Quadratic Gaussian (LQG) controller. This is simply a combination of a Kalman filter and a LQR controller. The separation principle guarantees that these can be designed and computed independently (Morimoto, 1991). LQG controllers can be used both in linear time-invariant (LTI) systems as well as in linear time-variant systems. The application to linear time-variant systems enables the design of linear feedback controllers for non-linear uncertain systems, which is the case for the WT system.

The schematics of a LQG is in essence similar to that depicted in Figure **??** in Section 3.4, the only difference is that the observer gain matrix L in this figure now can be defined as the Kalman gain K_f. However, we also assume disturbances in form of noise, such that the system with the LQG regulator in compressed form can be described as in Figure 6

4. Control design and simulations

4.1 Introduction

The purpose in this project is to investigate the application of modern control theories, such as the LQR and LQG, on WT systems and how a speed controller can be made with these theories to reduce torque variations due to a wind disturbance. In addition, a further idea is to investigate if a better load reduction can be obtained by using a dynamic compensator from the LTR algorithm, and whether factors as the LTR gain will affect this result.

The simulations are done in the MATLAB Simulink environment, enabling the LTI state space model described in Section 2 to be incorporated together with the different controllers in the convenient block diagram approach available in Simulink.
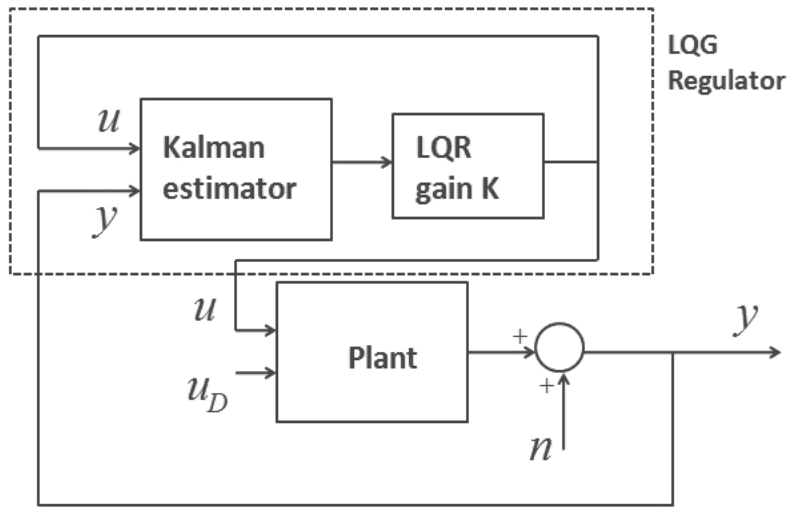
Fig. 6. LQG regulator

This Section presents results from the practical implementation of the WT control design. It is important to note that a test of the controlled system under various operating conditions has not been performed. This is mainly due to the fact that this work is not focused on a real-life application of the controller, but instead on the theoretical aspects of controller design. Also, the linearization of the WT plant at different operation points would have required a computer program, such as FAST[1]. Load mitigation in above rated wind speeds has already been described to be the focus of this work, and the operation point chosen will reflect this goal.

The first control approach that is being tested is the DAC theory, where the wind disturbance modeled in a straightforward way together with the LQR and observer procedures, as described in Section 3. The reason for starting with this method is to investigate if the results are comparable with the results from the LQG method, and if so; what is the difference in the results, and which results can be regarded as the "best" results.

It is important to note that for the simulations in this project are the actuator constraints, such as the dynamics of the pitch-system, not taken into consideration.

4.2 Linearization

As was described in Chaper 2 does the WT compose of a complex non-linear relationship between factors such as the aerodynamic properties of the blades, pitch angle, and wind speeds. The best approach is thus to build the model out from experimental data and a non-linear simulation model of the WT. Although it is possible to build a non-linear WT simulation model also in Simulink and extract linear models by utilizing the built-in `trim` and `linmod` functions, has this not been done in this work. Since the mathematical model presented in this paper is simplified a lot would this approach probably result in a more inaccurate model than with the use of the tailored WT simulation code provided by FAST,

---

[1] A popular aeroelastic design code for horizontal axis wind turbines developed by National Renewable Energy Laboratory, USA (Jonkman & Buhl, 2005)

where many aspects regarding the aerodynamics and structural dynamics are taken into account. The linearized state space model, which will be used in the control design is based on what is presented in (Wright, 2004) and (Balas et al., 1998).
The operation point, around which the linearization is done, is given as (Wright, 2004),
$V_0 = 18 m/s$
$\omega_{rot,0} = 42 rpm$
$\beta_0 = 12°$

The corresponding FAST linearization with reference to (Wright, 2004) around this point yields the following state space system

$$\begin{bmatrix} \dot{X_1} \\ \dot{X_2} \\ \dot{X_3} \end{bmatrix} = \begin{bmatrix} -0.145 & -3.108 \cdot 10^{-6} & 0.02445 \\ 2.691 \cdot 10^7 & 0 & -2.691 \cdot 10^7 \\ 0.1229 & 1.56 \cdot 10^{-5} & -0.1229 \end{bmatrix} \begin{bmatrix} X_1 \\ X_2 \\ X_3 \end{bmatrix} + \begin{bmatrix} -3.456 \\ 0 \\ 0 \end{bmatrix} \delta\beta + \begin{bmatrix} 1 \\ 0 \\ 0 \end{bmatrix} (\delta V)$$

(38)

$$y = \begin{bmatrix} 0 & 0 & 1 \end{bmatrix} \begin{bmatrix} X_1 \\ X_2 \\ X_3 \end{bmatrix}$$

where the factors C_d/I_{rot} and C_d/I_{gen} are calculated by using the known relation to the other parameters.
Recalling from Section 2 that Γ vector is given as $\frac{\alpha}{I_r}$, where α is describes the relationship between torque variations and wind variations, $\frac{\partial T_r}{\partial V}$. This means that if Γ is increased, it will follow that the torque is more sensitive to wind variations, which is surely a negative effect when the matter of fatigue is concerned. The torque is given as a non-linear function in Eqn (11), which shows the dependency on the wind speed, rotor speed and blade pitch, and will be fixed at the chosen operating point. However, the Γ vector is initially chosen to $[100]^T$.
The transfer function (TF) of the open loop system formed by the linearized state space system in Eqns. (4.2) is

$$G(s) = \frac{1.499 \cdot 10^{-14} s^2 - 0.4247 s - 1450}{s^3 + 0.374 s^2 + 503.3 s + 59.44}$$

(39)

extracted by using the MATLAB function `ss2tf`
One of the zeros of this TF is located at $s = 2.83 \cdot 10^{13}$ leading to a non-minimum phase system. Since the LTR procedure applied as an extension to the LQG later on is not feasible for non-minimum phase systems (Saberi et al., 1993) will this vector be formed as to represent rotor speed measurement instead, which changes the output to

$$y = \begin{bmatrix} 1 & 0 & 0 \end{bmatrix} \begin{bmatrix} X_1 \\ X_2 \\ X_3 \end{bmatrix}$$

(40)

4.3 Disturbance accommodating control
The DAC procedure has already been described in Section 3.6. The Simulink block digram shown in Figure 7 was set up according to the governing equations described in this section.

Fig. 7. Simulink block diagram of DAC
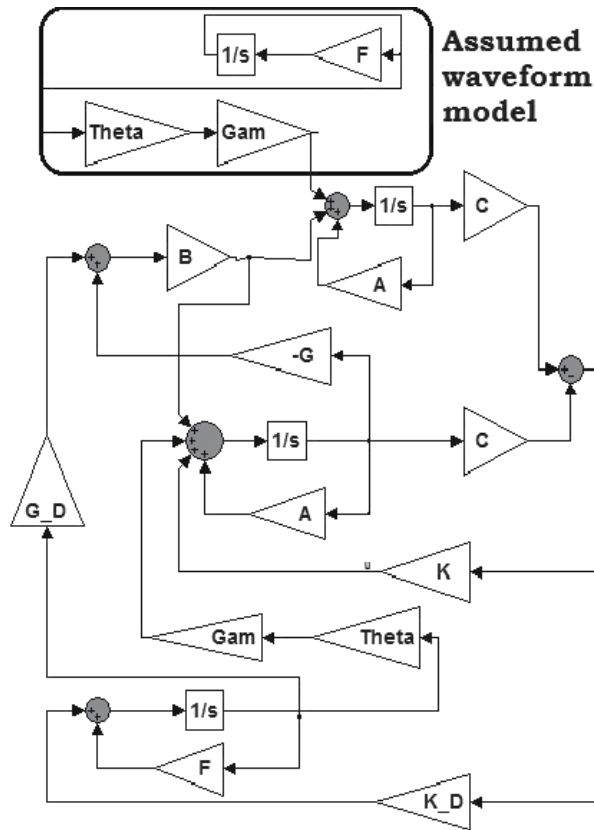
The assumed waveform model is shown in Figure 7. It is assumed a step input disturbance from the wind, hence $F = 0$ and $\Theta = 1$ will be chosen to reflect this (Henriksen, 2007). In order to "excite" the controller an initial condition (chosen as 1) were inserted into the integrator of the disturbance model.

4.3.1 Simulation without any control

It is interesting first to have a look at the response without any control at all. Then, after implementing the controller, is it easier to see how good the controller works in the disturbance accommodating task.

Now, by setting both the LQR and the wind disturbance gain equal to zero, perturbations in rotor speed (i.e. deviation from the operation point) shown in Figure 8 when simulating for 50 seconds. According to the simulation result, it is observed that the wind disturbance is not accommodated, and the rotor speed will increase.

4.3.2 Simulation with only wind disturbance gain

The next scenario which is to be simulated is a situation with the LQR control gain set to 0, but with the wind disturbance state gain G_D set to minimize the norm $|BG_D + \Gamma\Theta|$. The response of the rotor speed is shown in Figure 9 below.
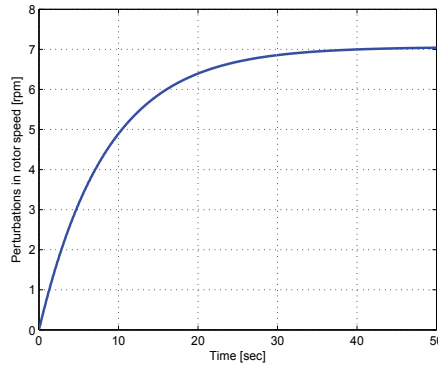
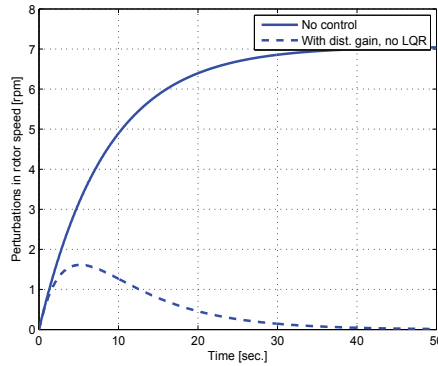Fig. 8. Perturbations in rotor speed with no control

Fig. 9. Perturbations in rotor speed with disturbance gain

As can be seen in this plot does G_D alone manage to regulate the speed, but with a long settling time.

4.3.3 Simulation of DAC with LQR

The final DAC approach will involve a LQR design. Hence, this design will be described in the following, with reference to the theories on LQR presented in Section 3.3. The initial parameters of the wighting functions Q and R are chosen arbitrarily. The next task is then to simulate to check whether the results correspond with the expected performance. After an iterative study while changing Q and R values, the following weighting matrices were chosen:

$$Q = \begin{bmatrix} 100 & 0 & 0 \\ 0 & 0 & 0 \\ 0 & 0 & 100 \end{bmatrix} \tag{41}$$

The control weight of the performance index R was set to 1.

The chosen values in Q will result in a relatively large penalty of the states x_1 and x_3. This means that if x_1 or x_3 is large, the large values in Q will amplify the effect of x_1 and x_3 in the optimization problem. Since the optimization problem are to minimize J, the optimal control u must force the states x_1 and x_3 to be small (which make sense physically since x_1 and x_3

represent the of the perturbations in rotor and generator speed, respectively). On the other hand, the small R relative to the max values in Q involves very low penalty on the control effort u in the minimization of J, and the optimal control u can then be large. For this small R, the gain K can then be large resulting in a faster response.

Since the system has been found to be observable the estimator poles can be arbitrarily placed. Hence, the poles were chosen to be at -10, -30, and -50 yielding the estimator gain matrix

$$K = \begin{bmatrix} 17,235 \\ 1.41 \cdot 10^8 \\ 89.626 \end{bmatrix} \tag{42}$$

The disturbance state estimator gain K_D is a scalar and chosen to 10.

It was found when doing these simulations and checking the results, that an exponential LQR were more appropriate for the current application. The exponential LQR gain were found by applying the code:

```
P=are(A+alpha*eye(3),inv(R)*B*B',Q);
Gdac=inv(R)*B'*P;
```

where alpha is the exponential time-constant chosen to 4. This resulted in the gain matrix:

$$Gdac = \begin{bmatrix} -18.2087 & -1.2265 \cdot 10^{-5} & -0.0425 \end{bmatrix} \tag{42}$$

Simulation of the time response of perturbations in rotor speed for ten seconds is shown in Figure 10.
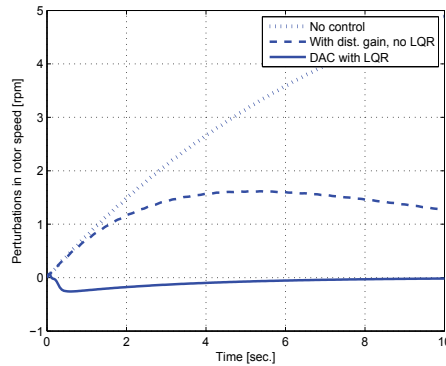
Fig. 10. Comparison of perturbations in rotor speed when applying DAC with LQR

When looking at the plots in Figure 10, it is clear that the disturbance now is much better attenuated while comparing with the first two scenarios. The reason why the speed have this undershoot is due to the right complex plane zeros the LQR controller gives to the closed loop system.

It is also of interest to see how the control signal changes in the three previous situations. This is shown in Figure 11.

As can be seen from Figure 11 does the pitch angle end up having a higher value. This is an expected situation since it is now assumed a constant wind disturbance which must be

Fig. 11. Comparison of control signal for three previous scenarios

accounted for by an increase in pitch angle. Otherwise, the step in the wind would result in a higher rotor speed, a situation we do not want to occur and the very reason for having a control system in the first place.
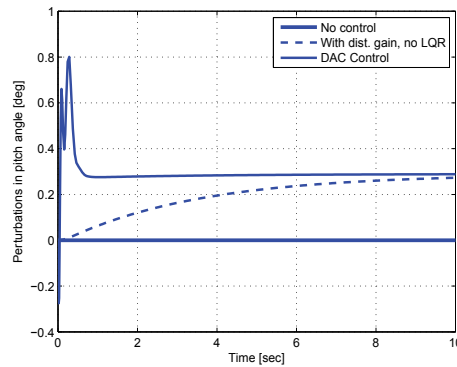
Another interesting signal is the error signal, which is the discrepancy between the "measured" output signal y and the estimated signal $\hat{y}$. This is shown in Figure 12 below.
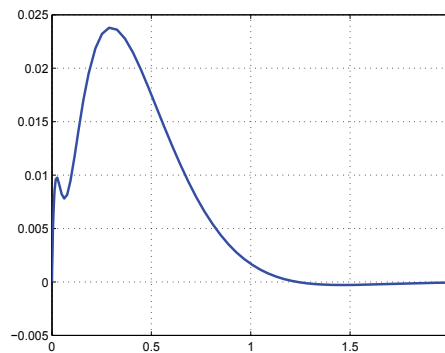
Fig. 12. Error signal for a step input

The DAC simulations in this section have shown that this control method enables to mitigate disturbance due to a wind assigned to affect the rotor state. However, the simulations show that the settling time is relatively long (approximately 10 sec). Whether it is possible to obtained a "better" result using a LQG controller, will be the task in the following section.

The disturbance will now be replaced by two step functions and the disturbance vector Γ in order to make the DAC more comparable with the LQG analysis. This gives the disturbance input signal as shown in Figure 13.

The output response when applying this disturbance model is given in Figure 14

4.4 LQG controller

The control objective is the same as for the DAC; make the perturbations in the rotor speed as small as possible in order to attenuate the wind disturbance. The wind disturbance is made
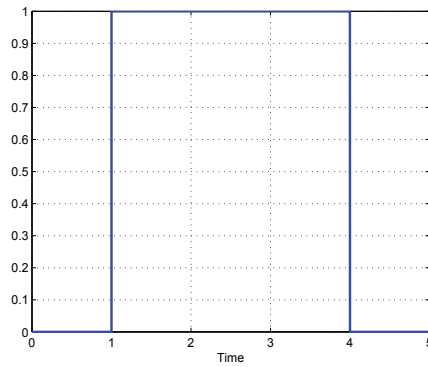
Fig. 13. Step signal for disturbance modeling
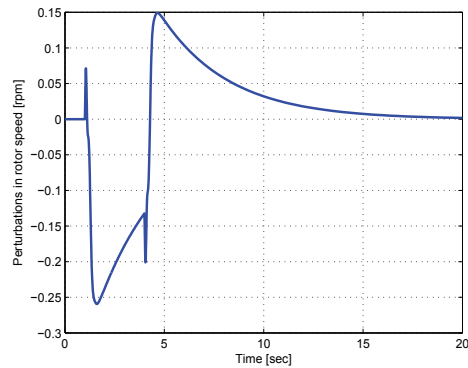
Fig. 14. Output response when applying step input

by using the combination of two step functions as described earlier. This will give a step input affecting the rotor state. Firstly, a situation without control is showed in Figure 15.
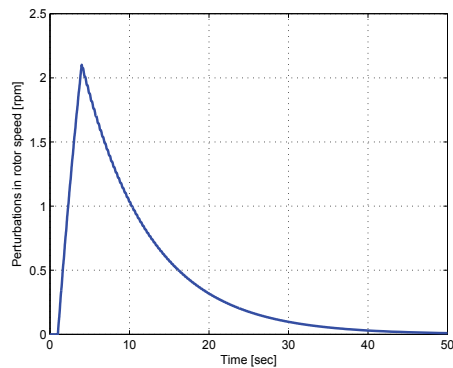
Fig. 15. Response in rotor speed without any control

The sudden change in the rotor speed after one second is due to the step input function. The figure show that without any control will the rotor speed increase to approximately 2 rpm

above the operational speed. After four seconds, when the disturbance is set to zero again, will the speed then decrease and be brought to zero after approximately 50 seconds.

Calculation of the Kalman gain used in the LQG controller is according to the theory discussed in Section 3. There are different methods to do this calculation in MATLAB. One is by applying the `kalman` function, and another is the `lqrc` function. The latter is for instance used in the LTR demo provided with the Robust Control Toolbox in MATLAB. When applying the same weighting as for the LQR in the DAC approach in the `lqrc` function, and the weighting functions

$$Q_n = \begin{bmatrix} 30 & 0 \\ 0 & 30 \end{bmatrix}$$
$$R_n = 1$$

representing the process and measurement noise covariances in the `kalman` function, did the `kalman` function yield much better disturbance attenuation for a given control effort (shown in Figure 16). The corresponding load attenuation for the two cases is shown in Figure 17 below
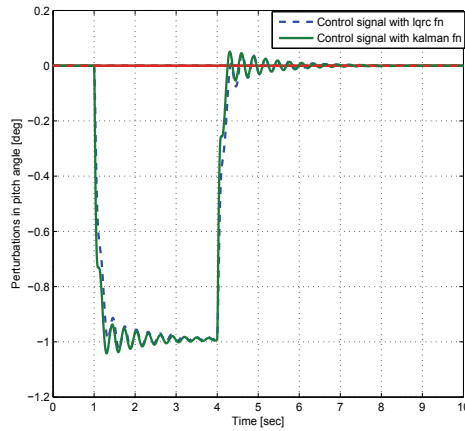

Fig. 16. Comparison of control effort while applying `kalman` and `lqrc` functions in MATLAB

The differences in the output response can be seen through the Kalman gain matrix, which when using the `lqrc` function were calculated to

$$Kf = \begin{bmatrix} 10.38 \\ -1.76 \cdot 10^{-6} \\ -1.65 \end{bmatrix} \tag{40}$$

Similarly, the Kalman gain matrix when using the `kalman` function is

$$Kf2 = \begin{bmatrix} 57.60 \\ 3.87 \cdot 10^{-6} \\ 1.07 \end{bmatrix} \tag{40}$$
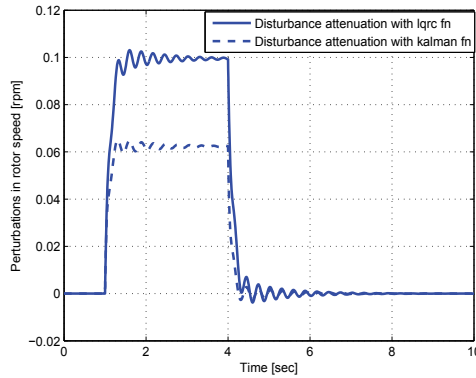
Fig. 17. Comparison of rotor speed for similar control effort while applying `kalman` and `lqrc` functions in MATLAB

The LQR gains were calculated with an exponential LQR with a time-constant α set to 10, and were given as

$$G = \begin{bmatrix} -25.78 & -2.68 \cdot 10^{-5} & -5.70 \end{bmatrix} \tag{40}$$

The perturbation in rotor speed when comparing the LQG with the DAC response is shown in Figure 18.
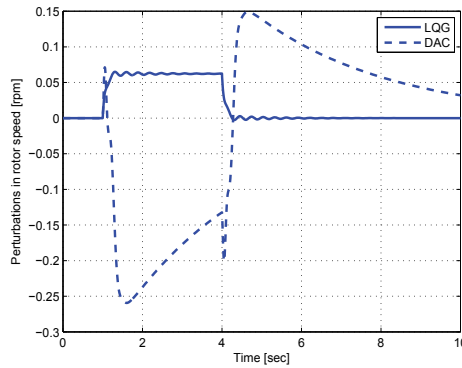
Fig. 18. Comparison of perturbations in rotor speed for LQG and DAC

Figure 18 makes it clear that the effect of the two different control methods is quite different when comparing the two output signals. The LQG controller will not force the disturbance to zero in the same way as the DAC does, which must be regarded as a disadvantage of the LQG. However, the DAC gives a much larger overshoot which is not very positive seen from a controller's perspective.

Similarly, the perturbations in pitch angle for the two methods is shown in Figure 19.

This figure shows that the control effort is much higher for the DAC approach than for LQG. To improve the robustness properties of the LQG will the LTR approach now be introduced as a way to ensure good robustness in spite of uncertainties in the plant model.
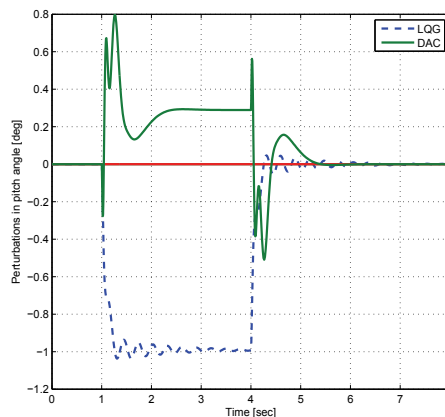
Fig. 19. Comparison of perturbations in pitch angle for the LQG and DAC

5. Conclusions and further works

The purpose of this thesis has been to reduce the loads on a WT for above rated wind speeds (Region III) by speed control when applying different controlling methods. This was first performed by pitch regulation with DAC. This regulation policy showed to have some regulation capacity, but also resulted in some bias in the control signal. It was found when utilizing the DAC controller that although the wind disturbance was well mitigated, the settling time was relatively long(approx. 10 sec). It could have been interesting to extend the work also to include torque regulation in below rated wind speeds. This regulation policy would aim at mitigation of speed and torque variations due to wind disturbances in Region II. The LQG regulator showed to give good speed attenuation, but since DAC and LQG is quite different approaches were a comparison between them not possible. It would have been of major interest to extend the work to also considering pitch actuator constraints to see how this would have affected the results, especially the control input signal.

6. Acknowledgment

7. References

Archer, C. L. & Jacobson, M. Z. (2005). Evaluation of global wind power, *Journal of Geophysical Research* Vol. 110: p. 17.

Athans, M. (1981). The Linear Quadratic LQR problem, *Massachusets Institute of Technology* .

Balas, M., Lee, Y. & Kendall, L. (n.d.). Disturbance tracking control theory with application to horizontal axis wind turbines, *Proceeding of the 1998 ASME Wind Energy Symposium, Reno, Nevada, 12-15 January* pp. 95–99.

Bianchi, F., Mantz, R. & Christiansen, C. (2004). Power regulation in pitch-controlled variable-speed WECS above rated wind speed, *Renewable Energy* Vol. 29(No. 11): pp. 1911–1922.

Bossanyi, E. A. (2000). The design of closed loop controllers for wind turbines, *Wind Energy* Vol.3: pp.149–163.

Bossanyi, E. A. (2003). Individual blade pitch control for load reduction, *Wind Energy* Vol. 6: pp.119–128.

Bossanyi, E. A. (2004). Developments in individual blade pitch control, *EWEA conference-The Science of Making Torque from Wind DUWIND Delft University of Technology April 19-21 2004* .

Bottasso, C. & Croce, A. (2009). Cascading kalman observers of structural flexible and wind states for wind turbine control, *Technical report*, Dipartimento di Ingegneria Aerospaziale, Politecnico di Milano, Milano, Italy.

Bottasso, C., Croce, A., Devecchi, D. & Riboldi, C. (2010). Multi-layer control architecture for the reduction of deterministic and non-deterministic loads on wind turbines.

Bottasso, C., Croce, A. & Savini, B. (2007). Performance comparison of control schemes for variable-speed wind turbines, *Journal of Physics: Conference Series 75, The Science of Making Torque from Wind* .

Burns, R. S. (2001). *Advanced Control Engineering*, Butterworth Heinemann.

Connor, B., Iyer, S., Leithead, W. & Grimble, M. (1992). Control of a horizontal axis wind turbine using H-infinity control, *First IEEE Conference on Control Applications*, pp. 117–122.

Gu D.-W., Petkov P.Hr. & Konstantinov, M. (2005). *Robust Control Design With MATLAB*, Springer.

Ekelund, T. (1997). *Modeling and Linear Quadratic Optimal Control of Wind Turbines*, PhD thesis, Chalmers University of Technology, Gothenburg, Sweden.

Elliot, A. S. & Wright, A. D. (2004). Adams/wt: An industry-specific interactive modeling interface for wind turbine analysis, *Wind Energy* .

Henriksen, L. C. (2007). Model Predictive Control of a Wind Turbine, *Informatics and Mathematical Modelling - Technical University of Denmark* .

Johnson, C. D. (1976). Theory of Disturbance- Accommodating Controllers, *Advances in Control and Dynamic Systems* Vol. 12: pp. 387–489.

Karimi-Davijani, H., Sheikholeslami, A., Livani, H. & Karimi-Davijani, M. (2009). Fuzzy logic control of doubly fed induction generator wind turbine, *World Applied Sciences Journal* Vol. 6 (4): pp. 499–508.

Lackner, M. A. & van Kuik, G. A. M. (2010). The performance of wind turbine smart rotor control approaches during extreme loads, *Journal of Solar Energy Engineering* Vol. 132(No.1).

Laks, J. H., Pao, L. Y. & Wright, A. D. (2009). Control of wind turbines: Past, present, and future, *University of Colorado at Boulder, USA* .

Lee, C.-H. (2004). Stabilization of nonlinear nonminimum phase systems: Adaptive parallel approach using recurrent fuzzy neural network, Vol. 34(No. 2): pp. 1075–1088.

Lee, J. & Kim, S. (2010). Wind power generations impact on peak time demand and on future power mix, *Green Energy and Technology* 3: 108–112.

Liebst, B. (1985). A pitch control system for the KaMeWa Wind Turbine, *Journal of Dynamic Systems and Control* Vol. 107(No.1): pp.46–52.

Liu, J.-H., Xu, D.-P. & Yang, X.-Y. (2008). Multi-objective power control of a variable speed wind turbine based in h infinite theory, *International Conference on Machine Learning and Cybernetics*.

Jonkman & Buhl Jr M.L. (2005). Fast's user guide, *National Renewable Energy Laboratory* .

Morimoto, H. (1991). Adaptive LQG regulator via the Separation Principle, *IEEE Transactions on Automatic Control* VOL. 35(No. I): 85–88.

Saberi, A., Chen, B. M. & Sannuti, P. (1993). *Loop Transfer Recovery, Analysis and Design*, Springer.

Mattson S.E. (1984). *Modeling and Control of Large Horizontal Axis Wind Power Plants*, PhD thesis, Lund Institute of Technology, Lund, Sweden.

Selvam, K. (2007). Individual pitch control for large scale wind turbines.

Waltz, E. (2008). Offshore wind may power the future, *Scientific American* .

Wilson, D. G., Berg, D. E., Barone, M. F., Berg, J. C., Resor, B. R. & Lobitz, D. W. (2009a). Active aerodynamic blade control design for load reduction on large wind turbines, *European Wind Energy Conference and Exhibition, 16-19 March*.

Wilson, D. G., Berg, D. E., Barone, M. F., Berg, J. C., Resor, B. R. & Lobitz, D. W. (2009b). Active aerodynamic blade control design for load reduction on large wind turbines, *AWEA Wind Power Conference* .

Wilson, D. G., Berg, D. E., Resor, B. R., Barone, M. F. & Berg, J. C. (2009). Combined individual pitch control and active aerodynamic load controller investigation for the 5mw upwind turbine, *AWEA Wind Power Conference* .

Wright, A. D. (2004). Modern control design for flexible wind turbines, *Technical report*, National Renewable Energy Laboratory.

Wright, A. D. & Fingersh, L. J. (2008). Advanced control design for wind turbines part i: Control design, implementation, and initial tests, *Technical report*, National Renewable Energy Laboratory.

Wright, A. & Stol, K. A. (2008). Designing and testing controls to mitigate dynamic loads in the controls advances research turbine, *Conference Paper 2008 ASME Wind Energy Symposium* .

Active Isolation and Damping of Vibrations for High Precision Laser Cutting Machine

Andrea Tonoli[1,2], Angelo Bonfitto[2] and Mario Silvagni[2],
Lester D. Suarez[2] and Enrico Zenerino[2]
[1]Mechanics Department
[2]Mechatronics Laboratory – Politecnico di Torino
Italy

1. Introduction

High precision industrial machines suffer the presence of vibrations due to several noise sources: ground vibration, acoustic noise, direct force disturbances. These are sources of several problems at different levels and of different natures causing the performance losses on sensitive systems (Crede, 1951), (Rivin, 1979).

In the last years the need of higher processing quality and throughput resulted in a continuing demand for higher accuracy. Therefore active isolation and vibration damping systems became mandatory to satisfy these requests (Preumont, 2002), (Hyde, 1997).

In general, machine supports are designed for high stiffness to obtain a robust machine alignment with respect to its surroundings. However, in the presence of significant ground vibration levels the support stiffness is commonly sacrificed to reduce the transmission to the payload stage. Efforts to go towards these issues are recorded in several applications and the solutions are different for any particular situation, depending on the nature of the vibration sources, the amount of the disturbances and the machine environment.

Three main categories of possible approaches can be identified: passive, active and semi-active configurations.

Completely passive solutions have almost reached their maximum potential which is still not sufficient to satisfy stringent requirements. On the opposite, the exponential growth in electronics and actuators fields made the use of active and semi-active isolation more feasible. In particular, active control architectures allow to perform an effective isolation at low frequencies, which is a common requirement for very demanding applications like micrometer motion control, defect inspections, critical dimensions measurement and overlay metrology.

Active control arrangements are provided with sensors, actuators and controllers (Watters, 1988). Each of them can be classified depending on their technology and physical working principle. For the application considered in this work, the main categories of sensors used are: displacement, velocity, acceleration, strain and force. In the same way, the most common types of actuators are: shape memory alloys, magnetic, piezoelectric, magnetostrictive and magneto-rheological fluids actuators (Thayer, 1998). The choice of sensors and actuators is strictly related to the type of application and requirements and has also influence on the selection of the control strategies to be

applied. Typically the main control approaches are feedback, classical or model based, and feed-forward technique, mostly with adaptive filtering of reference (Anderson, 1996). Depending on the type of the controller, the system model can be used to support the control design or can play itself a fundamental role on the control action (model based strategies) (Beadle et al, 2002), (Sullivan, 1997).

This chapter is focused on the evaluation of an active isolation and vibration damping device on the working cell of a micro-mechanical laser center, using active electromagnetic actuators. To clarify the goal of this study it is important to point out that: a) the vibration damping is defined as the reduction of the response amplitude of the system within a limited bandwidth near the natural frequencies of the system; b) vibration isolation is defined as the attenuation of the response of the system after its corner frequency to cut-off all disturbances after that frequency allowing all signals below it to pass with no alterations.

The machine object of study is composed by two main parts: a frame support and a payload stage where the laser cutting is performed. The system performance in terms of accuracy and precision is reduced by the presence of two main vibration sources: the ground and the stage itself. The active device should meet two main goals: the payload vibrations damping and the reduction of the transmissibility of ground disturbances.

In this work the phases followed to design, realize and validate the device are illustrated with a particular emphasis on the mechatronics aspects of the project.

A detailed analysis of the plant components is reported along with an exhaustive explanation of the supports, actuation and sensing subsystems design criteria.

The actuation block consists in four electromagnetic Lorentz type actuators (two per axis) (Brusa, 2001). The absolute velocities of the frame support and of the stage are measured by means of eight geophone sensors to determine the amount of the disturbances (Huan, 1985), (Riedesel, 1990). The considerations leading to the choice of this sensing system are reported along with the related signal conditioning stage. The design of the supports between the ground and the frame and of the connections between the frame and the stage is also explained.

Furthermore, all the subsystems described in the first part of the chapter are modeled along with their interactions. The Lagrange equations approach is used to represent the system behavior and in particular the links between the mechanical and electrical subsystems are illustrated. The model includes the plant, the sensing, the control and the actuation blocks. In particular, the mechanical subsystem is considered as a four degrees of freedom system. Time and frequency domain computations are carried out from the model to evaluate vibration levels and displacements and to identify which control parameters need to be carefully designed to satisfy the requirements.

The last section gives details about the proposed control action and the validation of the device. The control law consists in a couple of decentralized actions exerted along X and Y-axis allowing to minimize the ground vibrations transmission and damp the payload vibrations. A Lead-Lag control strategy, performed with a digital platform based on DSP and FPGA, is used to compensate the high-pass band dynamic of the geophone sensors and to damp the vibrations (Kuo, 1996), (Elliott, 2001). The payload isolation is achieved by feeding the control block with the difference of frame and stage velocities and giving the proper current command to the actuators.

The chapter concludes on the comparisons between simulation and experimental tests, illustrating the validity of the model and the effectiveness of the proposed approach. In particular, the performance of the vibration damping has been evaluated by using the frequency responses between the actuators force and the payload velocities and the active

isolation by simulating numerically the disturbances coming from the ground and by evaluating their transmission through all the system till the payload in closed loop configuration.

2. System architecture

In this section of the chapter a full description of all the machine subsystems is provided. The mechanical, electrical, electronic and control parts are identified and fully described separately in the first part. Furthermore, since the project can be assumed as a classical mechatronics application, the different blocks are analyzed in their interactions in order to provide an overall view of the system.
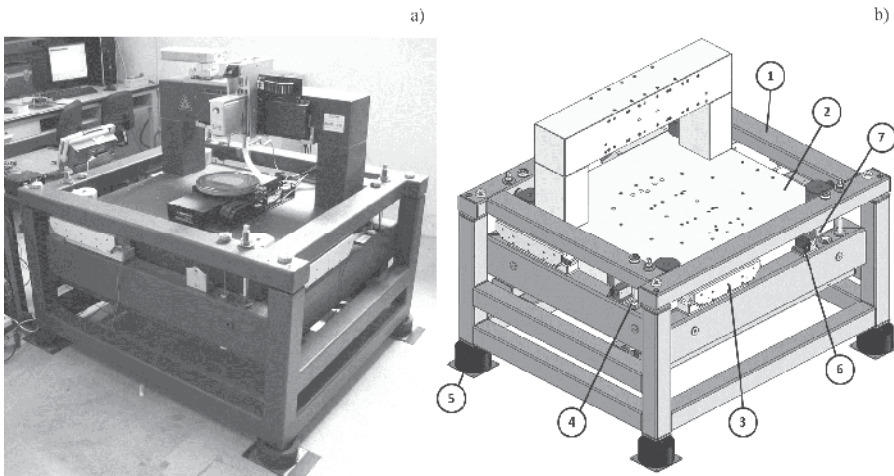

Fig. 1. a) Picture of the machine. b) Sketch of the system. 1: Frame; 2: Stage (Payload); 3: Actuators; 4: Frame – Stage Springs; 5: Air springs; 6: Frame sensors; 7: Stage sensors.

Figure 1.a shows a picture of the laser cutting machine while in the sketch of Figure 1.b all the components of the system are highlighted. The stage (payload) (2) consists in a granitic base that can move freely within the work volume and is surrounded by four electromechanical actuators (3) acting between the frame (1) and the stage. The machine is partially isolated from the ground by means of four air springs (5). Four mechanical springs (4) are vertically placed between the frame and the stage. The vibrations due to the machine process and coming from the ground are measured on the payload and on the frame by means of eight velocity inertial sensors (6, 7). A schematic representation of the actuators, sensors and springs position is reported in Figure 2 where c_{GF} and k_{GF} represent the damping and the stiffness introduced by the supports, c_{FS} and k_{FS} are the damping and the stiffness of the springs acting as connections between the frame and the stage. Actuators and sensors are placed so that they can be considered collocated in order to minimize the couplings between the axes actions by keeping the proper alternation between resonances and anti-resonances in the system dynamics. The main machine parameters and specifications are listed in Table 1.

The design phases have been performed considering the mechatronics nature of the system and the interactions between the machine subsystems, illustrated in Figure 3. A classical
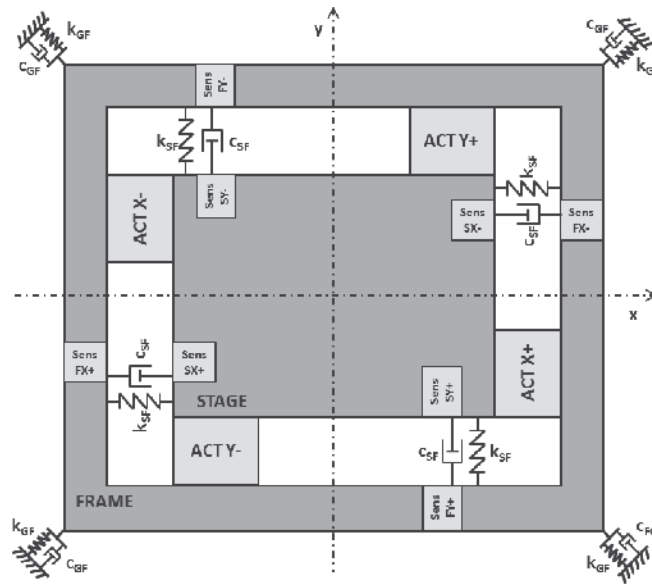
Fig. 2. XY plane view of the system. Frame-stage spring (k_{FS}, c_{FS}), electromagnetic actuator (ACT), velocity sensor (Sens.), Frame-Ground spring (k_{FG}, c_{FG}).

Stage mass	1450 kg
Frame mass	300 kg
Maximum displacement of the stage	2.5 mm
Inertia of the stage along X-axis in YZ-plane	200 kg m²
Inertia of the frame along X-axis in YZ-plane	100 kg m²

Table 1. Main parameters and specifications of the machine.
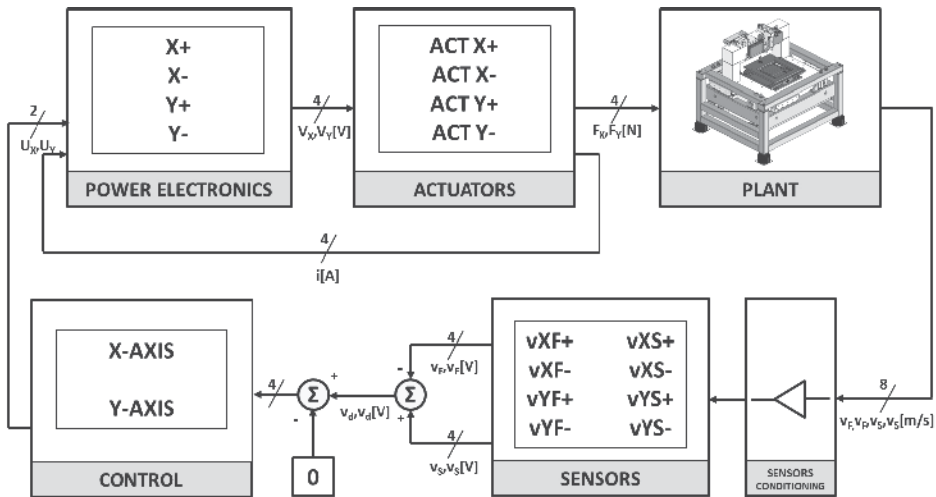
Fig. 3. Block diagram of the system.

feedback behavior is performed: eight velocities are acquired by the sensors measurements and elaborate with conditioning and filtering stages in order to feed the actuators with the proper commands by means of power electronics action. The filtering stage consists in the implementation of a Lead-Lag control strategy designed to fulfill the machine requirements in terms of: a) active isolation from the disturbances coming from the ground and b) damping of the vibrations generated by the machine processes.

2.1 Actuators subsystem

The actuation on the system is realized by means of four electromagnetic Lorentz type actuators placed as illustrated in Figure 1 and Figure 2.

The actuator configuration is reported in Figure 4 (a) Picture, b) Sketch), A and B are two permanent magnets while C indicates the coil.
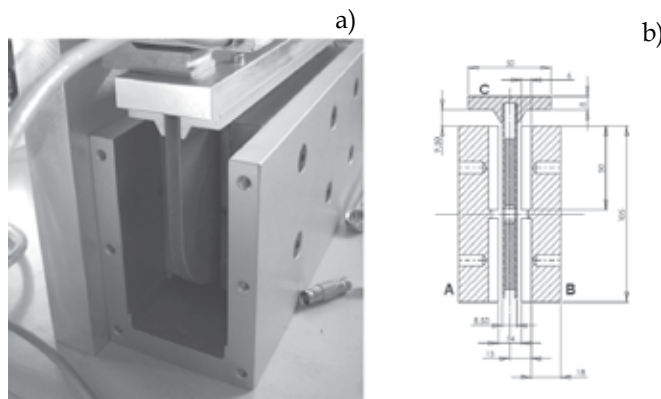
Fig. 4. a) Picture of the actuator, b) Section view (A and B: permanent magnets, C:coil).

The force F_{ACT} generated by each actuator is:

$$F_{ACT} = BNli \qquad (1)$$

where B is the magnetic field, N is the number of turns, i is the current flowing in the coil, l is the coil length. The direction of the resulting force is illustrated in Figure 5. The amount of required force for each actuator is equal to 200 N while the main parameters of the designed actuator are reported in Table 2.

Coil thickness	6	mm
Coil length	3.3	mm
Coil active section	198	mm²
Copper current density	12	A/mm²
Coil length (l)	200	mm
Coil max actuation force (F$_{ACT}$)	200	N
Number of turns (N)	263	-
Number of coils per axis	2	-

Table 2. Actuators main parameters.

The design of the actuators has been performed starting from the requirements of force and maximum displacement of the stage, then a current density and the wire section have been selected in order to perform a FEM analysis and to compute the magnetic field. Finally, once known all the electrical parameters, the coil length l has been computed.
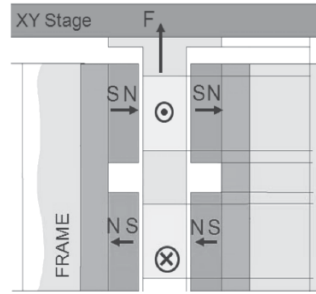
Fig. 5. Actuator force generation.

The actuators parameters have been identified experimentally. The resulting values are: resistance $R = 4.33\ \Omega$, $R = 9.64\ mH$. The actuator transfer function can be expressed as:

$$G_{ACT}(s) = \frac{1}{Z(s)} = \frac{1}{sL + R} = \frac{\dfrac{1}{L}}{s + \dfrac{R}{L}} \tag{2}$$

The stationary gain $G(s = 0)$ is:

$$G(s = 0) = 20\log_{10}\left(\frac{1}{R}\right) = -12.73\ dB \tag{3}$$

The electrical pole ω_e is:

$$\omega_e = \frac{R}{L} = 449\ rad/s = 72\ Hz \tag{4}$$

The resulting actuator trans-conductance transfer function is reported in Figure 6.
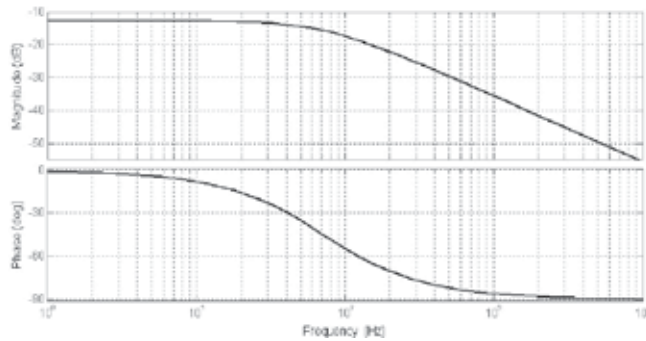
Fig. 6. Actuator trans-conductance transfer function (magnitude and phase).

2.2 Springs and supports

The frame and the stage are connected in the vertical direction by means of four linear springs placed as indicated by 4 in Figure 1 (c_{SF} and k_{SF} in Figure 2). The design has been performed computing displacements and stresses with a FEM software, starting from the following requirements:

- infinite fatigue life;

- stiffness $\begin{cases} k_{SFx} = 40\,N/mm; \\ k_{SFy} = 40\,N/mm; \\ k_{SFz} = 32500\,N/mm; \end{cases}$

- damping $\begin{cases} c_{SFx} = 228\,Ns/m; \\ c_{SFy} = 228\,Ns/m; \\ c_{SFz} = 4313\,Ns/m; \end{cases}$

- maximum displacement $z_{MAX} = 2.5mm;$

The designed spring is made of harmonic steel and is characterized by:

- length $l_{SPRING} = 125mm;$
- diameter $d_{SPRING} = 5mm;$
- maximum value of stress $\sigma_{MAX} = 500MPa.$

The supports chosen to provide the system with a partial level of isolation from the ground are four air-springs (5 in Figure 1, k_{GF} and c_{GF} in Figure 2) consisting in resilient element air and neoprene diaphragm. They are characterized by the following features:

- Nominal natural frequency: $\begin{cases} f_{GFx} = 12.3Hz; \\ f_{GFy} = 12.3Hz; \\ f_{GFz} = 5.4Hz; \end{cases}$

- stiffness $\begin{cases} k_{GFx} = 450\,N/mm; \\ k_{GFy} = 450\,N/mm; \\ k_{GFz} = 500\,N/mm; \end{cases}$

- damping $\begin{cases} c_{GFx} = 575\,Ns/m; \\ c_{GFy} = 575\,Ns/m; \\ c_{GFz} = 1700\,Ns/m; \end{cases}$

- Transmissibility at resonance: 8:1;
- The maximum load is equal to 545 kg;
- The maximum air pressure is equal to 80 psi (5.5 bar).

2.3 Sensing subsystem

The disturbances on the plant are evaluated by measuring the velocities on the stage and on the frame along X -axis and Y -axis by means of eight geophones placed as indicated in Figure 2. They can be considered as the most common velocity inertial sensors to measure seismic vibrations and can be classified as electromagnetic sensors that measure the velocity and produce a voltage signal thanks to the motion of a coil in a magnetic field (Hauge et al,

2002). One configuration of the conventional geophones consists of a cylindrical magnet coaxial with a cylindrical coil as shown in Figure 7. The coil is made up of a good conductor like copper and is wound around a nonconductive cylinder to avoid the effect of the eddy current that can be caused by the current induced in the coil. The wire diameter and the dimensions of the holding cylinder are designed according to the application requirements.
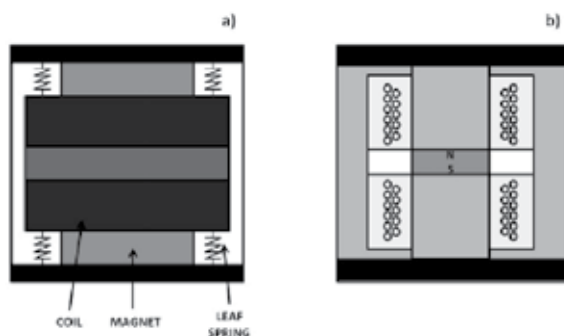
Fig. 7. Geophone active configuration scheme. a) Coil and springs installation. b) Cross section.

The internal core is a permanent magnet selected to give the highest possible magnetic field density to maximize the induced voltage in the coil. The coil is attached to the casing of the geophone by means of leaf springs (membranes); these springs are designed so as to maintain alignment in the motion of the coil relative to the magnet keeping the lowest stiffness possible in order to have a low resonant frequency for the geophone.

The reverse configuration (Figure 8) is realized using a coil fixed to the casing while the moving mass is the permanent magnet. Since the mass of the magnet is heavier than that of the coil, this configuration leads to a lower natural frequency, but the moving part is larger and heavier.
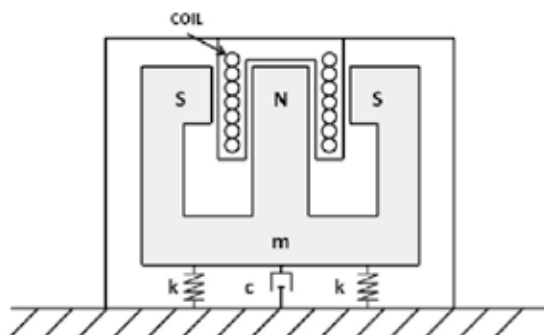
Fig. 8. Geophone reverse configuration scheme.

Two geophone sensors are tested in the system: active sensor LF24 (configuration in Figure 8) and passive sensor SM6 (configuration in Figure 7). The LF-24 Low Frequency Geophone is characterized by the following parameters: natural frequency at 1Hz, distortion measurement frequency at 12Hz and sensitivity equal to 15V/(m/s).

The sensor chosen is the passive sensor SM6 because it allows to have an extreme low noise though the output needs to be amplified by an active conditioning stage

The transfer function of the sensor response between the velocity of the casing and the induced voltage in the coil can be written in the form

$$TFG = -\frac{Gs^2}{s^2 + 2s\xi\omega_n + \omega_n^2}$$

(5)

where $\omega_n = \sqrt{K/m}$ is the natural frequency of the geophone, $\xi = C/2m\omega_n$ is the damping ratio including the effect of the eddy current and $G = Bl$ is the transduction constant, where B is the magnetic field generated by the permanent magnet and l is the length of the coil. Considering that the first natural frequency of the system is at about 1.8 Hz, close to the geophone natural frequency, the sensor sensitivity cannot be simply modeled as a constant value. Thus the transfer function of the geophone response must be identified to make the result more reliable.
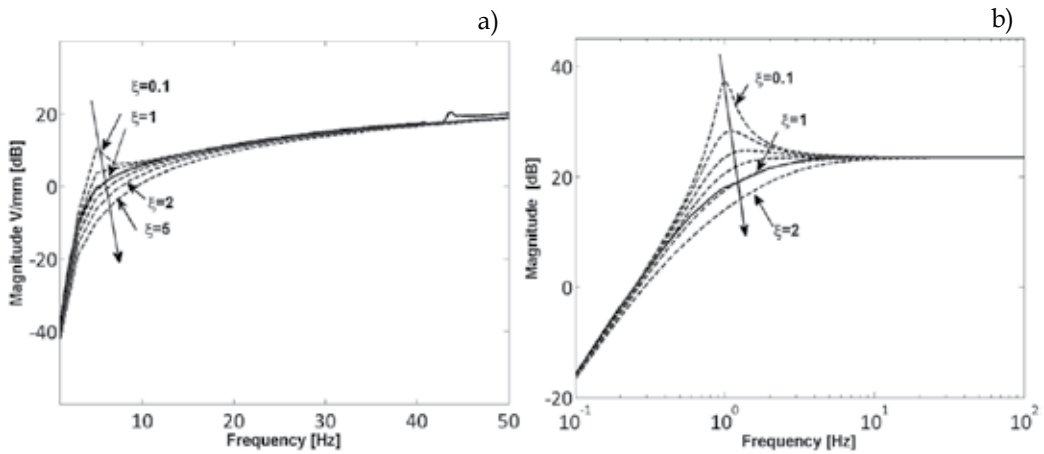
Fig. 9. Geophone damping ratio identification a) SM6 (Active configuration); b) LF24 (Reverse configuration).

SM6 is a passive velocity sensor with the following parameters: natural frequency is 4.5Hz, sensitivity is 28V/(m/s). The damping coefficient of SM6 can be indentified as the same way as LF24 in Figure 9.a and it is equal to 1.
Figure 9.b shows the LF24 transfer function expressed in Eq.5 identified experimentally. When the damping ratio is equal to 1, the experimental results fit quite well the model.
Since the generated voltage is proportional to the rate of crossing of the magnetic field, the output of the instrument will be proportional to the velocity of the vibrating body. A typical instrument of this kind may have a natural frequency between 1 Hz to 5 Hz. The sensitivity of such instrument may be in the range of 2 V/ms⁻¹ to 3.5 V/ms⁻¹ with the maximum displacement limited to about 5 mm peak to peak (Thomson, 1981). When a geophone is used to measure vibrations with a frequency below its natural frequency, the proof-mass tends to follow the motion of the vibrating body rather than staying stationary. This motion of the proof-mass following the casing reduces the relative motion which in turn reduces the induced voltage. Here the sensitivity of the sensor (ratio between the voltage and the casing velocity) becomes very small which restricts the performance of the sensor and limits the range of usage of the instrument to frequencies above its corner frequency. It is important to mention that

both displacement and acceleration can be obtained from the velocity sensor by means of the integral and derivative computation provided in most of the signal conditioner units.

2.4 Electronics subsystem

In this section the subsystems related to sensor acquisition and conditioning, power electronics and control implementation (Sensor conditioning, Power electronics, control blocks in Figure 3) are illustrated.

The electronics system architecture is shown in Figure 10. The main characteristic of this architecture is the serial communication input/output line that provides high noise immunity, which can be useful when signals must travel through a noisy environment, such as with remote sensors.
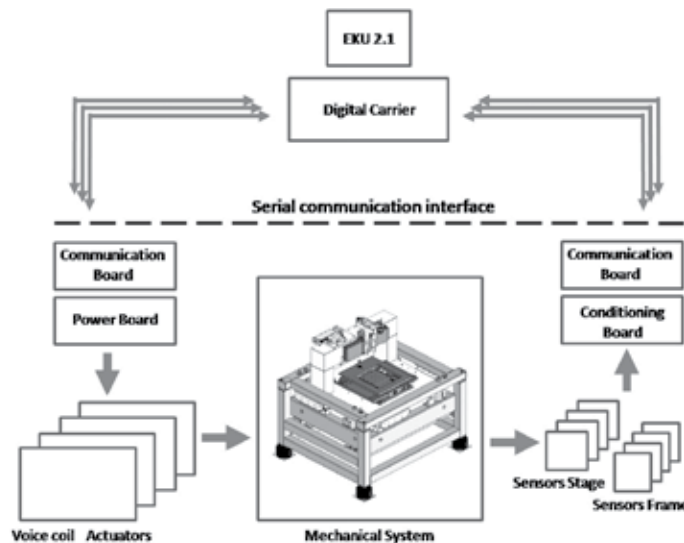
Fig. 10. Electronics subsystem.

The digital carrier is used like a buffer to provide the proper current level for the serial communication. Here, multiples system buses manage data exchange between the main serial communication core (FPGA) and the communication boards placed on the plant.

The communication boards are provided with one digital-to-analog converter (DAC) and two analog-to-digital converters (ADC). The DAC is a 16-bit, high-speed, low-noise voltage-output DAC with 30-MHz serial interface that is capable of generating output signal frequencies up to 1 MHz. The ADC is a single channel 12-bit analog-to-digital converter with a high-speed serial interface and sample rate range of 50 ksps to 200 ksps.

Control Unit (Control block in Figure 3)

The control module is supported by a DSP/FPGA–based digital control unit. Hence the overall control implementation can be divided between the two digital devices in order to fulfill different requirements: control strategy realization on DSP and serial communication implementation on FPGA.

The overall control strategy is characterized with a nested and decentralized control structure where only the outer loop is implemented on DSP while the inner loop (current loop) is realized on the power module directly. In particular, the outer loop computes the

right reference for the inner one starting from required error compensation. The same strategy is applied for each axis.

Sensors conditioning module (Sensor conditioning block in Figure 3)

The sensors conditioning module provides the output signal from geophone by means of an instrumentation amplifier circuits. The component is configured for dual-channel operation, in order to connect two geophones together. This conditioning circuit meets the needs of high performance and portable instrumentation when small signal amplitude conditioning brought out.

Figure 11, shows the circuit layout for dual-channel. R1A and R1B are the gain setting resistors.

With the ADC input in the range of [0-3] volt and assuming the maximum magnitude of noise on geophones measurement about 1000 m/s, the setting resistors are selected to achieve a gain of 100.
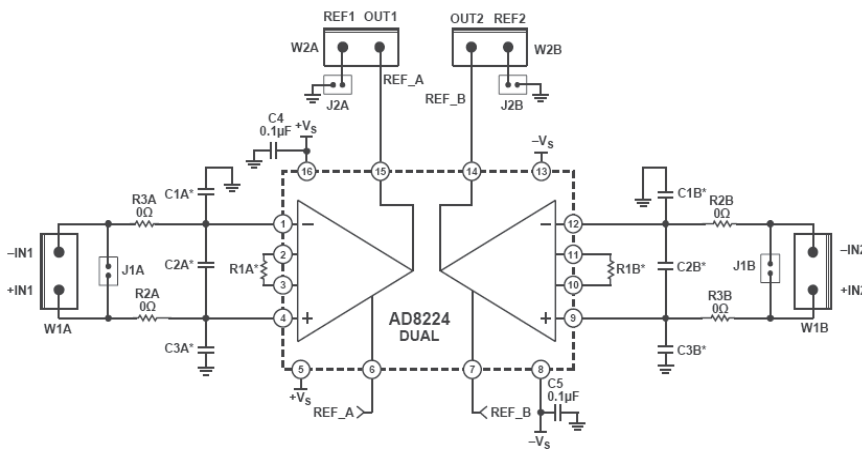
Fig. 11. Instrumentation amplifier circuits AD8224. R1A and R1B are the gain setting resistors.

Power electronics (Power electronics block in Figure 3)

The power module (Figure 12) is based on a trans-conductance amplifier instead of a switching amplifier in order to avoid noise due to the switching frequency. This kind of amplifier operates as a voltage-to-current converter whit a differential input voltage (voltage controlled current source configuration).

Figure 12 shows the electronics layout that is divided in three main stages: a) the trans-conductance amplifier (Trans Amp), b) the current amplifier (Curr Amp) and c) the feedback resistor (Feedback).

The power module uses the voltages reference (V_{in}) from the control unit to generate the proper current (I_L) to the load (electromagnetic actuator assumed as a RL load). The first stage performs the current control by means of an operational amplifier that is unity-gain stable with a bandwidth of 1.8MHz and it is internally protected against over-temperature conditions and current overloads. The second stage is a classical current amplifier with bipolar transistors in Darlington configuration to increase the current gain. The last stage provides the feedback signal to ensure the desired current in the load. The power supply is in the range of ±30V.
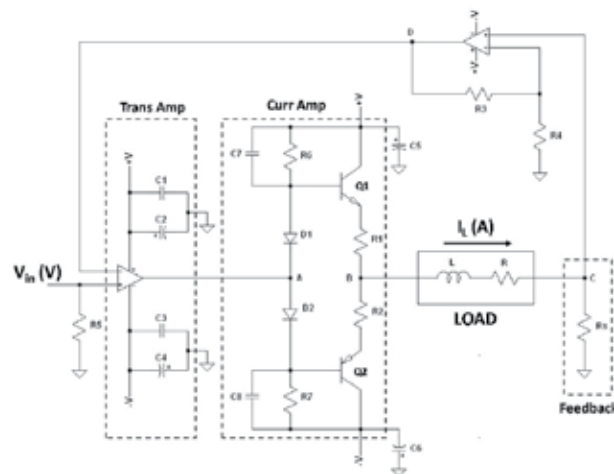
Fig. 12. Power electronic based on a trans-conductance amplifier.

3. Modeling

The system has been modeled by using four degrees of freedom considering that the dynamics along XZ and YZ planes are almost the same. As the vertical stiffness of the flexural springs is very high, it can be assumed that there is no relative displacement between stage and frame at vertical direction, which means the displacement in z axis about stage and frame are the same. Both the stage and the frame are assumed as moving about the frame mass center with the same rotating speed. Four flexural steel springs have been used to link the stage to the frame, four air springs are placed at the bottom of the frame, two actuators are working in series between the stage and the frame and two geophones are used to measure the velocities of stage and frame respectively. The model reference frames are defined in Figure 2 XY -plane view and in Figure 13, 16 YZ -plane view.
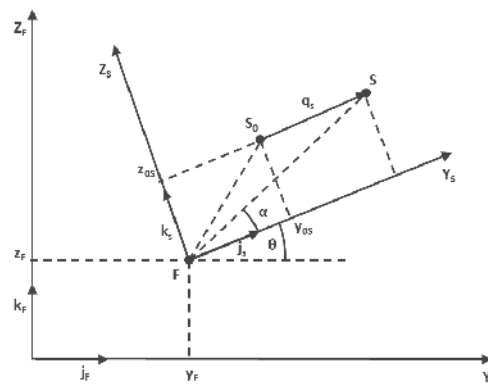
Fig. 13. YZ plane 4 dof kinematic relationships scheme.

The degrees of freedom of the model are:

$$\bar{X} = \begin{bmatrix} y_F; & z_F; & \theta; & q_S \end{bmatrix} \qquad (6)$$

that indicate the displacement of the frame along Y-axis and Z-axis, the rotation of the frame (and stage) around the X-axis mass center and the stage displacement along its Y-axis.

Referring to the illustration in Figure 14, it is possible to obtain the formulation of the velocity of a generic point S of the stage:

$$
\vec{V}_S = \vec{V}_F + \dot{q}_S \vec{j}_S + \dot{\theta} FS \left[\cos\alpha\, \vec{k}_S - \sin\alpha\, \vec{j}_S \right] =
$$
$$
= \dot{y}_F \vec{j}_F + \dot{z}_F \vec{k}_F + \left(\dot{q}_S - \dot{\theta} z_{0S} \right) \vec{j}_S + \dot{\theta}(y_{0S} + q_S)\vec{k}_S
$$
(7)
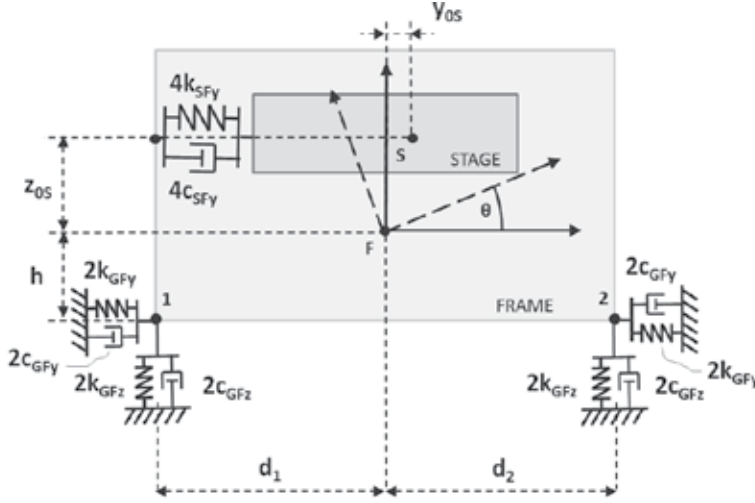
Fig. 14. YZ plane 4 dof model scheme.

The kinetic energy T of the system can be expressed as:

$$
T = \frac{1}{2} m_S \vec{V}_S^2 + \frac{1}{2} J_S \dot{\theta}^2 + \frac{1}{2} m_F \vec{V}_F^2 + \frac{1}{2} J_F \dot{\theta}^2
$$
(8)

where m_S, m_F, J_S and J_F are the mass and the rotating inertia of the payload (the stage S) and of the frame F.

The potential energy U is obtained starting from the diagram reported in Figure 14:

$$
U = k_{GFz}\left(z_F - \theta d_1 - z_G\right)^2 + k_{GFy}(y_F + \theta h - y_G)^2 + k_{GFz}\left(z_F + \theta d_2 - z_G\right)^2 + \ldots
$$
$$
+ k_{GFy}(y_F + \theta h - y_G)^2 + 2k_{SFy}q_S^2
$$
(9)

Owing to the Rayleigh dissipation formulation, the damping of the system is:

$$
\Re = c_{GFz}\left(\dot{z}_F - \dot{\theta} d_1 - \dot{z}_G\right)^2 + c_{GFy}(\dot{y}_F + \dot{\theta} h - \dot{y}_G)^2 + c_{GFz}\left(\dot{z}_F + \dot{\theta} d_2 - \dot{z}_G\right)^2 + \ldots
$$
$$
+ c_{GFy2}(\dot{y}_F + \dot{\theta} h - \dot{y}_G)^2 + 2c_{SFy}\dot{q}_S^2
$$
(10)

where each damping term c_i is obtained starting from the experimental identification of damping ratios ς_i:

$$c_i = 2\varsigma_i\sqrt{k_i m_i} \tag{11}$$

The inputs of the system are: the force of the electromagnet actuators F_{act}, the force of the stage F_S and the velocities from the ground in y direction v_{Gy} and z direction v_{Gz} v. The output are the velocities v_F of the frame and v_S of the stage measured with geophones sensors. Inputs and outputs are graphically represented in Figure 15.
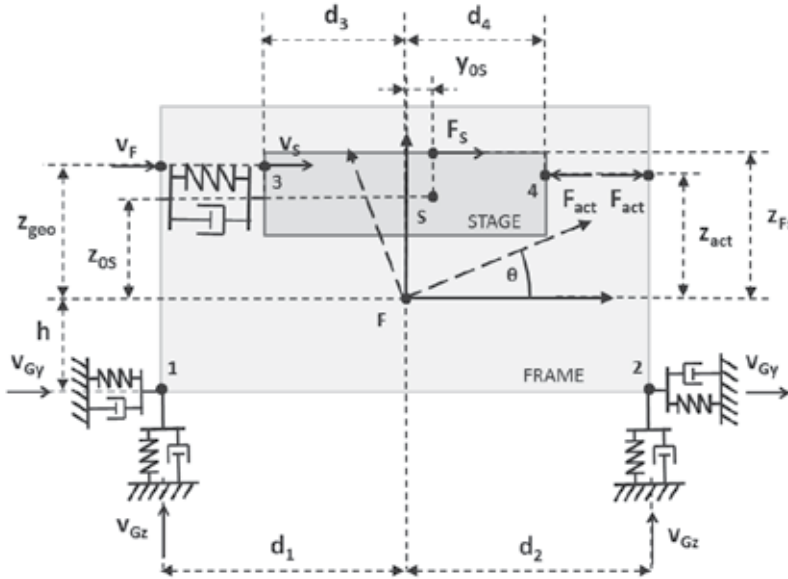
Fig. 15. YZ plane 4dof model scheme – input and output.

Using the Lagrange formulation is possible to write the equations of motion in the form:

$$M\ddot{q} + C\dot{q} + Kq = T\{F\} \tag{12}$$

where

$$q = \begin{pmatrix} y_F & z_F & \vartheta & q_S \end{pmatrix}^T \tag{13}$$

is the vector of the generalized coordinates,

$$F = \begin{pmatrix} v_{Gy} & v_{Gz} & F_S & F_{act} \end{pmatrix}^T \tag{14}$$

is the vector of the generalized forces and M is the mass matrix

$$M = \begin{bmatrix} m_{tot} & 0 & -m_S z_{0S} & m_S \\ 0 & m_{tot} & m_S y_{0S} & 0 \\ -m_S z_{0S} & m_S y_{0S} & J_{tot} & -m_S z_{0S} \\ m_S & 0 & -m_S z_{0S} & m_S \end{bmatrix} \tag{15}$$

with $m_{tot} = m_S + m_F$, $J_{tot} = J_S + J_F + m_S(y_{0S}^2 + z_{0S}^2)$. y_{0S}, z_{0S} are the initial position of the stage. The matrix is symmetric and not diagonal because it takes into account the coupling between the stage and the frame dynamics.

The stiffness matrix K is:

$$K = \begin{bmatrix} 4k_{GFy} & 0 & 4k_{GFy}h & 0 \\ 0 & 4k_{GFz} & -2k_{GFz}d_1 + 2k_{GFz}d_2 & 0 \\ 4k_{GFy}h & -2k_{GFz}d_1 + 2k_{GFz}d_2 & 2k_{GFz}d_1^2 + 4k_{GFy}h^2 + 2k_{GFz}d_2^2 & 0 \\ 0 & 0 & 0 & 4k_{SFy} \end{bmatrix} \tag{16}$$

The damping matrix C is:

$$C = \begin{bmatrix} 4c_{GFy} & 0 & 4c_{GFy}h & 0 \\ 0 & 4c_{GFz} & -2c_{GFz}d_1 + 2c_{GFz}d_2 & 0 \\ 4c_{GFy}h & -2c_{GFz}d_1 + 2c_{GFz}d_2 & 2c_{GFz}d_1^2 + 4c_{GFy}h^2 + 2c_{GFz}d_2^2 & 0 \\ 0 & 0 & 0 & 4c_{SFy} \end{bmatrix} \tag{17}$$

The selection matrix T of the generalized forces is:

$$T = \begin{bmatrix} -4k_{GFy} & 0 & -4c_{GFy} & 0 & 1 & 0 \\ 0 & -4k_{GFz} & 0 & -4c_{GFz} & 0 & 0 \\ 4k_{GFy}h & 2k_{GFz}d_1 - 2k_{GFz}d_2 & -4c_{GFy}h & 2c_{GFz}d_1 - 2c_{GFz}d_2 & 0 & 0 \\ 0 & 0 & 0 & 0 & 1 & -1 \end{bmatrix} \tag{18}$$

In the state space formulation the equations of motion of the system can rewritten as:

$$\dot{X} = AX + BU \tag{19}$$

where the state vector X and the input vector U are:

$$X = \{q \quad \dot{q} \quad y_G \quad z_G\}^T, U = \{v_{Gy} \, v_{Gz} \quad F_S \quad F_{act}\}^T \tag{20}$$

with A the state matrix, B the input matrix

$$A = \begin{bmatrix} 0 & I & 0 \\ -M^{-1}K & -M^{-1}C & M^{-1}T \\ 0 & 0 & 0 \end{bmatrix}, B = \begin{bmatrix} 0 \\ M^{-1}T \\ I \end{bmatrix} \tag{21}$$

The relationship between input and output can be represented as:

$$Y = CX + DU \tag{22}$$

where Y is the output vector, C the output matrix and D the feedthrough matrix

$$Y = \{v_S \quad v_F\}^T, C = \begin{bmatrix} 0 & 0 & 0 & 0 & 1 & 0 & -z_{geo} & 1 & 0 & 0 \\ 0 & 0 & 0 & 0 & 1 & 0 & -z_{geo} & 1 & 0 & 0 \end{bmatrix}, D = [0] \tag{23}$$

4. Control design & results

The control action is designed to achieve two main goals: active isolation of the payload from the ground disturbances and vibration damping during the machine work processes. These two actions allow to operate on the stage without external disturbances. The XZ and YZ are considered the same so the control laws along the two planes are equivalent.

Furthermore, from the control point of view, the adopted model is oversized respect to the control requirements if the goal is the isolation of the payload. As a matter of fact, in this case a two degrees of freedom model is sufficient while if also the dynamics of the frame is supposed to be controlled, then a 4 dof model is necessary.

The considered system can be considered as intrinsically stable due to the presence of mechanical stiffness between the payload and the frame allowing to obtain a negative real part for all the eigenvalues of the system.

Root loci of the system in open and closed loop configurations are reported in Figure 16.
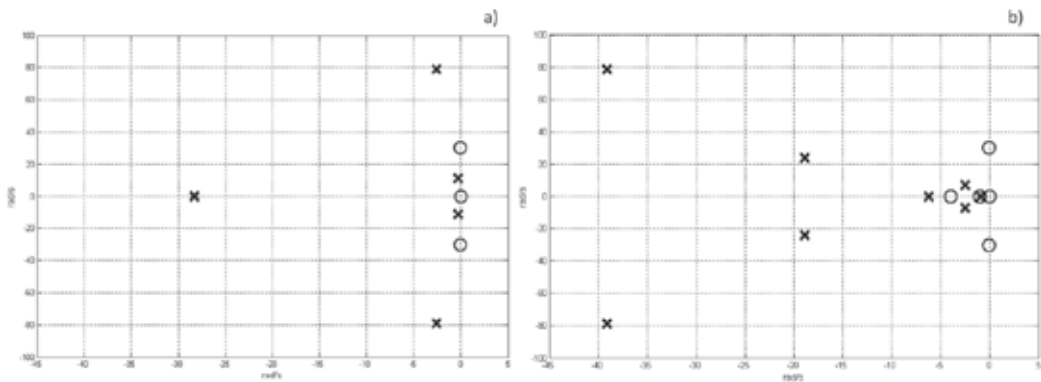
Fig. 16. Root loci of open loop (a) and closed loop (b) configurations (Circles: zeros; Crosses: poles).

Since the system along YZ (XZ) presents one actuation point and a couple of sensors (frame and stage velocities), a solution with a SISO control strategy is not feasible. A simplest solution to this problem considers the difference between the measured velocities as the feedback signal, so the system can be assumed as SISO and the control design becomes simpler.

Figure 17 shows that the system dynamics has a peak at 1.8 Hz related to the stage and higher modes related to the interaction of the stage with the frame and the ground at 10 Hz and beyond.

The control action is focused on damping the mode related to the stage by adding on the loop a lead-lag compensator.
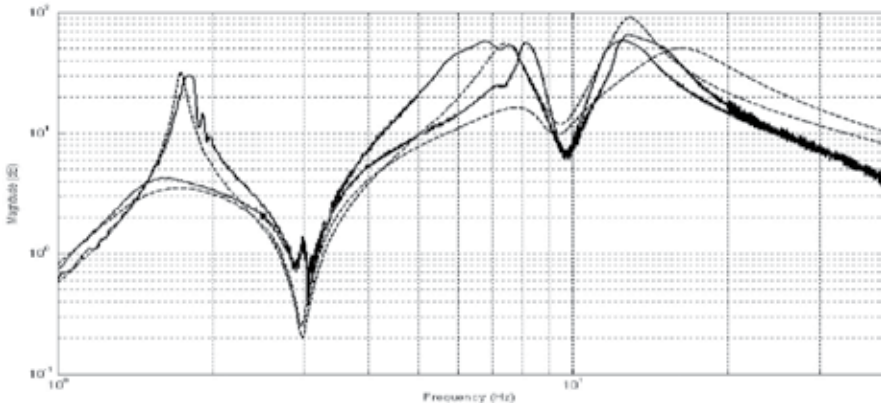
Fig. 17. Vibration damping action. Transfer function from the actuator force to the difference of frame and stage velocities ($(\dot{q}_S - \dot{q}_F)/F_{ACT}$). Open-loop vs Closed-loop. Solid line: experimental; Dashed line: numerical.

The two actions can be expressed as:

$$C_{LAG} = \frac{s + z_{LAG}}{s + p_{LAG}}$$

$$C_{LEAD} = \frac{s + z_{LEAD}}{s + p_{LEAD}}$$

(12)

The C_{LAG} action is used to improve the transient response at low frequency, while the C_{LEAD} is useful to increase the stability margin of the closed-loop system.

Therefore the resulting Lag-Lead action allows to compensate the geophone the critical phase behavior of the geophones and furthermore guarantees a quick damping action with good levels of stability margins.

The experimental tests have been performed to validate the two control actions. Figure 17 shows the frequency response function in open loop and closed loop, numerical and experimental calculated between the force of the actuator and velocity measured with the geophone on the stage. The force acts both on the stage and the frame, the dynamics of both the subsystems are visible. The vibration damping of the control action is validated on the stage mode (1.8 Hz peak) and the good correspondence between the simulated and experimental response is useful to validate the modeling approach.

A further demonstration of the correctness of the damping action is the velocity time response reported in Figure 18. In this case the system is excited with an impulse from the actuator and the velocity is measured on the stage. Numerical and experimental responses are superimposed to provide a further validation of the model (the position time response is not reported since the machine is not provided with displacement sensors and hence this validation could not be possible to perform). Figure 18.a shows open loop response, Figure 18.b shows closed loop response while in Figure 18.c the force exerted by the actuators is reported.
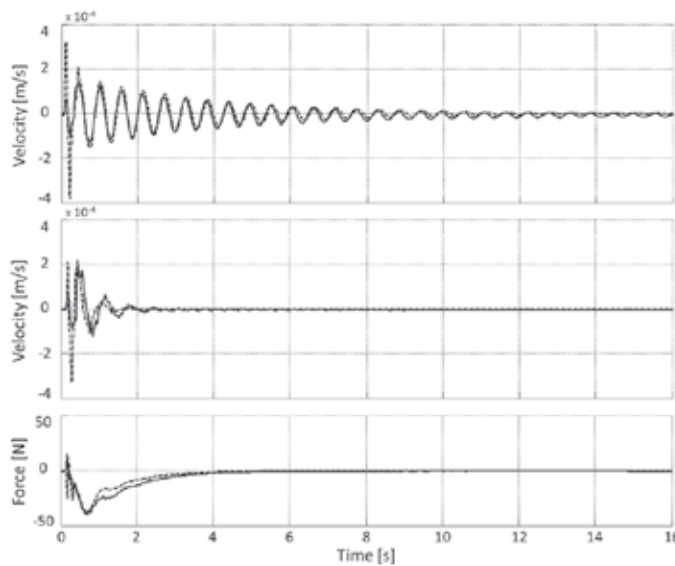
Fig. 18. Impulse time response, force from the actuator and velocity measured on the stage. Open-loop (a), Closed-loop (b), Force exerted by the actuators. Solid line: experimental results. Dashed line: numerical results.
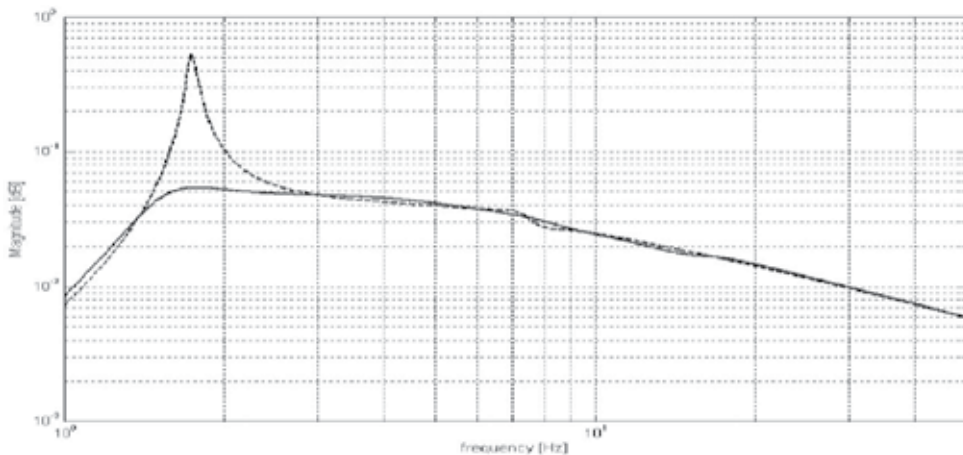
Fig. 19. Vibration damping action. Transfer function from a force applied on the stage to the velocity measured on the stage $(\dot{q}_S / F_{STAGE})$. Numerical response. Solid line: closed-loop; Dashed line: Open-loop.

The excitation coming from the laser-axis action on the payload is controlled in an effective way as shown in Figure 19 where the numerical transfer function between a force impulse on the stage and the related measured velocity is reported.

The active isolation action is verified by simulating the excitation coming from the ground. The experimental test in this case has not been performed since in reality it is difficult to excite the machine from the ground in a controlled and effective way. Nevertheless the

model is reliable as proved in Figure 15 and the obtained results can be assumed as a good validation of the control action.

Figure 20 illustrates that the closed loop system is capable to reject the disturbances coming from the ground in an effective way.
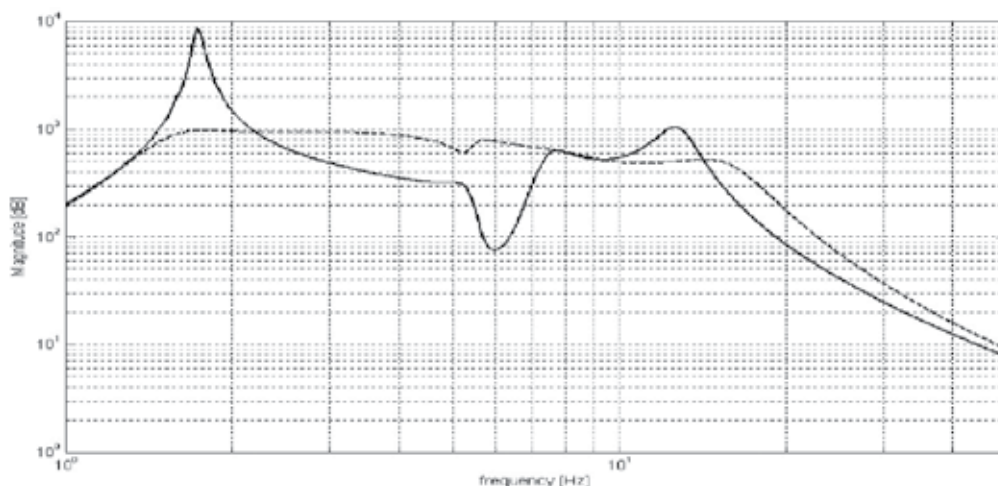
Fig. 20. Active isolation action. Transfer function from a simulated ground velocity to the velocity measured on the stage $(\dot{q}_S/\dot{q}_G)$. Numerical response. Solid line: Open loop configuration. Dashed line: Closed loop configuration.

5. Conclusions

In this chapter the realization of an active isolation and damping of vibrations for high precision laser cutting machine has been illustrated.

The literature analysis confirms that in the last decades active configurations had an exponential growth due to their high performance level.

The proposed solution uses Lorentz type electromagnetic actuators since they can be easily integrated in the mechanical structure and allow to reach good results.

A mechatronic approach has been used to manage the criticalities introduced by the subsystems interactions since it provides an overall view of the system.

A 4 degrees of freedom model has been carried out by means of Lagrange equations approach and was used to choose and set the control strategy. The proposed control technique is a lead-lag compensator able to control the stage dynamics and isolate it from the external disturbances.

The effectiveness of the vibration damping and the active isolation actions have been validated experimentally by analyzing the plant behavior in open-loop and closed-loop configurations with frequency and time responses. The results have been compared to the numerical computations to prove the correctness of the modeling approach.

Future works will be focused on the tests of new control strategies and on the evaluation of the adopted solutions compared to existing methods.

6. References

Anderson E., Leo D.J., Holcomn M.D, (1996). UltraQuiet platform for active vibration isolation, Proceedings Smart Structures and Integrated Systems 2717, San Diego, CA, pp. 436–451.

Beadle B.M., Hurlebaus S., Gaul L., Stöbener U. (2005). Active control strategies for vibration isolation, in Proc. IUTAM Symp. Vibration Control of Nonlinear Mechanisms and Structures 2005, Munich, Germany, pp. 91-100.

Brusa E., Carabelli S., Genta G., Maddaleno F., Silvagni M., Tonoli A. (2001). Voice coil actuator for Active Vibration Isolation in Microgravity, 6th ISMST, Torino.

Crede, C. (1951). Vibration and shock isolation, John Wiley and Sons Inc., New York, USA

Elliott S.J. (2001). Signal processing for active control, Academic Press.

Hauge, G.S. Campbell, M.E.. (2004). Sensors and control of a space-based six-axis vibration isolation system. Journal of Sound and Vibration 269. Pp 913–931.

Huan, S. L., & Pater, A. R. (1985). Analysis and prediction of geophone performance parameters. Geophysics, 50(8), 1221:1228.

Hyde T.T, (1997) An experimental study of active isolation. Proceedings of the 38th AIAA/ASME/ASCE/AHS/ASC, Structures, Structural Dynamics and Materials Conference, Orlando, FL, pp. 1763–1773.

Kuo S.M., Morgan D.R., (1996). Active noise control systems: algorithms and DSP implementations, John Wiley & Sons.

Preumont, A. (2002). Vibration control of Active Structures. Kluwer Academic Publishers, 2nd Edition, Netherlands

Riedesel, M., Moore, R. D., & Orcutt, J. A. 1990. Limits of Sensitivity of Seismometers with Velocity Transducers and Electronic Amplifiers. Bulletin of the Seismological Society of America, 80(6), 1725:1752.

Rivin, E. I. (1979). Principles and criteria of vibration isolation of machinery. Trans. of the ASME, Journal of Mechanical Engineering, 101:682–692.

Sullivan J., Rahman Z., Cobb R., Spanos J. (1997). Closed-loop performance of a vibration isolation and suppression system, Proceedings of the American Control Conference, Vol. 6, Albuquerque, NM, pp. 3974–3978.

Thayer, D., Vagners, J., von Flotow, A., Hardham, C. and Scribner, K., (1998). "Six Axis Vibration Isolation Using Soft Actuators and Multiple Sensors," Proceedings of the 21st Annual AAS Guidance and Control Conference, Feb 1998.

Thomson, W. (1971). Theory of vibration with applications. George Allen and Unwin.

Watters B.G., Coleman R.B., Duckworth G.L., Berkman E.F. (1988). A perspective on active machinery isolation, Proceedings of the 27th Conference on Design and Control, Vol. 3, Austin, TX, pp. 2033–2038.

Bearings Fault Detection Using Inference Tools

Miguel Delgado Prieto, Jordi Cusidó i Roura and
Jose Luis Romeral Martínez
MCIA Group, Technical University of Catalonia
Spain

1. Introduction

Electric motors are nowadays widely used in all kind of industrial applications due to their robustness and ease of control through inverters. Therefore, any effort, with the aim of improving condition monitoring techniques applied to them, will result in a reduction of overall production costs by means of productive lines stoppage reduction, and increment of the industrial efficiency. In this context, the most used electric machine in the industry is the Induction Motor (IM), due to its simplicity and reduced cost. The analysis of the origin of IMs failures exhibits that the bearings are the major source of fault (Singh et al., 2003), and even a common cause of degradation in other kinds of motors as Permanent Magnet Synchronous Machines. An IM failures percentage distribution, according to previous studies (O'Donell, 1986), is shown in figure 1, in order to highlight the bearings monitoring importance.
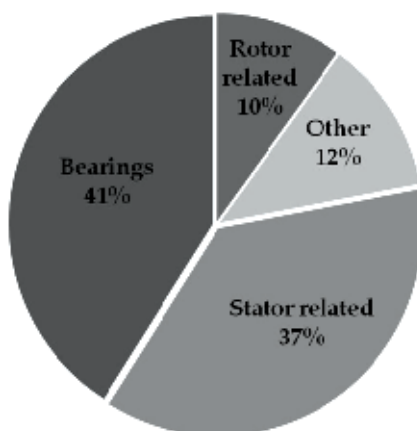
Fig. 1. IM failures percentage distribution.

Focusing in bearings defects, these have been typically categorized as distributed or local. Distributed defects include mainly surface roughness, waviness and misaligned races. Localized defects, however, include cracks, pits and spalls basically.
A great deal of studies concentrate their efforts in localized defects detection, because these defects are generally related with concrete fault indicators in the acquired signals, meanly

characteristics faults harmonics in machine vibrations. However, the issue related with the capability to detect both, localized and generalized bearings faults, is an important issue that should be attended (Cusido et al., 2009). Generalized degradation is difficult to detect because the lack of consistent characteristic fault harmonics in the spectral decomposition of any acquired signal. Therefore, it is difficult to inspect deeply motor bearings by analysing only some specific fault harmonics due to fault signal complexity (Obaid et al., 2003), and in the case of asynchronous motors the slip factor introduces additional difficulty. This fact makes necessary the diagnosis support of additional signal analysis (Frosini et al., 2008). The current trends in condition monitoring are related with the fusion of different features, which provide the possibility to merge fault indicators from different physical magnitudes (Cusido et al. 2010). This data fusion improves the diagnostic reliability, because fault indicators that are not descriptive enough themselves can contribute to detect faults in relation with others, especially if the features are extracted from different physical magnitudes, which enhance the monitoring capabilities. However, it is necessary to find the best and most useful fault indicators, and merge them by some kind of inference tool.

In this chapter, additional bearings fault features are introduced to be merged with traditional vibrations fault indicators. Hence, features from machine vibration, stator currents, stator common mode currents and acoustic emissions, are presented and related with bearing faults. With all these fault indicators diagnosis different systems based on multidimensional features fusion can be implemented. The bearing diagnosis capability and reliability are easily increased making possible the bearing fault detection even if the fault is localized or generalized. Regarding the inference tools for features fusion, it can be chosen a wide variety of methods such as statistical rules, expert systems or artificial intelligent techniques among others. In this chapter, two different inference tools are presented in order to generate two different diagnosis systems: Look-up tables, representing one of the easiest ways to merge information, and Fuzzy logic as a next step towards advanced diagnosis systems based on artificial intelligence.

2. Basic theory

A brief introduction of each proposed physical magnitude for bearings fault detection is presented next, with special attention to the specific bearings fault indicators.

2.1 Vibration analysis

Vibration analysis is one of the most extended condition monitoring techniques. Despite being a reliable, well studied robust technique, it requires that the motor under test has a vibration transducer installed. The measurements should be taken on the bearings, bearing support housing, or other structural parts that significantly respond to the dynamic forces and characterize the overall vibration of the machine. Therefore, the major disadvantage of vibration monitoring is that requires access to the machine, and specific accelerometers housing over the machine is sometimes required. For accurate measurements, sensors should be mounted tightly on the machine, and expertise is required in the mounting, condition that makes its online application expensive. Sometimes, other techniques without this kind of restriction are preferred or required.

The single-point bearing defects imply certain characteristic fault frequencies which will appear in the machine vibrations. The frequencies are predictable and depend on which surface of the bearings contains the fault. There is one characteristic fault frequency

associated with each of the four parts of the bearing. Vibration frequency components related to each of the four basic fault frequencies; (1) Fundamental train frequency, (2) Ball-spin frequency, (3) Ball pass outer race and (4) Ball pass inner race, can be calculated using the following expressions (Bellini et al., 2008):

$$FTF = \frac{1}{2} f_r \left(1 - \frac{P_d}{B_d} \right) \tag{1}$$

$$BSF = \frac{1}{2} \frac{P_d}{B_d} f_r \left[1 - \left(\frac{B_d}{P_d} cos\emptyset \right)^2 \right] \tag{2}$$

$$BPFO = \frac{n}{2} f_r \left(1 - \frac{B_d}{P_d} cos\emptyset \right) \tag{3}$$

$$BPFI = \frac{n}{2} f_r \left(1 + \frac{B_d}{P_d} cos\emptyset \right) \tag{4}$$

with:
n: Number of bearing balls
fr: Rotor speed
Bd: Ball diameter
Pd: Bearing Pitch diameter
β: Contact angle of the ball on the race
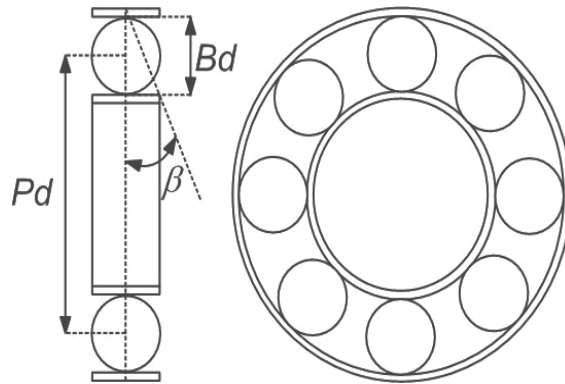
Fig. 2. Main bearing design parameters, B_d: ball diameter, P_d: pitch diameter, β: contact angle.

Regarding the roughness bearings defects, there is a wide variety of causes from contamination of the lubricant to the shaft currents or misalignment. The generalized roughness faults produce unpredictable broadband effects in the machines vibration spectrum, but it seems to be feasible the detection by means of the temporal vibration signal Root Mean Square (RMS) analysis. As some works and standards (Riley et al., 1999; Cabanas et al., 1996) set out, a RMS vibration value evaluation of the motor also provides a good indicator for motor health, allowing machine overall fault diagnosis.

2.2 Stator currents
A Motor Current Signature Analysis (MCSA) represents by the stator currents acquisition an interesting alternative method with its own particularities and benefits (Cusido et al., 2007a); the most interesting of them is to avoid accessing inside the motor making it easy to perform

its online fault analysis (Cusido et al. 2007b). It has been demonstrated (Schoen et al., 1995) that the characteristic bearing fault frequencies in vibration can be reflected on stator currents. As a result of motor airgap length variations due to bearings defect, flux density is influenced and then an additional magnetic flux appears. This magnetic flux, and its variations associated to rotor turning, creates additional components that can be found in the stator currents spectra (Cusido et al., 2005). Using this method it has been widely demonstrated in the literature (El Hachemi Benbouzid, 2000) that different faults like eccentricity, rotor asymmetry, stator winding failures, broken bars and bearings damage can be diagnosed. The relationship between the vibration frequencies and the current frequencies for bearing faults can be described by equation (5). Therefore, by means of (5), it is possible to analyze the specific fault harmonics in order to find abnormalities in their amplitude values.

$$f_{bg} = |f_e \pm m * f_v| \qquad (5)$$

with:

f_{bg}:   Electrical fault characteristic frequency
m: Integer
f_e: Electrical supply frequency
f_v: Vibration fault characteristic frequency {(1), (2), (3) or (4)}

It is well established that for bearing single-point defects, the characteristic stator current fault frequencies are good fault indicators. Even so, it was discovered in several studies, that for many in situ generated bearing faults, those characteristics fault frequencies are not observable and may not exist at all in stator current (Stack et al., 2004.). But it is demonstrated also that these same bearings faults have an effect over the motor eccentricity (Basak et al., 2006), and these characteristics stator current faults frequencies are easily detectable as sidebands over the fundamental motor current frequency. Therefore, the evaluation of the bearings characteristics stator current faults frequencies is useful for diagnosis proposes, because it can diagnose directly the bearing fault. But as a second diagnosis step, the analysis of stator current fundamental sidebands, in order to detect eccentricity, can be useful also for bearing diagnosis. However, it is necessary other fault indicators in order to classify correctly between eccentricity fault caused by bearing fault or eccentricity fault caused by other faults in the motor.

Regarding generalized bearing defects, previous works have shown the existing correlation between vibration and currents RMS values (Riley et al., 1999). Although it is a complex function that relates both magnitudes, this work tries to check the RMS currents reliability in order to perform the motor status diagnose.

2.3 High frequency common-mode pulses

One of the biggest culprits for bearings failure are common-mode circulating currents (CMC). The CMC are generated due to the inverter used to manage motors, because the inverter creates common mode voltage as figure 3 shows. Each high dv/dt over the inverter modulation implies a proportional current, which is propagated over the motor trough different paths to the ground in order to turn back to the inverter (Muetze and Binder, 2007a).

The CMC travels around the motor (and load if it is not electrically isolated), due to the capacitive effect that two conductive materials separated by means of some isolating material (dielectric) can create. For instance, the capacitive effect produced between the coil group and the chassis separated with air gaps in an induction motor.
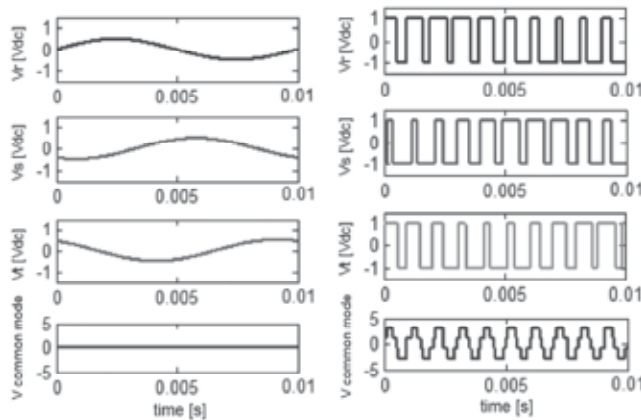
Fig. 3. Common mode voltage generated with PWM modulation.

The capacitances created inside the motor have a very low value, so the motor intrinsically gets filter the low frequency currents, but the high frequency currents see low impedance paths (Binder and Muetze, 2008.). Some current travel over the shaft, that in an electrical sense, find the bearing rail, lubricant and bearing ball capacitive coupling. The high frequency CMC pulses current that contain an important amplitude value, provoke a discharge over the capacitive coupling. This phenomenon is called EDM (Electric Discharge Machining) (Kar and Mohanty, 2008). The CMC influences on the bearings degradation due to the effect that every CMC discharge provoke over the lubricant that recover the bearing, because the continually application of these discharges implies lubricant degradation. This effect increases the contact between the bearings with the rail accelerating the final bearings degradation.

As it is shown in figure 4a, circulating currents could follow different paths to the ground through the stator windings or rotor. One important path of the circulating currents is through the bearings (Muetze and Binder, 2007b). The electrical scheme of parasitic capacitive couplings is shown also in figure 4b. This scheme represents the CMC path from inverter to bearings. As it has been explained previously, the inverter generates common mode voltage (V_{mc}) and at the same time, generates common mode current (I_{mc}) which is propagated trough the wire (L_C), motor (L_m) and through the coupling effect between the motor and chassis, and between the motor and rotor, this last ones cross finally the coupling effect between the shaft and the bearings.

A temporal CMC acquisition and a single common-mode discharge are shown in figure 5. These currents typically show a frequency range of mega-hertz with a period of micro-seconds between bursts. CMC discharges provoke bearings lubricant degradation. This effect provokes the contact between the bearings with the rail. Therefore, CMC discharges amplitude is directly depending of the parasitic capacitances which are depending of the lubricant state and the distance between bearings and rail mainly. Therefore, seems to be possible the bearings diagnosis by means of the number of CMC pulses that surpassed a prefixed amplitude threshold during a fixed time, in order to distinguish between fault and healthy bearings (Delgado et al., 2009). Analyzing the number of CMC pulses that surpassed a current amplitude threshold value, it is possible to see that a minor number of CMC pulses surpassing the threshold, is significant of a degradation state of the bearings, because the capacitive effect rail-lubricant-bearing needs a minor "*energy*" differential to allow an EDM.
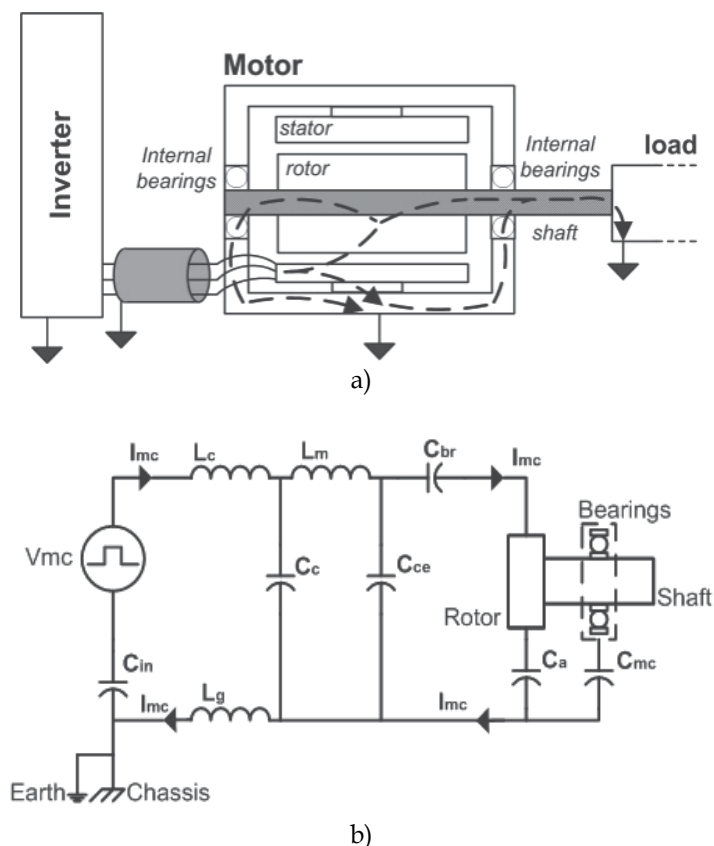
Fig. 4. a) Main CMC paths over inverter-motor-load system. b) Electrical Scheme for capacitive and parasitic couplings.

Therefore, the methodology consists in a first time acquisition over the stator CMC in a test bench with healthy bearings. The amplitude of the CMC pulses decrease at the same time that bearings degradation increase, so is necessary to specify a CMC pulses amplitude threshold and count the number of pulses that surpasses this threshold during a fixed time. Obviously, the time acquisition and the threshold value make depends the number of CMC pulses counted. An acquisition time of tens of milliseconds, and a threshold over the 75% of the maximum CMC pulses amplitude over healthy bearing, is enough to distinguish between healthy and degraded bearings.

In this work, to limit the CMC acquired signal to only pulses flowing through bearings (the responsible of balls degradation), a motor modification was introduced. All the ball bearing under test were isolated from the motor stator frame but in a point connected to ground through a cable where the pulses were measured. Bearings insulation was achieved by surrounding the piece with a polytetrafluoroethylene (PTFE) flat ring with a hole mechanized in it to let the cable pass through.

2.4 Acoustic Emissions

The Acoustic Emission Technique is a very promising tool that has practical application in several fields, and specifically, recent important relevance in condition monitoring of

machines. Acoustic Emission is defined as a radiation of mechanical elastic waves produced by the dynamic local rearrangement of the material internal structure. This phenomenon is associated with cracking, leaking and other physical processes and was described for the first time by Josef Kaiser in 1950. He described the fact that no relevant acoustic emission was detected until the pressure applied over the material under test surpassed the previously highest level applied.

a)

b)
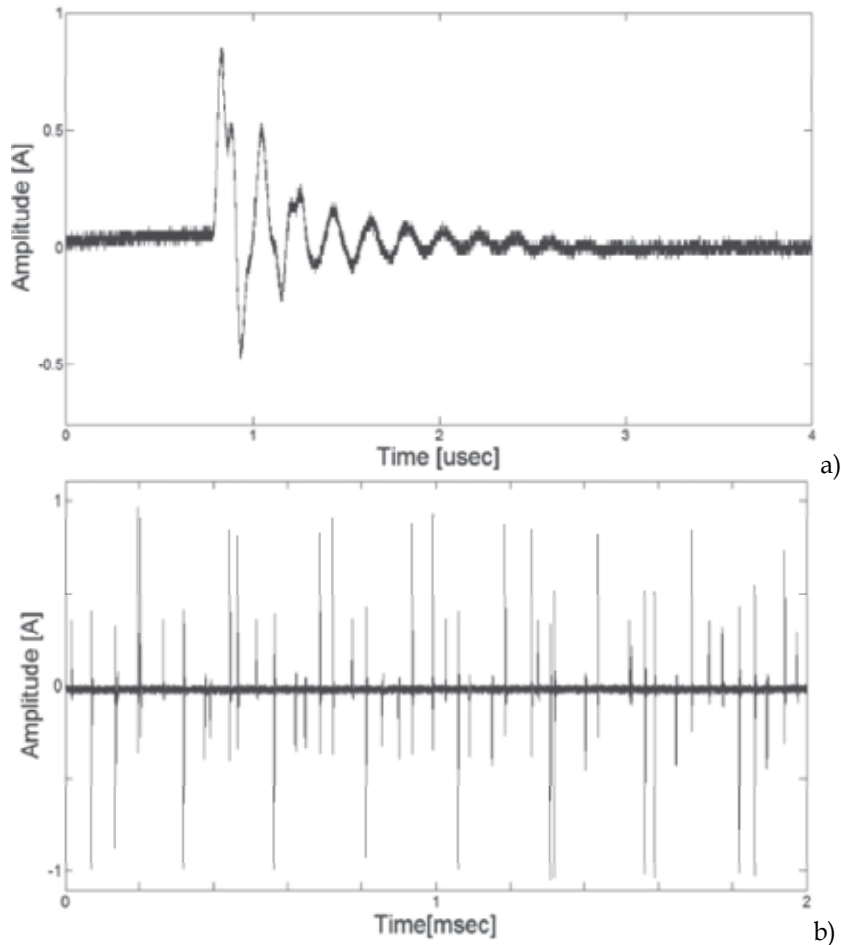
Fig. 5. Examples of common-mode current discharges, a) individual discharge, b) a set of discharges.

Acoustic Emissions Technique is classified as a passive technique because the object under test generates the sound and the Acoustic Emission sensor captures it. By contrast, Active methods rely on signal injection into the system and analysis of variations of the injected signal due to system interaction. Then an acoustic emission sensor captures the transient elastic waves produced by cracking or interaction between two surfaces in relative motion and converts their mechanical displacement into an electrical signal. This waves travel through the material in longitudinal, transverse (shear) or surface (Rayleigh) waves, but the majority of sensors are calibrated to receive longitudinal waves. Wherever the crack is

placed, the signal generated travels from the point of fracture to the surface of the material. The transmission pattern will be affected by the type of material crossed and then isotropic material will lead to spherical wave front types of propagation only affected by material surfaces or changes, where the Snell law rules their reflection and reflexion. On Figures 6 and 7 is shown the evolution of acoustic waves inside a Material. On figure 6 it is shown how reflections on waves due to the defect appear.
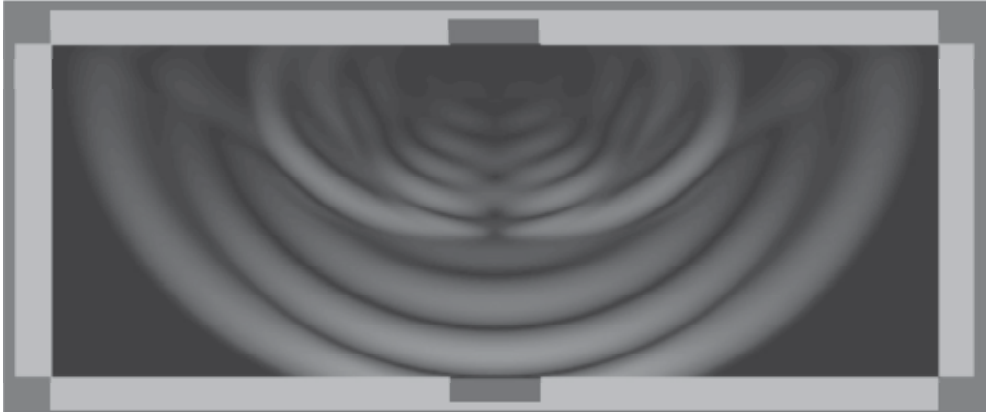
Fig. 6. Acoustic Emission Wave Propagation
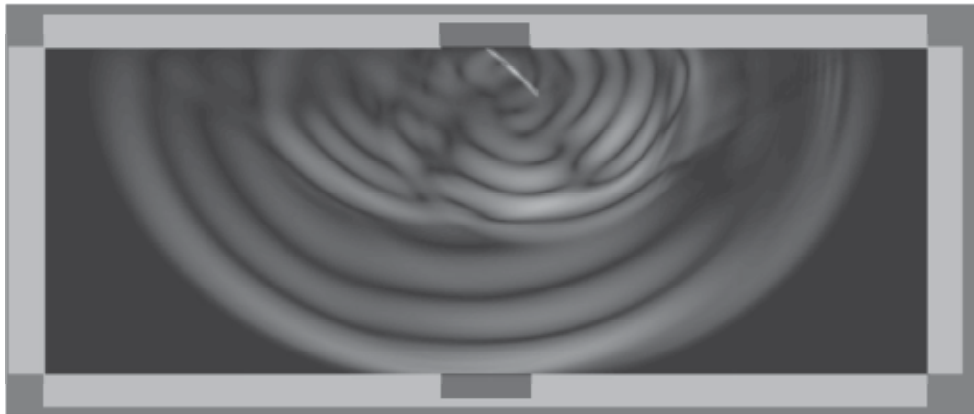
Fig. 7. Acoustic Emission Wave Propagation in fractured Material

The biggest advantage of this method is probably that it is capable of detecting the earliest cracks of the system and their posterior growth, making possible fault detection before any other current method. The main drawback is that it requires additional transducers and a well controlled environment.

3. Experimental results

Next, the experimental test bench and acquisition system, as well as the results obtained by each of the presented fault indicators are shown, finally, two inference methods are presented to merge the obtained information.

3.1 Experimental setup

The test rig used during this research work consists of four ABB M2AA 1.1kW induction motors, three of them with the drive-end ball bearings under test (with different bearing fault degradation level), and the other one used to regulate the applied load. Both driving and loading motors were controlled using independent inverters. Motors under test have also a cable attached to the drive-end bearings housing with the other side connected to ground (a hole was mechanized in order to pass the cable through the motor shield), allowing a low resistance path for CMC acquisition proposes.

The three motors under test have *SKF 6205* bearings with normal clearance and nine balls with diameter of 7.9 mm and pitch of 38.5 mm, and a contact angle of 0.66 radians. The bearings set under test (labeled *healthy*, *lightly* and *heavily damaged*), is composed by a healthy one (with very similar vibration levels to other new units tested in previous works) and other two units with different levels of damage due their operation hours, qualitatively evaluated with a shock pulse tester from *SPM Instruments*.
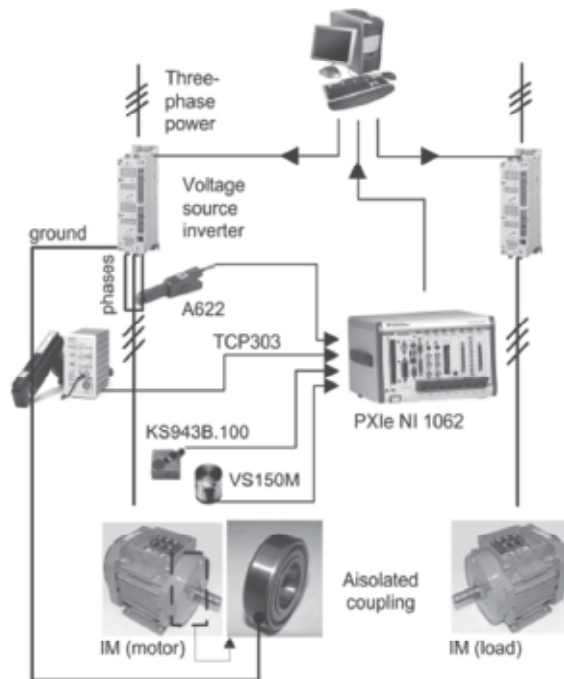
Fig. 8. Experimental test bench and acquisition system scheme.

Regarding the acquisition system, it is based on four different sensors connected to a main acquisition device. A triaxial shear design *MMF* branded piezoelectric accelerometer model *KS943B.100* with IEPE (Integrated Electronics Piezo Electric) standard output and linear frequency response from 0.5 Hz to 22 kHz, was attached using stud mounting to the drive-end motor end-shield and its data was collected at 20kS/s during 1 second for each measurement. Phase stator currents were acquired using Hall effect *Tektronix A622* probes with a frequency range from DC to 100 kHz and collected at 20 kHz during 1 second for each measurement. High frequency CMC signal was measured at the cable attached to the bearings housing with a *Tektronix TCPA300* amplifier and *TCP303* current probe, which

provides up to 15 MHz of frequency range, and acquired at 50 MHz during 100 ms for each measurement. Acoustic emissions were acquired with the use of a *Vallen-Systeme GmbH VS-150M* sensor unit with a range from 100 kHz to 450 kHz and resonant at 150 kHz. A *Vallen-Systeme GmbH AEP4 40dB* preamplifier was used before data acquisition at a sampling frequency of 25MS/s during 20ms each measurement. All the described sensors are connected to a *PXI* acquisition system from *National Instruments* formed by different specific boards.

3.2 Experimental results
3.2.1 Vibrations

The vibration signal RMS contributes clearly to bearings diagnosis. Figures 9, 10 and 11 show the evolution of the RMS value of each motor vibration signals for different speeds and load patterns tested. Clearly, the healthy motor, in figure 9, shows lower RMS values of vibration in comparison with the other two units. Figure 11, corresponding to the unit which was in the worst operational condition according to the *SPM* measurements performed, provide also the highest levels of RMS vibration values.
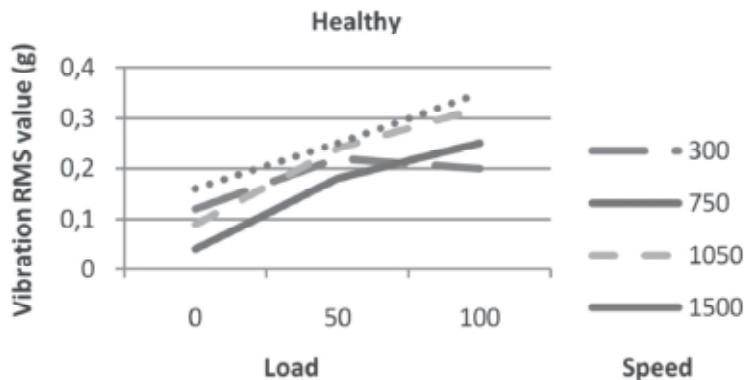
Fig. 9. RMS vibration for healthy unit, all speeds in rpm and loads in percentage of the nominal one.
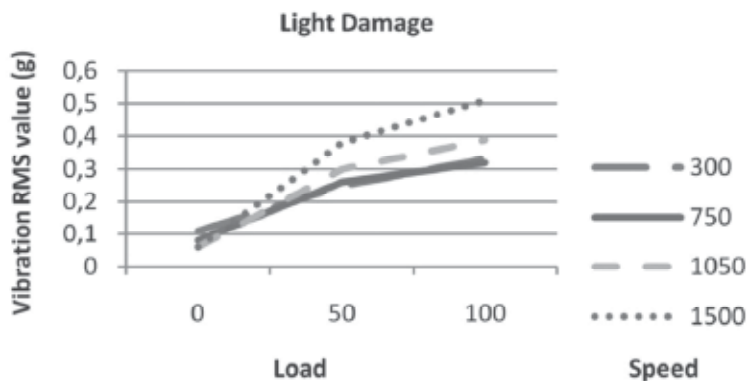
Fig. 10. RMS vibration for lightly damaged unit, all speeds in rpm and loads in percentage of the nominal one.
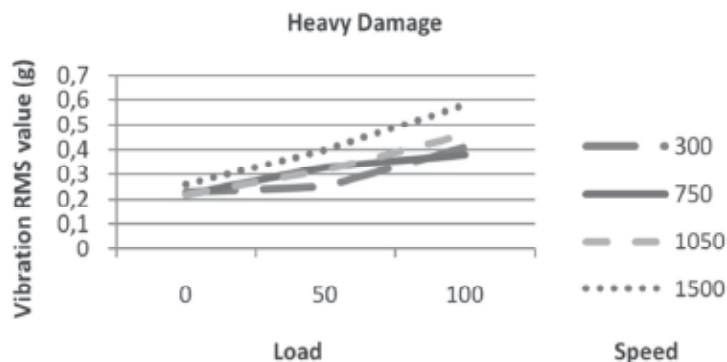
Fig. 11. RMS vibration for heavily damaged unit, all speeds in rpm and loads in percentage of the nominal one.

3.2.2 Stator currents

The figure 12a shows an example of stator-phase current in frequency domain over healthy test bench condition. The stator phase current characteristics bearing fault frequencies are related with the bearing construction parameters and the equations from (1) to (4) for m = 1 and 2 that are normally used (Obaid etal., 2003). These fault frequencies are not present along the frequency axis. The fault indicators thresholds for the stator phase current
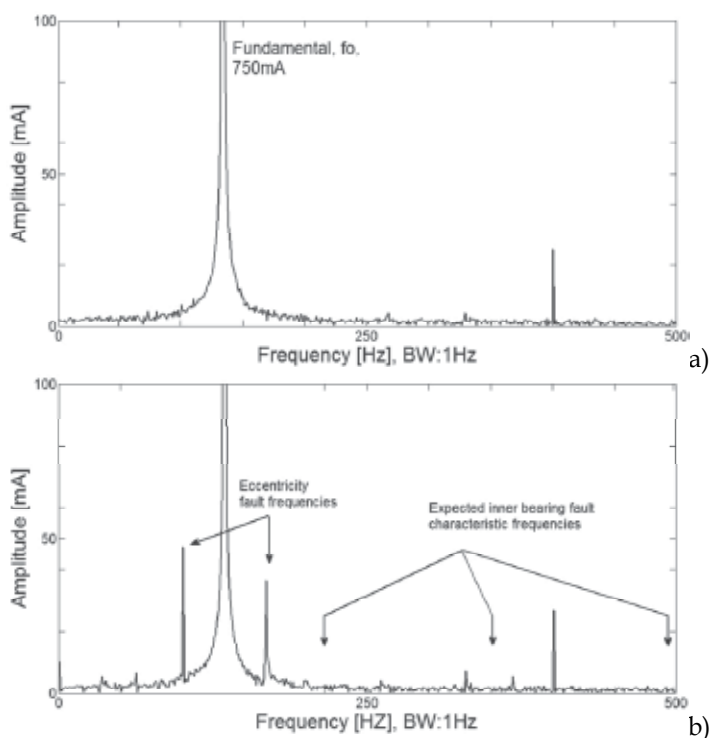
Fig. 12. Stator current frequency spectrum, from 0 to 500Hz, a) healthy bearings b) fault bearing

characteristic bearing fault frequencies can be fixed at 5% of the fundamental frequency amplitude, which is a demanding threshold for diagnosis proposes (Schoen et al., 1995). If the amplitude of these characteristic fault frequencies surpass the thresholds, imply that it can be diagnosed clearly the localized bearing fault related, but if this threshold is not surpassed for any characteristic frequency, it cannot be deduced that bearings are healthy (Zhou et al., 2009), maybe a generalized bearing defect or a non detectable single defect is occurring, then, the sidebands of the stator current fundamental harmonic will be analyzed as general eccentricity fault indicator (Bellini et al., 2008). The stator phase current spectra of a degraded bearings shows, at figure 10b, sidebands fault frequencies greater than 5% of fundamental amplitude, but there are not the characteristic bearing fault frequencies. This effect can be due to eccentricity between rotor and stator for different reasons, so it is necessary additional features in order to distinguish between eccentricity due to bearings degradation or due to other fault in the motor.

Regarding the other stator current feature presented, in order to avoid the influence of the main harmonic power value in the stator current RMS measurement, the acquired signals have been previously filtered using a band-rejection 5th order Butterworth filter centred in the power supply main harmonic with a bandwidth of 20 Hz between higher and lower cut-off frequencies. Tables 1 and 2 compare the RMS filtered values of the heavily and lightly damaged units with the healthy one.

Heavily Damaged-Healthy ([A] RMS)				
Load [% of nominal torque] \ Speed [rpm]	300	750	1050	1500
0	0,004	-0,006	-0,008	-0,007
50	0,036	0,03	0,073	0,044
100	0,018	0,026	0,024	0,024

Table 1. Difference in RMS filtered current value between heavily damaged unit and healthy one used as reference.

Lightly Damaged-Healthy ([A] RMS)				
Load [% of nominal torque] \ Speed [rpm]	300	750	1050	1500
0	0,008	0,002	-0,003	-0,003
50	0,002	-0,011	-0,002	-0,005
100	0,02	0,012	0,003	0,014

Table 2. Difference in RMS filtered current value between lightly damaged unit and healthy one used as reference.

A significant difference can be clearly appreciated when the motor is heavily damaged under load condition. Light damage is noticeable under nominal load conditions but its detection does not seem to be easily reliable.

3.2.3 High frequency bearings pulses

Bearings pulses threshold analysis has been executed to validate theories of correlation between bearings state (wear, lubrication, distributed defects, etc.) and pulses discharge over a threshold value. As it can be seen in figure 13 the stator CMC temporal analysis shows a decrement in the number of pulses surpassing a predefined threshold. The threshold value is fixed at 75% of the CMC pulse maximal amplitude in healthy cases. A number of counted pulses less than 75% of counted pulses in healthy bearings, will be the fault indicator threshold used to distinguish between healthy and degraded bearings.
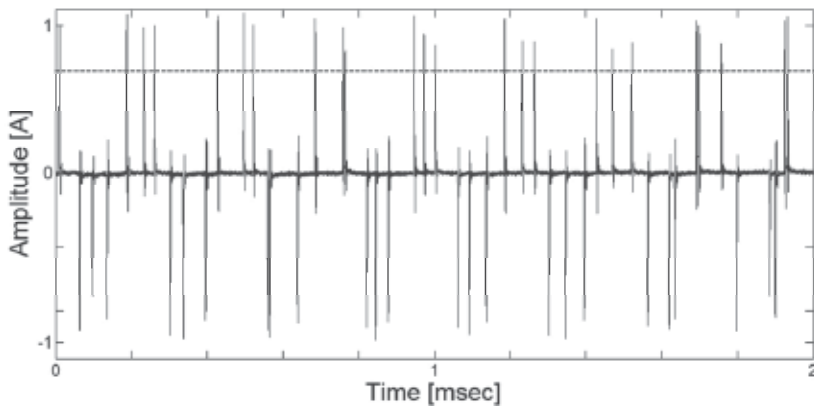
a)
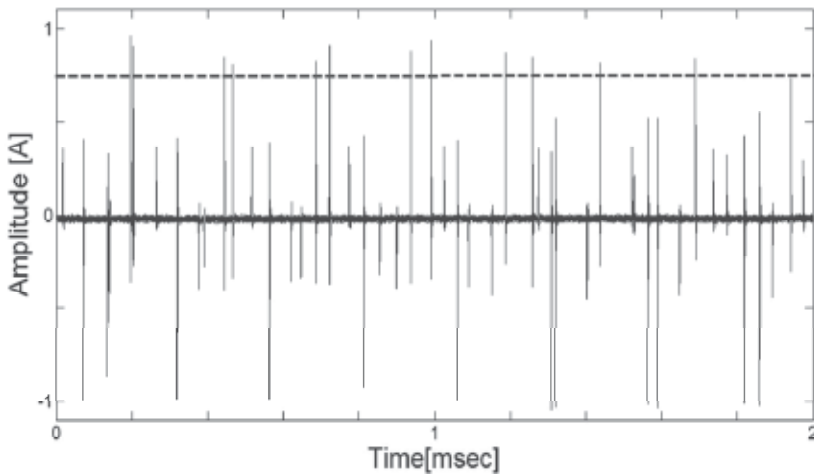
b)

Fig. 13. Example of common mode current signal acquisition, a) healthy bearings b) fault bearing.

The results summarized in figure 14, show that over a defined threshold level healthy bearings undergo a bigger number in comparison to the damaged units. It is noticeable also that this method is able to detect failure at its initial stage if the threshold is correctly placed.
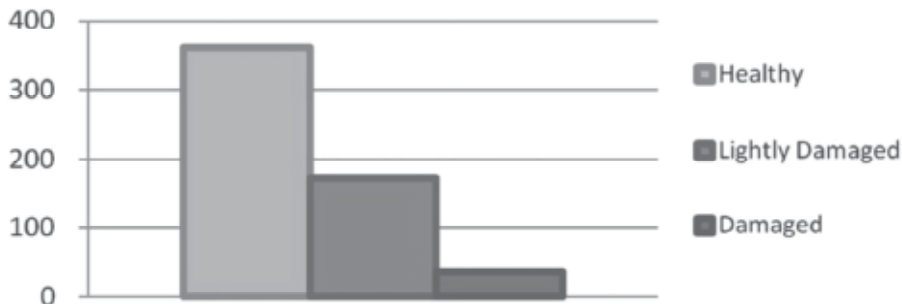
Fig. 14. Number of bearing pulses over threshold value for all motors under test. Healthy, lightly damaged and heavily damaged.

3.2.4 Acoustic Emission testing

Acoustic Emission acquired data has been statistically classified by means of value binning tools and histogram presentation. Fifteen sets of data were acquired for each motor and averaged. Figure 15 shows the results comparing the RMS voltage values acquired for the different units under test.
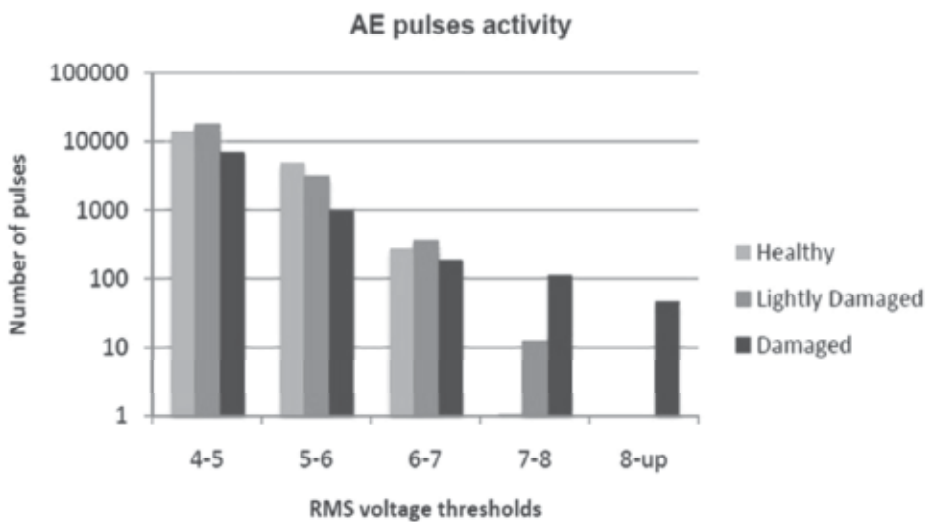
Fig. 15. Acoustic Emission voltage values classification

It is advisable that pulses over 8 V only appeared during the damaged motor testing while under 7 V that unit does not show more activity than the healthy and lightly damaged units. Then, the fuzzy inference system designed uses as reference the number of pulses that surpass the 7 V value, which is the zone where the distinction of the fault severity of the unit seemed to be more noticeable.

3.3 Inference tools
3.3.1 Look-up tables
A look-up table is a common tool applied in diagnosis field. It contents basically a set of simple association rules applied over obtained data. The operation consists in analyze a given combination of inputs in order to select one of the outputs. In the diagnosis field, this kind of inference tool is as a set of *if..then* rules collected in a table.

A proposed look-up table is shown in table 3, where a set of features, from the previously explained have been selected to generate an improved bearings diagnosis system.

FTF harmonic amplitude	BSF harmonic amplitude	BPFO harmonic amplitude	BPFI harmonic amplitude	Fundamental sidebands amplitude	Number of pulses over the threshold	Diagnosis
>5% of fundamental	Not necessary	Not necessary	Not necessary	Not necessary	< 75%	Bearing cage fault (Localized defect)
Not necessary	>5% of fundamental	Not necessary	Not necessary	Not necessary	< 75%	Bearing ball fault (Localized defect)
Not necessary	Not necessary	>5% of fundamental	Not necessary	Not necessary	< 75%	Bearing outer race fault (Localized defect)
Not necessary	Not necessary	Not necessary	>5% of fundamental	Not necessary	< 75%	Bearing inner race fault (Localized defect)
<5% of fundamental	<5% of fundamental	<5% of fundamental	<5% of fundamental	>5% of fundamental	< 75%	Bearing degradation (Distributed or non-detectable localized defect)
<5% of fundamental	<5% of fundamental	<5% of fundamental	<5% of fundamental	>5% of fundamental	< 75%	Eccentricity, but not for bearing degradation

Table 3. Look-up table considering single-point stator current characteristic harmonics, stator current fundamental frequency sidebands evaluation, and number of common mode pulses.

3.3.2 Fuzzy logic
Fuzzy logic is a useful tool in order to implement reasoning that is ambiguous or imprecise. In condition monitoring field, the implementation of tolerant and flexible rules is a more realistic way to generate a diagnosis than the use of crisp and categorical relations.

The analysis of the actual bearing status has been performed using a fuzzy logic inference implementation (Lou et al., 2004; Ballal et al., 2007), which maps given inputs (in this case current and vibration RMS values) to a single output, the different signals acquired are linked to a damage value scaled from 1 to 3.
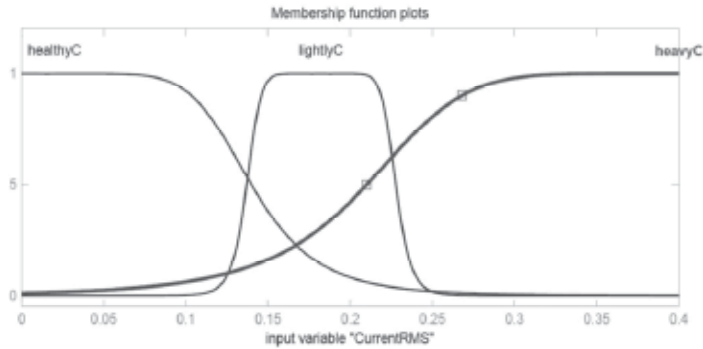
Fig. 16. Membership function plot for Current RMS. (motor speed: 1500 rpm, motor load: 0%).
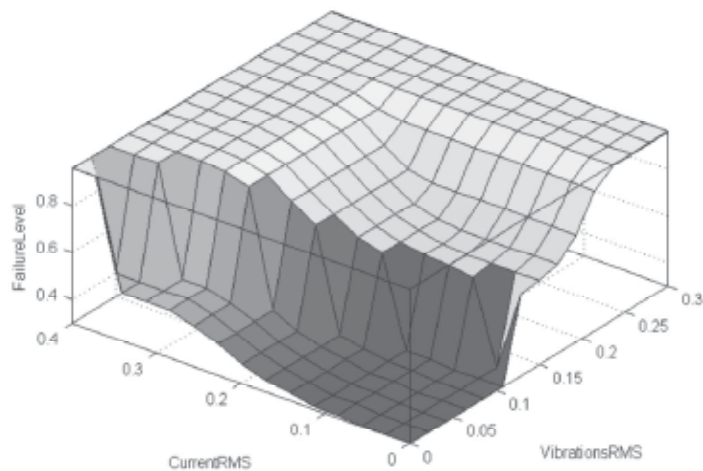
Fig. 17. Plotted surface showing the relationship between the system inputs Vibrations RMS value (g) and Stator Currents RMS value (A) versus the Failure Level output. (Motor speed: 1500 rpm, motor load: 0%)

Unit	Matches	Success %
Healthy	15	100 %
Lightly Damaged	14	93,33%
Heavy Damage	13	86,66%

Table 4. System testing results.

The membership functions, like figure 16, have been obtained through training and validation process, for each signal under analysis using real motor data. MATLAB "Adaptive neuro-fuzzy inference system" tool has been used for this purpose. Figure 17

shows the obtained relationship between Vibration and Stator Current RMS values against the Failure Level output for a motor speed of 1500 rpm and a load of 0%.

To perform the evaluation of the monitoring system designed, fifteen sets of data were collected from the same units and processed. Table 4 summarizes the obtained results.

All healthy data sets were correctly identified, whilst one of the lightly damaged was recognised as a heavily damaged set and two of the heavily damaged sets were identified as lightly damaged ones. The percentage of success was reasonably high and its improvement is still possible if more data sets are used during the system training stage.

4. Conclusions

This chapter tries to offer another point of view in the generation of diagnosis systems and the use of vibration signal analysis for machine condition monitoring. It has been presented an overview of multisensory inference approaches used to characterize motor ball bearings, and their application to a set of motors with distributed fault failure. The results show that a multivariable design contributes positively to damage monitoring of bearings, being a more solid solution than just using any of the single signals involved, which can be affected not only by external disturbances, but also by its own diagnosis limitations, especially dealing with damage severity evaluation. The selection and fusion of different fault indicators from different physical magnitudes has been solved by two examples: the application of simple look-up tables, and the development of a fuzzy system. In both proposed solutions, the bearings diagnosis reaches an important detection capability, including the possibility to detect different kinds of bearings faults and/or different levels of fault.

5. References

Ballal S., Khan Z. J., Suryawanshi H. M. & Sonolikar R. L., (2007). Adaptive Neural Fuzzy Inference System for the Detection of Inter-Turn Insulation and Bearing Wear Faults in Induction Motor, *IEEE Transactions on Industrial Electronics*, vol. 54, no. 1, pp. 250-258.

Basak D., Tiwari A. & Das S. P., (2006). Fault diagnosis and condition monitoring od electrical machines – a review, *IEEE International Conference on Industrial Technology,* pp. 3061-3066.

Bellini A., Filippetti F., Tassoni C. & Capolino G.-A., (2008). Advances in Diagnostic Techniques for Induction Machines," *IEEE Transactions on Industrial Electronics*, vol. 55, no. 12, pp. 4109-4126.

Binder A. & Muetze A., (2008). Scaling Effects of Inverter-Induced Bearing Currents in AC Machines, *IEEE Transactions on Industrial Applications*, vol. 40, no. 3, pp. 769-776.

Cabanas M. F., Melero M. G., Orcajo G. A., Cano Rodríguez J. M. & Juan Solares Sariego, (1996). Técnicas para el Mantenimiento y diagnóstico de Máquinas Eléctricas Rotativas, Marcombo, ISBN: 8426711669.

Cusido J., Delgado M., Navarro L., Sala V.M. & Romeral L., (2010). EMA fault detection using fuzzy inference tools, *IEEE AUTOTESTCON*, pp.1-6.

Cusido J., Garcia A., Navarro L. M., Delgado M., Romeral L. & Ortega A., (2009). On-line measurement device to detect bearing faults on electric motors, *IEEE Instrumentation and Measurement Technology Conference*, pp.749-752.

Cusido J., Romeral L., Delgado M., Garcia A., & Ortega J. A., (2007a). Induction machines fault simulation based on FEM modelling, *IEEE European Conference on Power Electronics and Applications*, pp.1-8.

Cusido J., Rosero J., Aldabas E., Ortega J.A. & Romeral L., (2005). Fault detection techniques for induction motors, *IEEE Compatibility in Power Electronics*, pp. 85- 90.

Cusido L. R., Garcia A., Rosero J. A. & Ortega J. A., (2007b). Fault detection in induction machines by using continuous and discrete wavelet decomposition, *IEEE European Conference on Power Electronics and Applications*, pp.1-8.

Delgado M., Garcia A., Ortega J. A., Urresty J. & Riba J. R., (2009). Bearing diagnosis methodologies by means of Common Mode Current, *European Conference on Power Electronics and Applications*, pp.1-10, 8-10.

El Hachemi Benbouzid M., (2000). A review of induction motors signature analysis as a medium for faults detection, *IEEE Transactions on Industrial Electronics,* vol. 47, no. 5, pp. 984-993.

Frosini L., Bassi E., Fazzi A. & Gazzaniga C., (2008). Use of the stator current for condition monitoring of bearings in induction motors, *Electrical Machines, International Conference on*, pp. 1-6.

Kar C. and Mohanty A. R., (2008). Vibration and current transient monitoring for gearbox fault detection using multiresolution Fourier transform, *Elsevier Journal of Sound and Vibration*, vol. 311, no. 1-2, pp. 109- 132.

Lou X., Kenneth K. A. & Loparo A., (2004). Bearing fault diagnosis based on wavelet transform and fuzzy inference, *Mechanical Systems and Signal Processing*, vol. 18, no. 5, pp. 1077-1095.

Muetze A. & Binder A., (2007). Calculation of Motor Capacitances for Prediction of the Voltage Across the Bearings in Machines of Inverter-Based Drive Systems, *IEEE Transactions on Industry Applications*, vol. 43, no. 3, pp. 665-672.

Muetze A. & Binder A., (2007). Calculation of Circulating Bearing Currents in Machines of Inverter-Based Drive Systems, *IEEE Transactions on Industrial Electronics*, vol. 54, no. 2, pp. 932-938.

O'Donell P., (1986). Report of large motor reliability survey of industrial and commercial installations, *IEEE Transactions on Industrial Applications*, vol. IA-21, no. 4.

Obaid R. R., Habetler T. G. & Stack J. R., (2003). Stator current analysis for bearing damage detection in induction motors, *Symposium on Diagnostics for Electric Machines, Power Electronics and Drives*, pp. 182-187.

Obaid, R. R, Habetler, T. G. & Stack, J. R. (2003). Stator current analysis for bearing damage detection in induction motors, *IEEE Proceeding on Power Electronics and Drives, Symposium on Diagnostics for Electric Machines*, pp. 182-187.

Riley C. M., Lin B. K., Habetler T. G. & Kliman G. B., (1999). Stator current harmonics and their causal vibrations: a preliminary investigation of sensorless vibration monitoring applications, *IEEE Transactions on Industry Applications,* vol. 35, no. 1, pp. 94-99.

Schoen R. R., Habetler T. G., Kamran F. & Bartfield R. G., (1995). Motor bearing damage detection using stator current monitoring, *IEEE Transactions on Industry Applications*, vol. 31, no. 6, pp. 1274-1279.

Singh G. K. & Saad Ahmed Saleh Al Kazzaz, (2003). Induction machine drive condition monitoring and diagnostic research-a survey, *Electric Power Systems Research*, vol. 64, no. 2, pp. 145-158.

Stack J. R., Habetler T. G. & Harley R. G., (2004). Fault Classification and Fault Signature Production for Rolling Element Bearings in Electric Machines, *Symposium on Diagnostics for Electric Machines, Power Electronics and Drives*, vol. 40, no. 3, pp. 735-739.

Zhou W., Lu B., Habetler T. G. & Harley R. G., (2009). Incipient Bearing Fault Detection via Motor Stator Current Noise Cancellation Using Wiener Filter, *IEEE Transactions on Industry Applications*, vol. 45, no. 4, pp.1309-1317.

Vibration Analysis of an Oil Production Platform Submitted to Dynamic Actions Induced by Mechanical Equipment

José Guilherme Santos da Silva, Ana Cristina Castro Fontenla Sieira,
Luciano Rodrigues Ornelas de Lima and Bruno Dias Rimola
State University of Rio de Janeiro (UERJ)
Brazil

1. Introduction

Structural engineers have long been trying to develop solutions using the full potential of its composite materials. At this point there is no doubt that the structural solution progress is directly related to an increase in materials science knowledge.

On the other hand, the competitive trends of the world market have long been forcing structural engineers to develop minimum weight and labour cost solutions. A direct consequence of this new trend design is a considerable increase in problems related to unwanted floor vibrations. For this reason, the structural floors systems can become vulnerable to excessive vibrations, for example, produced by impacts such as mechanical equipment (rotating machinery) (Rimola, 2010; Rimola, 2010a; Rimola, 2010b).

This way, the present paper investigated the dynamic behaviour of an oil production platform made of steel and located in Santos basin, São Paulo, Brazil. The structural model consists of two steel decks with a total area of 1915 m^2 (upper deck: 445 m^2 and lower deck: 1470 m^2), supported by vertical sections made of tubular steel members (steel jacket), and piled into the seabed. A variety of mechanical equipment was located on the steel decks of the structural model, related to electrical generators and compressors (Rimola, 2010).

The soil representation was based on the Winkler's Theory (Winkler, 1867). This theory simulates the soil behaviour as a group of independent springs, governed by the linear-elastic model. In the Winkler's model, the soil stiffness was considered as the necessary pressure to produce a unitary displacement (Winkler, 1867).

The proposed computational model, developed for the oil production platform dynamic analysis, adopted the usual mesh refinement techniques present in finite element method simulations implemented in the GTSTRUDL program (GTSTRUDL, 2009). In this finite element model, floor steel girders and columns were represented by three-dimensional beam elements, where flexural and torsion effects were considered. The steel decks were represented by shell finite elements. In this investigation, it was considered that both structural elements (steel beams and steel deck plates) have total interaction with an elastic behaviour.

The structural model dynamic response was determined through an analysis of its natural frequencies and peak accelerations. The results of the dynamic analysis were obtained from

an extensive numerical study, based on the finite element method using the GTSTRUDL program (GTSTRUDL, 2009). In this investigation, dynamic loadings coming from the rotating machinery (electrical generators and compressors) were applied on the steel decks of the structural system (production platform).

A numerical analysis was performed, in order to obtain the dynamic impacts on the deck structure coming from the electrical generators and compressors. Based on the peak acceleration values, obtained on the structure steady-state response, it was possible to evaluate the structural model performance in terms of human comfort, maximum tolerances of the mechanical equipment and vibration serviceability limit states of the structural system, based on the design code recommendations (CEB 209/91, 1991; ISO 1940-1, 2003; ISO 2631-1, 1997; ISO 2631-2, 1989; Murray et al., 2003).

2. Vibration analysis of steel floors

Besides the evaluation of the structural systems behaviour when submitted to dynamic loads, the causes and effects of vibration on people have been subject of many studies and experiments, due to the fact that they affect people in different ways, causing discomfort, health problems, reduced ability concentration and efficiency at work or sickness, in the case of vibrations of very low frequencies.

(Reiher & Meister, 1946) developed a scale used to determine levels of acceptable vibration in floors. This scale was developed based on experiments in which a group of people was submitted to vibration, whose frequency varied from 1 Hz to 100 Hz. According to this scale, the vibration levels can be classified into several levels, depending on the amplitude and frequency.

(Srinivasulu & Vaidyanathan, 1976) presented the principles of analysis, design and construction of machines of different types. The authors investigated several factors to be considered during the design of machine foundations, in order to obtain the best solution, leading to better operation and reduce the undesirable effects of vibrations on the structure.

(Bachmann & Ammann, 1987) have studied the necessary procedures for the analysis of structures under dynamic loads coming from machines, including machines with rotating parts. The authors treat from the load formulation, also dealing with the effects of machinery induced vibrations in structures and measures to avoid such a problem. In their work are also included the acceptance criteria, both from the point of view of the structure and the point of view of human comfort.

(Griffin, 1996) indicates some reasons to measure human exposure to vibration, especially the following: development of standardized documentation on vibrations in the human body; determination of vibration levels and reduction in frequency range that can prejudice the human body and providing data that may be used for comparison between two or more occupational environments.

(Lenzen, 1996) observed during the development of his research, that the scale developed by (Reiher & Meister, 1946) did not take into account the influence of damping on the human perception of vibration. Through his studies in the laboratory, it was modified the scale of (Reiher & Meister, 1946). This modified scale showed satisfactory results in floors with damping ratios of up to 5%.

According to (Vasconcelos, 1998), establishing the concept of human vibration discomfort can be a difficult task. There are several factors that can influence the subjective feeling of discomfort, such as the socio-cultural people, the type of activity performed, the person's

psychological state at the time of the event, environmental factors, noise, etc. It is not easy to simulate these conditions in the laboratory to reduce the variability of individual responses. Thus, the limit of comfort of people subjected to vibration can be regarded as a rather subjective measure, generating some controversy as to the acceptable values of accelerations imposed.

(Zhou & Shi, 2001) considered that the elimination of vibration of rotating machinery is an important engineering problem. In their study, they presented a detailed review of the developed research that deals with the active balancing of rotors in real time and active control of vibration of rotating machinery, as well as dynamic modelling and analysis techniques for rotating systems. The authors report that the major problem found by the scheme of active control of vibration is the limited number of actuators to control an unlimited number of vibration modes.

(Pereira, 2005) presents a study on the vibration related to human comfort and perception, focusing on the suitability of buildings for vibration levels, aiming the generation of curves related to the perception and human comfort and vibration by means of laboratory experiments and comparing the results to the limits of vibration to other investigations and the design codes (ISO 2631-2, 1989).

The experimental tests developed by (Pereira, 2005) considered 30 volunteers, 15 men and 15 women exposed to vertical vibration at a frequency band ranging from 12 to 80 Hz in sitting and standing posture. The author also performed an analysis on the uncertainty of the outcome of the limit of perception, verifying the existence of a range of vibration in which individuals are not sure whether or not they are able to detect the vibration. It also aimed to know the vertical vibration levels that people find uncomfortable at their home environment, to determine the relationship between the perception threshold and comfort. According to these results, it was proved that the reduction in amplitude of the movement to higher frequency vibration becomes more difficult to be detected, reducing the sensitivity of people.

(Milet, 2006) discusses the basic concepts of dynamic analysis of machine foundations, investigating some analytical strategies and numerical methods available for designing. In this work, some design recommendations were presented and discussed.

(Souza et al., 2007) developed a prototype that allows, looking through a simple system, based on an unbalanced rotor, possible structural data caused by the resonance phenomenon, also allowing comparisons to be made with more complex structural systems. Furthermore, the experiment presented as being practical and simple, can serve as an analytical tool in the classroom, thus giving a better understanding of phenomena related to the vibration system.

(Assunção, 2009) addressed the issues and the most important conditions for a dynamic analysis of elevated frame structures, where equipment were allocated for industrial processes. The author developed a study related to the main causes of dynamic actions coming from industrial equipment and examined a framed structure supporting an unbalanced machine. Through this investigation, the author demonstrated that the developed computational model was appropriate to simulate the transmission of efforts and contribution of the vibrating mass on the responses of the framed structures.

3. Loads generated by mechanical equipment (rotating machinery)

Knowledge about the dynamic behaviour of rotors of rotating machinery, even in the design phase, has become an increasingly crucial factor, considering that it is not desirable to take

corrective actions after the beginning of activities. Material costs and delivery of services are relatively high when compared with the profits increasingly reduced according to the rules imposed by the market and the fact that such corrective actions still involve a period in which the equipment will need to become inoperative, which means losses, because it will not generate any profit for the period.

According to (Dias Junior, 2009), among several factors that contribute to the transmission of rotational energy to the vibratory movements of the machine, the well-known is undoubtedly the unbalance of the rotor. The rotor is the rotating part of a machine or engine which may be coupled elements as disks, generators, gears, etc. According to (Dias Junior, 2009), due to the unbalance, the force that acts at the rotor gravity centre, pull the shaft out of the line joining the two bearings, forcing the shaft to rotate stressed. This movement is called precession movement.

Rotors are supported on bearings, which are the elements responsible for connecting the movable and fixed structure of a rotating machine. In addition to this point, to absorbing energy, another function of the bearings is to guide or restrict movement during the rotation axis (Silva, 2004).

The process of balancing a rotor is a key factor to minimize the vibrations generated by electric motors. Depending on the vibration level of these engines, the structural system that supports the equipment can be compromised by fatigue or even premature failure. The balancing process is intended to improve the distribution of mass of a body, so that by turning around their bearings, produces no unbalance forces, keeping the vibrations and dynamic loads within suitable limits for the machine operation.

The balance can be achieved up to a certain limit, since after this process the rotor still presents imperfection in the mass distribution, called residual unbalance. It is worth mentioning that there is a direct relationship between the residual unbalance and vibration level of the machine, which depends on many factors (mass housing and the foundation, stiffness of the bearings and foundation, occurrence of resonances etc.). Anyway, there are allowable levels of residual unbalance, consistent with good practice of machine design.

3.1 Excitation forces: Unbalanced mass

Unbalanced mass is defined as a mass located at a distance d measured from the geometric centre of the shaft. The mass remains in a plane perpendicular to the axis y and it is a constant coordinate, as illustrated in Figure 1.

Based on Figure 1, it can be deduced that the force caused by unbalanced mass, acting on the axis, according to directions in the shown coordinate system, can be written as presented in Equations (1) and (2). In Equations (1) and (2), the dynamic forces generated by unbalanced mass have a frequency similar to the rotational frequency of the axis

$$F_u = m_u \Omega^2 d \cdot \sin(\Omega t) \tag{1}$$

$$F_w = m_u \Omega^2 d \cdot \cos(\Omega t) \tag{2}$$

3.2 Unbalance quantification

As previously mentioned, the unbalance is characterized by a mass located at a certain distance from the rotation axis, see Figure 1. Therefore, the unbalance is always measured by a product mass x distance, see Equation (3). The rotor must be subjected to a balancing

procedure, in order to achieve a tolerable minimum. This value is called the Permissible Residual Unbalance and designated by the symbol U.

$$U = \text{mass} \times \text{distance} \tag{3}$$
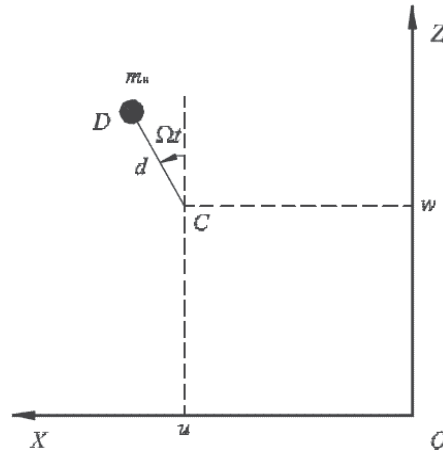
Fig. 1. Unbalanced mass (López, 2002)

It was observed in Equation (3), that the allowable residual unbalance is directly proportional to the mass of the rotor, i.e., as heavier was the rotor, greater it will be the permissible residual unbalance. It is appropriate to relate the allowable residual unbalance, U, and the rotor mass, m, in terms of the Specific Allowable Residual Unbalance, as shown in Equation (4).

$$e = \frac{U}{m} \tag{4}$$

As larger is the rotation speed, smaller should be the residual unbalance, since the centrifugal force, F_{cent}, increases with the square of the speed of it, as shown in Equation (5). In Equation (5) the centrifugal force, F_{cent} is expressed in N.

$$F_{cent} = m \cdot e \cdot \Omega^2 \tag{5}$$

Based on many years of experience, experts decided that the product of the angular velocity of rotor rotation and the specific allowable residual unbalance must be constant, i.e., to increase the speed of rotation it is necessary to reduce the specific residual unbalance.

This product is called Balance Quality Grade and it is designated by the letter G, see Table 1. To find a wide variety of existing rotors it was necessary to assign, depending on the type of rotor and its application, a value for this constant, see Table 1. Table 1 reproduces the G values which deals with quality of balancing rotating rigid bodies (ISO 1940-1, 2003).

3.3 Determination of unbalanced forces

As mentioned before, the unbalance of the rotor produces a dynamic load that depends on the mass, the equipment angular velocity and the eccentricity between the equipment

G	e x ω (mm/s)	Rotor Types - General Examples
G 4000	4000	Crankshaft/drives of rigidly mounted slow marine diesel engines with uneven number of cylinders.
G 1600	1600	Crankshaft/drives of rigidly mounted large two-cycle engines.
G 630	630	Crankshaft/drives of rigidly mounted large four-cycle engines; Crankshaft/drives of elastically mounted marine diesel engines.
G 250	250	Crankshaft/drives of rigidly mounted fast four-cylinder diesel engines.
G 100	100	Crankshaft/drives of fast diesel engines with six or more cylinders; Complete engines (gasoline or diesel) for cars, trucks and locomotives.
G 40	40	Car wheels, wheel rims, wheel sets, drive shafts; Crankshaft/drives of elastically mounted fast four-cycle engines with six or more cylinders; Crankshaft/drives of engines of cars, trucks and locomotives.
G 16	16	Drive shafts (propeller shafts, cardan shafts) with special requirements and parts of crushing machines; Individual components of engines (gasoline or diesel) for cars, trucks and locomotives; Crankshaft/drives of engines with six or more cylinders under special requirements.
G 6.3	6.3	Parts of process plant machines; Marine main turbine gears (merchant service); Centrifuge drums; Paper machinery rolls; print rolls; Fans; Assembled aircraft gas turbine rotors; Flywheels; Pump impellers; Machine-tool and general machinery parts; Medium and large electric armatures (electric motors having at least 80 mm shaft height) without special requirements; Small electric armatures, often mass produced, in vibration insensitive applications and/or with vibration-isolating mountings; Individual components of engines under special requirements.
G 2.5	2.5	Gas and steam turbines, including marine main turbines (merchant service); Rigid turbo-generator rotors; Computer memory drums and discs; Turbo-compressors; Machine-tool drives; Medium and large electric armatures with special requirements; Small electric armatures not qualifying for one or both of the conditions specified for small electric armatures of balance quality grade G 6.3; Turbine-driven pumps.
G 1	1	Tape recorder and phonograph (gramophone) drives; Grinding-machine drives; Small electric armatures with special requirements.
G 0.4	0.1	Spindles, discs and armatures of precision grinders; Gyroscopes.

Table 1. Balance quality values (ISO 1940-1, 2003)

gravity center and the rotation axis. In sequence, Equation (6) determines the dynamic load amplitude generated by the unbalance of a rotor, as follows:

$$P_0 = m \cdot R \cdot \Omega^2 = m \cdot (R\Omega) \cdot \Omega \tag{6}$$

Where:

P_0 : dynamic loading amplitude;

M   : total mass in rotation;

Ω : equipment frequency;

R. Ω = G : equipment balance quality grade, see Table 1: (ISO 1940-1, 2003).

For rotors of electric motors, R.Ω was considered equal to 0.0025 m/s. Substituting this value in Equation (6), it is obtained:

$$P_0 = m \cdot (0.0025) \cdot \Omega \tag{7}$$

Considering an unbalanced load spinning around an axis, the procedure for obtaining the global dynamic force acting on a plane is to apply the force in two orthogonal directions. One of these forces is applied in the horizontal direction with the angle phase ϕ equal to zero and the other in vertical direction with the angle phase ϕ equal to 1/4 of the period of vibration of unbalanced force.

Thus, as time increases, there is a variation of the two forces so that the composition (horizontal and vertical directions) results in a harmonic unbalanced force where one component will be multiplied by sin (Ωt) and the other by sin (Ωt + π/2). This way, when one harmonic component presents maximum values the other one is equal to zero and vice versa. The value of the dynamic force is obtained by the vector sum of the components in the vertical and horizontal directions as presented in Equation (8).

$$P(t) = P_0 \, \sin(\Omega t) + P_0 \, \sin(\Omega t + \frac{\pi}{2}) \tag{8}$$

3.3 Dynamic loading modelling

To perform the numerical analysis of the oil production platform developed in this investigation, it was used the data in accordance with Table 2. In sequence, Figure 2 shows the design of the equipment.

Equipment data	
Protective cover	1.2 kN
Coupling	5.3 kN
Gear unit	37.5 kN
Motor swing	15 kN
Rotor weight	10.8 kN
Input frequency	30 Hz
Output frequency	0.94 Hz

Table 2. Equipment data

The dynamic load modelling considered two components related to vertical and horizontal directions. Table 3 shows the dynamic loads applied on the structural system steel deck. These actions were properly combined in order to better represent the dynamic excitation induced by equipment on the structure.
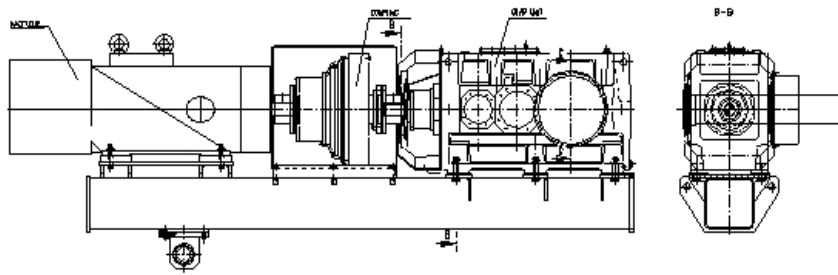
Fig. 2. Driving unit (motor, coupling and gear) supported by a steel beam (Rimola, 2010)

Equipment	Weight (kN)	Frequency (rad/s)	Rω (m/s)	P_0 (kN)
Rotor	10.80	188.49	0.0025	0.51
Gear	18.75	6.03	0.0025	0.028

Table 3. Dynamic actions related to the equipment

4. Investigated structural model

The structural system investigated in this paper is related to an oil production platform made of steel and located in Santos basin, São Paulo, Brazil. The structural model is supported by vertical sections made of tubular steel members (steel jacket), piled into the seabed by steel piles and consists of two steel decks with a total area of 1915 m² (upper deck: 445 m² and lower deck: 1470 m²), see Figures 3 and 4.

Fig. 3. Investigated structural model

The structural model is formed by steel beams and columns and steel deck plates, as presented in Figures 3 and 4. This platform is constituted by a lot of structural elements with very different geometrical characteristics; see (Rimola, 2010). A 2.05x105MPa Young's modulus was adopted for the steel beams, columns and decks.

Nodes: 1824
Elements: 3588
Beam: 3079
Shell: 509
Degrees of Freedom: 10872
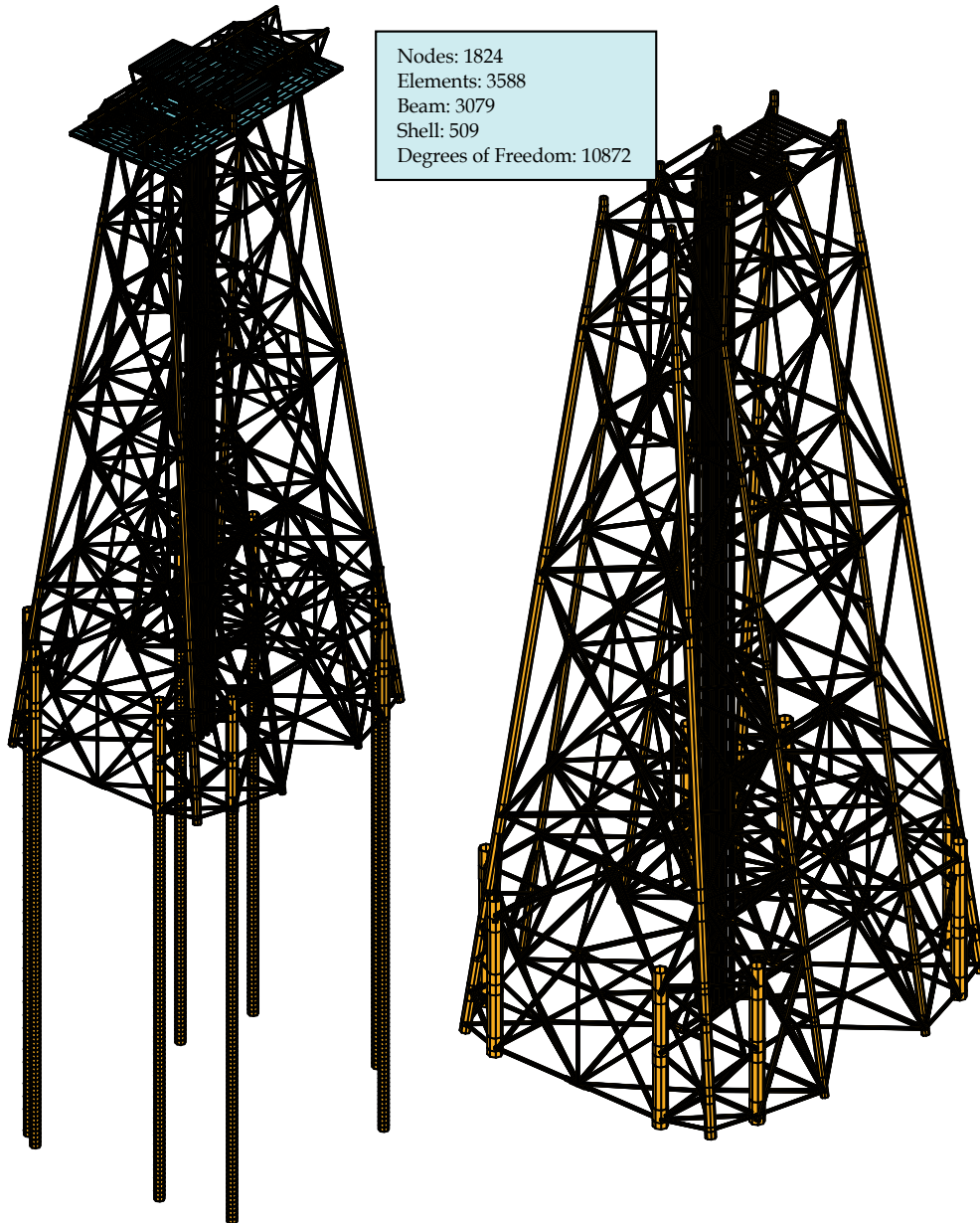
Fig. 4. Finite element model: oil production platform with steel jacket and piles

DEPTH	LAYERS DESCRIPTION	RESISTANCE PARAMETERS
6,090	Medium Sand	$\gamma_{sub} = 9,0 \text{ kN/m}^3$ $\phi=30°$
18,280	Stiff Clay	$\gamma_{sub} = 8,0 \text{ kN/m}^3$ $C = 70,75 \text{kN/m}^2$
21,940	Fine Sand	$\gamma_{sub} = 8,9 \text{ kN/m}^3$ $\phi=30°$
24,990	Medium Clay	$\gamma_{sub} = 8,0 \text{ kN/m}^3$ $C = 80,90 \text{kN/m}^2$
34,130	Medium Sand	$\gamma_{sub} = 8,9 \text{ kN/m}^3$ $\phi=35°$
42,970	Fine Sand	$\gamma_{sub} = 8,9 \text{ kN/m}^3$ $\phi=25°$
54,860	Stiff Clay	$\gamma_{sub} = 8,0 \text{ kN/m}^3$ $C = 113,55 \text{kN/m}^2$
67,050	Stiff Clay	$\gamma_{sub} = 8,0 \text{ kN/m}^3$ $C = 138,75 \text{kN/m}^2$
79,240	Stiff Clay	$\gamma_{sub} = 8,0 \text{ kN/m}^3$ $C = 164,20 \text{kN/m}^2$
103,00	Stiff Clay	$\gamma_{sub} = 8,0 \text{ kN/m}^3$ $C = 192,05 \text{kN/m}^2$

Fig. 5. Geotechnical profile

5. Computational modelling

The proposed computational model, developed for the structural system dynamic analysis, adopted the usual mesh refinement techniques present in finite element method simulations implemented in the GTSTRUDL program (GTSTRUDL, 2009).

In this computational model, floor steel girders and columns were represented by a three-dimensional beam element with tension, compression, torsion and bending capabilities. The element has six degrees of freedom at each node: translations in the nodal x, y, and z directions and rotations about x, y, and z axes. On the other hand, the steel deck plates were represented by shell finite elements (GTSTRUDL, 2009).

In this investigation, it was considered that both structural elements (steel beams and steel deck plates) have total interaction with an elastic behaviour. The finite element model has 1824 nodes, 3079 three-dimensional beam elements, 509 shell elements and 10872 degrees of freedom, as presented in Figure 4.

5.1 Geotechnical data

The data related to soil were obtained by means of three boreholes (Standard Penetration Tests: SPT) in a depth range varying from 43.5m to 178.3m. The boreholes allowed the definition of the geotechnical profile (Figueiredo Ferraz, 2004) adopted in the finite element modelling, see Figure 5. Characterisation and resistance tests performed in laboratory provided specific weight, friction angle and cohesion values illustrated in Figure 5. In Figure 5, γ_{sub} is the submerged specific weight (kN/m³); c represents the soil cohesion in (kN/m²) and ϕ is soil friction angle (degree).

5.2 Soil-structure interaction

When the study of half-buried columns is considered, the usual methodology to the formulation of the soil-structure interaction problem utilizes the reaction coefficient concept, originally proposed by (Winkler, 1867). In the case of laterally loaded piles, the analysis procedure based on (Winkler, 1867) is analogue to the one used for shallow foundations, see Figure 6.

The soil behaviour is simulated by a group of independent springs, governed by a linear-elastic model. The foundation applies a reaction in the column normal direction and it is proportional to the column deflection. The spring stiffness, designated by reaction coefficient (k_h) is defined as the necessary pressure to produce a unitary displacement (Winkler, 1867), as presented in Equation (9).
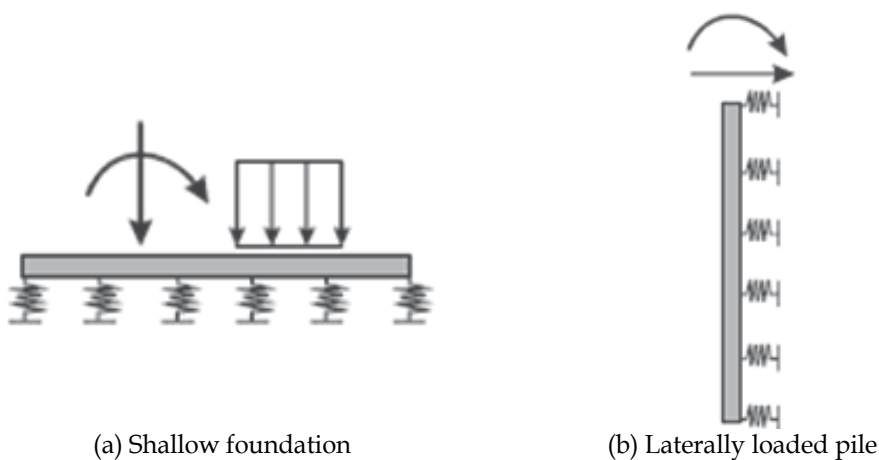

(a) Shallow foundation   (b) Laterally loaded pile

Fig. 6. Foundation analysis models

$$k_h = \frac{p}{y} \qquad (9)$$

Where:

p   : applied pressure, in (N/m²);

y   : soil deflection, in (m).

(Terzaghi, 1955) considered that the reaction coefficient (k_h) for piles in cohesive soils (clays), does not depend on the depth of the pile and may be determined by the following equation.

$$k_h = \frac{0.3048\,m}{1.5d} \times (k_{s1}) \qquad (10)$$

Where:

k_{s1} : modulus to a squared plate with a length of 0.3048m (1 ft), in (MN/m³);

d   : column width (pile), in (m).

Table 4 presents typical values for k_{s1} for consolidated clays.

Clay's consistency	k_{s1} (t/ft³)	k_{s1} (MN/m³)
Stiff	75	26.0
Very Stiff	150	52.0
Hard	300	104.0

Table 4. Typical values for k_{s1} (Terzaghi, 1955)

For piles in non-cohesive soils (sand), it is considered that the horizontal reaction coefficient (k_h) varies along the depth, according to Equation (11).

$$k_h = n_h \frac{z}{d} \qquad (11)$$

Where:

n_h : stiffness parameter for non-cohesive soils, in (MN/m³);

d   : column width (pile), in (m).

Typical values for n_h obtained by (Terzaghi, 1955), as a function of the sand relative density under submerged and dry condition, are presented in Table 5.

Relative density	n_h (dry) (t/ft³)	n_h (dry) (MN/m³)	n_h (submerged) (t/ft³)	n_h (submerged) (MN/m³)
Loose	7	2.4	4	1.4
Medium	21	7.3	14	4.9
Dense	56	19.4	34	11.8

Table 5. Typical values for n_h (Terzaghi, 1955)

Based on the horizontal reaction coefficients values (k_h) and the column width (d), the foundation stiffness parameter (k_0) is determined by using Equation (12) (Poulos & Davis, 1980):

$$k_0 = k_h \times d \qquad (12)$$

Based on the subsoil geotechnical profile (see Figure 5) and using the analysis procedure based on the Winkler model (Winkler, 1867) the horizontal reaction coefficients on the piles (k_h) were determined as a function of the type of the soil. Applying the horizontal reaction coefficients (k_h) on Equation (12), the foundation stiffness parameters values (k_0) were calculated.

The foundation stiffness parameters values (k_0) were used to determine the spring's stiffness (k) placed in the computational model to simulate the soil behaviour. The spring elements which simulate the piles were discretized based on a range with length equal to 1m (one meter). For each range of 1m it was placed a translational spring in the transversal direction of the pile section axis with a stiffness value equal to the value obtained for the horizontal reaction coefficient evaluated by the Winkler model (Winkler, 1867). Table 6 presents the spring's stiffness coefficients simulating.

Depth (m)	Layer Description	Pile Profile		Spring's stiffness
		Ø (mm)	Thickness (mm)	k (kN/m)
1	Medium sand	2108	55	4850.1163
2				9700.2327
3				14550.3490
4				19400.4653
5				24250.5816
6				29100.6980
7 a 18	Stiff clay	2134	55	5279.6981
19	Fine sand	2134	55	92152.2102
20				97002.3266
21				101852.4429
22				106702.5592
23 a 25	Medium clay	2134	55	281.5839
26	Medium sand	2134	55	126103.0245
27				130953.1408
28				135803.2572
29				140653.3735
30				145503.4898
31				150353.6062
32				155203.7225
33				160053.8388
34				164903.9551
35	Fine sand	2134	55	169754.0715
36				174604.1878
37				179454.3041
38				184304.4204
39				189154.5368
40				194004.6531
41				198854.7694
42				203704.8858
43				208555.0021
44 a 96	Stiff clay	2134	55	5279.6981

Table 6. Stiffness coefficients of soil representative springs

5.3 Structural damping modelling

It is called damping the process which energy due to structural system vibration is dissipated. However, the assessment of structural damping is a complex task that cannot be determined by the structure geometry, structural elements dimensions and material damping (Clough & Penzien, 1995).

According to (Chopra, 2007), it is impossible to determine the damping matrix of a structural system through the damping properties of each element forming the structure with the same way it is determined the structure stiffness matrix, for example. This is because unlike the elastic modulus, which is used in the stiffness evaluation, the damping materials properties are not well established.

Although these properties were known (Chopra, 2007), the resulting damping matrix would not take into account a significant portion of energy dissipated by friction in the structural steel connections, opening and closing micro cracks in the concrete, friction between structure and other elements that are bound to it, such as masonry, partitions, mechanical equipment, fire protection, etc. Some of these energy dissipation sources are extremely difficult to identify.

The physical evaluation of the damping of a structure is not considered properly as if their values are obtained by experimental tests. However, these tests often require time and cost that in most cases is very high. For this reason, damping is usually achieved in terms of contribution rates, or rates of modal damping (Clough & Penzien, 1995).

With this in mind, it is common to use the Rayleigh damping matrix, which considers two main parts, one based on the mass matrix contribution rate (α) and another on the stiffness matrix contribution rate (β), as can be obtained using Equation (13). It is defined **M** as the mass matrix and **K** as the stiffness matrix of the system (Craig Jr., 1981; Clough & Penzien, 1995; Chopra, 2007).

$$\mathbf{C} = \alpha\mathbf{M} + \beta\mathbf{K} \tag{13}$$

Equation (13) may be rewritten, in terms of the damping ratio and the circular natural frequency (rad/s), as presented in Equation (14):

$$\xi_i = \frac{\alpha}{2\omega_{0i}} + \frac{\beta\omega_{0i}}{2} \tag{14}$$

Where:

ξ_i : damping ratio related to the ith vibration mode;

ω_{0i} : circular natural frequency related to the ith vibration mode.

Isolating the coefficients α and β from Equation (14) and considering the two most important structural system natural frequencies, Equations (15) and (16) can be written.

$$\alpha = 2\xi_i\omega_{01} - \beta\omega_{01}\omega_{01} \tag{15}$$

$$\beta = \frac{2\left(\xi_2\omega_{02} - \xi_1\omega_{01}\right)}{\omega_{02}\omega_{02} - \omega_{01}\omega_{01}} \tag{16}$$

Based on two most important structural system natural frequencies it is possible to calculate the values of α and β. In general, the natural frequency ω_{01} is taken as the lowest natural

Vibration Analysis of an Oil Production
Platform Submitted to Dynamic Actions Induced by Mechanical Equipment
295

frequency, or the structure fundamental frequency and ω_{02} frequency as the second most important natural frequency.

In the technical literature, there are several values and data about structural damping. In fact, these values appear with great variability, which makes their use in structural design very difficult, especially when some degree of systematization is required. Based on the wide variety of ways to considering the structural damping in finite element analysis, which, if used incorrectly, provide results that do not correspond to a real situation, the design code CEB 209/91 (CEB 209/91, 1991) presents typical rates for viscous damping related to machinery support of industrial buildings, as shown in Table 7.

Construction Type	Minimum	Mean	Maximum
Reinforced Concrete	0.010	0.017	0.025
Prestressed Concrete	0.007	0.013	0.020
Composite Structures	0.004	0.007	0.012
Steel	0.003	0.005	0.008

Table 7. Typical values of damping ratio ξ for industrial buildings (CEB 209/91, 1991)

Based on these data, it was used a damping coefficient of 0.5% ($\xi = 0.5\%$ or 0.005) in all modes. This rate takes into account the existence of few elements in the oil production platform that contribute to the structural damping. Table 8 presents the parameters α and β used in the forced vibration analysis to model the structural damping in this investigation.

f_{01} (Hz)	f_{02} (Hz)	ω_{01} (rad/s)	ω_{02} (rad/s)	α	β
0.674	0.716	4.2364	4.4968	0.02172	0.00115

Table 8. Values of the coefficients α and β values used in forced vibration analysis

6. Natural frequencies and vibration modes

The production platform natural frequencies were determined with the aid of the numerical simulations, see Table 9, and the corresponding vibration modes are shown in Figure 7 and 8. Each natural frequency has an associated mode shape and it was observed that the first vibration modes presented predominance of the steel jacket system.

Natural Frequencies f_{0i} (Hz)		Vibration Modes	
f_{01}	0.67	Mode 1	Vibration modes with predominance of the steel jacket system.
f_{02}	0.71	Mode 2	
f_{03}	1.20	Mode 3	
f_{08}	1.99	Mode 8	Vibration modes with predominance of the steel deck displacements.
f_{17}	2.61	Mode 17	
f_{49}	4.14	Mode 49	

Table 9. Production platform natural frequencies

It can be observed in Figure 7, that the three first vibration modes presented predominance of displacements in the steel jacket system. In the 1st vibration mode there is a predominance of translational displacements towards the "y" axis in the finite element model. In the 2nd vibration mode a predominance of translational effects towards the axis "x" of the numerical model was observed. The third vibration mode presented predominance of torsional effects on the steel jacket system with respect to vertical axis "z". Flexural effects were predominant on the steel deck system and can be seen only from higher order vibration modes, see Figure 8.

However, flexural effects were predominant in the steel deck plate (upper and lower), starting from the eighth vibration mode (f_8 = 1.99 Hz - Vibration Mode 8), see Table 9. It is important to emphasize that torsional effects were present starting from higher mode shapes, see Table 9. Figures 7 and 8 illustrated the mode shapes corresponding to six natural frequencies of the investigated structural system.
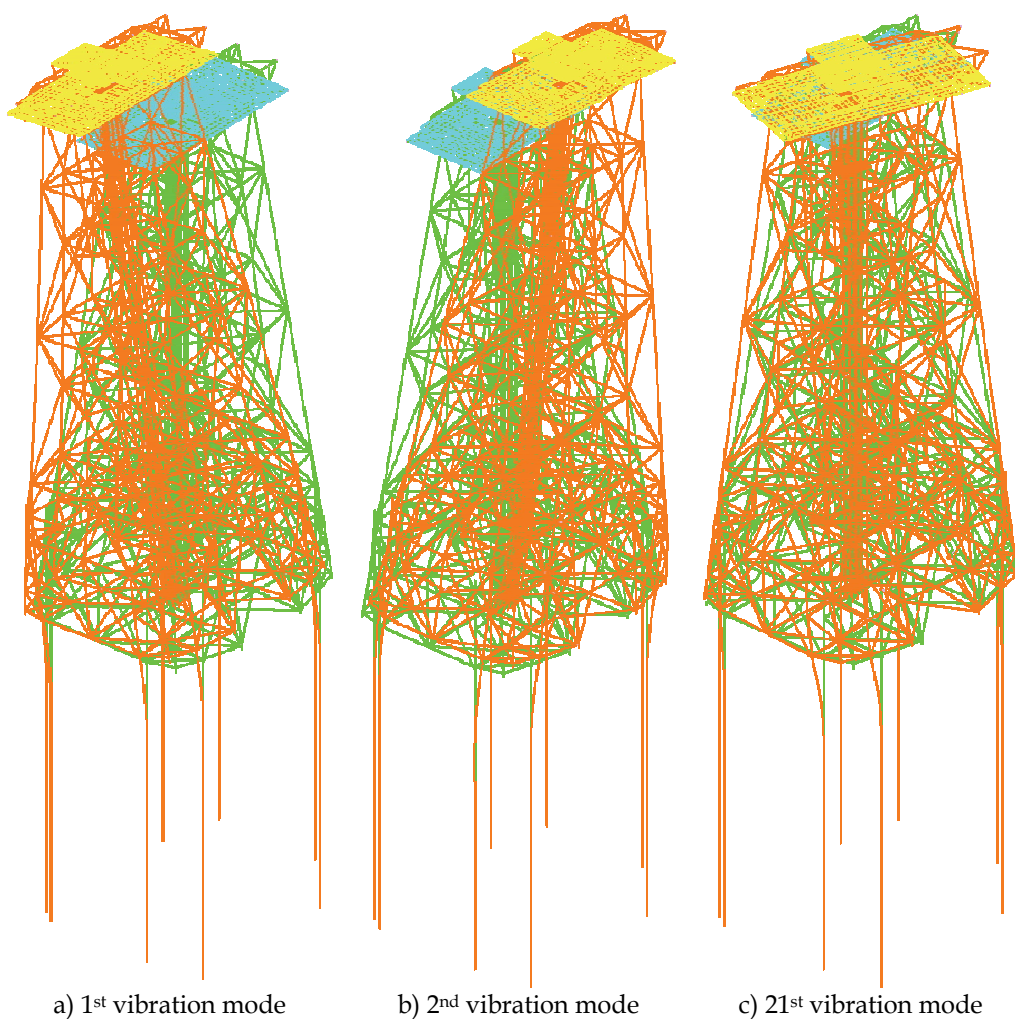

a) 1st vibration mode   b) 2nd vibration mode   c) 21st vibration mode

Fig. 7. Vibration modes with predominance of the steel jacket system

Vibration Analysis of an Oil Production
Platform Submitted to Dynamic Actions Induced by Mechanical Equipment
297

7. Structural system dynamic response

The present investigation proceeds with the evaluation of the steel platform's performance in terms of vibration serviceability effects, considering the impacts produced by mechanical equipment (rotating machinery). This strategy was considered due to the fact that unbalanced rotors generate vibrations which may damage their components and supports and produce dynamic actions that could induce the steel deck plate system to reach unacceptable vibration levels, leading to a violation of the current human comfort criteria for these specific structures. For this purpose, forced vibration analysis is performed through using the computational program (GTSTRUDL, 2009). The results of forced vibration models are obtained in terms of the structural system displacements, velocities and peak accelerations.

For the structural analysis, it was considered the simultaneous operation of three machines on the steel deck. The nodes of application of dynamic loads in this situation are shown in Figure 9. With respect to human comfort, some nodes of the finite element model were selected near to the equipment in order to evaluate the steel deck dynamic response (displacements, velocities and accelerations). These nodes are also shown in Figure 9.

The dynamic loading related to the rotor was applied on the nodes 9194, 9197 and 9224 and the corresponding dynamic loading associated to the gear was applied on the nodes 9193, 9196 and 9223, as presented in Figure 9. The description of the dynamic loadings (rotor and gear) was previously described on item 3. It should be noted that the positioning of the machines was based on the equipment arrangement drawings of the investigated platform (Figueiredo Ferraz, 2004).

The analysis results were compared with limit values from the point of view of the structure, operation of machinery and human comfort provided by international design recommendations (CEB 209/91, 1991; ISO 1940-1, 2003; ISO 2631-1, 1997; ISO 2631-2, 1989; Murray et al., 2003). It must be emphasized that only the structural system steady-state response was considered in this investigation.

The frequency integration interval used in numerical analysis was equal to 0.01 Hz ($\Delta\omega$ = 0.01 Hz). It was verified that the frequency integration interval simulated conveniently the dynamic characteristics of the structural system and also the representation of the proposed dynamic loading (Rimola, 2010).

In sequence of the study, Tables 10 to 12 present the vertical translational displacements, velocities and accelerations, related to specific locations on the steel deck, near to the mechanical equipment, see Figure 9, calculated when the combined dynamic loadings (rotor and gear) were considered.

These values, obtained numerically with the aid of the proposed computational model, were then compared with the limiting values proposed by design code recommendations (CEB 209/91, 1991; ISO 1940-1, 2003; ISO 2631-1, 1997; ISO 2631-2, 1989; Murray et al., 2003). Once again, it must be emphasized that only the structural system steady state response was considered in this investigation.

The allowable amplitudes are generally specified by manufactures of machinery. When manufacture's data doesn't indicate allowable amplitudes, design guides recommendations (ISO 1940-1, 2003) are used to determine these limiting values for machinery performance, see Table 10. The maximum amplitude value at the base of the driving support (Node 9197: see Figure 9), on the platform steel deck was equal to 446 µm (or 0.446 mm or 0.0446 cm), see Table 10, indicating that the recommended limit value was violated and the machinery performance can be inadequate (0.446 mm > 0.06 mm) (ISO 1940-1, 2003).

a) 8th vibration mode f_{08}=1.99 Hz

b) 17th vibration mode f_{17}=2.61 Hz
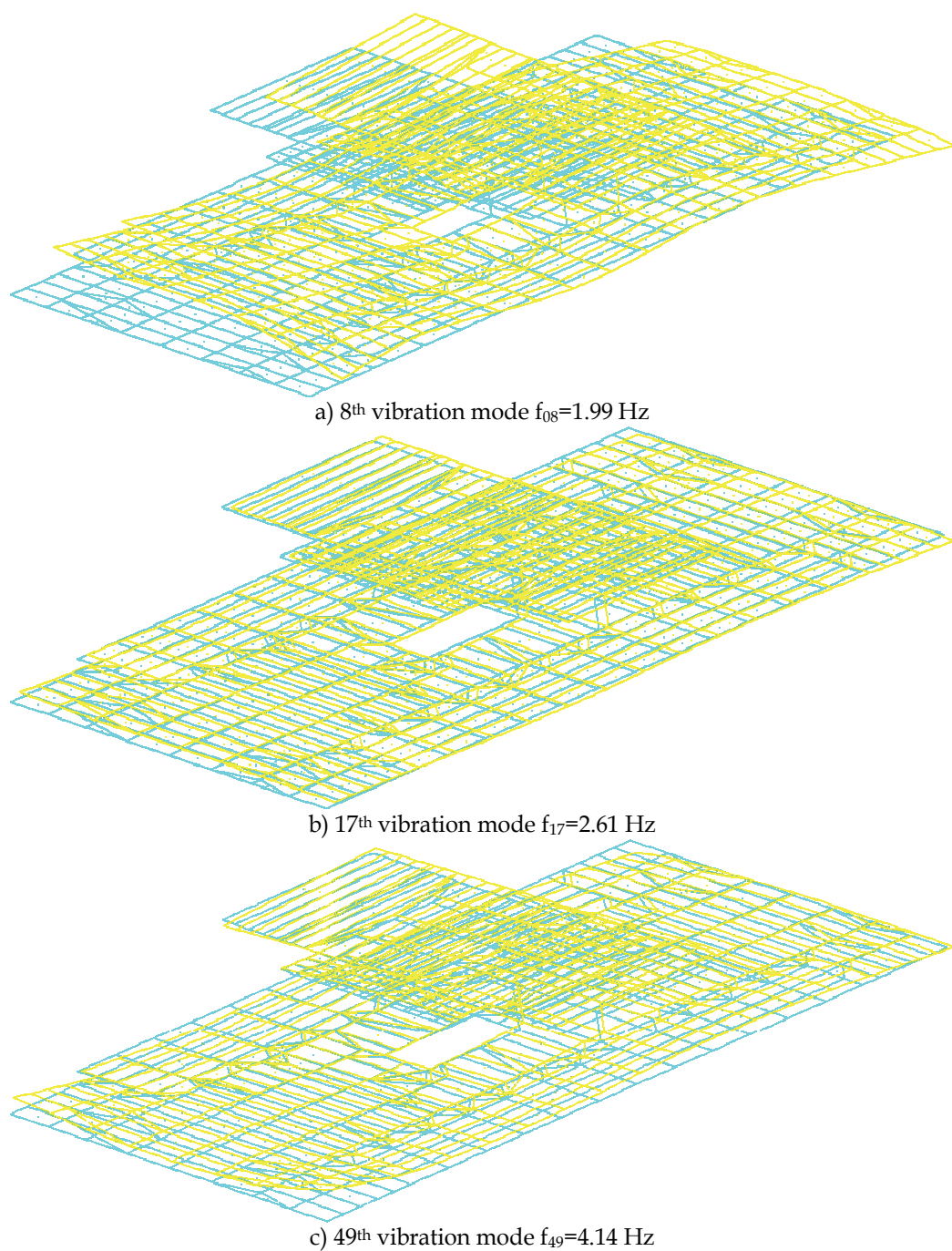

c) 49th vibration mode f_{49}=4.14 Hz

Fig. 8. Vibration modes with predominance of the steel deck system
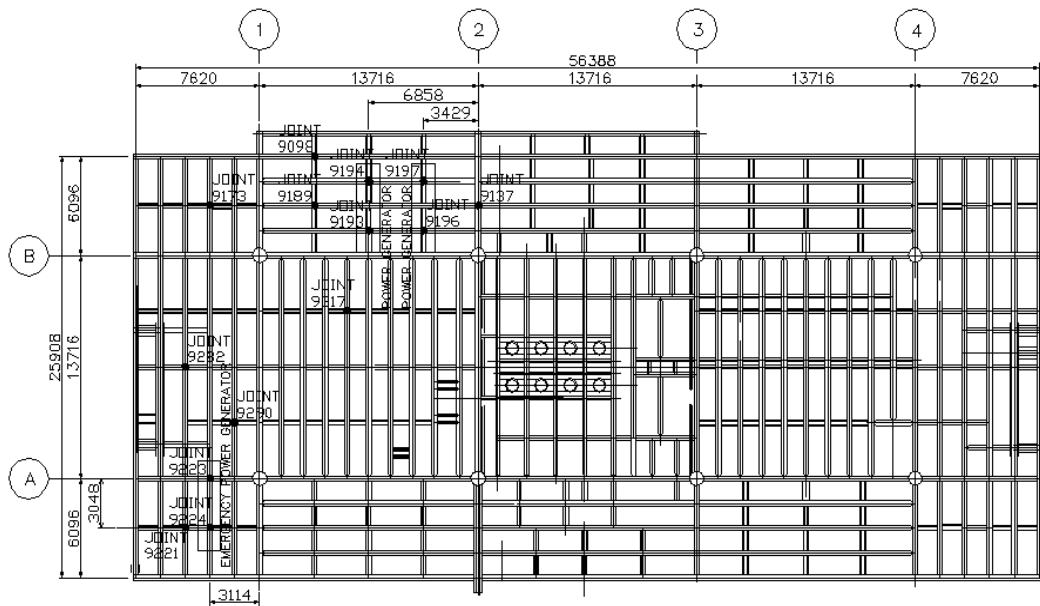
Fig. 9. Selected nodes for application of the dynamic loads

Rotor Support (Node: 9194) (µm)	Rotor Support (Node: 9197) (µm)	Rotor Support (Node: 9224) (µm)	Amplitude Limit Values (µm)
54	**446**	7	
Gear Support (Node: 9193) (µm)	Gear Support (Node: 9196) (µm)	Gear Support (Node: 9223) (µm)	40 to 60*
77	432	38	
* For vertical vibration for high speed machines (>1500 rpm) (ISO 1940-1, 2003).			

Table 10. Vertical displacements related to the combined dynamic loading (driving)

Rotor Support (Node: 9194) (mm/s)	Rotor Support (Node: 9197) (mm/s)	Rotor Support (Node: 9224) (mm/s)	Velocity Limit Values (mm/s)
10.18	**84.12**	11.89	
Gear Support (Node: 9193) (mm/s)	Gear Support (Node: 9196) (mm/s)	Gear Support (Node: 9223) (mm/s)	0.70 to 2.80*
14.49	81.46	7.27	
* Tolerable velocity for electrical motors according to (ISO 1940-1, 2003).			

Table 11. Velocities related to the combined dynamic loading (driving)

The maximum velocity value calculated at the base of the driving support (Node 9197: see Figure 9), on the platform steel deck was equal to 84.12 mm/s, see Table 11. The allowable velocity considering a perfect condition to machinery performance is located in the range of 0.7mm/s to 2.8 mm/s, see (ISO 1940-1, 2003), as presented in Table 11. This velocity value is

not in agreement with those proposed by the design codes (84.12 mm/s > 2.8 mm/s) (ISO 1940-1, 2003), violating the recommended limits.

Steel Deck (Node: 9098) (m/s^2)	Steel Deck (Node: 9137) (m/s^2)	Steel Deck (Node: 9173) (m/s^2)	Steel Deck (Node: 9189) (m/s^2)	Acceleration Limit Values (m/s^2)
5.62	6.16	4.67	**27.33**	
Steel Deck (Node: 9221) (m/s^2)	Steel Deck (Node: 9282) (m/s^2)	Steel Deck (Node: 9290) (m/s^2)	Steel Deck (Node: 9317) (m/s^2)	0.315 to 1.0*
11.62	8.19	11.77	0.61	
* Acceptable acceleration values for human comfort in accordance with (ISO 2631-1, 1997).				

Table 12. Accelerations related to the combined dynamic loading (driving)

People working temporarily near to driving could be affected in various degrees (human discomfort). The allowable acceleration value when the human comfort is considered (ISO 2631-1, 1997) is located in the range of 0.315 m/s^2 to 1.0 m/s^2, as illustrated in Table 12. The peak acceleration value calculated on the platform steel deck was equal to 27.33 m/s^2, see Table 12. This maximum acceleration value violated the recommended limits proposed by the design codes (27.33 m/s^2 > 1.0 m/s^2) (ISO 2631-1, 1997), causing human discomfort.

Based on the numerical results obtained with the present investigation, it was clearly demonstrated that the investigated structural model presented problems due to excessive vibration. This way, some changes on the horizontal steel bracing system were proposed by the authors, in order to reduce the vibration effects.

This way, Figure 10 shows the proposed steel bracing members which were added to the original design of the investigated structural model. The central idea was to propose a bracing system that produces an increasing in the steel deck stiffness and, consequently, can cause a reduction of the steel deck system dynamic response, when submitted to the rotor and gear dynamic loads.

In sequence, Figure 11 shows the vibration modes of the production platform steel deck system before and after the addition of the proposed bracing members shown in Figure 10. Comparing the presented vibration modes, it may be concluded that modal amplitudes have been modified, leading to a reduction of the structural system dynamic response, in terms of displacements, velocities and accelerations.

Figure 12 shows the response spectra of vertical translational displacements, for the supports and rotors, and, for particular nodes of the steel deck of the platform. Only three graphs were presented due to the fact that this figure (Figure 12) represents, in general, the dynamic response of the system. Based on the structure dynamic response, the peak of interest for the forced vibration numerical analysis, associated with the excitation frequency of the equipment (f = 30 Hz) is indicated in the Figure 12.

Tables 13 to 15 present the vertical translational displacements, velocities and accelerations, related to specific locations on the steel deck, near of the mechanical equipment, see Figure 9, calculated with the introduction of the proposed steel bracing system, when the combined dynamic loadings were considered.

The values presented in Tables 13 to 15 were obtained numerically with the aid of the developed finite element model. These values were then compared with the limiting values proposed by design code recommendations (CEB 209/91, 1991; ISO 1940-1, 2003; ISO 2631-1,
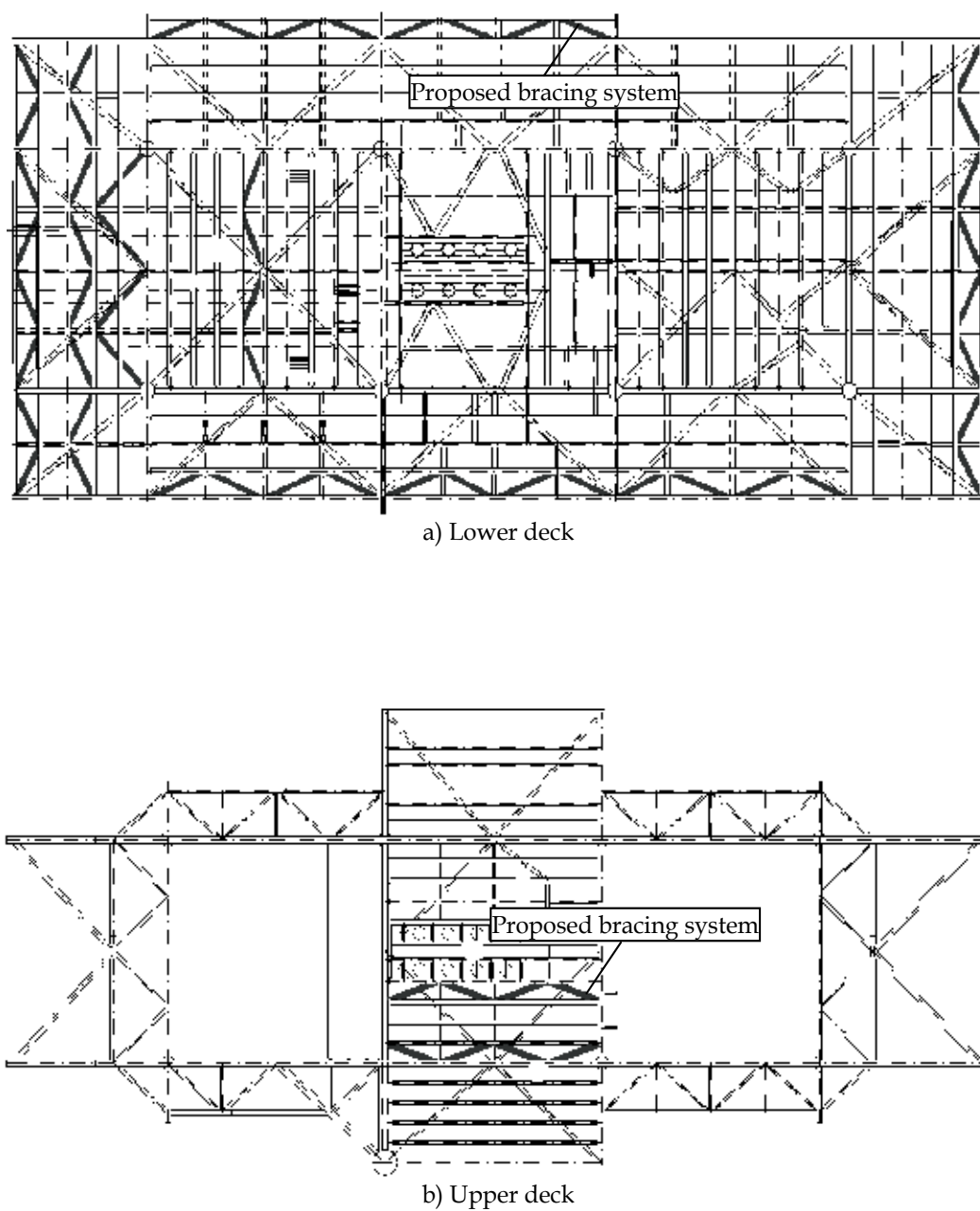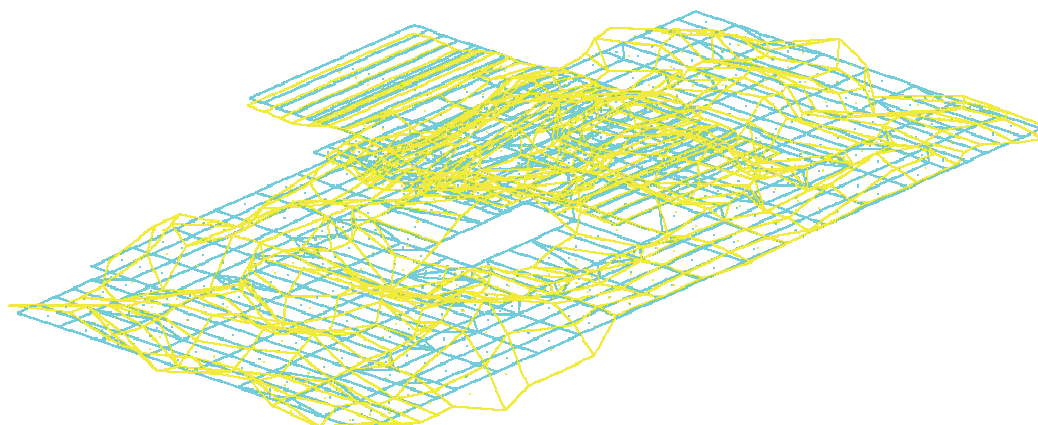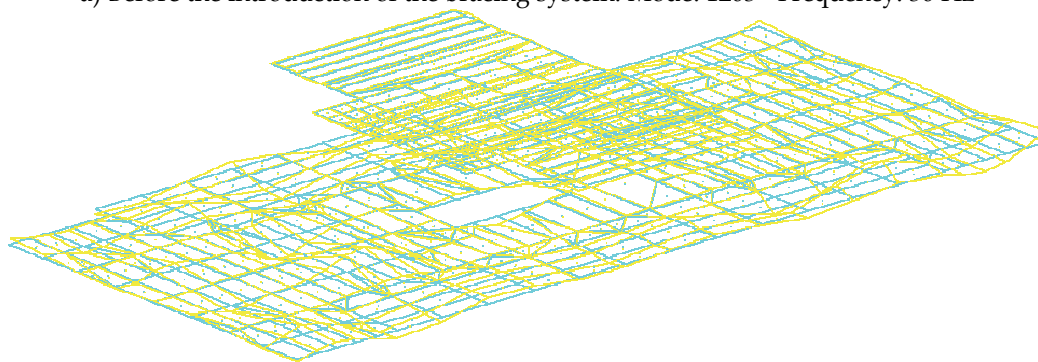
a) Lower deck

b) Upper deck

Fig. 10. Steel deck with the introduction of the proposed bracing system

a) Before the introduction of the bracing system. Mode: 1203 - Frequency: 30 Hz

b) After the introduction of the bracing system. Mode: 1195 - Frequency: 30 Hz

Fig. 11. Steel deck vibration modes

1997; ISO 2631-2, 1989; Murray et al., 2003), after the introduction of the proposed bracing system. It must be emphasized, that only the production platform steady state response was considered in this analysis.

Considering the Figure 12 (12a, 12c and 12e), related to the production platform steel deck dynamic response, it can be verified the existence of several energy transfer areas with several energy transfer picks, before the addition of the proposed bracing system.

The peak of interest for the forced vibration numerical analysis, associated with the excitation frequency of the equipment (f = 30 Hz) is clearly indicated in this figure, see Figure 12 (12a, 12c and 12e). However, after the introduction of the proposed bracing system, the energy transfer pick related to the excitation frequency of the equipment was significantly reduced, see Figure 12 (12b, 12d and 12f). This fact demonstrates the efficiency of the proposed bracing system and indicates that the structural system dynamic response can be significantly reduced.

Considering the same strategy previously presented, the design recommendations (see Tables 10 to 12) were utilized, in order to determine the limiting values for machinery performance, related to allowable amplitudes, velocities and accelerations (ISO 1940-1, 2003; ISO 2631-1, 1997).
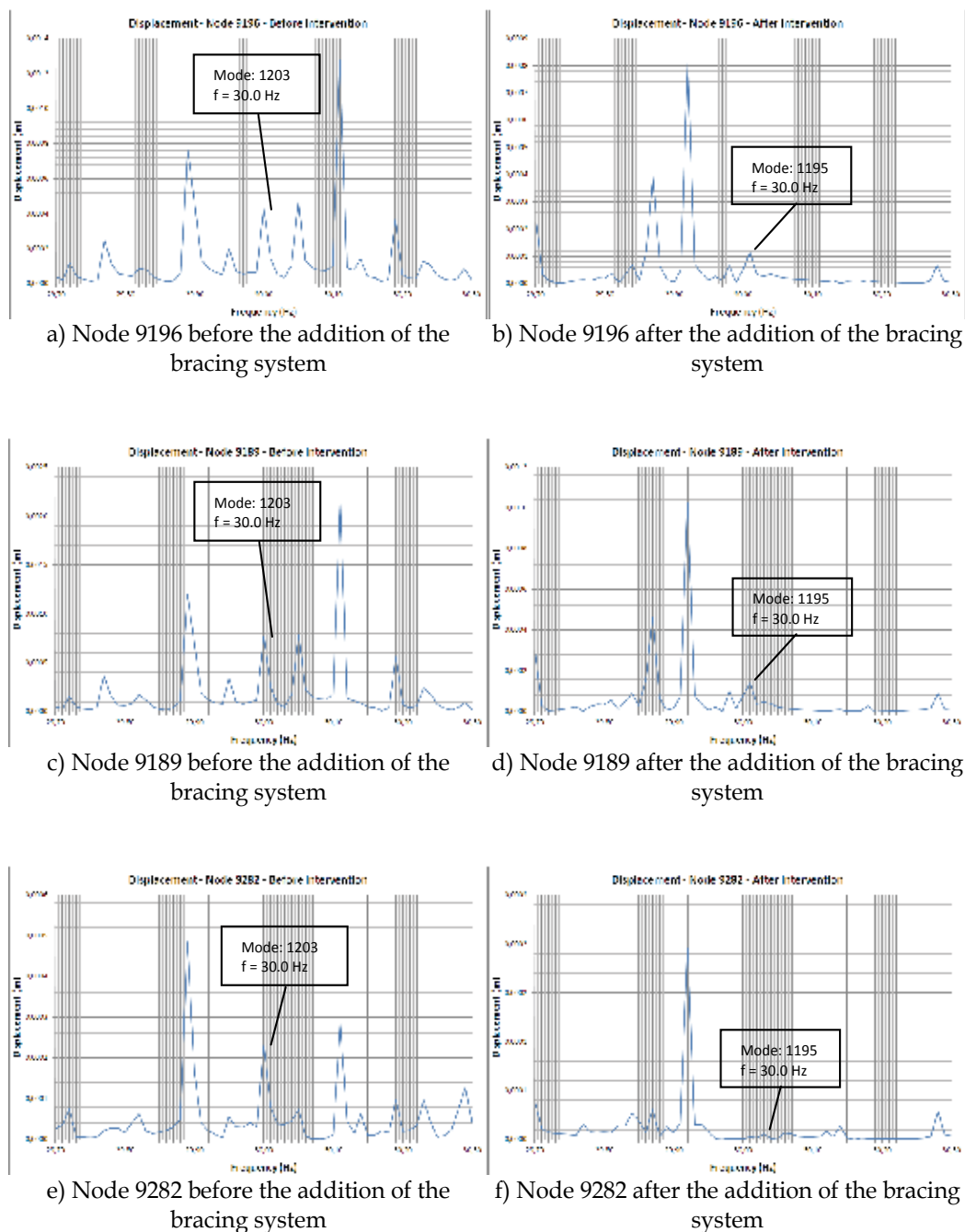
a) Node 9196 before the addition of the bracing system

b) Node 9196 after the addition of the bracing system

c) Node 9189 before the addition of the bracing system

d) Node 9189 after the addition of the bracing system

e) Node 9282 before the addition of the bracing system

f) Node 9282 after the addition of the bracing system

Fig. 12. Vertical displacements response spectra of the steel deck selected joints before and after the introduction of the proposed bracing system

Rotor Support (Node: 9194) (µm)	Rotor Support (Node: 9197) (µm)	Rotor Support (Node: 9224) (µm)	Amplitudes Limit Value (µm)
35	**96**	54	40 to 60*
Gear Support (Node: 9193) (µm)	Gear Support (Node: 9196) (µm)	Gear Support (Node: 9223) (µm)	
33	52	5	
* For vertical vibration for high speed machines (>1500 rpm) (ISO 1940-1, 2003).			

Table 13. Vertical displacements related to the combined dynamic loading (driving), after the addition of the proposed bracing system

Rotor Support (Node: 9194) (mm/s)	Rotor Support (Node: 9197) (mm/s)	Rotor Support (Node: 9224) (mm/s)	Velocities Limit Value (mm/s)
6.68	6.92	**10.36**	0.70 to 2.80*
Gear Support (Node: 9193) (mm/s)	Gear Support (Node: 9196) (mm/s)	Gear Support (Node: 9223) (mm/s)	
6.23	9.80	2.71	
* Tolerable velocity for electrical motors according to (ISO 1940-1, 2003).			

Table 14. Velocities related to the combined dynamic loading (driving), after the addition of the proposed bracing system

Steel Deck (Node: 9098) (m/s^2)	Steel Deck (Node: 9137) (m/s^2)	Steel Deck (Node: 9173) (m/s^2)	Steel Deck (Node: 9189) (m/s^2)	Amplitudes Limit Value (m/s^2)
1.39	0.50	2.63	**4.96**	0.315 to 1.0*
Steel Deck (Node: 9221) (m/s^2)	Steel Deck (Node: 9282) (m/s^2)	Steel Deck (Node: 9290) (m/s^2)	Steel Deck (Node: 9317) (m/s^2)	
3.44	0.20	1.23	2.75	
* Acceptable acceleration values for human comfort in accordance with (ISO 2631-1, 1997).				

Table 15. Accelerations related to the combined dynamic loading (driving), after the addition of the proposed bracing system

This way, after the addition of the bracing system, see Figure 10, the structural system dynamic response, submitted to the dynamic loadings (driving) coming from the machinery presented the following results: the maximum amplitude value at the base of the driving support (Node 9197: see Figure 9) on the platform steel deck was reduced of 446 μm (or 0.446 mm or 0.0446 cm) to 96 μm (or 0.096 mm or 0.0096 cm), see Tables 10 and 13; the maximum velocity value calculated at the base of the driving support (Node 9197: see Figure 9), on the steel deck was reduced of 84.12 mm/s to 6.92 mm/s, see Tables 11 and 14; the peak acceleration value calculated on the structure steel deck was reduced of 27.33 m/s² to 4.96 m/s², see Tables 12 and 15.

It must be emphasized that despite the fact that the limiting values for machinery performance, related to allowable amplitudes, velocities and accelerations (ISO 1940-1, 2003; ISO 2631-1, 1997) were violated, even after the addition of the proposed bracing system, the steady-state structural system dynamic response was considerably reduced.

8. Final remarks

This paper investigated the dynamic behaviour of an oil production platform made of steel and located in Santos basin, São Paulo, Brazil. The structural model consists of two steel decks with a total area of 1915 m² (upper deck: 445 m² and lower deck: 1470 m²), supported by vertical sections made of tubular steel members (steel jacket), and piled into the seabed, when subjected to impacts produced by mechanical equipment (rotating machinery). The main objective of the paper was to assess the dynamic impacts on the steel deck structure coming from the electrical generators and compressors.

Based on the peak acceleration values and maximum displacements and velocities, obtained on the structure steady-state response, it was possible to evaluate the structural model performance in terms of human comfort, maximum tolerances of the mechanical equipment and vibration serviceability limit states of the structural system, based on the design code recommendations.

It was concluded that the oil production platform displacements response spectra presented several energy transfer areas with several energy transfer picks. However, after the introduction of the horizontal steel bracing system proposed by the authors, the energy transfer pick related to the excitation frequency of the equipment was significantly reduced, demonstrating the efficiency of the idealized system.

After the addition of the horizontal bracing system the structural system dynamic response presented the following results: the maximum amplitude value at the base of the driving support on the steel deck was reduced of 0.0446 cm to 0.0096 cm; the maximum velocity value calculated at the base of the driving support on the deck was reduced of 84.12 mm/s to 6.92 mm/s and the maximum acceleration value calculated on the structure steel deck was reduced of 27.33 m/s² to 4.96 m/s².

However, even considering the improvement on the structural model bracing system and a considerably reduction on the structure dynamic response, the results obtained throughout this investigation indicated that the analysed platform steel deck violated the human comfort criteria, as well as its vibration serviceability limit states, inducing that individuals working temporarily near the machinery could be affected by human discomfort.

On the other hand, considering the machinery performance, it was also concluded that the platform steel deck design, should be revaluated, due to the fact that the displacements and velocities values related to the machinery supports were very high and violated the recommended limits proposed by design codes.

9. Acknowledgements

10. References

Assunção, T. M. R. C. (2009). "*Considerações sobre efeitos dinâmicos e carregamentos induzidos por fontes de excitação em estruturas*". MSc Dissertation (In Portuguese), Civil Engineering Post-graduate Programme, Federal University of Minas Gerais, UFMG, Minas Gerais, MG, Brazil.

Bachmann, H.; Ammann, W. (1987). *Vibrations in Structures: Induced by Man and Machines*, Structural Engineering Document 3rd Ed., International Association for Bridges and Structural Engineering.

Chopra, A. K. (2007). *Dynamics of Structures – Theory and Applications to Earthquake Engineering*. 3rd Ed., Pearson Education, Inc., New Jersey.

Clough, R. W.; Penzien, J. (1995). *Dynamics of Structures*, 3rd Ed., Computers and Structures, Inc., Berkeley.

Comité Euro-International Du Beton. (1991). *Vibration Problems in Structures - Practical Guidelines*. Bullitin dínformation nº 209.

Craig JR., R. R. (1981). *Structural Dynamics – An Introduction to Computer Methods*. John Wiley& Sons, Inc., New York.

Dias Junior, M. "Dinâmica de Rotores". Proceedings of IV Congresso da Academia Trinacional de Ciências, Paraná, PR, Brazil, October 2009, Fozdo Iguaçu.

Figueiredo Ferraz Consultoria e Engenharia de Projeto LTDA. (2004). "*Análise em Serviço da Plataforma de Merluza (PMLZ-1)*", Technical Report (In Portuguese).

Griffin, M. J. (1996). *Handbook of Human Vibration*. Ed. Academic Press, London.

GTSTRUDL. (2009). Structural Design & Analysis Software, Release 29.1.

ISO 1940-1. *Mechanical Vibration. (2003). Balance Quality Requirements for Rotors in a Constant (Rigid) State. Part 1: Specification and Verification of Balance Tolerances*.

ISO 2631-1. *Mechanical Vibration and Shock. (1997). Evaluation of Human Exposure to Whole-body Vibration. Part 1: General Requirements*.

ISO 2631-2. *Mechanical Vibration and Shock. (1989). Evaluation of human exposure to whole-body vibration. Part 2: human exposure to continuous and shock-induced vibrations in buildings (1 to 80Hz)*.

Lenzen, K. H. (1996). *Vibration of Steel Joist Concrete Slab Floors*. In: Engineering journal, v.3(3), p. 133-136.

López, E. J. (2002). *Dinámica de Rotores*. Graduation Monography. Universidad Nacional del Comahue.

Milet, R. R., (2006). "*Análise Comparativa de Métodos de Cálculo para Fundações de Máquinas*", MSc Dissertation (In Portuguese), Civil Engineering Post-graduate Programme, Federal University of Pernambuco, UFPE, Pernambuco, PE, Brazil.

Murray, T. M., Allen, D. E. and Ungar, E. E. (2003). *Floor vibration due to human activity*, Steel design guide series, AISC, Chicago, USA.

Pereira, C. C. G. (2005). "*Curvas de Percepção e Conforto Humano para Vibrações Verticais*". MSc Dissertation (In Portuguese), Civil Engineering Post-graduate Programme, Federal University of Ouro Preto, UFOP, Minas Gerais, MG, Brazil.

Poulos, H. G.; Davis, E. H. (1980). *Pile Foundation Analysis and Design*. John Wiley & Sons Inc., New York.

Reiher, H. E, Meister, F. J. (1946). *The Effect of Vibration on people*. Translated from Forsch Geb, p 381-386, Ohio.

Rimola, B. D. (2010). "*Análise Dinâmica de Plataformas de Aço a partir da Consideração do Efeito da Interação Solo-Estrutura*", MSc Dissertation (In Portuguese), Civil Engineering Post-graduate Programme, PGECIV, State University of Rio de Janeiro, UERJ, Rio de Janeiro, RJ, Brazil.

Rimola, B. D. ; Silva, J. G. S. da ; Sieira, A. C. C. F. ; Lima, L. R. O. de ; Neves, L. F. da C. (2010a). Vibration Analysis of a Production Platform Induced by Mechanical Equipments. Proceedings of The Tenth International Conference on Computational Structures Technology, CST 2010, Valência, Spain. Civil-Comp Press, Edinburg. v. 1. p. 1-12.

Rimola, B. D ; Silva, J. G. S. da ; Sieira, A. C. C. F. ; Lima, L. R. O. de. (2010b). Vibration Analysis of an Oil Production Platform. Proceedings of the CILAMCE 2010: XXXI Iberian Latin American on Computational Methods in Engineering and MECOM 2010: IX Argentinean Congress on Computational Mechanics, CILAMCE 2010, Buenos Aires, Argentina. AMCA (Argentine Association for Computational Mechanics). v. XXIX. p. 7529-7540.

Silva, E. L. da. (2004). "*Dinâmica de Rotores: Modelo Matemático de Mancais Hidrodinâmicos*". MSc Dissertation (In Portuguese), Federal University Paraná. Paraná,PR, Brasil.

Souza, M. G. de; Cicogna, T. R.; Chiquito, A. J. (2007). "*Excitação dos modos normais de um sistema usando um motor desbalanceado*". Revista Brasileira de Ensaio de Física, v. 29, n. 1, p.5-10, Brazil.

Srinivasulu, P.; Vaidyanathan, C. V. (1976). *Handbook of Machine Foundations*. McGraw-Hill, New Delhi.

Terzaghi, K. (1955). *Evaluation of Coefficients of Subgrade Reaction*. Géotechnique, London, v. 4, nº 4, p. 297-326.

Vasconcelos, R. P. (1998). "*Atenuações de Vibrações em Lajes Nervuradas de Piso em Concreto Armado*". MSc Dissertation (In Portuguese), Civil Engineering Post-graduate Programme, Federal University of Rio de Janeiro, UFRJ, Rio de Janeiro, RJ, Brazil.

Winkler, E. (1867). "*Die Lehre von Elastizitat und Festigkeit*" (On Elasticity and Fixity), Dominicus, Prague.

Zhou, S.; Shi, J. (2001). *Active Balancing and Vibration Control of Rotating Machinery: A Survey.* The Shock and Vibration Digest - Sage Public ations, Vol. 33, No. 4, p. 361-371.

MIMO Vibration Control for a Flexible Rail Car Body: Design and Experimental Validation

Alexander Schirrer[1], Martin Kozek[1] and Jürgen Schöftner[2]

[1]*Institute of Mechanics and Mechatronics, Vienna University of Technology*
[2]*Institute of Technical Mechanics (ACCM), Johannes Kepler University of Linz*
Austria

1. Introduction

Car bodies of modern rail vehicles are designed as lightweight structures with the aim to minimize mass and thus operational energy demand. The central structural design requirements are given by the main static and dynamic loads. However, ride comfort becomes an increasingly important issue because the softer, more compliant structure exhibits low eigenfrequencies that significantly affect perceived passenger ride comfort.

Various approaches have been taken to reduce comfort-relevant vibrations of the car body that can be grouped into vibration isolation and vibration damping approaches. The isolation approaches include passive, semi-active, and active concepts to decouple the car body from the bogeys and wheel sets. The active approaches are more complex and can affect the safety against derailment, but potentially lead to improved isolation performance over their passive counterparts (see Foo & Goodall (2000) and Stribersky et al. (1998)).

The complementary vibration damping approaches intend to increase the elastic eigenmodes' damping ratios. A passive approach is taken in Hansson et al. (2004), active control schemes have been proposed in Kamada et al. (2005) as well as Schandl et al. (2007) and Benatzky (2006). The latter two references treat the same metro configuration and actuation concept as the present work.

This chapter presents LQG and weighted $\mathcal{H}_2$ MIMO control design methods for the vibration control of lightweight rail car body structures. These designs are studied and compared to achieve vibration reduction and passenger ride comfort improvement in a highly flexible metro rail car body. The metro car body structure is directly actuated via locally mounted Piezo stack actuators. Utilizing strain measurement signals, the control law actuates the structure with the aim of minimizing ride comfort-relevant acceleration signals across the car body interior. This system is subject to variations in damping and frequency of the flexible modes which pose a challenge for control design; the two control methods are implemented in a simulation as well as in a scaled experimental setup and their capabilities are investigated. The work is embedded in a rich series of research and publications treating various aspects of control design for flexible rail car bodies. A robust $\mathcal{H}_\infty$-optimal control approach is surveyed in Kozek et al. (2011), including an overview on modeling, control design, simulation, identification, and experimental results. These research topics are focused on and detailed in Benatzky & Kozek (2005; 2007a;b); Benatzky et al. (2006; 2007); Bilik et al. (2006);

Popprath et al. (2006; 2007) and Schirrer et al. (2008). Further studies focus on Piezo stack actuators, their modeling and control (Schirrer, Kozek & Benatzky, 2008). Schirrer & Kozek (2008) and Schirrer (2010) report co-simulation studies of the multi-body system dynamics, the control law, and a non-linear actuator model. The underlying research project and its results are documented in two doctorate theses (Benatzky, 2006; Schandl, 2005), as well as in a series of master / diploma theses (Bilik, 2006; Schöftner, 2006; Schirrer, 2010). This work is based on the results of Schöftner (2006), Benatzky (2006), and Schirrer & Kozek (2008).

This text should provide the readers with first-hand experience of robust control design and implementation. It is intended to relate control theory results, simulation, and experimental results. This is done with the aim of improving one's understanding of relevant design parameters, caveats, and ways to successfully establish a working control law for challenging control problems. At the example of the application of modern control design methods to a complex, three-dimensional vibration control problem, a reliable methodology for tackling structurally new problems in vibration control is demonstrated. Additionally, the novel application of large-scale Piezo stack actuators for the vibration control of large and heavy flexible structures is studied.

This chapter is structured as follows: In the first section, a system description of the flexible metro car is given. The equations of motions are expressed by a first-order state-space representation obtained by a finite element analysis within the frequency range of interest. Details about the actuation, measurement, and performance variables are introduced which play an essential role for the MIMO controller design. Since the system order of the optimal state-space controller is equal to the order of the open-loop system, system order reduction is often necessary. The control laws designed for low-order plants then have to be validated on the original system for closed-loop stability and performance. Two types of optimal controllers are designed for a reduced-order plant model: an LQG and a weighted $\mathcal{H}_2$ controller. Simulation results are analysed and interpreted.

In an additional section, real-time control laws are designed with both design methodologies for a laboratory scale model of a rail car body. The redesigned controllers are validated in experimental test runs, providing an extended understanding on robustness, design parameter tuning, and real-time implementation issues. Finally, conclusions are drawn from both theoretical and experimental experience, and specific properties of the design methods are discussed.

2. System description - modeling of a flexible rail car body

2.1 Flexible rail car body model

For the different controller design procedures which will be explained in the next chapters a mathematical model of the flexible rail car body is necessary. The equations of motion of a linear time-invariant system can be stated in state-space form as:

$$\dot{x} = Ax + B_1w + B_2u$$
$$z = C_1x + D_{11}w + D_{12}u \qquad (1)$$
$$y = C_2x + D_{21}w + D_{22}u,$$

where the first line describes the differential equation of the physical system. The second and third lines are the output equations. The system matrix of the dynamic system and the input

matrices for the disturbance w and the actuation u are denoted by A, B_1, and B_2, respectively. The output matrices C_1 and C_2 as well as the feedthrough matrices D_{11}, D_{12}, D_{21}, and D_{22} depend on the locations and on the types of the measurements and the performance outputs. In the literature on $\mathcal{H}_2$ and $\mathcal{H}_\infty$ controller design, z is called the output performance vector to be optimized and y is the measurement vector.

The state-space model description (1) can be established through analytical modeling, typically via the Finite Element (FE) Method, or through data-based identification. These steps are detailed in Kozek et al. (2011) for the rail car body model. In this work, the simulation part is based on an analytic model and the experimental part utilizes a model identified from measured signal data.

Fig. 1 shows the rail car body containing the positions for the performance outputs ($P_1 - P_6$), the disturbances ($E_1 - E_4$), the feedback sensors ($S_1 - S_4$), and the actuators ($A_1 - A_4$). For a detailed discussion on optimal placement of sensors and actuators see Schirrer (2010).
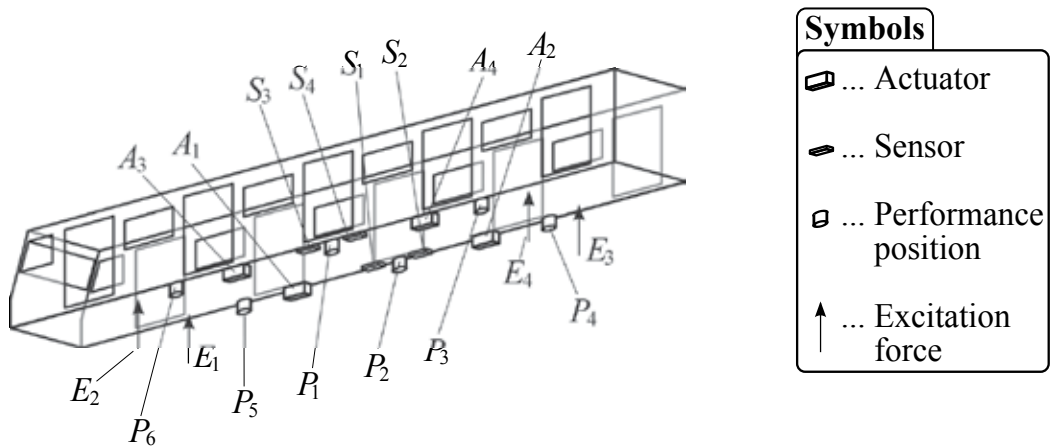

Fig. 1. Flexible rail car body: positions of input and output variables

The mathematical model of the rail car body, obtained by an FE model and subsequent order reduction steps, considers 17 elastic modes and 12 frequency-response-modes (FRM), see Schandl (2005). It is thus of order 58.

Fig. 2 shows the minimum and maximum singular values of the open-loop transfer function matrix T_{dz} which may be interpreted as the best- and the worst-case functional relationship from the white-noise disturbance vector d (related to w as shown below in Sec. 2.2) to the performance vector z. From the singular values of the frequency response (which is identical to the Bode magnitude response in the SISO case), one can observe the elastic modes in the frequency range $\omega = 40 - 200 \, \text{rad/s}$ (region 2, blue circles) as well as the FRM in the higher frequency domain (region 3, red squares). Note that no suspension (rigid-body) modes are modeled that typically lie at low frequencies (region 1), because only the flexible car body structure is considered. Full multi-body validation is studied via extensive co-simulations in Schirrer (2010). The main goal in the next sections is to design controllers which suppress elastic modes, but which are not active at other frequencies because the accuracy of the simulation model decreases with increasing frequency. The transfer function is likely to be dominated by other physical effects and nonlinearities for $\omega > 200 \, \text{rad/s}$ which have not been considered in obtaining the mathematical model. The FRM are special modes, which

are necessary to accurately describe highly localized deformations caused by the structure actuation at the actuator interfaces (see Schandl (2005)). They lie at high frequencies and can be treated here as testing modes, since the actuator action in the high-frequency domain is undesired. High-frequency modes that are always present in continuous structures, but which are not considered in the model used for the controller design may be excited and destabilize the closed-loop system.
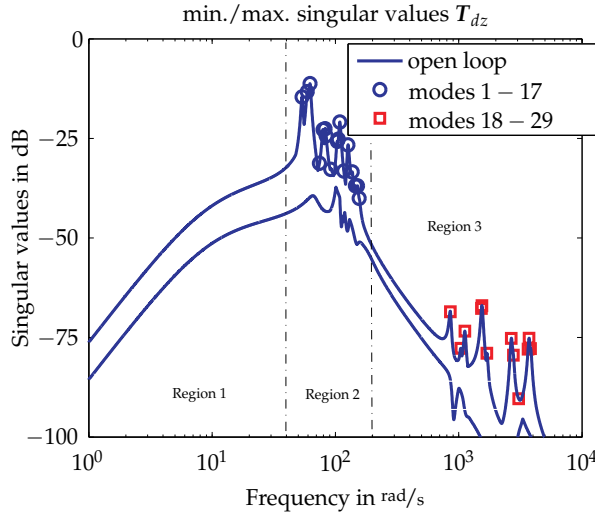

Fig. 2. Minimum and maximum singular values of the open-loop system showing the elastic modes. Modes denoted by squares are the frequency response modes (see Sec. 2.1).

2.2 Excitation

The rail vehicle runs on an imperfect track with misalignments and rail position variations. This track excitation is often characterized by its spatial frequency spectrum and associated filters, see Frederich (1984). For the studied rail car body dynamics, the disturbance w models the excitation of the car body by secondary suspension forces. Its spectrum is known from simulation and measurements and can be modeled by a colored noise sequence resulting from filtering a white noise disturbance input signal d by a second-order lag function with cut-off frequency $\omega_{\text{c.o.}} = 10\,\text{rad/s}$:

$$F(s) = 3000\frac{100}{s^2 + 20s + 100}. \tag{2}$$

The colored noise $w(t)$ is related to the white noise signal $d(t)$ by

$$\boldsymbol{W}(s) = F(s)\boldsymbol{D}(s) \quad \Leftrightarrow \quad \boldsymbol{w}(t) = \mathcal{L}^{-1}\{F(s)\boldsymbol{D}(s)\} \quad \text{with} \quad \boldsymbol{d}(t) = \mathcal{L}^{-1}\{\boldsymbol{D}(s)\}. \tag{3}$$

2.3 Actuators

A novel concept of structural actuation is applied here: Piezo stack actuators, mounted in consoles at the floor support trusses of the car body structure locally introduce bending moments into the structure. This allows direct actuation of the structural vibrations and is thus considered efficient. In this study, four stack actuators are considered in the full-size car body simulations (see Section 3 and Figure 1), whereas two stack actuators are utilized

in the experimental setup in Section 3.4, see Figure 25. For more detailed studies on the actuator concept refer to Kozek et al. (2011); the deformation characteristics of a simple console interface structure with a large-scale Piezo stack actuator have been investigated in Schirrer et al. (2008).
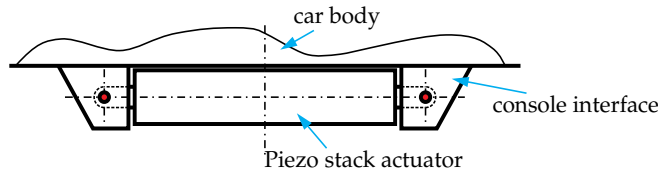

Fig. 3. Actuator mounted in a console to introduce torques into the attached flexible structure (rail car body)

2.4 Measurements

For the controller design, a signal-to-noise ratio (SNR) of about 10 is assumed, see Fig. 4. Two types of measurements are available: either using the acceleration or using strain sensor outputs proportional to the local structure curvature. The measurement positions are either collocated with the actuator or located in the middle of the car body underneath the doors (see Fig. 1). The latter case, when the actuator and sensor positions do not coincide, is called non-collocation. In general, non-collocated systems suffer from a lack of robustness and should not be used if the uncertainty of the system is large, but the controller performance may be better than for collocated systems if a sufficiently accurate mathematical model is available, see Preumont (2006).

In the present work, four strain sensors respectively six acceleration sensors are utilized in the full-size car body simulations. In the experimental setup, two strain sensors respectively one acceleration sensor are utilized for feedback (however, ride comfort performance is evaluated always at six acceleration performance positions as indicated in Figure 1).
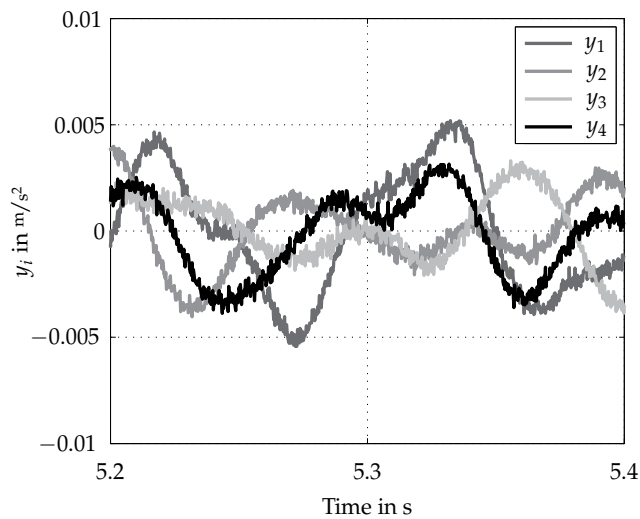

Fig. 4. Measured acceleration signals of the sensors showing a signal-to-noise ratio SNR = 10

2.5 Evaluation of passenger ride comfort according to ISO 2631

Whole-body vibrations are transmitted to the human body of the passengers in a bus, train or when driving a car. The ISO 2631 standard provides an average, empirically verified objective quantification of the level of perceived discomfort due to vibrations for human passengers (ISO, 1997). The accelerations in vertical and horizontal directions are filtered and these signals' root mean square (RMS) are combined into a scalar comfort quantity. Fig. 5 shows the ISO 2631 filter magnitude for vertical accelerations which are considered the only relevant component in the present study. For the heavy metro car, the highest sensitivity of a human occurs in the frequency range of $f \approx 4 - 10\,\mathrm{Hz}$. For the scaled laboratory model, all relevant eigenfrequencies are shifted by a factor of 8 compared to the full-size FEM model. For this reason, the ISO 2631 comfort filters and the excitation spectra are also shifted by this factor. Moreover, only unidirectional vertical acceleration signals are utilized as they represent the main contributions for the considered application.
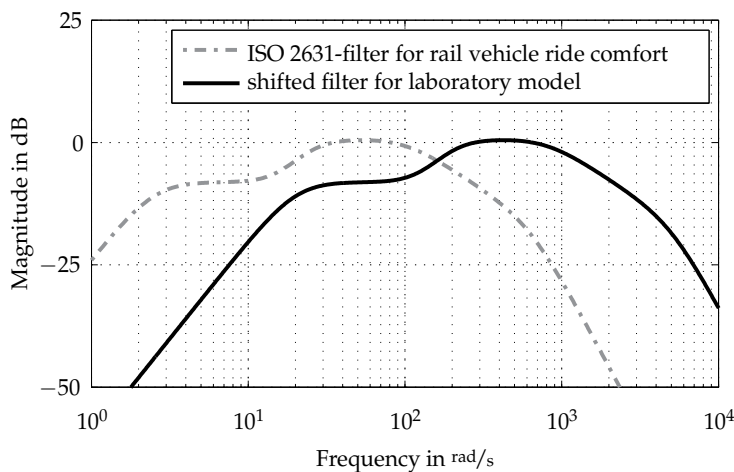

Fig. 5. Filter function according to ISO 2631 (yaw axis)

3. Optimal controller design for the metro car body

Two different methods for controller design are investigated in the following: an LQG and a frequency-weighted $\mathcal{H}_2$ controller are computed for a reduced-order plant model containing only the first 6 eigenmodes. The goal of this study is to obtain a deeper understanding on robustness and controller parameter tuning, since the LQG and the frequency-weighted $\mathcal{H}_2$ control methods are applied to design real-time state-space controllers for the laboratory setup in the next chapter.

3.1 LQG controller for a reduced-order system
3.1.1 Theory

The continuous-time linear-quadratic-gaussian (LQG) controller is a combination of an optimal linear-quadratic state feedback regulator (LQR) and a Kalman-Bucy state observer, see Skogestad & Postlethwaite (1996). Let a continuous-time linear-dynamic plant subject to

process and measurement noises be given in state space ($D = 0$ for compactness):

$$\dot{x} = Ax + Bu + Ew$$
$$y = Cx + v, \tag{4}$$

where w and v are assumed to be uncorrelated zero-mean Gaussian stochastic (white-noise) processes with constant power spectral density matrices W and V.

The LQG control law that minimizes the scalar integral-quadratic cost function

$$J = \mathrm{E}\left[\lim_{T \to \infty} \frac{1}{T} \int_0^T l(x, u)\mathrm{d}t\right] \tag{5}$$

with

$$l(x, u) = x^\mathrm{T} Q x + u^\mathrm{T} R u \tag{6}$$

turns out to be of the form

$$\dot{\hat{x}} = A\hat{x} + Bu + H(y - C\hat{x}) \tag{7}$$
$$u = \quad\quad -K_\mathrm{LQR}\hat{x}. \tag{8}$$

Thereby, $\mathrm{E}\left[\cdot\right]$ is the expected value operator, $Q = Q^\mathrm{T} \succeq 0$ and $R = R^\mathrm{T} \succ 0$ are constant, positive (semi-)definite weighting matrices (design parameters) which affect the closed-loop properties, (7) is the Kalman observer equation, and (8) is the LQR state feedback control law utilizing the state estimate.

The optimal LQR state feedback control law (Skogestad & Postlethwaite, 1996)

$$u = -K_\mathrm{LQR}x \tag{9}$$

minimizes the deterministic cost function

$$J = \int_0^\infty l(x, u)\mathrm{d}t \tag{10}$$

and is obtained by

$$K_\mathrm{LQR} = R^{-1}B^\mathrm{T}X, \tag{11}$$

where X is the unique positive-semidefinite solution of the algebraic Riccati equation

$$A^\mathrm{T}X + XA - XBR^{-1}B^\mathrm{T}X + Q = 0. \tag{12}$$

The unknown system states x can be estimated by a general state-space observer (Luenberger, 1964). The estimated states are denoted by $\hat{x}$, and the state estimation error ε is defined by

$$\varepsilon := x - \hat{x}. \tag{13}$$

Choosing the linear relation

$$\dot{\hat{x}} = F\hat{x} + Gu + Hy, \tag{14}$$

for state estimation, the following error dynamics is obtained:

$$\dot{\varepsilon} = F\varepsilon + (A - HC - F)x + (B - G)u. \tag{15}$$

If $F = A - HC$ and $G = B$ hold, and if the real parts of the eigenvalues of F are negative, the error dynamics is stable, $\hat{x}$ converges to the plant state vector x, and the observer equation (7) is obtained.

With the given noise properties, the optimal observer is a Kalman-Bucy estimator that minimizes $\mathrm{E}\left[\varepsilon^{\mathrm{T}}\varepsilon\right]$ (see Mohinder & Angus (2001); Skogestad & Postlethwaite (1996)). The observer gain H in (7) is given by

$$H = YC^{\mathrm{T}}V^{-1},\tag{16}$$

where Y is the solution of the (filter) algebraic Riccati equation

$$AY + YA^{\mathrm{T}} - YC^{\mathrm{T}}V^{-1}CY + EWE^{\mathrm{T}} = 0.\tag{17}$$

Taking into account the separation principle (Skogestad & Postlethwaite, 1996), which states that the closed-loop system eigenvalues are given by the state-feedback regulator dynamics $A - BK$ together with those of the state-estimator dynamics $A - HC$, one finds the stabilized regulator-observer transfer function matrix

$$G_{yu}(s) = -K[s\mathbf{I} - A + HC + BK]^{-1}H.\tag{18}$$

Remark: The solutions to the algebraic Riccati equations (12) and (17) and thus the LQG controller exist if the state-space systems $\left(A, B, Q^{\frac{1}{2}}\right)$ and $\left(A, W^{\frac{1}{2}}, C\right)$ are stabilizable and detectable (see Skogestad & Postlethwaite (1996)).

3.1.2 LQG controller design and results for strain sensors / non-collocation

The controller designs are based on a reduced-order plant model which considers only the lowest 6 eigenmodes. The smallest and largest singular values of the system are shown in Fig. 6 and Fig. 7 (compare Fig. 2 for the complete system). The eigenvalues are marked by blue circles. The red lines depict the singular values of the order-reduced $T_{dz,\mathrm{red}}$ (including the shaping filter (2) for the colored noise of the disturbance signal w).

Since a reduced-order system is considered for the controller design, the separation principle is not valid any longer for the full closed-loop system. Neither the regulator gain K_{LQR} nor the estimator gain H is allowed to become too large, otherwise spillover phenomena may occur that potentially destabilize the high-frequency modes. Therefore, the design procedure is an (iterative) trial-and-error loop as follows: in a first step, the weighting matrices for the regulator are prescribed and the resulting regulator gain is used for the full-order system where it is assumed that the state vector can be completely measured. If spillover occurs, the controller action must be reduced by decreasing the state weighting Q. In a second step, the design parameters for the Kalman-Bucy-filter are chosen, considering the fact that the process noise w is no white noise sequence any longer, see (2). Since the process noise covariance is approximately known as $(84.54\,\mathrm{N})^2$ for each channel, the weighting for the output noise V is utilized as a design parameter.

For the optimal regulator the weighting matrices for the states and the input variables are chosen as

$$Q = 9 \cdot 10^8 \cdot \mathbf{I}_{12 \times 12}, \qquad R = \mathbf{I}_{4 \times 4},\tag{19}$$
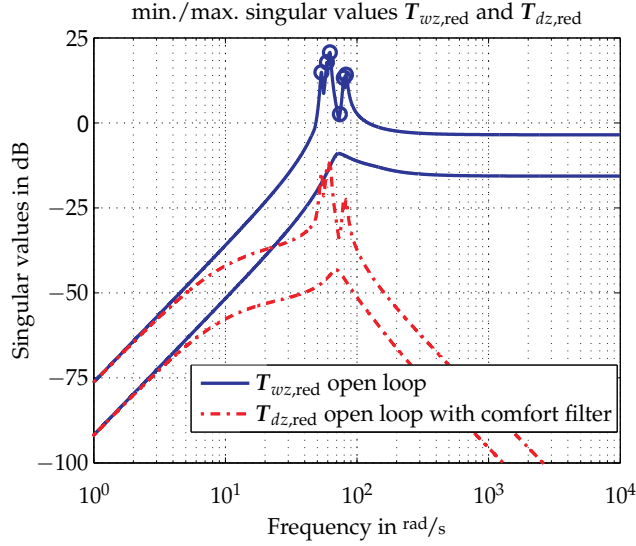
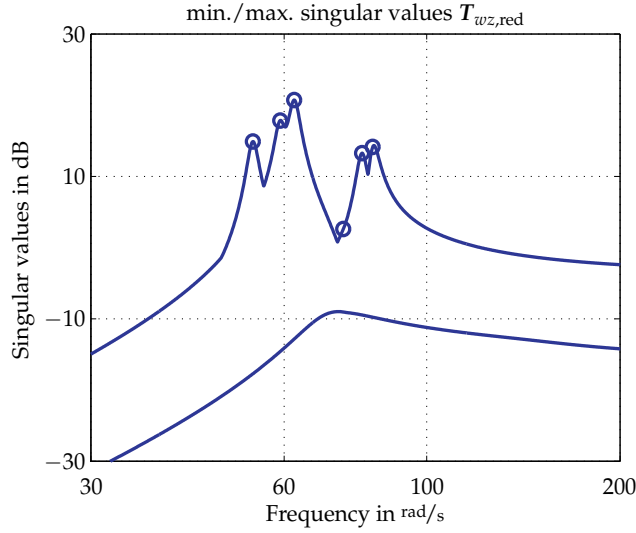Fig. 6. Smallest and largest singular values of the reduced-order open-loop system (6 modes)

Fig. 7. Smallest and largest singular values of the reduced-order open-loop system (6 modes, zoomed)

where $\mathbf{I}_{n \times n}$ is the identity matrix (n rows, n columns). The observer weightings are chosen to be

$$W = 84.54^2 \cdot \mathbf{I}_{4 \times 4}, \qquad V = (1.54 \cdot 10^{-6})^2 \cdot \mathbf{I}_{4 \times 4}. \qquad (20)$$

Table 1 lists the reduction of the ISO-filtered (see Fig. 5) RMS of each performance variable $z_{1,\mathrm{ISO}}$–$z_{6,\mathrm{ISO}}$ compared to open-loop results. Figures 8–11 contain the maximum/minimum singular values from the white noise input d (which is related to the colored noise input w by (3)) to the performance vector z, the time-domain response of two selected performance

variables z_1 and z_6, and two pole location plots (overview and zoomed) for the open- and the closed-loop results.

Performance position index i	1	2	3	4	5	6	avg.
RMS reduction $z_{i,\text{ISO}}$ in %	8.44	11.22	29.64	26.53	30.05	31.80	22.94

Table 1. RMS reduction of the performance vector z by LQG control (strain sensors / non-collocation), system order 12
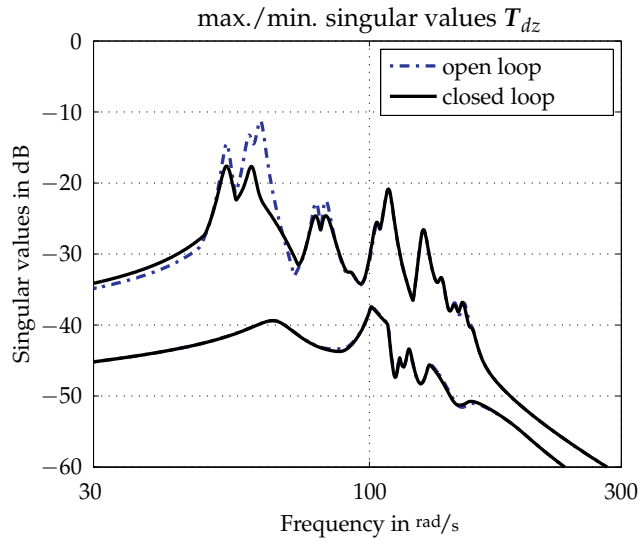

Fig. 8. Reduction of rail car disturbance transfer singular values with non-collocated LQG control
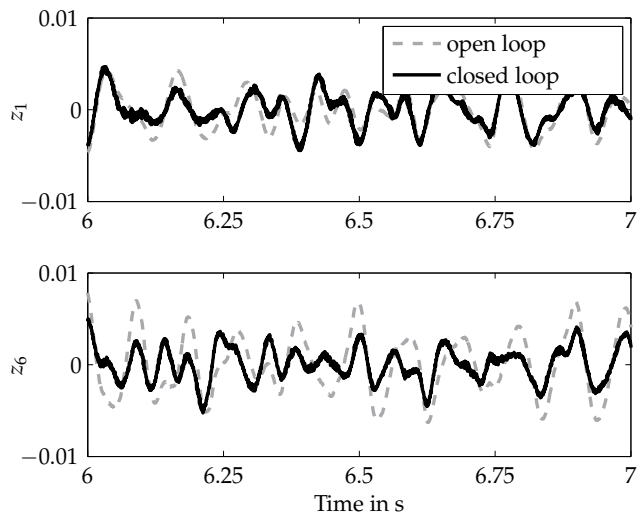

Fig. 9. Acceleration signals z_1 and z_6 without/with non-collocated LQG control
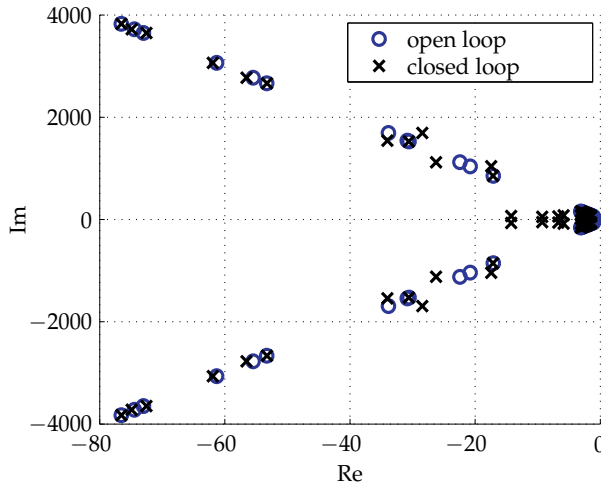
Fig. 10. Rail car model open-loop and non-collocated LQG closed-loop pole locations
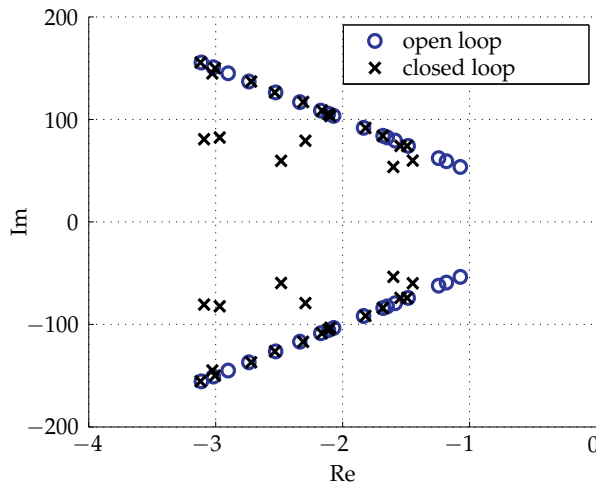

Fig. 11. Rail car model open-loop and non-collocated LQG closed-loop pole locations (zoomed)

3.1.3 Controller design and results for acceleration sensors / collocation

The optimal regulator is designed with the same weighting matrices for the states and the control variables as for the case strain sensors / non-collocation, see (19). The observer weightings are chosen to be

$$W = 84.54^2 \cdot \mathbf{I}_{4\times4}, \qquad V = 0.154^2 \cdot \mathbf{I}_{4\times4}. \tag{21}$$

Table 2 lists the reduction of the ISO-filtered (see Fig. 5) RMS of each performance variable $z_{1,\text{ISO}}$–$z_{6,\text{ISO}}$ compared to open-loop results. Figures 12–15 contain the maximum/minimum singular values from the white noise input d (which is related to the colored noise input w

by (3)) to the performance vector z, the time-domain response of two selected performance variables z_1 and z_6, and two pole location plots (overview and zoomed) for the open- and the closed-loop results.

Performance position index i	1	2	3	4	5	6	avg.
RMS reduction $z_{i,\text{ISO}}$ in %	7.83	8.36	8.04	7.02	8.79	10.23	8.38

Table 2. RMS reduction of the performance vector z by LQG control (acceleration sensors / collocation), system order 12
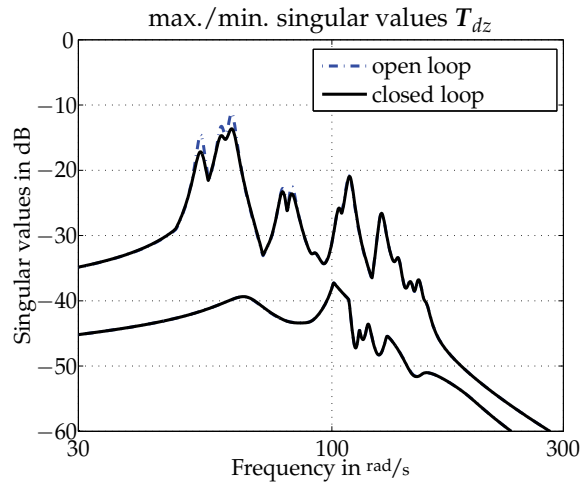

Fig. 12. Reduction of rail car disturbance transfer singular values with collocated LQG control
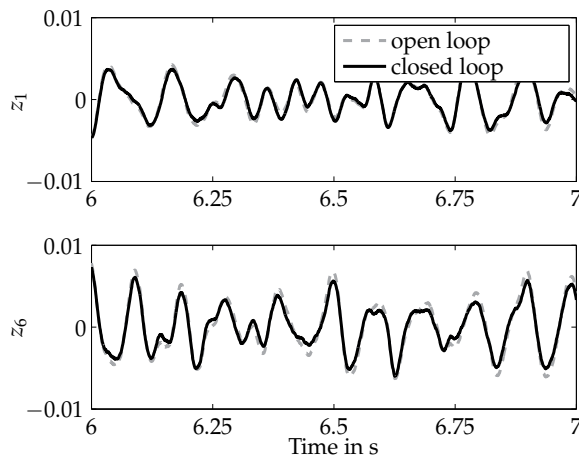

Fig. 13. Acceleration signals z_1 and z_6 without/with collocated LQG control
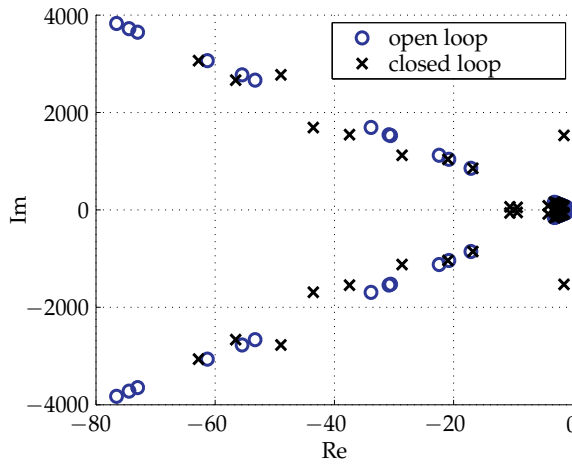
Fig. 14. Rail car model open-loop and collocated LQG closed-loop pole locations
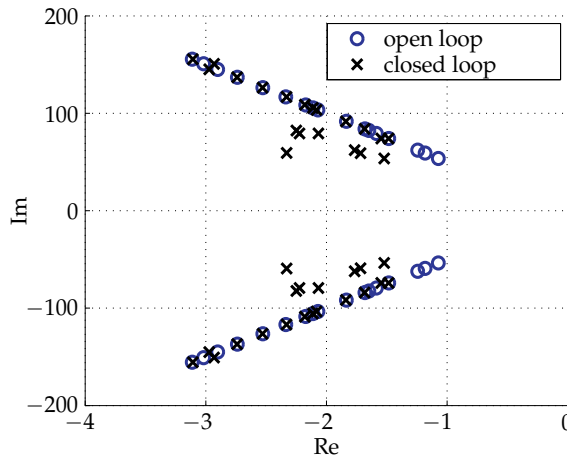

Fig. 15. Rail car model open-loop and collocated LQG closed-loop pole locations (zoomed)

3.2 Frequency-weighted $\mathcal{H}_2$ controller for a reduced-order system

The LQG controllers designed in the previous section do not take into account the performance vector z. The design of the regulator and the estimator gains are a trade-off between highly-damped modes, expressed by the negative real part of the closed-loop poles, and robustness considerations. The generalization of the LQG controller is the $\mathcal{H}_2$ controller, which explicitly considers the performance vector (e.g. one can minimize the deflection 2-norm at a certain point of a flexible system). Another advantage of this type of optimal controller is the possibility to utilize frequency-domain weighting functions. In doing so, the controller action can be shaped for specific target frequency ranges. In turn, the controller can be designed not to influence the dynamic behaviour where the mathematical model is uncertain or sensitive to parameter variations.
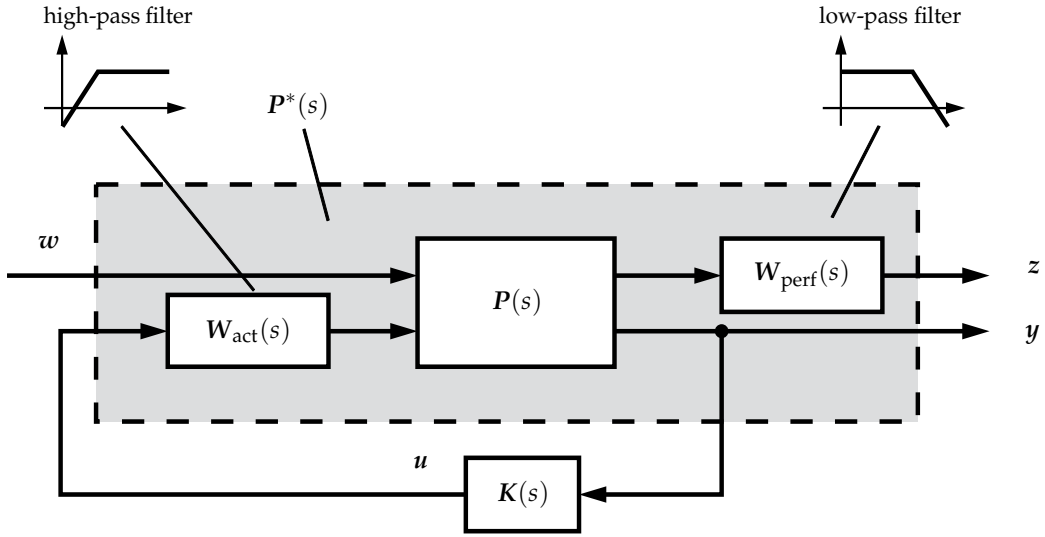
Fig. 16. Closed-loop system $P(s)$ with controller $K(s)$ and actuator and performance weighting functions $W_{\mathrm{act}}(s)$ and $W_{\mathrm{perf}}(s)$

Fig. 16 shows the closed-loop system, where the system dynamics, the controller, and the frequency-weighted transfer functions are denoted by $P(s)$, $K(s)$, $W_{\mathrm{act}}(s)$, and $W_{\mathrm{perf}}(s)$. Taking into account the frequency-weights in the system dynamics, the weighted system description of P^* can be formulated:

$$
\begin{bmatrix} z \\ y \end{bmatrix} = \begin{bmatrix} P_{11}^*(s) & P_{12}^*(s) \\ P_{21}^*(s) & P_{22}^*(s) \end{bmatrix} \begin{bmatrix} w \\ u \end{bmatrix},
\tag{22}
$$

where $P_{11}^*(s)$, $P_{12}^*(s)$, $P_{21}^*(s)$, and $P_{22}^*(s)$ are the Laplace domain transfer functions from the input variables u and w to the output variables y and z.

3.2.1 $\mathcal{H}_2$ control theory

Let the system dynamics be given in the state-space form (1), fulfilling the following prerequisites (see Skogestad & Postlethwaite (1996)):

- (A, B_2) is stabilizable

- (C_2, A) is detectable

- $D_{11} = 0, D_{22} = 0$

- D_{12} has full rank

- D_{21} has full rank

- $\begin{bmatrix} A - \mathrm{j}\omega\mathbf{I} & B_2 \\ C_1 & D_{12} \end{bmatrix}$ has full column rank for all ω

- $\begin{bmatrix} A - j\omega\mathbf{I} & B_1 \\ C_2 & D_{21} \end{bmatrix}$ has full row rank for all ω

For compactness the following abbreviations are introduced:

$$\overline{R} = D_{12}{}^{\mathrm{T}}D_{12}$$
$$\overline{S} = B_2\overline{R}^{-1}B_2{}^{\mathrm{T}}$$
$$\overline{A} = A - B_2\overline{R}^{-1}D_{12}{}^{\mathrm{T}}C_1$$
$$\overline{Q} = C_1{}^{\mathrm{T}}C_1 - C_1{}^{\mathrm{T}}D_{12}\overline{R}^{-1}D_{12}{}^{\mathrm{T}}C_1 \succeq \mathbf{0}$$
$$\overline{\overline{R}} = D_{21}D_{21}{}^{\mathrm{T}}$$
$$\overline{\overline{S}} = C_2{}^{\mathrm{T}}\overline{\overline{R}}^{-1}C_2$$
$$\overline{\overline{A}} = A - B_1D_{21}{}^{\mathrm{T}}\overline{\overline{R}}^{-1}C_2$$
$$\overline{\overline{Q}} = B_1B_1{}^{\mathrm{T}} - B_1D_{21}{}^{\mathrm{T}}\overline{\overline{R}}^{-1}D_{21}B_1{}^{\mathrm{T}} \succeq \mathbf{0},$$

where $\succeq \mathbf{0}$ denotes positive-semidefiniteness of the left-hand side. The $\mathcal{H}_2$ control design generates the controller transfer function $K(s)$ which minimizes the $\mathcal{H}_2$ norm of the transfer function T_{wz}, or equivalently

$$\|T_{wz}\|_2 = \sqrt{\frac{1}{2\pi}\int_{-\infty}^{\infty}T_{wz}{}^{\mathrm{T}}(j\omega)T_{wz}(j\omega)\mathrm{d}\omega} \to \min. \tag{23}$$

The controller gain K_c and the estimator gain K_f are determined by

$$K_c = \overline{R}^{-1}(B_2{}^{\mathrm{T}}X_2 + D_{12}{}^{\mathrm{T}}C_1) \tag{24}$$

and

$$K_f = (Y_2C_2{}^{\mathrm{T}} + B_1D_{21}{}^{\mathrm{T}})\overline{\overline{R}}^{-1}, \tag{25}$$

where $X_2 \succeq \mathbf{0}$ and $Y_2 \succeq \mathbf{0}$ are the solutions of the two algebraic Riccati equations

$$X_2\overline{A} + \overline{A}^{\mathrm{T}}X_2 - X_2\overline{S}X_2 + \overline{Q} = \mathbf{0}, \tag{26}$$
$$\overline{\overline{A}}Y_2 + Y_2\overline{\overline{A}}^{\mathrm{T}} - Y_2\overline{\overline{S}}Y_2 + \overline{\overline{Q}} = \mathbf{0}. \tag{27}$$

The state-space representation of the controller dynamics is given by

$$\begin{aligned} \dot{\widehat{x}} &= (A - B_2K_c - K_f(C_2 - D_{22}K_c))\widehat{x} + K_fy \\ u &= -K_c\widehat{x}, \end{aligned} \qquad \Rightarrow u = -K(s)y. \tag{28}$$

3.2.2 $\mathcal{H}_2$ controller design and results for strain sensors / non-collocation
The frequency-weighting functions have been specified as

$$W_{\mathrm{act}} = G_{\mathrm{act}} \cdot \mathbf{I}_{4\times 4} = 4967 \cdot \frac{(s+45)^4 \cdot (s^2 + 6s + 3034)}{(s+620)^4 \cdot (s+2000)^2} \cdot \mathbf{I}_{4\times 4} \tag{29}$$

$$W_{\text{perf}} = G_{\text{perf}} \cdot \mathbf{I}_{6\times 6} = 20 \cdot \mathbf{I}_{6\times 6} \tag{30}$$

As in the previous section, the $\mathcal{H}_2$ controller is designed for the reduced-order model (12 states). Considering the shaping filter (2) for the disturbance ($8 = 4 \cdot 2$ states) and the weighting functions (29) and (30) ($24 = 4 \cdot 6$ states), one finds a controller of order 44.

Table 3 lists the reduction of the ISO-filtered (see Fig. 5) RMS of each performance variable $z_{1,\text{ISO}}$–$z_{6,\text{ISO}}$ compared to open-loop results. Figures 17–20 contain the maximum/minimum singular values from the white noise input d (which is related to the colored noise input w by (3)) to the performance vector z, the time-domain response of two selected performance variables z_1 and z_6, and two pole location plots (overview and zoomed) for the open- and the closed-loop results.

Performance position index i	1	2	3	4	5	6	avg.
RMS reduction $z_{i,\text{ISO}}$ in %	26.27	27.95	28.71	27.84	30.99	34.31	29.35

Table 3. RMS reduction of the performance vector z by $\mathcal{H}_2$ control (strain sensors / non-collocation), system order 44
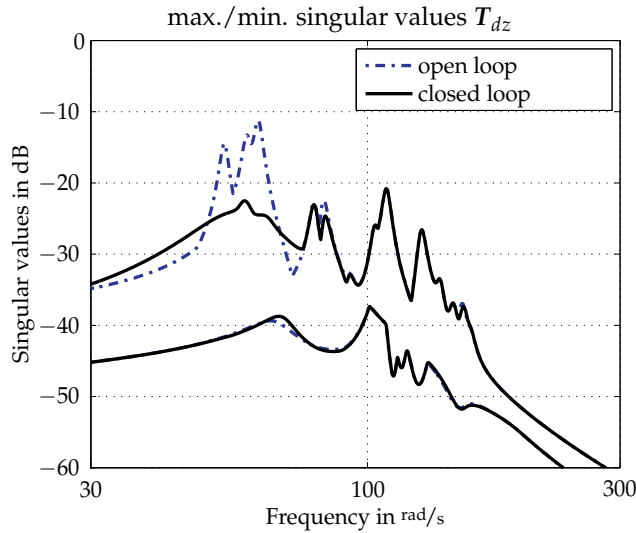

Fig. 17. Reduction of rail car disturbance transfer singular values with non-collocated $\mathcal{H}_2$ control

3.2.3 $\mathcal{H}_2$ controller design and results for acceleration sensors / collocation

The frequency-weighting functions have been specified as

$$W_{\text{act}} = G_{\text{act}} \cdot \mathbf{I}_{4\times 4} = 4967 \cdot \frac{(s+45)^4 \cdot (s^2 + 6s + 3034)}{(s+620)^4 \cdot (s+2000)^2} \cdot \mathbf{I}_{4\times 4}, \tag{31}$$

$$W_{\text{perf}} = G_{\text{perf}} \cdot \mathbf{I}_{6\times 6} = 20 \cdot \mathbf{I}_{6\times 6}. \tag{32}$$

Table 4 lists the reduction of the ISO-filtered (see Fig. 5) RMS of each performance variable $z_{1,\text{ISO}}$–$z_{6,\text{ISO}}$ compared to open-loop results. Figures 21–24 contain the maximum/minimum singular values from the white noise input d (which is related to the colored noise input w
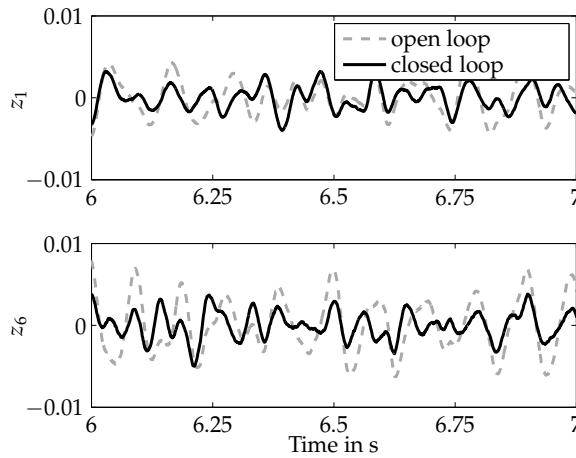
Fig. 18. Acceleration signals z_1 and z_6 without/with non-collocated $\mathcal{H}_2$ control
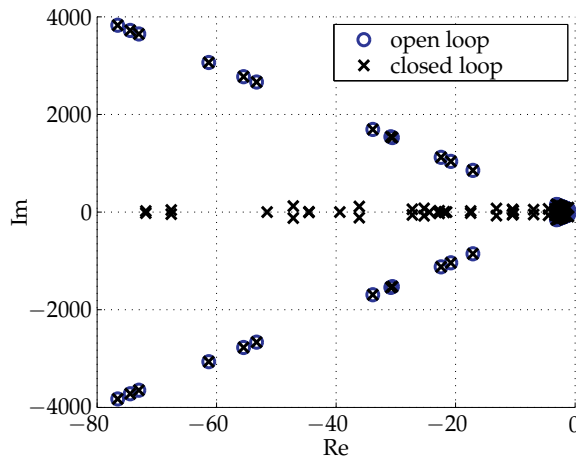

Fig. 19. Rail car model open-loop and non-collocated $\mathcal{H}_2$ closed-loop pole locations

by (3)) to the performance vector z, the time-domain response of two selected performance variables z_1 and z_6, and two pole location plots (overview and zoomed) for the open- and the closed-loop results.

Performance position index i	1	2	3	4	5	6	avg.
RMS reduction $z_{i,\mathrm{ISO}}$ in %	23.89	28.12	27.23	24.67	28.85	31.27	27.34

Table 4. RMS reduction of the performance vector z by $\mathcal{H}_2$ control (acceleration sensors / collocation), system order 44

3.3 Interpretation

The main goal for both the LQG and the $\mathcal{H}_2$ controller designs was to increase the damping of the first three eigenmodes. In the present design task, the LQG controller designed for
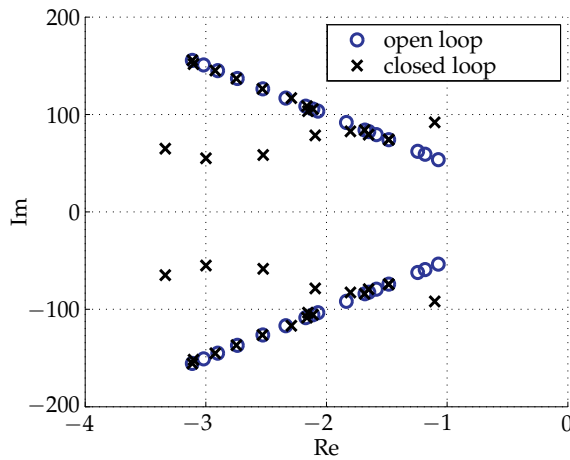
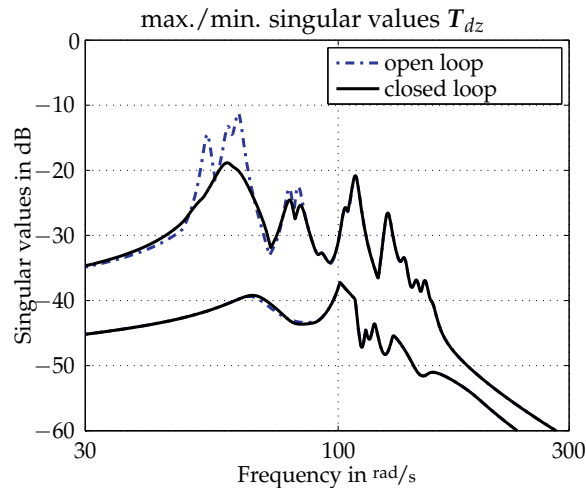Fig. 20. Rail car model open-loop and non-collocated $\mathcal{H}_2$ closed-loop pole locations (zoomed)

Fig. 21. Reduction of rail car disturbance transfer singular values with collocated $\mathcal{H}_2$ control

collocated acceleration sensors (see Section 3.1.3) did not yield satisfactory performance. The singular value plot shows only marginal magnitude reduction (Figure 12), and also a time-domain analysis of the performance signals z_1 and z_6 (see Figure 13) shows no significant improvement. According to Table 2, the reduction of the filtered performance vector is approximately 8%. However, at $\omega \approx 1500$ rad/s one of the frequency response modes approaches the imaginary axis (Fig. 14 and Fig. 15). Even though the simulated closed loop remains stable, this spillover is critical for operation at an uncertain real plant which possesses unknown high-frequency dynamics.

Considering the LQG design for non-collocated strain sensors in Section 3.1.2, the controller significantly improves the vibrational behaviour. The performance vector is reduced by 23% (Table 1) and a significant reduction is apparent for the time-domain evaluation in Fig. 9. The maximum singular values of the first three eigenmodes are reduced (e.g. third eigenmode
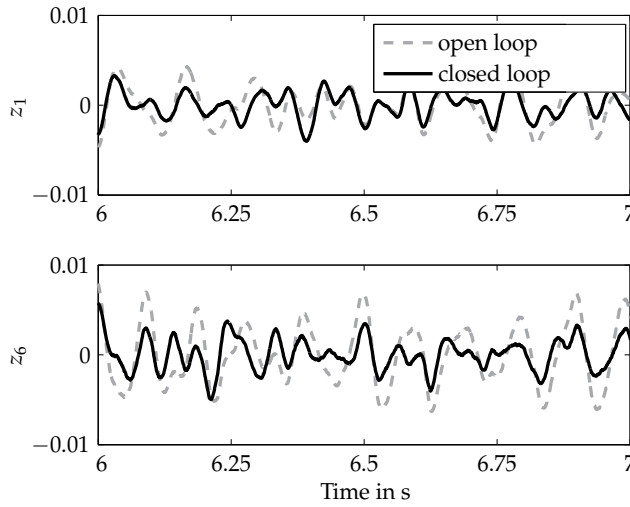
Fig. 22. Acceleration signals z_1 and z_6 without/with collocated $\mathcal{H}_2$ control
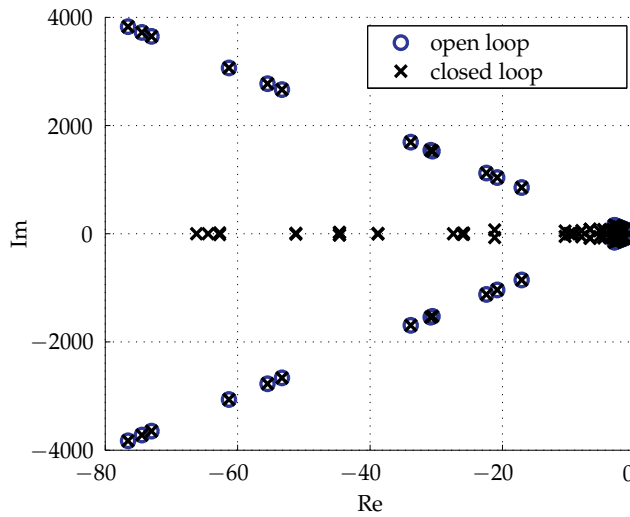

Fig. 23. Rail car model open-loop and collocated $\mathcal{H}_2$ closed-loop pole locations

$-11\,\mathrm{dB}$, see Fig. 8). From the pole location plot one concludes that in the higher frequency domain the frequency response modes remain unchanged (Fig. 10 and Fig. 11).

Both variants of the $\mathcal{H}_2$-optimal controllers (Section 3.2.2 and Section 3.2.3) show significantly higher performance in simulation than the controllers obtained by the LQG design procedure. The main advantage of the $\mathcal{H}_2$ design approach is the possibility to directly incorporate frequency weights to shape the design, see (29) and (31). Specifically, the frequency content of the actuator command signals can be modified. The control law actuates mainly within the frequency range $\omega \approx 50 - 70\,\mathrm{rad/s}$ due to the transmission zeros in the weighting functions W_{act}. In the high-frequency domain, W_{act} is large for both $\mathcal{H}_2$ designs, so only small actuator signal magnitudes result at these frequencies which is especially
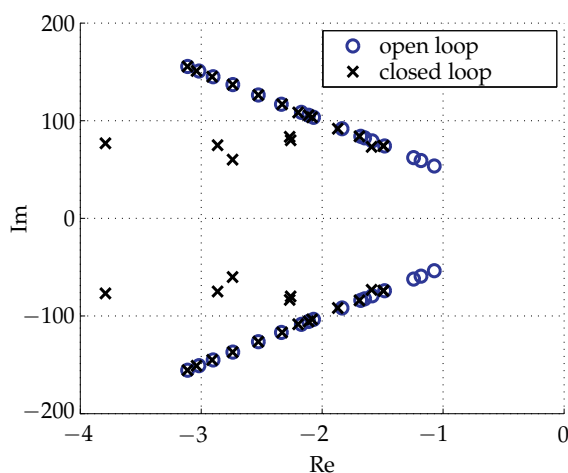
Fig. 24. Rail car model open-loop and collocated $\mathcal{H}_2$ closed-loop pole locations (zoomed)

favorable if the plant dynamics is unknown there. The results for strain/non-collocation and acceleration/collocation control designs are shown in Figs. 17–20 and Table 3 as well as in Figs. 21–24 and Table 4. In the first case the vibrations of the time-domain performance signals $z_{i,\text{ISO}}$ are reduced by 30% (Fig. 18), which is also indicated by the singular values plot (Fig. 17): the lowest three modes are reduced on average by 11 dB. Virtually no spillover occurs at high frequencies ($\omega \approx 150 - 4000\,\text{rad/s}$): The singular values are unchanged (not shown) and also the pole locations remain unchanged for $\omega > 150\,\text{rad/s}$ (seen in Fig. 19 and Fig. 20 where the open-loop poles (blue circles) and closed-loop poles (black crosses) coincide).

The acceleration sensor / collocation simulation results show similar improvement: Only the first three modes are strongly damped (Fig. 21 and Fig. 24), the other ones are hardly affected by the controller action due to the specific choice of the weighting function (31), see Fig. 23. The average reduction of the ISO-filtered performance variables is 27% (Table 4 and Fig. 22).

As a concluding remark, note that the combination of the $\mathcal{H}_2$ method with frequency-weighted transfer functions for the input and the performance signals (W_{act}, W_{perf}) provide satisfactory results, which are characterized by their high robustness and insensitivity to parameter uncertainties. It is shown that the frequency content of the controller action can be tuned by the input weight W_{act}, which affects only the first modes of interest. Higher modes, which are much more difficult to model, are hardly affected due to the roll-off of the $\mathcal{H}_2$ controller. Nevertheless, the LQG controller shows very promising results for the case of non-collocated strain sensors, although the controller is designed for a strongly reduced model containing only 6 modes (note that the full order model has 29 modes). If the acceleration signals are measured and sensor and actuators are collocated, the full-order plant is destabilized by the LQG controller (designed on the reduced-order plant).

Finally, it is noted that so-called reduced-order LQG controllers (see Gawronski (2004)) also have been designed to control the metro vehicle, see Schöftner (2006). By this method an LQG controller has been directly designed for the full-order plant model with 29 modes. Then, the controller transfer functions are evaluated (dynamic systems of order 58) and transformed to the Gramian-based input/output-balanced form. Hardly observable or controllable states, indicated by small Hankel singular values, are truncated, yielding a

low-order controller. While this procedure works well for academic problems (for example, a simply-supported beam), for the metro car body no low-order controller with good vibration reduction performance could be found, see Schöftner (2006).

3.4 Experimental setup of scaled metro car body
3.4.1 General remarks

Fig. 25 and Fig. 26 show the laboratory testbed in which the metro car body scale model is operated. The aluminum structure is excited via an electrodynamic shaker, two Piezo patches measure local structure strain, and two Piezo stack actuators, mounted in consoles on the structure, provide an efficient means of structural actuation. Fig. 26 also shows the actuation and measurement setup symbolically with actuator amplifier (AA), shaker amplifier (SA), antialiasing filters (AF), measurement amplifier (MA) and the laboratory computer (Lab.-PC) on which the real-time control algorithms are implemented.

Fig. 25. Scaled metro car body
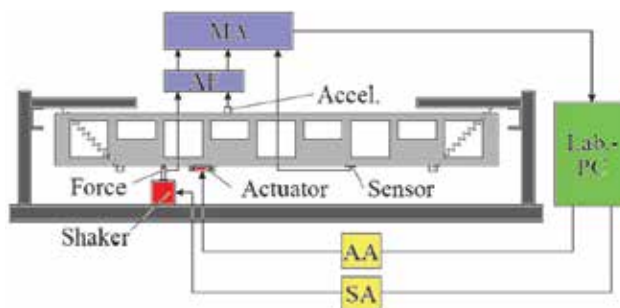

Fig. 26. Basic sketch of the scaled metro car body with actuators, sensors, and performance variables

The pole plot and the singular-value plot (Fig. 27 and Fig. 28) of the frequency response provide information on the identified dynamics of the laboratory setup (200 modes): the modes relevant for the control problem are the bending mode at $f \approx 65\,\mathrm{Hz}$ and the torsional

mode at $f \approx 75\,\text{Hz}$. The majority of the poles are either negligible high-frequency modes or other local oscillatory modes.
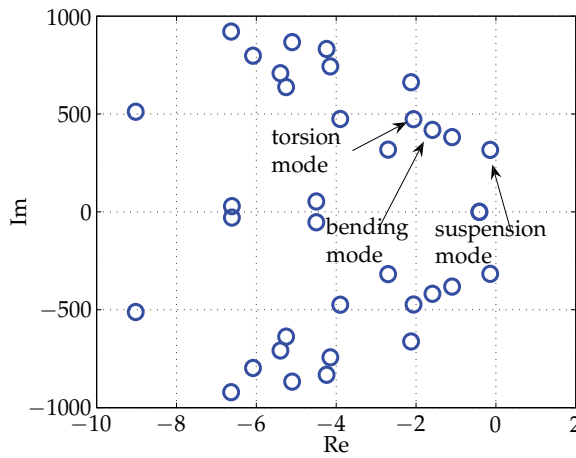
Fig. 27. Pole plot of the identified scaled metro car body (zoomed)
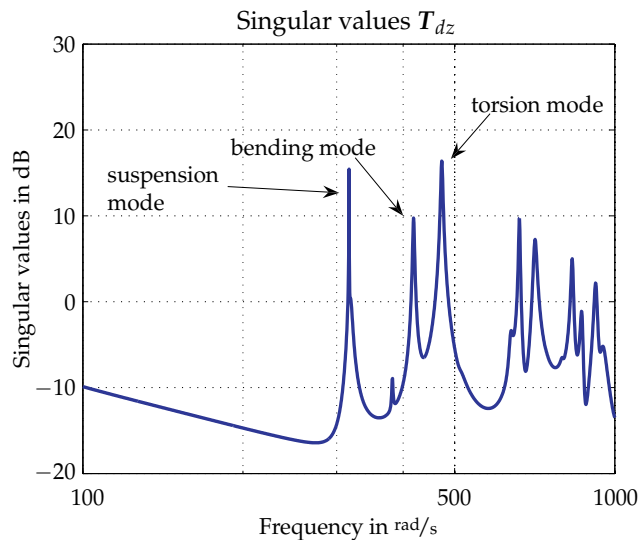
Fig. 28. Singular values of the identified scaled metro car body

The goal is to significantly dampen the torsional and the bending modes without destabilizing other oscillatory modes. For an objective evaluation of the active vibration control problem, the RMS of the frequency-filtered performance variables $z_{i,\text{ISO}}$ ($i = 1, \ldots, 6$) are compared in the open-loop and closed-loop responses. These six performance quantities represent a quantification of passenger ride comfort. A more detailed analysis can be found in Kozek & Benatzky (2008) and Schirrer (2010).

3.4.2 LQG controller design

An LQG controller is designed for a reduced-order plant model with 28 states (the system is identified with 200 states, see Kozek et al. (2011)). Hence the system is transformed into a modal state space representation and all eigenmodes with an eigenfrequency higher than $f \approx 75$ Hz are truncated and not considered for the controller design. The weighting functions for the regulator and the estimator design are

$$Q = \begin{bmatrix} \mathbf{I}_{24 \times 24} & \mathbf{0} \\ \mathbf{0} & 6 \cdot 10^6 \cdot \mathbf{I}_{4 \times 4} \end{bmatrix}, \qquad R = \mathbf{I}_{2 \times 2} \tag{33}$$

$$W = 0.0054, \qquad V = 2 \cdot 10^{-4} \mathbf{I}_{2 \times 2}. \tag{34}$$

Note that Q in (33) is chosen such that only the bending and the torsional vibrations should be significantly damped. A discussion of the results for the closed-loop system is given in Section 3.4.4.

3.4.3 $\mathcal{H}_2$ controller design

The $\mathcal{H}_2$ controller is designed for a plant model which only considers 3 eigenmodes (two of them describe the bending and torsional behaviour). For an efficient control design the frequency-dependent actuator and performance functions are specified as

$$W_{\text{act}} = G_{\text{act}} \cdot \mathbf{I}_{2 \times 2} = 188.5 \cdot 10^9 \cdot \frac{(s^2 + 77.91s + 151800)^4}{(s + 10000)^8} \cdot \mathbf{I}_{2 \times 2}. \tag{35}$$

$$W_{\text{perf}} = G_{\text{perf}} \cdot \mathbf{I}_{6 \times 6} = \mathbf{I}_{6 \times 6} \tag{36}$$

Note that the transmission zeros of W_{act} are near the two target modes to be damped, causing the actuator action to be a maximum for these frequencies. A discussion of the results for the closed-loop system are given in Section 3.4.4.

3.4.4 Results

Table 5 and Figures 29, 30, 31, and 32 show the damping ability of both types of controllers. In both cases, the vibrations of the actively controlled system are significantly reduced compared to the open-loop response of the system. The accelerations at both ends of the structures, expressed by the performance variables z_1, z_2, z_5 and z_6 can be significantly reduced, whereas z_3 and z_4 are close to the open-loop response. This is explained due to the fact that the first torsional mode dominates the bending vibrations for the scale laboratory setup. For the LQG controller the singular values only differ for the torsional and the bending vibrations (-14 dB and -10 dB). It is evident that only the eigenvalues of the two targeted flexible modes are affected by the controller. The unchanged mode at lower frequency is an almost uncontrollable suspension mode, while the higher flexible modes are not adversely affected by the control action.

Analogous results could be obtained using the frequency-weighed $\mathcal{H}_2$-optimal control design methodology: the achieved RMS reductions of the performance variables are approximately the same as for the LQG control method. Note that the bandwidth of the frequency-weighted controller is narrow around $f = 60 - 75$ Hz where the actuator weightings are small. Contrary to the LQG approach, the target modes as well as other modes with a higher negative real part are positively influenced. This indicates that the model quality is sufficiently high and that

the control laws are insensitive to the occurring differences between design plant and actual system.

Performance position index i	1	2	3	4	5	6	avg.
RMS reduction $z_{i,\text{ISO}}$ (LQG) in %	41.53	34.69	8.83	6.02	37.28	36.94	27.55
RMS reduction $z_{i,\text{ISO}}$ ($\mathcal{H}_2$) in %	41.31	35.69	-4.00	4.59	34.89	36.16	24.77

Table 5. Laboratory testbed results: RMS reduction of the performance vector z by an LQG (system order 28) and an $\mathcal{H}_2$ controller (system order 23) utilizing strain feedback sensors
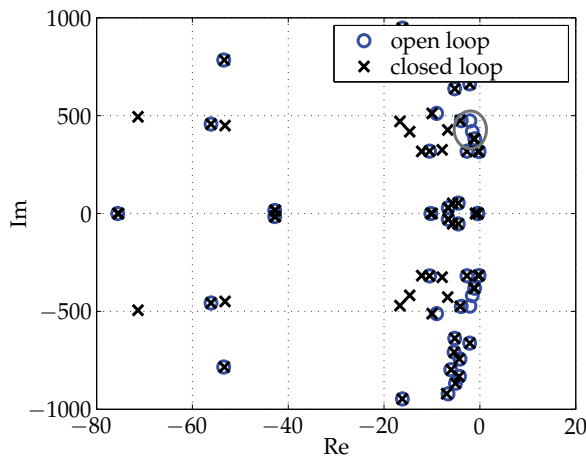

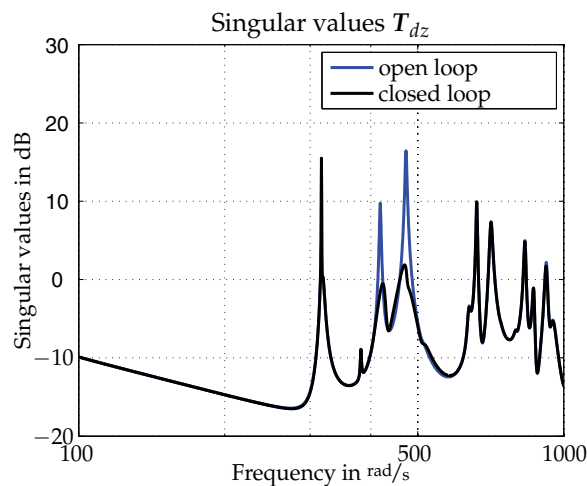Fig. 29. Pole plot with/without LQG controller

Fig. 30. Singular values of the frequency response plot with/without LQG controller
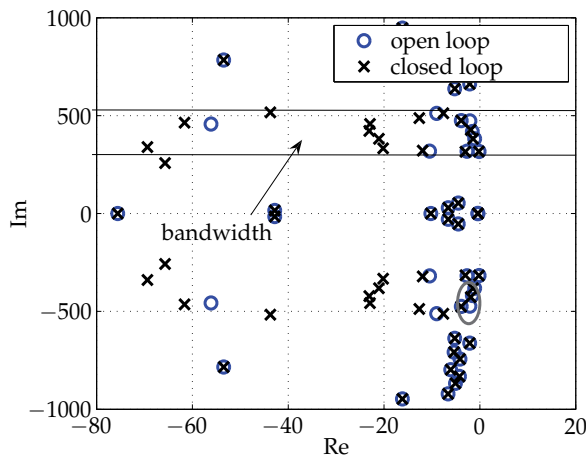
Fig. 31. Pole plot with/without $\mathcal{H}_2$ controller
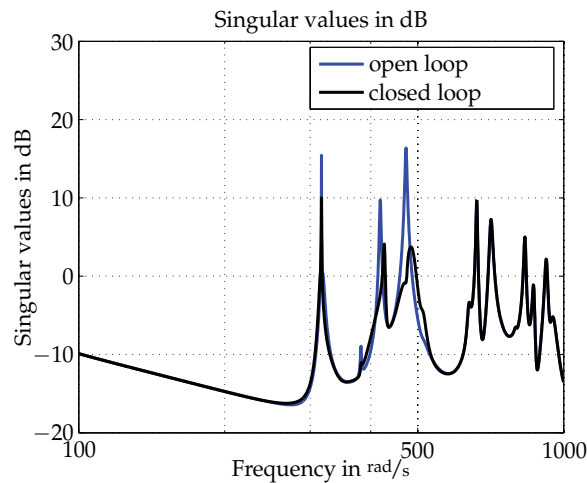
Fig. 32. Singular values of the frequency response plot with/without $\mathcal{H}_2$ controller

4. Conclusions

This chapter presents a case study on the design of MIMO control laws to reduce vibrations in a flexible metro rail car body and thus to improve passenger ride comfort. Direct structural actuation by Piezo actuators is considered and two sensor concepts – strain sensors (in a non-collocated setting) and acceleration sensors (collocated) – are evaluated. One part of the outlined studies focused on a simulation model of a full-size lightweight metro rail car body; the other part tests the control concepts on a laboratory testbed with a scale model of the car body. The control laws have been designed by LQG and by frequency-weighted $\mathcal{H}_2$-optimal control design methodologies. Both design methods are first studied in the simulation and compared. It is found that the weighted $\mathcal{H}_2$ designs yield controllers that perform satisfactorily in the presence of model uncertainty and independent of the sensor concept (strain sensors / non-collocation or acceleration sensors / collocation): the first three

modes of interest are significantly attenuated and the unknown modes in the high-frequency domain are hardly affected by the controller action, thus increasing the ride comfort for the passengers. The LQG controller minimizes the vibrations only for strain sensors in the non-collocated setup. Finally, both design methods, which have been studied for the lightweight rail car body simulations, are successfully implemented in a scaled laboratory setup: it is demonstrated that the target modes (torsion and bending) have been significantly damped by both controller types. A further advantage of the weighted $\mathcal{H}_2$ controller is that the controller action can be tuned for a specific bandwidth in the frequency domain, which is essential if the dynamics of the structure under consideration is uncertain or a control input is not desired for certain frequencies. The studies' results show the applicability of weighted $\mathcal{H}_2$ control for partially uncertain flexible-structure systems. The control goal of improving ride comfort is directly formulated as a weighted $\mathcal{H}_2$ minimization problem which justifies the presented study. However, a range of related publications show the design and application of robust $\mathcal{H}_\infty$-optimal controllers for this application, which can give robustness guarantees based on the structured singular value.

5. References

Benatzky, C. (2006). *Theoretical and experimental investigation of an active vibration damping concept for metro vehicles*, PhD thesis, Institute for Mechanics and Mechatronics, Division of Control and Process Automation, Vienna University of Technology, Austria.

Benatzky, C. & Kozek, M. (2005). Effects of local actuator action on the control of large flexible structures, *Proceedings of the 16th IFAC World Congress*, Prague, Chech Republic.

Benatzky, C. & Kozek, M. (2007a). An actuator fault detection concept for active vibration control of a heavy metro vehicle, *Proceedings of the 14th International Congress on Sound and Vibration (ICSV14), Cairns, Australia*.

Benatzky, C. & Kozek, M. (2007b). An identification procedure for a scaled metro vehicle - flexible structure experiment, *Proceedings of the European Control Conference ECC 2007, Kos, Greece*, Kos, Greece.

Benatzky, C., Kozek, M. & Bilik, C. (2006). Experimental control of a flexible beam using a stack-bending-actuator principle, *Proceedings of the 20th Scientific Conference*, Hanoi, Vietnam.

Benatzky, C., Kozek, M. & Jörgl, H. (2007). Comparison of controller design methods for a scaled metro vehicle - flexible structure experiment, *Proceedings of the 26th American Control Conference, New York, USA*.

Bilik, C. (2006). *Aufbau und Inbetriebnahme des Prüfstandmodelles eines Schienenfahrzeug-Wagenkastens zum Nachweis von aktiver Schwingungsdämpfung*, Diploma thesis, Vienna University of Technology, Vienna.

Bilik, C., Benatzky, C. & Kozek, M. (2006). A PC-based multipurpose test bed environment for structural testing and control, *Proceedings of the 3rd International Symposium on Remote Engineering and Virtual Instrumentation*, Maribor, Slovenia.

Foo, E. & Goodall, R. M. (2000). Active suspension control of flexible-bodied railway vehicles using electro-hydraulic and electro-magnetic actuators, *Control Engineering Practice* 8(5): 507–518.

Frederich, F. (1984). *Die Gleislage - aus fahrzeugtechnischer Sicht*, Vol. 108 (12) of *Gleislauftechnik*, Siemens Verlagsbuchhandlung, pp. 355 – 361.

Gawronski, W. (2004). *Advanced structural dynamics and active control of structures*, Springer, New York.

Hansson, J., Takano, M., Takigami, T., Tomioka, T. & Suzuki, Y. (2004). Vibration Suppression of Railway Car Body with Piezoelectric Elements, *JSME International Journal Series C* 47(2): 451–456.

ISO (1997). ISO2631-1: Mechanical vibration and shock - evaluation of human exposure to whole-body vibration. Part 1: General requirements, International Organization for Standardization. Corrected and reprinted July 15th, 2007.

Kamada, T., Tohtake, T., Aiba, T. & Nagai, M. (2005). Active vibration control of the railway vehicle by smart structure concept, *in* S. Bruni & G. Mastinu (eds), *19th IAVSD Symposium - Poster Papers*.

Kozek, M. & Benatzky, C. (2008). Ein maßstäbliches Experiment zur aktiven Schwingungsdämpfung eines Eisenbahn-Wagenkastens, *at - Automatisierungstechnik* 10(56): 504–512.

Kozek, M., Benatzky, C., Schirrer, A. & Stribersky, A. (2011). Vibration damping of a flexible car body structure using piezo-stack actuators, *Control Engineering Practice* 19(3): 298 – 310. Special Section: IFAC World Congress Application Paper Prize Papers.
URL: *http://www.sciencedirect.com/science/article/B6V2H-4X3MR4Y-2/2/3ef1d868e70c2b 6f10fd9412f9c8c1de*

Luenberger, D. G. (1964). Observing the state of a linear system, *IEEE Transactions on Military Electronics* 8(2): 74–80.

Mohinder, S. & Angus, P. (2001). *Kalman Filtering: Theory and Practice Using MATLAB*, Wiley Interscience, John Wiley & Sons, USA.

Popprath, S., Benatzky, C., Bilik, C., Kozek, M., Stribersky, A. & Wassermann, J. (2006). Experimental modal analysis of a scaled car body for metro vehicles, *Proceedings of the 13th International Congress on Sound and Vibration (ICSV13), Vienna, Austria*.

Popprath, S., Schirrer, A., Benatzky, C., Kozek, M. & Wassermann, J. (2007). Experimental modal analysis of an actively controlled scaled metro vehicle car body, *Proceedings of the 14th International Congress on Sound and Vibration (ICSV14), Cairns, Australia*.

Preumont, A. (2006). *Mechatronics: Dynamics of Electromechanical and Piezoelectric Systems*, Springer.

Schandl, G. (2005). *Methodenuntersuchung zur aktiven Schwingungsreduktion eines Schienenfahrzeugwagenkastens*, PhD thesis, Vienna University of Technology, Vienna.

Schandl, G., Lugner, P., Benatzky, C., Kozek, M. & Stribersky, A. (2007). Comfort enhancement by an active vibration reduction system for a flexible railway car body, *Vehicle System Dynamics* 45(9): 835–847.

Schöftner, J. (2006). *Aktive Schwingungsdämpfung eines Schienenfahrzeugwagenkastens durch $\mathcal{H}_2$-Regelung*, Master's thesis, Institute for Mechanics and Mechatronics, Division of Control and Process Automation, Vienna University of Technology.

Schirrer, A. (2010). *Co-Simulation of Rail Car Body Vibration Control with SimPACK®*, VDM Verlag Dr. Müller, Saarbrücken, Germany.

Schirrer, A. & Kozek, M. (2008). Co-simulation as effective method for flexible structure vibration control design validation and optimization, *Control and Automation, 2008 16th Mediterranean Conference on*, pp. 481 –486.

Schirrer, A., Kozek, M. & Benatzky, C. (2008). Piezo stack actuators in flexible structures: Experimental verification of a nonlinear modeling and identification approach, *6th EUROMECH Nonlinear Dynamics Conference (ENOC 2008), OPEN-ACCESS library*. URL: *http://lib.physcon.ru*

Schirrer, A., Kozek, M., Plank, A., Neumann, M., Badshah, S. & Wassermann, J. (2008). Vibration analysis of an actively controlled flexible structure using speckle interferometry, *Proceedings of 15th International Congress on Sound and Vibration (ICSV15)*.

Skogestad, S. & Postlethwaite, I. (1996). *Multivariable feedback control*, John Wiley & Sons.

Stribersky, A., Müller, H. & Rath, B. (1998). The development of an integrated suspension control technology for passenger trains, *Proceedings of the Institution of Mechanical Engineers, Part F: Journal of Rail and Rapid Transit*, Vol. 212, pp. 33–42.

Changes in Brain Blood Flow on Frontal Cortex Depending on Facial Vibrotactile Stimuli

Hisao Hiraba[1], Takako Sato[2], Satoshi Nishimura[2], Masaru Yamaoka[3],
Motoharu Inoue[1], Mitsuyasu Sato[1], Takatoshi Iida[1], Satoko Wada[1],
Tadao Fujiwara[3] and Koichiro Ueda[1]
[1]Departments of Dysphasia Rehabilitation
[2]Oral and Maxillofacial Surgery and
[3]Physics, Nihon University, School of Dentistry
Japan

1. Introduction

We provide patients who have problems with reduced salivation (hyposalivation) with artificial saliva treatment, humectants, and salivary gland massage (Ueda et al. 2005). However, treatment with artificial saliva and humectants is symptomatic, and although salivary gland massage can reinvigorate weak glands, to do so is difficult for people with disabilities and has varying effects, depending on operator skill. Thus, we have focused on increasing salivation through the use of vibrotactile stimulation, as reported by Hiraba et al. (2008). Before using this apparatus on patients, it was necessary to first estimate the effect on normal subjects.

The biggest challenge with continuous use of stimulation is an adaptive effect. In particular, we were interested in determining whether the effect was continuous without attenuation, when patients continue using the apparatus every day (Despopoulos and Silbernagel, 2003). We investigated adaptation to the continuous use of vibrotactile stimuli for 4 or 5 days in the same subjects to determine whether this resulted in a decrease in salivation (Despopoulos and Silbernagel, 2003; Principles of Neural Science. 2000a). Before this experiment was performed, it was necessary to compare resting and stimulating salivary secretion and to investigate the most effective frequency for increasing salivary secretion. We examined the amount of salivation during vibrotactile stimuli with a single motor (1.9 μm amplitude) on the bilateral masseter muscle belly (on the parotid glands), using a dental cotton roll positioned at the opening of the secretory duct for 3 min. Furthermore, we examined the amount of salivation during vibrotactile stimuli with single and double motors (1.9 μm and 3.5 μm amplitudes) on the bilateral submandibular angles (on the submandibular glands). Then, we compared resting and stimulating salivation and investigated the most effective frequency for increasing salivary secretion. The effect of increased salivation in normal subjects was determined as the difference between resting and stimulating salivation.

We defined a 5-min interval as the recovery time between resting and stimulating salivation from a preliminary study. First, we examined the most effective frequency for salivation of

the parotid glands among 89, 114, and 180 Hz with a single motor, and then we found the most effective frequency for salivation of the submandibular glands between 89 and 114 Hz with single and double motors. We discuss the effects of vibrotactile stimulation based on these results.

Furthermore, to study the mechanism of increased salivation evoked by vibrotactile stimuli, we recorded changes in brain blood flow (BBF) at the frontal cortex and the pulse frequency during stimulation. When subjects listen to classical music (particularly Mozart), they develop a relaxed feeling. Specifically, the feeling of relaxation is produced by decreasing BBF in the frontal cortex. In particular, we suggest that the relaxed feeling is produced by an increase in parasympathetic activity. Furthermore, we examined changes in the pulse frequency during vibrotactile stimulation. A decrease in pulse frequency suggests an increase in parasympathetic activity (Principles of Neural Science. 2000b). Thus, we assumed a mechanism of increased salivation by exploring oxyhemoglobin (oxyHb) concentration in the BBF of the frontal cortex and changes in pulse frequency. We believe that the coordination is carried out by a highly interconnected set of structures in the brain stem and forebrain that form a central autonomic network (Principles of Neural Science. 2000b).

2. Material and methods

2.1 Vibrotactile stimulation apparatus

The vibrotactile stimulation apparatus consists of an oscillating body and control unit, as shown in Hiraba et al. (2008) and Yamaoka et al. (2007). The oscillating body is composed of the headphone headset equipped with vibrators as a substitute for positions of the bilateral microphones, and vibrators utilizing the vibration electric motor (VEM) (Rekishin Japan Co., LE12AOG). The VEM was covered in silicon rubber (polyethyl methacrylate, dental mucosa protective material, Shyofu Co.) for conglobating the stimulation parts and preventing the warming of the VEM's temperature produced by the vibration of long periods (Hiraba et al. 2008). The control unit consists of three parts, the pulse width modulation (PWM) circuit in Figure 1A-a, LCD monitor circuit (Figure 1A-b) and power supply circuit (Figure 1A-c), and it interfaced with a PWN electric motor, delivered vibration frequencies in the 60-182 Hz range (Yamaoka et al. 2007).

We examined the amount of salivation during vibrotactile stimuli on the bilateral masseter muscle belly (on the parotid glands) and on bilateral parts of the submandibular angle (on the submandibular glands; Fig. 1B, 1C). We determined the amount of salivation using a dental cotton roll (1 cm across, 3 cm length) positioned at the opening of the secretory ducts (right and left sides of the parotid glands and right and left sides of the submandibular and sublingual glands), during vibrotactile stimulation of the bilateral parotid and submandibular glands. The weights of the wet cotton rolls after 3 min of use were compared with their dry weights (Hiraba et al. 2008).

2.2 Stimulating salivation in normal subjects

We determined that a 3-min salivation measurement with a 5-min recovery time was sufficient from a previous experiment (Hiraba et al. 2008). First, we used three frequencies with a single motor (89, 114, 180 Hz-S) on the parotid glands (Fig. 1B, 1D) and conducted a practice exercise so that the participants could learn to avoid the foreign-body sensation of the cotton rolls for 3 min. Next, after a 5-min rest, we examined the amount of salivation during 89 Hz-S vibrotactile stimulation for 3 min. After every 5 min of rest, we examined the

amount of salivation during 114 and 180 Hz-S vibrotactile stimulation for 3 min, respectively. We finally examined the amount of salivation on resting stimulation for 3 min (Fig. 1D). We conducted these tests with 19 normal subjects (6 males, 13 females; average age, 22 years). This experiment was performed between 3 and 5 pm in a temperature-controlled, quiet room.
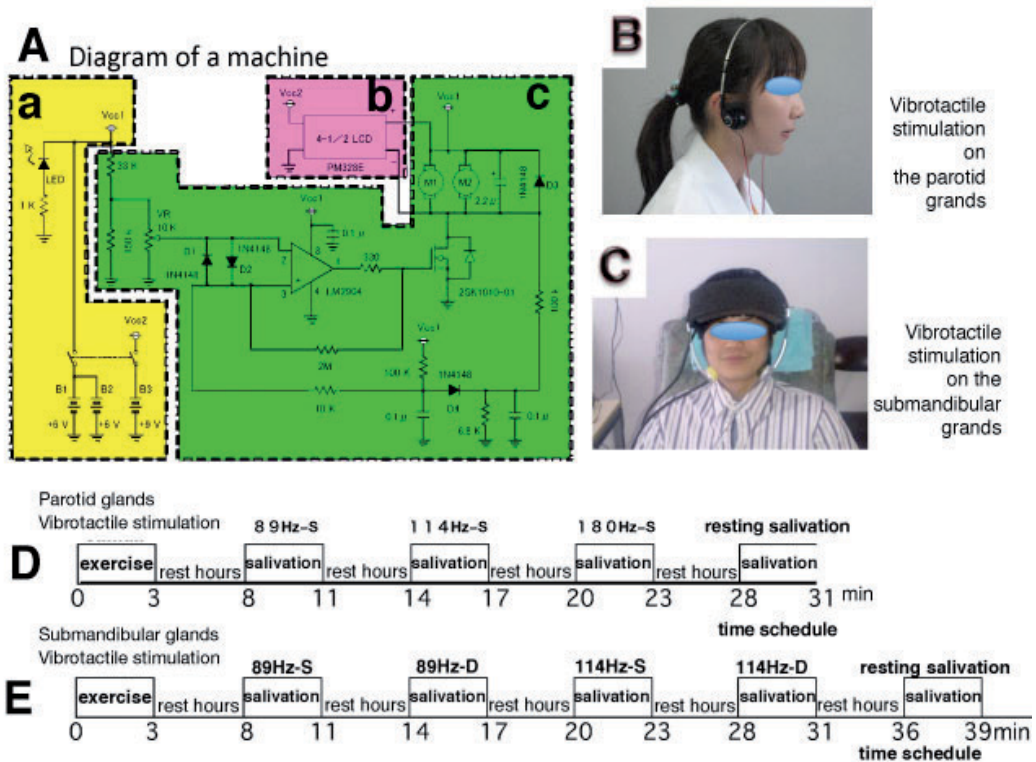

Fig. 1. Pictures and diagrams of the vibratory machine (A), experimental techniques (B and C) and experimental schedules (D and E). **B and C**. Measuring salivation amount during vibrotactile stimulation of the bilateral masseter muscle belly (on the parotid glands, B) and the bilateral angle of the mandibular body (on the submandibular glands, C), using dental cotton rolls positioned at the opening of the secretory ducts (right and left sides of parotid glands and right and left sides of submandibular and sublingual glands). **D and E**. Time schedules for the vibrotactile stimuli, respectively. The designations 89 Hz-S, 114 Hz-S and 180 Hz-S indicate vibrotactile stimuli at 89, 114, and 180 Hz, respectively, with a single motor. The designations 89 Hz-D and 114 Hz-D represent vibrotactile stimuli of 89 and 114 Hz with double motors. We allowed a 5-min recovery time shown as "rest hours." Variation per day in the effective salivation during 4 or 5 days of continuous use at 89 Hz-S vibrotactile stimulation for the right and left parotid glands, and the time schedule as shown in Figure 1D was repeated by subjects for 4 or 5 days.

After the three frequencies were tested on the parotid glands, we determined the most effective frequencies, which were 89 and 114 Hz-S. Second, we subjected the submandibular glands to the two frequencies (89 and 114 Hz) and two different amplitudes (Fig. 1C, 1E).

The amplitude of the oscillating bodies during vibrotactile stimulation was measured with a CCD laser displacement gauge (LK-G3000, Keyence Co., Osaka, Japan). We examined the 89 and 114 Hz frequencies and used oscillating bodies added as the frequency with double motors (single motor had a 1.9 µm amplitude, 89 and 114 Hz-S, and double motors had a 3.5 µm amplitude, 89 and 114 Hz-D). Specifically, 89 and 114 Hz-S, and 89 and 114 Hz-D were used in the next experiment. We examined the amount of salivation for the four frequencies (Fig. 1E). We conducted these experiments with 17 normal subjects (15 males, 2 females; average age, 22 years) for the resting-stimulation examination. This experiment was performed between 3 and 5 pm in a temperature-controlled, quiet room.

The most effective salivation amount by vibrotactile stimulating the parotid glands occurred at 89 Hz-S, so we examined changes in salivation for 4 or 5 continuous days with the same time schedule (Fig. 1D). We also investigated the adaptation periods during continuous use of vibrotactile stimulation for 4 or 5 continuous days in the same subjects. We conducted resting-stimulation examinations with 26 normal subjects (11 males and 15 females; average age 25 years). This experiment was performed between 3 and 5 pm in a temperature-controlled and quiet room.

2.3 BBF on the frontal cortex

The recording was conducted using a functional near-infrared spectroscopy (fNIRS) OEG16 instrument (Spectratech Inc., Shelton, CT, USA) from the frontal cortex. As shown in Figures 4A and 4B, the fNIRS probe assembly consisted of six LEDs as light sources, each of which emitted two wavelengths, 770 nm and 840 nm, and six photodiodes as detectors (Fig. 4A, 4B). The sources and detectors were symmetrically arranged in an area of 3.0×14.0 cm, with a nearest source-detector separation of 2.0 cm, and measurement points were at 16 points on the frontal cortex. During scanning, a Velcro band held the probe assembly securely to the forehead of subjects and extended from ear to ear horizontally and from hairline to eyebrows vertically. Each of the LEDs was turned on in sequence, and the diffuse NIR light from each source was acquired through the cortical region at the nearest detector. Thus, 16 source-detector pairs (channels) in total were measured (Fig. 4B). The sampling rate across all 16 channels was 0.76 Hz. In particular, we showed a 16-channel computerized analysis (as shown in Fig. 4B) and the original waves of four channel recording areas in the central parts (original waves in Fig. 4C recorded over the selected areas in Fig. 4A).

We recorded BBF during vibrotactile stimulation. We also conducted a BBF experimental recording as subjects listened to classical music (Mozart, Eine kleine Nachtmusik). We conducted the examinations with 10 normal subjects (6 males, 4 females; average age, 22 years) for the resting-stimulation and classical music examinations. This experiment was performed between 3 and 5 pm in a temperature-controlled, quiet room.

2.4 Pulse frequency during vibrotactile stimulation

We recorded changes in pulse frequency (P225F, Nihon-Kohden Co., Tokyo, Japan) during vibrotactile stimuli at 89 and 114 Hz-S. Because the hemoglobin in blood absorbs red light irradiation, a pulse wave was calculated using a ratio between red light irradiation (660 µm) and infrared light (940 µm). The pulse frequency indicated by this apparatus was measured by averaging the pulse frequency during the previous eight pulses (Fig. 5C). First, the pulse frequency during rest was recorded for 1 min, and then those during 89 and 114 Hz-S vibrotactile stimuli were recorded for 2 min each. A 1-min rest period was taken between

the 89 and 114 Hz-S vibrotactile stimuli. Finally, the pulse frequency during rest was recorded for 30 s. We conducted these examinations with 10 normal subjects (6 males, 4 females; average age, 22 years). This experiment was performed every day between 3 and 5 pm in a temperature-controlled, quiet room.

3. Results

3.1 Vibrotactile stimuli on the parotid and submandibular glands

We examined the differences between vibrotactile stimulating of parotid and submandibular glands (Fig. 1B, 1C). First, we tested three frequencies of vibrotactile stimulation, 89, 114, and 180 Hz-S, on the parotid glands and determined the frequency most effective for salivation (Fig. 2A). We found that the most effective frequencies for submandibular gland salivation were 89 Hz-S, 89 Hz-D, 114 Hz-S, and 114 Hz-D (Fig. 2B) and that the erase most effective stimulation was 89 Hz-S (Fig. 2A, 2B; $p < 0.05$).

We examined the most effective salivation in each gland, including the right parotid, left parotid, right submandibular and sublingual and left submandibular and sublingual glands. As a result, the most effective stimulation for salivation of the parotid and submandibular glands was 89 Hz-S (Fig. 2A-a, 2B-a; resting salivation, 0.89±0.61 mL; 89 Hz-S, 1.46±0.90 mL; 89 Hz-D, 1.04±0.78 mL; 114 Hz-S, 0.93±0.76 mL and 114 Hz-D, 0.80±0.53 mL). Furthermore, a significant difference was observed between the vibrotactile stimulation at 89 Hz-S and that at 114 Hz-D (paired t-test; $p < 0.05$). No other significant difference in each gland was observed (Fig. 2A-b, 2A-c, 2B-b, 2B-c, 2B-d and 2B-e).
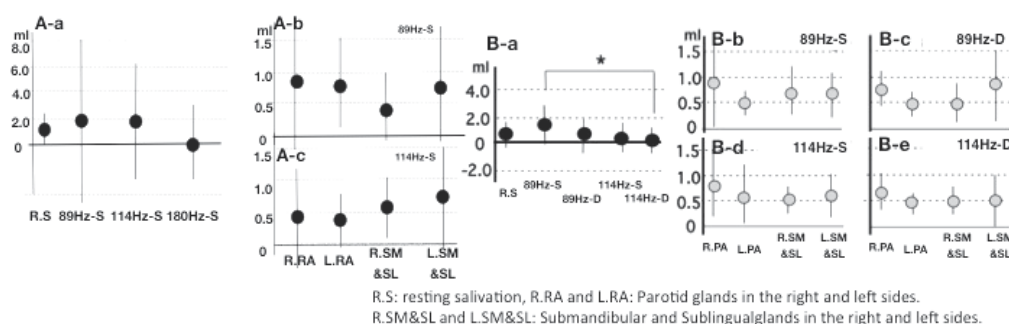

Fig. 2. Salivation from the parotid glands (A) and the submandibular glands (B) after each vibrotactile stimulation. **A-a and B-a**. Total number of salivations after each vibrotactile stimulation. **A-b, A-c, B-b, B-c, B-d and B-e**. Salivation amount for each gland after various vibrotactile stimuli. The increased salivation between 89 Hz-S and 114 Hz-D was significantly different (paired-t-test; $p < 0.05$). Stimulating the parotid or submandibular glands at 89 Hz-S was the most effective for salivation. Salivation was not different among the various glands (parotid and submandibular and sublingual glands on the right and left sides).

3.2 Variation in effective salivation per day during continuous vibrotactile stimulation

Because patients with hyposalivation often have a psychiatric disorder, we conducted an experiment to realistically approximate natural conditions. We examined whether effective salivation occurred continuously when vibrotactile stimulation was performed daily. In

particular, we used the 89 Hz-S from the previous experiment, and because no difference was found between vibrotactile stimulation of the parotid and submandibular glands, we analyzed salivation evoked by vibrotactile stimulation of the parotid glands. Normal subjects (15 males, 11 females; average age, 25 years) used this apparatus continuously for 4 or 5 days at the same time and place (Fig. 3). None of the glands (right and left parotid glands, and right submandibular and sublingual glands) showed an attenuated response. Regression curves for each gland (Fig. 3A, 3B, 3C and 3D) showed non-adaptation to continuous stimulation, because they showed parallel or over-increasing curves, indicating that continuous usage of this apparatus should not be a problem.
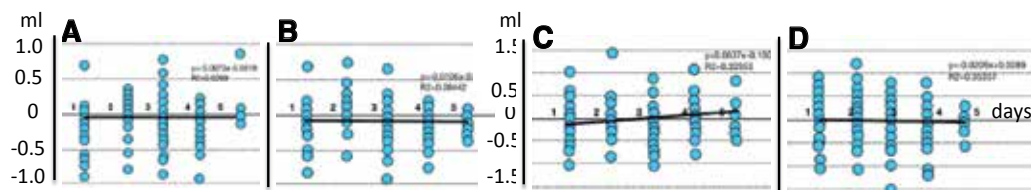

Fig. 3. Variation in effective salivation per day during 4 or 5 days of continuous use of 89 Hz-S vibrotactile stimulation in the right (A) and left parotid (B) and the right (C) and left submandibular and sublingual glands (D). The time schedule, as shown in Figure 1D, was repeated by subjects for 4 or 5 days. Vertical lines indicate the increase and decrease in vibrotactile salivation versus resting salivation (it is shown by a positive value when the vibrotactile salivation was greater than the resting salivation, and by a negative value when the vibrotactile salivation was lower than the resting salivation). Abscissa lines indicate time (4–5 days). Solid lines indicate the regression curve. There was no adaptation to the 89 Hz-S vibrotactile stimulation in the parotid, submandibular, or sublingual glands.

3.3 Relationship between each stimulation and fNIRS activity

The OEG16 spectroscope was used to record the hemoglobin concentration in the BBF from areas in the frontal cortex using 16 channels. In particular, we measured original waves in four channel recording areas (circled 1, 2, 3, and 4 in Fig. 4A). Figure 4B shows the schema of the oxyhemoglobin (oxyHb) concentration evoked by analyzing 16 channels during vibrotactile stimulation at 89 Hz-S. The contrasting red and blue zones indicate activity strength, and no response is shown in white (Fig. 4B). The results showed very weak oxyHb concentrations during the 89 Hz-S vibrotactile stimulation, as shown in Figure 4C-b.

We provided evidence of the real waves on the central parts (circled 1, 2, 3, 4; Fig. 4A) of the BBF recording in 16 channels (Fig. 4C). The red lines indicate changes in oxyHb concentrations, the blue lines indicate deoxyhemoglobin (deoxyHb), and the green lines indicate total hemoglobin (totalHb) during salivation measurements at rest and for each vibrotactile stimulation frequency. The first waves in Figure 4C(a) indicate changes during the resting condition, the second waves (b) show changes during 89 Hz-S vibrotactile stimulation, the third waves (c) show changes during 89 Hz-D, the fourth waves (d) show changes during 114 Hz-S, the fifth waves (e) show changes during 114 Hz-D and the bottom waves (f) show changes during "A-" phonation. Each wave was recorded for 3 min, and each vibrotactile stimulation provided for 2 min is shown between the vertical lines. However, "A-" phonation is shown by four applicable vertical lines. Although each wave
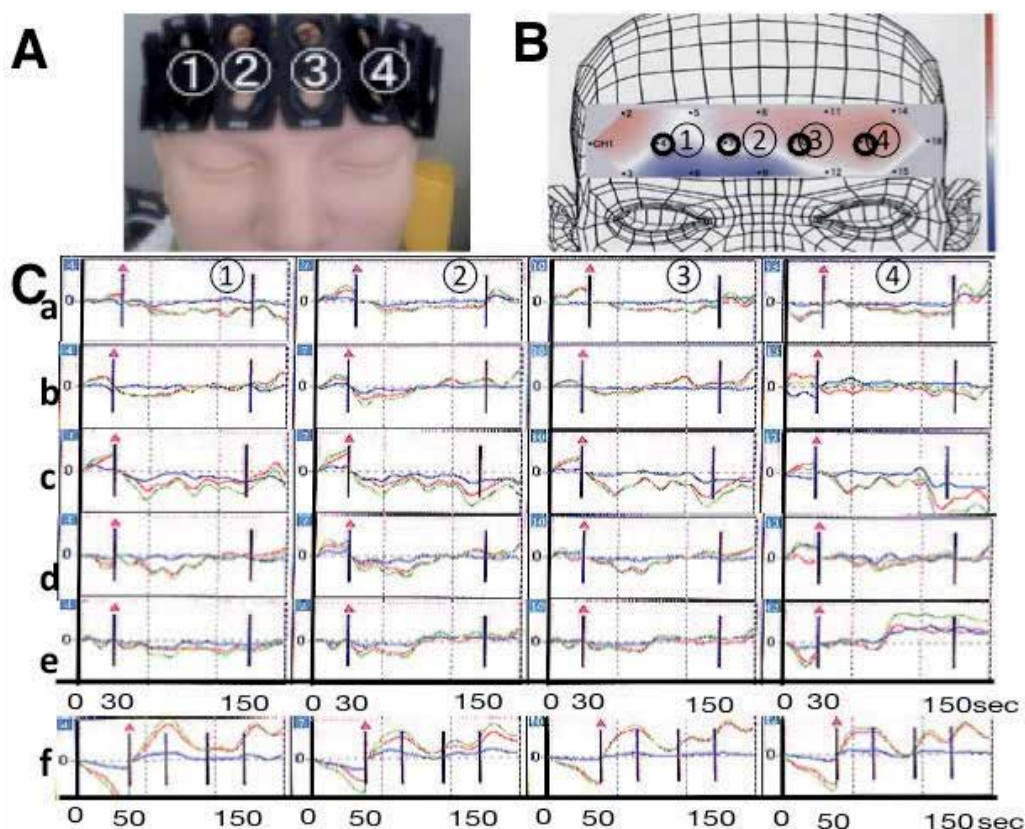
Fig. 4. A. Frontal cortex recording sites. The circled numbers 1, 2, 3, and 4 indicate the recording sites for each wave, as shown in **C**. **B**. A computerized numerical analysis of variations in oxyhemoglobin (oxyHb) concentration during 89 Hz-S vibrotactile stimulation. Red (plus) and blue shading (minus) indicates differences in frontal cortex activation, whereas the white band indicates non-activation. **C.** Changes in blood brain flow during 2 min of various vibrotactile stimuli and vocalizing "A-" sounds are shown at the central areas of the frontal cortex. **C-a**. During the resting condition. **C-b**. During 89 Hz-S vibrotactile stimulation. **C-c**. During 89 Hz-D vibrotactile stimulation. **C-d**. During 114 Hz-S vibrotactile stimulation. **C-e**. During 89 Hz-D vibrotactile stimulation. **C-f**. While vocalizing "A-" sounds. The spaces between the solid bars (2 min.) represents the stimulating period. However, vertical lines during vocalizing "A-" sounds were the timely accomplishment between good winds. Red, blue, and green lines indicate oxyhemoglobin, deoxyhemoglobin, and total hemoglobin concentrations, respectively.

measured during resting salivation, at 114 Hz-D, and during "A-" phonation showed increased activity, the 89 Hz-D and 114 Hz-S vibrotactile stimuli showed decreased activities. However, vibrotactile stimulation at 89 Hz-S was fairly close to zero value (0.14±1.10 mM mm · s). In particular, when we focused on changes in oxyHb based on these results, increased oxyHb occurred during "A-" phonation, the resting condition (5.20±6.78 mM mm · s) and at 114 Hz-D of vibrotactile stimulation (-0.13±3.54 mM mm · s), whereas a decrease in oxyHb was revealed during vibrotactile stimulation at 114 Hz-S (-5.48±7.12 mM mm · s) and at 89 Hz-D (-2.18±10.13 mM mm · s). However, oxyHb during vibrotactile stimulation at 89 Hz-D (0.29±2.26 mM mm · s) was near zero, similar to all of the data (oxyHb, deoxyHb, totalHb). From these results, we computed integral rates of oxyHb during 2 min, as shown by the area between the longitudinal bars in the central part (circled 1, 2, 3, and 4) of the recording wave (Fig. 4C).

Furthermore, we examined the integral rates while subjects listened to classical music for 2 min. We divided the subjects into two groups: one group did not like to listen to classical music (2.96±6.40 mM mm · s, n = 7) whereas the other group did (0.85±0.05 mM mm · s, n = 3; Fig. 5A and 5B, respectively). Although the subjects who enjoyed the music did not show a larger spread of values (±SD), the latter did. In particular, vibrotactile stimulation at 89 Hz-S revealed a small similar spread of values. Each integral rate during the vibrotactile stimulation at 89 Hz-S and while the listening to classical music showed similar averages and SDs (Fig. 5B-b).

3.4 Pulse frequency during vibrotactile stimulation and frontal cortex fNRS activity

We chose three typically responding subjects, as shown in Figure 5C. One subject showed a decrease in pulse frequency during both 89 Hz-S and 114 Hz-S vibrotactile stimulation, while the other two showed a decrease in pulse frequency at 89 Hz-S and an increase during 114 Hz-S stimulation (Fig. 5C). We divided the two groups into decrease pulse frequency and increase pulse frequency groups, based on 114 Hz-S vibrotactile stimulation. Although the 89 Hz-S vibrotactile stimulation created a sense of relaxation, the 114 Hz-S vibrotactile stimulation is either liked or disliked. Specifically, the 89 Hz-S vibrotactile stimulation will produce parasympathetic activity and evoke a relaxation response.

4. Discussion

4.1 Adaptation to vibrotactile stimulation

Continuous exposure to various sensory stimuli induces adaptation (Principles of Neural Science. 2000c). Thus, we examined whether adaptation occurred to the vibrotactile stimulation when normal subjects continuously used this apparatus every day for 4 or 5 days. However, we first investigated changes in total saliva secretion quantities by normal subjects in response vibrotactile stimulation by measuring the weights of cotton rolls set on the ducts of each gland. For the repeated measurements, we defined a recovery time of 5 min from a previous experiment, as resting salivation values before and after stimulating salivation were the same (Fig. 1D, 1E).

The most effective frequency for increasing the total amount of salivation during vibrotactile stimulation of the parotid and submandibular glands was 89 Hz-S (Fig. 2A-a, 2B-a). Furthermore, as shown in Figures 2A-b and 2A-c, and 2B-b, 2B-c, 2B-d and 2B-e, no difference was found among the various glands. Because 89 Hz-S vibrotactile stimulation of the parotid and submandibular glands showed the same results in all glands, the results

might not be directly affected by the vibrotactile stimulation on the parotid and submandibular glands. Specifically, the increased salivation evoked by vibrotactile stimulation at 89 Hz-S may be the result of somatosensory input from the facial skin and intraoral cavity.

Burdette and Gale (1988) reported that tonic masticatory muscle activity may be effective for treating patients with myofacial pain dysfunction. Furthermore, Vrjama and Vanharantra (1994) reported that discographically painful discs always decrease pain during a vibration examination. These results assume that the peripheral stimuli provided by the vibration arrive at the central nervous system (spinal cord and brain stem) and that these effects are produced by a depressant effect on the cerebral cortex, depending on the somatosensory information, although they are not clearly organized. We believe that their interpretation does not adequately explain this situation. We suggest that vibrating stimuli may promote parasympathetic effects by inhibiting the sympathetic effects elicited by pain. We know serous salivation is evoked only by a parasympathetic effect. Furthermore, we found that salivation production responded to a specific frequency and amplitude.

Vibration may effectively activate the muscle spindles of the masseter muscles, because the tonic vibration reflex (TVR) of the muscle spindles activates with 80–100Hz vibrations (Desmedt, Codaux 1975). However, we showed the same salivation response in various glands. We showed that increased salivation evoked by 89 Hz-S vibrotactile stimulation would be produced by somatosensory inputs from facial skin and the intraoral cavity, suggesting that increased salivation is not produced by a direct effect of muscle contraction.

Next, we examined the physiological characteristics of adaptation to vibrotactile stimulation by testing adaptation in 26 normal subjects for 4 or 5 days. Patients with decreased salivation (hyposalivation) would be using this machine daily; thus, we wanted to realistically approximate actual conditions. The results suggested that 89 Hz-S vibrotactile stimulation to the facial skin of the masseter belly may be appropriate for patients with decreased salivation, because the regression curve (negative gradient) did not decrease with continuous use of the apparatus (Fig. 3).

4.2 fNIRS activity in the frontal cortex

The frontal cortex is associated with cognitive function, including memory, attention, abstract reasoning and higher cognitive activity (Principles of Neural Science. 2000a).

We recorded changes in BBF in the frontal cortex to examine typical changes in fNIRS parameters based on increases in oxyHb and totalHb and decreased deoxyHb, as reported by Sakatani et al. (2006). In particular, increased fNIRS activity patterns in the frontal cortex are associated with speech, and decreased fNIRS activity patterns in the frontal cortex are associated with playing TV games and are thought to be dependent on network differences (Sakatani et al. 1999). The fNIRS responses may be influenced by mental stability, because they indicate control of sophisticated mental functions produced by complex networks. Because fNIRS activity increases while subjects are speaking and decreases while they play TV games, we suggest that the autonomic system has a profound effect. Specifically, we suggest that fNIRS activity during conscious speaking is associated with a sympathetic effect, and that playing a TV game is associated with reflective movement under a non-sympathetic effect.

The effect of 89 Hz-S vibrotactile stimulation was almost zero for oxyHb, deoxyHb, and totalHb (Fig. 4C-b). In particular, the fNIRS activity focuses on the excitatory behaviours to

increase oxyHb. In animal experiments, changes in oxyHb and BBF are related, and fNIRS activity changes in oxyHb are used as a neuronal activity index (Hoshi et al. 2001). Thus, changes in oxyHb produced by an 89 Hz-S vibrotactile stimulation on the parotid and submandibular glands may indicate mental stability. The reason may be due to the same tendency of oxyHb concentration between the 89 Hz-S vibrotactile stimulation and subjects who liked to listen to classical music (Fig. 5B-b). People relax when they listen to classical music, so we think that 89 Hz-S vibrotactile stimulation is produced by excitation of the parasympathetic system. In particular, although the 89 Hz-S vibrotactile stimulation always
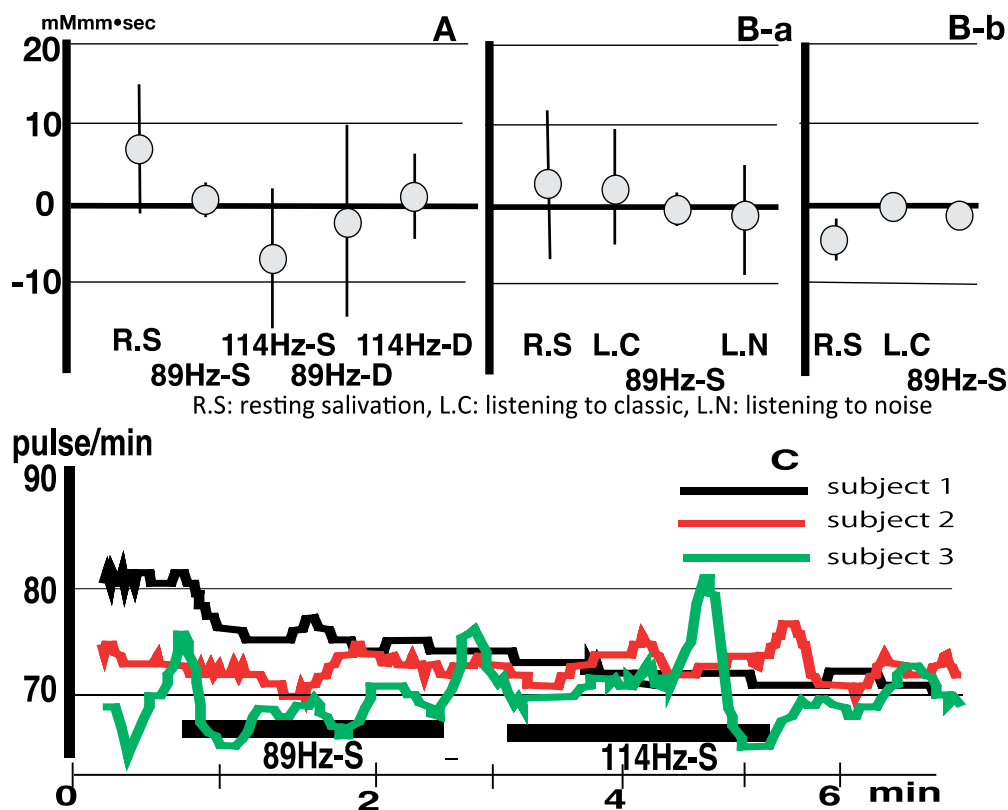

Fig. 5. Integral values of oxyhemoglobin (oxyHb) concentration produced by vibrotactile stimuli for 2 min are shown in A and B. **A**. Integral values produced in the resting condition and after each stimulation (*n* = 17). **B**. Integral values produced in the resting condition, listening to classical music (Mozart, Eine kleine Nachtmusik), 89 Hz-S and listening to noise (*n* = 10). One group enjoyed listening to classical music (D-b, *n* = 3), and one did not (D-a, *n* = 7). **C**. Changes in pulse frequency during vibrotactile stimulation (89 Hz-S and 114 Hz-S). We assessed 10 normal subjects, and changes in pulse frequencies are shown for three typical subjects. All subjects had decreased pulse frequency during 89 Hz-S vibrotactile stimulation, although the 114 Hz-S vibrotactile stimulation divided the subjects into two groups: one showed an increased pulse frequency and the other showed a decreased pulse frequency.

revealed parasympathetic excitation, listening to classical music showed different activity depending on music preference (Fig. 5B-a, 5B-b). Those subjects who enjoyed Mozart classical music accepted it as relaxing, whereas those who disliked it perceived it as noise. However, 89 Hz-S vibrotactile stimulation may produce a balanced mental condition, regardless of preference. This phenomenon suggests that the effect caused by the 89 Hz-S vibrotactile stimulation and the feeling sensed by those listening to Mozart who enjoyed it may be the same. Thus, we suggest that these feelings were produced by parasympathetic activity.

Burdette and Gale (1988) reported that tonic masticatory muscle activity might be effective for treating patients with myofascial pain-dysfunction. Furthermore, Vrjama and Vanharantra (1884) reported that discography always results in less pain during a vibration examination. They suggested that peripheral stimuli produced by the vibration arrive at the central nervous system (spinal cord and brain stem) and that these effects are caused by a depressant effect on the cerebral cortex, depending on the somatosensory information (Burdette and Gale, 1988; Vrjama and Vanharantra, 1884). However, we believe that somatosensory information via the thalamus produces excitability in the primary somatosensory cortex. Furthermore, somatosensory information in the primary somatosensory cortex may project to the frontal cortex via the parietal association area (Handbook of Neuropsychology 1994), and this information may cause the excitatory effects.

4.3 Parasympathetic effect based on 89 Hz-S vibrotactile stimulation

When we are frightened, our heartbeat increases (Principles of Neural Science. 2000b). The parasympathetic nervous system is responsible for rest and digestion, and maintaining basal heart rate, respiration, and metabolism under normal, resting conditions (Principles of Neural Science. 2000b). We examined the parasympathetic effects with changes in pulse frequency during vibrotactile stimulation. We showed changes in pulse frequency in typical normal subjects in response to 89 Hz-S and 114 Hz-S vibrotactile stimuli (Fig. 5C). These results showed a decrease in pulse frequency during 89 Hz-S stimulation, but an increase in pulse frequency following the 114 Hz-S vibrotactile stimulation, except for one subject. Specifically, the 114 Hz-S vibrotactile stimulation showed variable results, because one subject was relaxed, whereas the others were not. However, the 89 Hz-S vibrotactile stimulation resulted in decreased pulse frequency in all subjects, suggesting that stimulating the face evoked parasympathetic stimulation (Fig. 5C). Thus, the parasympathetic activity elicited by 89 Hz-S vibrotactile stimulation, may produce an increase in salivation. We reiterate that a relaxed feeling was produced in all subjects during 89 Hz-S vibrotactile stimulation.

We consider the following schema for this phenomenon. Vibrotactile stimulation to the face produces somatosensory information activity in the orofacial region, which projects to the trigeminal sensory complex (principal trigeminal sensory nuclei and trigeminal spinal tract nuclei) and solitary nuclei (Fig. 6). This somatosensory information is divided into the parabrachial nuclei, thalamus, and hypothalamus. Information projecting to the parabrachial nuclei arrives in the hypothalamus, amygdala, and frontal cortex and then to the thalamus and primary somatosensory cortex (SI). Petrides reported that information travelling to the SI goes around the frontal cortex via the parietal association area (Handbook of Neuropsychology 1994). We think that somatosensory information travelling

via the parietal association area represents excitability. If the BBF in the frontal cortex via the parietal association area is excitable and that via the parabrachial nucleus is inhibitory, which wave forms will be revealed? We believe that BBF to the frontal cortex evoked by various stimuli shows various wave forms, depending on the condition. In particular, the 89 Hz-S vibrotactile stimulation may produce a relaxed feeling.

4.4 Projection of autonomic activity in the frontal cortex

Autonomic function must ultimately be coordinated by adapting to environmental changes. The autonomic nervous system is a visceral sensory and motor system, and the visceral reflex is mediated by local circuits in the brain stem or spinal cord. These reflexes are regulated by networks of central autonomic control nuclei in the brain stem, hypothalamus and forebrain and are not under voluntary control, nor do they impinge on consciousness, with a few exceptions (Principles of Neural Science. 2000b). However, we think that changes in BBF in the frontal cortex may represent autonomic activity. This coordination is carried out by a highly interconnected set of structures in the brain stem and forebrain that form a central autonomic network (Fig. 6 and Principles of Neural Science. 2000b). Furthermore, the key component of this network is initiated by integral information in the parabrachial nucleus of the solitary tract and trigeminal sensory complex in the brain stem. These nuclei receive inputs from somatosensory and visceral afferents of the trigeminal, facial, glossopharyngeal, and vagus nerves and then use the information to modulate autonomic function. The somatosensory and visceral sensory outputs from the trigeminal and solitary nuclei are relayed to the forebrain and amygdala by the parabrachial nucleus, which is important for the behavioural responses to somatosensory, taste, and other visceral sensations (Principles of Neural Science. 2000b), and the information arriving in the amygdala will produce the pleasure-pain feeling. In contrast, the parabrachial nucleus is a taste-sensation relay nucleus in rats (Scott and Small 2009), and the rodent parabrachial nucleus sends integral limbic and reward system information (Yamamoto et al. 2009). Although their function in humans is unknown, we think that these nuclei may play a role as a relay nucleus for the autonomic system. On the other hand, we showed a projection from the trigeminal sensory complex, as the parabrachial nucleus can also record the response to tactile stimuli from facial skin (Chiang et al, 1994). Furthermore, somatosensory information is projected to the primary somatosensory cortex and is then relayed to the frontal cortex, via the parietal association area (Handbook of Neuropsychology 1994).

What does BBF activity in the frontal cortex mean? We think that the information via the parabrachial nucleus dominates that via the parietal association area. Thus, information in the frontal cortex is assumed to arrive via the parabrachial nucleus area. The hypothalamus is the centre of the autonomic system. We perceive emotional experiences such as fear, pleasure, and contentment and these reflect the interplay between higher brain centres and sub-cortical regions, such as the hypothalamus and amygdala (Principles of Neural Science. 2000a). Patients in whom the prefrontal cortex or the cingulate gyrus has been removed are no longer bothered by pain, but exhibit appropriate autonomic reactions; however, the sensation is not perceived as a powerfully unpleasant experience (Principles of Neural Science. 2000a). Furthermore, the anatomical connections of the amygdala with the temporal (cingulate gyrus) and frontal (prefrontal) association cortices provide the means by which visceral and somatosensory sensations trigger a rich assortment of associations or the cognitive interpretation of emotional states (Principles of Neural Science. 2000b).
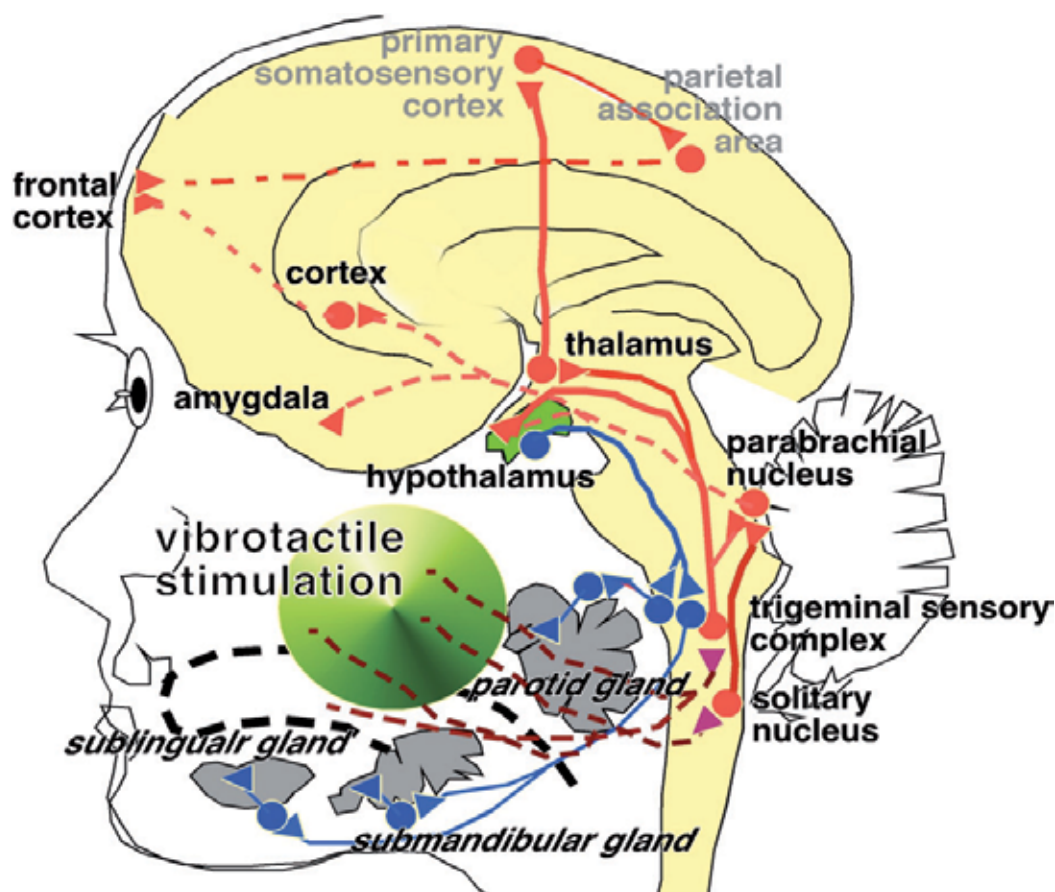
Fig. 6. Pathways distributing somatosensory information in the brain. Somatosensory information evoked by vibrotactile stimulation is relayed by the trigeminal sensory complex and solitary and parabrachial nuclei, which arrives at the hypothalamus, thalamus, amygdala and frontal cortex, respectively. The autonomic system (particularly the parasympathetic nervous system) produces increased salivation. The lateral branch of the trigeminal sensory nucleus is projected to the parabrachial nucleus. Information from the parabrachial nucleus is received by the amygdala and frontal cortex. Furthermore, somatosensory information is projected to the primary somatosensory cortex and relayed to the frontal cortex via the parietal association area. Thus, this information finally leads to a relaxed feeling and BBF waves reflect parasympathetic activity (modified from schemas in Principles of Neural Science 2000b and Handbook of Neuropsychology 1994).

Finally, we showed oxyHb activity during "A-" phonation (Fig. 4C-f). Sympathetic activity increases when we speak. From our data, the facial stimulation effects evoked by 89 Hz-S vibrotactile stimulation evoked parasympathetic activity, depending on the decrease in pulse frequency, and oxyHb concentration reflected the non-activation of BBF waves in the frontal cortex. We suggest that the 89 Hz-S vibrotactile stimulation produced a relaxing sensation depending on excitation in the amygdaloid complex and parasympathetic activity in the hypothalamic nuclei. The relaxing sensation was reflected by the oxyHb concentration of the BBF wave in the frontal cortex.

5. Conclusion

We showed that the most effective salivation response was produced by an 89 Hz vibrotactile stimulation with a single motor (1.9 μm amplitude) on the parotid glands, as reported previously (Hiraba et al. 2008). In this study, we focused on the submandibular glands secreting the greatest amount of saliva and explored changes in salivation during stimulation of the submandibular glands with 89 Hz and 114 Hz vibrotactile stimuli using single (89 Hz-S and 114 Hz-S) or double motors (3.5 μm amplitude, 89 Hz-D and 114 Hz-D), respectively. The increased salivation evoked by the 89 Hz-S vibrotactile stimulation was produced by somatosensory inputs from the facial skin and intraoral cavity. We examined the effects of vibrotactile stimulation on adaptation in normal subjects to test the effect of continuously using this apparatus every day by patients with hyposalivation. The results showed no adaptation with continuous use. Furthermore, we investigated changes in BBF in the frontal cortex during vibrotactile stimulation. Stimulating the submandibular and parotid glands at 89 Hz-S resulted in the most salivation. OxyHb concentrations in the BBF to the frontal cortex during an 89 Hz-S vibrotactile stimulation were the same as those in subjects who preferred listening to classical music. Furthermore, parasympathetic activity decreased pulse frequency during an 89 Hz-S vibrotactile stimulation, suggesting a close relationship between the BBF waves in the frontal cortex and the autonomic system. An 89 Hz-S vibrotactile stimulation may produce relaxation and salivation may be increased by parasympathetic excitation.

6. Acknowledgements

7. References

Ueda K. 2005. Sessyoku enge rehabilitation. In: Uematsu H, Inaba S, Watanabe M, editors. Koureishya Shika guidebook. Tokyo: Ishiyaku. pp 248–275 (in Japanese).

Hiraba H., M. Yamaoka, M. Fukano, K. Ueda and T. Fujiwara (2008) Increased secretion of salivary glands produced by facial vibrotactile stimulation. Somatosensory and Motor Research 25, 222–229.

Despopoulos, A. and Silbernagl, S (2003) 10 Nutrition and digestion. In: Color Atlas of Physiology. 5th ed. New York, Medical science international Ltd. pp 226–265.

Yamaoka, M., Hiraba, H., Ueda, K. and Fujiwara, T. (2007) Development of a vibrotactile stimulation apparatus for orofacial rehabilitation. *Nihondaigaku Shigakubu Kiyou* 35 , pp. 13–18. (in Japanese)

Burdette BH, Gale EN. (1988) The effects of treatment on masticatory muscle activity and mandibular posture in myofascial pain-dysfunction patients. J Dent Res 67; 1126–1130.

Vriama M, Vanharanta H.(1994) Bony vibrotactile stimulation: A new, non-invasive method for examining intradiscal pain. Eur Spine J 3; 233–235.

Desmedt JE, Codaux E. (1975) Vibration induced discharge patterns of single motor unit in the masseter muscle in man. J Physiol 253; 420–442.

Ivarsen S., Kupfermann F., Kandel ER. (2000a) 50, Emotional States and Feelings. In: Kandel ER., Schwartz JH., Jessell TM., editors, Principles of neuronal science, 4th ed, New York: McGraw-Hill. pp 982–997.

Sakatani K, Yamashita D, Yamanaka T (2006) Changes of cerebral blood oxygenation and optical path length during activation and deactivation in the prefrontal cortex measured by time-resolved near infrared spectroscopy. Life Sciences 78; 2734–2741.

Sakatani K, Lichty W, Xie Y (1999) Effects of aging on language-activated cerebral blood oxygenation changes of the left prefrontal cortex. Near infrared spectroscopy study. J Stroke Cerebrovascular Dis. 8; 398–403.

Hoshi Y, Kobayashi N, Tamura M. (2001) Interpretation of near-infrared spectroscopy signals: A study with a newly developed perfused rat brain model. J Appl Physiol. 90; 1657–1662.

Ivarsen S., Ivarsen L., Saper CB. (2000b) 49, The Autonomic Nervous System and the Hypothalamus. In: Kandel ER., Schwartz JH., Jessell TM., editors, Principles of neuronal science, 4th ed, New York: McGraw-Hill. pp 960–981.

Gardner EP, Martin JH. (2000c) 21, Coding of sensory information. In: Kandel ER., Schwartz JH., Jessell TM., editors, Principles of neuronal science, 4th ed, New York: McGraw-Hill. pp 411–429.

Chiang CY, Hu W and Sessle BJ (1994) Parabrachial area and nucleus raphe magnus-induced modulation of nociceptive and non-nociceptive trigeminal subnucleus caudalis neurons activated by cutaneous or deep inputs. J. Neurophysiol. 71, 2430–2445.

Petrides M (1994) Frontal lobes and working memory: evidence from investigations of the effects of cortical excisions in nonhuman primates. In: Handbook of Neuropsychology, Vol. 9, F. Boller and J. Grafman (eds.), Elsevier Science B.V., Amsterdam, pp. 50–82.

Yamamoto T, Takemura M, Inui T, Torii K, Maeda N, Ohmoto M, Matumoto I, Abe K. (2009) Functional organization of the rodent parabrachial nucleus. Ann N Y Acad Sci. 1170; 378–382.

Scott TR and Small DM (2009) The role of the parabrachial nucleus in taste processing and
        feeding. Ann N.Y. Acad Sci. 1170, 372–377.

Edited by Francisco Beltrán Carbajal

This book focuses on the important and diverse field of vibration analysis and control. It is written by experts from the international scientific community and covers a wide range of research topics related to design methodologies of passive, semi-active and active vibration control schemes, vehicle suspension systems, vibration control devices, fault detection, finite element analysis and other recent applications and studies of this fascinating field of vibration analysis and control. The book is addressed to researchers and practitioners of this field, as well as undergraduate and postgraduate students and other experts and newcomers seeking more information about the state of the art, challenging open problems, innovative solution proposals and new trends and developments in this area.

IntechOpen